

‘Shrink-Wrapping’ Nanoscale Objects

Patrick Louis Higgs



A thesis submitted for the degree of
Doctor of Philosophy in Chemistry

School of Natural and Environmental Sciences
Newcastle University

July 2020

Abstract of the Dissertation

'Shrink-Wrapping' Nanoscale Objects

Patrick Louis Higgs

This thesis describes the 'structural metamorphosis' of discrete single-chain polymer nanoparticles (SCPNS) – an architecture in which a linear polymer chain is intramolecularly crosslinked – into intermolecularly crosslinked polymer films. It was hypothesized that this process could be exploited for the 'shrink-wrapping' of 3D nanoscale objects, whereby SCPNs concentrate themselves onto the surface of the object through complementary non-covalent interactions and then spontaneously crosslink with their neighbouring polymer chains to afford a covalently crosslinked film. With the ambitious goal of 'shrink-wrapping' virus-like particles (VLPs) in mind, this thesis developed the concept by 'wrapping' nano- and microscale objects of increasing complexity. Chapter 1 proposes a definition for 'structural metamorphosis' and describes how this phenomenon could be exploited to drive 'shrink-wrapping' of virus-like particles. Chapter 2 explores the 'shrink-wrapping' of simian virus 40 and Model System I, where the 'wrapping' process is driven by simple electrostatic interactions. Chapter 3 describes Model System II, in which specific carbohydrate-receptor interactions drive the 'shrink-wrapping' of protein-functionalized silica micro- and nanoparticles. The success of these investigations is largely owed to the development of a highly hydrophilic aldehyde polymer scaffold that was constructed to circumnavigate issues of non-specific binding between polymers and the particle surface. Chapter 4 reports progress in the 'shrink-wrapping' of SV40 viral capsid, describing work towards the synthesis of SCPNs functionalized with the oligosaccharide GM1 – the native ligand of SV40. The 'shrink-wrapping' of sensitive biomacromolecular targets such as VLPs requires hydrazone exchange chemistry to operate on a reasonable timescale at physiological pH. Published work in Chapter 5 investigates rate-enhancing structural features which lead to rapid hydrazone exchange processes at neutral pH. These findings are anticipated to have important consequences on the development of structurally adaptive polymers, materials, molecular machines, nanoparticles and surfaces, where hydrazone exchange chemistry is commonly exploited to endow these systems with stimuli-responsive behaviour.

In dedication to Vera Merckel.

Acknowledgements

I would like to take this opportunity to thank all those who have contributed to the work described in this thesis. My thanks must firstly go to my PhD supervisor Dr David Fulton for his constant guidance, encouragement and unwavering enthusiasm, and most of all for providing a challenging but engaging research environment in which I learnt to become a tenacious and capable scientist. For this education and mentorship, I am truly grateful.

I have been fortunate to work alongside and collaborate with some extraordinarily talented and inspirational scientists during my time at Newcastle. I will be forever grateful to Dr Antonio Ruiz-Sanchez, Dr Clare Mahon, Dr Gema Dura, and Dr Osama El-Zubir who were so generous with their time and patience. I thank them all for their invaluable guidance and friendship. Thanks to all the friends I have met whilst working in the Chemical Nanoscience laboratory. Dr Chris McGurk, Dr Rachel Little, Dr Sam Lunn, Dr Tom Bamford, Cheney Leung, Pablo Rojas, it has been a great pleasure to work with you all.

Thanks to Michael Bracchi, Ben Jarman and Stuart Thompson for the evenings of music making in Newcastle and the great weekends away in Cumbria, which provided endless hours of entertainment when we needed it the most. Of course, thanks to Milene Dalmina, Liam Mistry and Jordan Appleton for your close friendships, and for many happy hours spent together in the lab.

Thank you to Prof Bruce Turnbull and his research group at the University of Leeds for providing samples of SV40 viral capsid which were utilized in Chapter 2. I have been fortunate to collaborate with Dr Andrew Leach at Manchester University, who I wish to thank for generously contributing his time and energy to the computational transition state modelling discussed in Chapter 5. My thanks must also go to Dr Benjamin Horrocks for his invaluable guidance on the fitting of kinetics data. It has been a pleasure to consult with such a knowledgeable, patient, and approachable physical chemist.

My deepest and most heartfelt thanks must go to my partner Laura for her support and encouragement, and for making the years that much more enjoyable! Thanks to my parents Tom and Jacqui, my siblings Tess and Ed, and to Laura's family Tom, Stella, and Hannah Kerigan. You all found your own way to help over the years, for which I am very grateful.

Lastly, I want to acknowledge the teachers who played an important role during my education: Dianna Green, Kevin Gough, Christine Smallwood, Rachel Steels, Michelle Thwaites, and Robin Young. Thank you, I certainly would not have made it this far without your kind words of encouragement that improved my sense of self-belief and pushed me to further my education.

Table of Contents

Chapter 1	1
'Structural Metamorphosis' in Chemistry	
Chapter 2	33
'Shrink-Wrapping' Through Complementary Electrostatic Interactions	
Chapter 3	90
'Shrink-Wrapping' Through Specific Ligand-Receptor Interactions	
Chapter 4	144
Progress Towards the 'Shrink-Wrapping' of SV40 Viral Capsid	
Chapter 5	175
Enhancing the Kinetics of Hydrazone Exchange Processes at Neutral pH	
Research Outlook	210
Manuscript A	216
Molecular Recognition-Mediated 'Wrapping' of Micron-Sized Spherical Objects	

Abbreviations

µg	Micrograms
µL	Microlitre
AFM	Atomic Force Microscopy
AIBN	2,2'-Azobis(2-methylpropionitrile)
Boc	<i>tert</i> -Butyloxycarbonyl protecting group
BSA	Bovine serum albumin
Con A	Concanavalin A
cNPs	Carboxylate-functionalized polystyrene nanoparticles
CTA	Chain transfer agent
DA	Diels Alder
Da	Dalton
DCB	Dynamic covalent bond
DCC	Dynamic combinatorial chemistry
DDMAT	S-1-Dodecyl-S'-(α,α'-dimethyl-α"-acetic acid)trithiocarbonate
DI	Deionized
D_h	Hydrodynamic diameter
DLS	Dynamic light scattering
DMA	<i>N,N</i> -Dimethylacrylamide
DMAP	4-(Dimethylamino)pyridine
DMF	Dimethylformamide
DMSO	Dimethylsulfoxide
dRI	Differential refractive index
<i>E. coli</i>	Escherichia coli
EDC	1-Ethyl-3-(3-dimethylaminopropyl)carbodiimide
ELISA	Enzyme-linked immunosorbent assay
ESI-MS	Electrospray ionisation mass spectrometry
FT-IR	Fourier transform infrared spectroscopy
GPC	Gel permeation chromatography
h	Hour
HEPES	4-(2-Hydroxyethyl)piperazine-1-ethanesulphonic acid
HRMS	High resolution mass spectrometry
IEP	Isoelectric point
K_a	Association constant
K_d	Dissociation constant
k_f	Forward rate constant
k_r	Backward rate constant

LTB	<i>E. coli</i> heat labile toxin
MeOH	Methanol
mg	Milligram
min	Minute
MGV	Mean grey value
MHz	Megahertz
mL	Millilitre
mM	Millimolar
<i>M_n</i>	Number average molecular weight
<i>M_w</i>	Weight average molecular weight
MW	Molecular weight
MWCO	Molecular weight cut-off
NH ₄ OAc	Ammonium acetate
NMR	Nuclear magnetic resonance
NPs	Nanoparticles
PD	Polymer dose
PDI	Polydispersity index
PE	Polyelectrolyte
PEG	Poly(ethylene) glycol
ppm	Parts per million
PS	Polystyrene
RAFT	Reversible addition-fragmentation chain transfer
rt	Room temperature
RT	Retention time (GPC analysis)
SCPNs	Single chain polymer nanoparticles
SDS-PAGE	Sodium dodecyl sulfate-polyacrylamide gel electrophoresis
sNPs	Sulfonate-functionalized polystyrene nanoparticles
TEM	Transmission electron microscopy
TFA	Trifluoroacetic acid
TR-DLS	Time-resolved dynamic light scattering
TS	Transition state
UV	Ultraviolet
UV-Vis	Ultraviolet-visible
ZP	Zeta potential

Chapter 1

‘Structural Metamorphosis’ in Chemistry

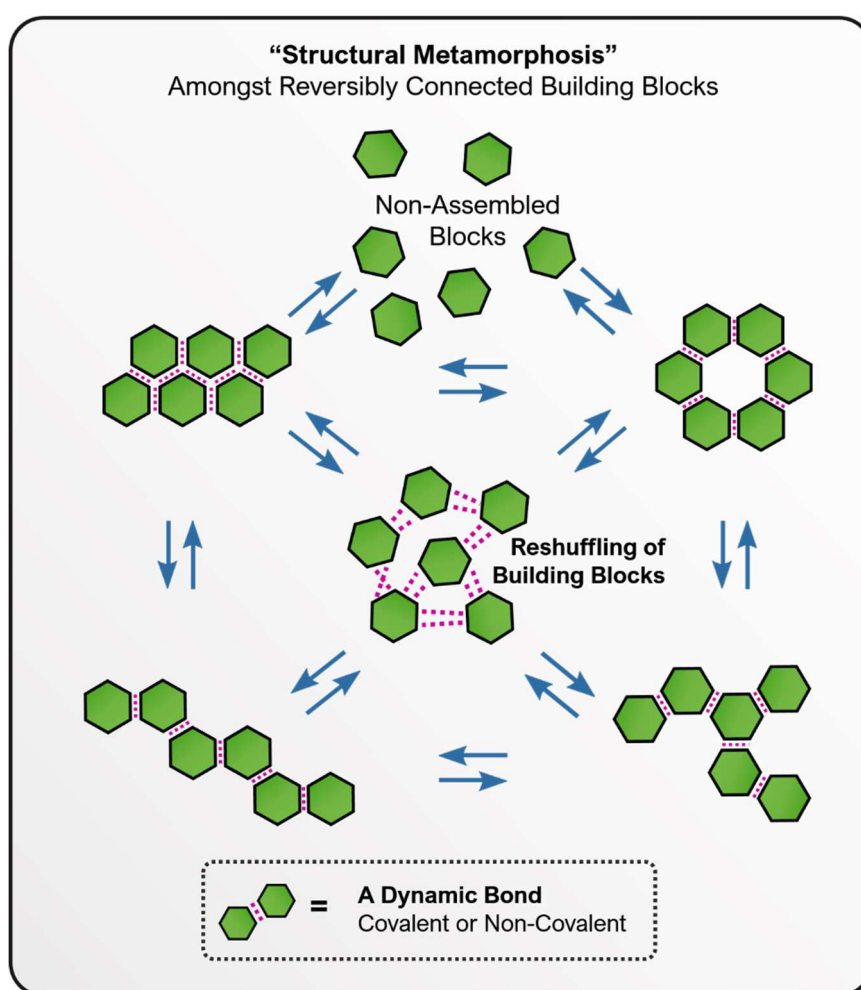


Table of Contents

1.1. Abstract	3
1.2. Introduction	4
1.2.1. What is 'Structural Metamorphosis'?	5
1.2.2. A Supramolecular Example of 'Structural Metamorphosis'	6
1.2.3. A Dynamic Covalent Example of 'Structural Metamorphosis'	7
1.2.4. Towards 'Structural Metamorphosis' within a Polymeric System	9
1.2.5. 'Structural Metamorphosis' of Polymeric Nanoparticles	11
1.2.6. Component Exchange of Hydrazone Crosslinks	12
1.2.7. Thermally Induced 'Metamorphosis' of Polymeric Nanoparticles	13
1.2.8. 'Shrink-Wrapping' of 2D Surfaces Displaying Carbohydrate Receptors	17
1.2.9. 'Shrink-Wrapping' of Viruses and Virus-Like Particles	20
1.2.10. Inspiration for the 'Encapsulation' of Viral Targets	21
1.2.11. Catching a Virus in a Molecular Net	25
1.3. Conclusion	27
1.4. Proposed Approach	28
1.5. References	29

1.1. Abstract

This chapter explores the concept of 'structural metamorphosis' by structurally dynamic chemical architectures. Based upon literature examples which showcase this phenomenon at play within chemical systems, the process of 'structural metamorphosis' was considered and a definition proposed. Literature examples were examined against the proposed definition of 'structural metamorphosis' to verify that it is robust and can be applied consistently. The 'structural metamorphosis' of structurally dynamic polymeric nanoparticles into intermolecularly crosslinked polymer films was considered in detail. A strategy to exploit this process for the 'shrink-wrapping' of virus-like particles was discussed and its potential applications proposed.

1.2. Introduction

Examples of metamorphosis are ubiquitous and displayed on many levels within the natural world: The biological transformation of *Danaus plexippus*, Monarch butterfly larvae (Fig. 1a) into their mature adult form,¹ the pH-responsive conformational switch of ‘inactive’ dengue virus (Fig. 1b)² into its pathogenically active form, or the ‘structural metamorphosis’ of the biofilm-surface layer protein A (**BsIA**)³ (Fig. 1c) into a crosslinked hydrophobic film upon a droplet surface.⁴ Imperatively, structure gives rise to properties in the natural world. Thus, metamorphosis is invoked by an abrupt transformation of bonding (connectivity of components) at the molecular level – a process that is often accompanied by a marked change in function at a macroscopic level. The monarch butterfly is, for example, capable of flight and yet the larvae are not. Whilst intriguing to a broad scientific community, these processes of transformation have seldom been explored within chemical systems, with chemists to date reporting just a handful of examples in which ‘structural metamorphosis’ was investigated at the molecular and/or supramolecular levels. This chapter will firstly define what is ‘structural metamorphosis’ and then interrogate this definition by review of select literature examples which exemplify this phenomenon at play within chemical systems.

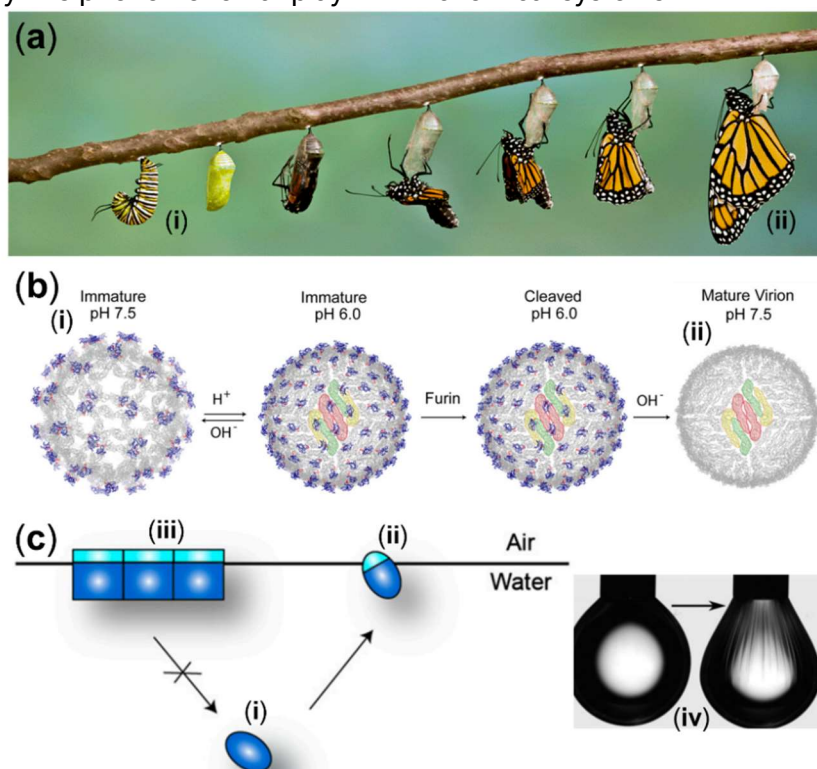


Figure 1: Three examples of metamorphosis from the natural world. (a) Biological metamorphosis of the monarch butterfly, *Danaus plexippus* from its larva (i) to the mature adult form (ii).¹ Image by Steve Greer Photography, copyright 2020. (b) Conformational ‘metamorphosis’ of **dengue virus** from its ‘inactive’ conformer (i) to the pathogenically active (ii) species is triggered by acidifying the virus to lysosomal conditions, pH ~ 4.5.² Reproduced with permission of ref. 2. (c) ‘Structural metamorphosis’ of the bacterial hydrophobin **BsIA**, a ‘coat’ protein crucial to biofilm formation. Wild-type **BsIA** (i) migrates to the water/air interface and the protein spontaneously undergoes a conformational ‘switch’ (ii), which drives the irreversible formation of a polymer-like ‘crosslinked’ protein film (iii) upon the droplet surface.^{3,4} Droplet compression experiments (iv) revealed that **BsIA** films are elastic in nature, encapsulating the water droplet within a plastic-like layer. Reproduced with permission of ref. 3.

1.2.1. What is ‘Structural Metamorphosis’?

Metamorphosis is defined⁵ as the process of changing shape, structure, or form. In the highlighted examples (Fig. 1a-c) of metamorphosis, these transformations are all triggered by a change in their external environments. Note that in each case, however, all the necessary components required to successfully undergo ‘metamorphosis’ are already present within the system, with no need for the input of additional external materials. ‘Structural metamorphosis’ is defined in this thesis as a transition between two discrete architectures, where components are neither added nor taken away, but the interconnectivity (bonding) of building blocks is changed (Fig. 2) at the molecular and/or supramolecular level, facilitating a switch from one architecture to another. The ‘reshuffling’ of molecular components which occurs during ‘structural metamorphosis’ requires a dynamic nature to the bonds that connect the building blocks within the system. A dynamic bond is defined⁶ as any class of chemical bond that can selectively undergo reversible breaking and reformation, usually under equilibrium conditions. These dynamic bonds can be either covalent or non-covalent in their nature, but crucially, it is the ability of these interactions to reversibly break and reform that allows for components to change their interconnectivities and for ‘structural metamorphosis’ to subsequently occur. There is no requirement within the definition proposed above for ‘structural metamorphosis’ to be a reversible or irreversible process.

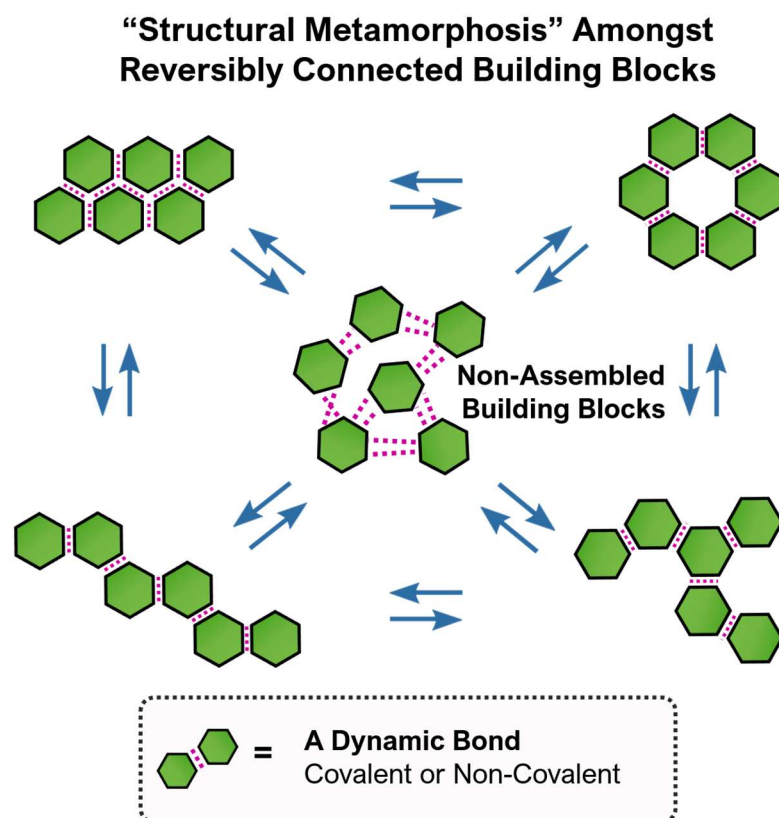


Figure 2: ‘Structural metamorphosis’ amongst reversibly connected building blocks permits a range of molecular architectures to be accessed. The ‘structurally adaptive’ nature of such species requires a dynamic bond between the assembled components.

1.2.2. A Supramolecular Example of ‘Structural Metamorphosis’

In 2016 Kumar *et al.* reported⁷ the ‘structural metamorphosis’ of **PDDA/FMOC-AA** coacervate droplets (Fig. 3a i) into branched star-like architectures (ii) displaying long outward-reaching appendages (Fig. 3c v). This pH-triggered ‘metamorphosis’ of coacervate droplets, was triggered by the addition of D-glucono- δ -lactone lactone (**GDL**), the hydrolysis (Fig. 3b) of which acidifies the solution, affording the protonation of carboxylate groups within **FMOC-AA**. When protonated, the **FMOC-AA** embedded within the **PDDA/FMOC-AA** coacervate rapidly aggregates to form long fibres (Fig. 3c ii), which entangle to form a weak hydrogel (Fig. 3c iii). Figure 3c shows confocal fluorescence microscope images of the coacervate droplet before (iii) and 10 min after (iv) the addition of **GDL**. Further experiments revealed that addition of 10 mM sodium hydroxide affords rapid collapse (Fig. 3c vi) of the star-like architecture back to its coacervate core (vi, 40s), thus demonstrating the pH-responsive nature of these delicate architectures.

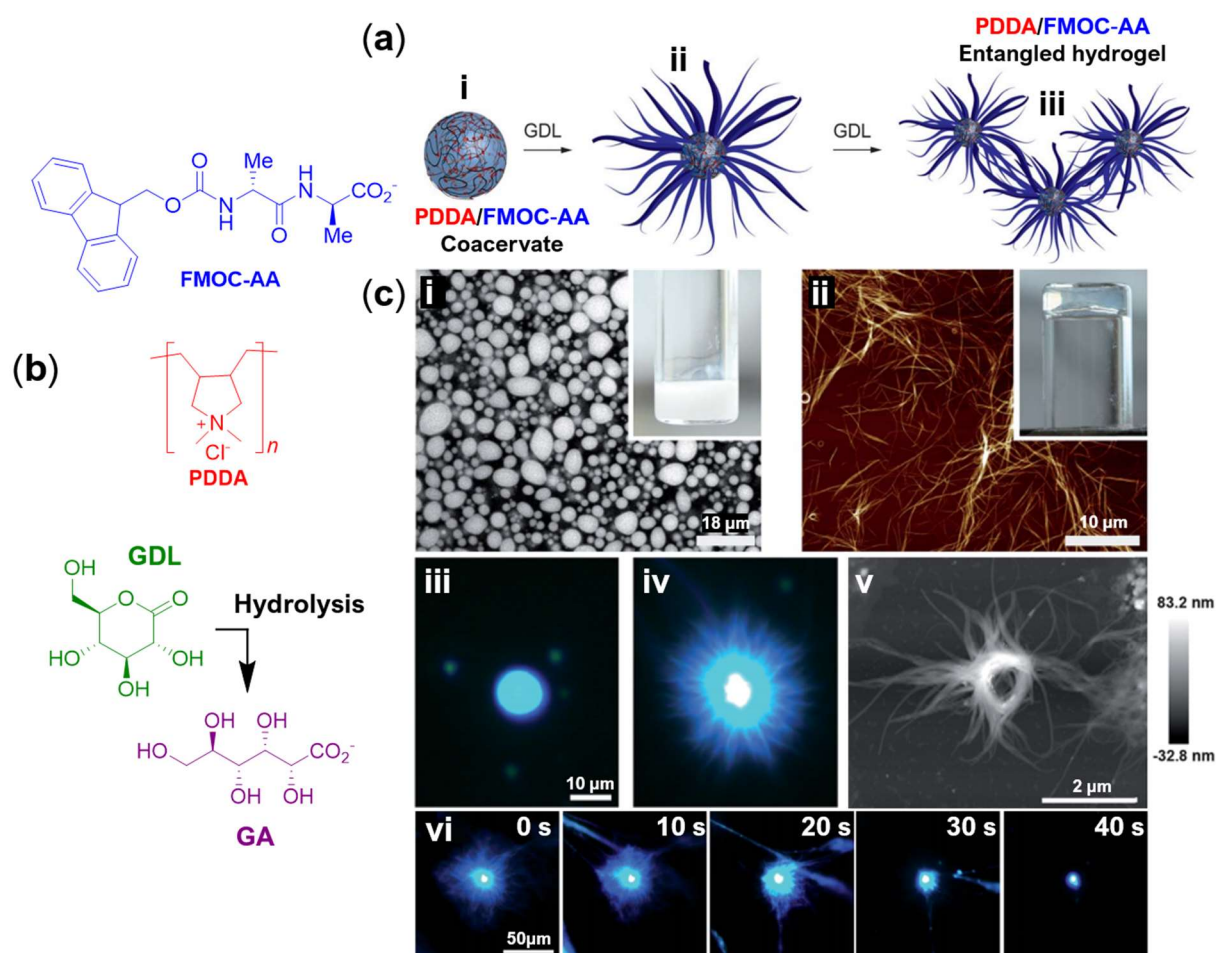


Figure 3: (a) ‘Structural metamorphosis’ of an **PDDA/FMOC-AA** coacervate droplet (i) into a branched star-like architecture (ii) upon addition of **GDL**. The entanglement the outward-reaching arm-like appendages affords the formation of hydrogel (iii). (b) Chemical structures of **FMOC-AA**, **PDDA**, **GDL** and **GA**. (c) Confocal fluorescence microscope (i, iii, iv, vi) and AFM micrographs (ii, v) characterizing the transition of **PDDA/FMOC-AA** coacervate droplets into branched star-like architecture. Fluorescence microscope images of **PDDA/FMOC-AA** coacervate before (iii) and after (iv) addition of **GDL**. (vi) A series of time-resolved fluorescence microscope images monitoring the rapid collapse of star-like architecture induced by the addition of sodium hydroxide. Reproduced with permission from ref. 7, copyright of Royal Society of Chemistry 2016.

This study demonstrates that rudimentary aspects of ‘structural metamorphosis’ can be integrated into these coacervate-based ‘protocells’, by incorporation of a pH-responsive **FMOC-AA** dipeptide building block. The ‘metamorphosis’ of coacervate droplets (Fig. 3c i, iii) into distinct star-like architectures (Fig. 3c ii, iv-v) was shown to be a quasi-reversible process. It was not, however, possible to continuously cycle between coacervate (Fig. 3a i) and star-like assembly (Fig. 3a ii). If repeated, the outward growth (Fig. 3c iii-iv) and subsequent pH-triggered collapse (Fig. 3c vi) of the arm-like tendrils would result in the depletion of **PDDA/FMOC-AA** material from the coacervate core, thus precluding an entirely reversible ‘metamorphosis’ between coacervate (Fig. 3a i) and star-like architectures (Fig. 3a ii). Nevertheless, this study is an excellent example of ‘structural metamorphosis’, where the transformation is triggered by adjusting protonation state of the pH-responsive building block **FMOC-AA**. This example clearly fits the above definition of structural metamorphosis, as the system traverses between two well-defined architectures (Fig. 3a), from the coacervate droplet (i) to the star-like structure (ii) without requiring the addition of further components.

1.2.3. A Dynamic Covalent Example of ‘Structural Metamorphosis’

Research from the laboratory of Sijbren Otto has demonstrated⁸ that shaking a dynamic combinatorial library (DCL) (Fig. 4a-b) made from thiol building block **1** gives rise to ‘stacks’ of disulfide macrocycles **1₆** (c) which were covalently captured by photoirradiation at 365 nm to produce polymers of **1** (d). Elongation of macrocycles **1₆** into fibres/polymers (c) was shown to be a mechanosensitive process,⁹ driven by the formation of weak β -sheet interactions between short peptide sidechains (b) located upon building block **1**. Fibre growth occurs spontaneously in aqueous solution. However, in the absence of mechanical agitation the DCL composition is dominated by macrocycles which do not aggregate into polymers; thus, fibre growth is slow and cannot reach completion. Shaking the DCL by was shown favour the formation of hexamer (**1₆**) fibres, which elongate *via* a chain-growth polymerization process. Shaking breaks the growing fibres into fragments, a process which produces new growing ends and accelerates the formation of hexamer fibres.⁹ Fibre growth thus drives the amplification of macrocycle **1₆** at the expense of the other library members, which leads to the complete consumption of thiol **1** *via* re-equilibration of the DCL. Hexamer fibre growth was monitored by cryo-TEM (g) and SDS-PAGE (f), revealing that the emergence of polymers of **1₆** correlated with a change in the bulk material properties, observed as a distinct sol-to-gel transition (e). In this elegantly designed system, the ‘structural metamorphosis’ of thiol **1** (e) into long fibres (d) relies upon a union of weak supramolecular (β -sheet) interactions and stable dynamic covalent (disulfide) bonds, between which a powerful synergy exists. In the absence of either of these interactions, macrocycles would not form, thus ‘structural metamorphosis’ would not be observed.

This system crucially achieves ‘structural metamorphosis’ by exploiting two key phenomena in unison: (i) Concentration (**b-c**) of molecular building blocks (stacking of macrocycles) through non-covalent interactions, followed by (ii) covalent crosslinking (**c-d**) of the stacked macrocycle building blocks. Importantly, note that stacked macrocycle oligomers (**c**) contain intramolecular disulfide bonds, whereas after covalent ‘trapping’ by irradiation with UV light (**d**) these oligomers become intermolecularly crosslinked, with disulfide bonds running between neighbouring macrocycles in the oligomer assembly. Covalent ‘trapping’ of intramolecularly crosslinked macrocycles (**c**) into intermolecularly crosslinked (**d**) polymers of thiol building block **1** was thus of crucial importance in obtaining mechanically stable oligomer species. These features are also shared by the polymer-based ‘structural metamorphosis’ observed by the Fulton research group, which will be later discussed on pages 11 – 19.

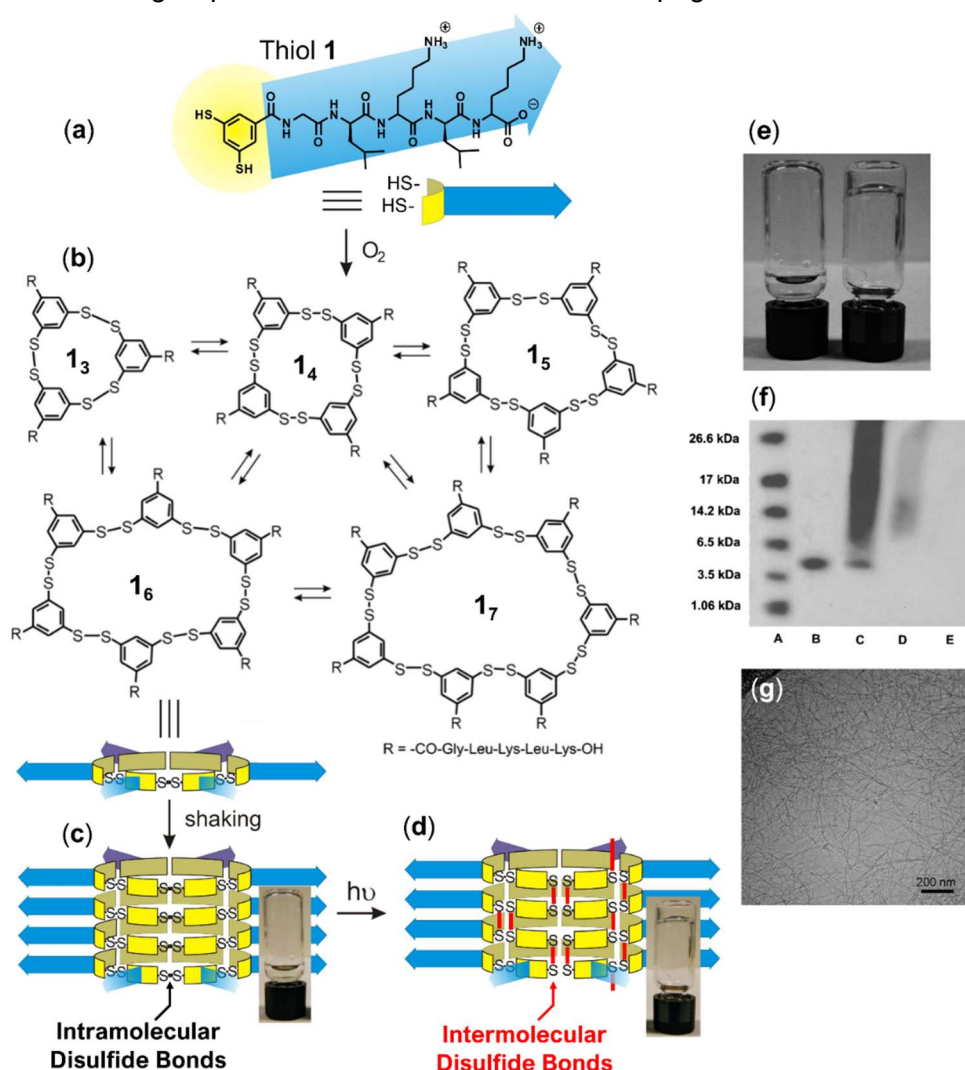


Figure 4: Shaking the dynamic combinatorial library (**b**) made from dithiol building block **1** (**a**) in aqueous borate buffer (50 mM, pH 8.1) gives rise to stacks of disulfide macrocycles **16** (**c**), which are covalently captured upon photoirradiation (365 nm) to produce polymers of **1** (**d**). Photographs (**e**) of samples containing predominantly **16** prior to (left) and after (right) 3 days of photoirradiation. (**f**) SDS-PAGE analysis of sample of **16** prior to photoirradiation (lane B) and after 1 day (lane C), 2 days (lane D) and 3 days (lane E). Lane A shows the standard molecular weight ladder. (**g**) Cryo-TEM image of a sample containing predominantly **16** after 3 days photoirradiation. Reproduced with permission from ref. 8, copyright of Wiley publishing 2011.

1.2.4. Towards ‘Structural Metamorphosis’ within a Polymeric System

Brent Sumerlin and co-workers first coined the term ‘macromolecular metamorphosis’ in 2017, describing¹⁰ an intriguing system in which structurally dynamic polymeric building blocks (Fig. 5a-b) undergo structural reconfiguration through Diels-Alder (DA) type diene displacement reactions (Fig. 5, i-v). These reactions facilitate the interconversion of macromolecular building blocks between an array of structurally diverse polymer architectures (a-g), in a process which is termed ‘macroscopic metamorphosis’. This study exploits a well-established difference in the thermodynamic stabilities of diene/dienophile [4+2] cycloaddition adducts¹¹ (Fig. 5, X-Y) to induce transformations in the interconnectivity of polymeric building blocks. Anthracene-maleimide (**Anth-Mal**) DA cycloaddition adducts (**Y**) are much more thermodynamically stable than the analogous furan-maleimide (**Fur-Mal**) adducts (**X**), thus formation of stable **Anth-Mal** adducts provides the driving force for ‘macroscopic metamorphosis’ of polymeric building blocks. Addition of anthracene-functionalized polymer building blocks (i-iii) with a range of topologies was thus envisaged to induce structural transformation of the amphiphilic block copolymer precursor (a) into comb polymer (c), hydrophobic block copolymer (d) or star polymer (e) architectures. Similarly, segmented hyperbranched polymer (b) was transformed into architectures (f) and (g) by addition of the appropriate anthracene-functionalized polymers (iv-v).

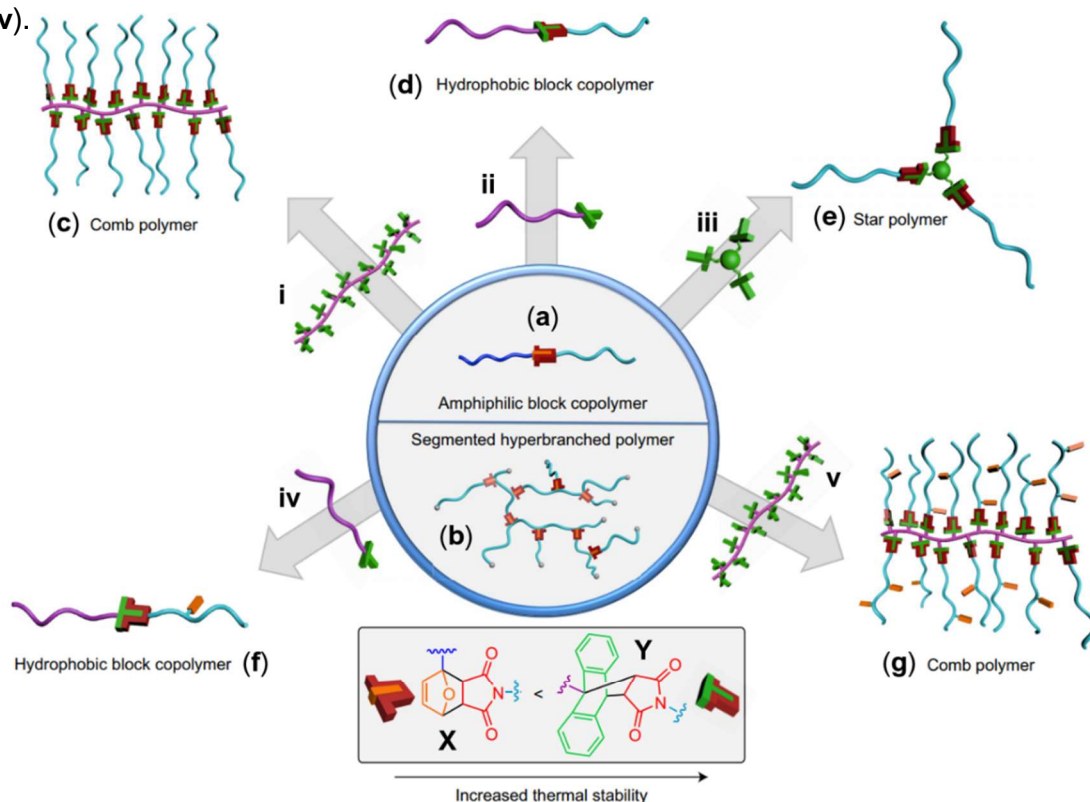


Figure 5: Structurally dynamic polymers (a) and (b) can undergo ‘macroscopic metamorphosis’ through diene displacement reactions (i-v), permitting their transformation between a structurally diverse array of different polymer architectures (a-g): Amphiphilic block copolymer (a), segmented hyperbranched polymer (b), comb polymer (c, g), hydrophobic block polymer (d, f) and star polymer (e). Process of ‘macroscopic metamorphosis’ are driven by the difference in thermodynamic stability of DA adducts X and Y. Reproduced with permission from ref. 10, copyright of Nature Chemistry 2017.

Diels-Alder adducts can be considered as a dynamic covalent bonds (DCBs),¹² thus and have been utilized to construct recyclable networks,¹³ self-healing materials¹⁴ and complex polymer architectures.¹⁵ However, the conditions for formation and cleavage of this 'reversible' linkage are harsh, with temperatures in excess of 100 °C typically required. Whilst the disassembly of architectures **c-g** should in principle be possible by inducing the retro-DA reaction to disconnect the polymer building blocks at very high temperatures, or under mechanochemical stress, this reaction was reported to be essentially irreversible on account of the highly stable anthracene-maleimide linkage (**Y**). The 'macroscopic metamorphoses' presented in Figure. 5 are therefore essentially irreversible processes, with no scope to traverse back and forth between the various polymer architectures (**a-g**). Whilst reversibility is not a specific requirement for 'metamorphosis' (as defined in this thesis), the potential applications of this work are restricted by the irreversible nature of the DA chemistry employed, which precludes the macroscopic building blocks from being 're-processed' into an array of polymer architectures (**a-g**). Redesigning the existing system such that the building blocks are instead connected by dynamic bonds – which can be readily broken or exchanged under ambient conditions – would thus address this deficiency. Utilization of dynamic covalent imine, acyl hydrazone or oxime bonds, for example, would permit scope for further modification to the polymer morphologies by component exchange processes. Moreover, the hydrolysis of acyl hydrazone or imine bonds – a processes which is readily achieved under acidic conditions – would permit the disassembly of polymer architectures, such that the constituent building blocks can be recovered and possibly recycled.

Whilst Summerlin *et al.* demonstrated an impressive level of control over the connectivity of macroscopic building blocks, the observed changes in polymer topology are not strictly an example of 'structural metamorphosis' as defined in this thesis, which demands that all components necessary for 'metamorphosis' are incorporated within the system prior to the transformation. The work reported by Summerlin *et al.* required the addition of external anthracene-functionalized polymer components to induce changes in polymer architecture, and thus should be considered as a synthetic modification of the existing polymer structure, rather than a 'metamorphosis'. A more elegant system design might be envisaged by incorporating all the key components for 'metamorphosis' within the polymer scaffolds. In this regard, the Fulton research group have recently reported several examples of 'structural metamorphosis' in polymeric systems that are entirely consistent with this approach, which will now be discussed.

1.2.5. 'Structural Metamorphosis' of Polymeric Nanoparticles

The transformation of discrete polymeric nanoparticles (Fig. 6, **a**) into covalently crosslinked polymer films (**b**) was first reported¹⁶ by Murray *et al.*, a process that can be considered as a 'structural metamorphosis'. In dilute aqueous solution (**a**) the single-chain polymer nanoparticles (**SCPNs**) feature intramolecular crosslinks (**red**) which are dynamic covalent acyl hydrazone linkages (**c**). The concentration of **SCPNs** (**i**) drives their 'structural metamorphosis' into a covalently interlocked polymer film (**b**) in which adjacent chains are now intermolecularly crosslinked (**purple**) with one another. Thus, the 'structural metamorphosis' of **SCPNs** (**a**) into an intermolecularly crosslinked polymer film (**b**) is a concentration-crosslinking phenomenon which in this example, was driven simply by the evaporation of solvent. It has, however, also been demonstrated that other strategies for concentrating the dynamic covalent **SCPNs**, such as weak non-covalent interactions between the polymer chains and a complementary surface can be utilized to drive the formation of intermolecularly crosslinked polymer films.

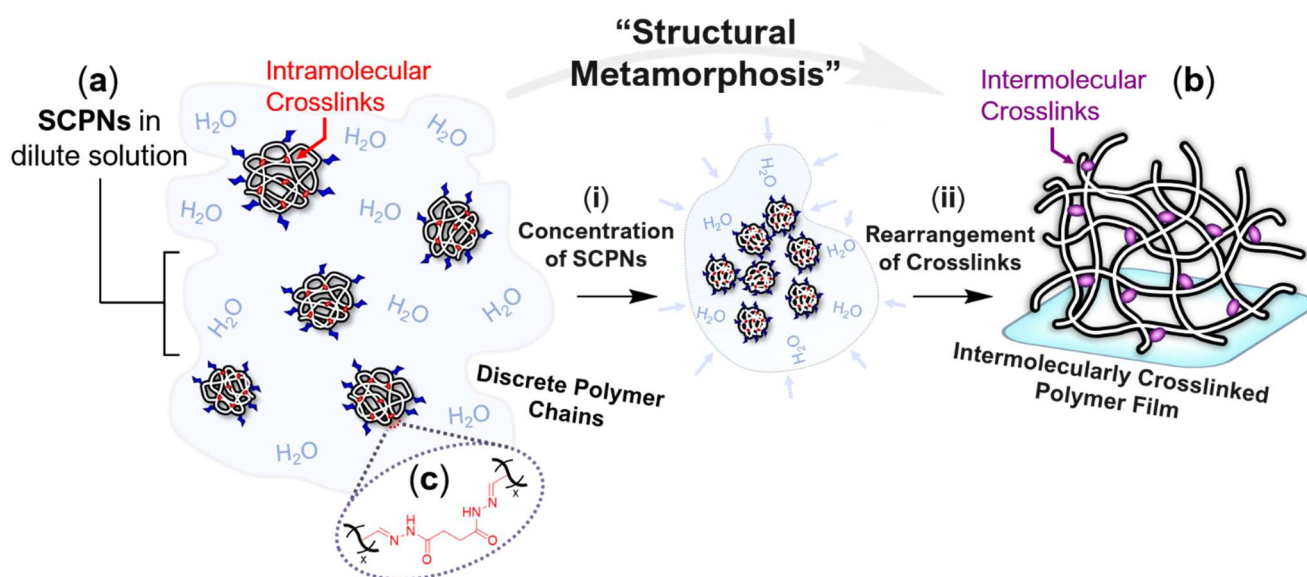


Figure 6: The transformation of discrete polymeric nanoparticles (**a**) into a covalently crosslinked polymer film (**b**) can be considered as a 'structural metamorphosis'. The intramolecular crosslinks (**red**) embedded within single chain polymer nanoparticles (**SCPNs**) (**a**) are dynamic covalent hydrazone linkages (**c**). Concentration (**i**) of these **SCPNs** from dilute aqueous solution, drives the structural rearrangement of crosslinks (**ii**) which in turn leads to the formation of polymer films (**b**) featuring intermolecular crosslinks (**purple**) between neighbouring polymer chains.

1.2.6. Component Exchange of Hydrazone Crosslinks

In the above example, ‘structural metamorphosis’ of **SCPNs** depends crucially upon the dynamic nature of the acyl hydrazone linkages embedded within the polymer chains to facilitate the transition from intra- to intermolecularly crosslinked polymer architectures. Crucially, acyl hydrazone bonds undergo component exchange processes (Fig. 7a) which facilitate the ‘structural metamorphosis’ of crosslinker residues embedded within the polymer chains. Although any dynamic covalent bond could, in principle, have been utilized to facilitate ‘structural metamorphosis’, the venerable acyl hydrazone linkage was employed on account of its proven track record of reliably facilitating component exchange reactions.^{12a} Figure 7b illustrates the hydrazone exchange process, within the context of a hypothetical crosslinked polymer system, whereby the reaction of **Chain A** with **Chain B** leads to the formation of an intermolecularly crosslinked polymer aggregate, **Complex A/B**. Continuation of this exchange process leads to the formation of an intermolecularly crosslinked polymer film, in which each polymer chain is covalently linked to its neighbours.

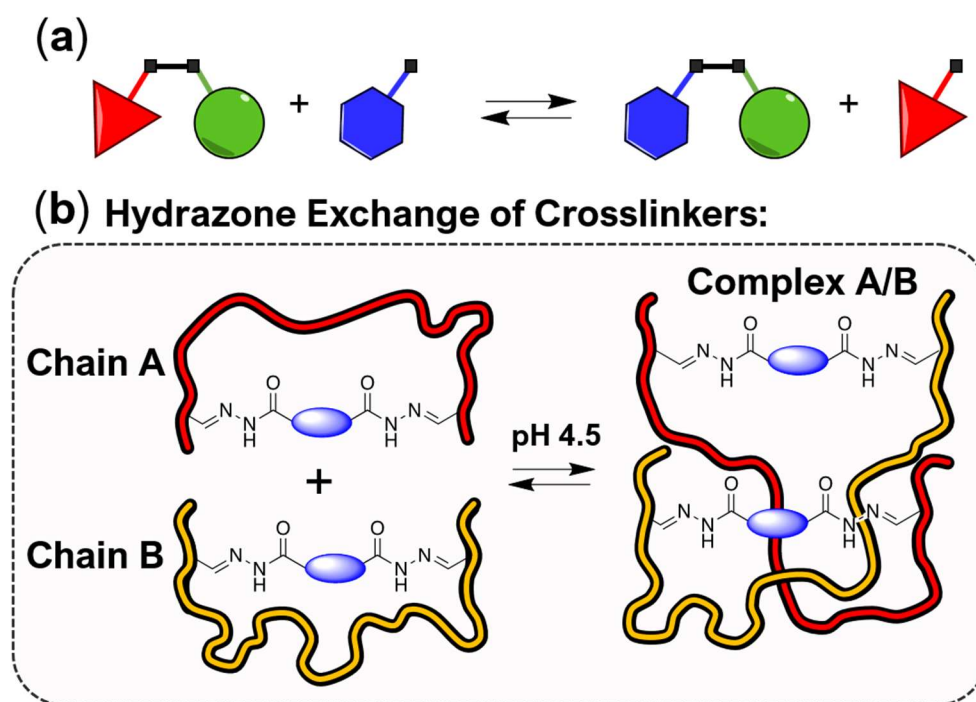


Figure 7: The process of ‘structural metamorphosis’ relies upon the component exchange of acyl hydrazone crosslinks, a reaction which displays optimal kinetics at pH 4.5. (a) A component exchange reaction in which one reaction partner (**blue hexagon**) displaces another (**red triangle**) to afford a new product species. These reactions are often entirely reversible and at equilibrium are governed by the relative thermodynamic stabilities of the products. (b) **Chain A** and **Chain B** – each contain a single intramolecular crosslink, however hydrazone exchange facilitates the formation of intermolecularly crosslinked species, such as the **Complex A/B**.

Single-Chain Polymer Nanoparticles

Single-chain polymer nanoparticles (**SCPNS**) (Fig. 8) are intriguing, bioinspired architectures that result from the ‘collapse’ or folding of an individual polymer chain by intramolecular crosslinking into a globular nanometer-sized particle. Nature presents a great source of inspiration for such architectures that aim to mimic the structural complexity as well as the functionality of the tertiary structure of proteins. Since their inception in 2002,¹⁷ **SCPNS** have been fabricated with a myriad of intramolecular crosslinking chemistries, including covalent,¹⁸ dynamic covalent¹⁹ metal-ligand coordination²⁰ and supramolecular interactions.²¹ Recent publications highlight that **SCPNS** show great promise in catalysis,²² drug-delivery systems,²³ chemical sensors,²⁴ enzyme mimics,²⁵ fluorescence probes²⁶ light-harvesting²⁷ and contrast imaging agents.²⁸

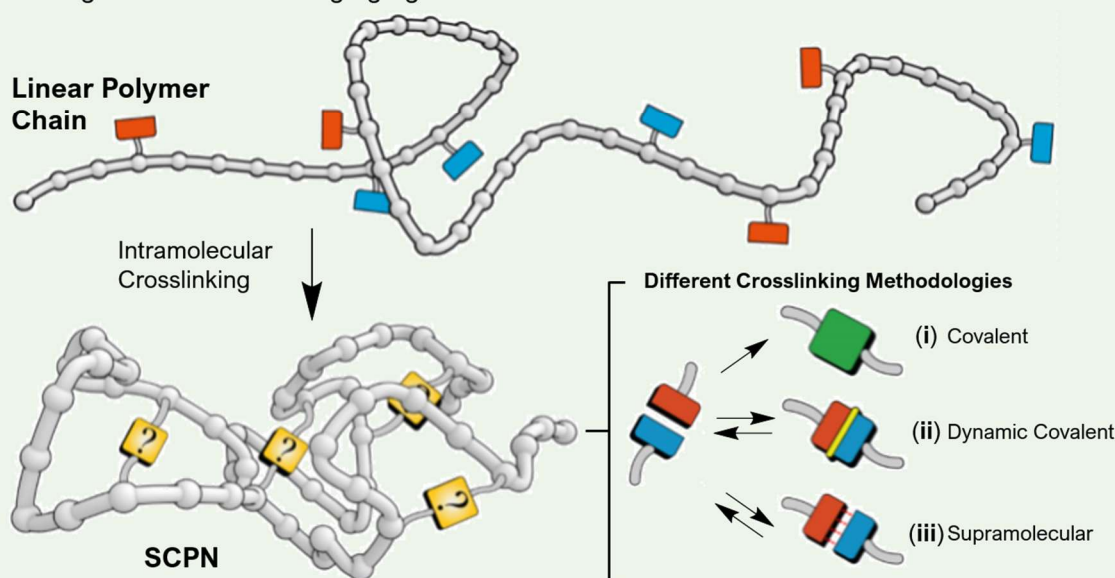


Figure 8: Collapse of an individual polymer chain into a single-chain polymer nanoparticle (**SCPNS**) via various intramolecular crosslinking chemistries: (i) Covalent, (ii) dynamic covalent or (iii) supramolecular interactions. Reproduced with permission from ref. 29, copyright of the Chinese Chemical Society 2019.

1.2.7. Thermally Induced ‘Metamorphosis’ of Polymeric Nanoparticles

To explore further the concept of ‘structural metamorphosis’ within polymeric systems, Whitaker *et al.* fabricated a novel class of ‘structurally-dynamic’ polymer nanoparticles (**NP1-NP4**) (Fig. 9b) which exhibited reversible sol-to-gel transitions (Fig. 9b-c) triggered by adjusting their temperature in aqueous solutions.^{30a} The single-chain polymer nanoparticles (**NP1-NP4**) were prepared (Fig. 9a-b) by addition of crosslinker (**SD**) (i) to linear copolymer scaffolds (**P1-P4**) at pH 4.5, thus yielding **SCPNS** (**NP1-NP4**) which feature intramolecular dynamic covalent acyl hydrazone linkages. The **SCPNS** (**NP1-NP4**) were thermo-responsive in nature, and when heated above their lower critical solution temperatures (LCSTs), they precipitated from aqueous solution (Fig. 9d).

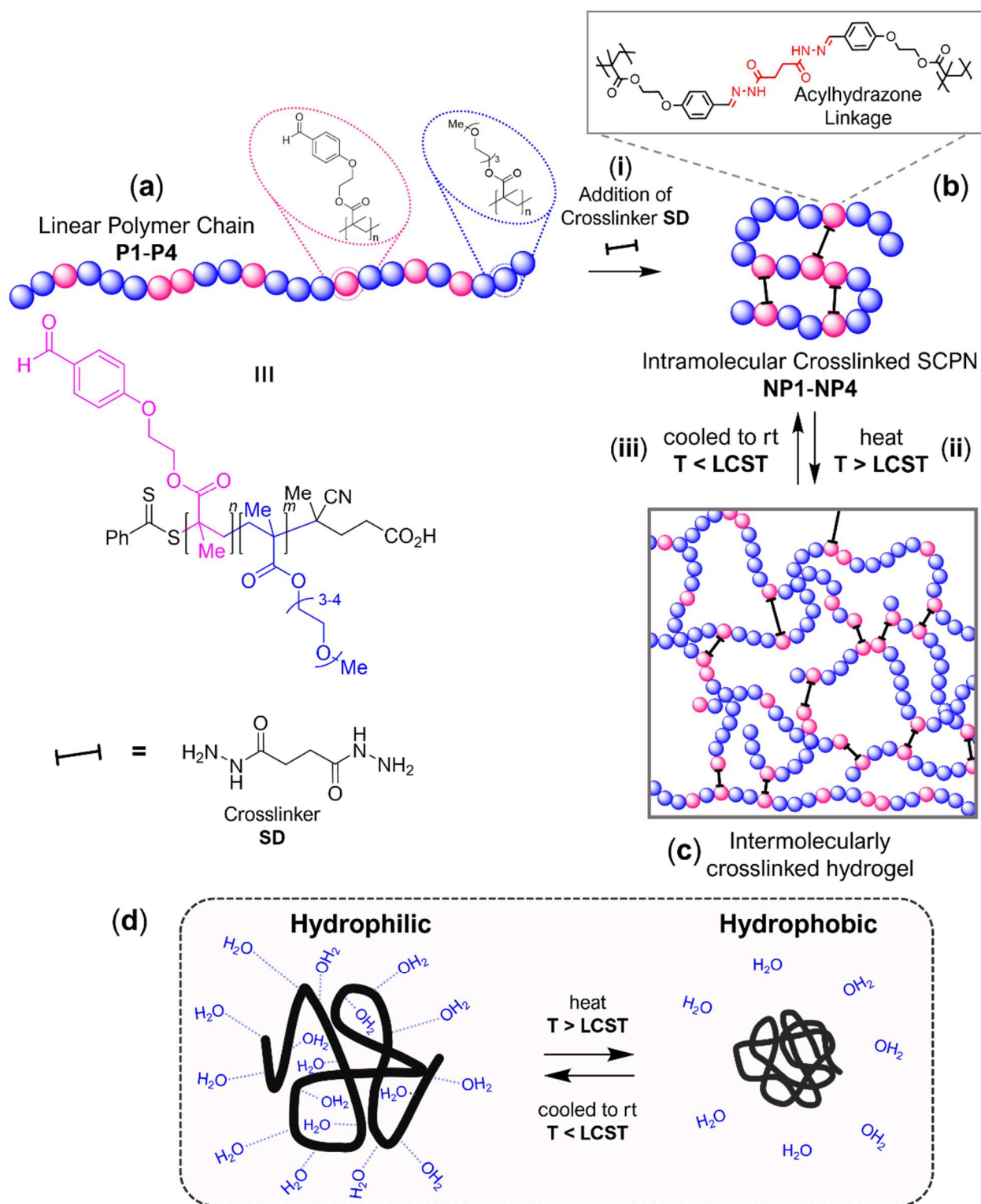


Figure 9: Thermally induced ‘structural metamorphosis’ of single-chain polymer nanoparticles (SCPNS) into an intermolecularly crosslinked hydrogel network. (a) Conjugation of polymer chains **P1** – **P4** with crosslinker **SD** to form intramolecularly crosslinked **SCPNS** (**NP1** – **NP4**) (b) and their subsequent reversible transformation into an intermolecularly crosslinked hydrogel (c). (d) In aqueous solution thermo-responsive polymers precipitate at temperatures above their LCST.

In this example, the ‘structural metamorphosis’ of **SCPNS** (**NP1** – **NP4**) into a crosslinked hydrogel network was triggered by raising the temperature of the nanoparticle solutions above

their LCST* (Fig. 9d) at pH 4.5. As anticipated, heating **SCP**Ns above their LCST afforded a white precipitate and after 5 min an opaque solid material formed. Vial inversion tests indicated that this material possessed hydrogel-like characteristics, which suggests the reorganisation of the polymer chains within the nanoparticles from intra- to intermolecularly crosslinked architectures. **SCP**Ns are stable for > 24 h in aqueous solution, however beyond this timescale evidence of aggregation was observed. Two distinct arguments can be made to rationalize the observed transformation of **SCP**Ns (Fig. 9b) into crosslinked hydrogel (c):

(1) **Kinetic Control:** The transformation of **SCP**Ns into crosslinked hydrogel is a thermodynamically favourable process, but kinetically disfavoured process (Fig. 10a) as the intra-to-inter transformation of acyl hydrazone crosslinks does not readily occur in dilute aqueous solution. Initially, **SCP**Ns are in dilute aqueous solution and remain ‘trapped’ in a meta-stable state by a kinetic barrier (i). Heating **NP1-NP4** above their LCST affords the precipitation of polymer chains, thus concentrating the **SCP**Ns (ii) from aqueous solution and significantly lowering the kinetic barrier (iii) for gel formation. The lowering of this kinetic barrier by concentration of polymer chains is a crucial step in allowing **SCP**Ns to undergo ‘structural metamorphosis’ into crosslinked hydrogel, a more thermodynamically stable state.

(2) **Thermodynamic Control:** The relative energies of **SCP**Ns *versus* the crosslinked hydrogel state are directly influenced by the concentration of polymer chains within the aqueous solution (Fig. 10b).[†] In dilute aqueous solution ($T < \text{LCST}$) **SCP**Ns are the most thermodynamically favourable state (Fig. 1b, **S1**), however, heating of polymer solutions above their LCST (i) drives the concentration of polymer chains and thus destabilizes **SCP**Ns (**S2**) relative to the hydrogel state (**S3**). Conversely, cooling of the sample to below the LCST permits swelling followed by steady dissolution of the gel (ii), which raises the energy of the hydrogel (**S4**) state relative to that of **SCP**Ns, thus ‘encouraging’ return to the initial state (**S1**). Such processes of reversible phase-separation/polymer dissolution are well known in the literature, and with many thermo-responsive polymer systems displaying this behaviour,^{30b-g} it can be readily explained within the framework of Flory-Huggins solution theory.^{30h-j}

Intriguingly, the gelation process was observed to be entirely reversible. Cooling the gel to below the LCST regenerated aqueous solutions of **NP1-NP4**, which indicates that the system is likely operating under thermodynamic control (Fig. 10b). The timescale of the reverse process, however, was significantly slower than gel formation, with the solid material requiring

* At $T < \text{LCST}$ many weak attractive (enthalpically favourable) interactions arise between water and hydrophobic moieties displayed upon the polymer scaffold. Heating the system above its LCST provides sufficient thermal energy to break these weak interactions, and thus polymer chains are dehydrated through the entropically favoured displacement of water molecules into the bulk solution.

[†] This argument operates on the assumption that the system is under thermodynamic control, where population of **SCP**Ns *versus* hydrogel is governed by the relative thermodynamic stabilities (ΔG) of these two states.

several days to several months to become fully re-dissolved in aqueous solution, depending upon the density of crosslinker units embedded within the polymer scaffold. These observations suggest that dissolution of the hydrogel material is limited by slow hydrolysis/exchange processes, which are required to break the intermolecular acyl hydrazone linkages on the way to re-forming intramolecularly crosslinked **SCPNS**. The low temperatures ($T < \text{LCST}$) required to facilitate gel-to-SCPNS transition will also likely contribute to the long dissolution times, as low temperatures provide less thermal energy to drive bond-breaking and disentanglement of polymer chains from the hydrogel network.

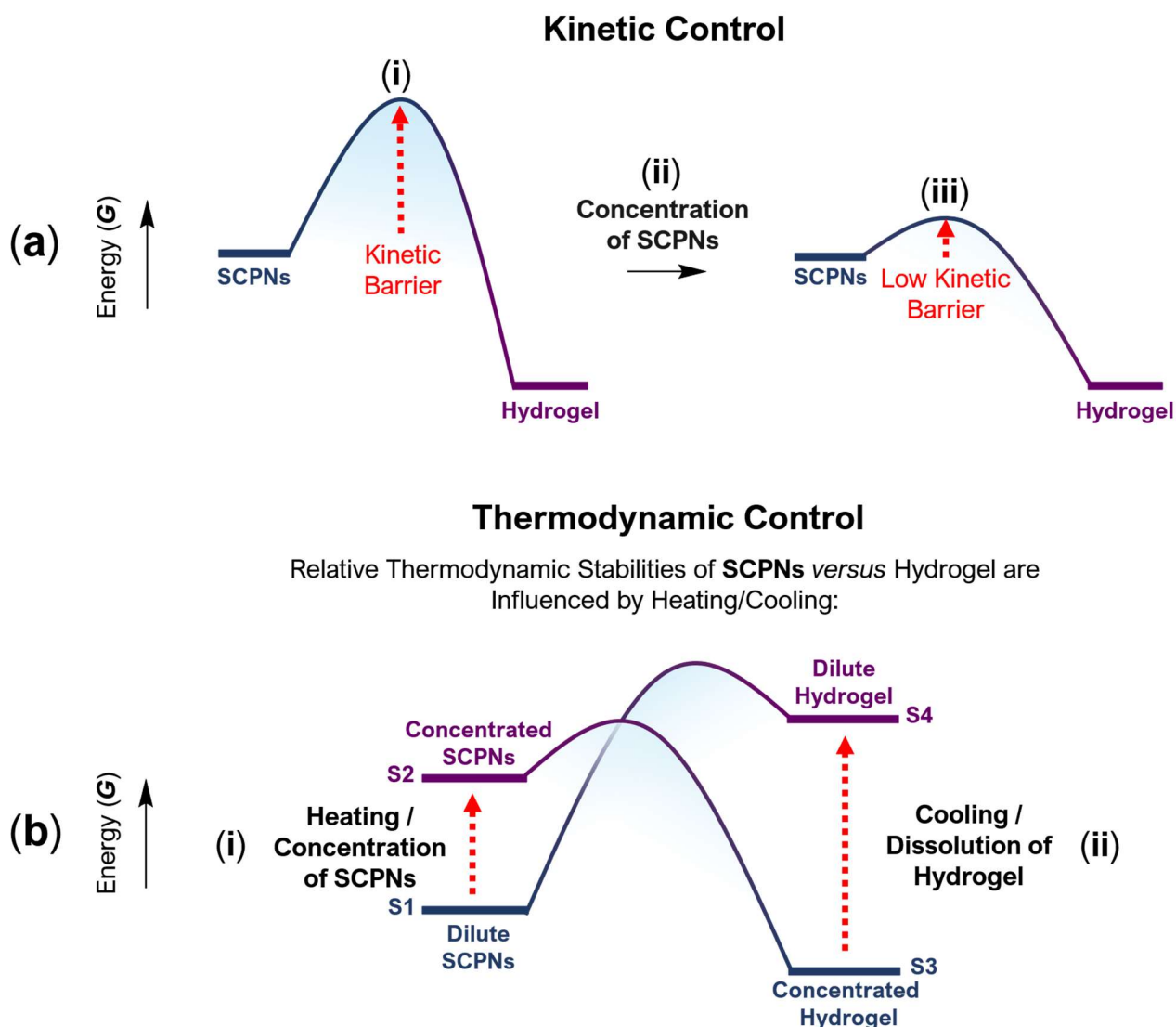


Figure 10: (a) **SCPNS** are ‘trapped’ in dilute aqueous solution by a kinetic barrier (i). Concentrating **SCPNS** (ii) from dilute solution, as accomplished in this example by heating polymer solutions above their LCST, lowers this kinetic barrier (iii) allowing **SCPNS** to undergo ‘structural metamorphosis’ into a crosslinked hydrogel, a more thermodynamically stable state. (b) The relative thermodynamic stabilities of **SCPNS** *versus* the hydrogel state are directly influenced by heating/cooling of the sample. Heating of polymer solutions to above their LCST drives the concentration of polymer chains and thus destabilizes **SCPNS** relative to the hydrogel state. Conversely, cooling to below the LCST permits swelling followed by steady dissolution of the gel, which raises the energy of the hydrogel state relative to that of **SCPNS**.

1.2.8. 'Shrink-Wrapping' of 2D Surfaces Displaying Carbohydrate Receptors

Research by the Fulton group has demonstrated^{16,30} that 'structural metamorphosis' of SCPNs is triggered by the concentration of polymer chains, either by evaporation of solvent or by thermally-induced precipitation of thermo-responsive polymer chains. However, it was hypothesized that SCPNs (Fig. 11a) might also be concentrated onto 2D surfaces (b) through weak non-covalent interactions (i), thus providing an additional approach to 'shrink-wrap' the surface within an intermolecularly crosslinked polymer film (d). Work by Mahon *et al.* recently confirmed this hypothesis, demonstrating³¹ that carbohydrate-decorated **glyco-SCPNs** possess the ability to concentrate themselves through specific molecular-recognition events at protein-functionalized surfaces (Fig. 11c), and thus spontaneously crosslink to form an intermolecularly crosslinked polymer film (Fig. 11d).

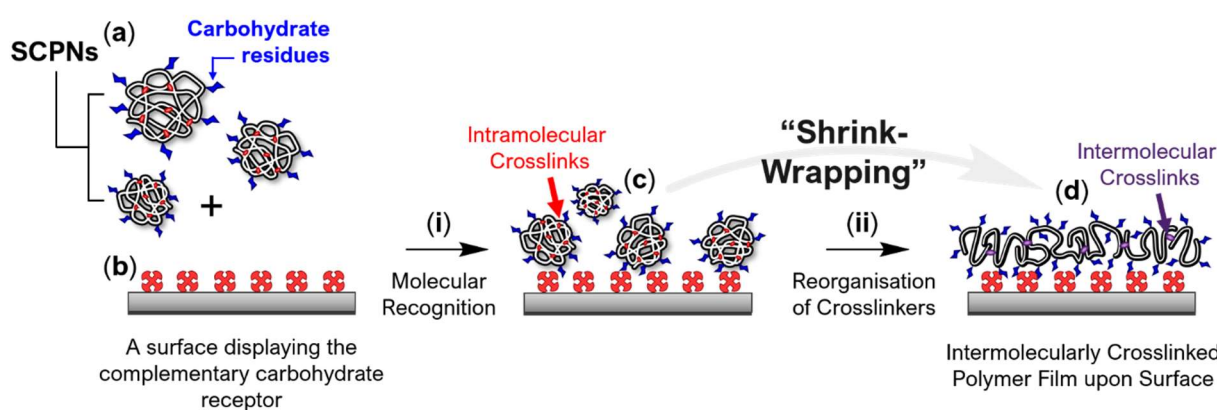


Figure 11: Addition of carbohydrate 'decorated' **SCPNs** (a) to a surface displaying the complementary carbohydrate receptor (b) concentrates the **SCPNs** onto the surface through specific molecular recognition events (i). An increase in the localized concentration of **SCPNs** triggers a structural reorganisation (ii) of dynamic covalent crosslinks to form an intermolecularly crosslinked polymer film (d) covering the protein-functionalized surface. The 'structural metamorphosis' of **SCPNs** into crosslinked polymer film is a process termed 'shrink-wrapping'.

In order to facilitate the formation of polymer films through specific molecular-recognition events two types of **glyco-SCPNs** were prepared: (i) **MAN-SCPNs**, whose intramolecularly crosslinked polymer backbone is decorated with mannosyl hydrazide (**MAN**) residues and (ii) **GAL-SCPNs**, which display galactosyl hydrazide (**GAL**) residues. Each of the **glyco-SCPNs** was shown to display a high binding affinity for surfaces functionalized with the complementary carbohydrate-binding protein (lectin). Surfaces functionalized with the mannose-binding protein Concanavalin A (**Con. A**) (Fig. 12a) were shown bound selectively to **MAN-SCPNs**, whereas surfaces displaying galactose-binding Heat Labile Toxin (**LBT**) bound selectively to **GAL-SCPNs**. AFM micrographs revealed that exposure of the protein-functionalized surfaces to their complementary **glyco-SCPNs** afforded a dramatic change in surface roughness arising on account of polymer film formation (Fig. 13). AFM was employed to monitor film formation

as a function of time, indicating the steady build-up of a glycopolymer film over a 24 h period. Control experiments were performed using the non-complementary pairing of (Fig. 12a) **MAN-SCPNS** + **LBT** surface and (Fig. 12b) **GAL-SCPNS** + **Con A** surface. In both cases, however, formation of the glycopolymer film was not observed, indicating that ‘shrink-wrapping’ of the 2D surface may only occur when **glyco-SCPNS** are concentrated through complementary molecular recognition events. Further control experiments also revealed that the ‘shrink-wrapping’ phenomenon was not observed unless the crosslinkers embedded within the **glyco-SCPNS** were dynamic covalent in nature. When ‘fixed’ **glyco-SCPNS**, containing non-dynamic (static) crosslinkers were employed, ‘shrink-wrapping’ of the complementary protein-functionalized surfaces was not observed, emphasizing the importance of hydrazone exchange in the ‘shrink-wrapping’ process.

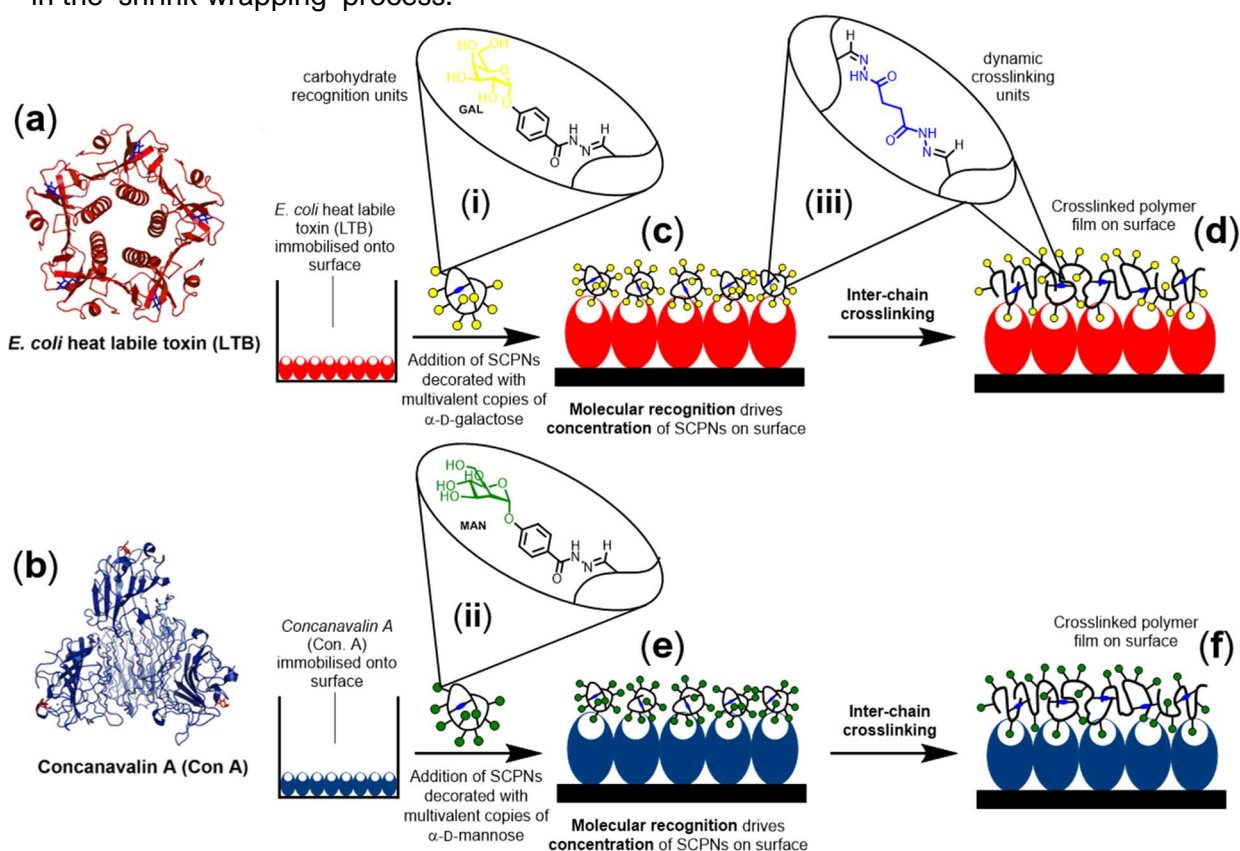


Figure 12: ‘Shrink-wrapping’ of 2D lectin-functionalized surfaces. (a) Heat labile toxin (**LBT**) shown with five associated galactose residues (**blue**). (b) Concanavalin A (**Con A**) shown in its tetrameric form with four associated mannose residues (**red**). **LBT**- (a, c-d) and **Con A**-functionalized (b, e-f) surfaces are ‘wrapped’ by **GAL-SCPNS** (i) and **MAN-SCPNS** (ii), respectively. **SCPNS** possessing intramolecular dynamic covalent crosslinks and carbohydrate residues (**GAL** or **MAN**) are stable in dilute solution. However, a combination of specific molecular recognition events (c and e) and rearrangement of dynamic covalent bonds (d and f) allows **SCPNS** to crosslink into polymer films. Polymer chains bind to lectin-functionalized surfaces through specific recognition events (c and e), leading to the concentration of **SCPNS** upon the surface. Surface-bound **SCPNS** become spatially closer to one another, thus their dynamic covalent intra-molecular crosslinkers undergo component exchange to form inter-chain crosslinks. This process is termed ‘shrink-wrapping’ and results in the formation of intermolecularly crosslinked polymer films (d and f).

AFM studies (Fig. 13, **g-h**) revealed that glycopolymer films can be readily removed by addition of hydroxylamine solution, which was hypothesized to cleave the inter-chain acyl hydrazone crosslinks by formation of the more stable³² oxime-functionalized polymer. Most importantly, the results from this investigation constitute firm evidence that the intra-to-intermolecular switch in crosslinking is a real phenomenon, which can be exploited to ‘shrink-wrap’ two-dimensional surfaces. In a natural progression of this work, the chemistry of ‘shrink-wrapping’ 2D immobilized protein surfaces should now be extended to the encapsulation of three-dimensional nano-assemblies, such as virus-like particles.

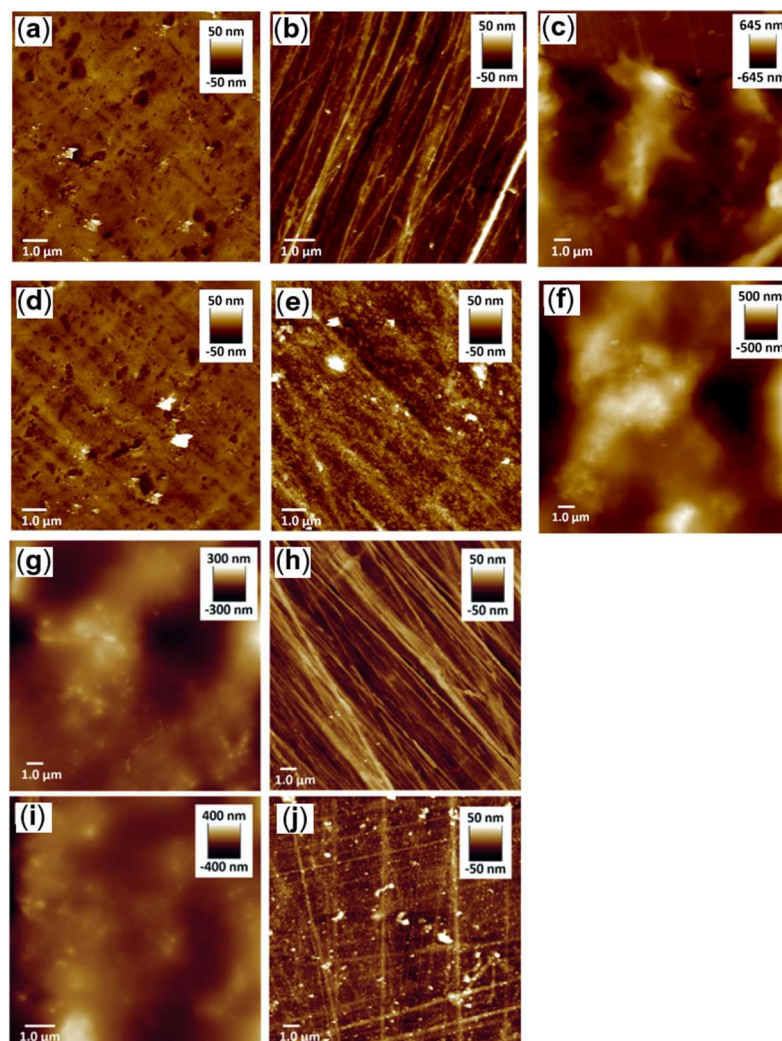


Figure 13: AFM images of 15 x 15 μm regions of streptavidin-coated polystyrene surfaces (**a**)(**d**) prior to any modification; (**b**) after functionalization with **Con A** via biotin-streptavidin linkage; (**c**) after functionalization with **Con A** and incubation in a solution of **SCPN-MAN** for 18 h at 5 °C; (**e**) after functionalization with **LTB** via biotin-streptavidin linkage; (**f**) after functionalization with **LTB** and incubation in a solution of **SCPN-GAL** for 18 h at 5 °C. (**g-j**) AFM images of 15 × 15 μm regions of surfaces displaying: (**g**) polymer film produced by exposure of **MAN-SCPNS** to a **Con A**-functionalised surface; (**h**) the same surface after exposure to hydroxylamine; (**i**) polymer film produced by exposure of **MAN-SCPNS** to a **Con A**-functionalised surface; (**j**) the same surface after exposure to methyl α-mannoside Reproduced with permission from ref. 31, copyright Wiley publishing 2017.

1.2.9. 'Shrink-Wrapping' of Viruses and Virus-Like Particles

Viruses, by their very nature, are designed to selectively target and infiltrate host cells with efficacies which have been fine-tuned through millions of years of evolution.³³ The first step in the infection pathway is attachment of the virus to the cell membrane,³⁴ a process which is facilitated by specific recognition events between cell-surface glycans and complementary carbohydrate receptors displayed on the periphery of the virus. Researchers are, however, still working to elucidate the intricate mechanisms by which viruses manage to evade the immune defences and facilitate cell entry.³⁵ A significant barrier to understanding these mechanisms and designing effective therapies to combat viral pathogens, however, is that the structure and composition of viral surfaces are in a constant state of flux. Viral surfaces evolve rapidly, with adjustments of their receptor compositions closely mirroring the changes in the glycans displayed upon the surface host cell surface that they are known to target. The development of technologies for 'neutralizing' such dynamic pathogens must therefore be equally as 'intelligent' if they are to have long-term success. One such strategy would be to interface viral targets with 'structurally adaptive' **SCPNs** (Fig. 14a) which, upon their binding to receptors located upon the viral surface (**b**), undergo 'structural metamorphosis' into an intermolecularly crosslinked polymer film (**c**). This strategy was envisaged to 'shrink-wrap' viral capsids within a 'protective' layer of glycopolymer film (Fig. 14), analogous to capturing the virus in a 'molecular net'. It is anticipated that 'unwrapping' (**iii**) of viral capsid could be triggered by the application of a specific stimulus, such as a drop in pH or addition of hydroxylamine, to afford displacement of acyl hydrazone crosslinks.

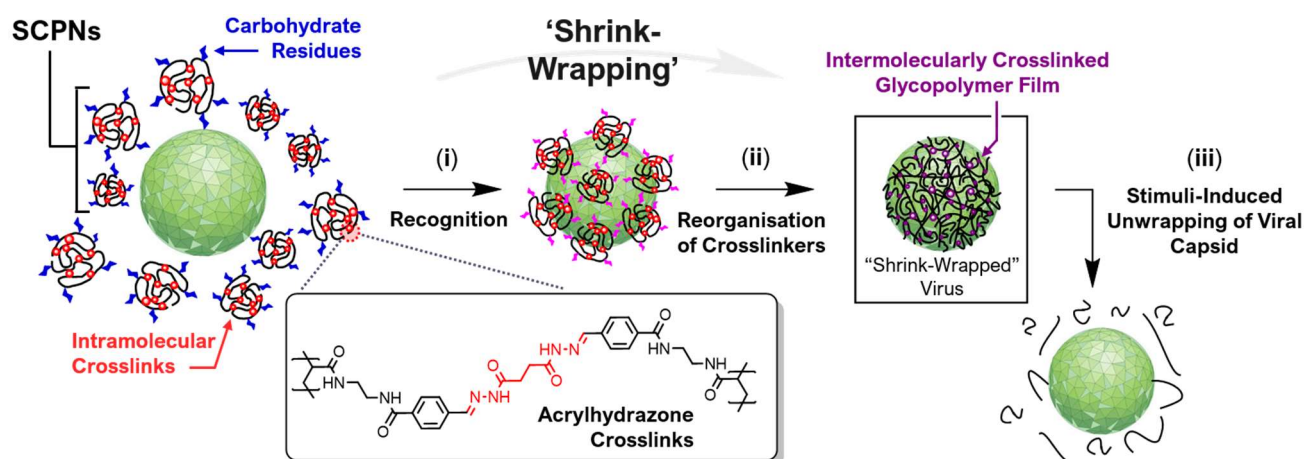


Figure 14: The 'shrink-wrapping' of a viral capsid within an intermolecularly crosslinked polymer film. In step (i) single-chain polymer nanoparticles (SCPNs) decorated with carbohydrate residues bind selectively to receptors situated on the periphery of the capsid. This process 'concentrates' the SCPNs, allowing their dynamic covalent crosslinkers to undergo intra- to inter-chain reorganisation in step (ii), resulting in the shrink-wrapping of the capsid within a layer of intermolecularly crosslinked polymer chains. In step (iii) the application of a stimuli such as a drop in pH or increase in redox potential is anticipated to induce cleavage of the crosslinks, triggering the 'unwrapping' of viral capsid.

It is hypothesized that ‘shrink-wrapping’ (Fig. 14) will proceed by the selective recognition of receptors (i) located upon the viral surface by **SCPNS** decorated with residues of the complementary carbohydrate, followed by the ‘structural metamorphosis’ of dynamic covalent crosslinks (ii) amongst neighbouring polymer chains. Initially, progress of the ‘shrink-wrapping’ process would be dependent on the formation of specific carbohydrate-virus recognition events. These weak supramolecular interactions concentrate **SCPNS** onto the periphery of the capsid, leading to a concentration-crosslinking phenomenon that drives ‘structural metamorphosis’ of **SCPNS** into covalently crosslinked polymer films.

In summary, the above description highlights that ‘shrink-wrapping’ is indeed a union of supramolecular (i) and dynamic covalent (ii) chemistry, both of which are essential to the ‘wrapping’ process. These two classes of dynamic bond can be judiciously combined and embedded within a single polymer chain to afford a class of ‘structurally dynamic’ **SCPNS** with the capacity to undergo ‘structural metamorphosis’. It is hypothesized that ‘metamorphosis’ of carbohydrate-decorated **SCPNS** would facilitate the ‘shrink-wrapping’ of virus-like particles displaying the complementary carbohydrate receptor. Initial inspiration for the ‘shrink-wrapping’ of virus-like particles came from research published by the group of Professor George Whitesides,³⁶ which demonstrated the ability of carbohydrate-functionalized poly(acrylamides) to inhibit viral surfaces with impressive selectivity (Fig. 15a-c).

1.2.10. Inspiration for the ‘Encapsulation’ of Viral Targets

During the early 1990s the laboratory of Professor George Whitesides investigated the inhibition of virus-cell binding by sialic acid (**SA**) decorated polyacrylamides (Fig. 15a). Their work^{36d} identified that the multivalent expression of carbohydrate residues upon a glycopolymer scaffold (Fig. 15e) drastically improves the efficacy of the inhibitor compared to that of monovalent carbohydrate ligands (Fig. 15d), thus presenting a useful strategy for interrupting virus-cell binding to prevent invasion of host cells by influenza virus (Fig. 15a-b). The multivalent inhibition (Fig. 15e) of virus-cell interactions by α -sialyl bearing polyacrylamide scaffolds arises from two effects: (i) multivalent capping or (ii) steric blocking of the viral surface by polymer. A series of carefully designed and rigorously conducted control experiments delineated the individual contributions of these two effects, revealing that multivalent capping (i) was predominantly responsible for inhibiting carbohydrate receptors displayed on the periphery of influenza virus. An ELISA-type assay (Fig. 17a) was developed to quantify the strength of the inhibitory effect by measuring the strength of polymer-virus binding. Binding was assessed with a comprehensive library of acrylamide-based glycopolymers displaying a range of carbohydrate types, carbohydrate densities and molecular weights were explored to determine optimum polymer composition for maximum inhibition of viral surfaces. Whilst it had

been reported³⁷ in 1995 that multivalence (cluster glycoside) effects play an important role in the strength of virus-cell binding, chemists at the time were only just beginning to realize the instrumental importance of multivalency effects, which are now known to have a multitude of biological consequences.³⁸ Seminal work by the Whitesides research group demonstrated that that multivalent effects can be exploited to disrupt virus-cell interactions, thus inhibiting entry of the virus into cell.

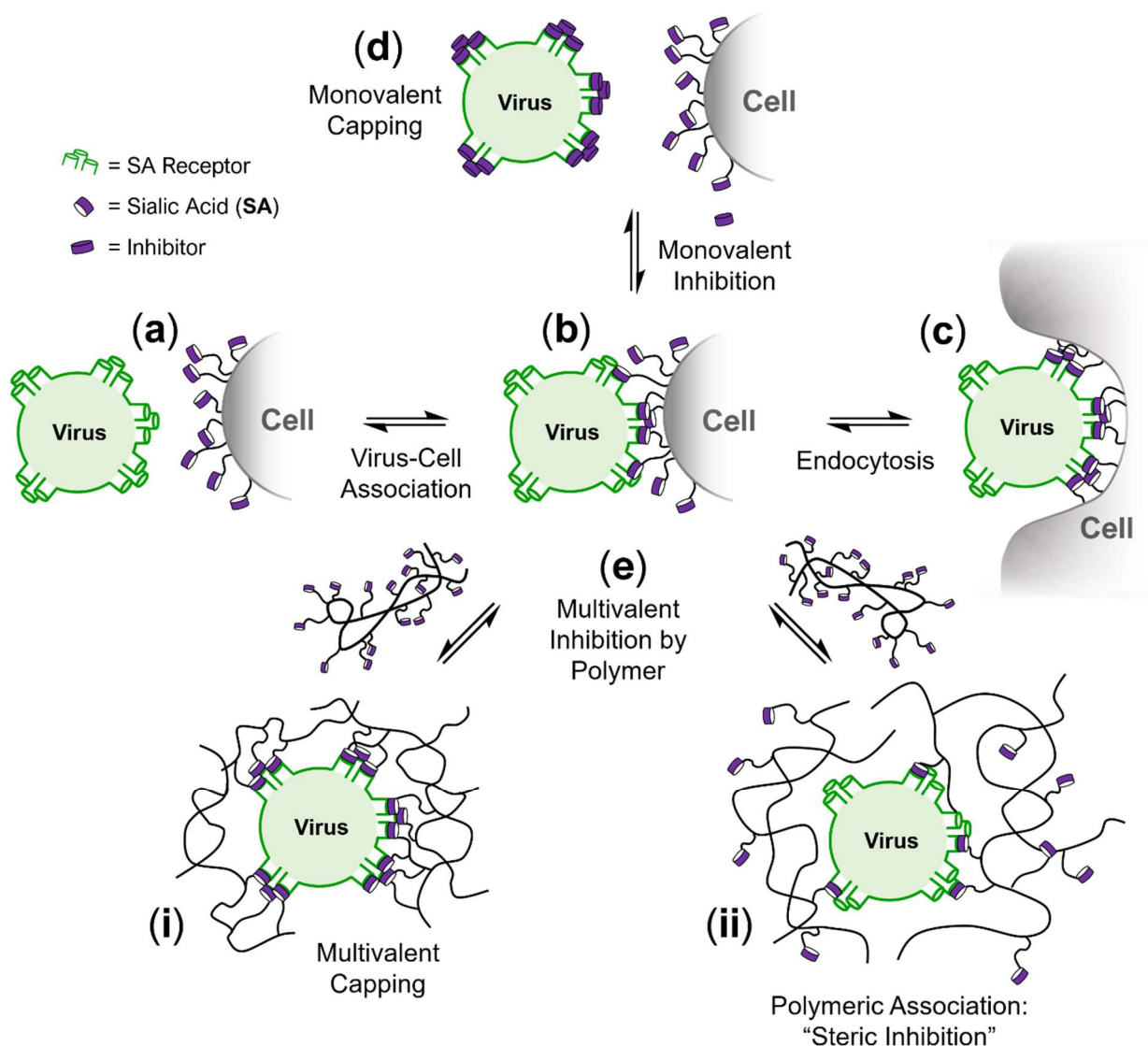


Figure 15: Possible explanations for the inhibition of attachment of influenza virus particles to sialic acid (SA) residues upon the cell surface by SA-polyacrylamide. Influenza virus (a) binds sialic acid residues displayed on the surface of cells (b) to induce cell entry (c) and invade the host organism. Inhibition of virus-cell interactions prevent influenza from binding the cell surface, thus preventing invasion of the host cell. Strategies for inhibiting virus-cell binding: monovalent capping (d) with a small molecule inhibitor, or multivalent inhibit with SA-functionalized polymer.

Lying at the vanguard of viral surface engineering and neoglycoconjugate chemistry, these seminal studies directly supported the hypothesis that multi-valency effects are crucial in mediating strong carbohydrate-protein recognition events between glycopolymers and receptors displayed upon the periphery of the virus. Of crucial importance to these investigations were: (i) The development of an ELISA assay (Fig. 17a) which estimated the affinity of **SA**-functionalized glycopolymer to the viral surface, and (ii) the utility of TEM imaging (Fig. 17b) to visualize the attachment of glycopolymers to the viral surface (Fig. 17b). In combination these two techniques provided a strong characterization handle with which the nature of virus-polymer interactions could be thoroughly interrogated.

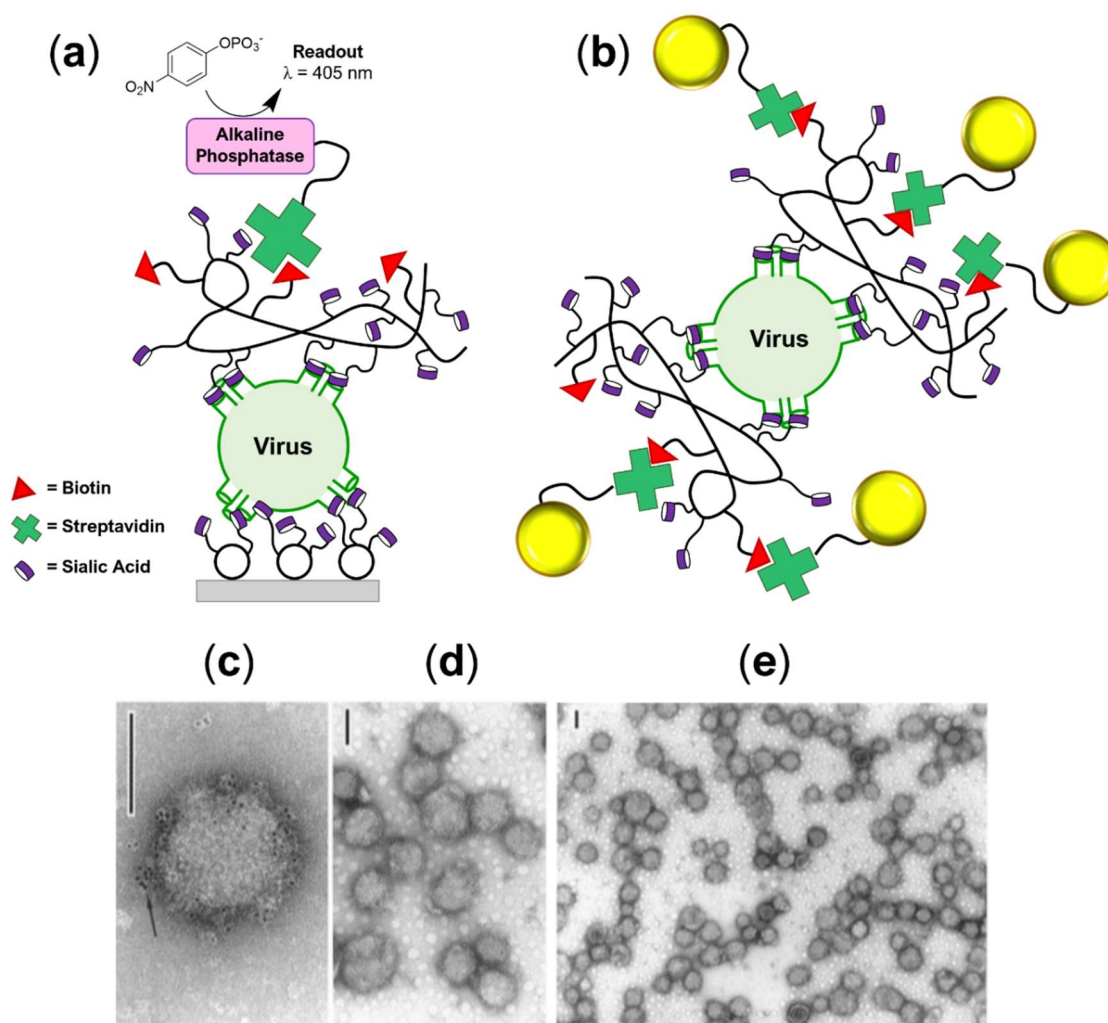


Figure 17: (a) ELISA-type assay for measuring the binding of biotin-labelled polymer-bearing sialic acid (**SA**) groups to the influenza virus. (b) Colloidal gold-labelled **SA**-functionalized polyacrylamide binding to influenza virus. (c-e) TEM micrographs showing gold-labelled polymer adhered to the periphery of influenza virus. Polymer-bound virus was labelled with streptavidin-coated colloidal gold and dark spots were observed around the periphery of the viral particles. Adsorbed polymer-virus complexes were stained with uranyl acetate negative stain prior to TEM. Scale bars all indicate 100 nm. Reproduced with permission from ref. 36d, copyright American Chemical Society 1996.

1.2.11. Catching a Virus in a Molecular Net

Virus-like particles have played an important role in vaccine development.^{39a,b} However, viral capsids are often susceptible to degradation upon exposure to elevated temperatures or dehydrating conditions.^{39c} Recent advances in virus engineering have demonstrated that virus-like particles can be protected from their external environment by covalent modification of the capsid exterior. In 2016, Delalande *et al.* reported^{39d} the capture of brome mosaic virus (**BMV**) within a ‘molecular net’ (Fig. 18, **a**). The metal-organic net was constructed around **BMV**, a small non-enveloped icosahedral virus, by the coordination of tannic acid (**TA**) with iron (III) (Fig. 18, **b-c**) to determine whether the net could act as a transport barrier for water. It was anticipated that the thin virus-bound layer of **Fe³⁺/TA** coordination polymer would maintain a hydrated environment around the virus, thus stabilizing **BMV** against disassembly in physically or chemically challenging environments. Reported characterization was consistent with a thin virus-adsorbed layer of **TA/Fe³⁺**, which was obtained by treating **BMV** with **FeCl₃** (Fig. 18a, **i**), removing the non-surface-bound **Fe³⁺** ions, then adding **TA** crosslinker (**ii**) to obtain the molecular net architecture. This modified protocol was necessary to ensure that **Fe³⁺/TA** coordination was localized to the virus surface and did not occur in the bulk solution, which was shown to lead to large crosslinked aggregates containing multiple virus particles buried within a thick layer of **Fe³⁺/TA**.

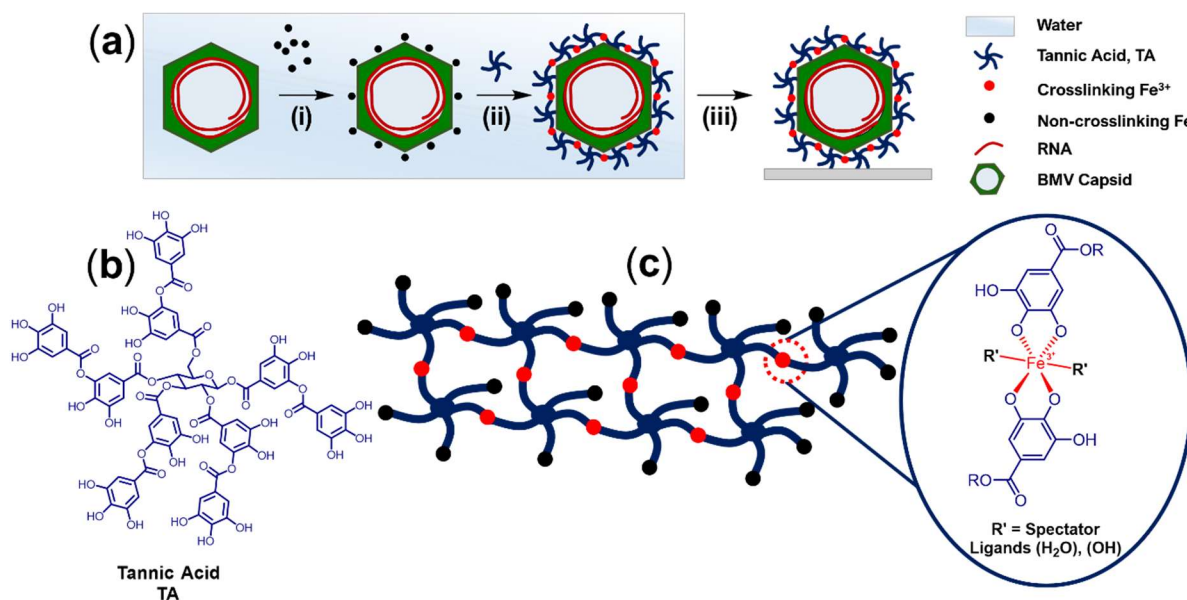


Figure 18: Catching a virus in a molecular net. (a) Overview of ‘coating’ **BMV** capsid with a crosslinked layer of **tannic acid/Fe³⁺** coordination polymer. Structures of **tannic acid**, **TA** (b) and **TA/Fe³⁺** coordination polymer (c).

AFM analysis and negative-stain TEM images revealed that **TA/Fe³⁺** coated virus (**Coated BMV**) featured remarkable stability against capsid disassembly in aqueous buffer (Fig. 19a, **c**) or by exposure to dehydrating conditions (Fig. 19b-c) and thus negligible size decreases were

observed by AFM (Fig. 19, **h-i**), whereas the unmodified virus (**Naked BMV**) was readily denatured, as evidenced by a collapse in the particle height by AFM (Fig. 19, **g, k**). Further experiments demonstrated that **Coated BMV** was stable for up to four weeks at pH 4.6 and low salt concentrations, as was evidenced by the negligible change in its electrophoretic mobility from one week to another. AFM analysis revealed that after storing **Coated BMV** in air for one year the virus remained remarkably intact, suggesting that the virus-adsorbed **TA/Fe³⁺** layer is highly effective in maintaining the native hydration state around the virus, thus protecting it against harsh external environments, even over relatively long timescales. Note that these studies remain distinct from the concept of ‘shrink-wrapping’, as preparation of the virus-adsorbed **TA/Fe³⁺** layer required the addition of external tannic acid crosslinker to obtain metal-ligand coordination network around the viral surface. This work highlights, however, the considerable potential of chemical approaches in stabilizing viral capsids, preventing their degradation, improving their shelf lives, and possibly circumnavigating their requirement for cold storage.

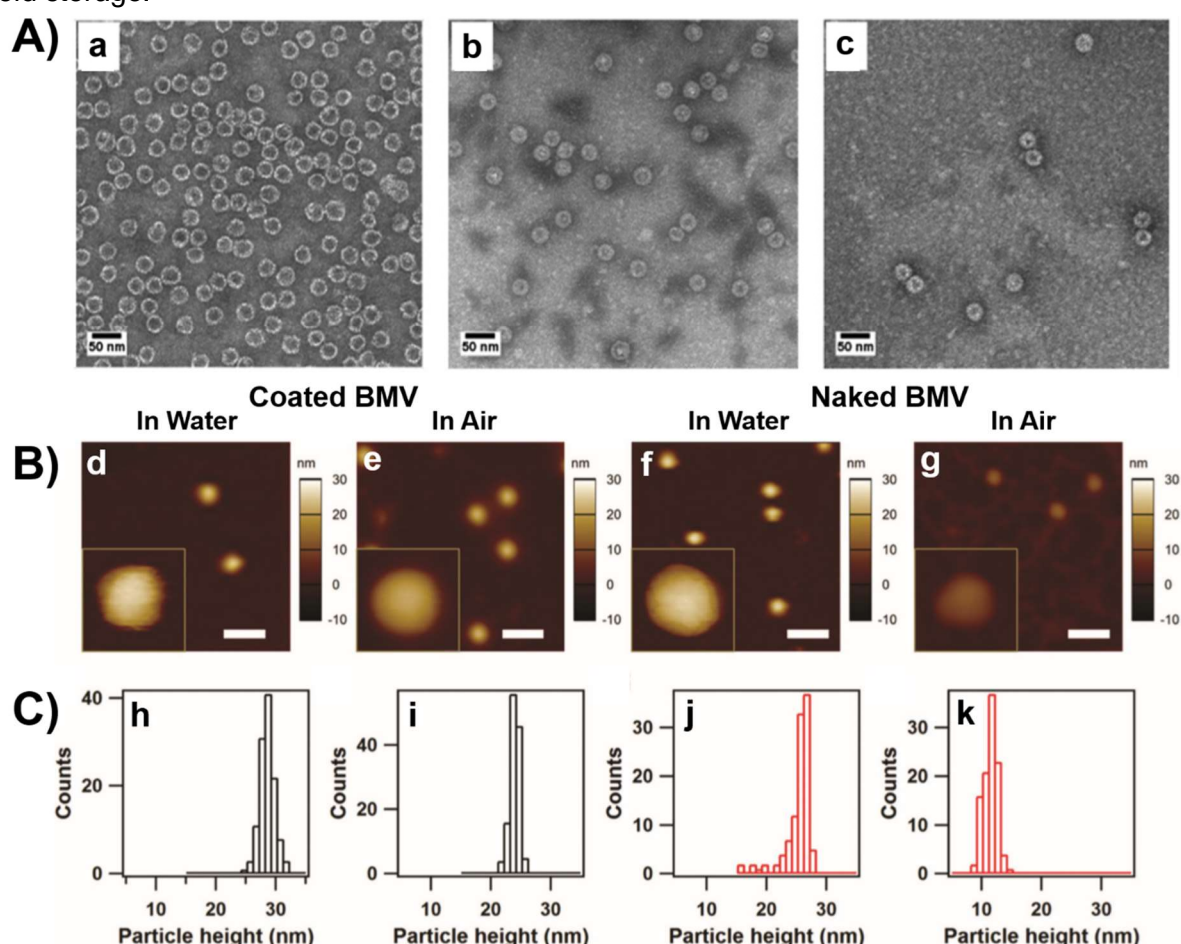


Figure 19: Experimental results demonstrating that a virus-adsorbed layer of **TA/Fe³⁺** protects the encapsulated **BMV** capsids against disassembly in aqueous buffer or by exposure to dehydrating conditions. (A) TEM images of: **Naked BMV** capsids (a), **Coated BMV** capsids (b) and **Coated BMV** capsids after 48 h incubation in disassembly buffer (c). Representative AFM micrographs (B) and height histograms (C) for **Coated BMV** and **Naked BMV** in water and in air, after drying. Reproduced with permission from ref. 39d, copyright of the Royal Society of Chemistry 2016.

1.3. Conclusion

Inspired by stimuli-responsive behaviour observed in nature, chemists have sought to incorporate rudimentary aspects of intelligence within simple molecular,⁴⁰ supramolecular,⁸ polymer systems^{10,30,31} and produce 'smart' materials⁷ which adapt to changes in their external environment. Review of this literature revealed surprisingly few examples of 'structural metamorphosis', an intriguing process in which 'structurally adaptive' systems traverse from one discrete molecular, macromolecular, or supramolecular architecture to another. This thesis was inspired by the emergence of this novel phenomenon and reports a strategy by which 'structural metamorphosis' of SCPNs might be exploited to drive the 'shrink-wrapping' of virus-like particles and other biologically relevant targets. Whilst 'metamorphosis' appears to be a thermodynamically favourable process, observations suggest that meta-stable SCPNs architectures may remain 'kinetically trapped' as discrete polymer chains in dilute aqueous solution. Early investigations have demonstrated^{30,31} that weak supramolecular interactions concentrate SCPNs, thereby triggering their 'metamorphosis' into polymer films. Furthering this work, it is anticipated that carbohydrate-receptor recognition events may drive the 'shrink-wrapping' of virus-like particles by triggering film formation upon the viral surface. It is hypothesized that 'shrink-wrapping' will protect the virus from its external environment and may present a strategy to engineer viral surfaces without requirement for covalent modification of the capsid. 'Shrink-wrapping' may also be utilized to 'capture' and 'neutralize' harmful pathogens within a polymer 'net'. Many bacterial and viral pathogens rely upon carbohydrate-receptor interactions to facilitate cell entry,³⁸ thus the presence of a 'shrink-wrap' layer is anticipated to mask carbohydrate-receptors displayed upon the antigen surface, thereby inhibiting cell entry. Development of the 'shrink-wrapping' concept is fundamentally a supramolecular chemistry project, in which utility structurally adaptive polymer architectures shall be explored. Progress towards the ambitious goal of 'shrink-wrapping' viral capsids will be incremental, gradually developing this novel concept by 'wrapping' biological targets of increasing complexity (Fig. 20a-d).

1.4. Proposed Approach

Research towards the ‘shrink-wrapping’ of complex biological targets such as ‘native’ influenza virus or *E. Coli* will follow a stepwise approach, steadily progressing the ‘shrink-wrapping’ concept to systems of increasing complexity (Fig. 20a-d). Investigations in this thesis began with **Model System I** (a) (Chapter 2) where electrostatically charged SCPNs were employed to ‘shrink-wrap’ negatively charged polystyrene nano- and microspheres. In these studies, it was hypothesized that simple electrostatic interactions drive the concentration aspect of the ‘shrink-wrapping’ process. In **Model System II** (b) (Chapter 3) specific molecular recognition events drive ‘shrink-wrapping’ by concentrating mannose-decorated glyco-SCPNs onto the periphery of protein-functionalized silica microparticles which display the complementary mannose receptor. Investigations towards the ‘shrink-wrapping’ of virus-like particles (c) were reported in Chapter 4, which details the synthesis of GM1-functionalized glycopolymers for binding to Simian Virus 40 (SV40), a small non-enveloped icosahedral viral capsid. Many such biomacromolecules display optimum stability at pH 7.4, yet acidic conditions (pH 4.5) are required to facilitate successful ‘shrink-wrapping’. To address this limitation and improve biocompatibility of the ‘wrapping’ approach, Chapter 5 investigates rate-enhancing structural features which facilitate rapid hydrazone exchange at neutral pH (e). Inclusion of these moieties upon polymer scaffolds is thus anticipated to yield next-generation polymer ‘wrapping agents’ which ‘shrink-wrap’ complex biological targets at physiological pH (f).

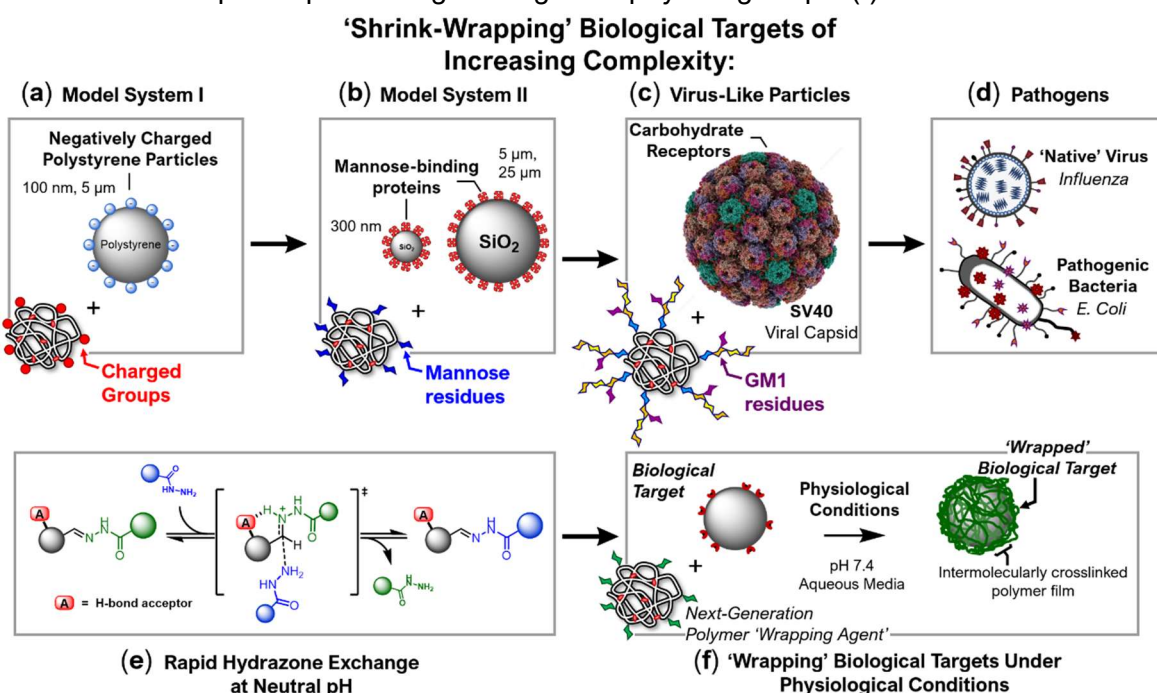


Figure 20: Research strategy for progressing the ‘shrink-wrapping’ concept towards biological targets of increasing complexity. (a) **Model System I:** Electrostatically charged SCPNs were adsorbed onto oppositely charged polystyrene nano- or microspheres. Electrostatic interactions drive the ‘shrink-wrapping’ process. (b) **Model System II:** Protein-functionalized silica nano- and microspheres displaying mannose-binding receptors were ‘shrink-wrapped’ with mannose-decorated SCPNs. (c) **Virus-Like Particles:** Investigations towards the ‘shrink-wrapping’ Simian virus 40 viral capsid. (d) ‘Shrink-wrapping’ of ‘native’ viruses such as influenza, or pathogenic bacteria such as *E. Coli*. (e) Rate-enhancing structural features (A) facilitate rapid hydrazine exchange at neutral pH, and thus their inclusion upon polymer scaffolds may permit ‘wrapping’ of biological targets under physiological conditions (f).

1.5. References

- [1] (a) K. S. Oberhauser and M. J. Solensky, *Monarch butterfly biology & conservation*. Ithaca, Cornell University Press, New York, 2004. (b) A. E. Pelling, P. R. Wilkinson, R. Stringer and J. K. Gimzewski, Dynamic Mechanical Oscillations During Metamorphosis of the Monarch Butterfly, *J. R. Soc. Interface*, 2009, **6**, 29–37
- [2] I. Yu, H. A. Holdaway, P. R. Chipman, R. J. Kuhn, M. G. Rossmann and J. Chen, Association of the pr Peptides with Dengue Virus at Acidic pH Blocks Membrane Fusion, *J. Virol.* 2009, **83**, 12101–12107.
- [3] R. J. Morris, M. Schor, R. M. C. Gillespie, A.S. Ferreira, L. Baldauf, C. Earl, A. Ostrowski, L. Hobley, K. M. Bromley, T. Sukhodub, S. Arnaouteli, N. R. Stanley-Wall and C. E. MacPhee, Natural variations in the biofilm-associated protein BslA from the genus *Bacillus*, *Sci. Rep.*, 2017, **7**, 1-13.
- [4] (a) K. M. Bromley, R. J. Morris, L. Hobley, G. Brandani, R. M. C. Gillespie, M. McCluskey, U. Zachariae, D. Marenduzzo, N. R. Stanley-Wall and C. E. MacPhee, Interfacial self-assembly of a bacterial hydrophobin, *Proc. Natl. Acad. Sci.*, 2015, **112**, 5419–5424. (b) L. Hobley, A. Ostrowski, F. V Rao, K. M. Bromley, M. Porter, A. R. Prescott, C. E. Macphee, D. M. F. van Aalten and N. R. Stanley-Wall, *Proc. Natl. Acad. Sci.*, 2013, **110**, 13600–13605.
- [5] C. Soanes, *Oxford Dictionary of Current English*, 4th edn., Oxford University Press, Oxford, 2009.
- [6] R. J. Wojtecki, M. A. Meador and S. J. Rowan, Using the dynamic bond to access macroscopically responsive structurally dynamic polymers, *Nat. Mater.*, 2011, **10**, 14–27.
- [7] R. K. Kumar, R. L. Harniman, A. J. Patil and S. Mann, Self-transformation and structural reconfiguration in coacervate-based protocells, *Chem. Sci.*, 2016, **7**, 5879–5887.
- [8] J. Li, J. M. A. Carnall, M. C. A. Stuart and S. Otto, Hydrogel Formation upon Photoinduced Covalent Capture of Macrocyclic Stacks from Dynamic Combinatorial Libraries, *Angew. Chem. Int. Ed.*, 2011, **50**, 8384–8386.
- [9] J. M. A. Carnall, C. A. Waudby, A. M. Belenguer, C. A. Marc, J. J. Peyralans and S. Otto, Mechanosensitive Self-Replication Driven by Self-Organization, *Science*, 2010, **327**, 1502–1506.
- [10] H. Sun, C. P. Kabb, Y. Dai, M. R. Hill, I. Ghiviriga, A. P. Bapat and B. S. Sumerlin, Macromolecular metamorphosis via stimulus-induced transformations of polymer architecture, *Nat. Chem.*, 2017, **9**, 817–823.
- [11] (a) B. Gacal, H. Durmaz, M. A. Tasdelen, G. Hizal, U. Tunca and Y. Yagci and A. L. Demirel, Anthracene-Maleimide-Based Diels-Alder ‘Click Chemistry’ as a Novel Route to Graft Copolymers, *Macromolecules*, 2006, **39**, 5330–5336. (b) R. Gheneim, C. Perez-Berumen and A. Gandini, R. Gheneim, C. Perez-berumen and A. Gandini, *Macromolecules*, 2002, **35**, 7246–7253.
- [12] (a) P. T. Corbett, J. Leclaire, L. Vial, K. R. West, J. Wietor, J. K. M. Sanders and S. Otto, Dynamic Combinatorial Chemistry, *Chem. Rev.*, 2006, **106**, 3652–3711. (b) P. Chakma and D. Konkolewicz, Dynamic Covalent Bonds in Polymeric Materials, *Angew. Chem. Int. Ed.*, 2019, **58**, 9682–9695. (c) S. J. Rowan, S. J. Cantrill, G. R. L. Cousins, J. K. M. Sanders and J. F. Stoddart, Dynamic Covalent Chemistry, , *Angew. Chem. Int. Ed.*, 2002, vol. 41.
- [13] J. Zhang, Y. Niu, C. Huang, L. Xiao, Z. Chen, K. Yang and Y. Wang, Self-healable and recyclable triple-shape PPDO – PTMEG co-network, *Polym. Chem.*, 2012, **3**, 1390–1393.
- [14] Y.-L. Liu and T.-W. Chuo, Dynamic Covalent Bonds in Polymeric Materials, *Polym. Chem.*, 2013, **4**, 2194–2205.
- [15] A. P. Bapat, J. G. Ray, D. A. Savin, E. A. Hoff, L. Patton and B. S. Sumerlin, Dynamic-covalent nanostructures prepared by Diels–Alder reactions of styrene-maleic anhydride-derived copolymers obtained by one-step cascade block copolymerization, *Polym. Chem.*, 2012, **3**, 3112–3120.

- [16] B. S. Murray and D. A. Fulton, Dynamic Covalent Single-Chain Polymer Nanoparticles, *Macromolecules*, 2011, **44**, 7242–7252.
- [17] E. Harth, B. Van Horn, V. Y. Lee, D. S. Germack, C. P. Gonzales, R. D. Miller and C. J. Hawker, A Facile Approach to Architecturally Defined Nanoparticles via Intramolecular Chain Collapse, *J. Am. Chem. Soc.*, 2002, **124**, 8653–8660.
- [18] (a) N. Ormategui, I. Garcia, D. Padro, G. Cabanero, H. J. Grande and I. Loinaz, Synthesis of single chain thermoresponsive polymer nanoparticles, *Soft Matter*, 2012, **8**, 734–740. (b) D. Chao, X. Jia, B. Tuten, C. Wang and E. B. Berda, Controlled folding of a novel electroactive polyolefin via multiple sequential orthogonal intra-chain interactions, *Chem. Commun.*, 2013, **49**, 4178–4180. (c) W. Fan, X. Tong, Q. Yan, S. Fu and Y. Zhao, Photodegradable and size-tunable single-chain nanoparticles prepared from a single main-chain coumarin-containing polymer precursor, *Chem. Commun.*, 2014, **50**, 13492–13494.
- [19] (a) B. T. Tuten, D. Chao, K. Lyon and E. B. Berda, Single-chain polymer nanoparticles via reversible disulfide bridges, *Polym. Chem.*, 2012, **3**, 3068–3071. (b) P. T. Dirlam, J. Kim, K. J. Arrington, J. Chung, R. Sahoo, L. J. Hill, P. J. Costanzo and P. Theato, Single chain polymer nanoparticles via sequential ATRP and oxidative polymerization, *Polym. Chem.*, 2013, **4**, 3765–3773. (c) A. Sanchez-Sanchez, A. Fulton and A. Pomposo, pH-responsive single-chain polymer nanoparticles utilising dynamic covalent enamine bonds, *Chem. Commun.*, 2014, **50**, 1871–1874. (d) A. P. P. Kröger, R. J. E. A. Boonen and J. M. J. Paulusse, Well-defined single-chain polymer nanoparticles via thiol-Michael addition, *Polymer*, 2017, **120**, 119–128. (e) Y. Zhou, Y. Qu, Q. Yu, H. Chen, Z. Zhang and X. Zhua, Controlled synthesis of diverse single-chain polymeric nanoparticles using polymers bearing furan-protected maleimide moieties, *Polym. Chem.*, 2018, **9**, 3238–3247.
- [20] (a) S. Mavila, C. E. Diesendruck, S. Linde, L. Amir, R. Shikler and N. G. Lemcoff, Polycyclooctadiene Complexes of Rhodium (I): Direct Access to Organometallic Nanoparticles, *Angew. Chem. Int. Ed.*, 2013, **2**, 5767–5770. (b) J. Jeong, Y. Lee, B. Kim, B. Kim, K. Jung and H. Paik, Colored single-chain polymeric nanoparticles via intramolecular copper phthalocyanine formation, *Polym. Chem.*, 2015, **6**, 3363–3550. (c) F. Wang and C. E. Diesendruck, Advantages and limitations of diisocyanates in intramolecular collapse, *Polym. Chem.*, 2017, **8**, 3712–3720.
- [21] (a) E. Huerta, P. J. M. Stals, E. W. Meijer and A. R. A. Palmans, Consequences of Folding a Water-Soluble Polymer Around an Organocatalyst, *Angew. Chem. Int. Ed.*, 2013, **52**, 2906–2910. (b) E. W. Meijer, Forced Unfolding of Single-Chain Polymeric Nanoparticles, *J. Am. Chem. Soc.*, 2015, **137**, 6880–6888. (c) G. Yilmaz, V. Uzunova, R. Napier and C. R. Becer, Single-Chain Glycopolymer Folding via Host–Guest Interactions and Its Unprecedented Effect on DC-SIGN Binding, *Biomacromolecules*, 2018, **19**, 3040–3047.
- [22] (a) T. Terashima, T. Mes, T. F. A. De Greef, M. A. J. Gillissen, P. Besenius, A. R. A. Palmans and E. W. Meijer, Single-Chain Folding of Polymers for Catalytic Systems in Water, *J. Am. Chem. Soc.*, 2011, **133**, 4742–4745. (b) M. A. J. Gillissen, I. K. Voets, E. W. Meijer and A. R. A. Palmans, Single chain polymeric nanoparticles as compartmentalised sensors for metal, *Polym. Chem.*, 2012, **3**, 3166–3174. (c) J. Willenbacher, O. Altintas, P. W. Roesky and C. Barner-Kowollik, Single-Chain Self-Folding of Synthetic Polymers Induced by Metal – Ligand Complexation, *Macromol. Rapid Commun.*, 2014, **35**, 45–51. (d) A. Sanchez-Sanchez, A. Arbe and J. Colmenero, Metallo-Folded Single-Chain Nanoparticles with Catalytic Selectivity, *ACS Macro Lett.*, 2014, **3**, 439–443. (e) P. W. Roesky and C. Barner-Kowollik, Pd-complex driven formation of single-chain nanoparticles, *Polym. Chem.*, 2015, **6**, 4358–4365. (f) Y. Liu, S. Pujals, P. J. M. Stals, T. Paulöhr, S. I. Presolski, E. W. Meijer, A. R. A. Palmans and L. Albertazzi, Catalytically active single-chain polymeric nanoparticles, *J. Am. Chem. Soc.*, 2018, **140**, 3423–3433. (g) H. Rothfuss, P. W. Roesky and C. Barner-Kowollik, Single-Chain Nanoparticles as Catalytic Nanoreactors, *J. Am. Chem. Soc.*, 2018, **140**, 5875–5881.
- [23] (a) S. K. Hamilton and E. Harth, Molecular Dendritic Transporter Nanoparticle Vectors Provide Efficient Intracellular Delivery of Peptides, *ACS Nano*, 2009, **3**, 402–410. (b) A.

- Sanchez-Sanchez, S. Akbari, A. J. Moreno, F. Lo Verso, A. Arbe, J. Colmenero and J. A. Pomposo, Design and Preparation of Single-Chain Nanocarriers Mimicking Disordered Proteins for Combined Delivery of Dermal Bioactive Cargos, *Macromol. Rapid Commun.*, 2013, **34**, 1681–1686. (c) Y. Bai, H. Xing, G. A. Vincil, J. Lee, E. J. Henderson, Y. Lu, N. Gabriel and S. C. Zimmerman, Practical synthesis of water-soluble organic nanoparticles with a single reactive group and a functional carrier scaffold, *Chem. Sci.*, 2014, **5**, 2862–2868. (d) A. P. P. Kro, N. M. Hamelmann, A. Juan, S. Lindhoud and J. M. J. Paulusse, Biocompatible Single-Chain Polymer Nanoparticles for Drug Delivery - A Dual Approach, *ACS Appl. Mater. Interfaces*, 10, 30946–30951.
- [24] (a) M. A. J. Gillissen, I. K. Voets, E. W. Meijer and A. R. A. Palmans, Single-chain polymeric nanoparticles as compartmentalised sensors for metal, *Polym. Chem.*, 2012, **3**, 3166–3174. (b) A. Latorre-Sanchez and J. A. Pomposo, A simple, fast and highly sensitive colorimetric detection of zein in aqueous ethanol via zein-pyridine-gold interactions, *Chem. Commun.*, 2015, **51**, 15736–15738.
- [25] (a) J. Colmenero and J. A. Pomposo, Endowing Single-Chain Polymer Nanoparticles with Enzyme-Mimetic Activity, *ACS Macro Lett.*, 2013, **2**, 775–779. (b) C. A. Tooley, S. Pazicni and E. B. Berda, Toward a tunable synthetic [FeFe] hydrogenase mimic: single-chain nanoparticles functionalized with a single diiron cluster, *Polym. Chem.*, 2015, **6**, 7646–7651. (c) T. S. Fischer, D. Schulze-Sünninghausen, B. Luy, O. Altintas and C. Barner-Kowollik, Supramolecular Chemistry Stepwise Unfolding of Single-Chain Nanoparticles by Chemically Triggered Gates, *Angew. Chem. Int. Ed.*, 2016, **55**, 11276–11280. (d) J. Rubio-Cervilla, E. González and J. Pomposo, Advances in Single-Chain Nanoparticles for Catalysis Applications, *Nanomaterials*, 2017, **7**, 341.
- [26] Y. Liu, T. Pauloeherl, S. I. Presolski, L. Albertazzi, A. R. A. Palmans and E. W. Meijer, Modular Synthetic Platform for the Construction of Functional Single-Chain Polymeric Nanoparticles: From Aqueous Catalysis to Photosensitization, *J. Am. Chem. Soc.*, 2015, **137**, 13096–13105.
- [27] (a) A. B. Benito, M. K. Aiertza, M. Marradi, L. Gil-Iceta, T. S. Zahavi, B. Szczupak, T. Reese, E. Scanziani, L. Passoni, M. Matteoli, M. De Maglie, A. Orenstein, M. Oron-Herman, G. Kostenich, L. Buzhansky, E. Gazit, H. Grande and V. Gómez-Vallejo, J. Llop and I. Loinaz, Functional Single-Chain Polymer Nanoparticles: Targeting and Imaging Pancreatic Tumors in Vivo, *Biomacromolecules*, 2016, **17**, 3213–3221. (b) J. De-La-Cuesta, E. González and J. A. Pomposo, Advances in Fluorescent Single-Chain Nanoparticles, *Molecules*, 2017, **22**, 1–14. (c) A. P. P. Kröger, M. I. Komil, N. M. Hamelmann, A. Juan, M. H. Stenzel and J. M. J. Paulusse, Glucose Single-Chain Polymer Nanoparticles for Cellular Targeting, *ACS Macro Lett.*, 2019, **8**, 95–101. (d) D. N. F. Bajj, M. V. Tran, H. Tsai, H. Kim, N. R. Paisley, W. R. Algar and Z. M. Hudson, Fluorescent Heterotelechelic Single-Chain Polymer Nanoparticles: Synthesis, Spectroscopy, and Cellular Imaging, *ACS Appl. Nano Mater.*, 2019, **2**, 898–909.
- [28] I. Perez-Baena, I. Loinaz, D. Padro, I. García, J. Grande and I. Odriozola, Single-chain polyacrylic nanoparticles with multiple Gd (III) centres as potential MRI contrast agents, *J. Mater. Chem.*, 2010, **20**, 6916–6922.
- [29] G. M. ter Huurne, A. R. A. Palmans and E. W. Meijer, Supramolecular Single-Chain Polymeric Nanoparticles, *CCS Chem.* 2019, **1**, 64–82.
- [30] (a) D. E. Whitaker, C. S. Mahon and D. A. Fulton, Thermoresponsive dynamic covalent single-chain polymer nanoparticles reversibly transform into a hydrogel, *Angew. Chem. Int. Ed.*, 2013, **52**, 956–959. (b) J. S. Scarpa, D. D. Mueller and I. M. Klotz, Slow hydrogen-deuterium exchange in a non- α helical polyamide, *J. Am. Chem. Soc.*, 1967, **89**, 6024–6030. (c) J. Lutz and A. Hoth, Preparation of Ideal PEG Analogues with a Tunable Thermosensitivity by Controlled Radical Copolymerization of 2-(2-Methoxyethoxy)ethyl Methacrylate and Oligo(ethylene glycol) Methacrylate, *Macromolecules*, 2006, **39**, 893–896. (d) Felix A. Plamper, Markus Ruppel, Alexander Schmalz, Oleg Borisov, Matthias Ballauff and Axel H. E. Müller, Tuning the Thermoresponsive Properties of Weak Polyelectrolytes: Aqueous Solutions of Star-Shaped and Linear Poly(N,N-

- dimethylaminoethyl Methacrylate, *Macromolecules*, 2007, **40**, 8361-8366. (e) V. Aseyev, H. Tenhu and F. M. Winnik, Non-ionic Thermoresponsive Polymers in Water, *Adv. Polym. Sci.*, 2011, **242**, 29-89. (f) M. A. Ward and T. K. Georgiou, Thermoresponsive Polymers for Biomedical Applications, *Polymers*, 2011, **3**, 1215-1242. (g) D. Roy, W. L. A. Brooks and B. S. Sumerlin, New Directions in Thermoresponsive Polymers, *Chem. Soc. Rev.*, 2013, **42**, 7214-7243. (h) W. Burchard, "Solution Thermodynamics of Non-Ionic Water-Soluble Polymers" in *Chemistry and Technology of Water-Soluble Polymers*, ed. C. Finch, Springer, New York, 1983, pp. 125-142. (i) F. Franks, "Water Solubility and Sensitivity-Hydration Effects" in *Chemistry and Technology of Water-Soluble Polymers*, ed. C. Finch, Springer, New York, 1983, pp. 125-142. (j) M. A. van Dijk and A. Wakker, *Concepts in Polymer Thermodynamics*, CRC Press., Florida, 1998, pp. 61-65
- [31] C. S. Mahon, C. J. McGurk, S. M. D. Watson, M. A. Fascione, C. Sakonsinsiri, W. B. Turnbull and D. A. Fulton, Molecular Recognition-Mediated Transformation of Single-Chain Polymer Nanoparticles into Crosslinked Polymer Films, *Angew. Chem. Int. Ed.*, 2017, **56**, 12913-12918.
- [32] J. Kalia and R. T. Raines, *Angew. Chem. Int. Ed.*, Hydrolytic stability of hydrazones and oximes, 2008, **47**, 7523-7526.
- [33] Z. Chen, N. Li, S. Li, M. Dharmawardana, A. Schlimme and J. J. Gassensmith, Viral chemistry: the chemical functionalization of viral architectures to create new technology, *Viral Chem.*, 2016, **8**, 512-534.
- [34] A. Imberty and A. Varrot, *Curr. Opin. Struct. Biol.*, Microbial recognition of human cell surface glycoconjugates, 2008, **18**, 567-576.
- [35] (a) L. J. Str and T. Stehle, Glycan Engagement by Viruses: Receptor Switches and Specificity, *Annu. Rev. Virol.*, 2014, **1**, 285-306. (b) M. H. Dietrich, C. Harprecht and T. Stehle, The bulky and the sweet: How neutralizing antibodies and glycan receptors compete for virus binding, *Protein Sci.*, 2017, **26**, 2342-2354.
- [36] (a) A. Spaltenstein and G. M. Whitesides, Polyacrylamides Bearing Pendant α -Sialoside Groups Strongly Inhibit Agglutination of Erythrocytes by Backbone Linkages Department of Chemistry, *J. Am. Chem. Soc.*, 1991, **113**, 686-687. (b) M. A. Sparks, K. W. Williams and G. M. Whitesides, Neuraminidase-Resistant Hemagglutination Inhibitors: Acrylamide Copolymers Containing a C-Glycoside of JV-Acetylneuraminic Acid, *J. Med. Chem.*, 1993, **36**, 778-783. (c) M. Mammen, G. Dahmann and G. M. Whitesides, Effective Inhibitors of Hemagglutination by Influenza Virus Synthesized from Poisoners Having Active Ester Groups. Insight into Mechanism of Inhibition, *J. Med. Chem.*, 1995, **38**, 4179-4190. (d) G. B. Sigal, M. Mammen, G. Dahmann and G. M. Whitesides, Polyacrylamides bearing pendant α -sialoside groups strongly inhibit agglutination of erythrocytes by influenza virus: The strong inhibition reflects enhanced binding through cooperative polyvalent interactions, *J. Am. Chem. Soc.*, 1996, **118**, 3789-3800.
- [37] (a) Y. C. Lee and R. T. Lee, Carbohydrate-Protein Interactions: Basis of Glycobiology, *Acc. Chem. Res.*, 1995, **28**, 321-327. (b) J. J. Lundquist and E. J. Toone, The Cluster Glycoside Effect, *Chem. Rev.*, 2002, **102**, 555-578.
- [38] P. Compain, Multivalent Effect in Glycosidase Inhibition: The End of the Beginning, *Chem. Rec.*, 2019, **19**, 1-14.
- [39] (a) A. Roldão, M. C. M. Mellado, L. R. Castilho, M. J. Carrondo and P. M. Alves, Virus-like particles in vaccine development, *Expert Rev. Vaccines*, 2010, **9**, 1149-1176. (b) A. Zeltins, Construction and Characterization of Virus-Like Particles: A Review, *Mol. Biotechnol.*, 2013, **53**, 92-107. (c) A. Arkhipov, P. L. Freddolino and K. Schulten, Construction and Characterization of Virus-Like Particles: A Review, *Structure*, 2006, **14**, 1767-1777. (d) L. Delalande, I. B. Tsvetkova, C. Zeng, K. Bond, M. F. Jarrold and B. Dragnea, Catching a virus in a molecular net, *Nanoscale*, 2016, **8**, 16221-16228.
- [40] B. M. Matysiak, P. Nowak, I. Cvrtila, C. G. Pappas, B. Liu, D. Komáromy and S. Otto, Antiparallel Dynamic Covalent Chemistries, *J. Am. Chem. Soc.*, 2017, **139**, 6744-6751

Chapter 2

'Shrink-Wrapping' Through Complementary Electrostatic Interactions

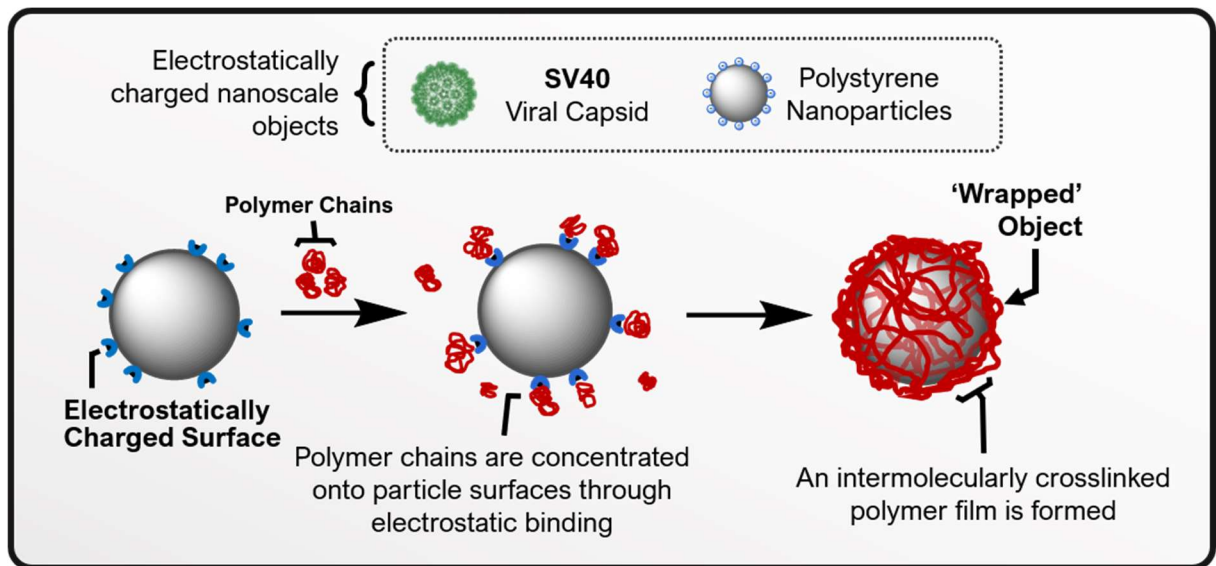


Table of Contents

2.1. Abstract	35
2.2. Introduction	36
2.3. Results and Discussion	37
2.3.1. Synthesis of and Characterization of Aldehyde Polymer Scaffold	37
2.3.2. Synthesis of Hydrazide Residues	39
2.3.3. Preparation of Dynamic Covalent Polyelectrolytes	40
2.3.4. Synthesis and Characterization of ‘Soft’ Polycation	42
2.3.5. Synthesis and Characterization of Polyelectrolyte SCPNs	43
2.3.6. ‘Shrink-Wrapping’ Studies with SV40 Viral Capsid	46
2.3.7. Fluorescence Titration Experiments Investigating Electrostatic Binding of Polyelectrolytes to SV40 Viral Capsid	52
2.3.8. Investigations on the ‘Shrink-Wrapping’ of Polystyrene NPs	54
2.3.9. Triggered ‘Unwrapping’ of Polystyrene Nanoparticles	63
2.3.10. Attempted Removal of ‘Hard’ Polyelectrolyte Coatings	65
2.3.11. Adsorption of ‘Soft’ Polyelectrolytes onto Polystyrene NPs	69
2.3.12. Adsorption of Linear Polycation upon SV40 Viral Capsid	73
2.4. Conclusion	77
2.5. Future Work	78
2.6. Experimental	79
2.7. References	85
2.8. Appendix A	86

2.1. Abstract

This chapter explores the ‘shrink-wrapping’ of electrostatically charged 3D nanoscale objects within dynamic covalent polyelectrolyte films. The incorporation of acyl hydrazone covalent crosslinks within these polyelectrolyte films was anticipated to impart additional stability to the adsorbed polymer, beyond that observed for the corresponding non-crosslinked polyelectrolyte layer. Experiments began with the ‘shrink-wrapping’ of Simian Virus 40 (**SV40**), a small icosahedral DNA tumour virus which displays a net negative surface charge upon the capsid exterior. Single-chain polymer nanoparticles (SCPNs) were engineered to display the complementary positively charged quaternary ammonium appendages upon their surfaces. It was hypothesized that favourable electrostatic polymer-virus interactions would thus concentrate SCPN chains onto the viral surface, and then drive ‘shrink-wrapping of **SV40** capsid. Dynamic light scattering (DLS) and zeta potential measurements were employed to monitor the ‘wrapping’ process, and fluorescence titration experiments provided fundamental insights regarding the nature of the interaction between polymer and capsid. To further explore ‘shrink-wrapping’ of electrostatically charged nanoscale objects, ‘wrapping’ experiments were conducted with a basic model system (**Model System I**) based upon sulfonate-functionalized polystyrene nanoparticles. Time-resolved DLS experiments were employed to monitor the adsorption of polyelectrolyte layers onto the periphery of the colloidal particles, which revealed a subtle increase hydrodynamic diameter of 10 – 30 nm, consistent with the formation of thin (5 – 15 nm) adsorbed polymer coating. This observation was corroborated by TEM (polymer coating \approx 4 nm) and zeta potential measurements, which revealed an increase in positive charge at the polystyrene surface that correlated with the administered Polymer Dose (PD). Upon addition of excess polycation, a complete surface-charge reversal was achieved, thus affording ‘wrapped’ polystyrene nanoparticles with good colloidal stability on account of their net positive charge. Control experiments were then undertaken to demonstrate the intermolecularly crosslinked nature of surface-bound polymer ‘wrapping’, by attempting to displace non-crosslinked polymer layers. These studies revealed that that the adsorption of ‘hard’ polyelectrolytes onto colloidal particles is an essentially irreversible process, a result which posed a significant challenge to experiments designed to demonstrate the intermolecularly crosslinked nature of the adsorbed polymer films. To circumnavigate the issues of irreversible polymer-particle binding, ‘wrapping’ experiments were conducted with ‘soft’ polyelectrolytes, the deprotonation of which permitted the displacement of the now charge-neutral polymer layer from the particle surface. These experiments produced encouraging results which support the hypothesis that nano- and microscale objects were successfully ‘shrink-wrapped’, however additional work is needed to adapt this strategy to the ‘wrapping’ of complex biological targets such as **SV40**.

2.2. Introduction

In recent years, the rapid formulation of novel vaccines has strongly benefitted from the development of virus-like particles (VLPs) for use as non-infectious virus alternatives, which lack all harmful genetic information but still retain the same protein surface structure and identical immunogenic properties to the naturally-occurring infectious virus.¹ A great limitation, however, is that viral capsids are delicate self-assembled protein structures which may suffer severe physical instability when placed in environments outside of physiological conditions.² Exposure to high temperatures and dehydrating conditions results in the eventual denaturing of proteins, rapidly followed by disassembly of the viral capsid.² By constructing a robust synthetic polymer 'wrapping' it is anticipated that VLPs can be protected from 'harsh' external environments, which may prevent their degradation and possibly even eliminate the requirement for cold transport and storage, two factors which add significant cost to vaccination programs in developing nations. Successful 'shrink-wrapping' of viral capsid also presents exciting opportunities in targeted-drug delivery, where VLPs have become increasingly popular vehicles³ for controlled-release on account of their uniform nanoscale size, well-defined surface structures, ease of fabrication and accessible chemical modification.⁴ Recent literature reports encapsulation of pharmaceutical compounds within the capsid (vector) interior, followed by molecular recognition of its outer surface to 'concentrate' the release of the drug at a target cell.⁵ 'Shrink-wrapping' thus presents a potential strategy to engineer viral surfaces, for example to introduce drug-delivery markers onto the capsid exterior, without requiring direct covalent modification of the virus proteins. Furthermore, in drug-delivery applications the presence of 'foreign' capsid within the body often provokes an immune-response, resulting in the reduced bioavailability of the drug. It is also hypothesized that development of an effective mechanism for on-demand 'wrapping' and 'unwrapping' of the capsid could mask the viral surface from the immune system, thus may offer scope to control the rate of cargo release and minimize any undesirable immune-response.⁶ This chapter reports studies on the 'shrink-wrapping' of a virus-like particle (Simian Virus 40) and a VLP model system (**Model System I**) based on polystyrene-sulfonate nanoparticles (**sNPs**), where SCPNs are concentrated onto the periphery of these substrates through complementary electrostatic interactions.

2.3. Results and Discussion

2.3.1. Synthesis and Characterization of Aldehyde Polymer Scaffold

Aldehyde acrylamide monomer **M1** (Fig. 1a) was synthesized in four steps and isolated as a white solid (3.05 g, 43 % overall yield). Monomer **M1** was prepared (Fig. 1a) by treatment of 4-carboxybenzaldehyde with trimethylorthoformate in acidic methanol (i) affording the acetal-protected intermediate **1**. The methyl ester of **1** was subjected to aminolysis with a large excess of 1,2-ethylenediamine (ii) to furnish intermediate **2**. Following purification by column chromatography, the primary amine group of **2** was acetylated by dropwise addition of acryloyl chloride to yield the acrylamide **3**. Treatment of **3** with 2 M HCl afforded monomer **M1**, which was isolated by column chromatography. The assigned ^1H NMR spectrum of **M1** (Fig. 1b) matched the expected structure and was entirely consistent with the literature reports.⁷

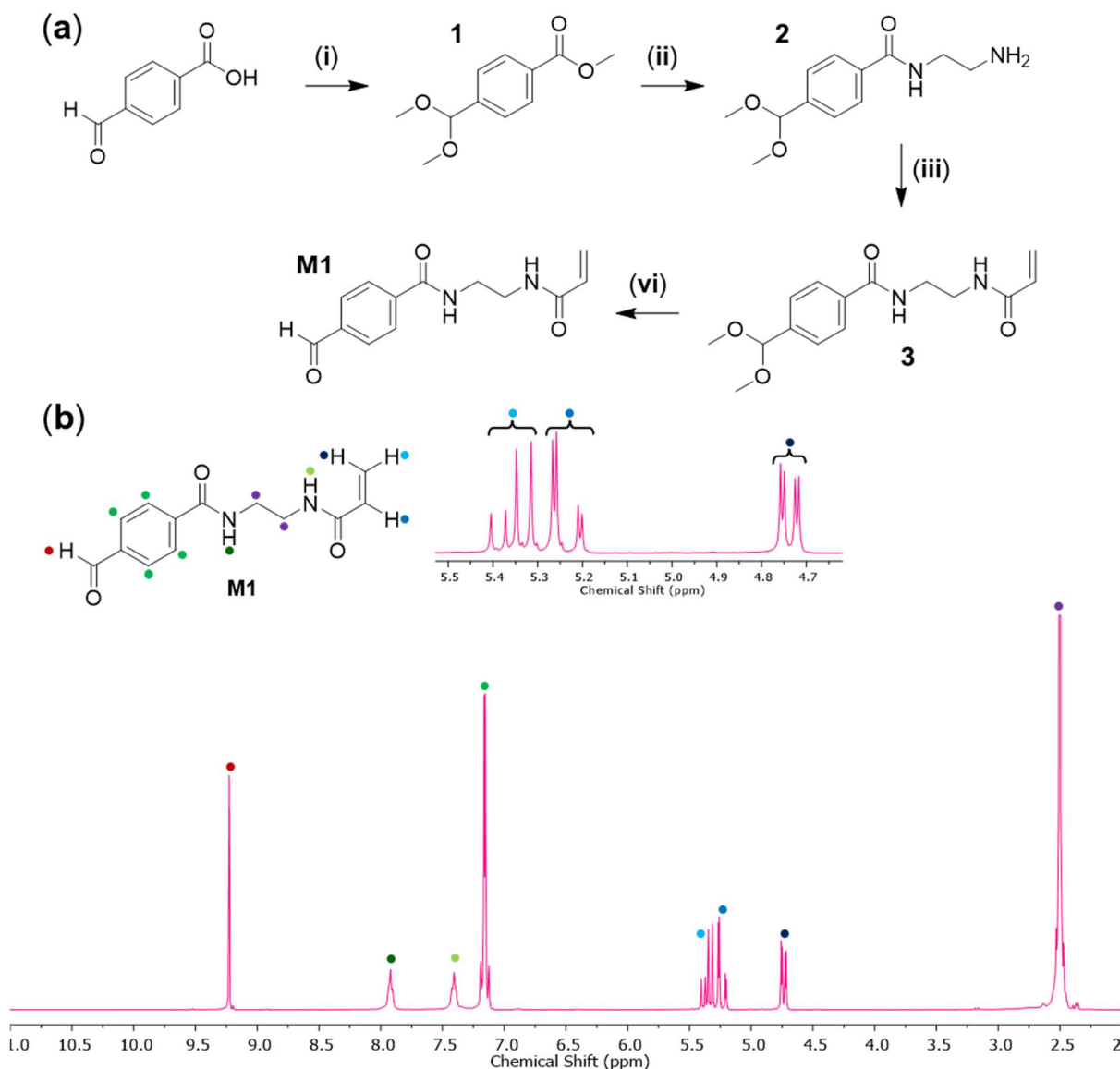


Figure 1: (a) Synthesis of aldehyde acrylamide monomer **M1**. Step (i) CH(OMe)₃, H₂SO₄, MeOH, reflux, 18 h. Step (ii) 1,2-ethylenediamine, reflux, 48 h. Step (iii) acryloyl chloride, Et₃N, CH₂Cl₂, 0 °, 18 h. Step (iv) 50:50 Acetone:2M HCl_(aq). (b) ^1H NMR spectrum (d_6 -DMSO, 400 MHz) of monomer **M1**, with structural assignments shown.

Aldehyde-functionalized scaffold (**P1**) was prepared (Fig. 2a) by reversible addition-fragmentation chain-transfer (RAFT)⁸ copolymerization of aldehyde monomer **M1** with *N,N*-dimethylacrylamide (**DMA**), a comonomer selected to impart aqueous solubility to the resulting polymer scaffold. Copolymer **P1** was shown by ¹H NMR spectroscopy (Fig. 2b) to have a degree of polymerization (D_p) of 89, containing approximately 21 aldehyde units (n) and 68 DMA (m) units, as determined by ¹H NMR end group analysis (Fig. 2d). Gel permeation chromatography (GPC) analysis of **P1**^{*} (Fig. 2c) revealed a monomodal distribution of polymers with a low PDI of 1.15, indicative of a well-controlled polymerization.

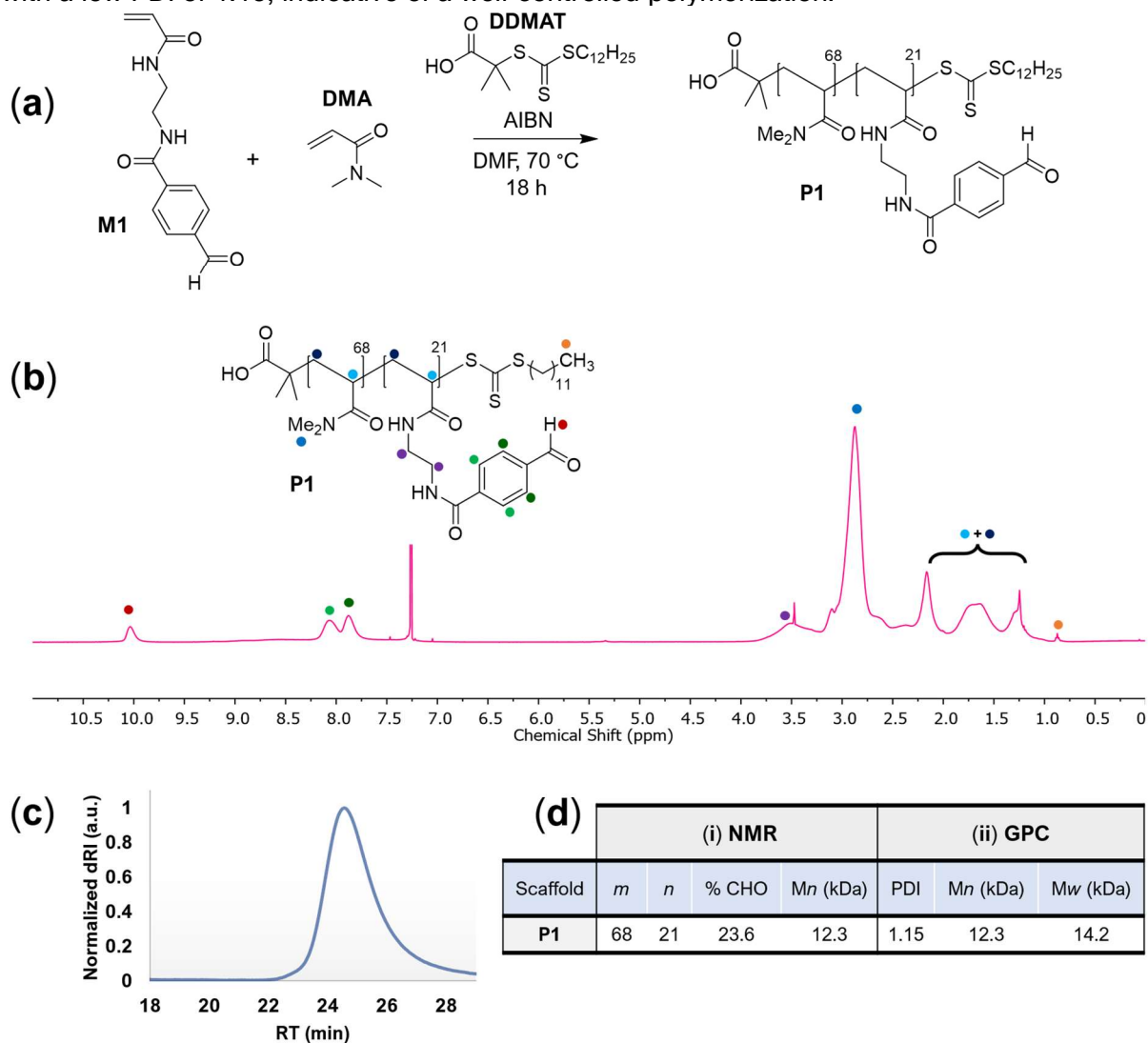
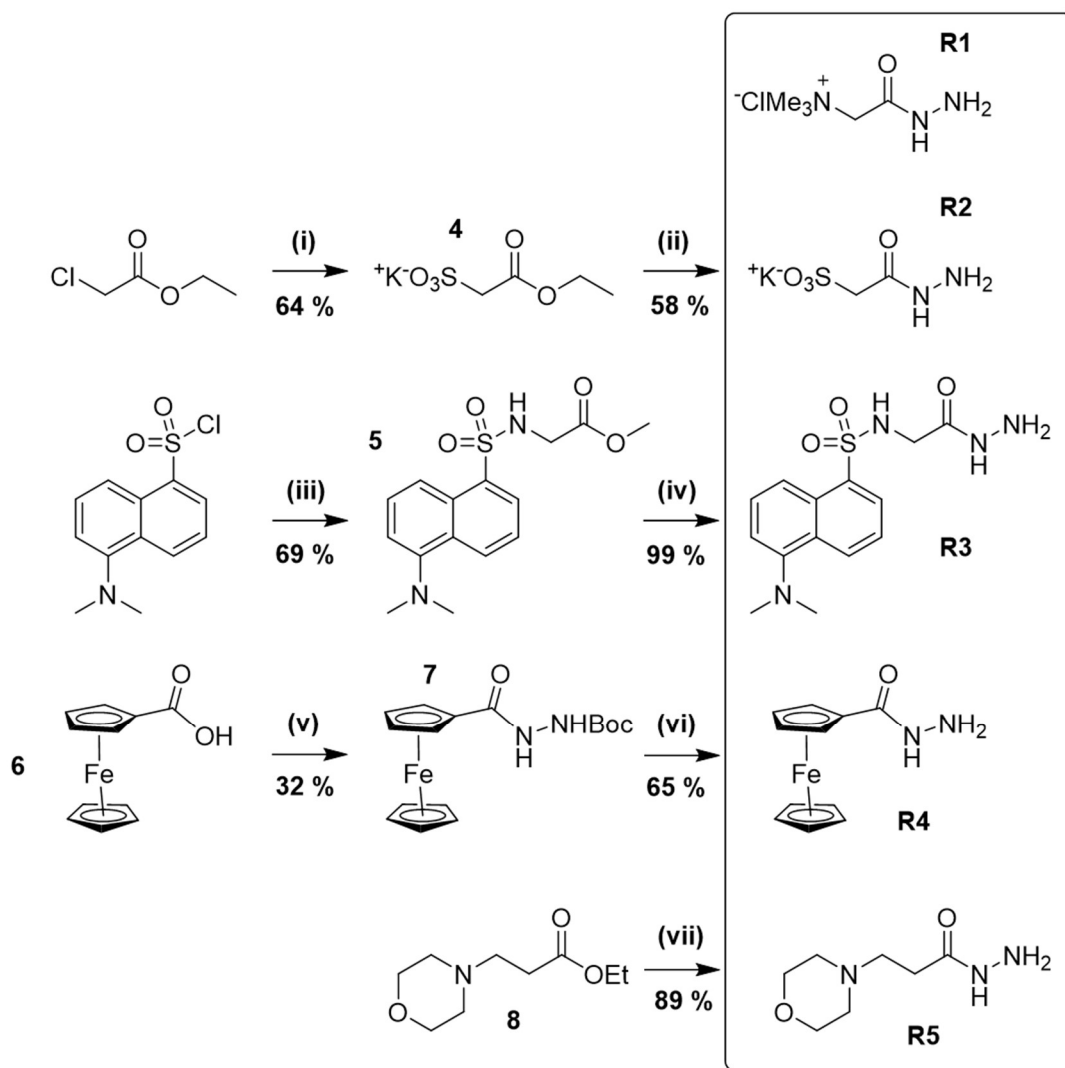


Figure 2: Synthesis and characterization of aldehyde-functionalized polymer scaffold **P1** (a) RAFT copolymerization of aldehyde monomer **M1** and *N,N*-dimethylacrylamide (**DMA**) affording aldehyde copolymer **P1**. (b-c) Characterization of aldehyde scaffold **P1** by ¹H NMR (CDCl₃, 300 MHz) spectroscopy (b) and GPC analysis (c). (d) Table of characterization data of **P1** by ¹H NMR spectroscopy (i) and GPC analysis (ii).

* Molecular weight (MW) of polymer samples were determined by calibration of the GPC instrument with a set of near-monodisperse poly(methylmethacrylate) (pMMA) standards. A calibration plot of MW versus retention time (RT) was obtained from pMMA standards. Comparison of the retention time at the polymer peak maximum (RT_{max}) to the RT versus MW calibration plot allowed for the MW of the polymer sample to be deduced. Whilst this is method

2.3.2. Synthesis of Hydrazone Residues

Hydrazone residues **R2-R5** were prepared according Scheme 1, and hydrazone **R1** (Girard's Reagent T) is commercially available. Dansyl hydrazone **R3** was synthesized by Dr Clare Mahon.^{9a} See experiment section for full synthetic protocols, characterization and ¹H NMR data.



Scheme 1: Synthesis of hydrazone residues (**R2 - R5**) used for the preparation of polyelectrolyte scaffolds. Step (i) K_2SO_3 , H_2O , reflux, 8 h. Step (ii) $\text{N}_2\text{H}_4\cdot\text{H}_2\text{O}$, MeOH, reflux 16 h. Step (iii) Et_3N , CH_2Cl_2 , rt, 24 h. (iv) $\text{NH}_2\text{NH}_2\cdot\text{H}_2\text{O}$, MeOH, rt, 18 h. Step (v) *tert*-Butylcarbazate, EDC, CH_2Cl_2 , rt, 18 h. Step (vi) 1:1 TFA/ CH_2Cl_2 , 0 °C. Step (vii) $\text{N}_2\text{H}_4\cdot\text{H}_2\text{O}$, EtOH, reflux 18 h.

Sulfonate residue **R2** was prepared as previously reported,^{9a} whilst morpholine hydrazone (**R5**) was prepared^{9b} (Scheme 1, step vii) by hydrazinolysis of ethyl ester **8** and isolated in an 89 % yield. After workup **R5** was characterized by ¹H NMR spectroscopy and used without further purification. Ferrocene hydrazone **R4** was prepared by a modified literature protocol,¹⁰ as it could not be prepared by hydrazinolysis of the corresponding methyl ester (see page 87).

of analysis yields only an approximate molecular weight, these values were entirely consistent with MWs deduced by ¹H NMR end group analysis, indicating a good level of accuracy in MW determination

2.3.3. Preparation of Dynamic Covalent Polyelectrolytes

'Hard' polyelectrolytes[†] (**P2** - **P3**) were prepared (Fig. 3) by grafting hydrazide residues (**R1/R2**) onto aldehyde scaffold **P1**. Aldehyde groups displayed along **P1** were 'decorated' with sulfonate residue (**R2**) (Fig. 3a) and Girard's reagent T (**R1**) (Fig. 3b), to afford linear polyanion **P2** and linear polycation **P3**, respectively.[‡] 'Unbound' hydrazide residues and other non-solvent contaminants were removed from the 'decorated' polymer scaffolds by dialysis against water. Subsequent lyophilization afforded the charged polymers (**P2** - **P3**) as low-density solids which were characterized by ¹H NMR spectroscopy (Fig. 4a-b).

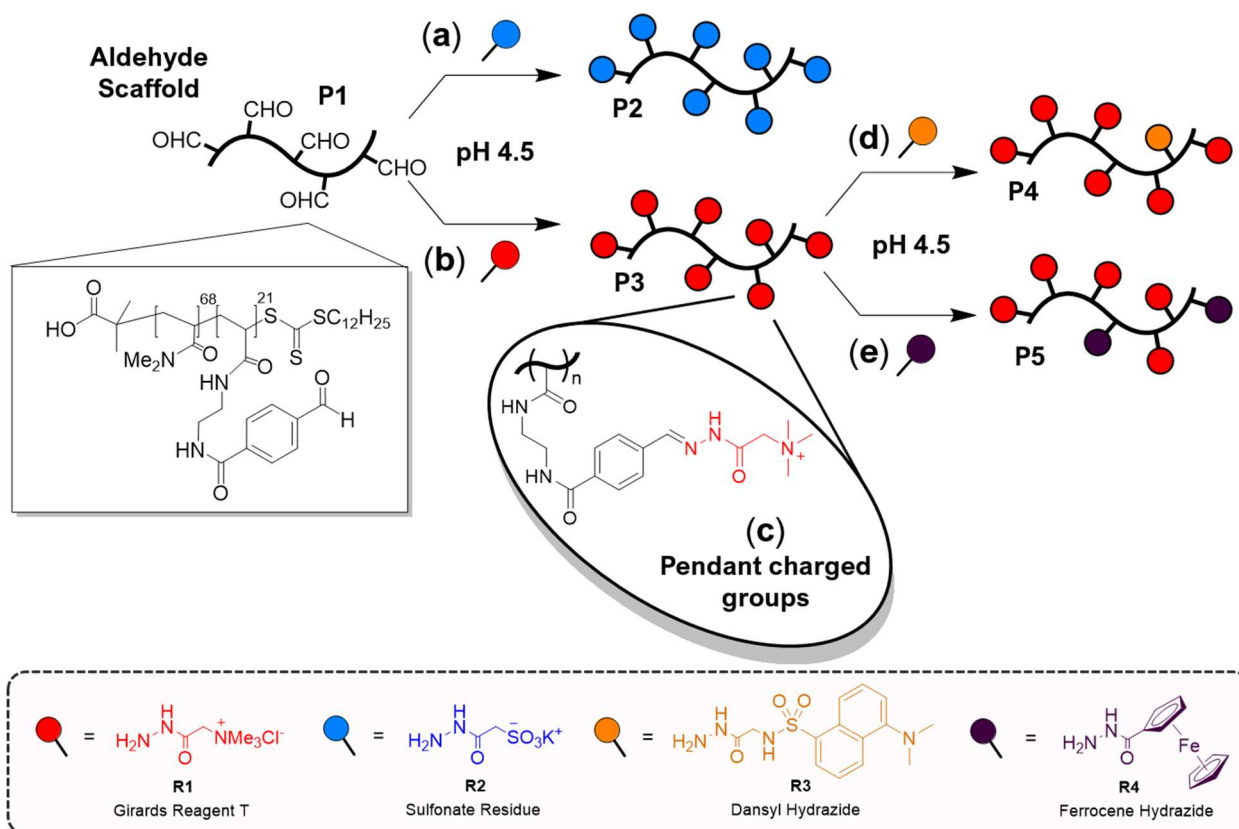


Figure 3: Preparation of 'hard' polyelectrolytes (**P2-P5**). (a-b) Decoration of aldehyde scaffold **P1** with hydrazide residues (**R1-R2**) to afford hydrazone-functionalized polymers (**P2/P3**) with pendant charged groups (c). Cationic polyelectrolyte **P3** (b) was further labelled (d) with dansyl hydrazide (**R3**) and ferrocene hydrazide (**R4**) (e) to afford **P4/P5**, which could be visualized by fluorescence microscopy (**P4**) and TEM (**P5**), respectively.

[†] A polyelectrolyte is defined as a polymer chain which displays multiple electrostatic charges. 'Hard' polyelectrolytes are polymers which display multiple electrostatically charged groups which cannot be readily neutralized by protonation or deprotonation. Sulfonate (SO_3^-)-functionalized polymers (**P2**) are thus 'hard' polyanions and quaternary ammonium (NMe_3^+)-functionalized polymers (**P3** - **P5**) are 'hard' polycations.

[‡] Condensation reaction between polyaldehyde scaffold **P1** and hydrazides (**R1** - **R2**) was quantitative in aqueous solution, with formation of the thermodynamically stable hydrazone bond (Fig. 3c) being fast under mildly acidic conditions.

^1H NMR spectra (Fig. 4a-b) of polyanion **P2** and polycation **P3** revealed complete disappearance of the aldehyde signal (δ 10.04 ppm) and the concomitant emergence of hydrazone C-H signals (orange) at δ 8 – 10 ppm. Multiple resonances were observed for the hydrazone C-H environment on account of hindered rotation about the amide bond, giving rise to *syn/anti* isomerization, consistent with previous literature reports.¹¹ These observations demonstrate aldehyde scaffold **P1** was completely ‘decorated’ with hydrazides **R1/R2** to afford the corresponding hydrazone-functionalized polyelectrolytes **P2/P3**, which display 21 sulfonate and quaternary ammonium residues, respectively. ^1H NMR spectra obtained after purification of **P2/P3** by dialysis, confirmed that these polyelectrolytes were essentially free of small molecule impurities.

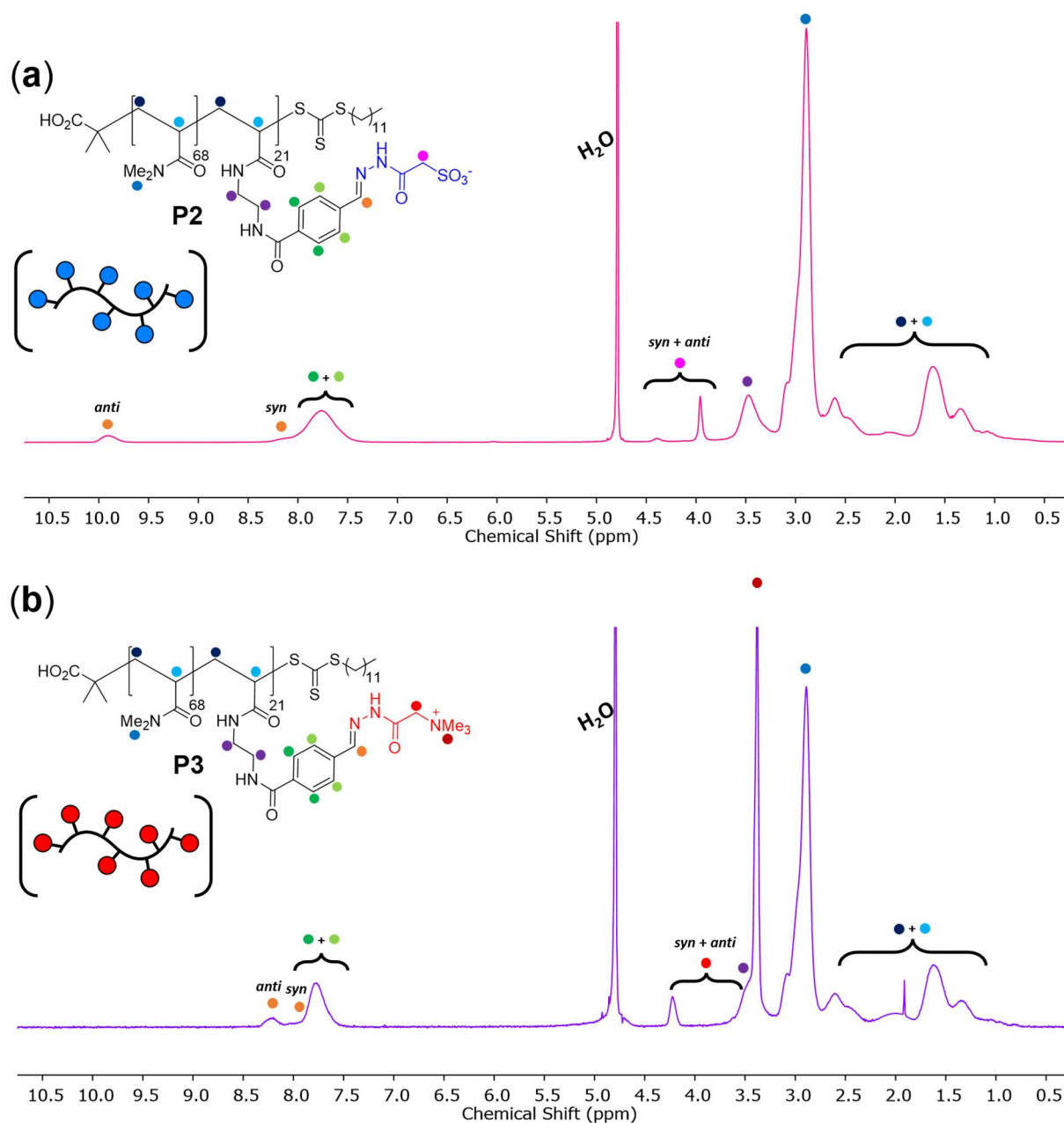


Figure 4: Assigned ^1H NMR spectra (400 MHz, D_2O) of linear polyanion **P2** (a) and linear polycation **P3** (b) after their purification by dialysis.

2.3.4. Synthesis and Characterization of ‘Soft’ Polycation

‘Soft’ polycation **P7**[§] bearing pendant morpholine moieties was prepared by ‘decoration’ of aldehyde scaffold **P6** with morpholine hydrazide **R5** (Fig. 5a). Aldehyde-functionalized scaffold **P6** (Fig. 5b) is a highly water-soluble poly(ethylene glycol)acrylate-based polymer, the synthesis and characterization of which is discussed in Chapter 3.

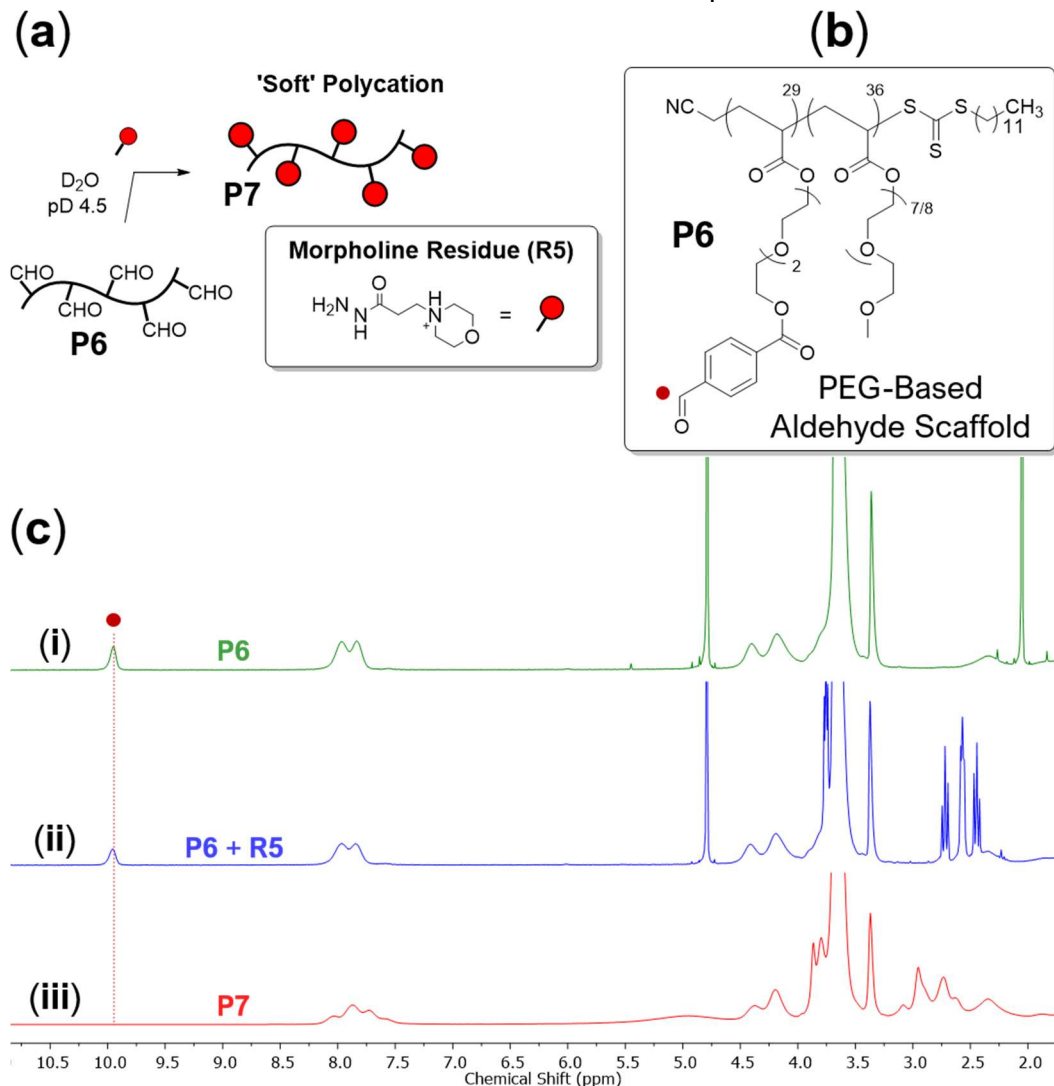


Figure 5: (a) Preparation of morpholine-functionalized ‘soft’ polyelectrolyte (**P7**) by grafting of morpholine hydrazide (**R5**) onto aldehyde scaffold **P6**. **P6** (b) is a poly(ethyleneglycol)acrylate-based aldehyde copolymer. (c) 1H NMR spectra (D₂O, 300 MHz) of aldehyde scaffold **P6** (i), **P6** + morpholine hydrazide **R5** (ii) and ‘soft’ morpholine polycation **P7** (iii), after purification by dialysis.

1H NMR spectroscopy (Fig. 5c) was employed to monitor the reaction of morpholine hydrazide **R5** with aldehyde scaffold **P6**, with complete disappearance of the ‘diagnostic’ aldehyde signal at ~ 10 ppm (Fig. 5c, iii) revealing complete ‘decoration’ of all 29 aldehyde moieties upon **P6** with **R5**. Figure 5c, iii shows the 1H NMR spectrum of **P7** after its purification by dialysis.

[§] **P7** is classed as a ‘soft’ polycation, as the electrostatically charged morpholine appendages can be readily protonated/deprotonated by adjusting the pH of solution.

2.3.5. Synthesis and Characterization of Polyelectrolyte SCPNs

Cationic single chain polymer nanoparticles (**Cationic SCPNs**) displaying ‘hard’ quaternary ammonium positive charges were synthesized (Fig. 6a) by intramolecular crosslinking of the linear polyelectrolyte chain (**P3**) with succinic dihydrazide (**SD**) (i-ii) under high dilution of ≤ 5 mg/mL. Appropriate conditions for controlled SCPN formation were determined from preliminary experiments; dropwise addition of 0.33 mM **SD** into a fast-stirred aqueous solution of **P3** (5.00 mg/mL), which afforded ‘dynamic’ **Cationic SCPNs** (**1**). Two crosslinker stoichiometries were explored; **Cationic SCPN-1** (a) and **Cationic SCPN-2** (b) which were engineered to contain 1 and 2 crosslinks per polymer chain, respectively. The covalent crosslinks embedded within these SCPNs were acyl hydrazone linkages (Fig. 6a, iii), the dynamic covalent nature of which is key to the concept of ‘structural metamorphosis’.

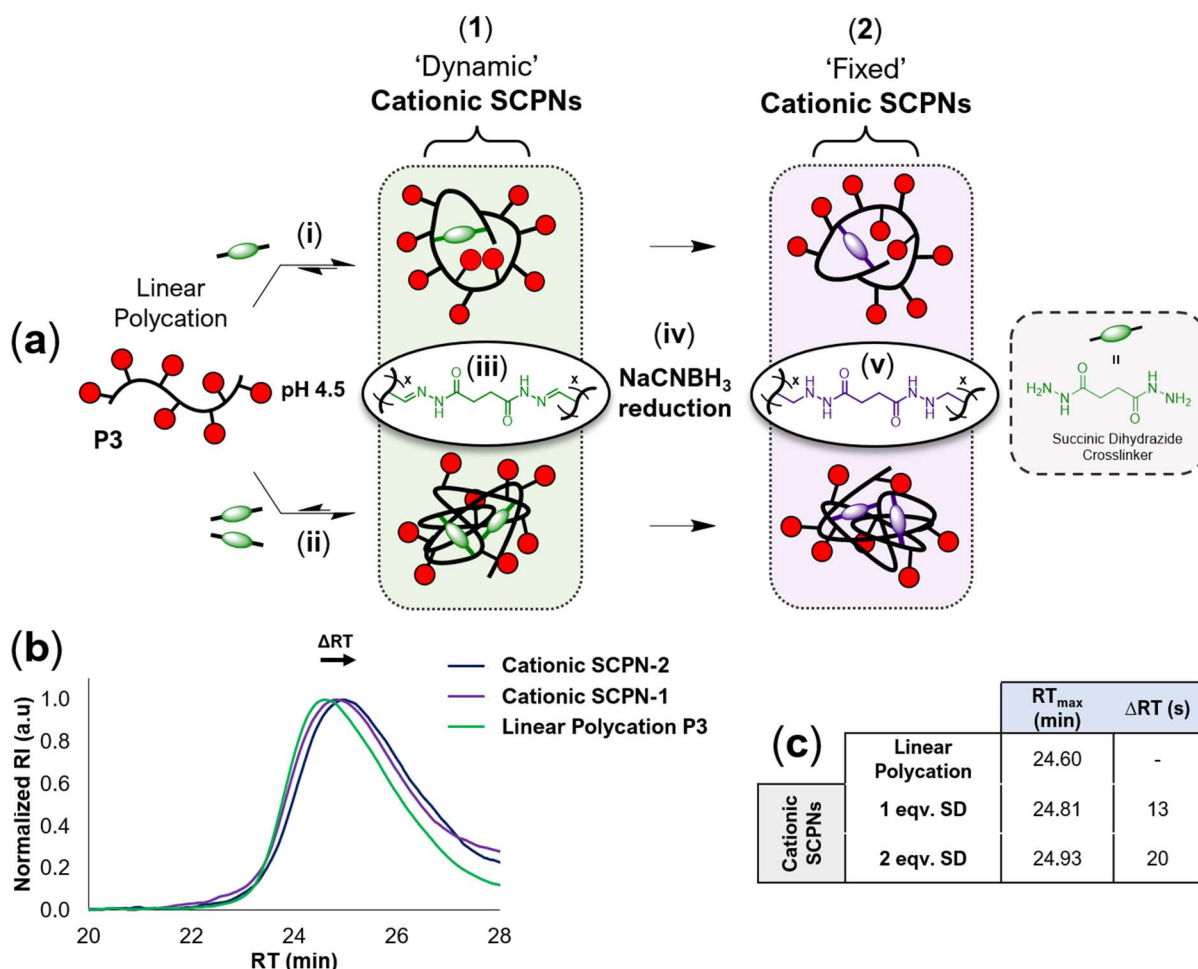


Figure 6: Synthesis (a) and characterization (b) of **Cationic SCPNs**. (a) Addition of 1-2 equivalents of succinic dihydrazide (i-ii) induced intra-chain crosslinking of linear polycation **P3** to yield **Cationic SCPNs** (**1**), which contain dynamic covalent acyl hydrazone crosslinks (iii). Chemical reduction (iv) of ‘dynamic’ **Cationic SCPNs** afforded ‘fixed’ **Cationic SCPNs** (**2**), whose crosslinks were no longer dynamic on account of their reduction from acyl hydrazone (a dynamic bond) (ii) to the corresponding amine (non-dynamic / fixed) (v). (b) Normalized differential refractive index (dRI) traces revealed a small increase in retention time (RT) for **Cationic SCPN-1** (purple) and **Cationic SCPN-2** (blue) relative to that of the linear polycation **P3** (red), consistent with chain collapse. (c) Retention times at peak maxima (RT_{max}) and shift in retention time (ΔRT) relative to the linear chain (**P3**).

To ensure that no unwanted ‘structural metamorphosis’ occurred during their characterization, cyanoborohydride reduction (Fig. 6a, **iv**) of the ‘dynamic’ acyl hydrazone bonds (**iii**) within the SCPNs was employed to chemically ‘fix’ the crosslinks as the corresponding amine (**v**), thus preventing any further structural rearrangement by component exchange. These ‘fixed’ **Cationic SCPNs** (Fig. 6a, **2**) were then characterized by GPC (Fig. 6b-c).

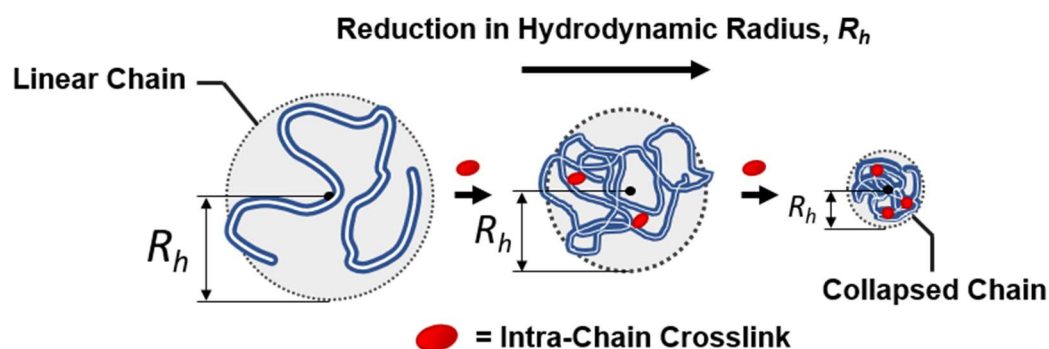


Figure 7: Chain collapse upon formation of **SCPns**. Increasing the density of intra-chain crosslinks affords a contraction of the polymer chain, resulting in a reduction in hydrodynamic diameter, R_h .

Successful formation of **SCPns** was confirmed by GPC analysis (Fig. 6b), which revealed a chain collapse consistent with intra-chain crosslinking.¹² The GPC traces (Fig. 6b) of **Cationic SCPN-1** (purple) and **Cationic SCPN-2** (blue) – which contain 1 and 2 equivalents of **SD**, respectively – showed a slight increase in retention time (RT) relative to linear polycation (**P3**) (green). Furthermore, GPC traces of **Cationic SCPN-1** and **Cationic SCPN-2** revealed a steady increase in RT as the density of **SD** crosslinker was increased. These observations were entirely consistent with literature,¹² which states that the observed increase in RT can be rationalized by the formation of intra-chain crosslinks, which cause a collapse of linear polymer chain (Fig. 7), thus reducing the hydrodynamic radius (R_h) and increasing the time to be eluted from the GPC column (RT).

Morpholine SCPNs were prepared (Fig. 8a) by intramolecular crosslinking of morpholine-functionalized scaffold **P7** with 1 equivalent of succinic dihydrazide under high dilution (5 mg/mL **P7**). Chemical reduction of ‘dynamic’ **Morpholine SCPNs** (i) with sodium cyanoborohydride afforded ‘fixed’ **Morpholine SCPNs** (ii), which were characterized by GPC (Fig. 8b). GPC of **Morpholine SCPNs** (red GPC trace) revealed the anticipated increase in RT, relative the linear polymer chain **P7**, which was consistent with the formation of intramolecularly crosslinked SCPNs.

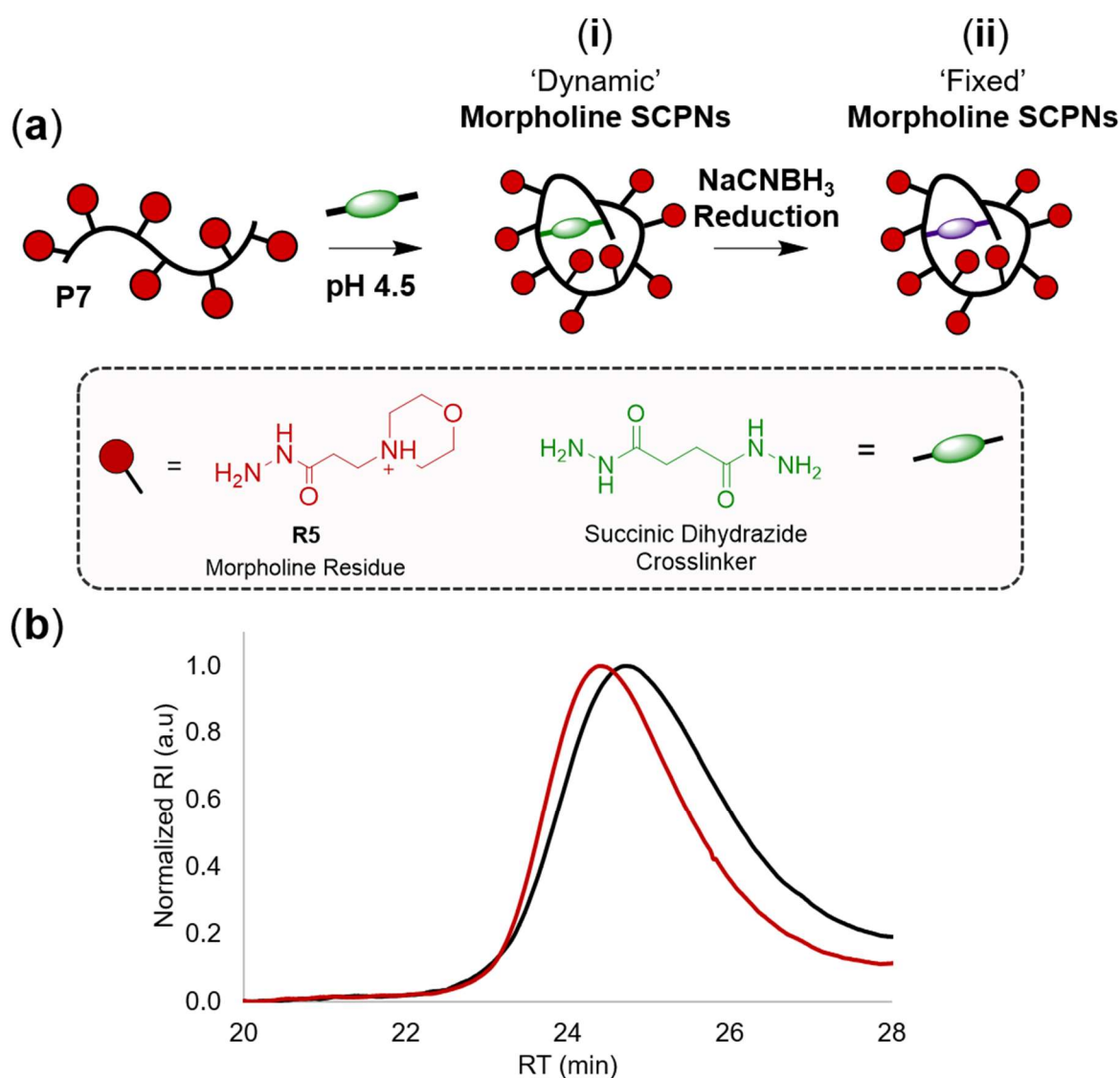


Figure 8: (a) Preparation of **Morpholine SCPNs** (i) by intramolecular crosslinking of linear morpholine scaffold **P7** (ii) with succinic dihydrazide under high dilution. (b) GPC characterization of ‘fixed’ **Morpholine SCPNs** (black line) and linear polymer chain **P7** (red line).

2.3.6. ‘Shrink-Wrapping’ Studies with SV40 Viral Capsid

To address the objective of developing a polymer ‘wrap’ for virus-like particles (VLPs), initial work focussed on ‘wrapping’ samples of **SV40** viral capsid. The **SV40** VLPs were produced in the laboratory of Prof. W. B. Turnbull at the University of Leeds by recombinant expression of the major capsid protein (**VP1**) from *E. Coli*. Dialysis of **VP1** pentamer (Fig. 9b) against increasing concentrations of ammonium sulfate afforded successful assembly of the complete **SV40** viral capsid (Fig. 9a), which was confirmed by TEM (Fig. 9d) and DLS analysis (Fig. 10). The icosahedral viral capsid of **SV40** (Fig. 9a) is a spherical protein assembly whose outer shell is comprised of 72 pentamer subunits (360 copies of **VP1** total), which are connected predominantly through disulfide linkages and calcium-mediated interactions,¹³ to afford a ‘hollow’ football-like structure with an external diameter ≈ 50 nm.¹⁴

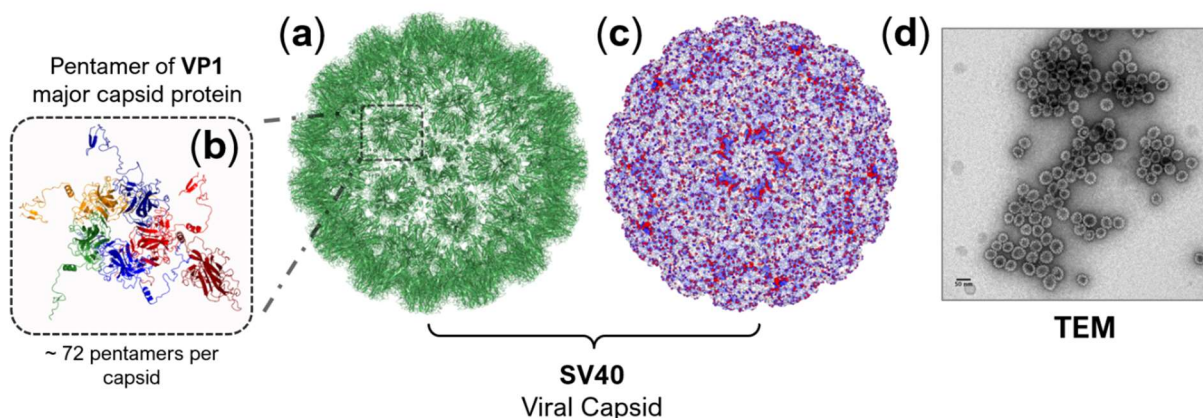


Figure 9: (a) The cryoEM-derived structure (PDB entry: 1sva) of **SV40** viral capsid (ribbon representation) and its associated electrostatic charge map (c). Positive and negative charges are shown in red and blue, respectively. **SV40** is assembled from pentamers of **VP1** (c), the major capsid protein. (d) TEM micrograph of assembled **SV40** capsids stained with uranyl acetate contrast agent, obtained by the laboratory of Prof. W. B. Turnbull.

SV40 capsid was characterized by dynamic light scattering (DLS) (Fig. 10a-d, f) and zeta potential (ZP) (Fig. 10e) measurements. ZP measurements revealed that the capsid possessed a net negative surface charge ($ZP = -34 \pm 3$ mV) at neutral pH, consistent with the reported electrostatic surface (Fig. 9b) and ZP values reported¹⁵ for the major capsid protein (**VP1**), which was $ZP_{VP1} = -15$ mV at neutral pH. This result suggests moderate stability against the aggregation of viral capsids in aqueous solution, on account of significant electrostatic repulsion between approaching particles. Importantly, the negative surface charge implies that the **SV40** viral capsid would interact favourably with polycations at neutral pH. Strong electrostatic interactions between **Cationic SCPN-1** and viral capsid are crucial, as this binding provides a driving force for the concentration of **Cationic SCPN-1** chains upon the capsid surface (Fig. 11b) and their subsequent ‘metamorphosis’ into an intermolecularly crosslinked polyelectrolyte film.

On account of the reported¹⁴ 50 nm diameter of **SV40** virus, it was strongly anticipated that the capsid would have a hydrodynamic diameter of 50 – 65 nm. Whilst DLS (Fig. 10c-d) consistently reported a **number-average** D_h of 59 ± 6 nm, the **z-average** and **volume-average** D_h were significantly larger than expected, at 106 and 186 nm, respectively. These observations suggest the presence of multi-capsid aggregate species, which may distort the measured hydrodynamic diameters (D_h) to larger than expected values,¹⁶ in excess of 180 nm. Furthermore, DLS reported a PDI of 0.265, considerably higher than what would be expected for a mono-disperse sample of viral capsids.

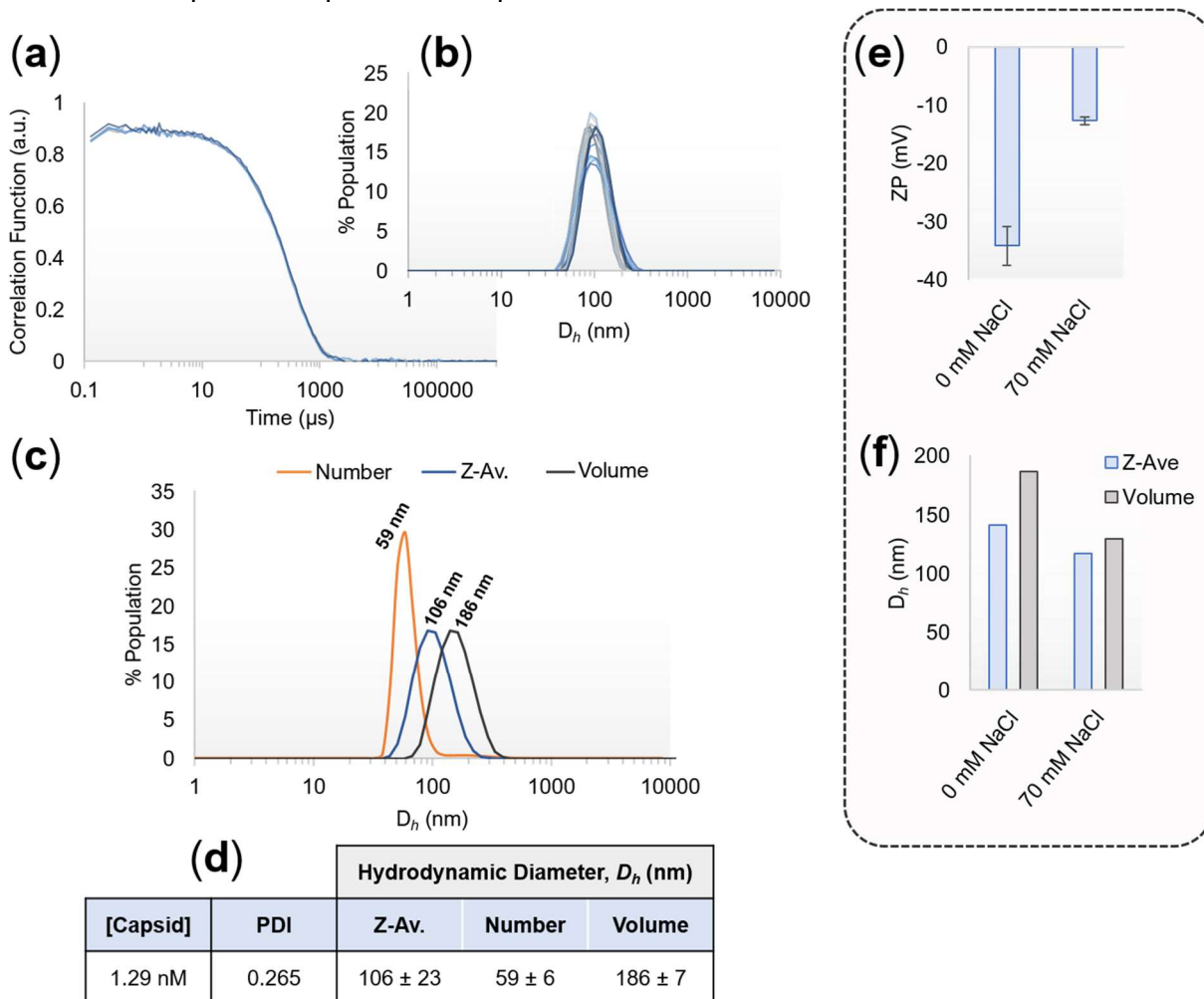


Figure 10: DLS (a-d) and zeta potential (e) characterization of **SV40** viral capsid: (a) Representative DLS correlation functions and (b) their associated z-average particle-size distributions (PSDs). (c) PSDs derived from the number-average (orange), z-average (blue) and volume-average (grey) data. (d) DLS summary table. Zeta potential (e) and DLS (f) of **SV40** capsid in the presence (70 mM NaCl) and absence of salt. All measurements were made with [capsid] = 1.29 nM in 10 mM TRIS (pH 7.4), 1 mM CaCl_2 , 0 - 100 mM NaCl, conditions under which **SV40** is known to have good stability against capsid disassembly.

In the hope of eliminating any capsid aggregation, stability screenings were conducted to identify conditions under which the **SV40** capsid displayed good colloidal stability, and thus the DLS results obtained should be more optimal, with values closer to those expected ($D_h \approx 50 - 65$ nm) for near-monodisperse **SV40** VLPs. A range of aqueous buffers types (TRIS, HEPES, phosphate), salt compositions and concentrations (0 – 200 mM NaCl) (Fig. 10e-f) were explored, and a range of capsid concentrations (0.01 - 120 nM) were investigated. Successive filtering/sonication of the sample and addition of SDS surfactant did not yield significant improvements to the observed DLS of viral capsid – observations which suggest that the viral capsid supplied was slightly polydisperse in nature, perhaps containing partially assembled or capsid was progressed to further experimental study, on account of the possibility that the adsorption of a virus-bound polyelectrolyte layer might improve the colloidal stability of the **SV40** and thus suppress aggregation, leading to DLS analysis of improved quality. Adsorption of polycation (**Cationic-SCPN-1**) (Fig. 11b, i) onto the periphery of the negatively-charged **SV40** capsid (Fig. 11b, ii) was monitored by DLS analysis (Fig. 12), which was anticipated to reveal a subtle increase in hydrodynamic diameter (D_h) of the ‘coated’ virus (Fig. 11b, v) relative to the D_h of ‘naked’ capsid that would be consistent with the formation of a virus-adsorbed polyelectrolyte layer of thickness, L (Fig. 11b, v).

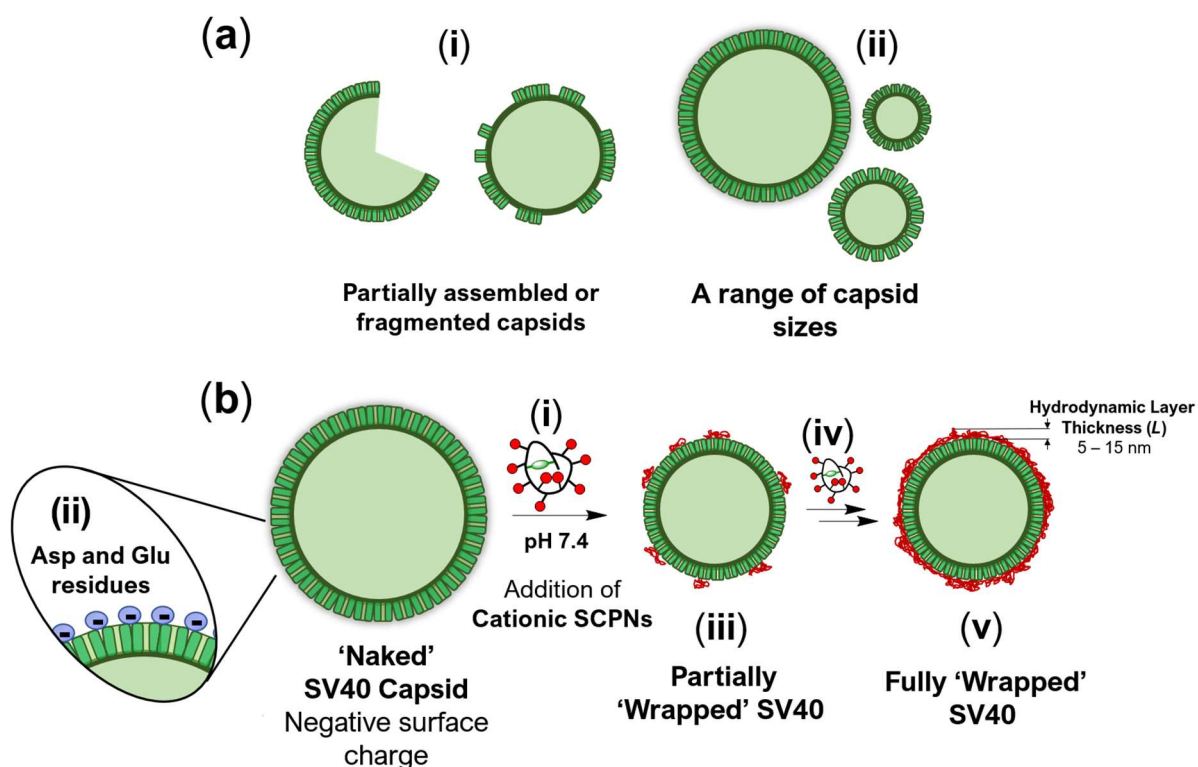


Figure 11: (a) The slightly polydisperse nature of **SV40** viral capsid by DLS may be explained by the presence of partially formed/fragmented capsids (i) or a range of capsid sizes (ii) within the sample. (b) Adsorption (i) of **Cationic SCPNs** onto negatively-charged (ii) **SV40** viral capsid to form a thin polyelectrolyte ‘coating’ (iii) within a thin polyelectrolyte layer. Addition of excess **Cationic SCPNs** (iv) was required to obtain **SV40** capsid which were fully ‘wrapped’ (v) within a polyelectrolyte layer with hydrodynamic thickness, L .

SV40 viral capsid was ‘wrapped’ (Fig. 11b, i-v) with a polyelectrolyte layer by titrating small quantities of **Cationic SCPN-1** into a buffered (pH 7.4) solution of **SV40** capsid and the hydrodynamic diameter (D_h) was monitored by DLS analysis (Fig. 12a, ii). The **z-average** D_h of ‘naked’ viral capsid was reported as 121 ± 5 nm (Fig. 12a, i), whilst the **Cationic SCPN-1** ‘wrapped’ capsid had D_h 155 ± 10 nm, thus revealing a 34 nm increase in D_h , consistent with the formation of a thin polyelectrolyte layer (17 nm) adsorbed onto the periphery of the viral capsid. The apparent thickness of this polyelectrolyte layer (L) was calculated by subtracting the hydrodynamic radius, R_h of the ‘coated’ capsid (77 ± 5 nm) from that of the naked capsid (60 ± 2), giving a layer thickness, L of 17 ± 7 nm.

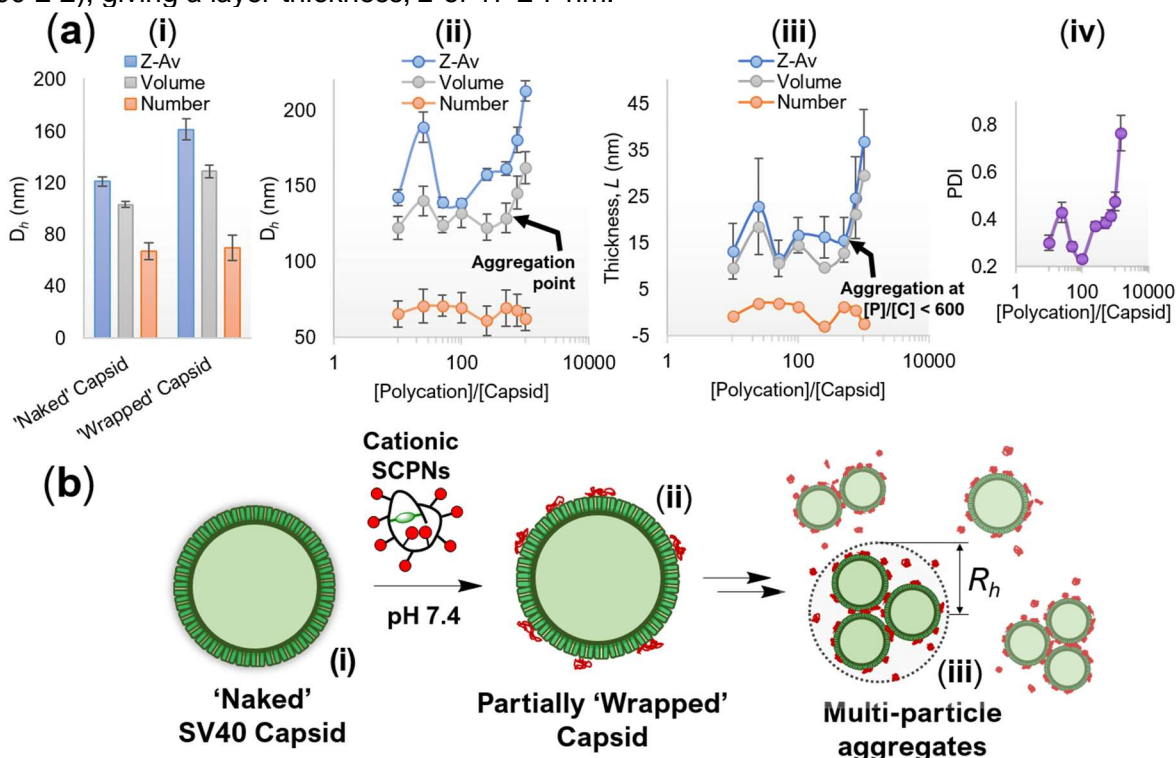


Figure 12: (a) DLS characterization of ‘wrapped’ **SV40** capsids. [capsid] = 29.3 nM in 7.7 mM TRIS (pH 7.4), 20 mM NaCl, 1 mM CaCl₂. (i) Hydrodynamic diameter (D_h) of ‘naked’ capsid and polyelectrolyte ‘wrapped’ **SV40** capsid ([Polycation]/[Capsid] = 500). (ii) DLS titration profiles for addition of **Cationic SCPN-1** into **SV40** capsid, where D_h of the ‘wrapped’ viral capsids is given as a function of the [polycation]/[capsid] ratio. The apparent thickness (L) of the adsorbed polymer layer (iii) was derived from changes in the particle diameter (D_h). (iv) Polydispersity index (PDI) versus [Polycation]/[Capsid] stoichiometry. Error bars show standard deviation. (b) Addition of **Cationic SCPN-1** to viral capsid was hypothesized to drive the formation of multi-particle aggregate species (iii), as were observed by DLS.

The titration profiles for the addition of **Cationic SCPN-1** into **SV40** capsid were obtained by DLS (Fig. 12a, ii), where D_h (**z-average**, **volume**, **number**) is plotted as function of the molar concentration ratio [polycation]/[capsid] and error bars indicate standard deviation. The corresponding polymer layer thickness, L values were calculated and plotted (Fig. 12a, iii) as a function of [polycation]/[capsid]. DLS results (Fig. 12a, ii) revealed that the **number-average** D_h showed an average of 67 ± 3 nm over the entire titration profile, indicating a negligible (0 ± 2 nm) increase in particle size upon increasing the concentration of **Cationic SCPN-1** – an observation which suggests no polymer is bound upon the periphery of **SV40** capsid. The

volume and **z-average** D_h , however, revealed a significant increase in particle size, especially when **Cationic SCPN-1** was present in greater than a 600-fold excess relative to the viral capsid ($[\text{polycation}]/[\text{capsid}] > 600$). At $[\text{polycation}]/[\text{capsid}] \approx 500$ the **volume-average** D_h was 129 ± 10 nm, a number which sharply increased to $D_h = 162 \pm 11$ nm at $[\text{polycation}]/[\text{capsid}] \approx 1000$, with no evidence of reaching a plateau. The latter D_h value corresponded to a thickness, L of 30 nm (Fig. 12a, **iii**), a number which is significantly larger than expected.^{**} Furthermore, the sample polydispersity index (PDI)(Fig. 12a, **iv**) was observed to dramatically increase at $[\text{polycation}]/[\text{capsid}] > 600$. These observations, together with an observed decrease in the quality of the DLS correlation function, suggests that above $[\text{polycation}]/[\text{capsid}] = 600$ the particle sizes measured by DLS were significantly distorted by aggregation which leads to larger than expected D_h values,¹⁶ (Fig. 12a, **i-ii**) most likely on account of the formation of multi-particle aggregates (Fig. 12b, **iii**). DLS results obtained at $[\text{polycation}]/[\text{capsid}] > 600$ were thus considered unreliable and discounted from the discussion, whilst DLS obtained below $[\text{polycation}]/[\text{capsid}] \approx 600$ was considered acceptable, on account of minimal levels of aggregation being observed by DLS. Below $[\text{polycation}]/[\text{capsid}] \approx 600$, the ‘coated’ particle size (Fig. 12a, **ii**) was approximately constant, with $D_h = 128 \pm 6$ nm, indicating a polymer layer thickness, $L \approx 10 - 15$ nm (Fig. 12a, **iii**).

Intriguingly, repetition of the above experiment in the absence of 20 mM NaCl – a salt which was anticipated to exacerbate aggregation of ‘wrapped’ **SV40** capsids in aqueous solution^{††} – afforded slightly inferior DLS results (Fig. 13), with aggregation processes now dominating DLS at $[\text{polycation}]/[\text{capsid}] < 250$. An extended range of polycation:capsid stoichiometries were explored ($[\text{polycation}]/[\text{capsid}] = 0 - 7500$) to investigate whether a large excess of polycation would afford colloiddally stable ‘wrapped’ **SV40** capsids (Fig. 11b, **v**). However, it did not. Aggregation was still observed and increased scatter (larger error bars) within the DLS measurements (Fig. 13a, **ii**) was significant, particularly upon increasing the concentration of **Cationic SCPN-1** beyond $[\text{polycation}]/[\text{capsid}] = 1000$. It was observed that the addition of **Cationic-SCPN-1** destabilizes the colloidal suspension of **SV40** capsids, thus driving the formation of multiparticle aggregates. It was hypothesized that these aggregates form on account of ‘patchy’ adsorption of **Cationic-SCPN-1** onto the viral surface to afford partially ‘wrapped’ capsids (Fig. 12b, **ii**), which display both regions of positive and negative charge and thus drive the formation of aggregates containing multiple capsids (Fig. 12b, **iii**).

^{**} **SV40** capsid is a particle with a hydrodynamic diameter, $D_h \approx 60$ nm. The adsorption of a 30 nm polycation (**P3**) layer adsorbed onto its surface thus seems unlikely, but not inconceivable. DLS measurements report the hydrodynamic diameter. If the polycation-coated **SV40** is highly hydrated, this may account for why the DLS-reported polymer layer thicknesses (L) are ≈ 30 nm at $[\text{polycation}]/[\text{capsid}] = 1000$.

^{††} The presence of NaCl ‘screens’ electrostatic forces of repulsions between approaching colloidal particles, and thus decreases the energy barrier to their aggregation in aqueous solution.

Finally, a control experiment (Fig. 13b) was conducted, in which small volumes of TRIS buffer were titrated into the viral capsid, instead of the **Cationic SCPN-1**. The titration volumes of the control experiment, and thus the concentrations of viral capsid, matched exactly those used in the previous titration with **Cationic SCPN-1**. Although DLS measurements (Fig. 13b, i) revealed that the mean particle size ($D_h = 196 \pm 16$ nm),[‡] was approximately constant over the range of capsid concentration employed during the titration experiment, the observed scatter in the DLS measurements was significant (± 16 nm), and comparable to the apparent thickness of the adsorbed polyelectrolyte layer (10 – 15 nm) deduced from previous DLS experiments (Fig. 12a).

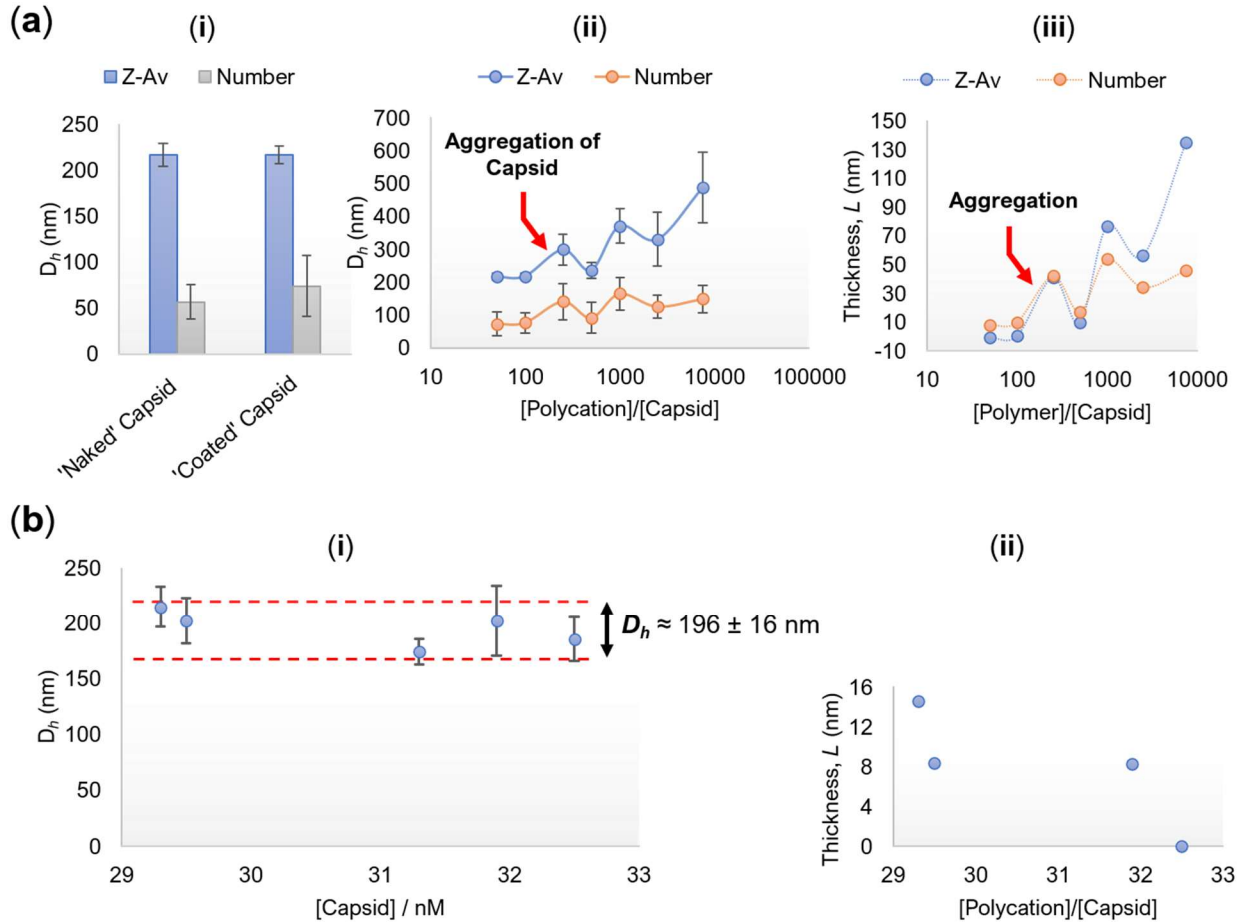


Figure 13: DLS characterization for titration of **Cationic SCPNs** into **SV40** capsid (a) and control experiment (b) in which buffer was titrated in SV40 capsid. $[\text{Capsid}]_{\text{init}} = 29.3$ nM in 7.7 mM TRIS (pH 7.4), 1 mM CaCl_2 . The apparent hydrodynamic diameter (D_h) of 'naked' capsid and polyelectrolyte 'coated' **SV40** capsid. (ii) DLS titration profiles for addition of **Cationic SCPN-1** into **SV40** capsid, where D_h of the 'coated' viral capsids is given as a function of the $[\text{Polycation}]/[\text{Capsid}]$ ratio. The apparent thickness (L) of the adsorbed polymer layer (iii) was derived from changes in the particle diameter (D_h). (b) Dilution of **SV40** capsid in control titration experiment was monitored by DLS, revealing significant scatter in particle size ($D_h = 196 \pm 16$ nm).

[‡] A large particle size was obtained on account of the low colloidal stability of **SV40**. Processes of particle-particle aggregation have been reported to decrease the reliability of DLS analysis for measuring accurate particle sizes, as transiently formed aggregate species distort the measured D_h values to larger than expected values.¹⁶

It was thus concluded that although **Cationic SCPN-1** may have been successfully adsorbed onto the periphery of **SV40** capsid, DLS failed to provide an accurate characterization handle for monitoring the ‘shrink-wrapping’ process, largely on account three contributing factors: (1) The ‘naked’ **SV40** capsid was moderately polydisperse ($PDI \approx 0.30$) in nature, leading to increased scatter in subsequent DLS measurements. (2) The ‘naked’ capsids lacked colloidal stability, leading to larger than expected particle sizes (**z-average** $D_h > 120$ nm, whereas $D_h \approx 50$ nm was expected). (3) The adsorption of **Cationic SCPN-1** onto the viral capsid modulates the colloidal stability of the resulting particle, often giving rise to increased scatter in the measured DLS data. In isolation, these factors can be dealt with, however in unison they preclude the highly accurate DLS analysis required to rigorously characterize a 5 – 15 nm polymer layer attached to the surface of a ≈ 50 nm capsid.

2.3.7. Fluorescence Titration Experiments Investigating Electrostatic Binding of Polyelectrolytes to SV40 Viral Capsid

In order to further understand the nature of the interaction between polyelectrolytes and **SV40** capsid, a fluorescence titration experiment was conducted in which three polymers were gradually titrated into a solution of the capsid (Fig. 14a): Aldehyde scaffold **P1**, linear polyanion **P2** and linear polycation **P3**. It was anticipated that only polycation **P3** would bind to the negatively-charged surface **SV40**, on account of a complementary electrostatic interaction between the two species. In this experiment, the intrinsic emission of tryptophan residues ($\lambda_{em} = 325$ nm) (Fig. 14) located within **SV40** capsid proteins was observed by excitation at $\lambda_{ex} = 280$ nm. Emission quenching (Fig. 14c) was observed as the polymer concentration increased, an observation consistent with binding interactions between the polymer and viral capsid surface. A steep decrease in the emission intensity of the capsid as polymer is titrated into solution, is indicative of stronger binding. It was therefore deduced that the linear polycation **P3** (Fig. 14c, iii) binds to **SV40** more strongly than the aldehyde polymer **P1** (Fig. 14c, i), which displays a gradual decrease in emission. Weak binding by **P1** was expected, as this scaffold exhibits little electrostatic attraction to the negatively-charged surface of **SV40**. The gradual emission quenching observed for **P1** was rationalized as non-specific binding of aldehyde polymer scaffold onto the viral surface. Whilst polycation **P3** featured the greatest quenching in the emission, the control experiment with negatively-charged **P2** also exhibited quenching, albeit to a lesser extent. This surprising result was rationalized by the mixed electrostatic nature of the viral capsids surface, which displays both regions of positive and negative charge (see Fig. 9c), and so regions of positive charge may bind with polyanion **P2**.

The polymer:capsid binding stoichiometry at saturation was deduced as approximately 1000:1 for linear polycation (**P3**), since no further decrease in emission was observed above $[\text{polycation}]/[\text{capsid}] \approx 1000$, implying saturation of the viral surface with polymer. Although quantitative analysis of polymer-capsid binding would be beneficial, this unfortunately was not possible on account of significant scatter in the data set. Careful repetition of anomalous measurements did not significantly improve the quality of the dataset. The observed ‘scatter’ in the data was attributed to high PDI of the supplied **SV40** samples, which were believed to contain a partially assembled or fragmented capsids (Fig. 11a, i), leading to error in the $[\text{polymer}]:[\text{capsid}]$ ratio at which saturation was observed.

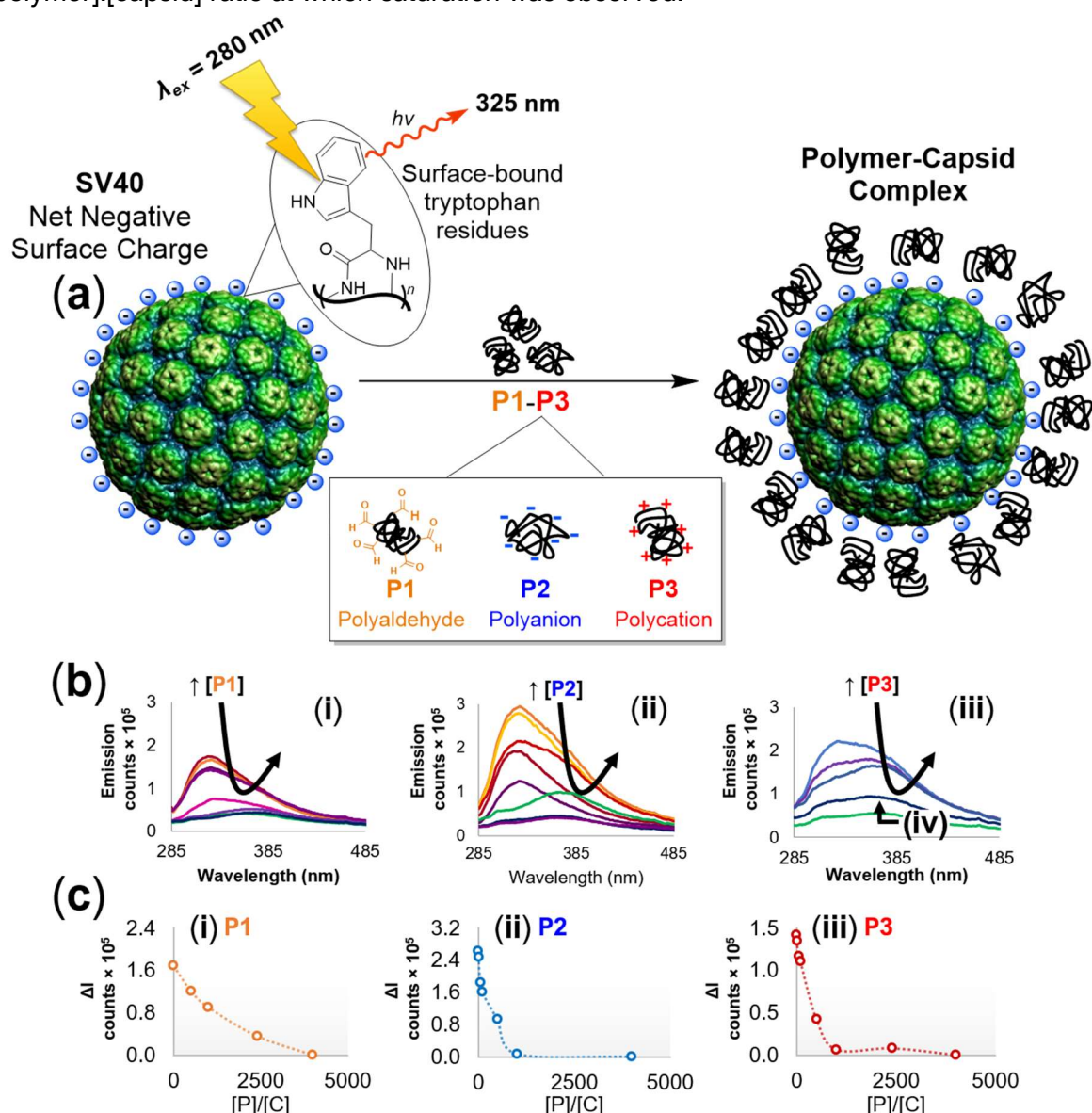


Figure 14: (a) Titration of polymers (**P1**, **P2**, **P3**) into an aqueous solution of **SV40** viral capsid affords emission quenching of surface-bound tryptophan residues on account of polymer-capsid binding. (b) Emission spectra show the quenching observed for linear polyaldehyde **P1** (i), linear polyanion **P2** (ii) and linear polycation **P3** (iii). (iv) Broad emission peak was observed at $\lambda \approx 380 \text{ nm}$ on account of an increasing polymer concentration, where each chain contains ~ 21 aromatic hydrazone units. (c) Emission quenching profiles of polymers **P1**, **P2** and **P3**, where the corrected emission intensity ΔI (see experimental) at 325 nm , is given as a function of the molar concentration ratio $[\text{Polycation}]/[\text{Capsid}]$.

Summary of work with SV40

The process of shrink-wrapping the viral surface of **SV40** was studied by zeta potential measurements and DLS analysis. A fluorescence spectroscopy titration also revealed that ‘hard’ polycations bind to the viral capsid surface, presumably through multiple non-specific electrostatic interactions. However, despite careful repetition of experimental work, quantitative binding analysis could not be obtained on account of inconsistencies observed in data observed from all these experiments. These inconsistencies are attributed to a relatively high polydispersity of the **SV40** samples. In the absence of structurally well-defined **SV40** viral capsid, and without analytical techniques available which could accurately characterize formation of thin polymer films upon the viral surface, an alternative approach was adopted to allow the continued development of the ‘shrink-wrapping’ concept.

2.3.8. Investigations on the ‘Shrink-Wrapping’ of Polystyrene NPs

To circumnavigate the issues of sample polydispersity (DLS) found with **SV40** viral capsid, the ‘shrink-wrapping’ of alternative 3D nanoscale objects was explored. Sulfonate-functionalized polystyrene latex nanoparticles constitute a good VLP model system on account of their commercial availability, their high colloidal stability and extremely monodisperse size distributions. DLS revealed that these particles typically had excellent PDI values of < 0.05 and (under the appropriate conditions) their hydrodynamic diameters could consistently be measured to an accuracy of ± 1 nm, a value which was substantially less than the anticipated thickness of the adsorbed polyelectrolyte layers located upon the particle surface. An established protocol¹⁷ was available for time-resolved dynamic light scattering (TR-DLS) and zeta potential (ZP) measurements to monitor the adsorption of ‘hard’ polyelectrolytes (**P2**, **P3** and **Cationic SCPN-1**) onto the charged surfaces of polystyrene-sulfonate nanoparticles (**sNPs**). Experiments began with **Cationic SCPN-1** (prepared from **P3**) which was anticipated to ‘shrink-wrap’ (Fig. 15a), the polystyrene substrate within an intermolecularly crosslinked polyelectrolyte film (Fig. 15d) on account of the ‘structural metamorphosis’ of the dynamic covalent acyl hydrazone crosslinks (Fig. 15b-c) embedded within the SCPN architecture.

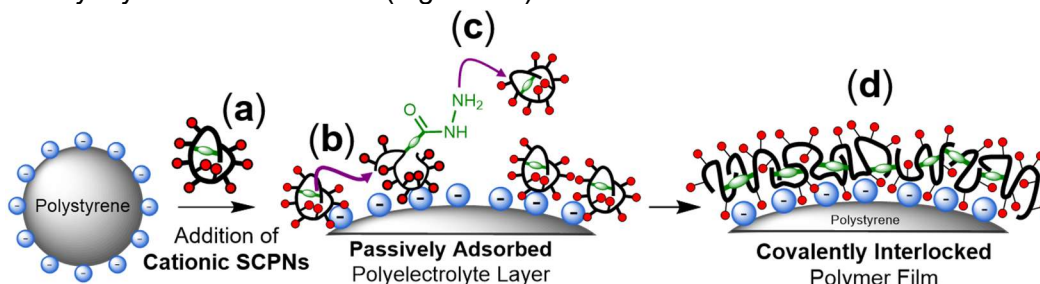


Figure 15: An overview of the hypothesized polyelectrolyte film formation upon the surface of polystyrene nanoparticles. (a) It is hypothesized that **Cationic SCPN-1** chains adsorb onto the polystyrene surface and the intra-chain crosslinks ‘reach’ out (b) and react (via hydrazone exchange) with ‘neighboring’ polymer chains on the surface (b) or capture SCPNs from solution (c) to form an intermolecularly crosslinked polymer film (d) upon the nanoparticle surface.

In this experiment, small amounts of **Cationic SCPN-1** were titrated (Fig. 16a) to a 1 mg/mL suspension (50 mM $\text{H}_4\text{NOAc-AcOH/H}_2\text{O}$, pH 4.5) of negatively-charged **sNPs** and the subsequent change in the hydrodynamic diameter (D_h) of the resulting particles was monitored as a function of time by TR-DLS (Fig. 16b). Prior to the addition of polymer, the ‘naked’ **sNPs** (Fig. 16b, i) featured a mean size of $D_h = 108 \pm 2$ nm, which remained constant with respect to time, indicative of excellent colloidal stability. Upon the addition of **Cationic SCPN-1** to the **sNPs**, D_h revealed a step-like increase in particle size (Fig. 16b, blue to orange), from 108 to 112 nm, which was immediately followed by a stable period in which the D_h of the ‘wrapped’ **sNPs** remained constant with time. These observations were consistent with the rapid adsorption of **Cationic SCPN-1** onto the periphery of **sNPs** and suggest that the resulting polyelectrolyte ‘wrapped’ particles featured reasonable colloidal stability.

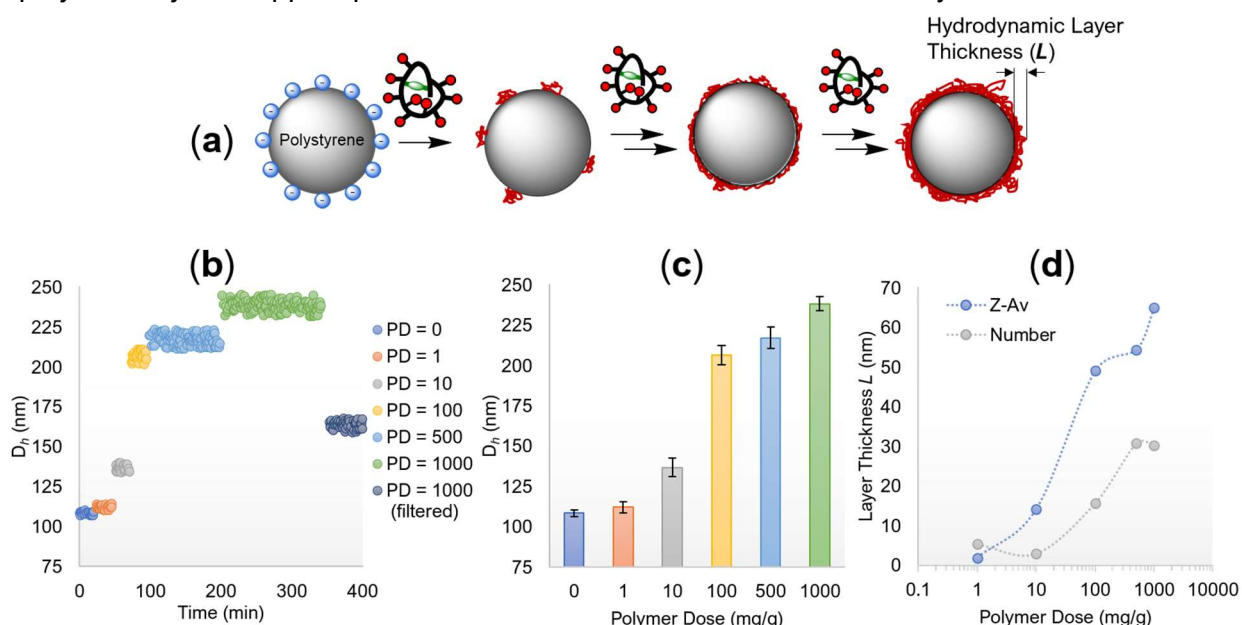


Figure 16: (a) Adsorption of **Cationic SCPN-1** chains onto negatively-charged **sNPs** was monitored by TR-DLS. (b) TR-DLS measurements showing the z-average hydrodynamic diameter (D_h) as a function of time during the titration of **Cationic SCPN-1** into **sNPs** (1 mg/mL). A range of polymer doses (PD = 0 – 1000 mg/g) were explored, where polymer dose is defined as the number of mg of polymer per g of **sNPs**. (c) Z-average diameter, D_h as a function of polymer dose. Error bars show standard deviation. (d) The apparent hydrodynamic layer thickness (L) of the adsorbed polyelectrolyte film.

In subsequent additions of **cationic SCPNs** further step-like increases in D_h (Fig. 16b-c) were observed. Figure 16c gives the mean diameters D_h of the ‘wrapped’ **sNPs** as a function of polymer dose (PD), a mass/mass ratio defined as:

$$\text{Polymer Dose (PD)} = \frac{\text{mass of polymer (mg)}}{\text{mass of polystyrene NPs (g)}} \quad (\text{Eqn. 2})$$

The observed increase in particle size (D_h) correlated with the amount of polymer added (Fig. 16b-c), with a significant (70 nm) increase in particle size at PD = 10 – 100 mg/g (red/yellow). Beyond PD = 500 mg/g, further additions of **Cationic SCPN-1** did not yield significant increases

in particle size, thus indicating that saturation of the **sNP** surface had likely been achieved. Passing the polymer 'wrapped' **sNPs** through a 450 nm filter afforded a notable (79 nm) (Fig. 16b, ii) decrease in particle size (**green** to **dark blue**), an observation that indicated a small population of multi-particle aggregates was present within the sample, which distort the measured particle sizes towards larger than expected values.^{16,17} The hydrodynamic thickness (L) of the adsorbed polymer layers were calculated, as outlined in earlier discussion, and presented as a function of polymer dose (Fig. 16d). The number-average layer thickness L (**grey**)(Fig. 16d) revealed saturation of the **sNP** surface, with a maximum layer thickness of 30 nm. In contrast, the z-average data revealed thick polymer layers of > 65 nm, significantly thicker than could feasibly adsorb onto a 100 nm particle. These results were rationalized by the fact that adsorption of polyelectrolytes onto oppositely-charged colloidal particles (Fig. 17a, i) is often accompanied by particle-particle aggregation processes (ii) which distort DLS towards larger than expected D_h values (Fig. 17c), thus leading inaccurate determination of the hydrodynamic thickness L . Figure 17 shows the difference between a stable (b) and aggregating system (c). In the stable system, the measured hydrodynamic diameter rapidly reaches a plateau after addition of polymer, which indicates the sample has good colloidal stability and so should afford DLS measurements free from the effects of aggregation. Crucially, high precision (error < ± 3 nm) D_h measurements were required to accurately determine the thickness (L) of the adsorbed polyelectrolyte layer by DLS analysis.

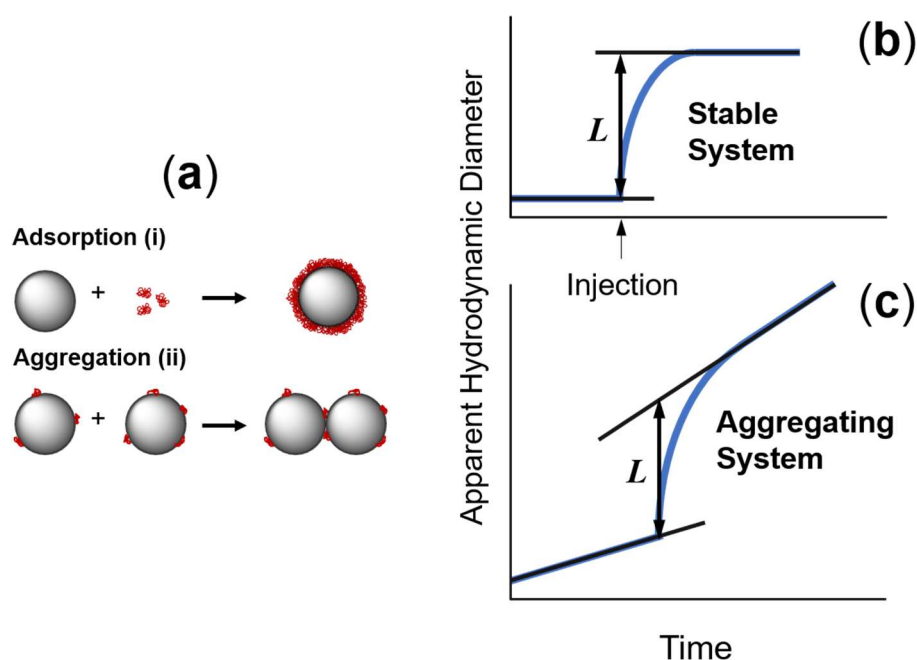
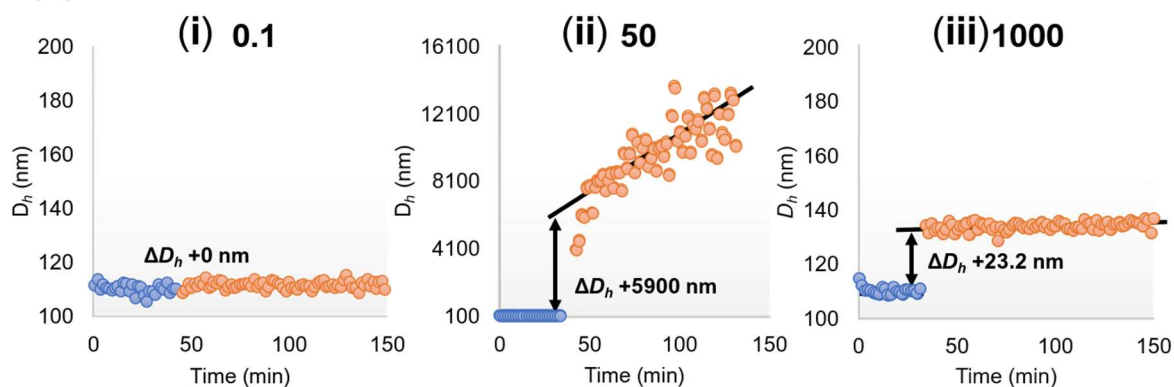


Figure 17: (a) Adsorption (i) of polyelectrolytes on oppositely charged colloidal particles is often accompanied by particle aggregation (ii). Scheme for measurement of the hydrodynamic layer thickness L in a stable (b) and aggregating system (c).¹⁷

In order to more accurately characterize the hydrodynamic thickness of polyelectrolyte films present upon the particle surface, further TR-DLS experiments (Fig. 18a) were undertaken in which **Cationic SCPN-1** was added to aqueous suspensions of **sNPs** at pH 4.5. A range of polymer doses (PD = 0.01 – 5000 mg/g) were investigated. TR-DLS allows for the D_h to be monitored as a function of time, and processes of particle-particle aggregation (Fig. 17a, ii) can be observed as a steady increase in D_h (Fig. 17c).¹⁷ Identifying conditions in which the colloidal particles are stable towards aggregation processes allows for the D_h , and thus thickness of the particle-bound **Cationic SCPN-1** layers to be determined with a high level of accuracy. To assist with the accuracy of DLS measurements, a reduced **sNP** concentration of 0.2 mg/mL was employed. This dilute particle concentration was observed to suppress the rate of particle-particle aggregation processes. TR-DLS results were compiled into Figure 18b, which shows the hydrodynamic thickness of the **Cationic SCPN-1** ‘wrapping’ as a function of polymer dose.

(a) Polymer Dose (mg/g):



(b)

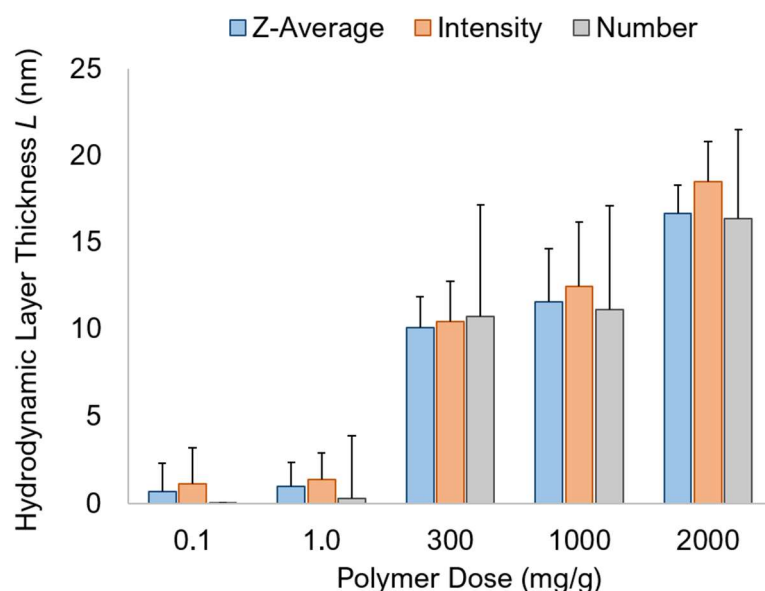


Figure 18: (a) Representative TR-DLS traces showing the expected increase in hydrodynamic diameter D_h upon addition of **Cationic SCPN-1** to **sNPs**, consistent with the formation of an adsorbed polyelectrolyte layer upon the particle surface. A range of polymer doses (PD = 0.1 – 2000 mg/g) were explored. Measurements of D_h (z-average data shown) were made before (blue circles) and after (orange circles) addition of **Cationic SCPN-1** to **sNPs**. (b) Hydrodynamic layer thickness L , given as a function of polymer dose. Error bars indicate the standard deviation.

At PD = 0.1 mg/g (see Fig. 18a, i) negligible increase in particle size was observed, thus the deduced hydrodynamic layer thickness, L was zero \pm the error associated with the DLS measurement. The TR-DLS trace at PD = 50 mg/g (see Fig. 18a, ii) was typical of an aggregating system (cf. Fig. 17c), in which the polyelectrolyte-covered particles are close to their isoelectric point, thus DLS was dominated by multi-particle agglomerate species. L values obtained for PD = 10 – 100 mg/g, were therefore omitted from Figure 18b on account of aggregation processes leading to inaccurate measurement of the polymer layer thickness by DLS. In contrast, at high polymer doses, PD > 300 mg/g (Fig. 18b) the system was stable towards aggregation (cf. Fig. 17b), with TR-DLS revealing an immediate ‘step’ increase in D_h upon addition of polyelectrolyte (Fig. 18a, iii), which was consistent with the rapid formation of a polyelectrolyte layer and indicates good colloidal stability. Thus, under these conditions accurate L values were obtained, indicating that the hydrodynamic layer of **Cationic SPCN-1** on the polystyrene surface was 10 – 15 nm thick, depending on the precise PD used.

To gain additional insight to the formation of polyelectrolyte films, the zeta potential measurements (Fig. 19a) were also obtained, which revealed that the polystyrene substrate becomes positively charged as the polymer dose increased, consistent with the formation of a thin polyelectrolyte layer adsorbed at the nanoparticle surface. At low polymer doses (PD < 10 mg/g), the zeta potential remained constant at ZP \approx - 62 \pm 8 mV (Fig. 19a), indicating a strongly negative surface charge, very similar to that observed for the ‘naked’ polystyrene particles (ZP = - 63 \pm 4 mV). These observations were consistent with a partially ‘wrapped’ species (Fig. 19a, i), where the number of negative surface charges far exceeds the number of positively charged quaternary ammonium groups on the surface-bound polyelectrolyte. At a polymer dose of 30 – 40 mg/g, the polyelectrolyte ‘coated’ polystyrene particles passed through an isoelectric point (IEP) (Fig. 19a) – where the total number of positive charges on the adsorbed polyelectrolytes exactly matches the number of negative charges on the particle surface – and with further addition of polycation underwent a reversal of the electrostatic charge upon their surface. This phenomenon is well known in colloid chemistry, and is commonly observed when multivalent ions, such as polycations, adsorb onto oppositely-charged surfaces.¹⁸ When working near the IEP (Fig. 19a) particle-particle aggregation presented a significant issue to obtaining reliable DLS characterization of the adsorbed polyelectrolyte layer. The particles no longer electrostatically repel one another, and thus, poor colloidal stability was observed in the form of precipitation (Fig. 19b). By avoiding working near the IEP it was possible to suppress these aggregation processes and obtain colloidally stable ‘wrapped’ **sNP** nanoparticles, whose sizes could readily be accurately determined by DLS analysis. At PD > 100 mg/g, the particles possessed a net positive charge (ZP = \approx + 35 mV) and their colloidal stability was regained (Fig. 19b) on account of the ‘over-charging’ effect,¹⁹ whereby the an excess of polyelectrolytes

(Fig. 19a, **iii**) is adsorbed onto oppositely-charged surfaces. Consequently, at PD > 300 mg/g, the polystyrene surface becomes supersaturated with polyelectrolyte and good colloidal stability was achieved.

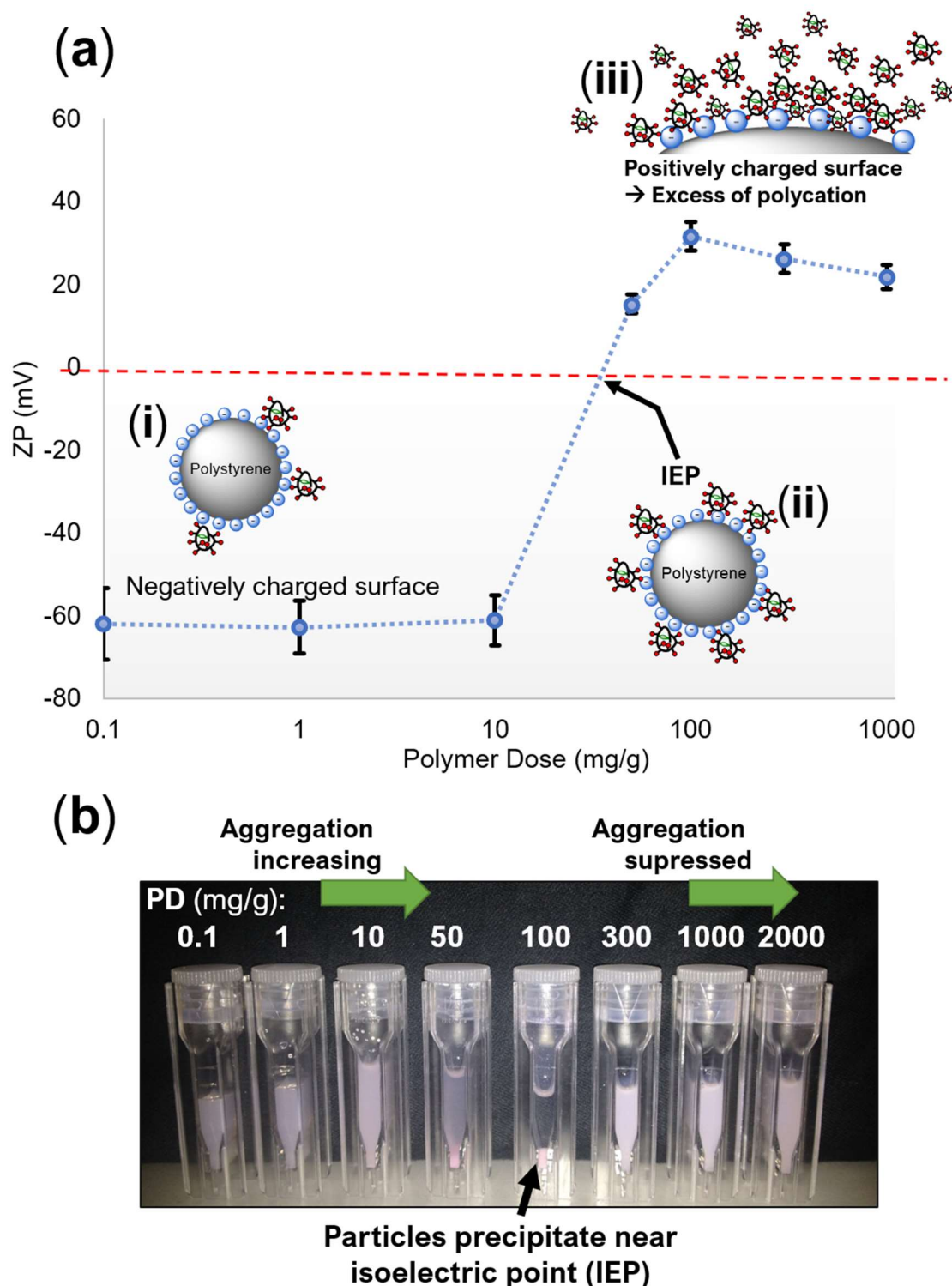


Figure 19: (a) Plot showing zeta potential of **Cationic-SCPN-1** 'wrapped' **sNPs** as a function of polymer dose (PD) added. (b) Image showing the loss of colloidal stability near the isoelectric point (IEP), which results in precipitation of particles from the suspension.

Further TR-DLS measurements were undertaken to investigate the thickness of polyelectrolyte layers formed from linear polycation (**P3**) and linear polyanion (**P2**), which were adsorbed onto polystyrene nanoparticles. Figure 20a-b reveals the hydrodynamic thickness, L of the polyelectrolyte layer for **Cationic SCPN-1** (red), linear polycation **P3** (orange) and linear polyanion **P2** (blue). It was anticipated that polyanion (**P2**) would show no increase in particle size, on account of the electrostatic repulsion between pendant sulfonate groups on the polymer scaffold and the negatively-charged polystyrene surface. Surprisingly, the addition of **P2** also afforded an increase in D_h , consistent with the adsorption of a 9 nm polyanion (**P2**) layer onto the negatively-charged polystyrene particles. This observation was initially rationalized by the presence of electric double layer (Fig. 20c) which effectively ‘screens’ the charge-charge repulsion between polyanions and polystyrene nanospheres. Counteranions in the Stern layer permit the association of polyanion within a loosely bound diffuse layer (DL) which surrounds the particle. It was later understood that the adsorption of polyanion **P2** onto negatively-charged **sNPs** is an entropically driven process, which will be discussed on page 61. Figure 21 shows the ZP of polystyrene particles as a function of polymer dose, for **Cationic SCPN-1** (red), polycation **P3** (orange) and polyanion **P3** (blue). As anticipated, polyanion **P2** does not afford charge reversal of the particle surface, whereas linear polycation **P3** and **Cationic SCPN-1** do, indicating that **sNPs** have been ‘coated’/‘wrapped’ with a positively charged layer of polymer.

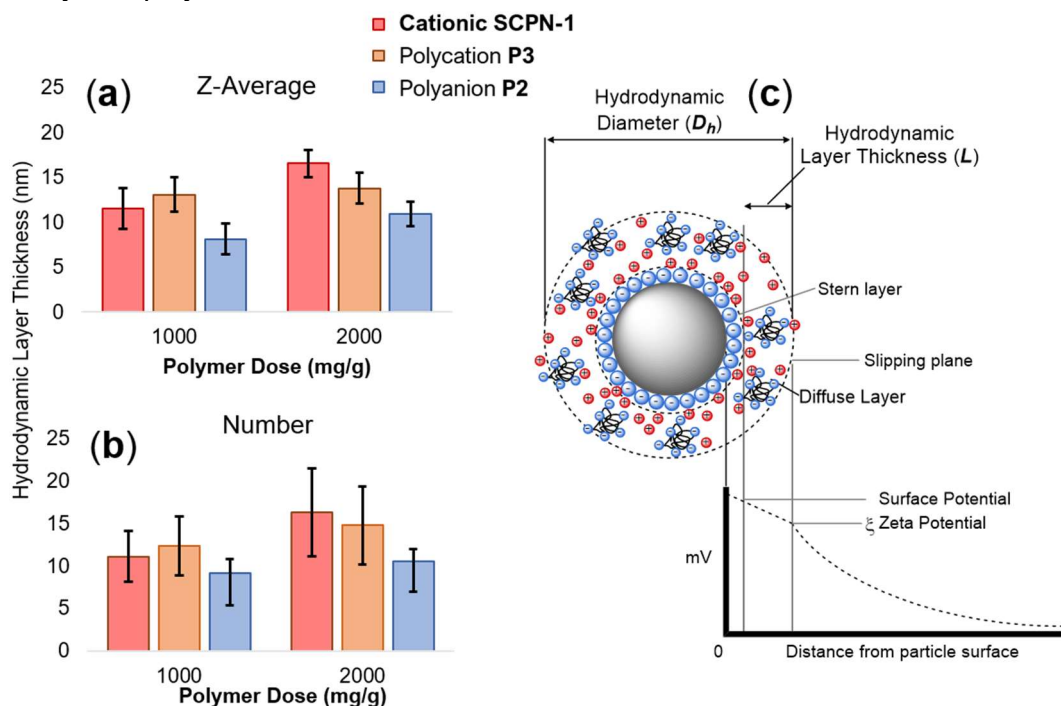


Figure 20: Z-average (a) and number average (b) hydrodynamic thickness (L) of polyelectrolyte layers formed by adsorption of **Cation SCPN-1** (red), polycation **P3** (orange) and polyanion **P2** (blue) onto **sNPs**. These values were determined by TR-DLS experiments. Error bars indicate standard deviation. (c) Electric double layer arrangement of ions surrounding polystyrene colloidal particle. Counteranions at the Stern layer were initially hypothesized to ‘shield’ the negatively-charged polystyrene surface from polyanions in the diffuse layer.

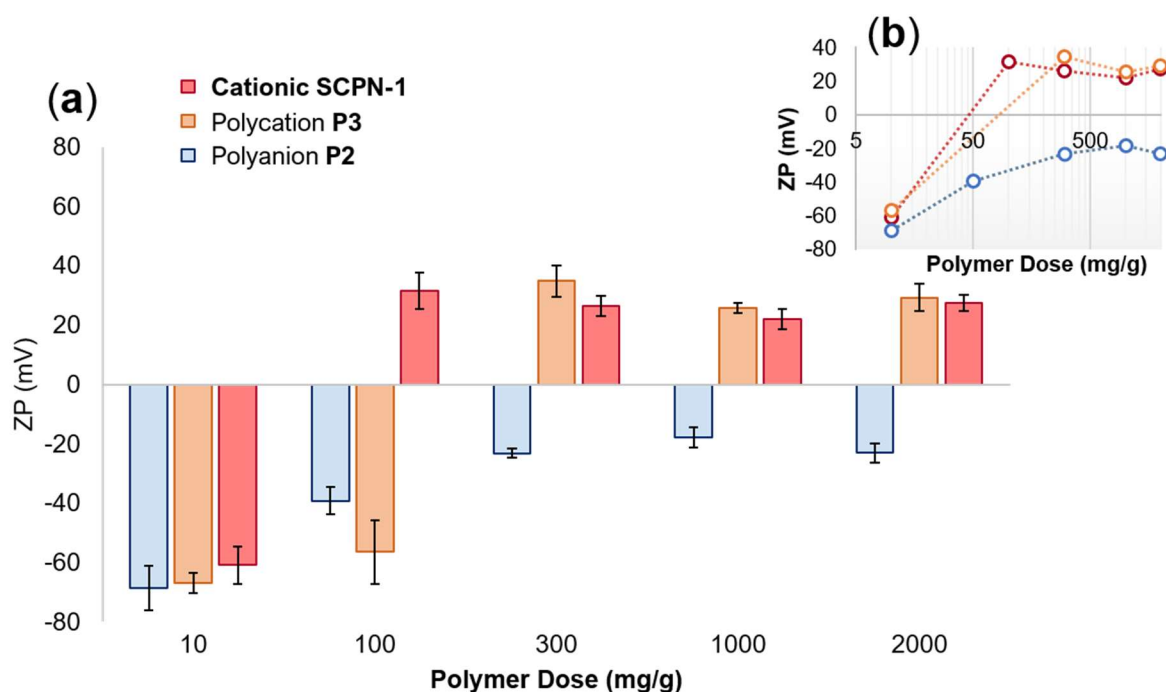


Figure 21: (a) Zeta potential of sNPs 'coated' in linear polyanion P2 (blue), linear polycation P3 (orange), or 'wrapped' in Cationic SCPN-1 (red). Error bars show standard deviation. (b) Zeta potential of 'coated' and 'wrapped' sNPs expressed as a function of the polymer dose (mg/g).

Surprisingly, the addition of polyanion P2 to sNPs revealed a + 46 mV increase in the measured zeta potential (Fig. 21a). This observation was consistent with the previous DLS data, and indicates that polyanion P2 attaches onto the surface negatively-charged sNPs, and strongly suggest that the adsorption of polyelectrolytes is not solely governed by electrostatic attractions/repulsions, but was likely a more complex process driven by the entropically favourable displacement of counterions from the polystyrene surface to the bulk solution (Fig. 22).²⁰ The observation that adsorption of polyanion P2 increases the measured ZP from - 66 mV to - 23 mV (see Fig. 21b) instead of maintaining a constant ZP value close to that of the 'naked' sNPs (ZP \approx - 66 mV) could be rationalized by partial protonation of dimethylacrylamide units located upon the polymer scaffold, which effectively decrease the overall negative charge within the adsorbed polyelectrolyte layer.

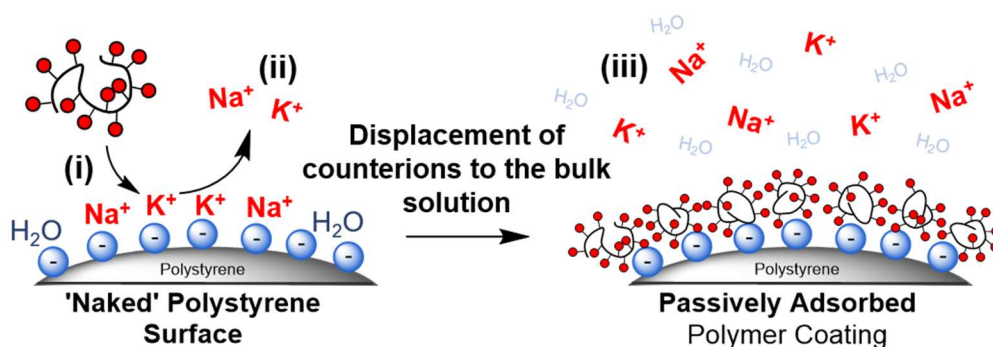


Figure 22: Adsorption of a 'hard' polyelectrolytes (i) onto the surface of polystyrene-sulfonate nanoparticles is an entropically favourable process driven by the displacement (ii) of counterions to the bulk solution (iii).

Negative-stain transmission electron microscopy (TEM) provided further evidence that **sNPs** were successfully encapsulated within a polyelectrolyte layer (Fig. 23). TEM analysis (Fig. 23f) obtained before (**orange**) and after (**blue**) the addition of **Cationic SCPN-1**, revealed a significant shift (Δ) in the observed particle size distributions (PSDs), consistent with the formation of a thin polyelectrolyte film upon the **sNPs** surface. Analysis of TEM micrographs revealed the average thickness of the polyelectrolyte film was 5 ± 3 nm, consistent with the hydrodynamic layer thickness (L) measured by TR-DLS (13 ± 2 nm). Uranyl acetate staining allowed for **Cationic SCPN-1** to be visualized by TEM (Fig. 23b), where discrete light ‘patches’ approximately measuring 15×30 nm were observed. These particles were significantly larger than expected for individual SCPNs ($D_h = 7.7$ nm by DLS), thus were likely multi-chain polymer aggregates formed by concentrating the **Cationic SCPNs** onto the TEM grid by slow evaporation. TEM micrographs of ‘shrink-wrapped’ **sNPs** (Fig. 23d) revealed a ‘bumpy’ surface morphology compared to the ‘naked’ **sNPs** (Fig. 23e), which appeared to have ‘smooth’ surfaces, observations which further indicate successful ‘wrapping’ of **sNPs**. Figure 23c-d show the ‘wrapped’ **sNPs** were surrounded by light-coloured patches, consistent with regions of ‘unbound’ **Cationic SCPN-1**, which overlapped more extensively and were less regular in

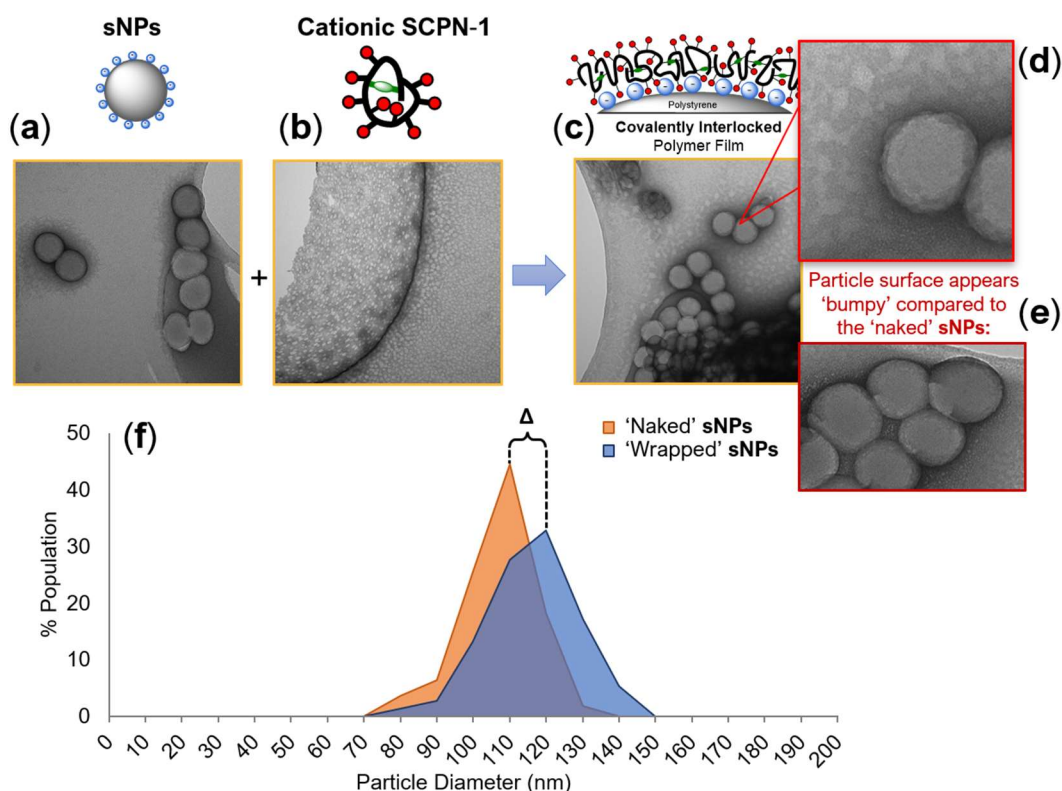


Figure 23: TEM images of (a) 100 nm polystyrene nanospheres (**sNPs**), (b) **Cationic SCPN-1**, and (c) ‘shrink-wrapped’ **sNPs** (PD = 2000 mg/g, **Cationic SCPN-1**). Magnified TEM image of ‘wrapped’ **sNPs** (d) and ‘naked’ **sNPs** (e). (f) TEM particle size distributions (PSDs) before (**orange**) and after (**blue**) ‘shrink-wrapping’ with **Cationic SCPN-1**. PSD histograms were obtained by measuring the diameters of 50 particles, so to produce statistically significant mean values, and revealed a shift (Δ) in the mean particle diameter upon addition of **Cationic SCPN-1**.

appearance compared to those seen in Figure 23b, suggesting that the ‘discrete’ **Cationic SCPN-1** had undergone more widespread ‘shrink-wrapping’ to form an extensively intermolecularly crosslinked polymer films.

Results thus far have successfully demonstrated that **Cationic SCPN-1** chains are adsorbed onto the periphery of negatively-charged polystyrene nanoparticles. Zeta potential (Fig. 21) measurements revealed a strongly positive surface charge ($ZP = 35 \pm 5$ mV) of the **Cationic SCPN-1** ‘wrapped’ **sNPs** and DLS analysis (Fig. 20) consistently showed the thickness of the **Cationic SCPN-1** ‘wrapping’ to be 10 - 15 nm, results which were then further corroborated by TEM (Fig. 23). Whilst it is highly likely that **sNPs** were successfully ‘shrink-wrapped’ within a crosslinked polyelectrolyte film (Fig. 23c) after the addition of **Cationic SCPN-1**, definitive proof of the crosslinked nature of this polyelectrolyte film is yet to be demonstrated. Contrary to expectations, negligible differences between **Cationic SCPN-1** and linear polycation **P3** were observed by DLS and ZP measurements. Addition of **Cationic SCPN-1** was anticipated to afford thicker polyelectrolyte films upon the particle surface than were linear polycation (**P3**), on account of **Cationic SCPN-1** chains having the capacity to ‘grow’ the thickness of the adsorbed film through component exchange of the dynamic covalent crosslinkers (Fig. 15b-d). DLS, TEM and ZP measurements did not, however, reveal significant differences between adsorption of linear (non-crosslinked) polycation **P3**, which cannot crosslink, and **Cationic SCPN-1** which does have the capacity to form crosslinks. These observations revealed that the ‘structural metamorphosis’ of **Cationic SCPN-1** chains into an intermolecularly crosslinked polymer film was a subtle process, thus obtaining definitive proof of this process would be challenging to elucidate, as will be later discussed on page 65.

2.3.9. Triggered ‘Unwrapping’ of Polystyrene Nanoparticles

DLS, zeta potential and TEM results have confirmed the successful attachment of **Cationic SCPN-1** chains onto the surface of **sNPs**. In order to demonstrate reversible and on-demand ‘un-wrapping’ of this VLP model system, experiments were undertaken to displace the **Cationic SCPN-1** film to re-expose the underlying substrate. **Cationic SCPN-1** ‘wrapped’ **sNPs** were incubated with hydroxylamine (Fig. 24a), followed by centrifugal dialysis to remove ‘unbound’ polymer chains. Hydroxylamine was anticipated to displace all charged (**R1**) and crosslink (**SD**) residues from the polymer backbone, in favour of forming the more thermodynamically stable²¹ oxime-functionalized polymer scaffold (Fig. 24a, i). This chemical modification breaks the electrostatic attraction between the polymer and polystyrene surface, which was anticipated to afford dissociation of the now neutrally charged coating from the surface (Fig. 24a, ii). Removal of the polyelectrolyte film was then observed by DLS (Fig. 24b) and ZP measurements (Fig 24c). DLS (Fig. 24b) revealed a 13 nm contraction in mean particle

diameter (Fig. 20a) and the corresponding shift in the particle size distribution, whilst the zeta potential decreased by 37.5 mV (from ZP \approx + 27.4, to - 10.1 mV) (Fig. 20c), indicating a reduction of positive charge at the polystyrene surface. Figure 20c shows the shift in zeta potential distribution, towards but not fully returning to that of the ‘naked’ particle (ZP \approx - 60 mV). These results show that a combined approach of hydroxylamine addition, followed by centrifugal dialysis afforded partial removal of the polymer coating. With firm evidence of particle ‘unwrapping’ in hand, studies were undertaken to demonstrate the **Cationic SCPN-1** chains adsorbed upon the surface of ‘wrapped’ **sNPs** have in fact formed an intermolecularly crosslinked film. This evidence is important in demonstrating that the ‘structural metamorphosis’ of SCPN chains into crosslinked polymer films has occurred, and thus should prove that ‘shrink-wrapping’ can be achieved upon the surface of nanoscale objects. Figure 25 describes the experiments which were undertaken to investigate the crosslinked nature of **Cationic SCPN-1** polymer films, and the control experiment (Fig. 25a-c) which should provide evidence to support the hypothesized ‘shrink-wrapping’.

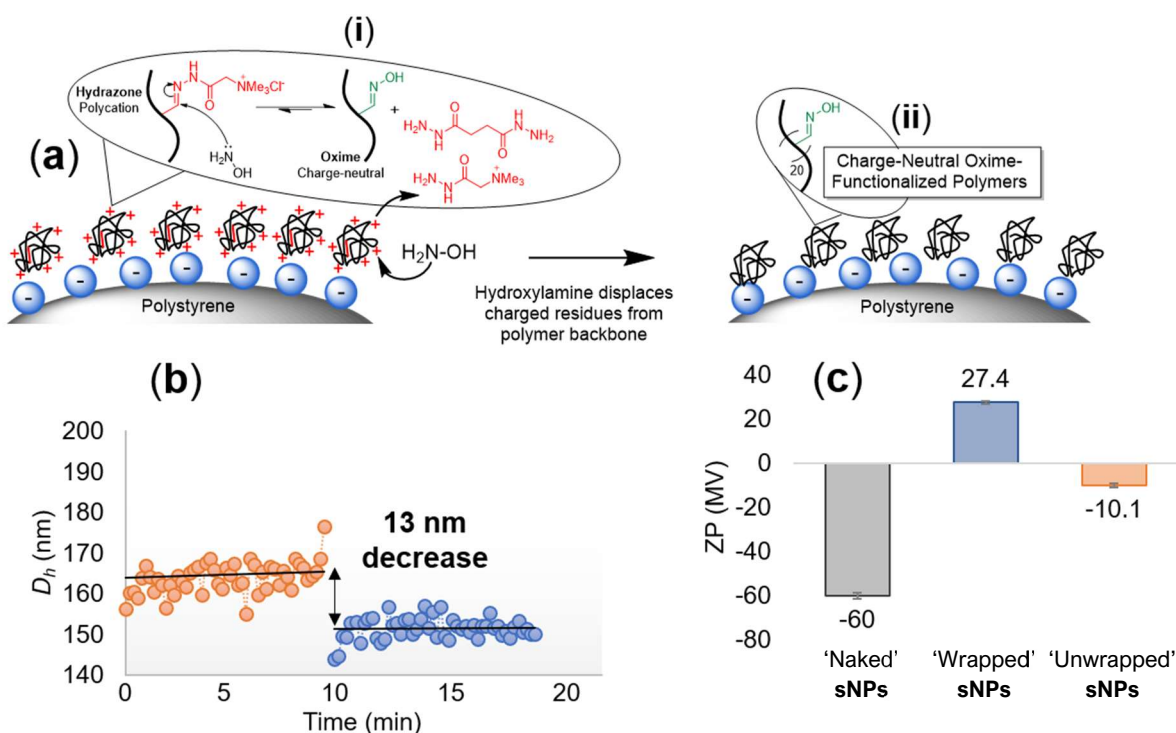


Figure 24: (a) Addition of hydroxylamine (i) cleaves hydrazide residues from the polymer scaffold, in favour of forming the more hydrolytically stable oxime polymer (ii), which is charge neutral, thus anticipated to dissociate from the polystyrene (**sNP**) surface. (a) TR-DLS before (orange) and after (blue) removal of coating revealed a 13 nm decrease in z-average size, D_h . (b) ZP values of ‘naked’ **sNPs**, polycation ‘coated’ **sNPs**, and ‘unwrapped’ **sNPs** after treatment of hydroxylamine and centrifugal dialysis to remove unbound polymer. A 38 mV decrease in zeta potential, towards that of the naked particle (- 60 mV).

2.3.10. Attempted Removal of ‘Hard’ Polyelectrolyte Coatings

It was strongly anticipated that experiments investigating the removal of polyelectrolyte layers would provide firm evidence that **sNPs** were successfully ‘shrink-wrapped’ within intermolecularly crosslinked polyelectrolyte films. Appropriate control experiments, with polycation (**P3**), were expected to show that polyelectrolyte ‘coatings’ consisting of non-crosslinked (linear) polymer chains (Fig. 25a-b) can easily be removed (Fig. 25c) through a combination of sonication, washing, and centrifugal dialysis, whereas the polyelectrolyte ‘wrapping’ formed by **Cationic SCPN-1** (Fig. 25d-e) should remain attached (Fig. 25f) on account of intermolecular covalent crosslinks having formed within the adsorbed polyelectrolyte layer. These observations are required to prove that the substrate was indeed ‘shrink-wrapped’ within a crosslinked polyelectrolyte film, thus differentiating this novel chemistry from passive adsorption of linear (i.e. non-crosslinked) polymer chains (Fig. 25b) onto colloidal particles. Initial experiments focused on the displacement of **P3** ‘coatings’ from particle surfaces, as getting this key control experiment (Fig. 25a-c) to work was crucial to obtaining proof of successful ‘shrink-wrapping’.

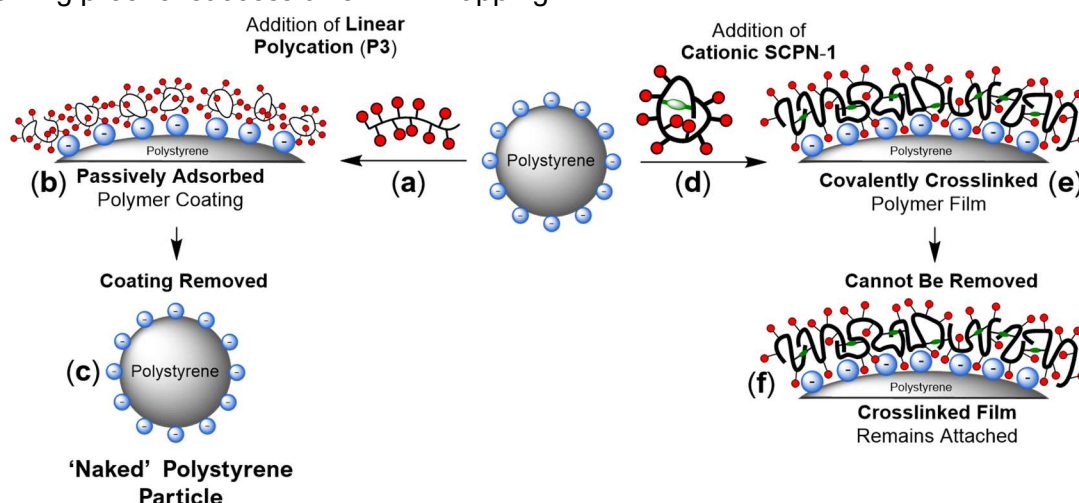


Figure 25: (a) Addition of linear polycation **P3** results in a passively adsorbed polyelectrolyte layer (b), which should easily be removed through a combination of centrifugation/washing, salt addition and dialysis. Complete removal of the **P3** coating would afford ‘naked’ polystyrene particles (c). (d) Addition of **Cationic SCPN-1** is anticipated to result in the ‘shrink-wrapping’ of **sNPs** (e). The formation of a covalently interlocked polymer film, which cannot be removed (f), on account of the intermolecular crosslinks which provide mechanical stability.

Suspensions of linear polycation (**P3**) ‘coated’ **sNPs** (Fig. 25b) were incubated with a range of different salt/surfactant solutions for 48 h, which were anticipated to ‘screen’ electrostatic interactions between **P3** and the negatively-charged polystyrene surface, thus facilitate the removal of the surface-bound polymer layer. Unbound polymer chains were then removed by centrifugal filtering and the ‘uncoated’ particles were analyzed by DLS (Fig. 26a) and ZP (Fig. 26b). Of the conditions explored for polyelectrolyte coating removal, 2M KBr afforded the largest reduction in ZP, which decreased from + 34 mV (‘coated’ **sNPs**) down to + 2 mV, suggesting that partial removal of the polymer coating had at least been achieved.

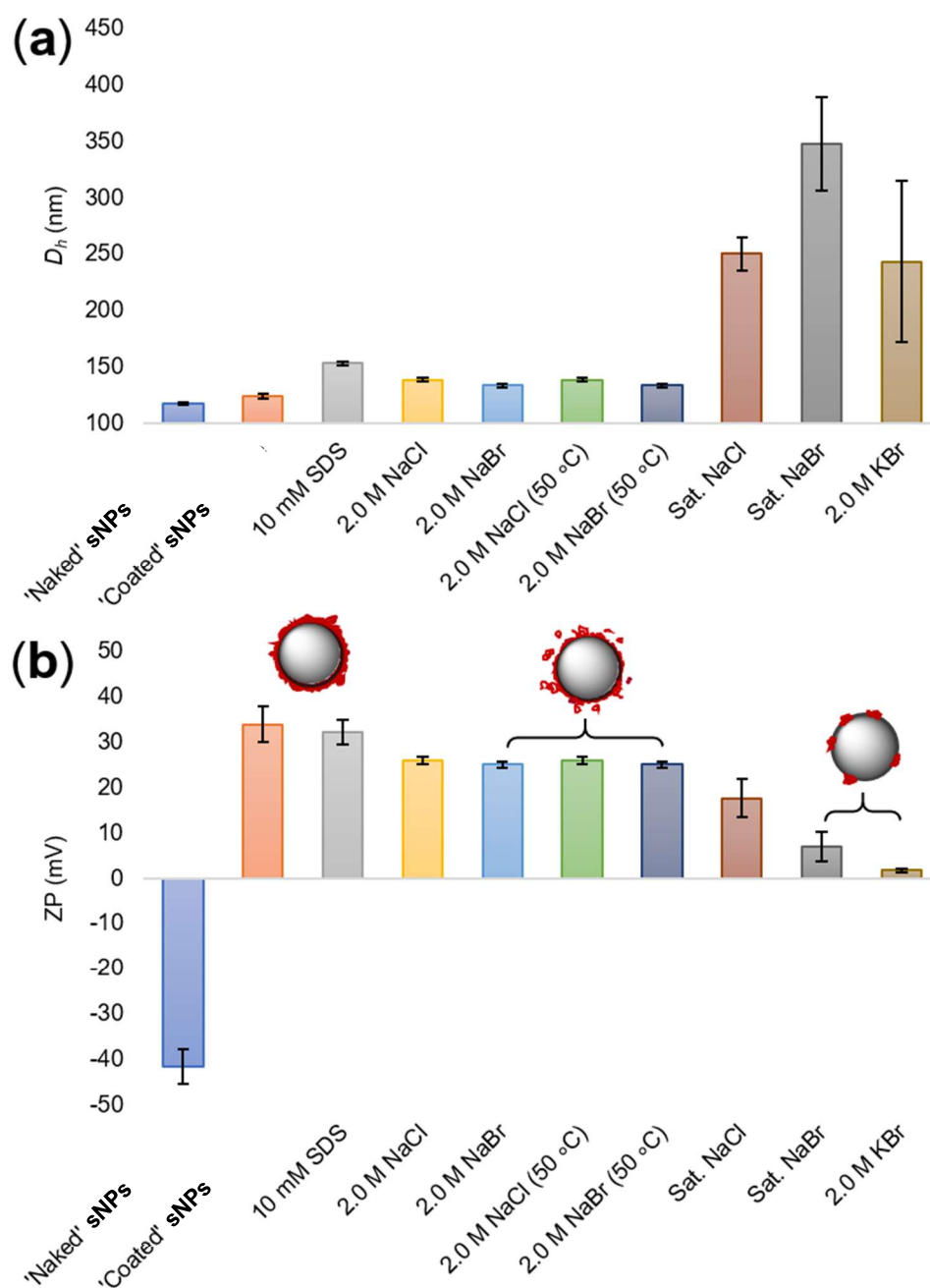


Figure 26: A summary of experimental conditions explored to facilitate the removal of the adsorbed polycation (**P3**) layer from the surface of **sNPs**. Particle size and surface charge were measured by DLS (**a**) and zeta potential (**b**), respectively. In both plots, the error bars show standard deviation.

In contrast, DLS (Fig. 26a) revealed that conditions where polymer coating had been most successfully removed (sat. NaCl, sat. NaBr, 2M KBr) also featured significant aggregation, leading to large particle sizes, where $D_h > 250$ nm. This observed decrease in colloidal stability was rationalized by the removal of excess polyelectrolyte from the **sNP** surface, which pushes the particle back towards the isoelectric point (where ZP = 0, Fig. 26b). Although DLS/ZP results suggest that incubation of ‘coated’ **sNPs** with high salt concentrations may afford at least partial removal of the polymer layer, complete coating removal was incredibly challenging to achieve for ‘hard’ polyelectrolytes, which are thought to adsorb irreversibly onto oppositely-charged colloidal particles.²² Furthermore, it was concluded that the challenges associated for accurately monitoring the removal of 5 – 15 nanometre thick ‘hard’ polyelectrolyte coatings from the surface of polystyrene nanoparticles using DLS were too great, on account of the colloidal stability of **sNPs** being modified by the adsorption of polymer chains, which influenced the quality of the DLS analysis obtained. Extensive experiments to facilitate the complete removal of ‘hard’ polyelectrolyte ‘coatings’ from the oppositely-charged polystyrene surface were largely unsuccessful. Whilst partial removal of the polymer coating was achieved by washing with excess salt, these conditions severely degraded the quality of the DLS analysis, making it difficult to accurately characterize the thickness of the remaining polymer layer.^{§§} It was concluded that adsorption of ‘hard’ polyelectrolytes onto oppositely-charged colloidal particles is essentially an irreversible process, driven by the entropically favourable displacement of counterions into the bulk solution,²⁰ rather than simply an electrostatic attraction between oppositely-charged species.

To circumnavigate the characterization issues associated with monitoring the displacement of polyelectrolyte ‘coatings’ by DLS, the decision was made to check for coating removal from microparticles, large enough to be visualized by microscopy. Further evidence that adsorption of ‘hard’ polycations is irreversible was observed by a fluorescence microscopy (Fig. 27) experiment, in which dansyl polycation (**P4**) was adsorbed onto 5 μ m sulfonate-functionalized polystyrene microparticles (**sMPs**) (Fig. 27a). The inclusion of dansyl fluorophores within

^{§§} Additional experiments were conducted in which alternating layers of ferrocene-labelled polycation **P5** and polyanion **P2** were built up layer-by-layer (*LbL*) upon surface of **sNPs**, and this process was monitored by TEM, DLS and ZP (see Appendix A, Fig. 40 - 41 for details). *LbL* assemblies contain several layers of loosely-bound polyelectrolyte upon the particle surface, and so it was hypothesized that *LbL* assemblies consisting of non-crosslinked polyelectrolytes would readily collapse upon addition of salt. In contrast, *LbL* assemblies containing crosslinked polyelectrolytes (e.g. **Cationic-SCPN-1**) were expected to be more difficult to displace, on account of inter-chain crosslinks having formed between adjacent polymer layers. Whilst these experiments were anticipated to provide access to the control experiments required to demonstrate successful ‘wrapping’ of **sNPs** within crosslinked polyelectrolyte film, DLS, ZP and TEM analysis showed that *LbL*-covered **sNPs** had low colloidal stability and tended to form ill-defined aggregates, thus making it difficult to characterize the formation and displacement of polymer layers from the particle surface. Therefore, no further experiments were conducted with *LbL*-covered **sNPs** as these ill-defined constructs were unlikely to afford clear evidence of successfully ‘wrapping’ by the available methods of analysis.

polycation **P4** allowed for the surface-bound polyelectrolyte layer to be observed as brightly emissive corona (Fig. 27b, i), which were exclusively localized to particle surfaces, indicating that no ‘unbound’ **P4** was present. Removal of the polycation ‘coating’ was then attempted by repeatedly washing, centrifuging and re-suspending the ‘coated’ **sMPs** with saturated NaCl solution. After 10 consecutive washes with sat. NaCl fluorescence microscope images (Fig. 27b, ii) revealed that the **sMPs** remained covered with a layer of polycation **P4**, as was evident by the brightly emissive coronas, which persisted upon the surface of **sMPs**.

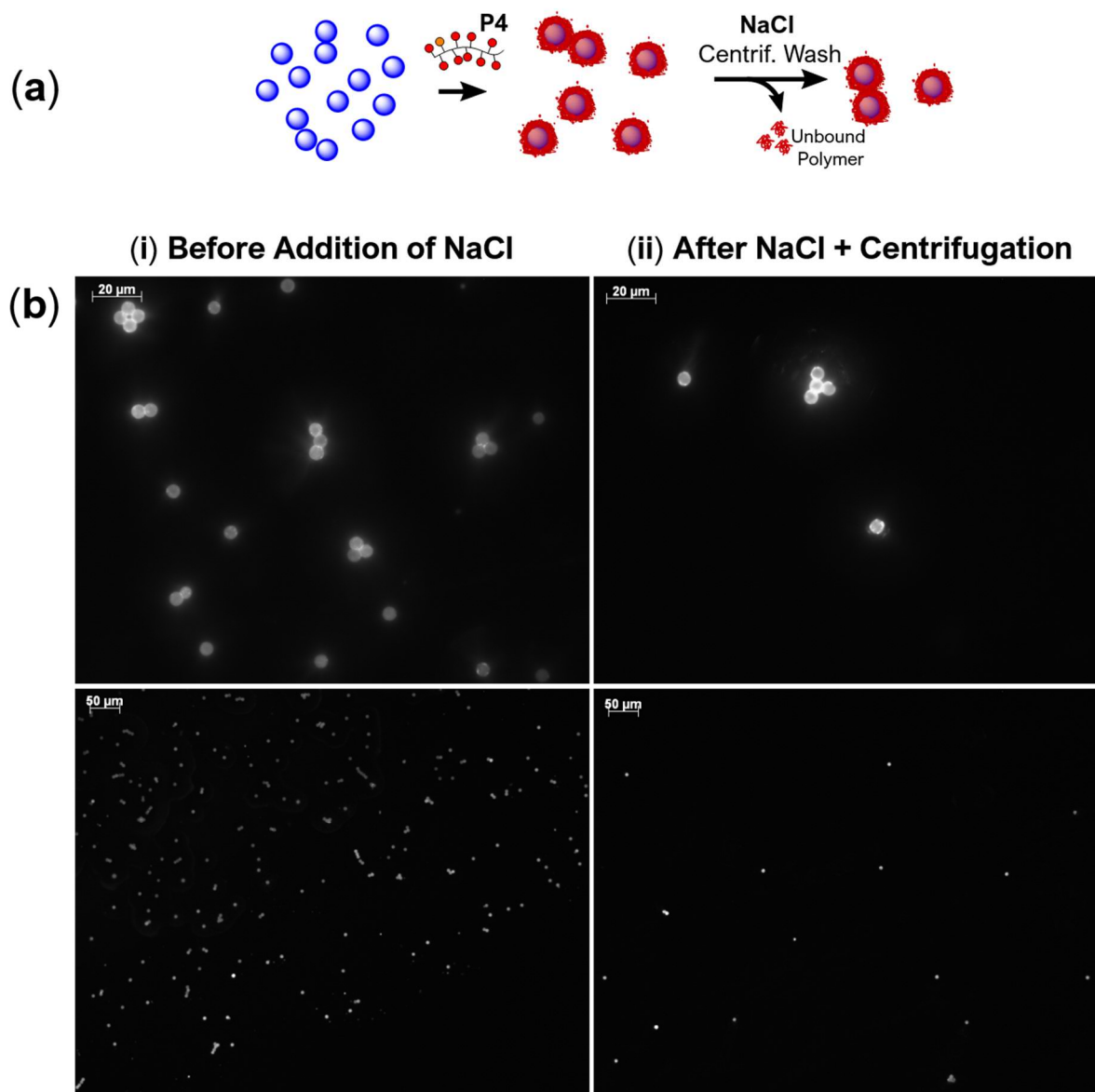


Figure 27: (a) Preparation of dansyl polycation (**P4**) ‘coated’ 5 μm sulfonate-functionalized microparticles (**sMPs**) and attempted ‘coating’ removal (b) by repeated washes with sat. NaCl solution, followed by centrifugation to remove the ‘unbound’ polyelectrolyte. (b) Fluorescence microscope images of ‘coated’ **sMPs** before (i) and after (ii) exhaustive centrifugal washing with sat. NaCl.

2.3.11. Adsorption of 'Soft' Polyelectrolytes onto Polystyrene NPs

On account of the challenges associated with removing 'hard' quaternary ammonium polyelectrolyte layers (**P3**, **P4**) from the surface of oppositely-charged polystyrene particles, an alternative class of 'soft' polyelectrolytes were prepared. These 'soft' polyelectrolytes feature morpholine moieties (Fig. 28, i), which upon increasing the pH of solution (ii), can be deprotonated (iii) to effectively 'switch off' the electrostatic charge attraction between polymer and the polystyrene surface to which the polymer layer was adsorbed. It was thus hypothesized that 'switching off' the electrostatic binding between polymer and particle, that the charge-neutral layer would be re-dispersed into the bulk solution (iv), effectively displacing adsorbed polymer coating from the **sNPs** surface to again yield the 'naked' polystyrene particles (v).

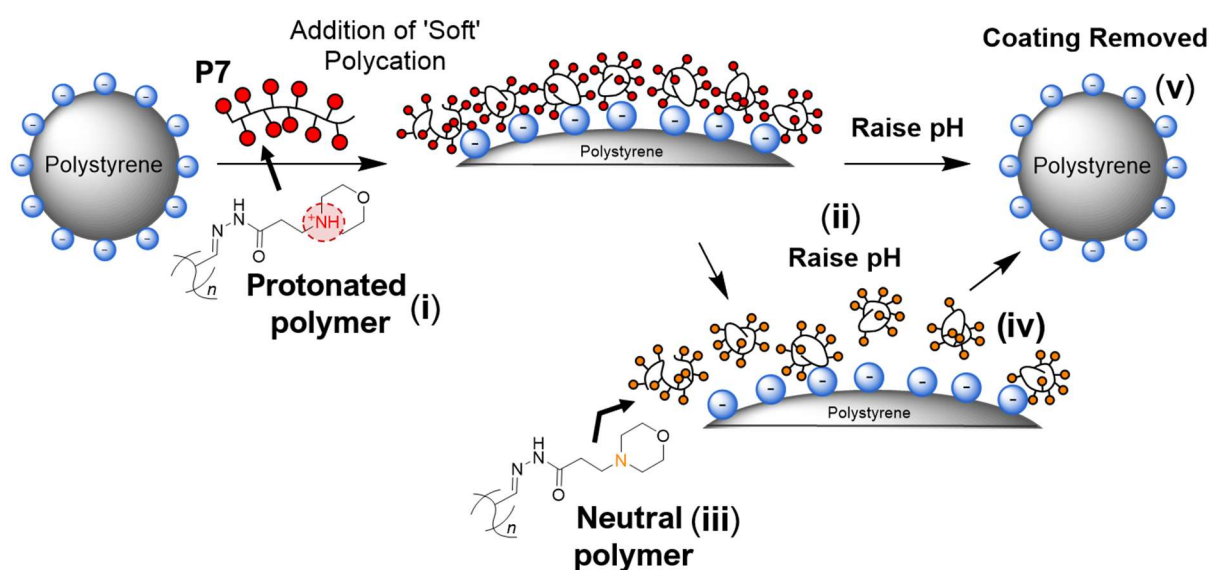


Figure 28: Adsorption of a 'soft' polycation **P7** onto **sNPs** yields a polymer coating which can be removed by raising the pH. Charged groups (i) within 'soft' polycation **P7** can be deprotonated by raising the pH of solution (ii), which renders a charge-neutral polymer (iii) which should be displaced from the polystyrene surface (iv), to afford the 'naked' polystyrene particles (v).

It was anticipated that the reversible formation/removal of the adsorbed 'soft' polyelectrolyte (**P7**) layer (Fig. 28) would permit access to the key experiment for definitive proof of 'shrink-wrapping' (Fig. 29a). In this key experiment, the adsorbed layer of linear 'soft' polycation (Fig. 29a, i) should be displaced by raising the pH (ii), whereas the same experiment with **Morpholine SCPNs** (Fig. 29b) was expected to yield 'wrapped' **sNPs** (i), where the polymer film cannot be displaced (ii) on account of the intermolecular crosslinks which hold the film in place. pH titration (Appendix A, Fig. 37c) revealed that the morpholine nitrogen of hydrazide **R5** (Fig. 30) was weakly basic, with a pK_a of 6.4. It was therefore anticipated that 'soft' polyelectrolytes displaying pendant morpholine (**R5**) residues would be fully deprotonated above pH 8, thus have no electrostatic charge to hold the polymer coating on the periphery of the polystyrene nanoparticles.

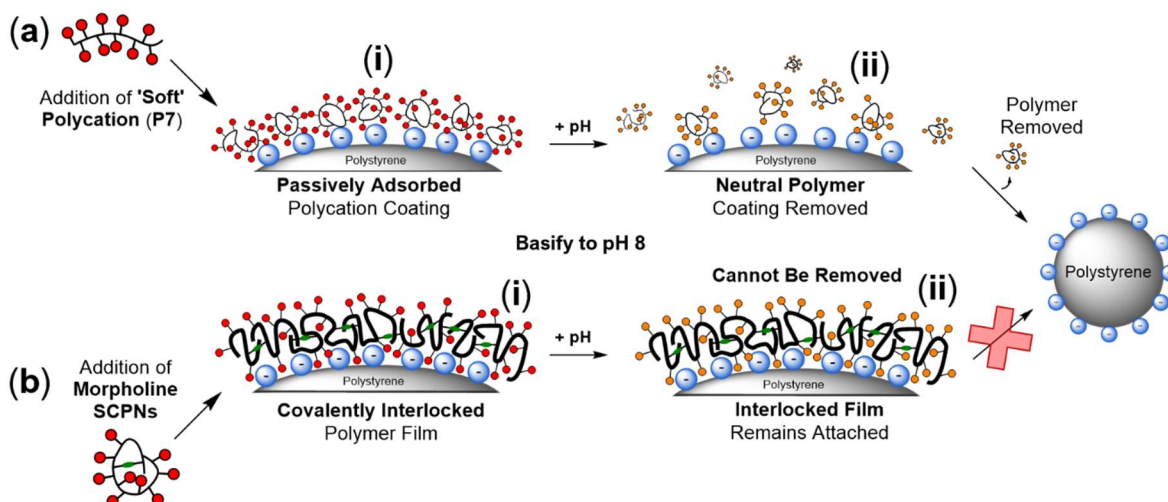


Figure 29: Key experiments to demonstrate the successful 'shrink-wrapping' of **sNPs**. **(a)** Control experiment with linear 'soft' polycation (**P7**). The adsorbed 'soft' polyelectrolyte **(i)** should be displaced **(ii)** by basifying the solution to pH 8 and removal of the unbound polymer should yield 'naked' **sNPs**. **(b)** Concentration of **Morpholine SCPNs** on to the surface of **sNPs** was anticipated to yield within an intermolecularly crosslinked polymer film **(i)**, which cannot be displaced **(ii)** by raising the pH.

The protonation state of morpholine decorated scaffold **P7** (Fig. 30a) was studied as a function of pH by zeta potential measurements (Fig. 30b, **iii**), which revealed a the 'soft' polycation was protonated, and thus positively charged ($ZP = 37 \pm 2$ mV) at pH 3. In contrast, **P7** was deprotonated, hence charge-neutral above pH 7.2, where $ZP = -1.1 \pm 1$ mV. These results indicate that it should be possible to reversibly 'switch' on/off the electrostatic charge upon the 'soft' morpholine polycation **P7**, simply by adjusting the pH of solution after **P7** has been adsorbed onto the periphery of **sNPs**.

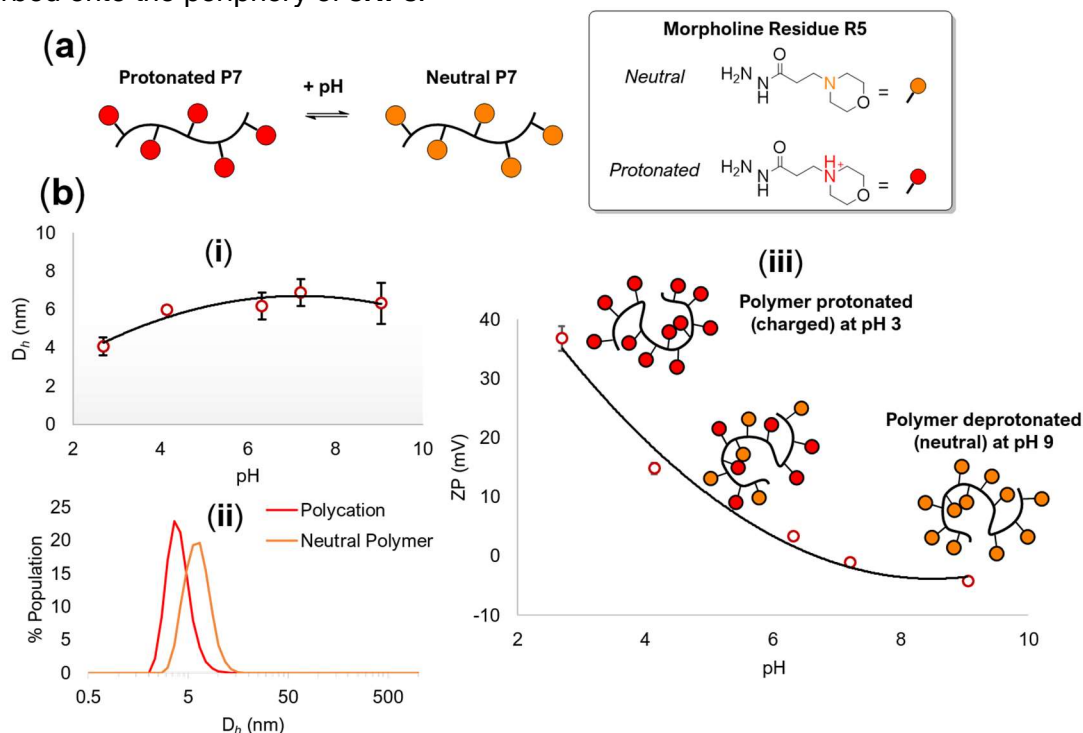


Figure 30: **(a)** Reversible deprotonation of 'soft' morpholine polycation **P7**. **(b)** DLS **(i-ii)** and ZP **(iii)** characterization of **P7**, as a function of pH. **(i)** Z-average D_h of **P7** as a function of pH. **(ii)** Z-average particle size distributions of **P7** in its positively-charged (pH 3)(red) and charge-neutral (pH 9)(orange)

In this experiment **sNPs** were added to varying doses (PD = 0 – 10000 mg/g) of morpholine polycation **P7**. Zeta potential and DLS measurements (Fig. 31a) were obtained to determine the surface charge of the resulting particles, over a range of pH values (pH 1 – 9.0).

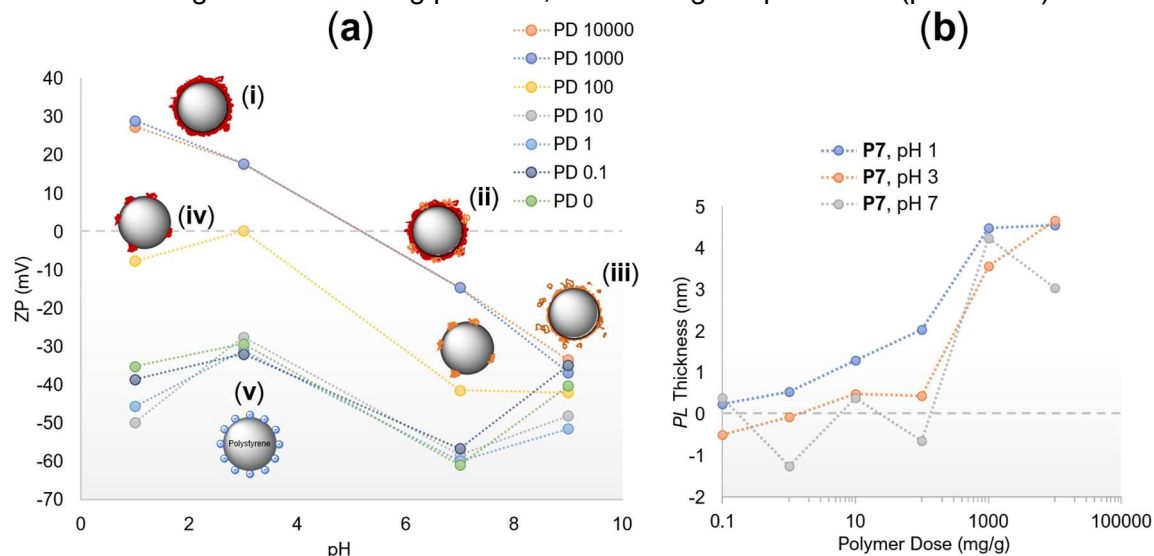


Figure 31: (a) Zeta potential as a function of pH. Polymer Doses 0 – 10000 mg/g were explored. (b) Hydrodynamic thickness (L) of the adsorbed polymer layer presented as a function of Polymer Dose at pH 1 (blue), pH 3 (orange) and pH 7 (grey).

ZP revealed that low polymer doses of 0.1 – 10 mg/g (Fig. 31a, v) did not afford positively charged particles, and featured ZP values close to that of the ‘naked’ **sNPs** ($ZP \approx -40$ mV), even under acidic conditions (pH 1), where all morpholine residues would be positively charged. Note that the ZP of ‘naked’ **sNPs** (Fig. 31a) (PD = 0 mg/g, green) remain approximately constant over the range pH = 1 – 9. Intermediate polymer doses (PD = 100 mg/g) (yellow) afforded ‘partially’ coated particles (Fig. 31a, iv) at pH 1 - 3, with a $ZP \approx 0$ mV, close to the isoelectric point (IEP). At PD = 100, just enough polymer is present to balance the total number of negative charges on the particle surface, thus no net charge is observed for the particle as it is close to the IEP. Raising pH partially deprotonated the positive charges on morpholine scaffold, thus the particles ZP value was shifted back to negative surface charge and away from the IEP. Addition of a large excess of morpholine polycation **P7**, however, afforded fully ‘coated’ **sNPs** (Fig. 31a, i) under acidic conditions, as was evident from their strong positive surface charge ($ZP = +30$ mV). Encouragingly, both PD = 1000 and 10000 mg/g afforded an identical ZP profile, which implies saturation of the particle surface with polymer. Increasing the pH, however, afforded deprotonation of morpholine residues within the adsorbed polymer layer (Fig. 31a, ii), until the ‘coated’ particle was no longer positively charged (iii), as evidenced by the now negative zeta potential ($ZP = -30$ mV at pH 9), with a very similar value to that of the ‘naked’ **sNPs** ($ZP = -40$ mV for PD = 0 mg/g at pH 9). The hydrodynamic thickness (L) of the adsorbed polymer layers (Fig. 31b) were obtained from DLS analysis and were expressed as a function of the polymer dose (PD). These results (Fig. 31b) were consistent with the adsorption of a thin polymer layer, with the maximum hydrodynamic thickness being 5 nm.

Further DLS/ZP experiments were conducted using morpholine polycation (**P7**) (Fig. 32c-d), a polymer which was absent in covalent crosslinks and **Morpholine SCPNs** (Fig. 32a-b), which were prepared by intramolecular crosslinking of **P7** with 1 equivalent of succinic dihydrazide. **Morpholine SCPNs** were anticipated to ‘shrink-wrap’ the periphery of **sNPs** (Fig. 29b) on account the dynamic covalent nature of their crosslinkers, whilst **P7** will form non-crosslinked polymer ‘coatings’, and thus were employed for control experiments. **P7** ‘coated’ (Fig. 32c) and **SCP** ‘wrapped’ (Fig. 32a) **sNPs** were prepared at pH 1 (red) and the zeta potentials were measured for each sample. Figures 32a,c report ZP as a function of the polymer dose. Under acidic conditions (pH 1) the expected surface charge reversal was observed at PD \approx 100, with positive ZP at PD > 1000 indicating that the **sNPs** were ‘coated’ in polymer. Morpholine polymer **P7** showed a more positive surface charge than the crosslinked polymer, which was rationalized by the crosslinked **Morpholine SCPNs** having a slightly lower density of positively charged morpholine residues than the parent linear polymer **P7**.^{***} After basifying the samples

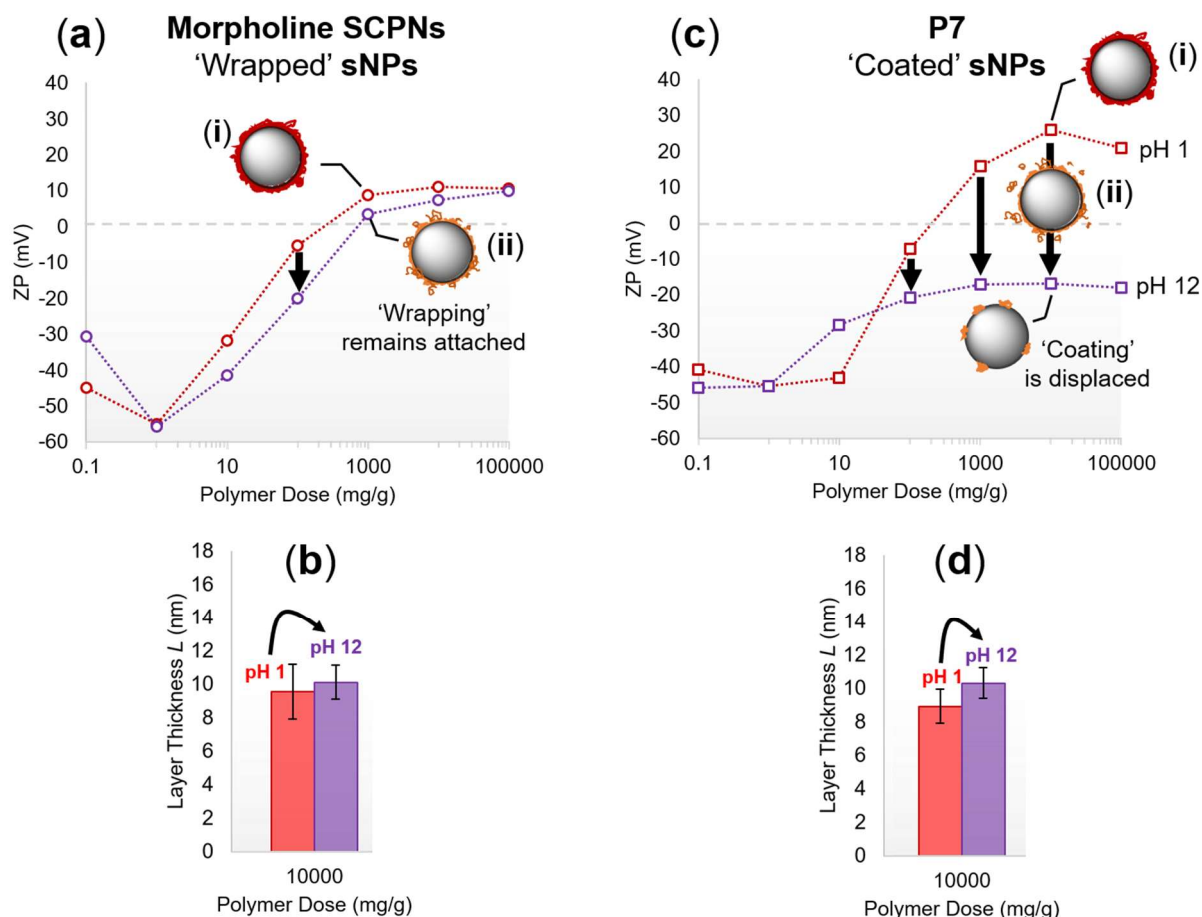


Figure 32: ‘Shrink-wrapping’ experiment with **Morpholine SCPNs** (a-b) and control experiment with morpholine polymer **P7** (c-d). (a and c) Zeta potential as a function of pH. Polymer doses 0 – 10000 mg/g were explored. (b) Hydrodynamic thickness (L) of the adsorbed polymer layer before (pH 1) and after (pH 12) removal of the polymer layer. These DLS results show negligible decrease in particle size.

^{***} Crosslinking of **P7** with succinic dihydrazide results in the displacement morpholine hydrazide, and thus **Morpholine SCPNs** have few morpholine residues per polymer chain.

to pH 9 (Fig. 32a,c), morpholine residues within the polymer coating were neutralized, and thus the surface charge of the polymer-encapsulated **sNPs** reverted back to negative zeta potentials ($ZP \approx -20$ mV), towards that of the 'naked' **sNPs** ($ZP = -43 \pm 3$ mV). This observation may suggest the polymer is still loosely associated with the surface of **sNPs** and has not been fully displaced. Intriguingly, after basifying the samples to pH 9 the ZP profile for **Morpholine SCPNs** (Fig. 32a, ii) was less negative (closer to neutral) than that of the non-crosslinked polymer **P7** (Fig. 32b, ii). These observations suggest that the 'wrappings' formed from **Morpholine SCPNs** tend to 'resist' displacement of the surface-bound polymer layer, whereas **P7** (non-crosslinked) layers are more easily displaced. This subtle difference in the behaviour of these two polymers is consistent with the hypothesis that **Morpholine SCPNs** have formed an intermolecularly crosslinked film upon the **sNPs**. Unfortunately, DLS results (Fig 32a and b) revealed negligible changes in the thickness of the adsorbed polymer layer. It was observed that both **P7** and **Morpholine SCPNs** were adsorbed onto **sNPs** with a layer thickness approximately 10 nm. After attempting to displace the polymer layer, these numbers had not significantly decreased, which indicates the polymer layers remained bound to the particle surface in both cases.

In summary, although DLS results suggest polymer layers had not been displaced, zeta potential measurements hint at subtle differences in the behaviour of crosslinked (**Morpholine SCPNs**) and non-cross linked (**P7**) polymers. Having established robust analytical protocols to investigate the adsorption of polyelectrolyte chains onto the surface of colloidal particles, studies returned to focus on the 'shrink-wrapping' of **SV40** capsids.

2.3.12. Adsorption of Linear Polycation upon SV40 Viral Capsid

Collaborators from the laboratory of W. B. Turnbull delivered a fresh batch of **SV40** capsid, which was rigorously characterized by DLS. Experiments with the previous batch of **SV40** suggested that **Cationic SPCN-1** had successfully adsorbed onto the viral surface, yet definitive proof of the intermolecularly crosslinked nature of the observed polyelectrolyte film was difficult to obtain. It was very likely that viral capsid had been successfully 'shrink-wrapped' by **Cationic SPCN-1**. Thus, present experiments focused predominantly on getting the troublesome control experiment with linear polycation **P3** to operate as anticipated, with the view of later returning to the 'shrink-wrapping' experiments with **Cationic SPCN-1**. In these experiments, solutions of 'coated' **SV40** were prepared by addition of linear polycation **P3** (Fig. 33a) into a 29.3 nM solution of viral capsid at pH 7.4. A series containing a range of [polycation]/[capsid] stoichiometries ($[Polycation]/[Capsid] = 0.3 - 23\ 000$) were prepared and after incubation at room temperature for 2 h, the 'unbound' excess of polycation **P3** was removed by centrifugation (40 000 rpm). Suspensions of the 'coated' viral capsids were then

characterized by DLS (Fig. 33b) and ZP (Fig. 33d), revealing the anticipated increase in particle size (D_h) and reverse in electrostatic charge present upon the periphery of **SV40** capsid, respectively. DLS (Fig. 33b) revealed a 2 - 30 nm increase in D_h , which was consistent with a polyelectrolyte bound upon the capsid surface, with a hydrodynamic layer thickness (L) of 1 – 15 nm depending on the [Polycation]/[Capsid] stoichiometry (Fig. 33c). Encouragingly, both the z-average (orange) and number-average (blue) data afforded similar values, despite the fact that the raw z-average DLS data (Fig. 33b, orange) was slightly skewed towards larger particle sizes, on account of a small population of multiparticle particle aggregates within the sample.

The next stage of this investigation involved the removal of the surface-bound ‘hard’ polycation layer by addition of excess salt, which was anticipated to displace the **P3** ‘coating’ from the viral surface, by disrupting the electrostatic interactions between polymer and capsid. Whilst the adsorption of **P3** onto oppositely-charged **sNPs** – a hard polyanion with high density of sulfonate groups – was an essentially irreversible process, it was hypothesized that the adsorbed **P3** layer should be reversibly displaced from **SV40** capsid, on account of the viral surface being only a ‘soft’ polyelectrolyte which displays both regions of both regions of positive and negative charge. Furthermore, the density of ‘soft’ negative charges displayed by the **SV40** capsid was expected to be considerably lower than that of ‘hard’ anionic groups upon the polystyrene-sulfonate (**sNPs**) particles. To displace the surface-bound **P3** layer from **SV40**,

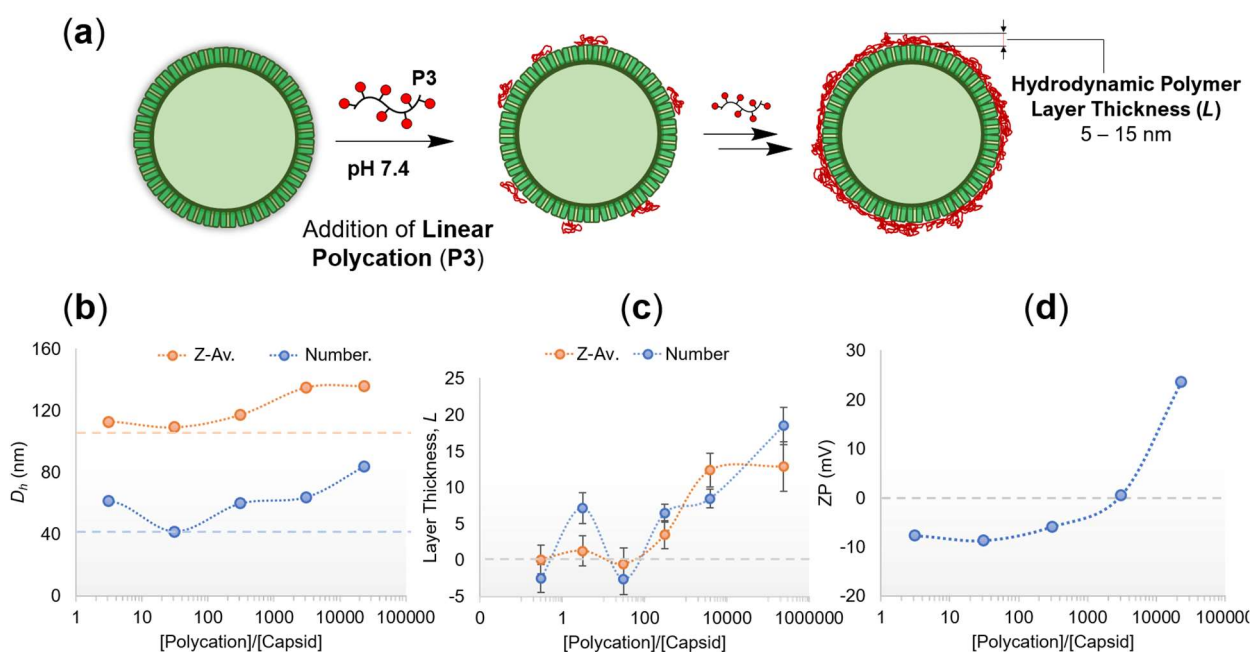


Figure 33: (a) Adsorption of linear polycation **P3** onto **SV40** viral capsid results in ‘coated’ **SV40**, with a polyelectrolyte layer thickness (L) of 2 – 15 nm, depending on the polymer dose. (b-c) DLS and ZP measurements of ‘coated’ **SV40** capsid. (b) Z-average (orange) and number average (blue) D_h given as a function of [Polycation]/[Capsid] stoichiometry. (c) Hydrodynamic layer thickness (L) of surface-bound polycation ‘coating’ upon the viral capsid, expressed as a function of [Polycation]/[Capsid] ratio. (d) ZP of ‘coated’ **SV40** as function of [Polycation]/[Capsid].

a range of salt concentrations (0 mM – 2M NaCl) and salt types (NaCl, NaBr, KCl etc.) were explored. However, the conditions ($[\text{NaCl}] > 200 \text{ mM}$) required to displace the polyelectrolyte layer was sufficient to drive particle-particle aggregation of viral capsids, which was observed by DLS (Fig. 34) as sharp increase in the polydispersity index.

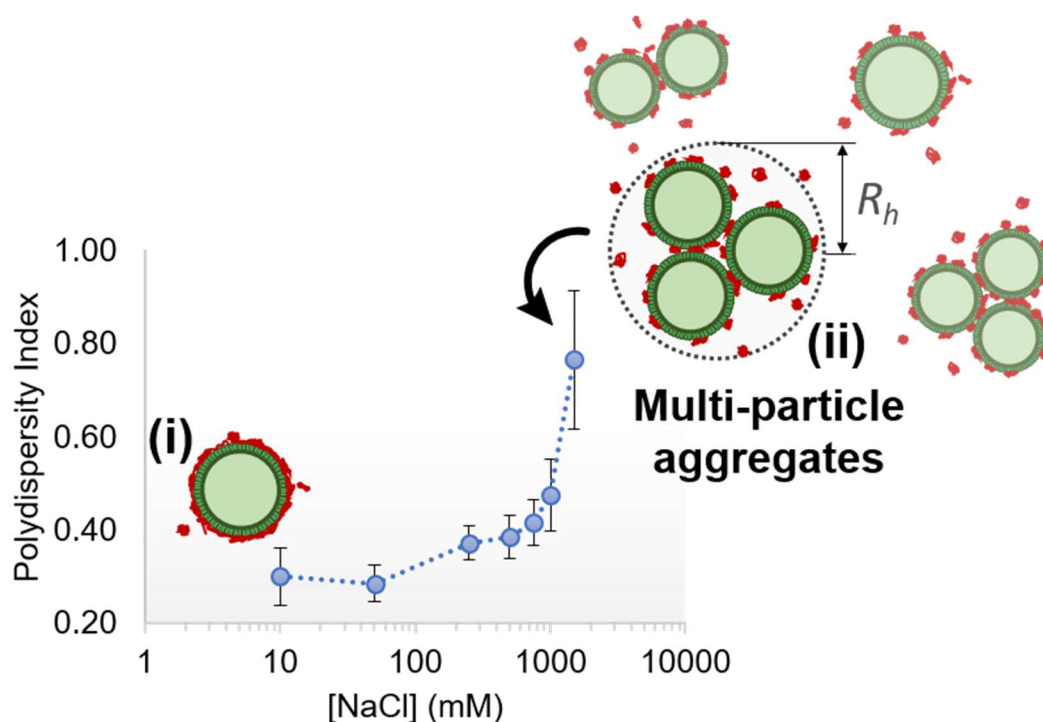


Figure 34: DLS polydispersity index (PDI) for **P3** 'coated' **SV40** (i), given as a function of $[\text{NaCl}]$. Where high salt concentrations of $[\text{NaCl}] > 200 \text{ mM}$ led to a sharp increase in polydispersity, on account the formation of multi-particle aggregates (ii).

In an alternative approach (Fig. 35a), the reversible adsorption of ‘soft’ morpholine-functionalized polycation **P7** onto **SV40** capsid was considered. **P7** required mildly acidic media ($\text{pH} < 4$) (see Fig. 30b, iii) to ensure protonation of morpholine residues located upon the polymer scaffold and basic conditions ($\text{pH} \approx 9$) to facilitate removal of the adsorbed polymer layer. Thus, the pH-stability of **SV40** capsid was investigated by measuring the zeta potential of **SV40** as a function of pH (Fig. 35b).

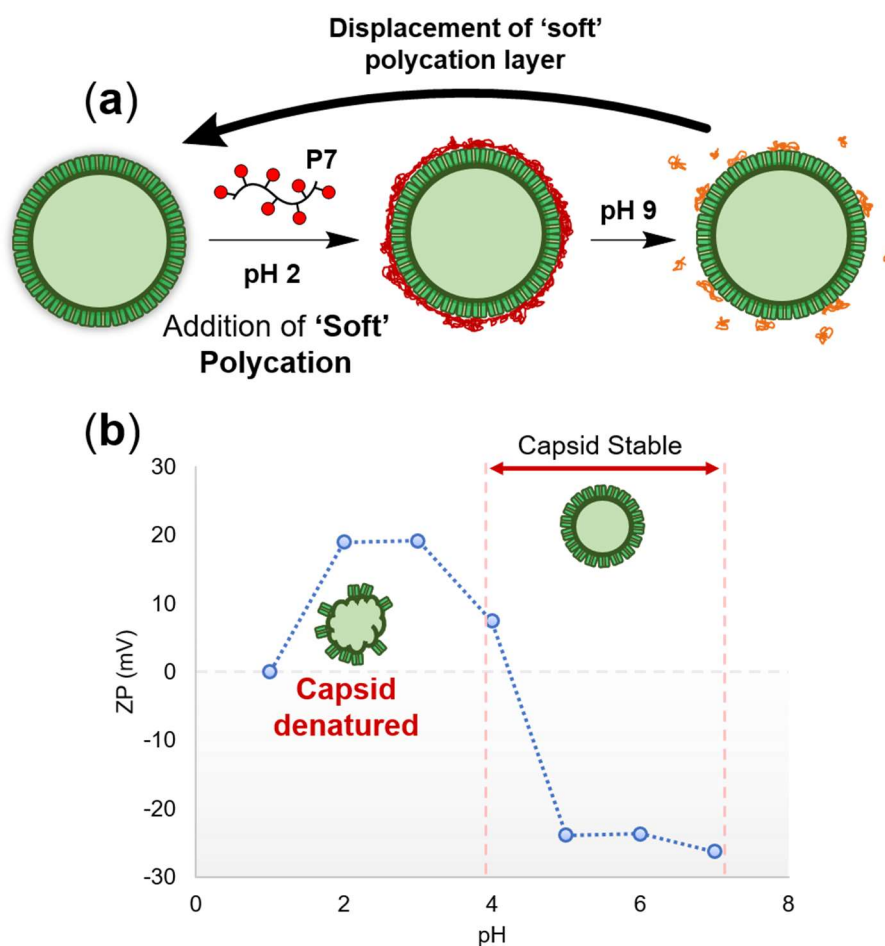


Figure 35: (a) Adsorption of morpholine-functionalized ‘soft’ polycation (**P7**) onto **SV40** was anticipated to allow for the reversible displacement of the surface-bound polymer layer from the viral surface by basifying to pH. Positively charged/protonated polymer layer (red), charge neutral/deprotonated **P7** (orange). (b) ZP of **SV40** viral capsid as a function of pH. **SV40** capsid was stable at pH 4 – 7.5, but denatured below pH 4 and had completely dissociated into its constituent protein subunits at pH < 2.

DLS and ZP measurements revealed that **SV40** capsid was stable in the range pH 4 - 7.4, whilst moderately acidic conditions ($\text{pH} < 2$) afforded disassembly/denaturing of the viral capsid into its constituent protein subunits. Zeta potential of **SV40** at pH 5 – 7 was $\text{ZP} \approx -24$ mV, a strong negative surface charge indicative of good colloidal stability. ‘Soft’ morpholine polycation (**P7**) is partially protonated at 5 (Fig. 30b, iii), and thus presents positive charges for complexing with **SV40** capsid. Future work aims to explore interface **SV40** capsid with ‘soft’ polyelectrolytes such as **Morpholine SCPNs/P7**, with the hope of demonstrating successful ‘shrink-wrapping’ of the viral capsid within intermolecularly crosslinked polymer films.

2.4. Conclusion

‘Shrink-wrapping’ studies were undertaken in which **SV40** viral capsid was interfaced with SCPNs displaying multiple positively-charged quaternary ammonium appendages, which were anticipated to concentrate polymer onto the virus surface through complementary electrostatic interactions, and thus drive covalent crosslinking of adjacent chains into a net-like polymer film. Characterisation of the ‘wrapped’ **SV40** capsid was consistent with this hypothesis, revealing the attachment of a thin (5 - 30 nm) virus-bound polymer layer and a distinct reversal in the electrostatic surface charge present upon viral surface. To demonstrate the successful ‘shrink-wrapping’ led to the formation of intermolecularly crosslinked polymer films, key control experiments were undertaken to highlight that crosslinked films are more difficult to displace from the virus surface than are non-crosslinked polymer coatings. It was observed that the high salt concentrations required to drive the displacement of non-crosslinked polymer coatings from **SV40** significantly disrupted the colloidal stability of the viral capsid, thus driving processes of particle-particle aggregation which decreased quality of DLS analysis obtained. Although **SV40** had likely been successfully ‘shrink-wrapped’ by **Cationic SCPN-1**, challenges associated with characterizing the displacement of polyelectrolyte layers from the particle surface meant that definitive proof of ‘shrink-wrapping’ has so far remained elusive.

In pursuit of strong evidence to support the ‘shrink-wrapping’ hypothesis, further investigations were conducted upon polystyrene nanoparticles (**sNPs**), a model system that has a similar size and surface charge to **SV40**. DLS, zeta potential TEM characterization revealed the successful adsorption of a thin (5 – 25 nm) layer of polymer chains located upon the particle surface. Although extensive efforts were made to demonstrate the crosslinked nature of these polymer layers, evidence of this could not be easily obtained. DLS and ZP measurements revealed that the adsorption of ‘hard’ polyelectrolytes layers onto particle surfaces, is essentially an irreversible process, which consequently denied access to the key control experiment that was anticipated to prove ‘shrink-wrapping’. This chapter was concluded by experiments to circumnavigate the irreversible binding of ‘hard’ polycations to polystyrene surfaces. It was anticipated that the reversible deprotonation/protonation of ‘soft’ morpholine polyelectrolytes would permit access to the key control experiment by presenting a means to ‘switch off’ the electrostatic charges associated with irreversible binding to particle surfaces. In this system the key control experiment operated as exactly anticipated with non-crosslinked morpholine polymers being successfully displaced after neutralizing their positive charges under basic conditions. ‘Wrapping’ experiments revealed that **Morpholine SCPNs** tended to resist displacement of polymer films from the particle surface, thus providing some evidence of successful ‘shrink-wrapping’.

2.5. Future Work

Future work looks to interface ‘soft’ **Morpholine SCPNs** with **SV40** capsid to see if strong evidence for the ‘shrink-wrapping’ of viral targets can be obtained. Furthermore, we are keen to investigate the effect that the polycation ‘wrapping’ has upon the stability of the virus-like particle to elevated temperatures and dehydrating conditions. It is anticipated that the surface-bound polymer layer will protect the viral ‘cargo’. Verification of this hypothesis should thus be explored through a combination of DLS, SDS-PAGE, ELISA, AFM and cryo-TEM experiments to reveal if the polymer coating ‘masks’ and thus protects the viral surface over prolonged exposure to stimuli known to denature the assembled capsid.

For example, the addition of reducing agents such as **DTT** or **glutathione** (Fig. 36a) are known¹³ to trigger the disassembly of **SV40** capsid into its constituent protein subunits (i.e. pentamers of **VP1**) – a process which could readily be monitored by time-resolved DLS analysis (Fig. 36b) to reveal a distinct collapse in hydrodynamic diameter (Fig. 36a, i). Future studies will examine the differences in stability between ‘naked’ (Fig. 36b) and ‘wrapped’ (Fig. 36c) **SV40** capsids, to understand how polymer ‘wrappings’ could be employed to engineer the properties of viral surfaces, extend their ‘shelf-lives’ and improve their performance.

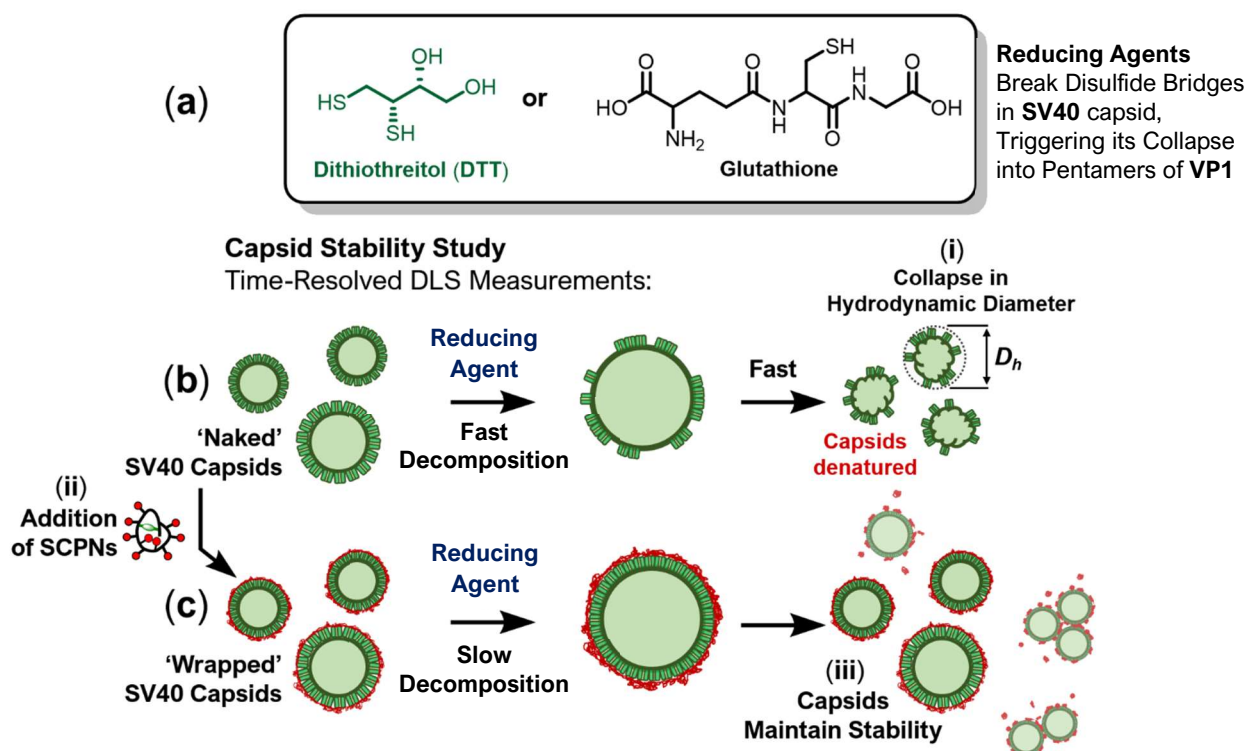


Figure 36: Addition of reducing agents (a) to **SV40** capsids is known to trigger their dissociation into pentamers of **VP1**,¹³ thus driving their degradation by cleaving disulfide bridges that hold the capsid together. (b) Addition of reducing agent to an aqueous dispersion of ‘naked’ **SV40** capsids is thus hypothesized to trigger a collapse (i) in its hydrodynamic diameter, D_h – a process which could be monitored by time-resolved DLS. In contrast, the reduction of ‘wrapped’ **SV40** (c) should be stable over longer periods (iii) and thus resist collapse in D_h , on account of its protective polymer ‘wrapping’. DLS studies should elucidate key differences between ‘naked’ and ‘wrapped’ **SV40**, thus demonstrating the potential of the ‘wrapping’ approach to engineer the properties of viral surfaces.

2.6. Experimental

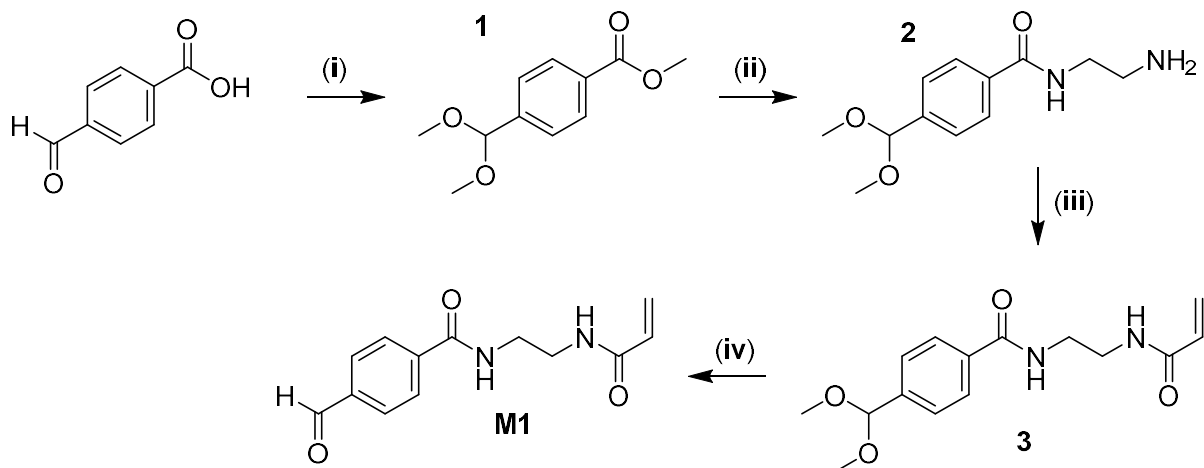
2.6.1. General Experimental

All chemicals were purchased from Sigma-Aldrich, Fisher Scientific or Alfa Aesar and were used as received without further purification. Functionalized-polystyrene latex nano- and microparticles were purchased from Sigma-Aldrich. All solvents were dried prior to use according to standard methods. *N,N*-dimethylacrylamide was purified by vacuum distillation at 60 °C. All solvents used for flash chromatography were GPR grade, except hexane and ethyl acetate, when HPLC grade was used. Unless state otherwise, all synthetic procedures were performed in oven-dried glassware under a N₂(g) atmosphere.

2.6.2. Instrumentation

¹H and ¹³C NMR spectra of synthesised compounds were recorded on a Bruker Avance 300 spectrometer (300 and 75 MHz respectively), Bruker Avance 400 spectrometer (400 MHz and 100 MHz, respectively), Bruker Avance III HD spectrometer (at 500 MHz and 125 MHz, respectively), or Bruker 700 Avance III HD spectrometer (700 MHz and 175 MHz, respectively). In all cases, the residual solvent signal was used as an internal standard. High-resolution mass spectrometry was performed on a Waters LCT Premier mass spectrometer^a. Gel permeation chromatography (GPC) was conducted on a on a Varian ProStar instrument (Varian Inc.) equipped with a Varian 325 UV-Vis dual wavelength detector with a 254 nm laser, a Dawn Heleos II multi-angle laser light scattering detector (Wyatt Technology Corp.), a Viscotek 3580 differential refractive index detector and two PL gel 5 µm Mixed D 300 × 7.5 mm columns with guard column (Polymer Laboratories Inc.) in series. Chromatogram analysis was performed on Galaxie software (Varian Inc.) and analyzed with the Cirrus software (Varian Inc.) and Astra software (Wyatt Technology Corp.). Near monodisperse poly(methyl methacrylate) standards (Agilent Technologies) were used for calibration. DLS and zeta potential measurements were performed on a Malvern Instruments Nano ZS. Fluorescence microscopy images were obtained were obtained using Zeiss Axioskop 2 Plus. pH measurements were made using a Hanna HI 90103 instrument which was calibrated before use using commercial buffer solutions (Sigma-Aldrich).

2.6.3. Synthesis of Aldehyde Monomer M1



Scheme 2: Synthesis of aldehyde acrylamide monomer **M1**. Step (i) $\text{CH}(\text{OMe})_3$, H_2SO_4 , MeOH, reflux, 18 h. Step (ii) 1,2-Ethylenediamine, reflux, 48 h. Step (iii) Acryloyl chloride, Et_3N , CH_2Cl_2 , 0° , 18 h. Step (iv) 50:50 Acetone:2M $\text{HCl}_{(\text{aq})}$.

Synthesis of Methyl 4-(dimethoxymethyl)benzoate (**1**):

4-Carboxybenzaldehyde (15.4 g, 102.6 mmol), trimethylorthoformate (32.7 g, 308.1 mmol) and H_2SO_4 (12 drops) were dissolved in MeOH (100 mL) and the mixture was refluxed for 48 h. The reaction mixture was neutralized with saturated $\text{NaHCO}_3(\text{aq})$ (100 mL) and the product was extracted with CH_2Cl_2 (3×150 mL). The organic extract was dried over MgSO_4 , filtered, and dried under vacuum to afford the title product as a clear oil (19.8 g, 92 %). ^1H NMR (CDCl_3 , 300 MHz) δ (ppm): 8.00 (d, 2H, Ar, $J_3 = 8.1$ Hz), 7.54 (d, 2H, Ar, $J_3 = 8.1$ Hz), 5.41 (s, 1H, $\text{CH}(\text{OCH}_3)_2$), 3.85 (s, 3H, COOCH_3), 3.31 (s, 6H, $\text{CH}(\text{OCH}_3)_2$). ^{13}C NMR (CDCl_3) δ (ppm): 167.1, 143.8, 130.8, 129.8, 127.1, 103.1, 53.0, 52.1. FT-IR (wavenumber, cm^{-1}): 2943 (C–H), 2904 (C–H), 2836 (C–H), 1724 (C=O), 1450 (C=C), 1434 (C=C), 1409 (C=C).

Synthesis of N-(2-Aminoethyl)-4-(dimethoxymethyl)benzamide (**2**):

Methyl 4-(dimethoxymethyl)benzoate **1** (6.0 g, 28.5 mmol) was dissolved in 1,2-diaminoethane (100 mL), heated to reflux for 24 h and then evaporated to dryness to afford a viscous yellow oil. Crude product **2** was dissolved in a minimal volume of CH_2Cl_2 , then filtered to remove residual 1,2-diaminoethane, which was observed as a white precipitate. **2** was purified by column chromatography (SiO_2 , $\text{CH}_2\text{Cl}_2/\text{EtOH}/\text{Et}_3\text{N}$ 80:15:5) to afford the product as a yellow oil (4.1 g, 61 %). ^1H NMR (CDCl_3) δ (ppm): 7.73 (d, 2H, Ar, $J_3 = 9.0$ Hz), 7.38 (d, 2H, Ar, $J_3 = 9.0$ Hz), 7.33 (t, 1H, NH), 5.30 (s, 1H, $\text{CH}(\text{OCH}_3)_2$), 3.61 (br s, 2H, NH_2), 3.46 (q, 2H, CH_2), 3.22 (s, 6H, $\text{CH}(\text{OCH}_3)_2$), 2.91 (t, 2H, CH_2). (CDCl_3 , 100 MHz) δ (ppm): 166.4, 143.0, 130.2, 129.6, 126.8, 102.3, 52.6, 52.1, 42.3. HRMS $^+$ $\text{C}_{12}\text{H}_{18}\text{N}_2\text{O}_3$: Theoretical: 238.1317. Actual: 238.1320

Synthesis of *N*-Ethylacrylamide-2-(4-(dimethoxymethyl)benzamide (**3**):

A solution of **2** (4.1 g, 17.2 mmol) and Et₃N (5.2 g, 51.3 mmol) in CH₂Cl₂ (100 mL) was cooled to 0 °C and acryloyl chloride (2.3 g, 25.8 mmol) in CH₂Cl₂ (50 mL) was added dropwise over 1 h. The reaction was stirred overnight, gently allowing to warm back to room temperature, then washed with saturated NaHCO_{3(aq)} (150 mL). The aqueous layer was extracted with CH₂Cl₂ (2 × 150 mL) and the combined organic extracts were dried over MgSO₄, filtered, and evaporated to dryness. The crude solid was purified by column chromatography [SiO₂, EtOAc-Et₃N (95:5)], affording the title product as a white solid (2.0 g, 40 %). ¹H NMR (300 MHz, CDCl₃) δ (ppm): 7.82 (s, 1H, NH), 7.79 (d, 2H, Ar, *J*₃ = 8.1 Hz), 7.44 (d, 2H, Ar, *J*₃ = 8.1 Hz), 7.36 (s, 1H, NH), 6.21 (dd, 1H, alkene CH, *J* = 17.2 Hz), 6.13 (dd, 1H, alkene CH, *J* = 17.2 Hz), 5.56 (dd, 1H, alkene CH, *J* = 9.7 Hz), 5.34 (s, 1H, CH(OCH₃)₂), 3.50 (m, 4H, (CH₂)₂), 3.28 (s, 6H, CH(OCH₃)₂). ¹³C NMR (75 MHz, CDCl₃) δ (ppm): 168.6, 167.5, 142.1, 134.6, 133.3, 131.3, 130.0, 128.2, 127.3, 103.1, 53.1, 41.3.

Synthesis of *N*-Ethylacrylamide-2-(4-formylbenzamide) (**M1**):

N-ethylacrylamide-2-(4-(dimethoxymethyl)benzamide) **3** (2.0 g, 6.8 mmol) was dissolved in 1:1 Acetone:1M HCl_(aq) (15 mL), stirred at room temperature for 1 h and neutralized with sat. NaHCO_{3(aq)} (85 mL). The aqueous layer was extracted with EtOAc (3 × 120 mL). The organic extracts were combined and dried over MgSO₄, filtered, and evaporated to afford the title product as a white solid (1.4 g, 84 %). ¹H NMR (300 MHz, *d*₆-DMSO) δ (ppm): 10.07 (s, 1H, CHO), 8.23 (s, 1H, NH), 8.79 (s, 1H, NH), 8.03 (d, 2H, Ar, *J*₃ = 8.4 Hz), 7.99 (d, 2H, Ar, *J*₃ = 8.4 Hz), 6.23 (dd, 1H, alkene CH, *J* = 17.1 Hz), 6.09 (dd, 1H, alkene CH, *J* = 17.1 Hz), 5.59 (dd, 1H, alkene CH, *J* = 9.6 Hz), 3.72 (m, 4H, (CH₂-CH₂)). ¹³C NMR (75 MHz, *d*₆-DMSO) δ (ppm): 193.0, 166.1, 165.5, 140.1, 138.2, 132.3, 129.6, 128.3, 125.2, 39.6, 38.7. FT-IR (wavenumber, cm⁻¹): 3264 (N-H), 3091 (C-H, alkene), 2943 (C-H, alkyl), 1699 (C=O, aldehyde), 1627 (C=O, amide), 1549 (C=O, amide), 1447 (C=C, aromatic), 1414 (C=C, aromatic). HRMS⁺ C₁₃H₁₅N₂O₃: Theoretical: 247.1083. Actual: 247.1081.

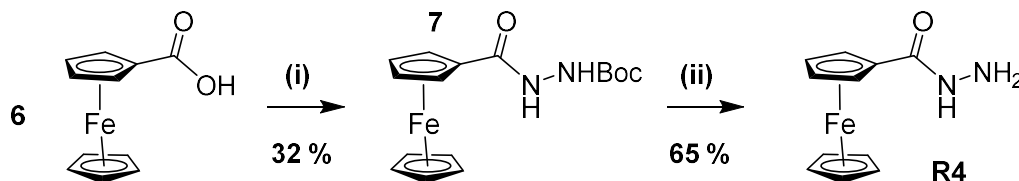
2.6.4. Synthesis of Hydrazide Residues (R2/R4)

Synthesis of Potassium ethyl sulfoacetate (**4**)

Ethyl chloroacetate (5.00 g, 4.08 mmol) and potassium sulfite (6.46 g, 4.08 mmol) were combined in H₂O (40 mL) and heated under reflux for 8 h, then left to stir at room temperature for 18 h. The solution was evaporated to dryness, yielding a white powder. Recrystallisation from hot 70:30 EtOH/H₂O yielded the title compound as a white solid (5.39 g, 64%). ¹H NMR (300 MHz, D₂O) δ (ppm): 4.14 (q, 2H, *J* = 6 Hz), 3.86 (s, 2H, -O₃SCH₂), 1.18 (t, 3H, *J* = 6 Hz, CH₂CH₃). ¹³C NMR (100 MHz, D₂O) δ (ppm): 166.93 (C=O), 62.93 (-O₃SCH₂), 56.10 (CH₂CH₃), 13.42 (CH₂CH₃). Melting point: 209 - 211°C.

Synthesis of Sulfoacetylhydrazide (**R2**)

Hydrazine hydrate (3.52 mL, 72.7 mmol) was added to a stirred solution of ethyl sulfoacetate **6** (1.00 g, 4.85 mmol) in H₂O (20 mL). The reaction mixture was left to stir at room temperature for 18 h, then evaporated to dryness, yielding a colourless oil (4.02 g). The oil was cooled in an ice-bath, and MeOH was added dropwise to yield the title product as a white precipitate which was isolated by filtration (0.54 g, 58%). ¹H NMR (300 MHz, D₂O) δ (ppm): 3.10 (s, -O₃SCH₂). ¹³C NMR (100MHz, D₂O) δ (ppm): 165.57 (C=O). 55.43 (-O₃SCH₂). HRMS(ES-) C₂H₅N₂O₄S: Actual: 153.0660. Theoretical: 152.9970.



Scheme 3: Synthesis of ferrocene hydrazide (**R4**). Step (i): *tert*-Butyl carbazate, EDC, CH₂Cl₂, rt, 18 h. Step (ii): H₂NN₂.H₂O, EtOH, reflux, 18 h.

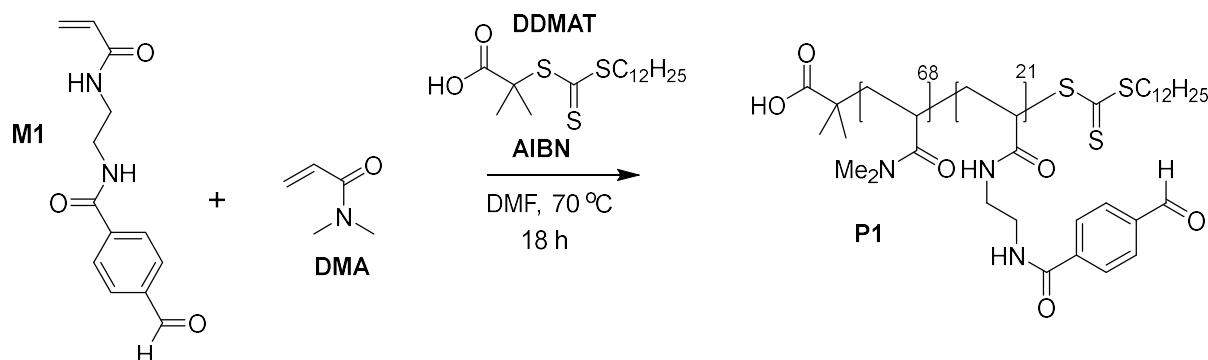
Synthesis of Ferrocenylhydrazide-Boc (**7**):

Ferrocene carboxylic acid (1.00 g, 4.35 mmol) was dissolved in CH₂Cl₂ (30 mL) and stirred under nitrogen at RT. EDC (574.8 mg, 4.35 mmol) and *tert*-butyl carbazate (835.8 mg, 4.36 mmol) were each dissolved in CHCl₃ (20 mL) and added to the vessel and stirred for 18 h. Reaction was judged complete by TLC (6:4 CH₂Cl₂/EtOAc, ninhydrin stain, product *R_f* = 0.7). The reaction mixture was washed with brine (140 mL), the organic extract was dried over MgSO₄, filtered, and then evaporated to afford the crude product as a brown solid. The product was purified by column chromatography (SiO₂, 6:4 CH₂Cl₂/EtOAc) to afford the product as an orange solid (482 mg, 32 % yield). ¹H NMR (CDCl₃, 300 MHz) δ (ppm): 7.45 (1H, s, -CO-NH-NH-), 6.54 (1H, s, -CO-NH-NH-), 4.73 (2H, t, subst. Fc), 4.39 (2H, t, subst. Fc), 4.29 (5H, s, unsubst. Fc), 1.51 (9H, s, -O(CH₃)₃).

Synthesis of Ferrocylhydrazide (**R4**):

Ferrocenylhydrazide-Boc **R4** (311 mg, 0.90 mmol) was dissolved in CH₂Cl₂ (6 mL) and TFA (3.3 mL, 14.4 mmol) was added dropwise at 0°C and stirred for 1 h then allowed to gently warm to room temperature. The reaction was neutralized by dropwise addition of sat. Na₂CO_{3(aq)} (10 mL), diluted with DI water (40 mL) and the product extracted with CHCl₃ (3 x 50 mL). The organic extracts were combined, dried over MgSO₄, filtered, and evaporated to dryness. The product was dissolved in CDCl₃ (6 mL) and dried under N₂ flow, then under high vacuum for 12 h. Product was obtained as an orange solid (142.5 mg, 65 % yield). ¹H NMR (CDCl₃, 300 MHz) δ (ppm): 6.92 (1H, s, -CO-NH-NH₂), 4.65 - 4.37 (5H, m, Fc), 4.21 (5H, s, unsubst. Fc), 3.99 (2H, s, -NH-NH₂).

2.6.5. Preparation of Aldehyde-Functionalized Polymer Scaffold P1



Scheme 4: Preparation of aldehyde-functionalized dimethylacrylamide copolymer scaffold.

S-1-Dodecyl-S'-(α,α -dimethyl- α'' -acetic acid)trithiocarbonate5 (**DDMAT**) (1 eq, 22.35 mg, 61 μ mol) and **AIBN** (0.2 eq, 2.05 mg, 12.5 μ mol) were added to a small schlenk tube. *N,N'*-Dimethylacrylamide (**DMA**) (80 eq, 0.545 g, 5.50 mmol) and *N*-ethylacrylamide-2-(4-formylbenzamide) (**M1**) (20 eq, 0.363 g, 1.37 mmol) were then added followed by DMF (3 mL). The reaction mixture was degassed five times, and then the vessel was backfilled and purged with N_2 , then allowed to warm to room temperature. The reaction mixture was then placed in an oil bath at 70 °C, and the polymerization was quenched in liquid N_2 after 18 h. The reaction mixture was dissolved in a minimal amount of THF and added dropwise to a large excess of ice-cold diethyl ether. The polymer was then isolated by filtration and the precipitation was repeated before drying under high vacuum. Polymer **P1** was obtained as a pale yellow solid. 1H NMR (300 MHz, $CDCl_3$) δ (ppm): 10.04 (br, *CHO*), 8.59 (br, *NH*), 8.07 (br, Ar), 7.88 (br, Ar), 3.4 – 3.6 (br, $(CH_2)_2$), 2.88 (br, $N(CH_3)_2$), 2.2 - 2.7 (br, $CHCH_2$, polymer backbone), 1.4 - 1.8 (br, $CHCH_2$, polymer backbone). The composition of **P1** can be determined by comparing the integration of the aldehyde protons of **M1** with the integration of the $N(CH_3)_2$ protons of **DMA**. The composition (**DMA:M1**) of monomer units within the polymer chain, as determined by 1H NMR spectroscopy, were not identical to the feed ratios on account of a difference in monomer reactivity.

2.6.6. General Procedure for 'Decoration' of Aldehyde Copolymers

Aldehyde copolymer **P1** or **P2** were dissolved in 100 mM H_4NOAc - $AcOH$, pD 4.5 (5 mL) for a polymer concentration of 20 mM. Hydrazide residues (**R1** - **R3**) (400 - 750 mM) were dissolved in 100 mM acetate/ D_2O buffer and then stirred at rt for 12 h and the reactions were then judged to be complete by 1H NMR spectroscopy, which revealed the complete disappearance of aromatic aldehyde signal. All unbound contaminants, such as excess hydrazide residue and acetate buffer were removed by dialysis in water (Spectra por, 3kDa MWCO), and then freeze drying to afford the hydrazide-decorated polymer scaffolds (**P1** - **P3**, **P7**) as white solids.

2.6.7. General Procedure for the Preparation of SCPNs

Linear polyelectrolytes (**P2**, **P3** or **P7**) were dissolved in 100 mM H₄NOAC-AcOH/H₂O buffer, pH 4.5, [Polymer] = 2 mg/mL. To the rapidly stirred polymer solution, succinic dihydrazide (1 – 3 mL, 1 – 3 eqv. relative to the number of hydrazone units displayed upon the polymer scaffold) was added dropwise over 1 h via an automated syringe-pump. The solution was stirred for a further 17 h at rt. Small (200 µL) aliquots of the polymer solution were removed and reduced by NaCNBH₃ (see below) to chemically ‘fix’ the acyl hydrazone crosslinkers. SCPN formation was confirmed by GPC analysis of the reduced SCPNs. Although SCPNs display reasonable kinetic stability in aqueous solution, samples were then flash frozen at – 78 °C and stored at – 20 °C to prevent unwanted structural rearrangement of intra-chain acyl hydrazone crosslinks through component exchange.

2.6.8. Reduction of SCPNs and Analysis by GPC

Small (400 µL) aliquots of SCPNs (≈ 2 mg/mL) were removed from reduced by addition of 400 µL 100 mM NaCNBH₃ (in DI H₂O) stirred for 4 h, then dried under vacuum and re-dissolved in 10 g/L LiBr in DMF ([polymer] = 2 mg/mL) for analysis by GPC. Successful SCPN formation is observed as an increase in retention time (RT) relative to the linear (non-crosslinked) polymer chain, consistent with the expected chain collapse through intramolecular crosslinking. Each sample was run three times to ensure negligible drift in RT between runs.

2.6.9. Emission-Quenching Experiment with SV40 Capsid

Aqueous solutions of polymers **P1**, **P2** or **P3** were titrated into **SV40** (29.3 nM viral capsid, 20 mM NaCl, 1 mM CaCl₂, 10 mM TRIS, pH 7.4) to achieve [Polymer]/[Capsid] stoichiometries in the range 0 – 5000, and then emission spectra were measured.

Emission quenching plots shown in Figure 14c show the corrected emission intensity (ΔI) as a function of [Polymer]/[Capsid] stoichiometry. ΔI was calculated according to **Eqn. 2**:

$$\Delta I = I_x - I_{end} \quad (\text{Eqn. 2})$$

Where I_x is the measured intensity at [Polymer]/[Capsid] = x , and I_{end} is the emission intensity measured at the titration endpoint. *i.e.* the emission at titration endpoint (I_{end}) was subtracted from each of the measured emission values during the titration (I_x).

2.6.10. Time-Resolved DLS Measurement Protocol

Measurements were performed on a Malvern Instruments Zetasizer Nano ZS, which employs a He/Ne laser operating at 633 nm as a light source and an avalanche photodiode as a detector. For TR-DLS each correlation function was accumulated for 30 s, and the apparent hydrodynamic radius was calculated with a second order cumulant fit. Because of the low polymer concentrations, no viscosity corrections are necessary. Such measurements were repeated for 1 - 2 h and continued after the polymer addition for about the same period.

2.7. References

- [1] A. Zeltins, Construction and Characterization of Virus-Like Particles: A Review, *Mol. Biotechnol.*, 2013, **53**, 92-107.
- [2] M. G. Mateu, Assembly, stability and dynamics of virus capsids, *Archives of Biochemistry and Biophysics*, 2013, **531**, 65-79.
- [3] (a) Y. Kitai, H. Fukuda, T. Enomoto, Y. Asakawa, T. Suzuki, S. Inouye and H. Handa, Cell selective targeting of a simian virus 40 virus-like particle conjugated to epidermal growth factor, *J. Biotechnol.*, 2011, **155**, 251-256. (b) C. Goldmann, N. Stolte, T. Nisslein, G. Hunsmann, W. Luke and H. Petry, Packaging of small molecules into VP1-virus-like particles of the human polyomavirus JC virus, *Journal of Virological Methods*, 2000, **90**, 85-90.
- [4] (a) M. G. Mateu, Virus engineering: functionalization and stabilization, *Protein Engineering, Design & Selection*, 2011, **24**, 53-63. (b) A. J. Patil, N. McGarth, E. J. Barclay, D. J. Evans, H. Cölfen, I. Mannes, A. Perriman and S. Mann, Liquid Viruses by Nanoscale Engineering of Capsid Surfaces, *Material Views*, 2012, **24**, 4557-4563.
- [5] (a) N. Kushnir, S. J. Streatfield and V. Yusibov, Virus-like particles as a highly efficient vaccine platform: Diversity of targets and production systems and advances in clinical development, *Vaccine*, **31**, 2012, 58-83. (b) A. P. J. Middelberg, T. Rivera-Hernandez, N. Wibowo, L. H. L. Lua, Y. Fan, G. Magor, C. Chang, Y. P. Chuan, M. F. Good and M. R. Batzloff, A microbial platform for rapid and low-cost virus-like particle and capsomere vaccines, *Vaccine*, 2011, **29**, 7154-7162.
- [6] E. A. Teunissen, M. de Raad and E. Mastrobattista, Production and biomedical applications of virus-like particles derived from polyomaviruses, *J. Control Release*, 2013, **172**, 305-321.
- [7] C. S. Mahon, M. A. Fascione, C. Sakonsinsiri, T. E. McAllister, W. B. Turnbull and D. A. Fulton, *Org. Biomol. Chem.*, 2015, **13**, 2756-2761.
- [8] (a) G. Moad, A. E. Rizzardo and S. H. Thang, *Aust. J. Chem.*, 2005, **58**, 379-410. (b) G. Moad, A. E. Rizzardo and S. H. Thang, *Aust. J. Chem.*, 2006, **59**, 669-692. (c) G. Moad, B. E. Rizzardo and S. H. Thang, *Aust. J. Chem.*, 2009, **62**, 1402-1472.
- [9] (a) C. S. Mahon and D. A. Fulton, *Chem. Sci.*, 2013, **4**, 3661-3666. (b) R. Yao, S. Wu, L. Jiang, S. Deng and S. Yu, *Res. Chem. Intermed.*, 2010, **36**, 523-528.
- [10] S. R. Beeren and J. K. M. Sanders, *Chem. Sci.*, 2011, **2**, 1560-1567.
- [11] W. Fieber, J. M. Lehn and A. Herrmann, *Helv. Chim. Acta*, 2007, **90**, 2281-2314.
- [12] P. Frank, A. Prasher, B. Tuten, D. Chao and E. Berda, *Appl. Petrochem. Res.*, 2015, **5**, 9-17.
- [13] K. Ishizu, H. Watanabe, S. Han, S. Kanesashi, M. Hoque, H. Yajima, K. Kataoka and H. Handa, *J. Virol.*, 2001, **75**, 61-72.
- [14] T. Stehle, S. J. Gamblint, Y. Yan and S. C. Harrison, *Structure*, 1996, **4**, 165-192.
- [15] M. Kawano, K. Doi, H. Fukuda, Y. Kita, K. Imai, T. Inoue, T. Enomoto, M. Matsui, M. Hatakeyama, Y. Yamaguchi and H. Handa, *Biotechnol. Reports*, 2015, **5**, 105-111.
- [16] H. Holthoff, S. U. Egelhaaf, M. Borkovec, P. Schurtenberger and H. Sticher, *Langmuir*, 1996, **12**, 5541-5549.
- [17] I. Szilagyi, A. Vaccaro and M. Borkovec, *Macromolecules*, 2010, **43**, 9108-9116.
- [18] M. Quesada-Pérez, E. González-Tovar, A. Martín-Molina, M. Lozada-Cassou and R. Hidalgo-Álvarez, *ChemPhysChem*, 2003, **4**, 234-248.
- [19] (a) S. Barany, *Adv. Colloid Interface Sci.*, 2015, **222**, 58-69. (b) T. T. Nguyen and B. I. Shklovskii, *Physica A*, 2001, **293**, 324-338.
- [20] J. Fu and J. B. Schlenoff, *J. Am. Chem. Soc.*, 2016, **138**, 980-990.
- [21] (a) J. Kalia and R. T. Raines, *Angew. Chem. Int. Ed.*, 2008, **47**, 7523-7526. (b) C. S. Mahon, C. J. McGurk, S. M. D. Watson, M. A. Fascione, C. Sakonsinsiri, W. B. Turnbull and D. A. Fulton, *Angew. Chem. Int. Ed.*, 2017, **56**, 12913-12918.
- [22] I. Szilagyi, G. Trefalt, A. Tiraferri, P. Maroni, and M. Borkovec, *Soft Matter*, 2014, **10**, 2479-2502.

2.8. Appendix

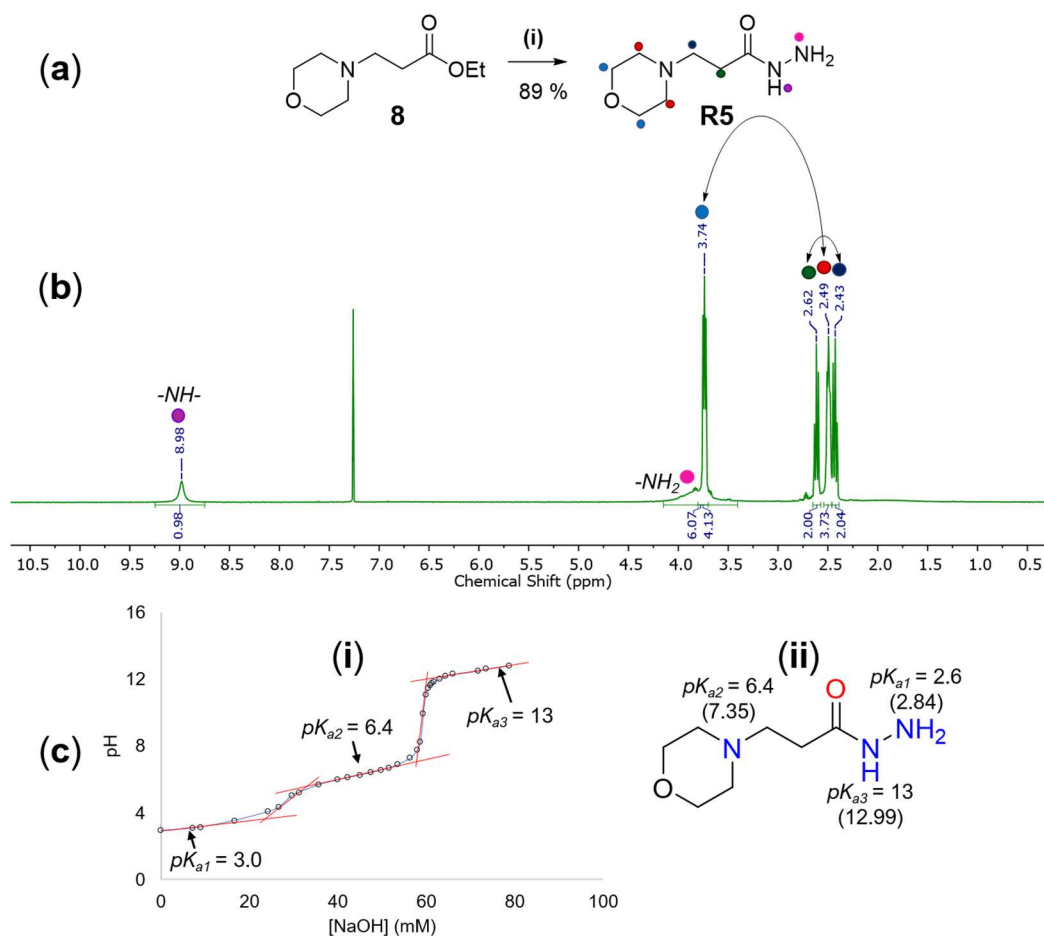


Figure 37: Synthesis (a) and characterization (b) of morpholine hydrazide **R5**. (a) Synthesis of **R5** by hydrazinolysis of ethyl ester **7**. Step (i): $\text{N}_2\text{H}_4 \cdot \text{H}_2\text{O}$, EtOH, reflux, 12 h. (b) ^1H NMR spectrum (CDCl_3 , 300 MHz) of **R5** with structural assignments shown. Arrows indicate J_3 coupling observed by COSY NMR spectroscopy. (c) pH titration profile (i) of **R5** revealed that the morpholine nitrogen had a $pK_a = 6.4$, slightly lower than that predicted (ii) by Chemicalize online platform (Chemaxon).

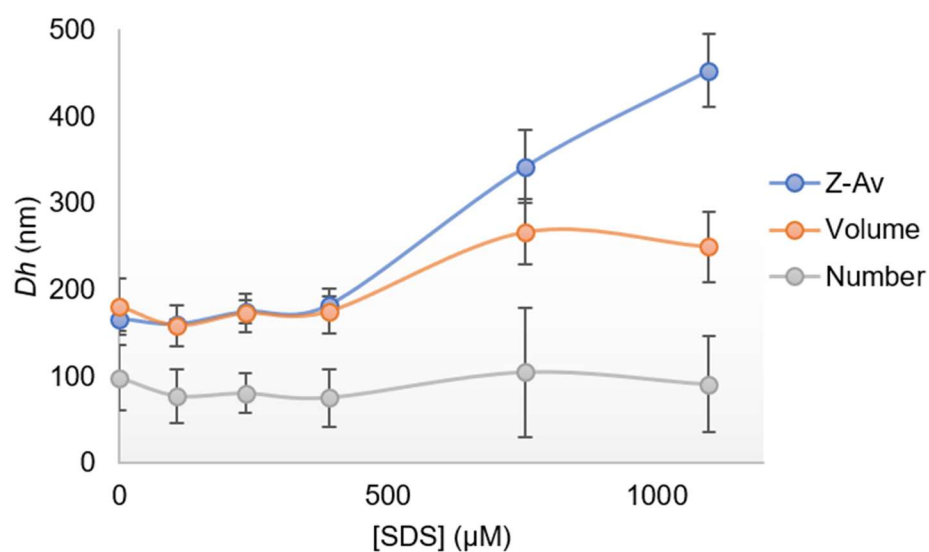


Figure 38: DLS titration profile for addition of SDS surfactant into SV40 capsid. [Capsid] = 117 nM in 1.8 mM TRIS, 18 mM NaCl, 0.9 mM CaCl_2 , pH 7.4

Ferrocene hydrazide (**R4**) was prepared in two steps (Fig. 39a) and isolated by column chromatography as an orange solid (21 % yield). Surprisingly, the alternative synthetic route (Fig. 39b) was unsuccessful on account of failed hydrazinolysis of methyl ester **7**.

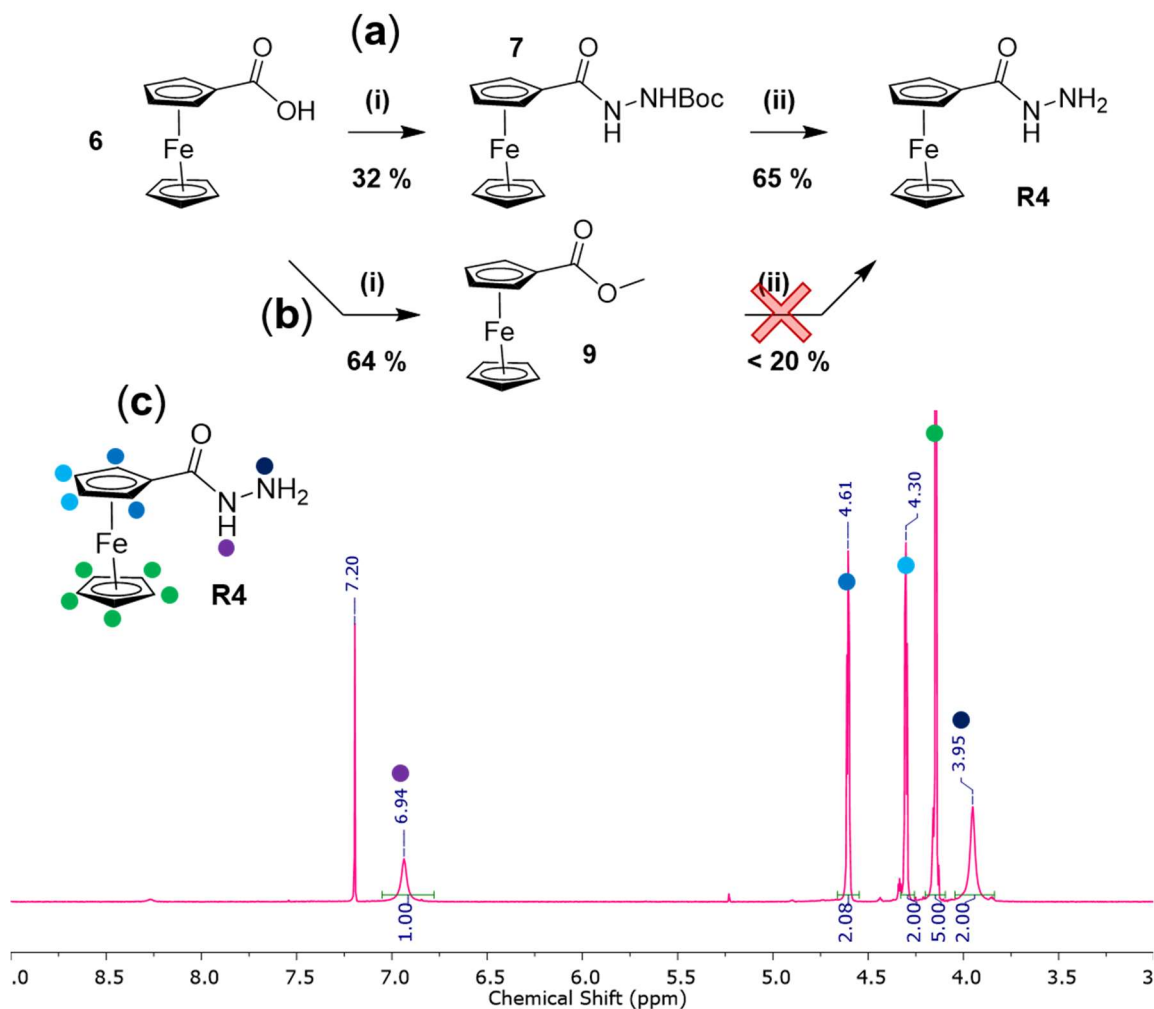


Figure 39: Successful (a) and failed (b) synthesis of ferrocenyl hydrazide **R4** and its characterization by ¹H NMR spectroscopy (c) (a) Step (i) *tert*-Butylcarbazate, EDC, CH₂Cl₂, rt, 18 h. Step (ii) 1:1 TFA, CH₂Cl₂, 0°C. (b) Step (i) H₂SO₄, MeOH, reflux, 18 h. Step (ii) N₂H₄.H₂O, MeOH, reflux 18 h. (c) ¹H NMR spectrum (CDCl₃, 300 MHz) of ferrocene hydrazide **R4**, with structural assignments shown.

Ferrocene polycation (**P5**) was adsorbed onto **sNPs** in the presence of NaCl (0 – 200 mM)(Fig. 40a). These experiments revealed that thicker adsorbed polyelectrolyte layers were obtained at higher salt concentrations, see Fig. 40d for DLS hydrodynamic layer thickness (L), which is given as a function of $[\text{NaCl}]$.

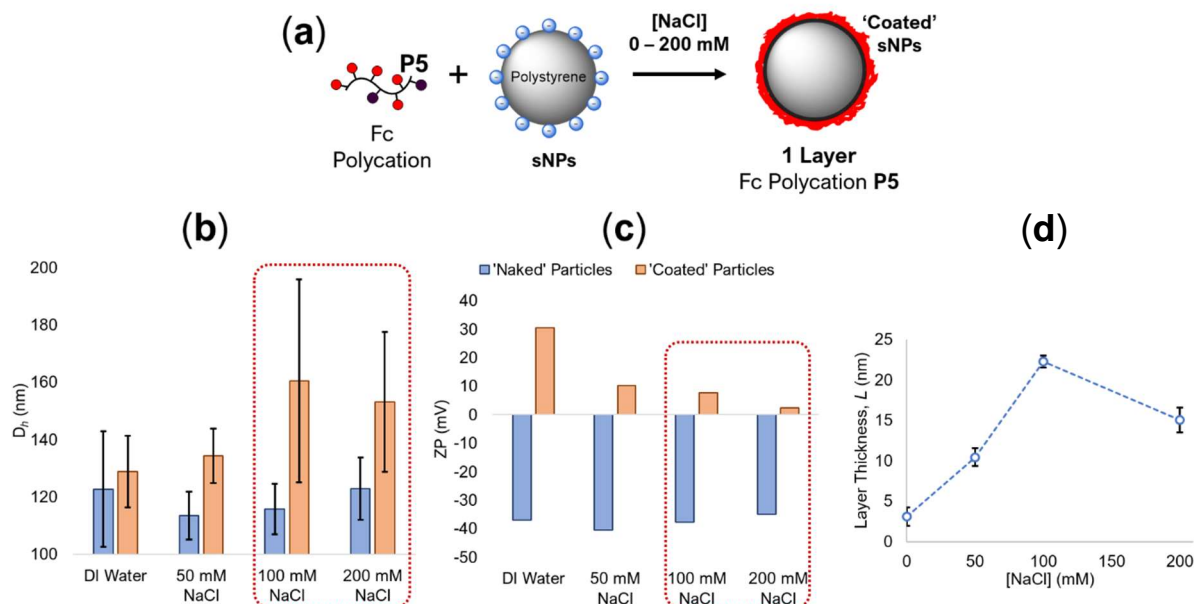


Figure 40: (a) Adsorption of ferrocene polycation **P5** onto negatively-charged **sNPs**. (b) DLS and ZP (c) characterization of **P5**-‘coated’ **sNPs** prepared in the presence of different salt concentrations, $[\text{NaCl}] = 0 - 200$ mM. (d) Hydrodynamic layer thickness (L) as a function of NaCl concentration.

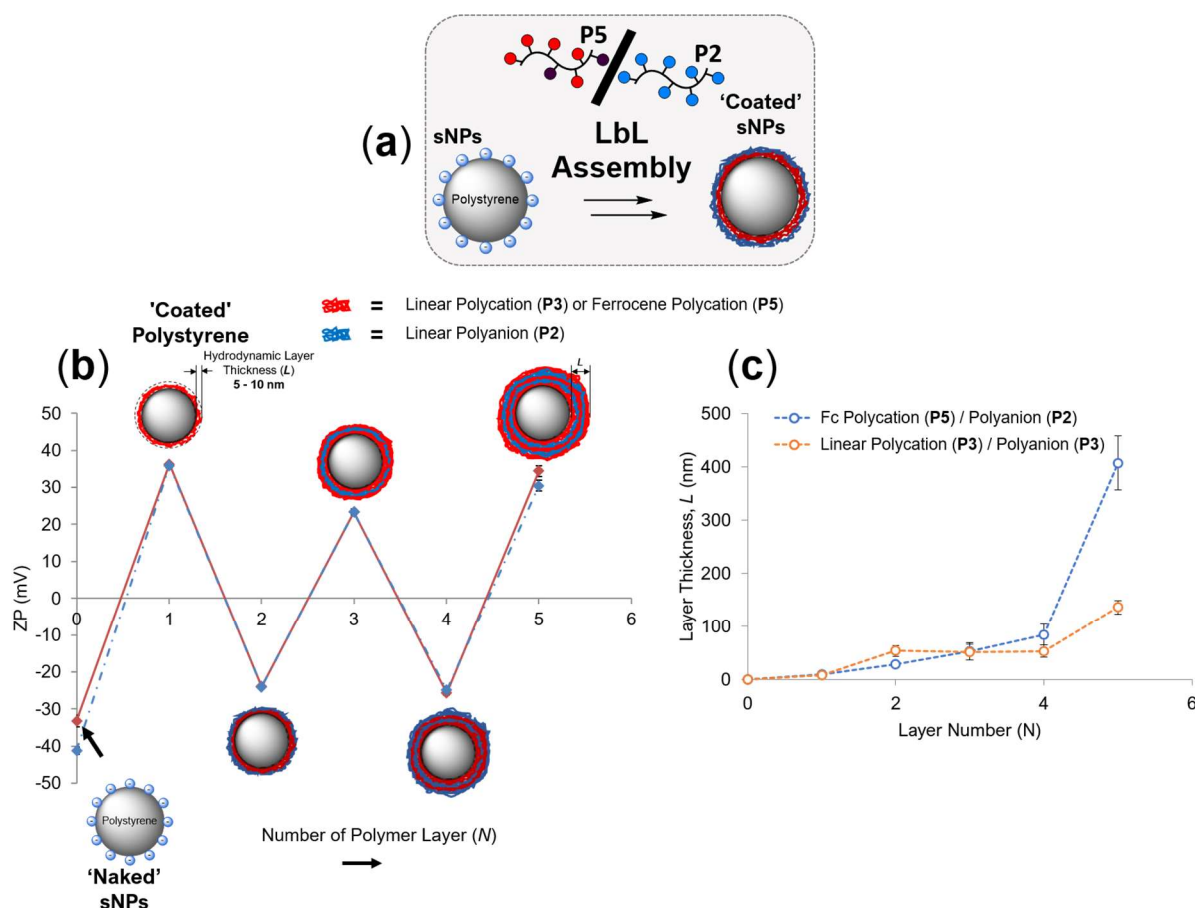


Figure 41: (a) Layer-by-layer (*LbL*) adsorption of ferrocene-labelled polycation **P5** and polyanion **P2**, which form alternating layers upon polystyrene nanoparticles (**sNPs**). Between each addition of polyelectrolyte the 'unbound' polymer chains were removed by repeated centrifugation wash cycles. (b) Zeta potential characterization of *LbL* 'coated' **sNPs**, which is given as a function of the number of polymer layers (*N*). (c) DLS analysis of *LbL* **P5/P2** adsorption on **sNPs**. These experiments set out to prepare thick polyelectrolyte layers upon **sNPs**, in the hope that addition of salt would 'screen' electrostatic interactions between oppositely charged polyelectrolyte chains in the *LbL* assembly, and thus result in a clear 'collapse' of this architecture by DLS. It was hypothesized that *LbL* architectures formed from **Cationic SCPN-1** would resist collapse upon addition of salt on account of intermolecularly crosslinking of the adjacent polymer layers. DLS analysis (c), however, revealed larger than expected particle sizes (and an increase in PDI) as the number of polymer layers (*N*) was increased, and thus this approach was not further explored.

Chapter 3

‘Shrink-Wrapping’ Through Specific Ligand-Receptor Interactions

Manuscript submitted, see page 216

Patrick L. Higgs, Jordan L. Appleton, W. Bruce Turnbull
and David A. Fulton

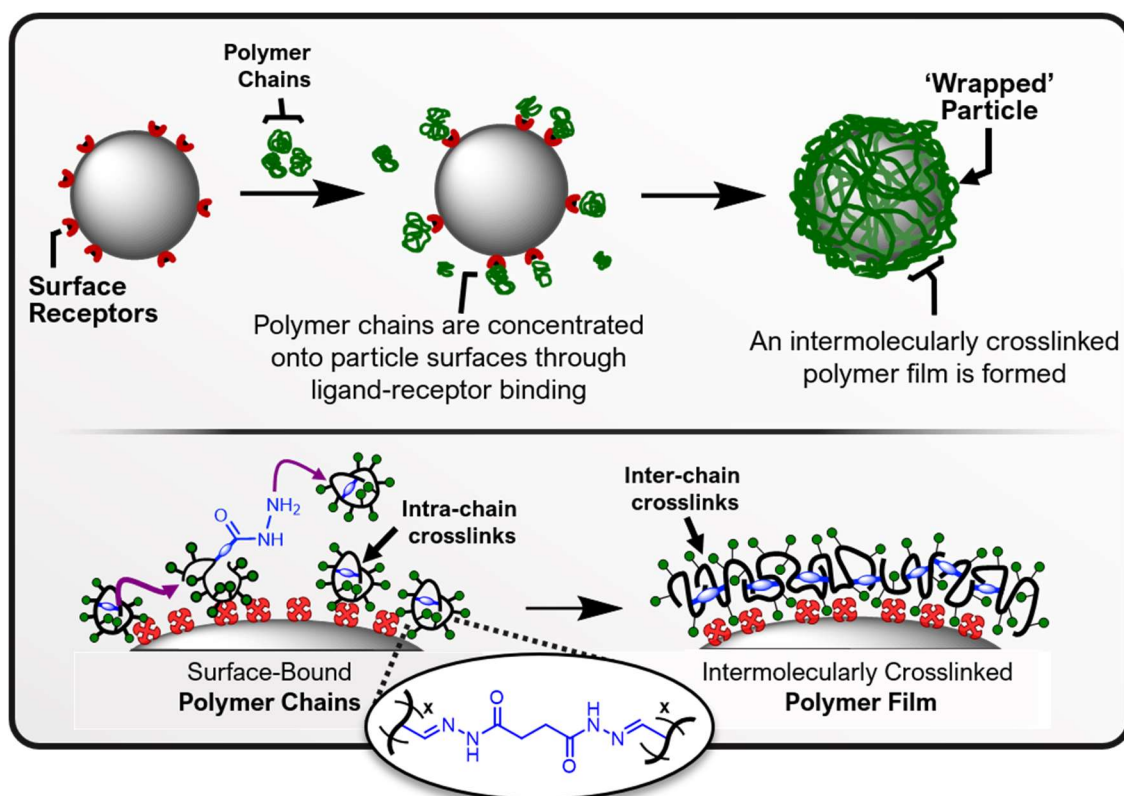


Table of Contents

3.1. Abstract	92
3.2. Introduction	93
3.2.1. Carbohydrate-Binding Pathogens	94
3.3. Results and Discussion	95
3.3.1. ‘Shrink-Wrapping’ Overview	95
3.3.2. Specific Carbohydrate-Receptor Recognition Events	96
3.3.3. Synthesis of Aldehyde-Functionalized poly(Acrylamide) Scaffolds	97
3.3.4. Synthesis of Mannose Hydrazide	98
3.3.5. Synthesis and Characterization of Mannose-Grafted Scaffolds	99
3.3.6. Synthesis and Characterization of Acrylamide Glyco-SPCNs	101
3.3.7. GPC Characterization of SCPN Formation	101
3.3.8. Preparation of Protein-Functionalized Nano- and Microparticles	104
3.3.9. ‘Shrink-Wrapping’ Studies with Con A-Immobilized Streptavidin-Modified Polystyrene NPs and Acrylamide-Based Glycopolymers	107
3.3.10. Factors Inhibiting the ‘Shrink-Wrapping’ of 3D Nano- and Micro-Objects	119
3.3.11. Synthesis and Characterization of PEG-Based Glyco-SPCNs	121
3.3.12. Fluorescence Microscopy ‘Shrink-Wrapping’ Studies with PEG-Based Glycopolymers and Lectin-Functionalized Silica Microparticles	126
3.4. Conclusion	132
3.5. Experimental	133
3.6. References	143

3.1. Abstract

In nature, complementary carbohydrate-protein recognition events trigger essential biological processes and play a central role in interactions and communication between living cells.¹ In this chapter, a chemical system is described, in which carbohydrate-receptor interactions were exploited to trigger the ‘structural metamorphosis’ of discrete polymer chains into intermolecularly crosslinked glycopolymer films upon the surface of 3D nano- and microscale objects. Carbohydrate-decorated single chain polymer nanoparticles (**glyco-SCPns**) were prepared in aqueous solution by intramolecular crosslinking of a linear glycopolymer chain with succinic dihydrazide. Specific molecular recognition events between the protein-functionalized particles and carbohydrate appendages displayed upon the **glyco-SCPns** concentrate polymers onto the surface. Crosslinks embedded within these **glyco-SCPns** possess a dynamic covalent nature that allows for their intra- to inter-chain conversion, which thus facilitates the ‘shrink-wrapping’ of particles within an intermolecularly crosslinked polymer film. This chapter builds upon previous studies² on the ‘shrink-wrapping’ of 2D surfaces by demonstrating that the ‘shrink-wrapping’ concept can be adapted to the encapsulation of three-dimensional substrates with micro- and nanoscale dimensionality. Nano-dimensional objects possess large surface areas with considerable surface energies, and thus are incredibly vulnerable to non-specific adsorption and particle-particle aggregation. These unwanted processes presented a considerable barrier in obtaining reliable DLS characterization of polymer ‘wrapped’ nanoparticles, and thus the ‘shrink-wrapping’ of 3D nanoscale objects proved to be particularly difficult to investigate in the absence of analytical techniques which can accurately characterize the formation of nanometre-thick polymer films upon colloidal particles. Thus, the ‘shrink-wrapping’ of larger objects of microscale dimensionality was investigated, revealing a facile method to probe the ‘wrapping’ process by fluorescence microscopy. The successful ‘shrink-wrapping’ of lectin-functionalized silica microspheres was accomplished, which constitutes the very first step towards the end goal of ‘wrapping’ bacteria, and thus may afford a ‘smart’ polymer technology for the selective ‘capture’ of harmful pathogens.

3.2. Introduction

Cell surfaces display a structurally rich array of membrane-bound glycolipids and glycoproteins, the exact 'glycolandscape' of which are often specific to the species, tissue, and cell type.³ Through evolution spanning millions of years, pathogens have learnt to exploit these glycolandscapes with great effect, recognising the unique 'barcode' of their target host cell and tissues. Amongst the vast array of strategies that pathogens use to exploit the host surface and escape the defence mechanisms, they display proteins – either lectins, toxins or adhesins – which have the capacity to selectively recognize complex oligosaccharides present upon the host tissue (Fig. 1) through specific molecular recognition events. Once established, these key interactions provide the 'foothold' by which pathogens gain first entry to susceptible host cells, thus infiltrating the defences to facilitate invasion of the organism.

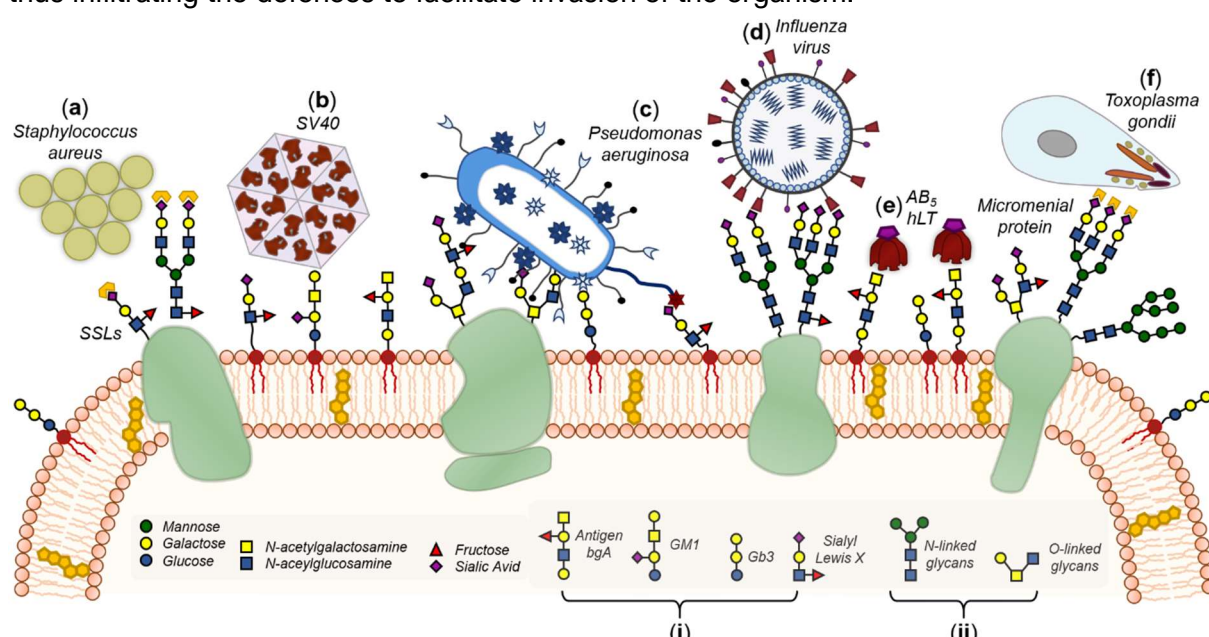


Figure 1: Pathogens (a-f) interact with or adhere to cell surfaces by selective binding of specific membrane-bound carbohydrates (i-ii). These recognition events facilitate their entry into cells, thus promoting invasion of the host organism.

Whilst diverse in their shape, size, surface morphology and density of carbohydrate receptors, pathogens a-f (Fig. 1) represent a mere cross-section of the > 1400⁴ antigens known to cause infectious diseases in humans. Collectively, they impose a great burden on human health, the economy and stretch healthcare systems worldwide. Influenza virus (d) alone was predicted to have cost the U.S. \$10.4 billion in direct medical expenses (2017),⁵ with annual outbreaks causing 3 – 5 million severe illnesses globally⁶ and up to 646,000 deaths.⁷ In contrast to the serious risk to human health posed by influenza, the bacteria *staphylococcus aureus* (a), *pseudomonas aeruginosa* (*P. aeruginosa*)(c) and *toxoplasma gondii* (f) are often responsible for less acute illnesses, typically colonising immuno-compromised patients as part of a secondary infection, and are thus categorised as 'opportunistic' pathogens. The combined effect of these antigens, however, places a substantial burden on healthcare systems, with secondary

infections often increasing the length of hospital admissions.⁸ Whilst diverse in their structure and the diseases that they cause, pathogens **a-f** are united in their dependence on specific carbohydrate recognition events to facilitate cell entry. A pathogen ‘capture’ mechanism was envisaged in which **glyco-SCPNs** bearing carbohydrate residues bind to complementary receptors located upon the pathogen surface through specific molecular recognition events. These interactions are anticipated to concentrate **glyco-SCPNs** onto the receptor-displaying surface and thus drive ‘shrink-wrapping’ of the pathogen within a glycopolymer film.

3.2.1. Carbohydrate-Binding Pathogens

The class of carbohydrate-binding proteins known as lectins have significant biological consequences, which are often implicated with disease. Pathogens *Escherichia coli* (*E. coli*)⁹ (Fig. 2a-b) and *P. aeruginosa*¹⁰ (Fig. 1c) are rod-shaped Gram-negative bacteria which display mannose- and galactose-binding receptors upon their surfaces, respectively. These receptors (lectins) recognise specific carbohydrate residues located upon the surface of host cells, and thus facilitate adhesion to host tissues. Carbohydrate receptors are displayed at the ends of micro-length hair-like appendages (Fig. 2a) named fimbriae (Fig. 2c), which enhance adhesion to host tissues through a ‘catch-bond’ mechanism¹¹ and thus promote colony formation. These carbohydrate-binding bacteria have a micron-sized dimensionality, and thus lectin-displaying microparticles (Fig. 3) constitute a good model system to begin initial developments towards the ‘shrink-wrapping’ of pathogenic bacteria. The overarching aim of this chapter was thus to encapsulate nano- and microscale spherical objects within covalently crosslinked polymer films.

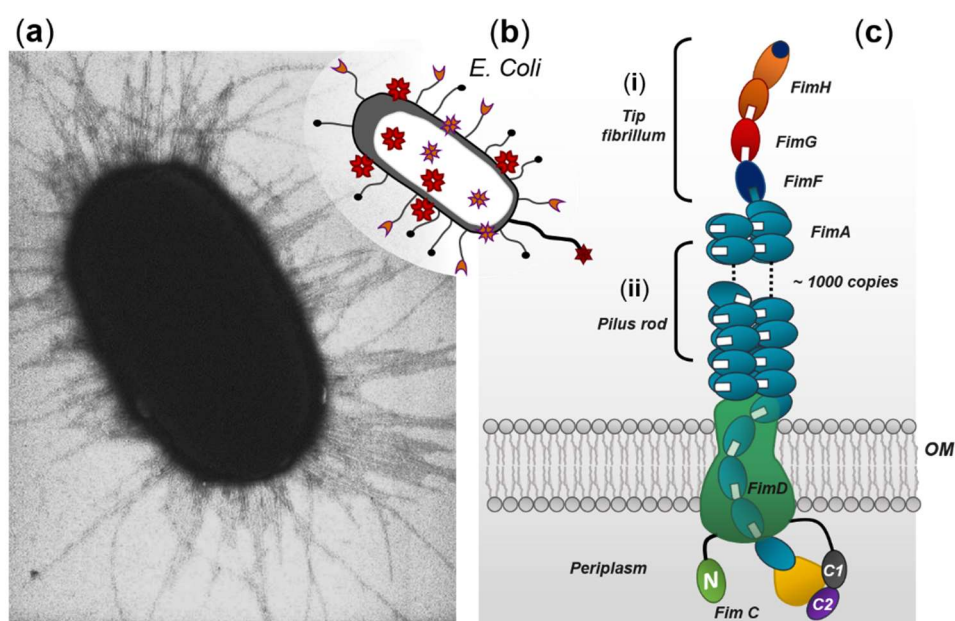


Figure 2: (a) TEM micrograph showing the long ‘sticky’ filaments of *E. coli*, known as fimbriae. Reproduced with permission of ref. 12, copyright of PLoS Biology, 2006. These fimbriae display carbohydrate-binding proteins to facilitate adherence to host cells and promote the colonization by attachment to neighbouring bacteria.¹³ (b) Schematic representation of *E. coli* and its type 1 pili (c) assembled by the Fim system. Fim H, located upon the fimbriae tip, is a mannose-binding lectin.

3.3. Results and Discussion

3.3.1. 'Shrink-Wrapping' Overview

In the previous chapter, complementary electrostatic interactions – the nature of which are omni-directional and non-specific – were employed to drive the 'shrink-wrapping' of nano- and microscale objects. In contrast, this chapter exploits specific molecular recognition events between carbohydrate-functionalized SCPNs (**glyco-SCPNs**) (Fig. 3a, i-ii) and lectin-functionalized silica particles to facilitate successful 'wrapping'. These specific interactions were hypothesized to drive the concentration of **glyco-SCPNs** upon the surface of the spherical object. Now spatially close, the subsequent 'structural metamorphosis' would lead to the formation of covalently crosslinked glycopolymer films (Fig. 3a, v). 'Structural metamorphosis' should be facilitated by the dynamic covalent nature of acyl hydrazone bonds (Fig. 3, iv) embedded within the glycopolymer film. Although deceptively simple, this subtle 'structural metamorphosis' of the dynamic covalent crosslinkers constitutes a central pillar underpinning the 'shrink-wrapping' concept, differentiating this novel concept from rudimentary adsorption of non-crosslinked polymer chains (Fig. 3b).

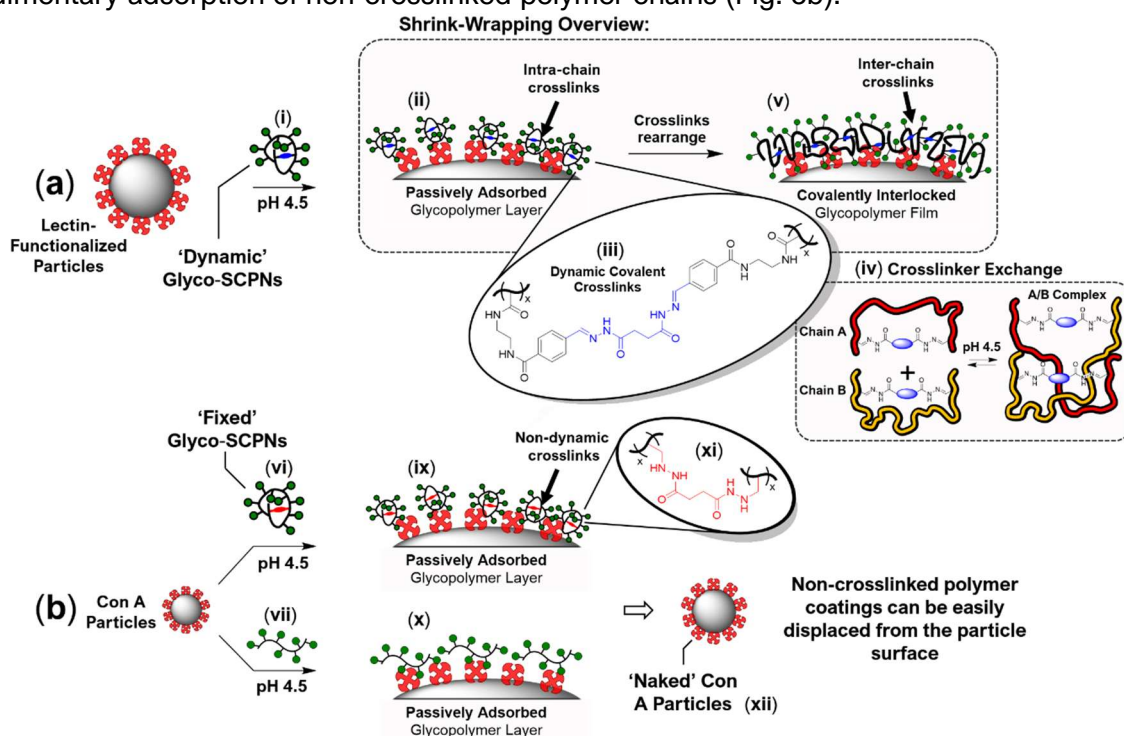


Figure 3: (a) Overview of the 'shrink-wrapping' of lectin-functionalized particles. (i) Concanavalin A functionalized nano- or microparticles were incubated with **glyco-SCPNs** grafted with the complementary carbohydrate (**mannose hydrazide**). (ii) Specific molecular recognition events concentrate the **glyco-SCPNs** upon the Con A particle surface, and this increase in local polymer concentration initiates 'structural metamorphosis' of the dynamic covalent hydrazone crosslinks (iii) contained within the **SCPNs**. Rearrangement of the intra-chain crosslinks proceeds *via* component exchange (iv) and ultimately leads to the formation of covalently crosslinked polymer films (v) featuring inter-chain hydrazone crosslinks which remain 'dynamic' in nature. (b) Control experiments with '**fixed**' **glyco-SCPNs** (vi) where the crosslinks are 'non-dynamic', and linear glycopolymer (vii) where no crosslinks are present will demonstrate that the particles have been 'shrink-wrapped' within a covalently crosslinked polymer film and not simply 'coated' in a non-crosslinked polymer layer.

3.3.2. Specific Carbohydrate-Receptor Recognition Events

In this chapter **glyco-SCPNs** were designed to exploit specific molecular recognition between the carbohydrate-binding protein (lectin) Concanavalin A (Con A) (Fig. 4a, I) and its complementary carbohydrate ligand (mannose), which was grafted onto polymer scaffolds and intramolecularly crosslinked to produce mannosylated **SCPNs** (Fig. 4c). Con A is isolated from *Canavalia ensiformis* (Jack Bean) and at neutral pH exists as a tetrameric protein complex¹⁴ (Fig. 4a, I) consisting of four identical 26.5 kDa protein subunits, each containing a single carbohydrate binding site. Con A (Fig. 4a, I) possesses a pH-dependent structure, with the tetramer (1) dissociating into dimeric structures at pH < 6 (2). Mn²⁺ and Ca²⁺ metal ions are shown as purple and green spheres, respectively, (Fig. 4a, I) and play a crucial role in stabilizing the 'active' protein conformation for carbohydrate binding.¹⁵ An alternative lectin, heat-labile

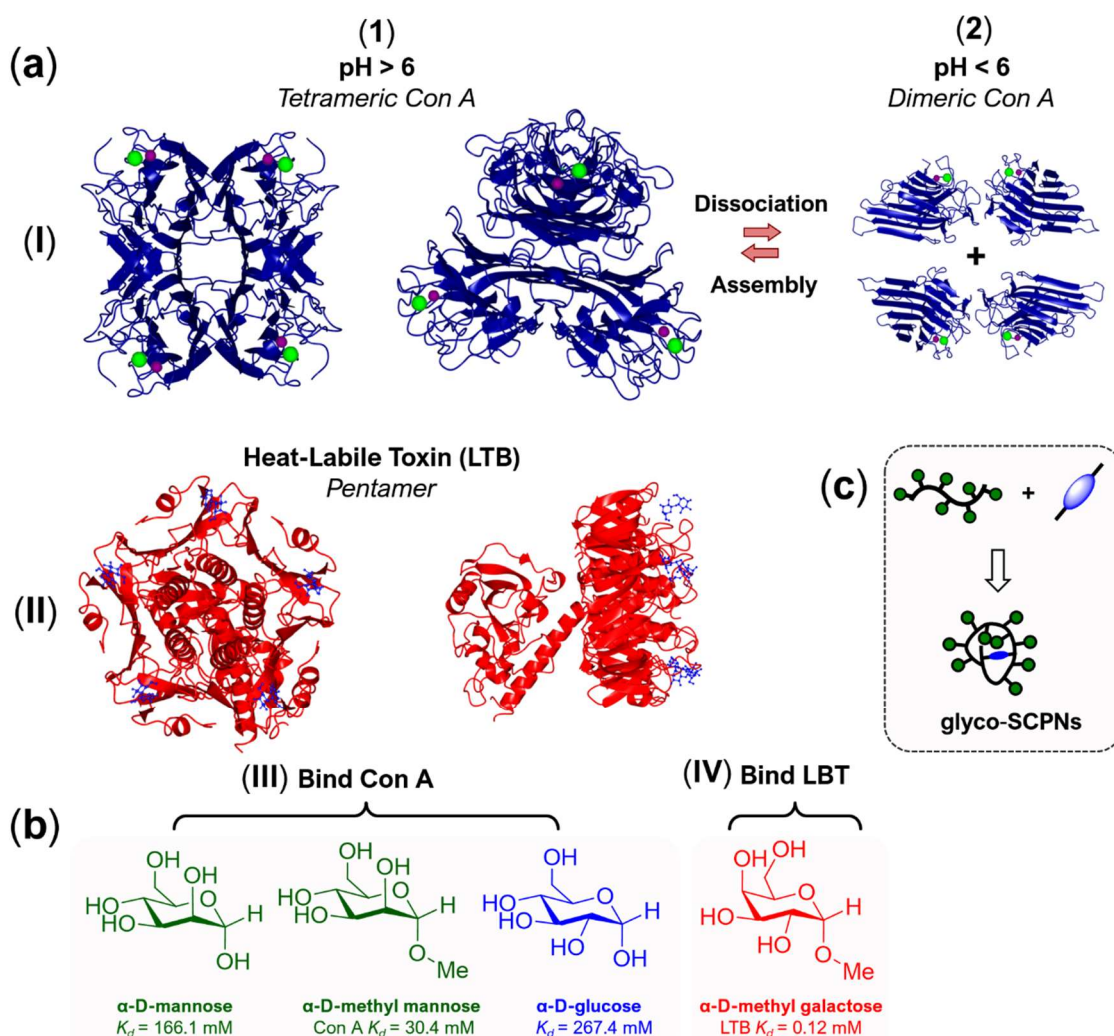


Figure 4: (a) Structures of lectins Concanavalin A (I), Heat-Labile Toxin (II) and their complementary carbohydrate ligands (b). At pH > 6 Con A exists as a tetramer (1) consisting of four identical 28 kDa subunits. Mn²⁺ (purple) and Ca²⁺ (green) metal ions – the positions of which are highlighted – are necessary to maintain Con A in an 'active' conformation for carbohydrate binding. At pH < 6 Con A dissociates into dimeric structures (2). (II) Structure of Heat-Labile Toxin pentamer, with its associated carbohydrate ligands. (b) Structures of carbohydrate ligands which selectively bind to Con A (c) and LTB (d). The respective K_d values are given for binding to tetrameric Con A¹⁶ and pentameric LTB at pH 7.4. (c) Preparation of **glyco-SCPNs**.

toxin (LTB) (Fig. 4a, II) was also employed for control experiments,^{*} on account of its lack of binding to mannose residues located upon the glycopolymer scaffolds. LTB (Fig. 4a, II) is a galactose-binding protein secreted by the pathogenic bacteria *E. Coli*. Belonging to the AB₅ family of toxins, LTB features a ring-like structure (Fig. 4a, II) consisting of five 18.5 kDa B subunits, each of which presents a single carbohydrate binding site. LTB selectively binds galactose residues (Fig. 4b, IV) and its complex oligosaccharide derivatives with moderate binding constants. In contrast, Con A selectively binds **D-glucose** ($K_d \approx 267$ mM),¹⁶ **D-mannose** ($K_d \approx 166$ mM),¹⁶ and **α -D-methyl mannopyranoside** ($K_d \approx 30$ mM),¹⁶ with a slight preference for the latter carbohydrates (Fig. 4b, III). Although these binding constants appear relatively low, this issue can be circumnavigated by multivalent expression of carbohydrates upon a polymer scaffold, where an ensemble of low-affinity supramolecular interactions reinforce one another to facilitate high-affinity binding of glycopolymer to the lectin substrate.¹⁷ **Glyco-SCPNs** bearing multiple pendant mannosyl groups were thus selected for synthesis (Fig. 4c). The building blocks from which these **glyco-SCPNs** are constructed will now be discussed, starting with the aldehyde-functionalized polymer scaffolds onto which mannose hydrazide is grafted.

3.3.3. Synthesis of Aldehyde-Functionalized poly(Acrylamide) Scaffolds

Aldehyde-functionalized copolymer scaffolds (**P1** - **P5**) were prepared by RAFT polymerization (Fig. 5a) of aldehyde monomer **M1** and *N,N*-dimethylacrylamide (**DMA**), affording a range (5 – 25 %) of aldehyde densities (Fig. 5b). ¹H NMR spectroscopy and gel permeation chromatography (GPC) characterization of acrylamide-based scaffolds **P1** - **P5** was entirely consistent with previous literature reports² and allowed for the polymer composition ($m + n$), degree of polymerization (D_p), molecular weight and polydispersity index (PDI) to be determined (Fig. 5b). GPC traces of **P1** - **P4** (Fig. 5c) revealed monomodal distributions with low PDI values, indicative of controlled RAFT polymerization processes. A limitation of the acrylamide-based aldehyde scaffolds, however, is their poor solubility in aqueous solutions. Polymer scaffolds which contained > 30 % aldehyde (**M1**) unit were virtually insoluble in aqueous solution, and thus were excluded from further study.[†]

^{*} In order to prove that the ‘shrink-wrapping’ of Con A-functionalized microparticles (**MP2**) was driven by specific mannose-Con A recognition events, ‘wrapping’ experiments were performed on silica microparticles functionalized with the galactose-binding lectin LTB to afford microparticles (**MP5**) (see page 105, Table 1) which were absent in the complementary receptor for the mannose residues located upon the SCPNs.

[†] The observed lack of aqueous solubility was rationalized by the highly hydrophobic nature of the benzaldehyde (**M1**) moiety, which was not sufficiently compensated by the hydrophilicity of **DMA** comonomer. To address these inadequacies with the acrylamide scaffold, a new generation of aldehyde-functionalized scaffold was prepared (see pages 121-122), which featured high aqueous solubility even at > 50 % aldehyde content. The abundance of hydrophilic poly(ethylene glycol) units offsets the highly hydrophobic nature of the benzaldehyde unit, whilst allowing for a neutral polymer backbone which carries no electrostatic charge – an important requirement when the intention is to reversibly bind to polymer scaffolds with complex biomacromolecular targets, such as virus-like particles, which often present highly charged surfaces.

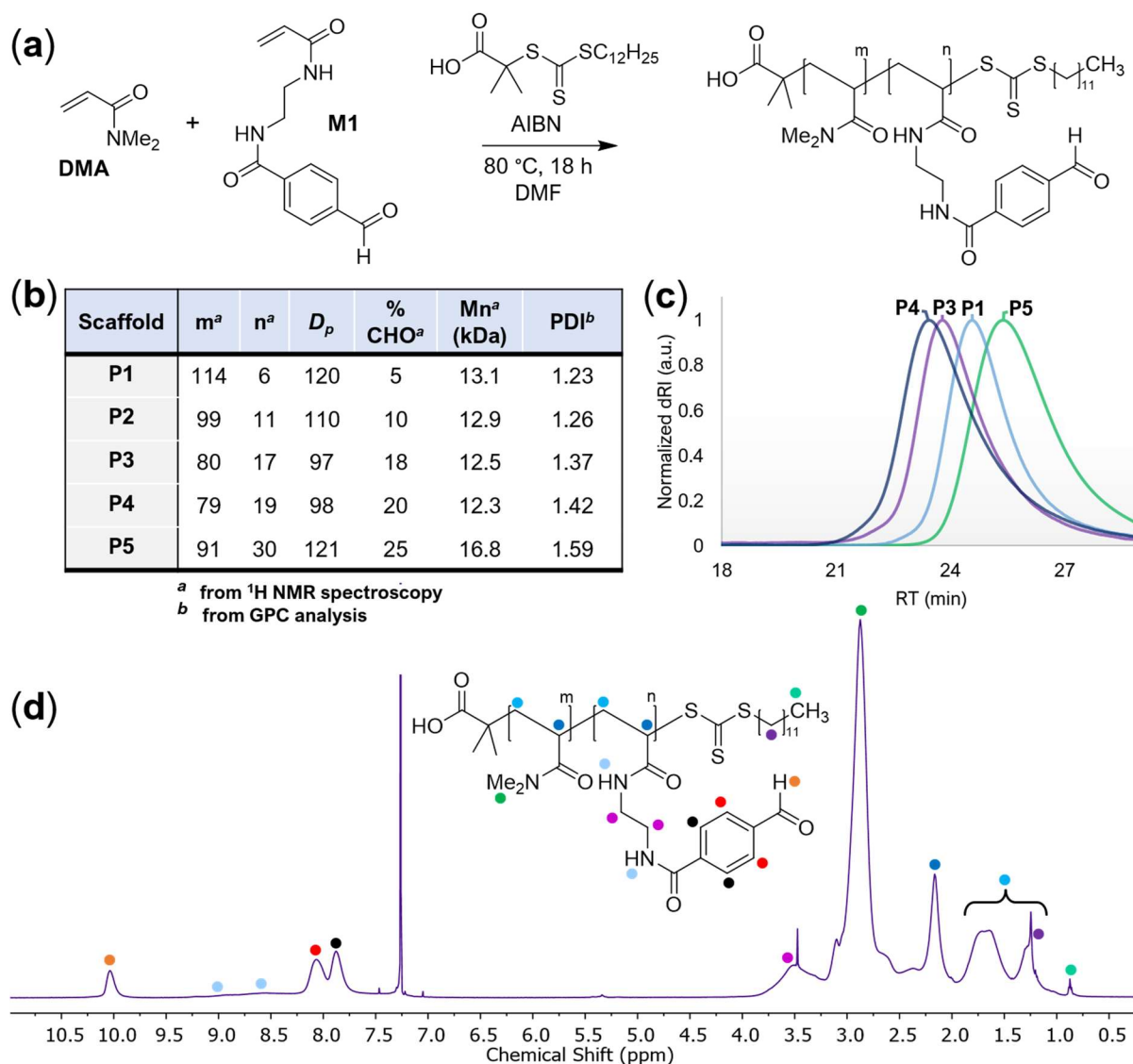


Figure 5: (a) Preparation of aldehyde-functionalized polymer scaffolds (**P1-P4**) by RAFT polymerization of **M1** with dimethylacrylamide. (b) Table of GPC^b and ¹H NMR spectroscopy^a end-group characterization. (c) GPC traces of **P1** and **P3-P5**, obtained in DMF + 1 g/L LiBr. (d) ¹H NMR (CDCl₃, 300 MHz) spectrum of acrylamide aldehyde scaffold **P3**.

3.3.4. Synthesis of Mannose Hydrazone

Mannose hydrazone residue (**MAN**) was synthesized in three steps and isolated as an off-white solid (1.36 g, 40 % yield) (Fig. 6a). Characterization of **MAN** was consistent with previous literature reports,² revealing successful isolation of the α -anomer. Deliberate inclusion of the hydrophobic phenyl moiety at the reducing end of the carbohydrate was anticipated to enhance the binding constant of **MAN** to its complementary carbohydrate-binding proteins. Intermediate **3** was prepared by a Lewis acid-catalysed glycosylation (Fig. 6a, i) of acetate-protected **D-Mannose**, purified by column chromatography and isolated by recrystallization to afford large cubic platelets of the α -anomer **3**. Deacetylation of **3** furnished the deprotected sugar **4** and subsequent hydrazinolysis of the methyl ester afforded mannose hydrazone (**MAN**). ¹H NMR spectroscopy (Fig. 6b) revealed **MAN** was isolated as the α -anomer (●, δ 5.68 ppm).

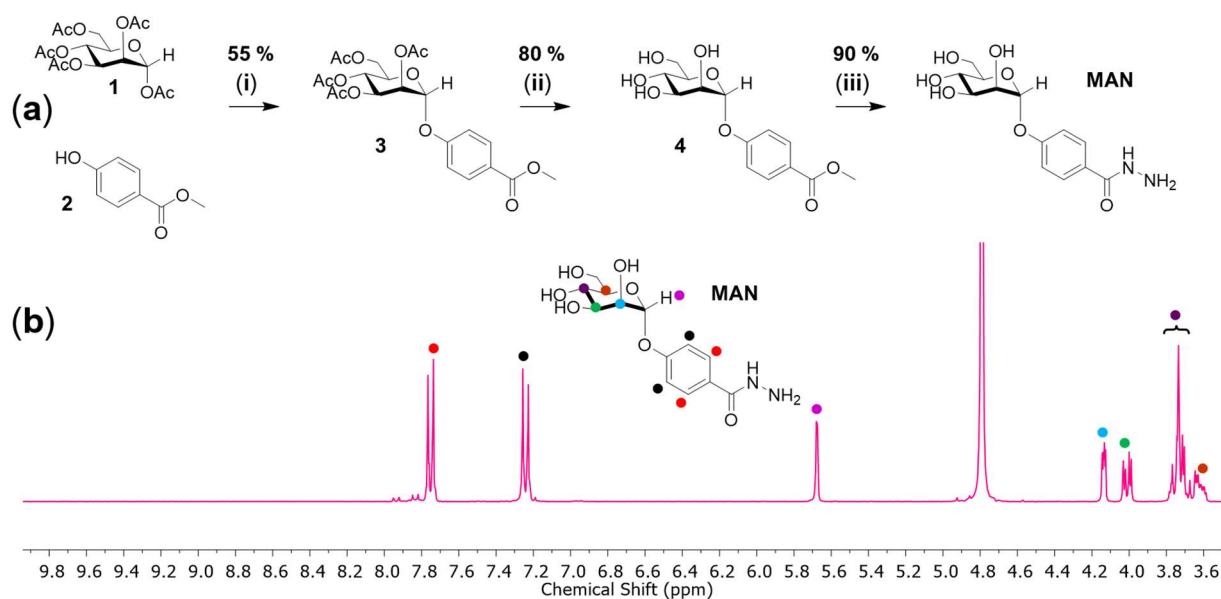


Figure 6: (a) Synthesis of mannose hydrazide residue (**MAN**). Step (i) BF₃·Et₂O, dichloroethane, 50 °C, 18 h. Step (ii) NaOMe, anhydrous MeOH. Step (iii) H₂NNH₂·H₂O, MeOH, reflux, 18 h. (b) Partial ¹H NMR spectrum (D₂O, 300 MHz) of **MAN**.

3.3.5. Synthesis and Characterization of Mannose-Grafted Scaffolds

Mannose hydrazide (**MAN**) was grafted onto aldehyde-functionalized copolymers (**P1** - **P5**) (Fig. 7a) through hydrazone formation to afford a series of glycopolymers (**P1-MAN** - **P5-MAN**) that display a range of carbohydrate (**MAN**) densities. **P1-MAN** - **P5-MAN** were then purified by dialysis against DI water, lyophilized to afford white solids and then characterized by ¹H NMR spectroscopy. Figure 8e shows a representative ¹H NMR spectrum of mannose-functionalized scaffold **P3-MAN** after purification by dialysis. For fluorescence microscopy experiments, glycopolymers (**P1-MAN** - **P5-MAN**) were additionally labelled (Fig. 7b) with small quantities of dansyl hydrazide (**DAN**) (1 - 2 equivalents per polymer chain).

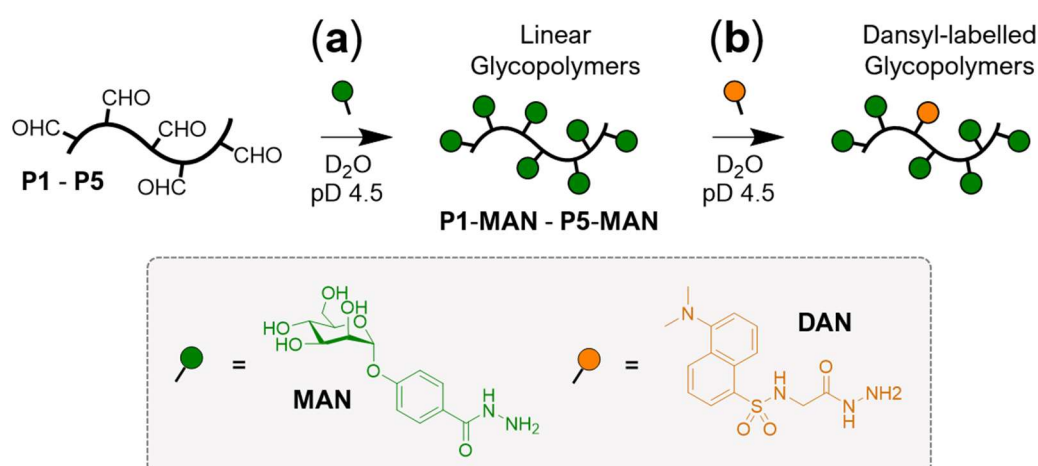


Figure 7: Aldehyde scaffolds (**P1** - **P5**) were 'decorated' with mannose hydrazide (**MAN**) (a) to afford linear glycopolymers (**P1-MAN** - **P5-MAN**) of varying mannose density. For fluorescence microscopy experiments, these glycopolymers were additionally labelled (b) with small quantities of dansyl fluorescence tag (**DAN**).

Grafting of **MAN** onto polymer scaffolds (**P1-P5**) was monitored by ^1H NMR spectroscopy (Fig. 8a-d), which revealed complete 'decoration' of aldehyde functionality, as evidenced by the disappearance of 'diagnostic' (●) aldehyde signal at δ 10.02 ppm and broadening of signals associated with mannose hydrazide (**MAN**).

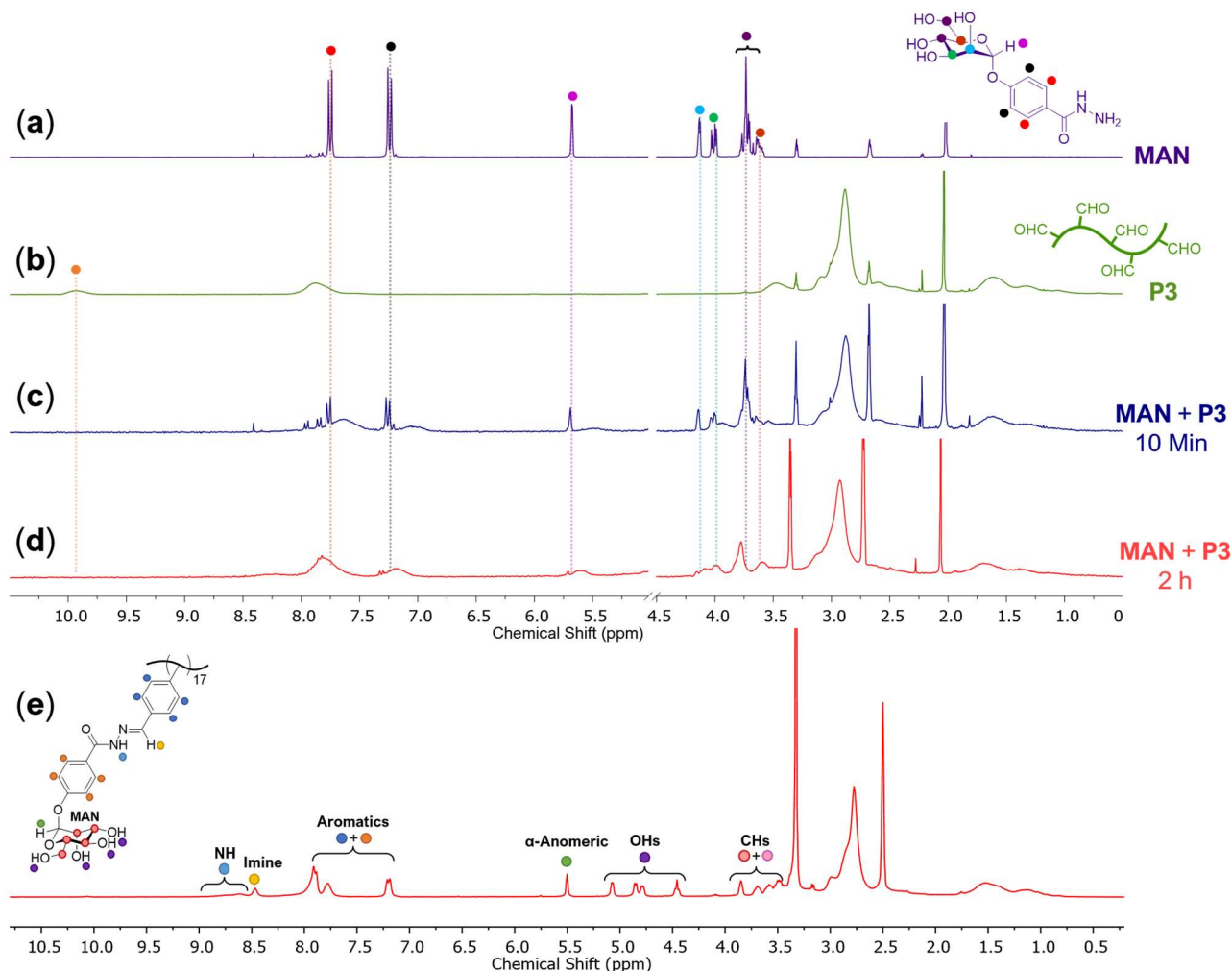


Figure 8: Grafting of mannose hydrazide (**MAN**) to aldehyde-functionalized copolymers (**P1 - P5**) was monitored by ^1H NMR spectroscopy. Representative ^1H NMR spectra (D_2O , 300 MHz) of: (a) Aldehyde scaffold **P3** (b) **MAN** residue, (c) **P3** (1.2 mM) + **MAN** (30.2 mM) after 10 min and (d) after 2 h at room temperature, 50 mM $\text{H}_4\text{NOAc-AcOH/D}_2\text{O}$ (pD 4.5), stoichiometry of aldehyde unit (**P3**) : **MAN** = 1 : 1.50. (e) Assigned ^1H NMR spectrum (d_6 -DMSO, 300 MHz) of **MAN**-grafted polymer scaffold (**P3-MAN**) after purification by dialysis.

3.3.6. Synthesis and Characterization of Acrylamide Glyco-SCPNs

A series of glyco-SCPNs bearing pendant mannose groups (MAN-SCPNs) were prepared by intramolecular crosslinking of linear glycopolymer chains (**P1-MAN** - **P5-MAN**) with succinic dihydrazide (**SD**) (Fig. 9a), which afforded MAN-SCPNs featuring a range of mannose densities. Addition of excess NaCNBH_3 to 'dynamic' MAN-SCPNs (**dyn-MAN-SCPNs**) (Fig. 9b) afforded chemical reduction of the dynamic covalent hydrazone bonds to the corresponding amine, thus yielding 'fixed' MAN-SCPNs (**fix-MAN-SCPNs**). This step was taken as precautionary measure to ensure that no unwanted intermolecular crosslinking of MAN-SCPNs occurred during their characterization by GPC analysis (Fig. 10b-e).

3.3.7. GPC Characterization of SCPN Formation

The successful formation of SCPNs can be confirmed by GPC, which reveals a chain collapse consistent with intra-chain crosslinking (Fig. 10a), if successful intramolecular crosslinking has occurred.¹⁸ MAN-SCPNs were thus characterized by GPC analysis (Fig. 10b-c), which revealed the intramolecularly crosslinked **fix-MAN-SCPN** chains displayed a small increase in retention time (RT) relative to their corresponding linear glycopolymer scaffolds (**P2-MAN** - **P3-MAN**), an observation which was consistent with the intra-chain crosslinking expected during the formation of SCPNs.

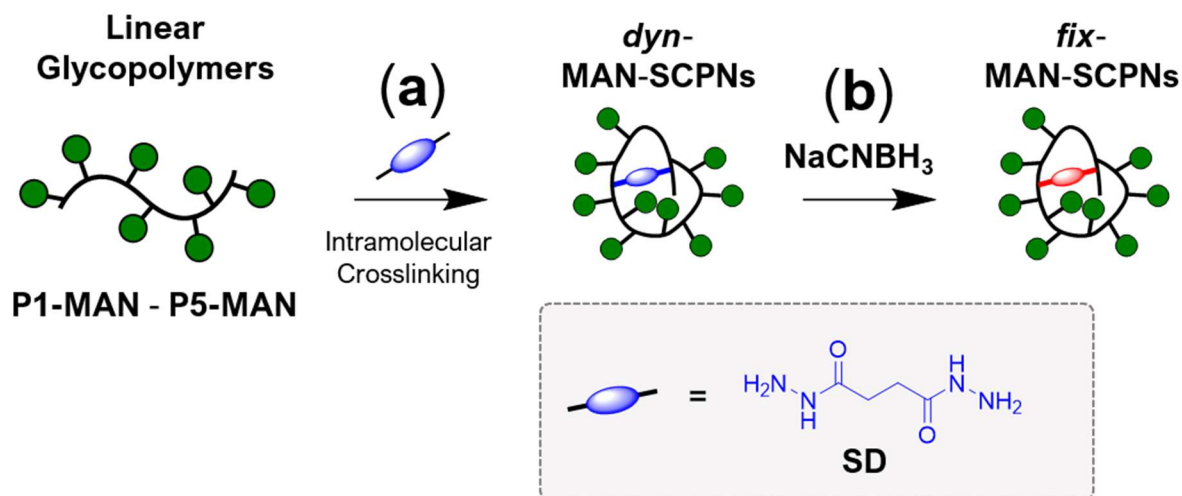


Figure 9: Preparation of MAN-SCPNs. Linear glycopolymers (**P1-MAN** – **P5-MAN**) were intramolecularly crosslinked (a) with succinic dihydrazide (**SD**) under high dilution to afford **dyn-MAN-SCPNs**. (b) Addition of excess NaCNBH_3 to **dyn-MAN-SCPNs** afforded chemical reduction of the dynamic covalent hydrazone bonds to the corresponding amine, thus yielding **fix-MAN-SCPNs**.

Glycopolymers that featured **MAN** densities > 18 % (**P4-MAN** – **P5-MAN**) were observed to have (i) broadening of their GPC traces (Fig. 10d-e), (ii) evidence of peak tailing and (iii) less pronounced RT shift, observations which indicated that these glycopolymers exhibited an interaction with the GPC columns. Furthermore, these same high **MAN** density glycopolymers featured diminished aqueous solubility, such that the 25 % **MAN** polymer (**P5-MAN**) was almost completely insoluble in water at > 5 mg/mL.[‡] Intriguingly, the corresponding aldehyde scaffolds (**P2** – **P5**) were all water soluble at 10 mg/mL, and solubility issues only arose after grafting with mannose hydrazide, a residue which was anticipated to be highly hydrophilic in nature. It was hypothesized that the poor aqueous solubilities of **P4-MAN** and **P5-MAN** arises on account of these mannosylated polymer scaffold containing two aromatic moieties (Fig. 11c, shown in blue/red), which present a highly hydrophobic region within the grafted glycopolymers, sufficient to disrupt the hydrophilic/hydrophobic balance in favour of precipitation in water.[§]

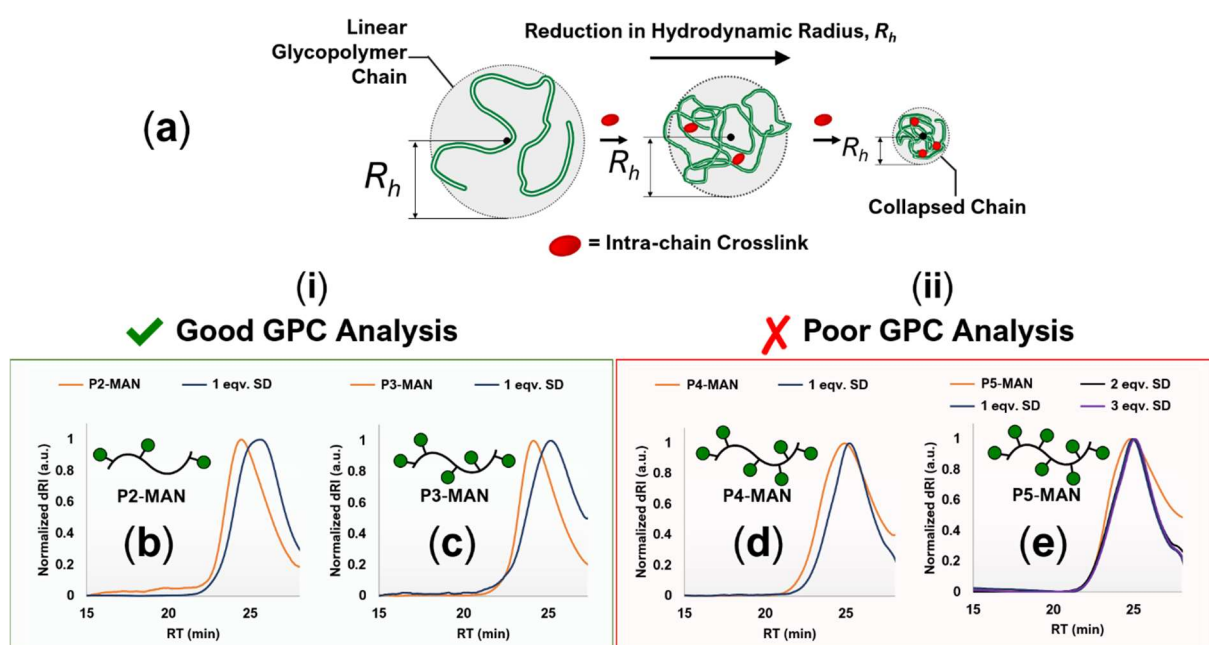


Figure 10: (a) Intramolecular crosslinking of **P1-MAN** – **P5-MAN** with succinic dihydrazide (**SD**) was anticipated to afford contraction of the polymer chain, resulting in a smaller hydrodynamic diameter and corresponding increase in the retention time observed by GPC. (b-e) GPC characterization of linear glycopolymers (**P2-MAN** – **P5-MAN**) (orange lines) and their corresponding **fix-MAN-SCPNs** (blue, black, purple lines), containing 1, 2 or 3 equivalents of crosslinker (**SD**). (b-c) GPC traces showing successful formation of SCPNs, as evidenced by the increase in RT upon crosslinking. (d-e) Failed GPC characterization (ii) of **fix-MAN-SCPNs**, was observed on account of broadening of the GPC traces which was observed at for scaffolds displaying higher carbohydrate densities. All GPC analysis was performed in DMF + 10 g/L LiBr, with PLgel Mixed-D 5 μ m GPC columns.

[‡] **P3-MAN** and their corresponding SCPNs (**dyn-MAN-SCPNs**) were employed for ‘shrink-wrapping’ experiments within this chapter, on account of this polymer scaffold displaying a reasonable aqueous solubility of ≥ 5 mg/mL, together with it displaying a relatively high number of carbohydrate (**MAN**) residues.

[§] It was observed that small changes in the polymer composition afforded significant changes in the aqueous solubility of glycopolymers **P1-MAN** – **P5-MAN**. **P3-MAN** afforded the optimum balance between high mannose density *versus* reduced aqueous solubility.

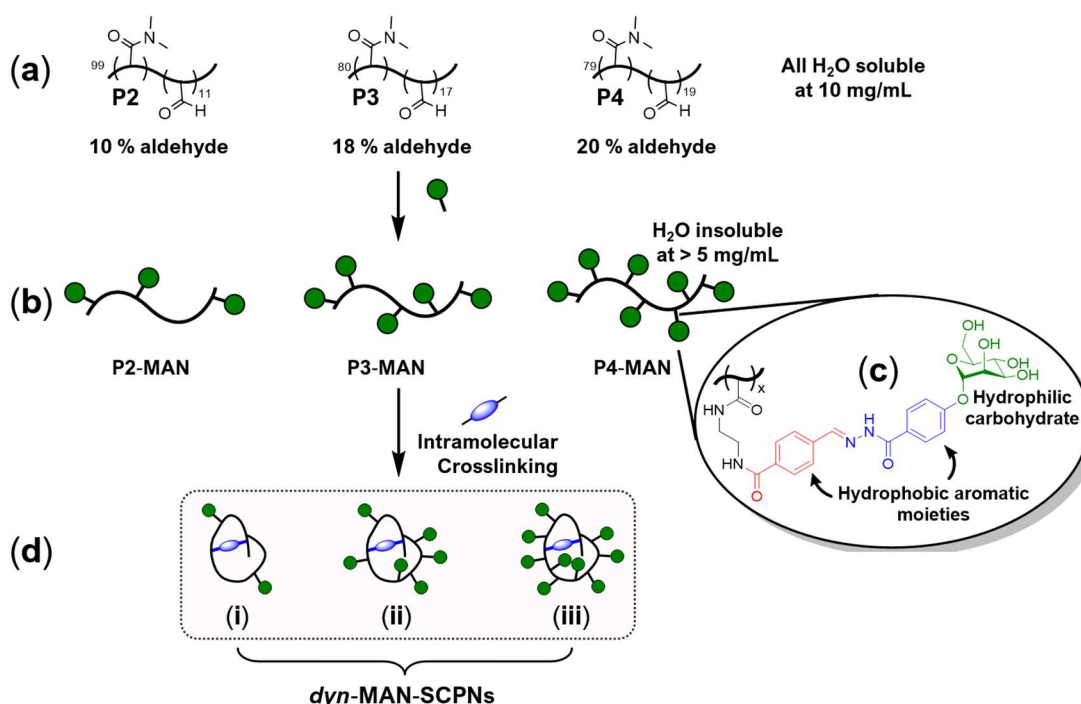


Figure 11: (a) Acrylamide-based aldehyde scaffolds (**P1**, **P2**, **P4**) with varying aldehyde densities, all were water-soluble at 10 mg/mL (b) Linear mannose-grafted polymers **P1-MAN**, **P2-MAN** and **P4-MAN** display increasing carbohydrate densities. (c) Mannose was grafted to polymer scaffolds through dynamic covalent acyl hydrazone bonds. Inconveniently, the hydrophobic aromatic moieties (shown in red/blue) reduced the aqueous solubility of the ‘decorated’ glycopolymers, presumably by disrupting the hydrophilic/hydrophobic balance. Glycopolymers with > 18 % **MAN** displayed very limited water solubility, with > 20 % **MAN** being virtually insoluble. (d) Intramolecular crosslinking of **P2-MAN** – **P4-MAN** afforded **dyn-MAN-SCPNS** with a range of carbohydrate densities.

To achieve the goal of ‘shrink-wrapping’ Con A-functionalized nano- and microparticles within aqueous solution requires mannosylated glycopolymers with good water solubility, but also a sufficient number of mannose units located upon their periphery for binding to Con A. However, mannosylated polymers prepared from acrylamide-based scaffolds (Fig. 11a-b), featured poor aqueous solubilities on account of the hydrophobic nature of the benzaldehyde unit of **M1** (Fig. 11c). In order to satisfy the requirements for aqueous solubility, glycopolymers featuring ≤ 18 mannose (**MAN**) units per polymer chain were prepared. This number, however, is further decreased to just 10 - 15 **MAN** units after intramolecular crosslinking (Fig. 11d) of the linear glycopolymer with succinic dihydrazide, on account of mannose hydrazide being displaced through hydrazone exchange reactions.** **MAN-SCPNS** prepared from **P3-MAN** were utilized for the ‘shrink-wrapping’ experiments discussed within this chapter, on account this glycopolymer featuring the highest density of mannose, whilst retaining reasonable aqueous solubility. In the next section (pages 107 - 120), “**dyn-MAN-SCPNS**” refers specifically to **SCPNS** prepared from **P3-MAN**, which contain 1 dynamic covalent acyl hydrazone crosslink per polymer chain, and “**fix-MAN-SCPNS**” are the corresponding non-dynamic form.

** Note that future optimization of the ‘shrink-wrapping’ chemistry will likely require the density of both **MAN** and crosslinker (**SD**) residues to be adjusted, such that **dyn-MAN-SCPNS** display the optimal carbohydrate/crosslinker composition for the complete encapsulation of Con A substrates within covalently crosslinked glycopolymer films.

3.3.8. Preparation of Protein-Functionalized Nano- and Microparticles

Con A particles were prepared in a range of particle sizes (diameters: 100 nm – 20 μ m) to allow for ‘shrink-wrapping’ to be investigated on nanoscale and microscale substrates. Initial experiments typically utilized Con A particles with smaller diameters (100 nm, 300 nm) to allow for ‘shrink-wrapping’ to be monitored by DLS measurements. Later investigations were performed on much larger Con A microspheres (5 μ m and 20 μ m), the ‘wrapping’ of which was probed by fluorescence microscopy. Table 1 provides a summary of all the particles employed in this chapter, detailing their size, ‘core’ material, and surface functionality. Con A-functionalized particles were prepared *via* two methods: (i) Immobilization of biotinylated Con A onto streptavidin-functionalized polystyrene particles (Fig. 12a), and (ii) covalent attachment of Con A onto NHS-functionalized silica particles (Fig. 12b). Con A particles were then purified by six consecutive centrifuge-wash-resuspend cycles to remove the excess ‘unbound’ Con A.

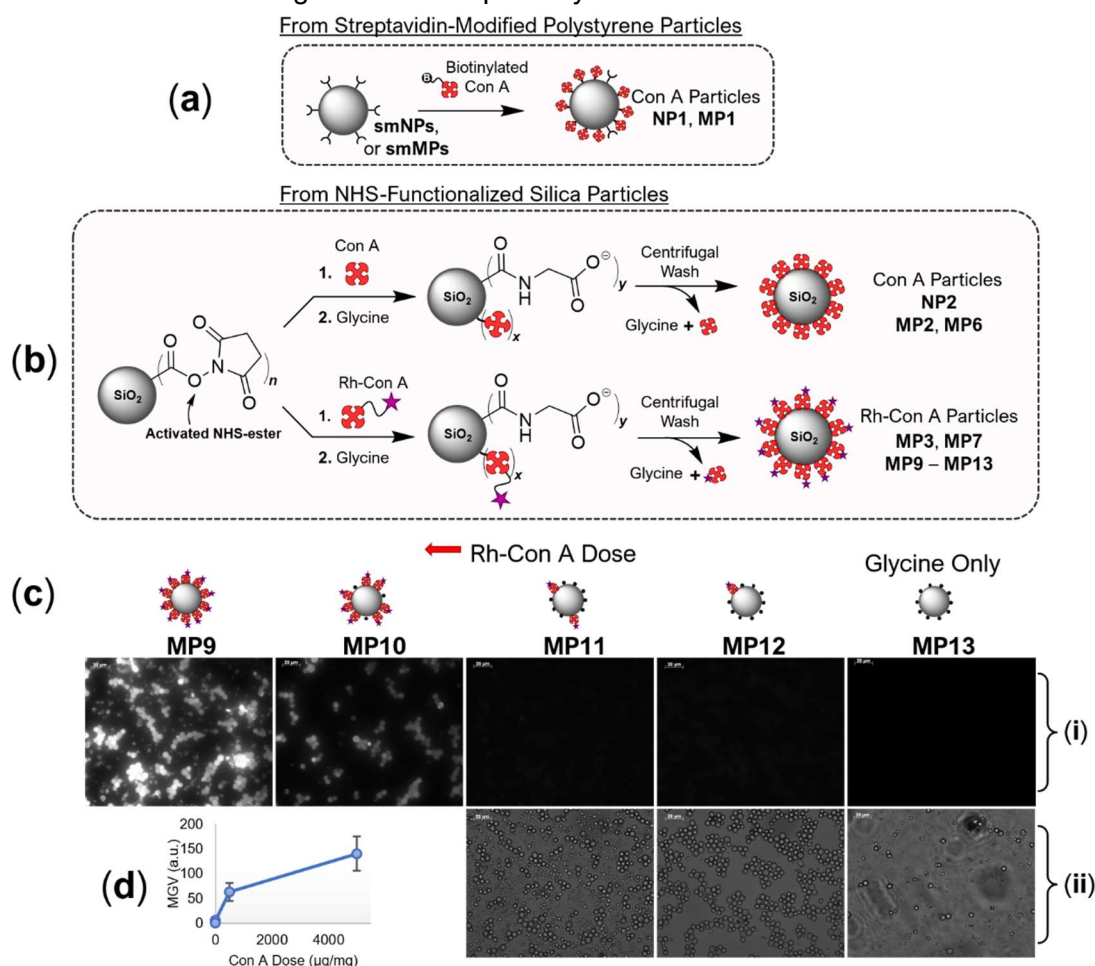


Figure 12: Preparation of Con A-functionalized particles. (a) Immobilization of biotinylated-Con A onto streptavidin-modified polystyrene particles (smNPs or smMPs). (b) Covalent attachment of Con A onto NHS-functionalized silica particles. Unreacted NHS-ester sites were then ‘capped’ with glycine and the particles purified by centrifugation. (c) Preparation of Con A microparticles (b) was optimized by preparing a range of 5 μ m microparticles (MP9 – MP13) with varying surface densities of Rh-Con A. MP9 – MP13 were observed by fluorescence microscopy (i), which revealed emissive coronas localized to the particle surface, indicating successful modification with the lectin. (ii) Bright field microscope images. The measured particle brightness (MGV) (d) was observed to directly correlate with the dose of Rh-Con A added.

Initial ‘wrapping’ experiments were conducted on **NP1** and **MP1**, particles which consist of a streptavidin-functionalized polystyrene ‘core’ (Fig. 12a).^{††} Later ‘wrapping’ experiments utilized **MP2 – MP5**, 5 µm microparticles which contain a silica-NHS ‘core’ (Fig. 13b).^{‡‡}

Particles	Particle Core	Surface Functionality	Protein Dose (µg/mg)	Particle Diameter
smNPs	Streptavidin-Modified Polystyrene	-	0	100 nm
smMPs	Streptavidin-Modified Polystyrene	-	0	5 µm
NP1	Streptavidin-Modified Polystyrene	Biotin-Con. A	500	100 nm
MP1	Streptavidin-Modified Polystyrene	Biotin-Con. A	500	5 µm
NP2	NHS-Functionalized Silica	Con. A	500	300 nm
MP2	NHS-Functionalized Silica	Con. A	500	5 µm
MP3		Rh-Con. A	500	
MP4		Glycine Only	0	
MP5		LBT	500	
MP6	NHS-Functionalized Silica	Con. A	500	20 µm
MP7		Rh-Con. A	500	
MP8		Glycine Only	0	
MP9	NHS-Functionalized Silica	Rh-Con. A	5000	5 µm
MP10			500	
MP11			50	
MP12			5	
MP13			0	

Table 1: Summary of nano- and microparticles utilized throughout experimental investigations.

Con A nanoparticles (**NP1**) were prepared by titration of biotinylated-Con A (**b-Con A**) into a solution of streptavidin-modified polystyrene nanoparticles (**smNPs**) with a diameter of 100 nm. The resultant Con A particles (**NP1**) were characterized by DLS (Fig. 13b), which revealed a 14 nm increase in hydrodynamic diameter, D_h , consistent with the attachment of a **b-Con A** monolayer (7 nm layer thickness, L) onto the particle surface. To confirm the successful immobilization of **b-Con A** onto **smNPs**, a fluorescence assay (Fig. 13c) (see experimental, page 140 for procedure) was conducted with biotin-4-fluorescein (**B4F**).

^{††} Results obtained by DLS (page 107), ELLA assay (pages 109 - 112) and fluorescence microscope (pages 112 - 117), however, revealed that acrylamide-based glycopolymers bind non-specifically to the underlying streptavidin-modified particle surface. These issues of non-specific binding are discussed on pages 117 - 119.

^{‡‡} The ‘shrink-wrapping’ of 20 µm Con A microparticles (**MP6 – MP8**) was also explored, however, these particles were observed to undergo fragmentation during their purification by centrifugation, and thus ‘wrapping’ experiments were instead conducted with 5 µm microparticles (**MP2 – MP5**), which were not observed to fragment under centripetal force.

The **B4F** assay reported (Fig. 13d, i) the ‘free’ biotin binding capacity (BC) of **smNPs** to be 57 pMol/mg – a value which was anticipated to decrease upon the addition of biotinylated-Con A, on account of it binding to the available streptavidin sites upon the particle surface. As anticipated, the assay results (Fig. 13d, ii) revealed a decrease in BC relative to **smNPs** (Fig. 13d, i), consistent with the attachment of **b-Con A**.

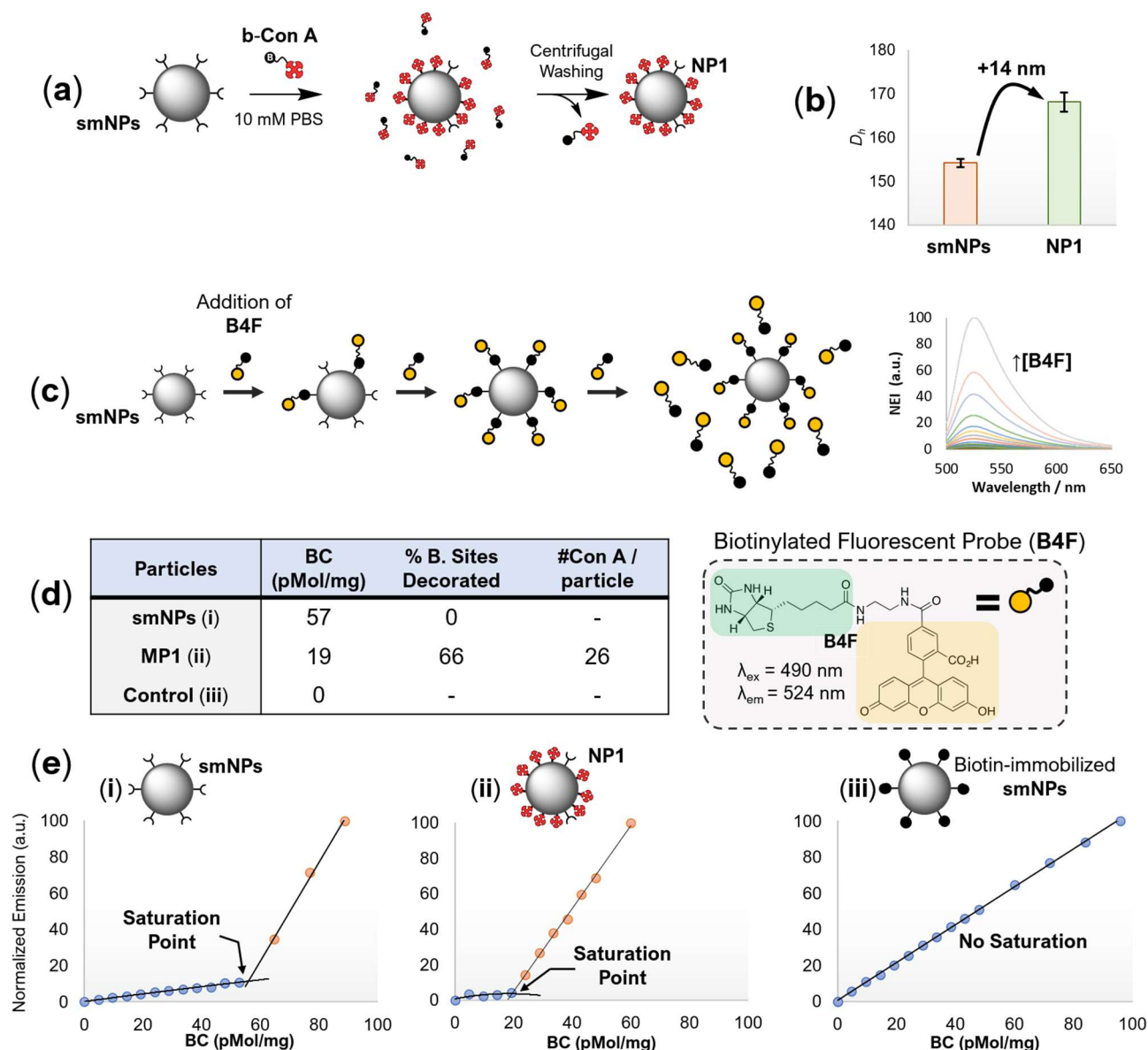


Figure 13: (a) Immobilization of biotinylated Con A onto **smNPs** (streptavidin-modified particles, 100 nm). The resulting Con A NPs (**NP1**) were purified by centrifugal washing. Attachment of biotinylated Con A (**b-Con A**) onto **smNPs** was confirmed by DLS (b), which revealed a small (14 nm) increase in hydrodynamic diameter (D_h), and **B4F** fluorescence assay (c) where the anticipated reduction in the biotin binding capacity (BC) was observed. (b) DLS analysis of ‘naked’ **smNPs** and Con A-immobilized **NP1**. (d) Table of biotin binding capacity of (i) ‘naked’ **smNPs**, (ii) Con A-immobilized **NP1** and (iii) biotin-immobilized **smNPs** (negative control) and the approximate number of Con A tetramers per particle. (e) Normalized emission profiles obtained by titration of **B4F** into particles (i)-(iii). Details of the normalization procedure are given in the experimental section (see page 140).

3.3.9. ‘Shrink-Wrapping’ Studies with Con A-Immobilized Streptavidin-Modified Polystyrene NPs with Acrylamide-Based Glycopolymers

DLS ‘Wrapping’ Experiments

DLS studies were conducted to investigate the ‘shrink-wrapping’ of 100 nm Con A particles (NP1) within glyco-SCPN films (Fig. 14a). Con A particles (NP1) were incubated with both crosslinked SCPNs (**dyn-MAN-SCPNs**) (Fig. 14a, 1) and linear glycopolymer (**P3-MAN**) (Fig. 14a, 2) for 24h at pH 4.5, which afforded suspensions of ‘wrapped’ NP1 (Fig. 14a, ii) and ‘coated’ NP1 (Fig. 14a, v), respectively. ‘Unbound’ glycopolymer chains were removed by centrifugation and then the ‘wrapped’/‘coated’ particles were characterized by DLS (Fig. 14b, before α MM).

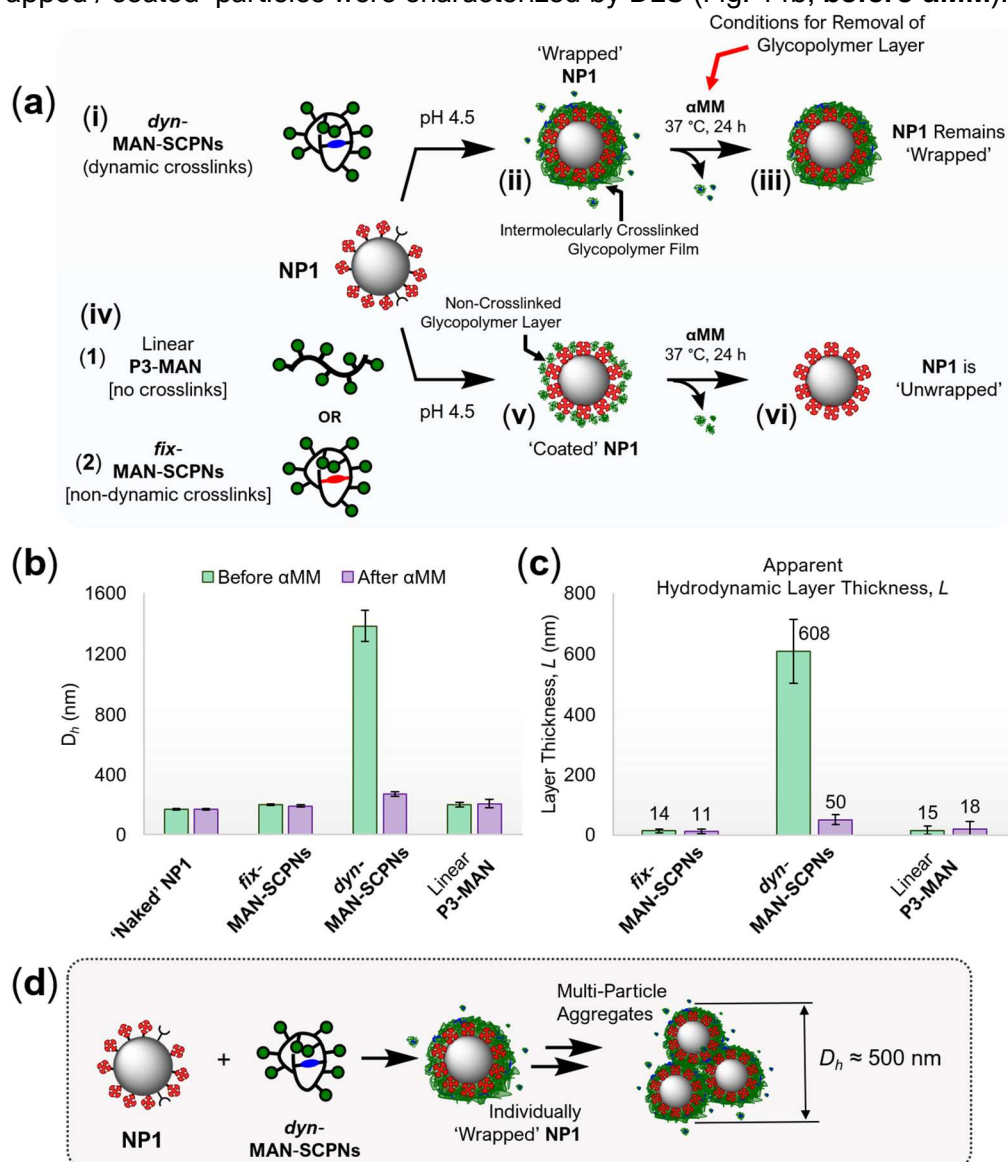


Figure 14: ‘Shrink-wrapping’ of Con A particles (NP1) was investigated by DLS analysis. (a) Schematic overview of the ‘wrapping’ experiment. Addition of **dyn-MAN-SCPNs** (i) was anticipated to afford Con A particles ‘wrapped’ within a covalently crosslinked glycopolymer film (ii), which cannot be displaced upon addition of α MM (iii). Control experiments with linear glycopolymer **P3-MAN** (1) and **fix-MAN-SCPN** (2), however, were expected to afford ‘coated’ particles, which can readily be displaced by incubation with α MM (vi). (b) DLS analysis during ‘wrapping’ experiment (a). Z-average hydrodynamic diameter, D_h is reported. (c) Apparent thickness of particle-bound glycopolymer layers. (d) Addition of **dyn-MAN-SCPNs** to NP1 was observed drive the formation of multi-particle aggregates.

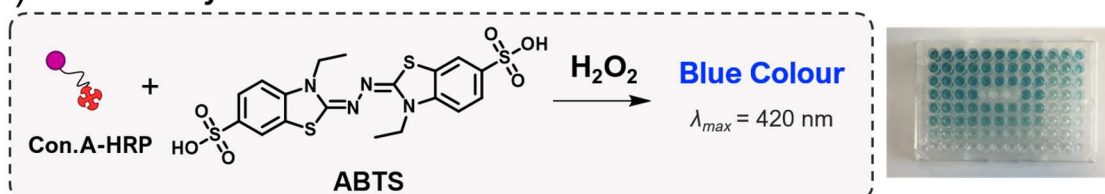
As described in Chapter 2 the apparent thickness, L (Fig. 14c) of the adsorbed polymer layer was derived by subtracting D_h of the ‘naked’ particle (**NP1**) from that of the ‘wrapped’/‘coated’ particles and then dividing by 2. Results in Figure 14c show that ‘coatings’ formed from **fix-MAN-SCPNs** and linear glycopolymer **P3-MAN** were 14 and 18 nm thick, respectively, whereas polymer ‘wrappings’ formed from **dyn-MAN-SCPNs** were reported to be > 608 nm. Whilst this number is not an accurate reflection of the polymer layer thickness, it suggests that the addition **dyn-MAN-SCPNs** drives the formation of multi-particle aggregates (Fig. 14d), whereas the control polymers (**fix-MAN-SCPNs** and **P3-MAN**) do not. Next, the displacement of the polymer layers was attempted (Fig. 14a), in order to provide further evidence of successful ‘shrink-wrapping’.

‘Wrapped’ and ‘coated’ particles were incubated with excess α -methyl mannose (**α MM**), a monosaccharide which was anticipated to fully displace the bound glycopolymer from the particle surfaces by out-competing the polymer chains in their binding to the surface-bound Con A. It was hypothesized that glycopolymer films formed from **dyn-MAN-SCPNs** (Fig. 14a, i - iii) should not be displaced on account their ability to undergo ‘structural metamorphosis’ and form inter-chain crosslinks, and thus cannot be removed by simply inhibiting the mannose-Con A interaction. Control experiments with **fix-MAN-SCPNs** and **P3-MAN**, however, do not contain intermolecular crosslinks, and thus should be readily displaced. However, layer thicknesses determined after **α MM** incubation (Fig. 14c, **green bars**) revealed that control polymers showed little or no reduction in the thickness of the adsorbed glycopolymer layer (relative to **purple bars**), which suggests that the polymer chains remain adhered to **NP1**. As anticipated the thickness of the **dyn-MAN-SCPN** ‘wrapped’ layer decreased substantially after **α MM**, now a plausible value of 50 nm. Intriguingly, the ‘wrapped’ layers were considerably thicker than of the control polymers, consistent with a network of multiple crosslinked layers upon the particle surface. In summary, these DLS studies provided some evidence of successful ‘shrink-wrapping’. However, issues of low colloidal stability were observed, leading to particle-particle aggregation. These unwanted processes were shown to increase the sample polydispersity, thereby reducing the accuracy with which DLS analysis can characterize the thickness (L) of surface-bound polymer films. It was thus concluded that numbers deduced from DLS ‘wrapping’ experiments should be treated with caution and the decision was made to explore alternative techniques for monitoring the ‘shrink-wrapping’ process.

Enzyme-Linked Lectin Assay (ELLA)

To further investigate the displacement of glycopolymer films from Con A nanoparticles (**NP1**), an enzyme-linked lectin assay (ELLA) protocol was developed (Fig. 15). This inhibition-type ELLA reported the relative concentrations of mannose-functionalized polymer scaffold (**P3-MAN**) with an assay readout (absorbance) that was inversely proportional to the glycopolymer concentration bound upon the particle surface. This ELLA experiment utilizes **Con A-HRP** conjugate, where enzyme (HRP) is covalently linked to the mannose-binding lectin Con A, thus allowing for the inhibition assay. Readout was observed as a blue colour, which develops on account of the **ABTS** substrate with the enzyme horseradish peroxidase (HRP) (Fig. 15a).

(a) ELLA Assay Readout:



(b) ELLA Assay Protocol:

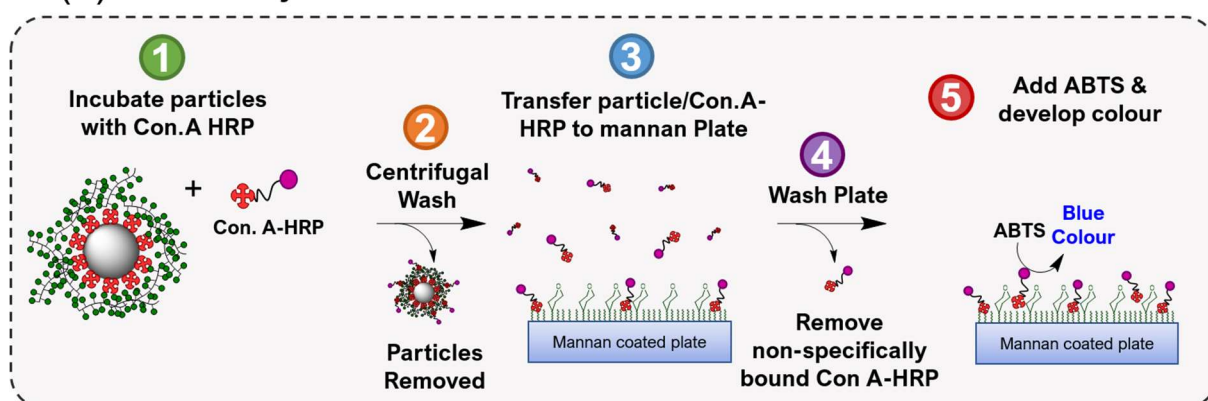


Figure 15: Inhibition-type ELLA assay of glycopolymer ‘coated’ Con A particles. (a) Assay readout is produced by the reaction of **ABTS** with the enzyme horseradish peroxidase, which was covalently linked to the lectin Con A. (b) Protocol for running ELLA assay. (1) ‘Coated’ Con A particles were incubated with **Con. A-HRP** for 1 h at rt, then the particles were pelleted by centrifugation (2), and thus ELLA reports the readout from **Con A-HRP** which is not bound to the particle. The supernatant liquid was transferred (3) to a mannan-immobilized 96-well plate and incubated for 1 h at rt. Mannan is a plant-derived oligosaccharide (a linear polymer of the sugar mannose) onto which **Con A-HRP** will bind. Washing (4) the 96-well plate ensured the removal of non-specifically adhered objects. (5) Peroxide/**ABST** solution was added and readout (absorbance) was measured at $\lambda_{max} = 420 \text{ nm}$

The standard protocol for the inhibition-type ELLA experiment (Fig. 15b) begins (1) with the incubation of glycopolymer ‘coated’ Con A particles in 0.25 mg/mL **Con A-HRP**, pH 7.4 PBS, rt, 1 h. Of the total number of **Con A-HRP** conjugates X_{TOT} , a portion X_A (Fig. 15b, 2) will bind to the glycopolymer upon the Con A particle surface, and thus be removed by the subsequent washing step (2). Step (2) was employed to remove the particles from the solution by successive pelleting (5 x 25 min 15 000 rcf), after which the supernatant liquid was transferred (3) to a mannan-coated 96-well plate and incubated for 1 h at rt, allowing the remaining **Con**

A-HRP to bind to the mannan surface. Non-specifically bound **Con A-HRP** was removed by washing (4) the plate three times with 0.01% Tween 20-PBS buffer (PBST), then assay readout was obtained by addition of **ABTS**/H₂O₂ solution to develop the blue colour. After 30 min the reaction was quenched by addition of 100 mM H₂SO₄ and the absorbance ($\lambda_{\text{max}} = 420 \text{ nm}$) was measured on a plate reader. Utilizing this protocol, an ELLA experiment (Fig. 16a) was performed on Con A particles (**NP1**) which had been ‘coated’ with a range of glycopolymer doses ranging from 0 - 5 $\mu\text{g}/\text{mg}$ (μg glycopolymer per mg of **NP1**)(Fig. 16a).

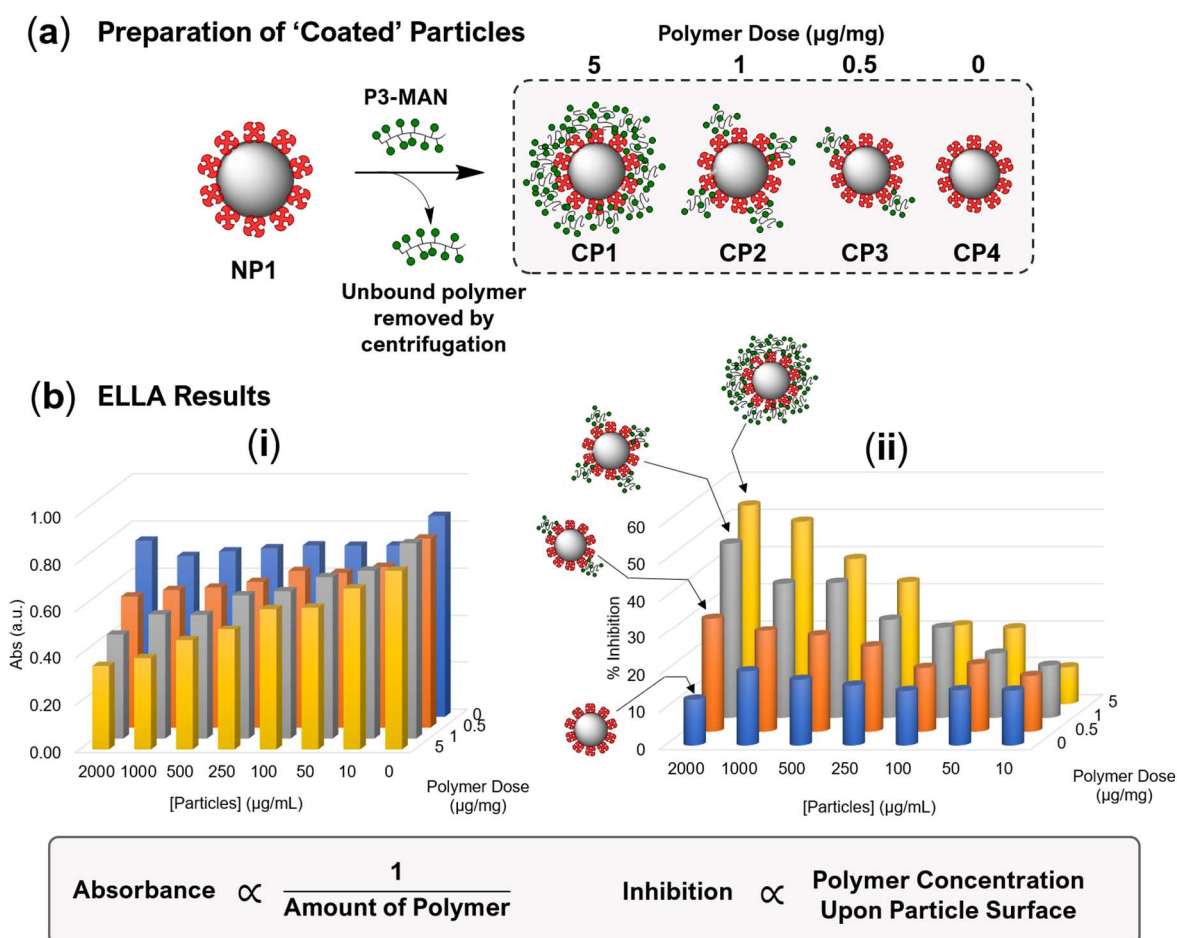


Figure 16: (a) Preparation of glycopolymer ‘coated’ particles (**CP1-CP4**) with a range of polymer doses. Coated particles were purified by centrifugation to remove any unbound glycopolymer. (b) ELLA assay results for coated particles **CP1-CP4**. Bars show the average absorbance, where $n = 3$. Concentrations of assay reagents were [**Con A-HRP**] = 15 $\mu\text{g}/\text{mL}$ and [**ABTS**] = 0.25 mg/mL .

‘Coated’ particles **CP1 - CP4** were purified by centrifugal washing to ensure the removal of ‘unbound’ glycopolymer. ELLA results (Fig. 16b, i) revealed that, as anticipated, readout (absorbance) was inversely proportional to the polymer dose (**CP1** and **CP2** feature low absorbance relative to **CP4**). Alternatively, these results can be presented as a % inhibition plot (Fig. 16b, ii). Note that the x- and y-axes indicate; (i) the concentration of particles and (ii) the polymer dose present in each sample prior to running the ELLA protocol. As anticipated, the control samples (PD = 0 $\mu\text{g}/\text{mg}$) where no glycopolymer was added showed the highest

absorbance values (Fig. 16b, i) and, importantly, no significant absorbance decrease was observed upon increasing the particle concentration (**blue bars**, right-to-left). In contrast, the PD = 5 $\mu\text{g}/\text{mg}$ results (**yellow bars**) revealed a steady absorbance decrease as particle concentration was increased, which manifests as an increase in % inhibition (Fig. 16b, ii). Taken together, these observations indicate that it is the concentration of glycopolymer present upon the surface of ‘coated’ Con A particles which gives rise to the observed inhibition effect. Whilst it was not possible to determine the absolute glycopolymer concentrations bound to the particle surfaces, the ELLA could, however, report the relative amounts of surface-bound glycopolymer with reasonable accuracy – a parameter which was more than adequate to the purposes of investigating the displacement of glycopolymer films from particle surfaces.

Further ELLA experiments (Fig. 17) were undertaken to investigate the displacement of the glycopolymer layers from ‘coated’ Con A particles. ‘Coated’ Con A particles **CP5-CP11** (Fig. 17a) were prepared (PD = 0 – 15 $\mu\text{g}/\text{mg}$)(see Fig. 17b) and the excess glycopolymer was removed by centrifugal washing. After purification **CP5-CP11** were each split into two equal aliquots: (A) which were incubated with **αMM** for 24 h at 37 °C and thus was anticipated to have no surface-bound glycopolymer. The control experiment (B) was absent in **αMM** , and thus no displacement of the glycopolymer layer was anticipated.

(a) Preparation of ‘Coated’ Particles and Displacement of Polymer Layer

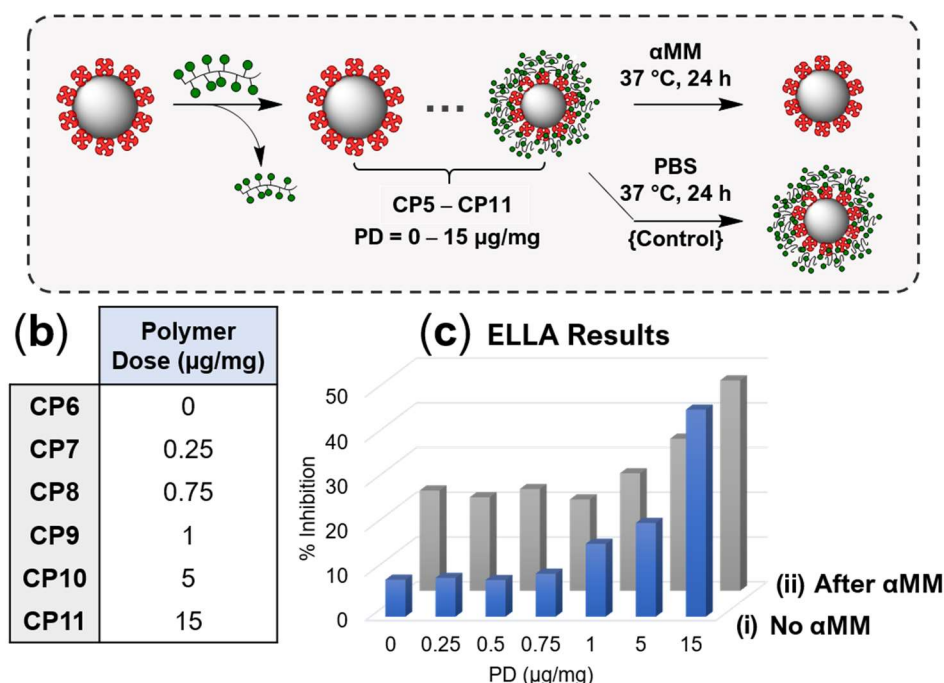


Figure 17: ELLA assay to investigate the displacement of **P3-MAN** glycopolymer coating. (a) Preparation of glycopolymer (**P3-MAN**) coated particles (**CP5-CP11**) with polymer doses (**(b)**) ranging between 0 – 15 $\mu\text{g}/\text{mg}$. (c) ELLA assay results before (i) and after (ii) incubation with **αMM** to displacement of the glycopolymer coating. Concentrations of assay reagents were [**Con A-HRP**] = 15 $\mu\text{g}/\text{mL}$ and [**ABTS**] = 0.25 mg/mL .

Surprisingly, the subsequent ELLA results revealed only subtle differences before (Fig. 17c, i) and after (ii) incubation with **α MM**. Both showed 50 % inhibition at PD = 15 μ g/mg, an observation which indicates that the glycopolymer layer was not successfully displaced by the conditions employed. Note that the 30 % ‘background’ inhibition observed in the **α MM** dataset (Fig. 17c, ii) at PD < 1 μ g/mg was rationalized by the presence of residual **α MM** monosaccharide, which was not fully removed by 5 x centrifugal washes.

In summary, although the ELLA assay offered a method for quantifying relative amounts of glycopolymer upon the surface of Con A particles, the results indicated that incubation with **α MM** did not successfully displace the linear (**P3-MAN**) glycopolymer layer. This observation suggests that the glycopolymer was perhaps non-specifically bound to the particle surface. The failure of this control experiment was significant, in that it was important to successfully demonstrate that linear glycopolymers (non-crosslinked) can successfully be displaced, whereas **dyn-MAN-SCPNS** form crosslinked glycopolymer films which cannot be displaced. In the absence of this control experiment, it would not be possible to prove the ‘shrink-wrapping’ concept occurred as envisaged.

On account of both ELLA assay and DLS affording somewhat inconclusive results, the decision was made to utilize an alternative strategy involving the ‘shrink-wrapping’ of 5 μ m lectin-modified microparticles, which were large enough to be investigated by fluorescence microscopy. Inclusion of the fluorescent dye (dansyl hydrazide) within the polymer scaffold, facilitated imaging of the glycopolymer as it adhered to the periphery of the particles (Fig. 18). The decision to move towards the ‘shrink-wrapping’ of micron-sized objects, and away from unreliable light-scattering measurements of nanometre-sized objects, is a significant turning point in this chapter, which allowed the project to successfully develop.

Monitoring ‘Shrink-Wrapping’ by Fluorescence Microscopy

‘Shrink-wrapping’ of micron-sized lectin-immobilized substrates was studied by fluorescence microscopy. Dansyl fluorescence tags incorporated upon the polymer scaffold enabled the visualization of its attachment to particle surfaces. Preliminary ‘wrapping’ experiments (Fig. 18a) with **dyn-MAN-SCPNS** (prepared from dansyl-labelled **P3-MAN** with 1 eqv. of crosslinker) were undertaken to identify the optimal polymer dose to successfully encapsulate Con A microparticles (**MP1**, Table 1) within a glycopolymer film. **MP1** (1 mg/mL) were treated with **dyn-MAN-SCPNS** at a range of polymer doses (PD \approx 0 – 1000 μ g/mg), then the particles were visualized by fluorescence microscopy (Fig. 18b).

Microscope images (Fig. 18b) revealed that in the absence of glycopolymer (i) no emission was observed, whilst at higher polymer doses (PD \approx 1 - 100 $\mu\text{g}/\text{mg}$) (iii - v) the glycopolymer was observed as a bright emissive corona localized at the particle surface. At PD = 1000 $\mu\text{g}/\text{mg}$ (vi), however, the emission observed from dansyl-labelled **dyn-MAN-SCPNS** were not exclusively localized at the particle surface (see Fig. 18b, vi), indicating the presence of excess glycopolymer which was not interacting with the Con A-functionalized surface. Intriguingly, the addition of relatively low polymer doses (PD = 0.1 - 1 $\mu\text{g}/\text{mg}$) (see Fig. 18b, iii, x 40) afforded particles which were encapsulated within thick glycopolymer layers, with large polymer-coated aggregates observed after several hours. To further investigate this phenomenon, the gradual build-up of glycopolymer films upon Con A microparticle surfaces was monitored as a function of time (Fig. 19a) for three polymer doses: (i) 0.1 $\mu\text{g}/\text{mg}$, (ii) 1 $\mu\text{g}/\text{mg}$ and (iii) 100 $\mu\text{g}/\text{mg}$.

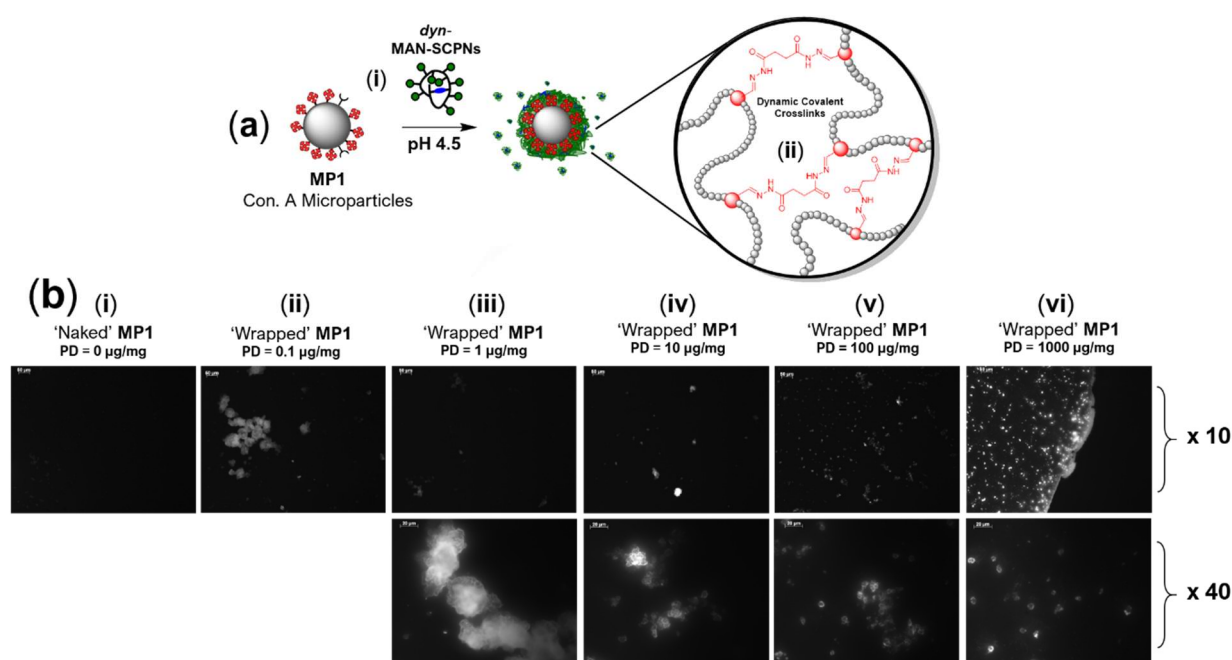


Figure 18: (a) Shrink-wrapping of Con A particles **MP1** by **dyn-MAN-SCPNS**. (b) Fluorescence microscope images (x 10 and x 40 magnification) were obtained for 'shrink-wrapped' particles after 24 h. A range of polymer doses (0 – 1000 $\mu\text{g}/\text{mg}$) were explored (i-vi), where polymer dose (PD) is defined as the mass ratio μg polymer / mg Con A particles.

dyn-MAN-SCPNS were incubated with **MP1** and microscope images (Fig. 19a) were obtained after 10 min, 3 h, 5 h and 18 h. Inspection of these images reveals that **dyn-MAN-SCPNS** build up slowly into thick glycopolymer films over an 18 h timeframe, eventually leading to the formation of 10 - 50 μm 'wrapped' multi-particle aggregates which were entirely encapsulated with glycopolymer film. This promising result was entirely consistent with the hypothesis that thick glycopolymer films may slowly build up over time, as succinic dihydrazide residues undergo slow component exchange processes which leads to the steady 'growth' of intermolecularly crosslinked films (Fig. 19c) located upon the particle surface.

The brightness of ‘wrapped’ **MP1** aggregates was determined by further processing of microscope images within ImageJ software to afford the mean gray value (MGV), a parameter which correlates with the brightness of particles within the image.^{§§} MGV values report on the brightness of fluorescence within the image, and thus a higher MGV indicates a higher concentration of dansyl-labelled polymer upon the particle surface. The mean gray values (MGVs) of the ‘wrapped’ **MP1** aggregates were plotted as a function of time (Fig. 19b, **iv-vi**).

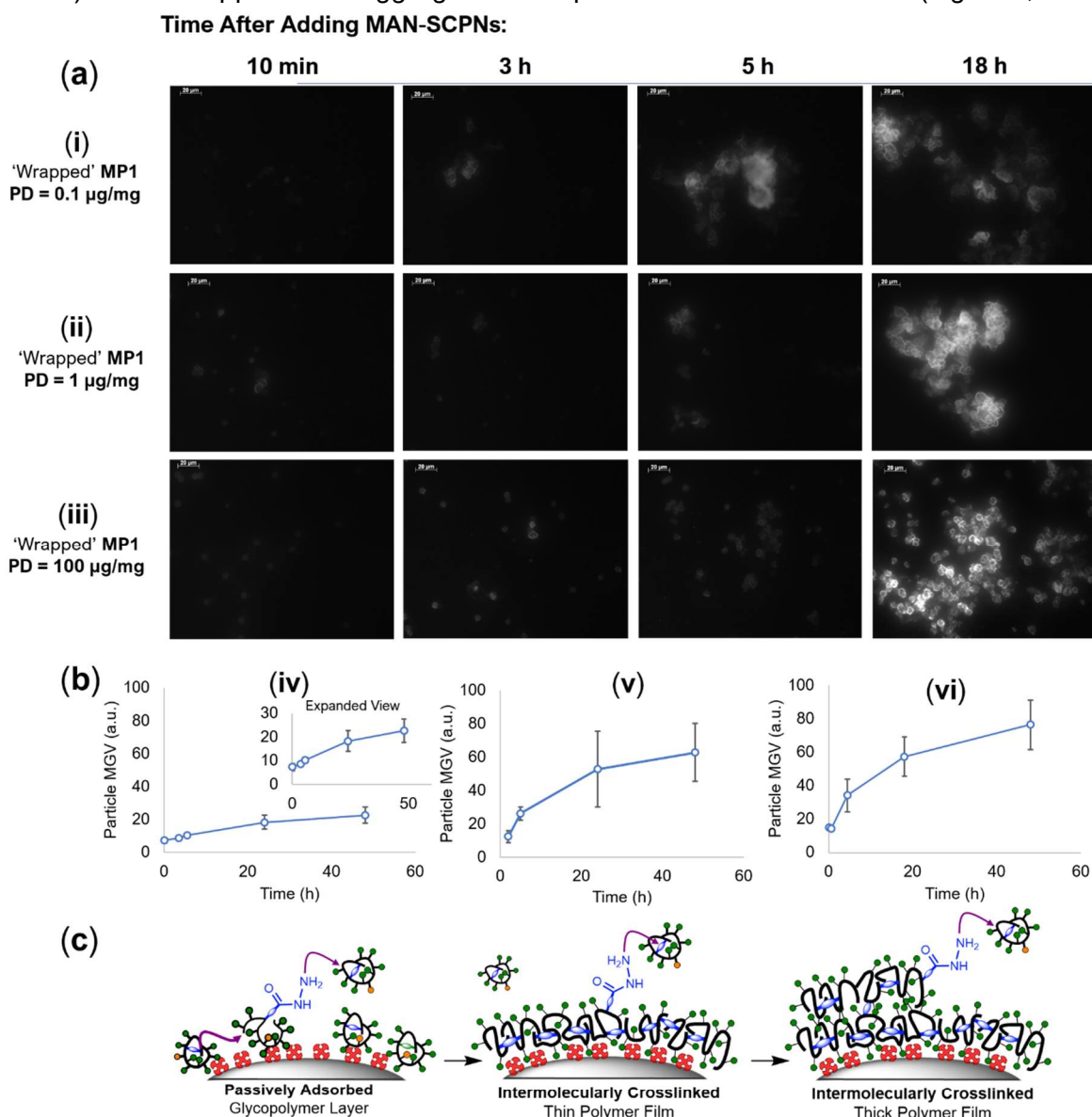


Figure 19: Time-resolved shrink-wrapping experiment. Fluorescence microscope images **(a)** were obtained at different time points after adding **dyn-MAN-SCPNs** to **MP1** (Con A particles). A range of polymer doses were explored: **(i)** 0.1 µg/mg, **(ii)** 1 µg/mg and **(iii)** 100 µg/mg. The slow emergence of a brightly emissive corona around the periphery of the particles suggests that glycopolymer films build up gradually upon the particle surface over a 24 h timescale. Further analysis of these images afforded the average particle brightness as function of time, which is expressed as the mean gray value (MGV). **(b)** MGV plots **(iv-vi)** were obtained from image sets **(i-iii)** and error bars indicate the standard deviation.

^{§§} Mean Gray Value (MGV) is defined as the average gray value within the selection. This is the sum of the gray values of all the pixels in the selection divided by the number of pixels. MGV has a maximum value 255 (a white pixel) and a minimum of 0 (a black pixel). The higher the MGV, the brighter the pixels within the selection, which is indicative of a higher fluorescence from the sample.

Repeating the above experiment with **P3-MAN**, a linear glycopolymer which contains no crosslinks, afforded ‘coated’ particle aggregates (Fig. 20) which were very similar in appearance to the ‘wrapped’ Con A particles (Fig. 19a). Furthermore, the non-crosslinked glycopolymer films build up at a comparable rate to those formed from **dyn-MAN-SCPNs**, indicating that the gradual build-up of glycopolymer-coated aggregates should not be attributed to the formation of intermolecularly crosslinked glycopolymer films. Although **dyn-MAN-SCPNs** had most likely undergone successful ‘metamorphosis’ to form crosslinked glycopolymer films upon the microparticle surface, fluorescence microscope images revealed no obvious differences in the appearance of **dyn-MAN-SCPNs** ‘wrapped’ **MP1** (Fig. 19a) and **P3-MAN** ‘coated’ **MP1** (Fig. 20). In pursuit of definitive evidence of ‘shrink-wrapping’, experiments were conducted to investigate the displacement of glycopolymer layers from the particle surface (Fig. 21).

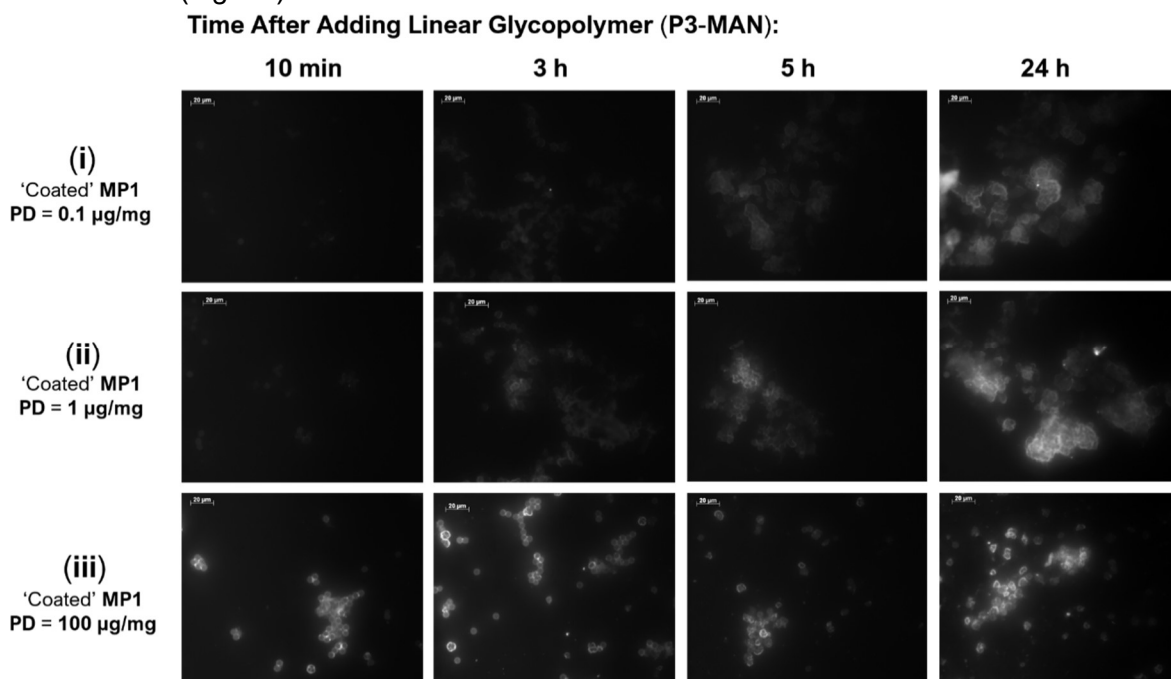


Figure 20: Control experiment in which **MP1** (Con-A immobilized particles, 5 µm) were incubated with linear glycopolymer **P3-MAN** to form ‘coated’ particles, whose glycopolymer layers lack the dynamic covalent crosslinks required for ‘shrink-wrapping’. Formation of **P3-MAN** encapsulated particles was studied as a function of time for three polymer doses: (i) 0.1 µg/mg (ii) 1 µg/mg and (iii) 100 µg/mg. All microscope images were obtained under UV light at 40 x magnification.

It was hypothesized, on account of their intermolecularly crosslinked nature, that **dyn-MAN-SCPN** films (Fig. 21a, i - iii) should be significantly more difficult to displace from the particle surface than ‘coatings’ formed from linear glycopolymer. If **dyn-MAN-SCPNs** (i) have successfully ‘shrink-wrapped’ **MP1** with an intermolecularly crosslinked polymer film (ii), then incubation with overnight **αMM** will reveal that those polymer films cannot be displaced, and thus **MP1** should remain ‘wrapped’ (iii). In contrast, a control experiment with non-crosslinked glycopolymer **P3-MAN** (Fig. 21a, iv) yields ‘coated’ **MP1** (v). Incubation with **αMM** is thus

anticipated to fully displace the glycopolymer chains from the particle surface. Consistent with this hypothesis, the fluorescence microscope images indicated that ***dyn*-MAN-SCPN** ‘wrappings’ were not displaced, as evidenced by the brightly emissive corona, which remains present even after treating ‘wrapped’ **MP1** with **α MM** (Fig. 21b, ii). The control experiment with **P3-MAN** (Fig. 21c), however, did not return the expected result, with fluorescence microscope images after **α MM** incubation (ii) revealing that **MP1** remained coated in an emissive glycopolymer layer. Although ‘shrink-wrapping’ had likely occurred, the failure of this control experiment to return the anticipated result denied access to convincing evidence of this phenomenon. Furthermore, the intriguing observation that **P3-MAN** was not significantly displaced by excess **α MM**, was highly indicative of non-specific binding between **P3-MAN** and

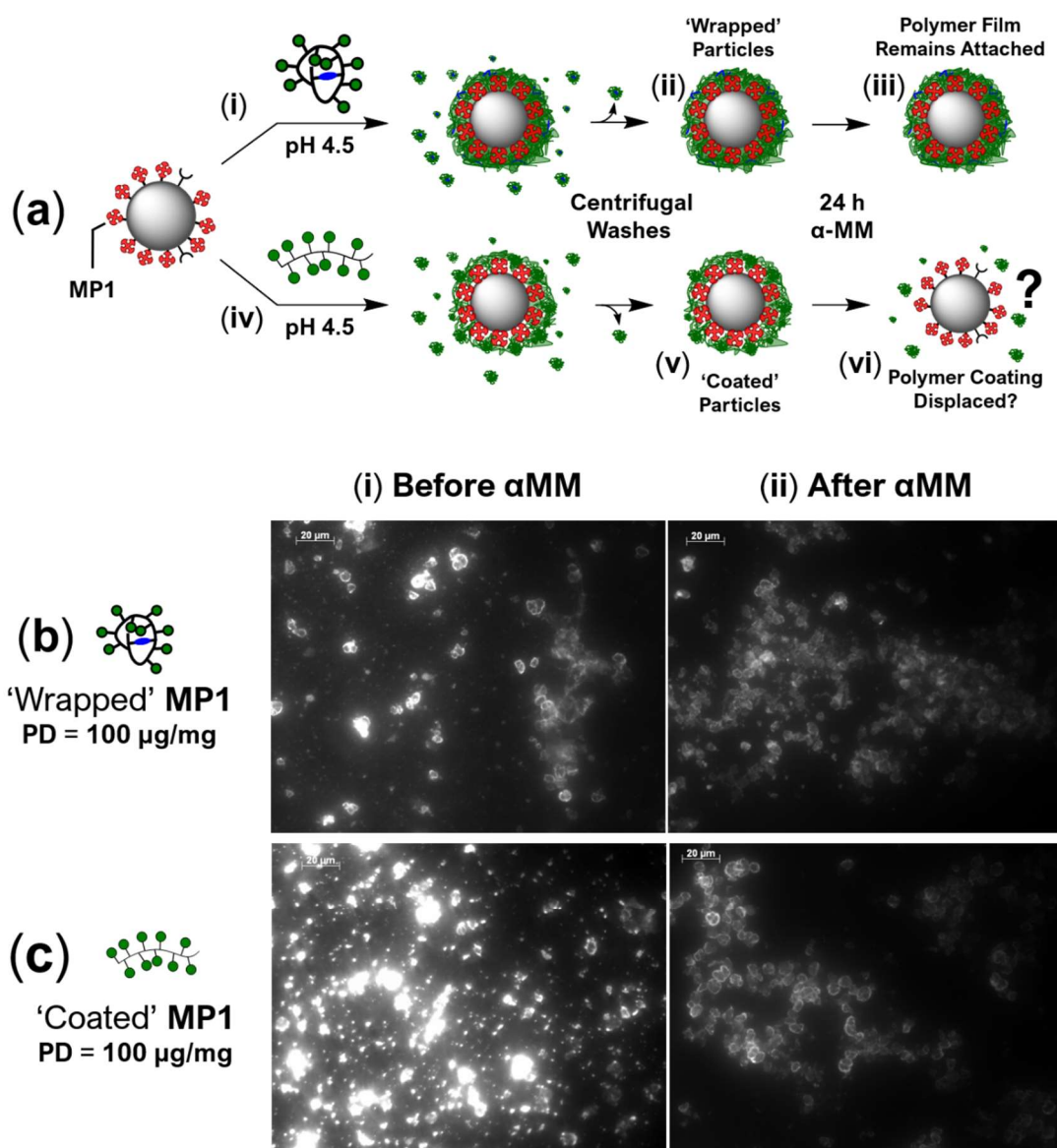


Figure 21: (a) Overview of the ‘shrink-wrapping’ experiment. (b-c) Fluorescence microscope images of ‘wrapping’ experiments performed with Con A particles (b) and control experiments with streptavidin-modified particles (c). Images were obtained before (i) and after (ii) incubation with **α MM**, which was anticipated to displace the glycopolymer coatings from particle surfaces. Experimental conditions: 1 mg/mL particles, PD = 100 μ g/mg, T > 18 h.

the particle surface of **MP1**. To further investigate this possibility, a series of control experiments (Fig. 22a) was undertaken to investigate whether glycopolymers **P3-MAN** and **dyn-MAN-SCPNs** were bound to **MP1** through specific recognition of Con A by their mannose residues, or if they simply adhered on account of non-specific interactions with the underlying streptavidin-modified particle surface. Figure 22a provides a schematic overview of these experiments and their outcomes.

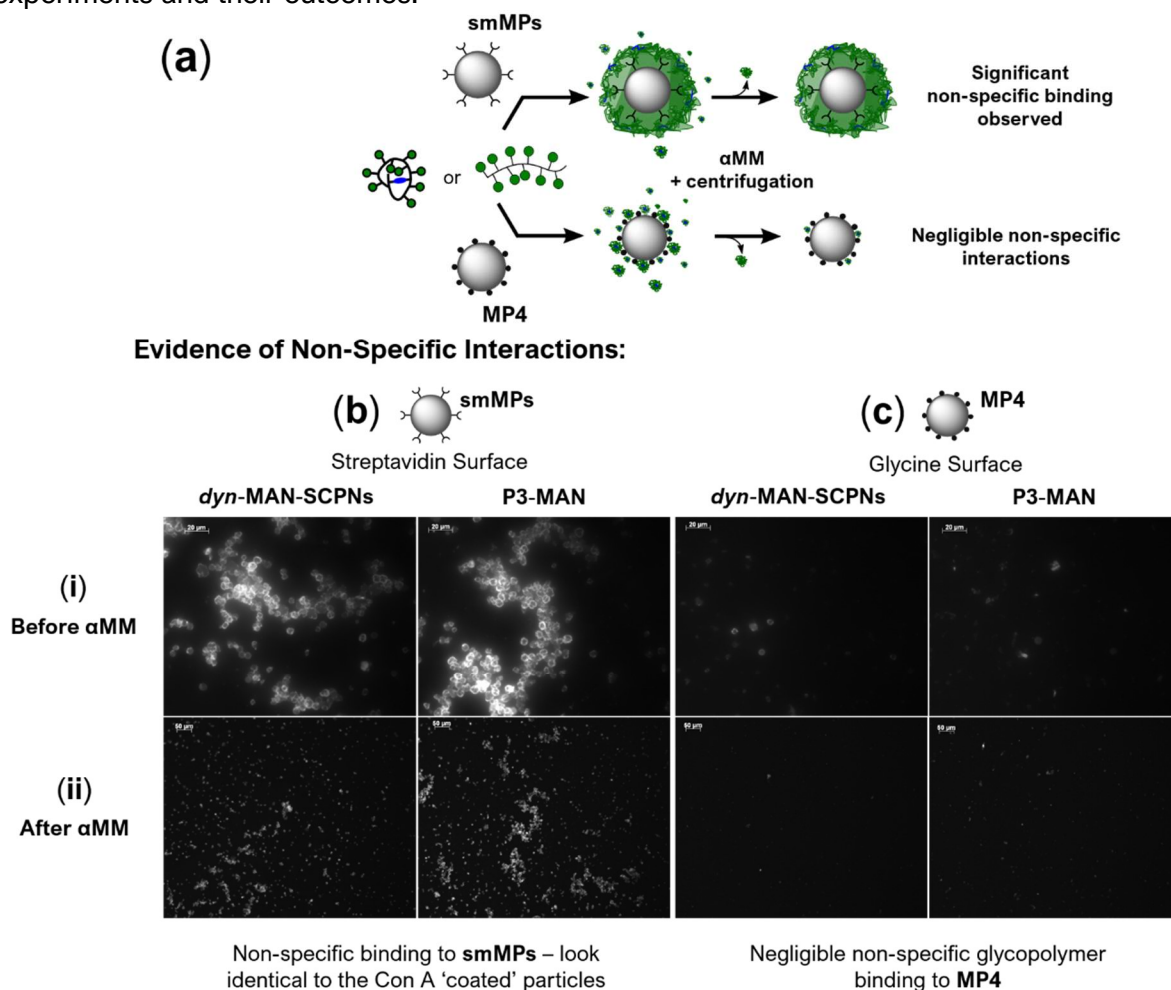


Figure 22: (a) Schematic overview of control experiments undertaken to investigate possible non-specific binding between the glycopolymers (**P3-MAN/dyn-MAN-SCPNs**) and **smMPs/MP4**, microparticles which are absent of Con A, thus lack the carbohydrate receptors required to drive concentration of polymer chains onto particle surfaces through specific molecular recognition events. (b-d) Fluorescence microscope images from control ‘wrapping’ experiments performed with streptavidin-modified microparticles (**smMPs**) (b) and glycine-capped silica microparticles (**MP4**) (c). Images were obtained before (i) and after (ii) incubation with **αMM**, which was anticipated to displace the glycopolymer coating. Experimental conditions: 1 mg/mL particles, PD = 100 µg/mg.

P3-MAN or **dyn-MAN-SCPNs** (Fig. 22a) were added to (i) streptavidin-modified polystyrene microparticles and (ii) glycine-capped silica microparticles (**MP4**), both of which are absent of Con A, and thus lack the carbohydrate receptors required to drive the concentration of glycopolymers onto the particle surfaces through specific molecular recognition events. After incubating **P3-MAN/dyn-MAN-SCPNs** with the particles for 24 h, ‘unbound’ polymer chains were removed by five consecutive centrifuge-wash-resuspend cycles, and then the particles were imaged under the microscope (see Fig. 22b-c, i). Bright coronas in these images revealed

that both **dyn-MAN-SCPNs** and **P3-MAN** remained bound non-specifically upon the streptavidin particles despite there being no Con A proteins present to recognise the glycopolymers. Glycine-capped silica particles (**MP4**)(Fig. 22c, i), however, showed little or no emission, which was indicative of negligible non-specific interactions. Further microscope images (Fig. 22b-c, ii) were obtained after treatment of these control experiments with **α MM**. After removal of ‘unbound’ glycopolymer by centrifugal washing, images revealed a very slight decrease in emission upon the streptavidin-modified particles (Fig. 22b, ii), however, significant non-specific binding was still observed. It was therefore concluded that acrylamide-based glycopolymers bind to **MP1** predominantly through ill-defined non-specific interactions.^{***} These observations were corroborated by, and entirely consistent with the earlier ELLA assay results (Fig. 17), which also showed that incubation of glycopolymer-coated **NP1** with **α MM** caused little or no removal of the polymer coating.

Further evidence of non-specific binding was observed by DLS studies (Fig. 23b) in which **P3-MAN** (Fig. 23a) was titrated into streptavidin-modified nanoparticles (**smNPs**). The DLS titration profile (Fig. 23b) which revealed a dramatic increase in particle size (D_h) and polydispersity index, consistent with the binding of **P3-MAN** onto the particle surface (Fig. 23c). Streptavidin particles which are partially ‘coated’ with glycopolymer feature low colloidal stability and thus exhibit a tendency to aggregate with one another (Fig. 23a). Continuation along this pathway diminishes the quality of DLS analysis, which is known to require a dispersion of colloiddally stable particles in order to return accurate particle size data. In combination, these unwanted processes of non-specific binding and particle-particle aggregation rationalize why ‘shrink-wrapping’ could not be accurately characterized by DLS analysis.

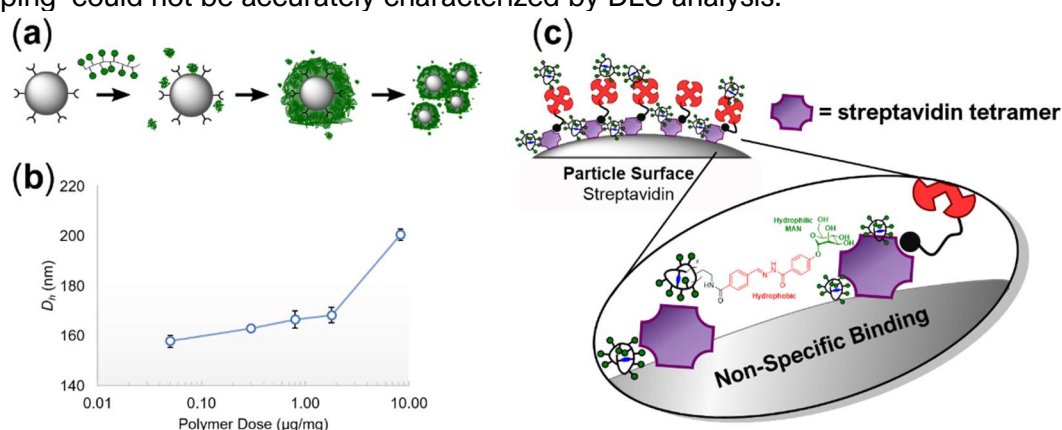


Figure 23: Non-specific binding was confirmed by a DLS titration experiment. (a) Control experiment in which **P3-MAN** was titrated into **smNPs** (streptavidin-modified nanoparticles, 100 nm) to afford DLS titration profile (b). (b) DLS titration profile for **smNPs/P3-MAN** revealed significant aggregation at polymer doses > 2 µg/mg. These observations further indicate that **P3-MAN** exhibits non-specific binding (c) to the underlying streptavidin particle core.

^{***} It has, however, been reported¹⁹ that streptavidin-biotin interactions can be inhibited by millimolar concentrations of mannose. An observation which suggests that pendant mannosyl groups displayed upon **P3-MAN** and **dyn-MAN-SCPNs** most likely interact with residues in the biotin binding pocket of streptavidin.

3.3.10. Factors Inhibiting the ‘Shrink-Wrapping’ of 3D Nano- and Micro-Objects

Two factors inhibited the ‘shrink-wrapping’ of 3D nano- and microscale objects: (i) Non-specific binding of glycopolymers to the underlying streptavidin particle surface and (ii) the hydrophobic nature of acrylamide-based glycopolymers.

(i) Non-Specific Binding:

Observations by DLS (Fig. 23b), ELLA assay (Fig. 17c) and fluorescence microscopy (Fig. 22b) were consistent with one another and provided strong evidence that **dyn-MAN-SCPNs** were concentrated onto **NP1/MP1** predominantly through ill-defined non-specific interactions between the mannose-functionalized polymer scaffolds and the underlying streptavidin-modified particles. These non-specific interactions prevented correct operation of the control experiment in which non-crosslinked glycopolymer ‘coatings’ should be displaced from the particle surface, and thus stifled progress of the ‘shrink-wrapping’ project. Furthermore, the scope of the chapter was to demonstrate that lectin-functionalized particles can be selectively ‘shrink-wrapped’ through specific molecular recognition between the glycopolymers and the particle surfaces, and thus the presence of non-specific polymer-particle interactions fundamentally undermines this objective and presented a significant barrier to investigating the ‘shrink-wrapping’ of 3D nano- and microscale objects.^{†††} To address the issues of non-specific binding, all future ‘wrapping’ experiments were conducted with microparticles (**MP2 - MP8**) prepared from a silica-based particle core, which displayed negligible non-specific binding to glycopolymers (Fig. 22c, ii).

(i) Hydrophobic Nature of Acrylamide-Based Glycopolymers

Results in this chapter revealed that acrylamide-based glycopolymers constituted a poor choice of polymer scaffold for ‘shrink-wrapping’ of 3D nano- and microscale objects in aqueous media. Acrylamide-based glycopolymers displayed low aqueous solubility on account of their hydrophobic nature (Fig. 11). Fluorescence images (Fig. 24a, i) show that acrylamide-based glycopolymers (**P3-MAN**) exhibit a strong tendency to aggregate in aqueous solution on account of their intrinsic hydrophobicity.^{†††} These aggregation processes (Fig. 24b, iv) are thought to present a kinetic barrier (Fig. 24b, iii) to the individual ‘shrink-wrapping’ of 3D nano- and microscale objects within a homogeneous layer of glycopolymer film. Acrylamide glycopolymer chains are relatively hydrophobic, and thus are hypothesized to contract in an aqueous environment in order to minimize their interactions with water. These processes of

^{†††} It should be noted that the issues of non-specific binding observed for the microparticle system **P3-MAN/MP1** (Fig. 21c/22b) will likely be amplified significantly for 3D nanoscale objects on account of their high surface areas.

^{††} Acrylamide-based glycopolymers (**P3-MAN** and the corresponding **dyn-MAN-SCPNs**) formed large multi-chain polymer aggregates, with diameters in well excess of 20 μm . The presence of these aggregate species in fluorescence microscope ‘shrink-wrapping’ experiments made it difficult to differentiate ‘wrapped’ Con A microparticles from polymer-only aggregates during analysis of the micrographs.

hydrophobic aggregation are anticipated to inhibit the binding of acrylamide-based glycopolymers onto the surface of Con A microparticles through specific Con A-mannose interactions. To address the inherent hydrophobicity of acrylamide glycopolymers and the related issues, a highly hydrophilic poly(ethylene glycol)-based polymer scaffold (**P6**) was prepared, from which the next-generation of polymer ‘wrapping agents’ were constructed (Fig. 25), and will now be discussed.

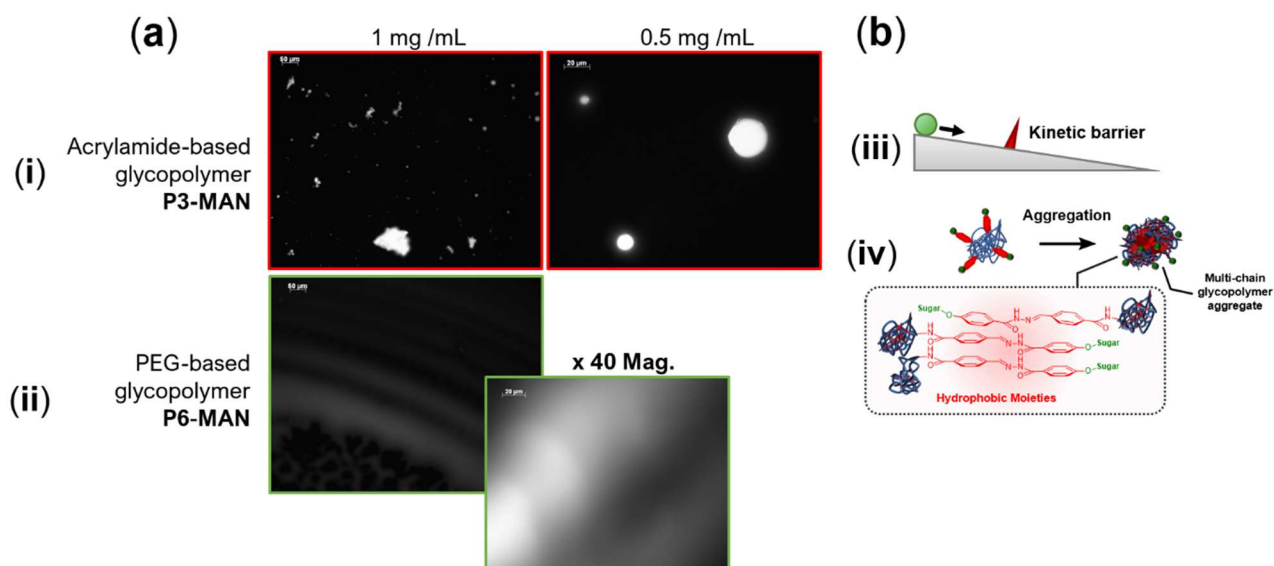


Figure 24: (a) Fluorescence microscope images of (i) acrylamide-based glycopolymer **P3-MAN** and (ii) PEG-based glycopolymer **P6-MAN** in aqueous solution. (b) It is hypothesized that acrylamide-based glycopolymers (i) aggregate in aqueous solution on account of their intrinsic hydrophobicity (iv). It is hypothesized that acrylamide glycopolymers aggregate to minimize contact with water on account of their relatively hydrophobic nature. These aggregation processes are anticipated to present a kinetic barrier to the individual ‘shrink-wrapping’ of 3D nano- and microscale objects within a homogeneous polymer film. In contrast, PEG-based glycopolymers (such as **P6-MAN**) (a, ii) are highly hydrophilic in nature, and thus constitute an idea scaffold for ‘coating’ aqueous dispersions of Con A-functionalized microparticles within a thin, but even distributed polymer layer.

3.3.11. Synthesis and Characterization of PEG-Based Glyco-SCPNS

PEG-based **dyn-MAN-SCPNS** were prepared (Fig. 25) using the previously described method of grafting mannose hydrazide (**MAN**)(a) onto aldehyde-functionalized copolymer (**P6**) followed by intramolecular crosslinking (b). For the remainder of this chapter, all references to “**dyn-MAN-SCPNS**” and “**fix-MAN-SCPNS**” relate to glycopolymers derived from **P6-MAN**.

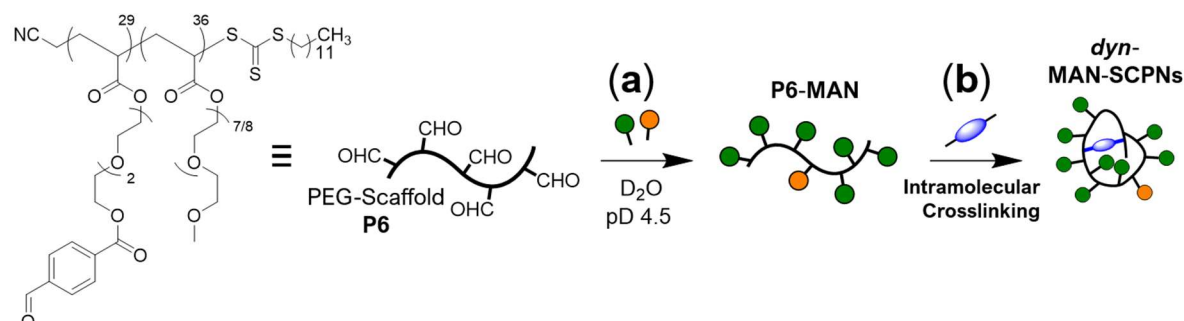


Figure 25: Preparation of **dyn-MAN-SCPNS** from PEG-based aldehyde scaffold **P6**. (a) **P6** was ‘decorated’ with mannose (**MAN**) and dansyl (**DAN**) hydrazide residues (pD 4.5), followed by intramolecular crosslinking (b) with succinic dihydrazide (**SD**) to afford **dyn-MAN-SCPNS**.

Preparation of Aldehyde-Functionalized PEG Copolymer Scaffolds

The preparation of PEG-based aldehyde scaffold polymer scaffold (**P6**) first required the synthesis of aldehyde-TEGA monomer (**M2**), which was synthesized (Fig. 26a) by the activation of **5** with thionyl chloride to afford acid chloride **6**. Esterification of **6** with a large excess of triethylene glycol (TEG) afforded predominantly the mono ester **7**, the terminal hydroxyl of which was then acetylated by dropwise addition of acryloyl chloride, thus affording the acrylate ester **M2**. Purification by column chromatography isolated **M2** as a colourless oil (2.59 g, 33 % yield overall), which was diluted in CH_2Cl_2 and stored at $-20\text{ }^{\circ}C$ to prevent autopolymerisation.

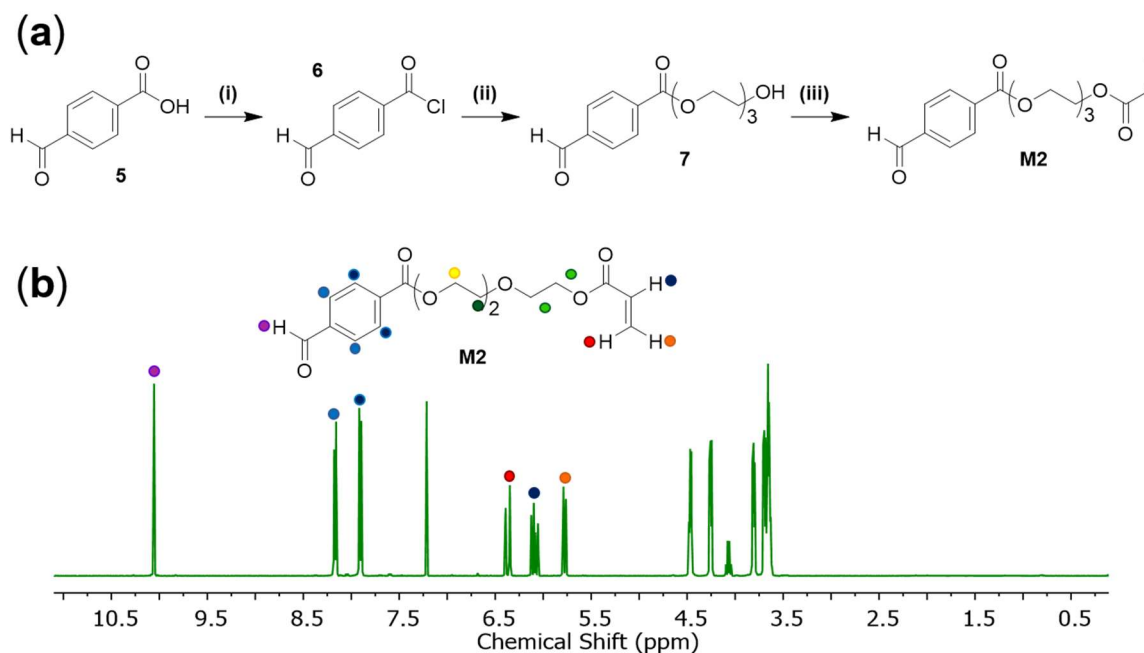


Figure 26: (a) Synthesis of aldehyde-TEGA monomer, **M2**. Step (i) 5 eqv. $SOCl_2$, 18 h reflux in toluene. Step (ii) Intermediate **6** was added dropwise into triethylene glycol, Et_3N , CH_2Cl_2 , 8 h at $0\text{ }^{\circ}C$. Step (iii) acryloyl chloride, Et_3N , CH_2Cl_2 , 18 h at $0\text{ }^{\circ}C$. (b) Assigned 1H NMR ($CDCl_3$, 300 MHz) spectrum of **M2**.

PEG-based aldehyde scaffolds (**P6-P7**), which differ in their molecular weights on account of different reaction times T_r (Fig. 27b), were prepared by RAFT polymerization of aldehyde monomer **M2** with the commercially available and highly hydrophilic comonomer **OEGA₅₀₀** (Fig. 27a). GPC analysis revealed monomodal polymer distributions of low polydispersity, consistent with controlled polymerization processes. PEG scaffolds **P6 – P7** were characterized by ^1H NMR spectroscopy (Fig. 27b, 28) to determine (i) polymer composition (**m/n**) (ii) the number-average molecular weight (M_n) by end group analysis. The kinetics of RAFT polymerization (Fig. 27c) were determined for **P6** using ^1H NMR spectroscopy to monitor the % conversion as a function of time, which revealed the polymerization was controlled and completed (> 80 % monomer conversion) within 2.5 h. Additionally, GPC analysis revealed a subtle increase in PDI throughout the polymerization process. DLS analysis of **P6** revealed a monomodal size distribution (Fig. 27d) with average hydrodynamic diameter, $D_h \approx 5.8 \pm 0.2$ nm, indicating excellent aqueous solubility and negligible aggregation of polymer chains.

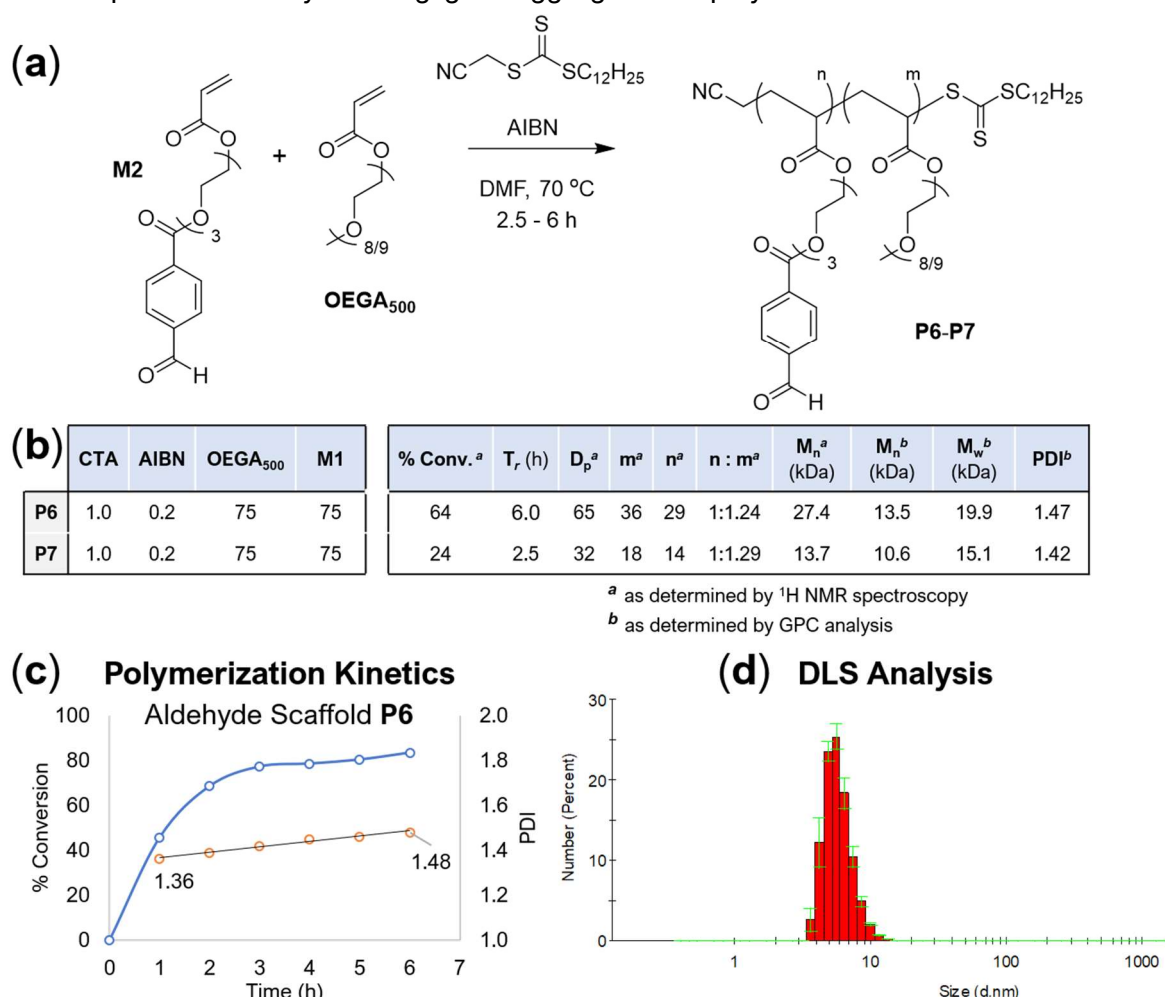


Figure 27: (a) Preparation of highly hydrophilic water-soluble aldehyde copolymer scaffolds (**P5-P6**) by RAFT polymerization of aldehyde monomer **M2** with **OEGMA₅₀₀**. (b) Table of characterization for scaffolds **P5-P6**: stoichiometries of CTA, AIBN and monomer feed ratios. Characterization: % monomer conversion (% Conv.), reaction time (T_r) degree of conversion (D_p), polymer composition (**m**, **n**), molecular weights (M_n , M_w) and polydispersity index (**PDI**). (c) Polymerization kinetics of **P6**, showing % conversion and PDI as a function of time. (d) DLS analysis of **P6** in water revealed a monomodal particle size distribution. Where superscripts ^a and ^b denote parameters determined by ^1H NMR spectroscopy or GPC, respectively.

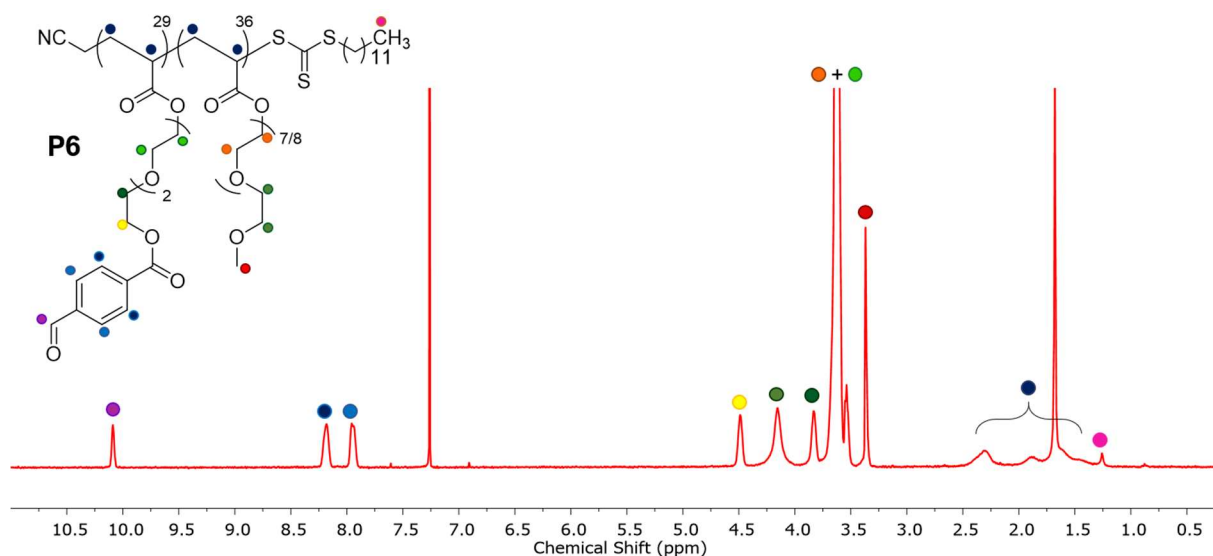


Figure 28: ^1H NMR (CDCl_3 , 300 MHz) spectrum of PEG scaffold **P6** with structural assignments shown.

Preparation of Mannose-Grafted Polymer Scaffolds

The ‘decoration’ **P6** with **MAN** was monitored by ^1H NMR spectroscopy (Fig. 29a-c), which revealed complete disappearance of the ‘diagnostic’ aldehyde (●) signal at δ 9.98 ppm (Fig. 29b) and peak broadening of the signals (●, ●, ●) associated with **MAN** (Fig. 28a), thus confirming successful synthesis of **P6-MAN**. **P6-MAN** was purified by dialysis against water and characterized by ^1H NMR spectroscopy (Fig. 29d), which indicated unconjugated **MAN** had been successfully removed.

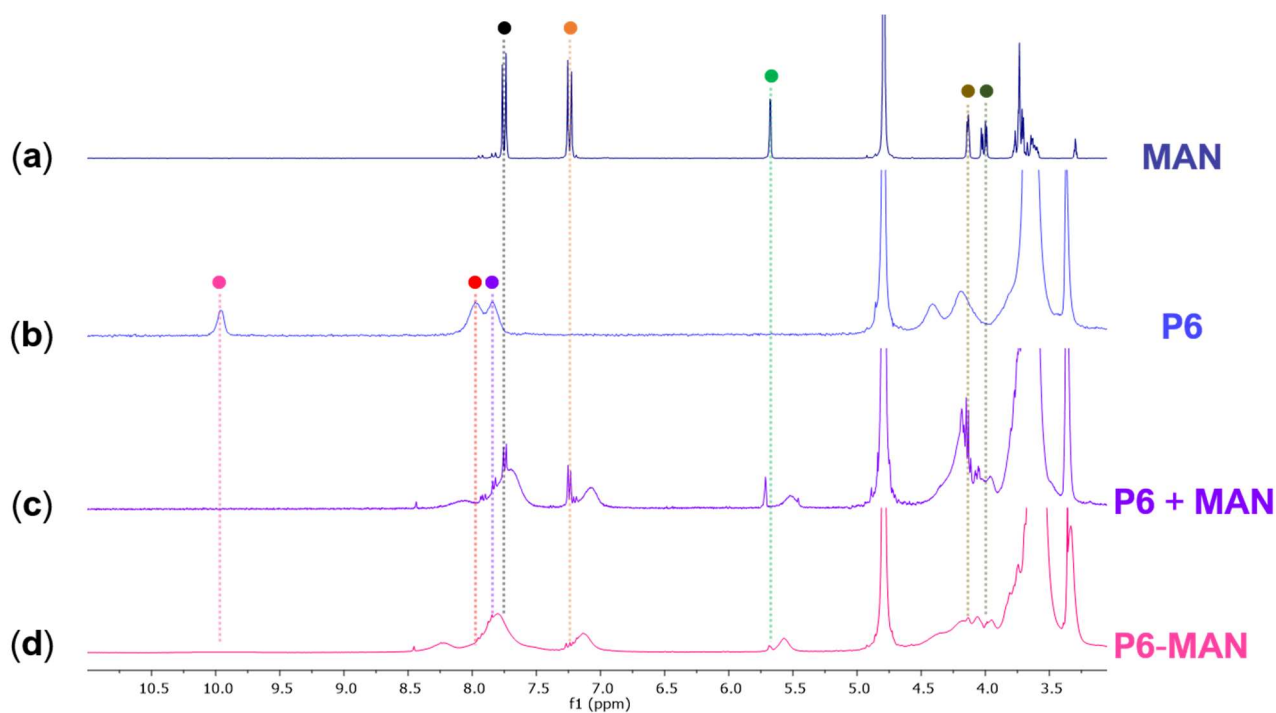


Figure. 29: Partial ^1H NMR (D_2O , 300 MHz) spectra of (a) mannose hydrazide, **MAN**, (b) aldehyde scaffold **P6**, (c) **P6 + MAN** after 10 min and (d) **P6-MAN** after purification by dialysis.

Synthesis and Characterization of MAN-SCPNs

dyn-MAN-SCPNs were prepared (Fig. 30a) by intramolecular crosslinking of **P6-MAN** with succinic dihydrazide at pH 4.5. SCPNs containing two crosslinker stoichiometries were explored: (i) **dyn-MAN-SCPN-1** which contains one intra-chain crosslink and (ii) **dyn-MAN-SCPN-2** which contains two intra-chain crosslinkers. These **dyn-MAN-SCPNs** (1) contain dynamic covalent hydrazone crosslinks (iii) which were reduced to the corresponding amine (v) to afford **fix-MAN-SCPNs** (2) by addition of cyanoborohydride (iv). SCPN formation was then characterized by GPC analysis (Fig. 30b) of **fix-MAN-SCPN-1** and **fix-MAN-SCPN-2**, which revealed the characteristic increase in retention time as the density of intramolecular crosslinker was raised.

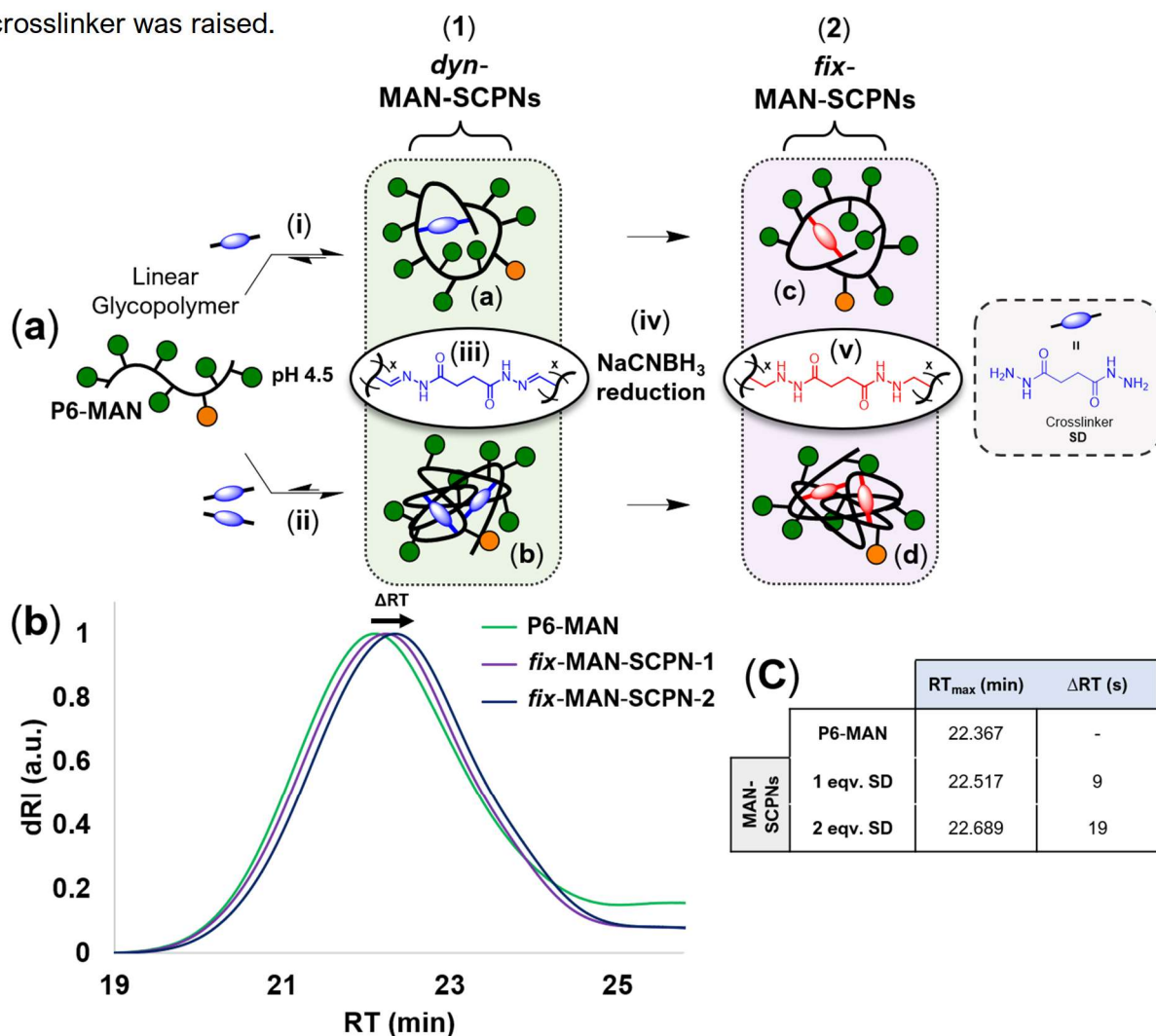


Figure 30: Synthesis (a) and GPC characterization (b) of **fix-MAN-SCPNs** prepared from **P6-MAN**. (a) Addition of 1-2 equivalents of succinic dihydrazide (i-ii) induced intra-chain crosslinking of linear polymer **P6-MAN** to yield **dyn-MAN-SCPNs** (1), which contain dynamic covalent acyl hydrazone crosslinks (iii). Chemical reduction (iv) of **dyn-MAN-SCPNs** afforded **fix-MAN-SCPNs** (2), whose crosslinks were no longer dynamic on account of their reduction from acyl hydrazone (a dynamic bond) (ii) to the corresponding amine (non-dynamic / fixed) (v). (b) Normalized GPC traces revealed a small increase in retention time (RT) for **fix-MAN-SCPN-1** (purple) and **fix-MAN-SCPN-2** (blue) relative to that of the linear glycopolymer (**P6-MAN**) (green), consistent with chain collapse. (c) Retention times at peak maxima (RT_{max}) and shift in retention time (ΔRT) relative to the linear chain (**P6-MAN**).

SCPN formation was further characterized by DLS analysis (Fig. 31a-b), which revealed a subtle decrease in the hydrodynamic diameter (D_h) of **dyn-MAN-SCPN-1** relative to that of the linear (non-crosslinked) glycopolymer **P6-MAN** (Fig. 31b). This observation was entirely consistent with SCPN formation by intramolecular crosslinking of **P6-MAN**.^{§§§} DLS experiments (Fig. 31c) demonstrated the kinetic stability of **dyn-MAN-SCPN-1** towards the formation of intermolecularly crosslinked aggregates upon the concentration of polymer chains in aqueous solution (50 mM H₄NAcO-AcOH, pH 4.5). **dyn-MAN-SCPN-1** were stable towards aggregation below 10 mg/mL.^{****} It should also be noted that, in contrast to the hydrophilic acrylamide glycopolymers, DLS analysis obtained for PEG glycopolymers always showed monomodal size distributions and no signs of aggregation were observed at polymer concentrations < 10 mg/mL. These observations suggest that PEG-based scaffolds present an ideal scaffold for the ‘shrink-wrapping’ of 3D nanoscale objects in aqueous media on account of their highly hydrophilic nature, which gives rise to excellent water-solubility even at high densities of aldehyde-containing unit **M2**. These scaffolds are thus unlikely to exhibit non-specific binding to nanoparticle surfaces, and furthermore may permit parameters such as the carbohydrate and crosslinker densities to be adjusted, without impacting on aqueous solubility.

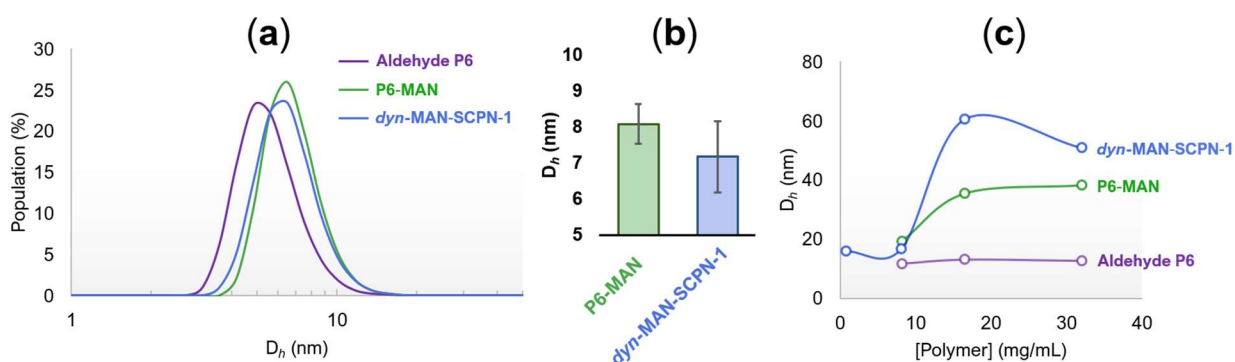


Figure 31: DLS analysis of PEG polymers: (i) Aldehyde Scaffold **P6**, (ii) **P6-MAN** and (iii) **dyn-MAN-SCPN-1**. (a) Particle size distributions (z-average D_h) for polymers (i) - (iii). (b) Number-average D_h shows collapse in hydrodynamic diameter of **dyn-MAN-SCPN-1** relative to the linear glycopolymer **P6-MAN**, consistent with SCPN formation by intramolecular crosslinking. (c) DLS (z-average D_h) revealed the stability of glycopolymers (i) - (iii) upon their concentration in aqueous solution.

^{§§§} It was also observed that mannose-decorated glycopolymer **P6-MAN** possessed a slightly larger hydrodynamic diameter than did the parent aldehyde polymer scaffold **P6**, which is consistent with **MAN** decoration of **P6**.

^{****} Intriguingly, **P6-MAN** was also observed to aggregate at concentrations > 10 mg/mL, whilst the parent aldehyde scaffold **P6** remained a stable size of $D_h \approx 12$ nm. It is hypothesized that **P6-MAN** aggregates more than **P6** in aqueous solution, on account of hydrogen bonding which may arise between **MAN** residues displayed upon neighbouring polymer chains

3.3.12. Fluorescence Microscopy ‘Shrink-Wrapping’ Studies with PEG-Based Glycopolymers and Lectin-Functionalized Silica Microparticles

Proof of Successfully ‘Shrink-Wrapping’ Microscale Objects

Convincing evidence of successful ‘shrink-wrapping’ was observed by fluorescence microscopy experiments which utilized a palette of four different glycopolymers architectures (Fig. 32a, i-iv). In these experiments, 5 μm Con A microparticles (**MP2**) (1 mg/mL) were incubated with dansyl-labelled glycopolymers (i-iv) (2.5 mg/mL) for 18 h. The particles were then purified by centrifugation and washing to remove any glycopolymers chains which were not adhered onto the particle surfaces. Three 5 μL aliquots of each sample were then deposited onto a clean glass slide, dried and then carefully imaged on the fluorescence microscope.

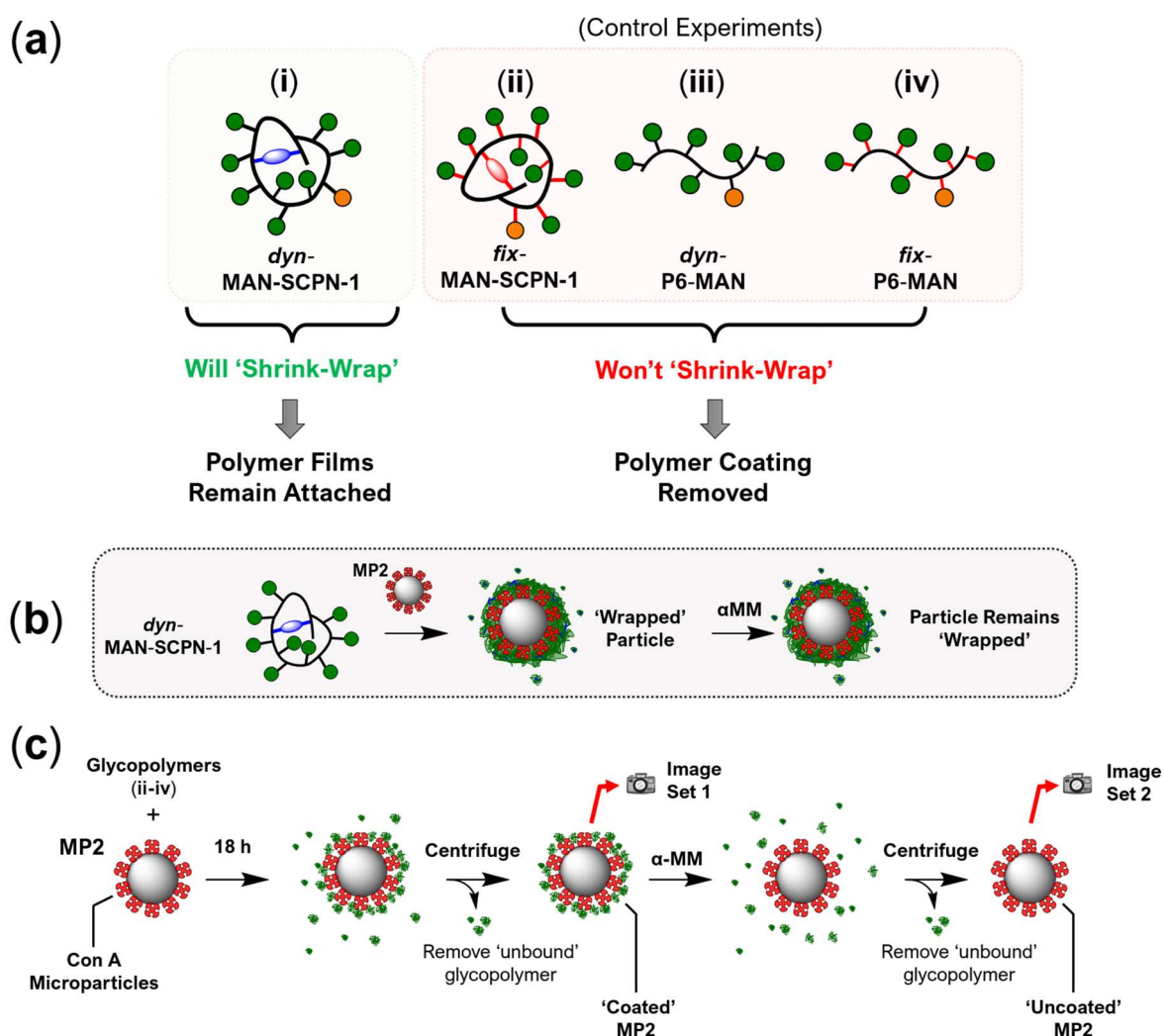


Figure 32: (a) The four types of glycopolymers architecture (i-iv) which were employed for ‘shrink-wrapping’ studies. **dyn-MAN-SCPN-1** (i) were anticipated to ‘shrink-wrap’ microparticle surfaces and thus resist displacement by incubation with αMM . Linear glycopolymers (iii-iv) and **fix-MAN-SCPN-1** (ii) were anticipated to only ‘coat’ the microparticles within non-crosslinked layers, and thus should be readily displaced by incubation with αMM . (b) **dyn-MAN-SCPN-1** is hypothesized to form a crosslinked glycopolymers film upon **MP2** which cannot be displaced by αMM incubation. (b) Schematic overview of the ‘shrink-wrapping’ experiment protocol, which is shown with control glycopolymers (ii-iv). Incubation of **MP2** with glycopolymers (ii - iv) affords ‘coated’ particles, which should be displaced by αMM .

It is anticipated that the structurally dynamic polymer ***dyn*-MAN-SCPN-1** (i) will 'shrink-wrap' the surface of complementary Con A microparticles (**MP2**) within intermolecularly crosslinked polymer films, and thus should resist displacement by incubation with α -methyl mannose (Fig. 32b). However, control experiments (Fig. 32c) undertaken with linear glycopolymers (**iii-iv**) and ***fix*-MAN-SCPN-1** (ii) are anticipated to only 'coat' the microparticles within non-crosslinked layers, thus should be readily displaced by incubation with α MM. With these predictions in mind, we now turn our attention to the inspection of the fluorescence microscope images shown in Figure 33.

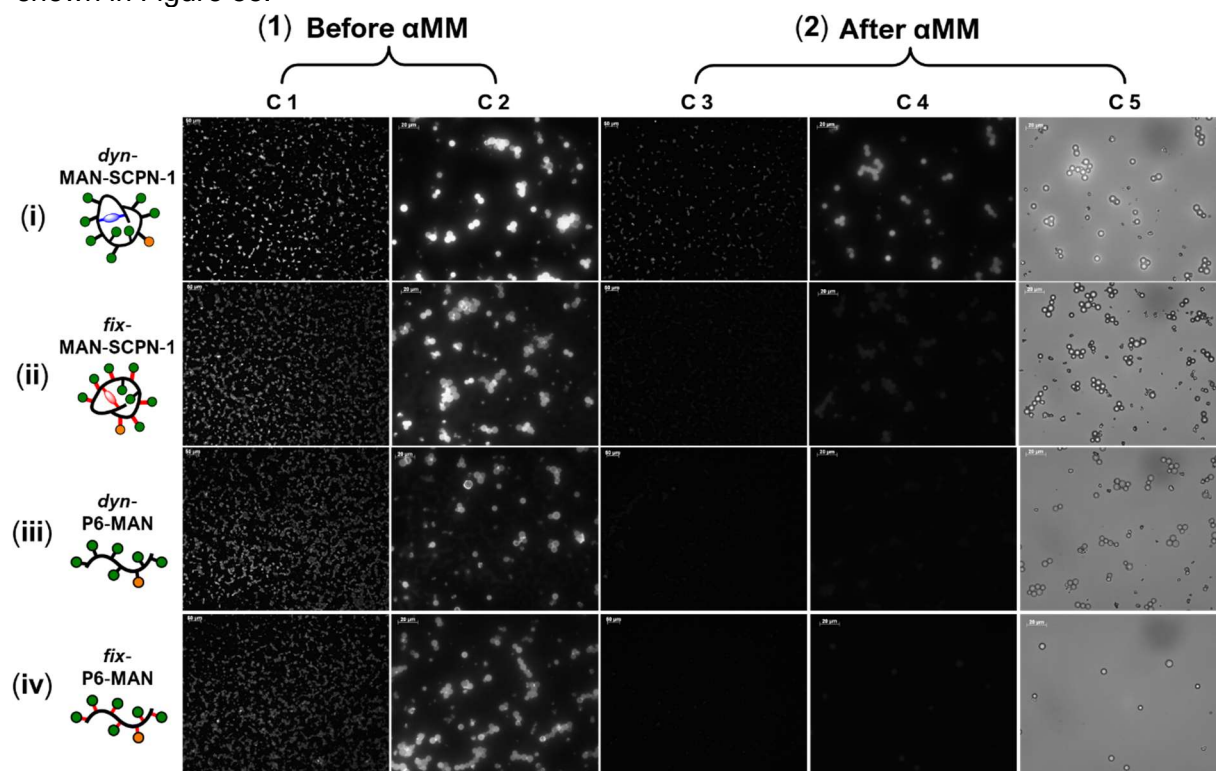


Figure 33: Representative fluorescence microscope images of 'wrapped' (i) and 'coated' (ii-iv) 5 μ m Con A microparticles (**MP2**) before (1) and after (2) incubation with α MM, which facilitated the removal of non-crosslinked glycopolymer 'coatings' (ii-iv) but not crosslinked glycopolymer 'wrappings' (i). Care was taken to obtain images of the exact same particles under both normal light (**C 5**) and UV irradiation (**C 4**), in order to successfully demonstrate the presence of non-emissive particles.

Fluorescence microscope images (Fig. 33) displayed in **C 1** (10 x mag) and **C 2** (40 x mag) were obtained 18 h after mixing glycopolymers (i - iv) with **MP2** and show that the polymers were bound onto the periphery of Con A microparticles as evidenced by their bright coronas, which were localized to the particles surface.⁺⁺⁺ It should be noted that at this stage in the experiment, all particles will have glycopolymer bound onto their surface, and thus all particles were observed to be emissive. After α MM incubation (**C 3 - C 5**), however, only the ***dyn*-MAN-SCPN-1** (i) 'wrapped' particles remained emissive, indicating successful 'shrink-wrapping' of

⁺⁺⁺ Great care was taken to maintain identical imaging conditions when obtaining fluorescence microscope images, in order to ensure that image brightness correlates with the concentration of dansyl-labelled glycopolymers observed within each image.

the particle surface within an intermolecularly crosslinked glycopolymer film. The observation that non-crosslinked glycopolymers (iii-iv) and non-dynamic SCPNs (ii) were displaced from the particle surface indicates that: (i) the presence of a covalent crosslinker brings additional stability beyond that of non-crosslinked films, and (ii) 'shrink-wrapping' can only occur when crosslinks within the SCPN architecture are dynamic covalent in their nature. Figure 34 shows representative fluorescence images which clearly highlight that the glycopolymer 'wrapping' (Fig. 34, i) cannot be fully displaced from **MP2**, whereas glycopolymer 'coatings' (Fig. 34, iii) are readily removed. Further processing of the fluorescence microscope images (shown in Figure 33) allowed for the MGTV values (Fig. 35a-b) to be determined, thus allowing for more accurate comparison of particle brightness to be deduced (see experimental, page 142).

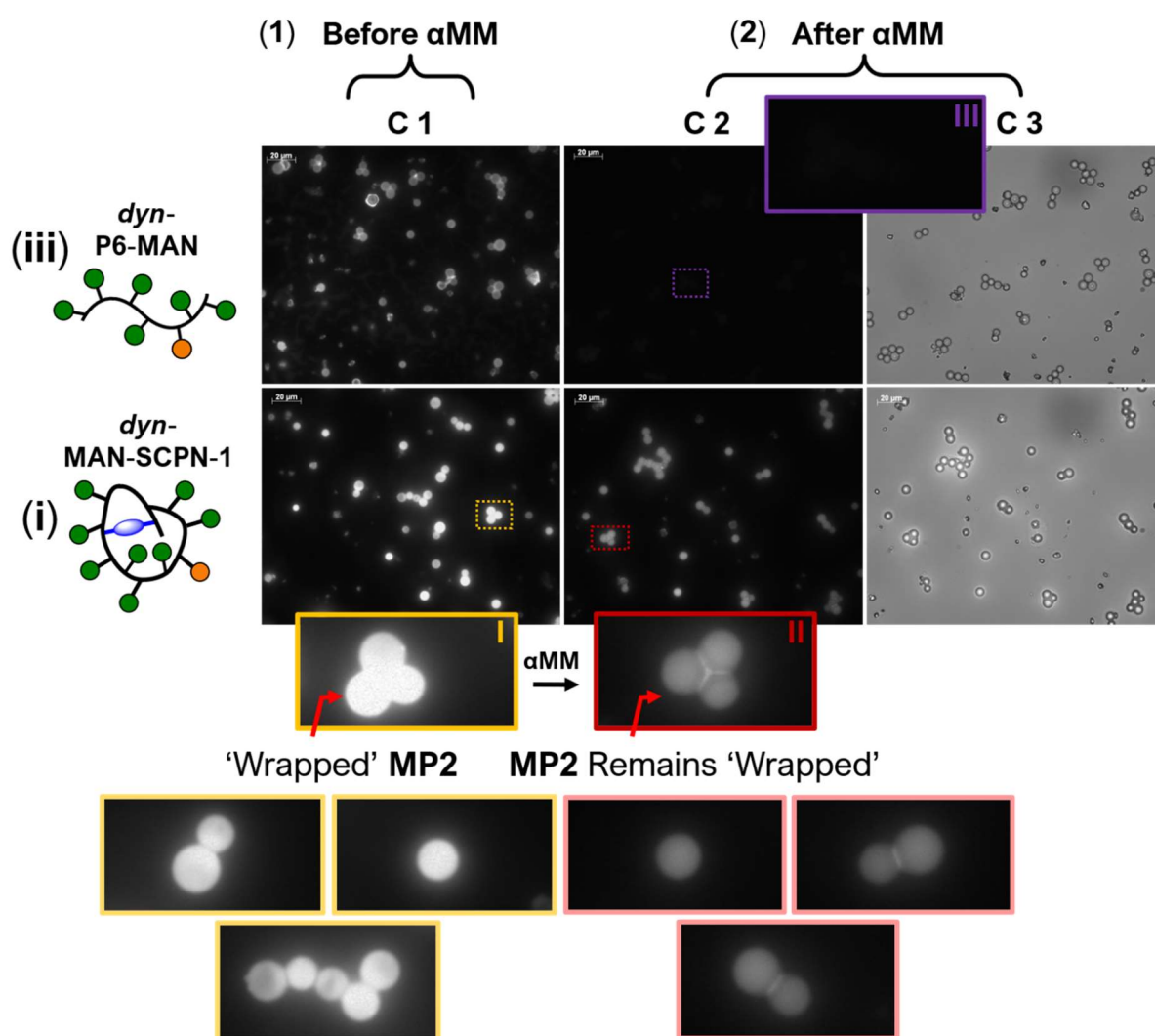


Figure 34: Representative fluorescence (C 1, C 2) and brightfield (C 3) microscope images of 'wrapped' (*dyn*-MAN-SCPN-1) (i) and 'coated' (*dyn*-P6-MAN) (iii) particles before (1) and after (2) incubation with α MM. Insets I-III: Further magnified images produced for regions of interest (see highlighted areas) within selected micrographs.

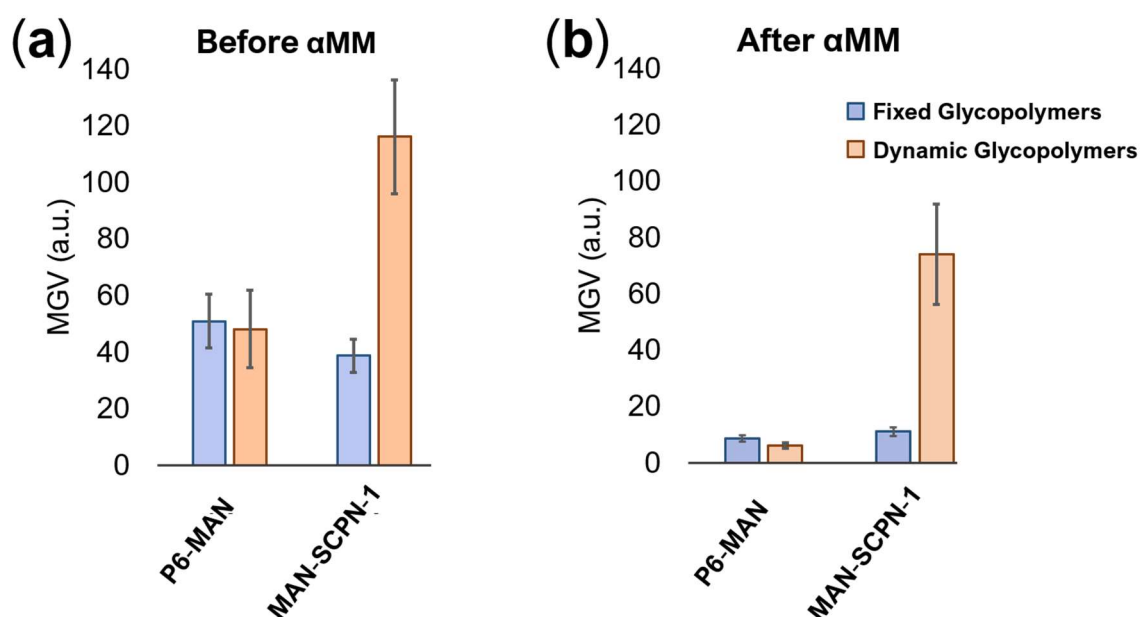


Figure 35: Analysis of fluorescence microscope images (shown in Fig. 33) yielded the average particle brightness (MGV) of the polymer-covered particles before (a) and after (b) incubation with α MM. The bars report the average MGV obtained for analyzes performed on > 100 particles. Error bars report standard deviation for these measurements.

Before their treatment with excess α MM (Fig. 35a), all glycopolymer (ii-iv) ‘coated’ particles are of comparable brightness and thus feature similar MGVs of $\approx 50 \pm 13$, with the exception of **dyn-MAN-SCPN-1**, which was significantly brighter (MGV = 120 ± 15). This observation was rationalized by the formation of inter-chain crosslinks that facilitate the formation of thicker glycopolymer films upon the particle surface. Following incubation with α MM, MGV values (Fig. 35b) for control glycopolymers (**dyn-P6-MAN**, **fix-P6-MAN**, **fix-MAN-SCPN-1**) were all observed to decrease significantly (MGV: $\approx 50 \rightarrow \approx 10$), whereas the MGV of **dyn-MAN-SCPN-1** remained relatively high (MGV: $\approx 120 \rightarrow \approx 70$). These observations show that control glycopolymers (ii-iv) were all successfully displaced from the surface of **MP2** by incubation with α MM, whereas **dyn-MAN-SCPN-1** could not be readily displaced, which is entirely consistent with the proposed hypothesis. It was thus concluded that **dyn-MAN-SCPN-1** yielded intermolecularly crosslinked glycopolymer films, and thus resisted displacement from the Con A particle surface, whereas all control glycopolymers (ii-iv) afforded non-crosslinked polymer layers which were significantly less robust. Furthermore, the observation that **fix-MAN-SCPN-1** coatings – whose crosslinks were non-dynamic on account of chemical reduction – were fully displaced (low MGV $\approx 10 \pm 5$) after α MM, whereas the **dyn-MAN-SCPN-1** films remained attached suggests that the dynamic covalent nature of the embedded crosslinker residues plays a crucial role which is essential to the observed ‘shrink-wrapping’ phenomenon. With definitive evidence of ‘shrink-wrapping’ now in hand, further experiments were undertaken to prove that **dyn-MAN-SCPNs** were concentrated onto the surface of **MP2** through specific molecular recognition events.

Evidence that Specific Carbohydrate-Receptor Interactions Drive ‘Shrink-Wrapping’

A control experiment (Fig. 36a) was undertaken in which glycopolymers (**i-vi**) were incubated with **MP5**, a 5 μm particle whose surface displays LTB, a galactose-specific lectin. On account of **MP5** displaying recognition only for galactose-functionalized polymers, it was anticipated that **dyn-MAN-SCPNs** would not ‘shrink-wrap’ **MP5**, and thus emission would not be observed. Fluorescence microscope images (Fig. 36b) revealed that (before centrifugation) glycopolymers (**i-iii**) did not significantly bind onto **MP5**, as evidenced by the observation that emission was not localized to the particle surface. After centrifugation (Fig. 36b), images revealed no emission, indicating that all glycopolymers (**i-iii**) (including **dyn-MAN-SCPN-1**) had been removed. It was thus concluded that **dyn-MAN-SCPN-1** must ‘shrink-wrap’ Con A microparticle (**MP2**) through specific molecular recognition events. In the absence of the complementary carbohydrate-binding protein upon the particle surface, however, no ‘shrink-wrapping’ was observed.

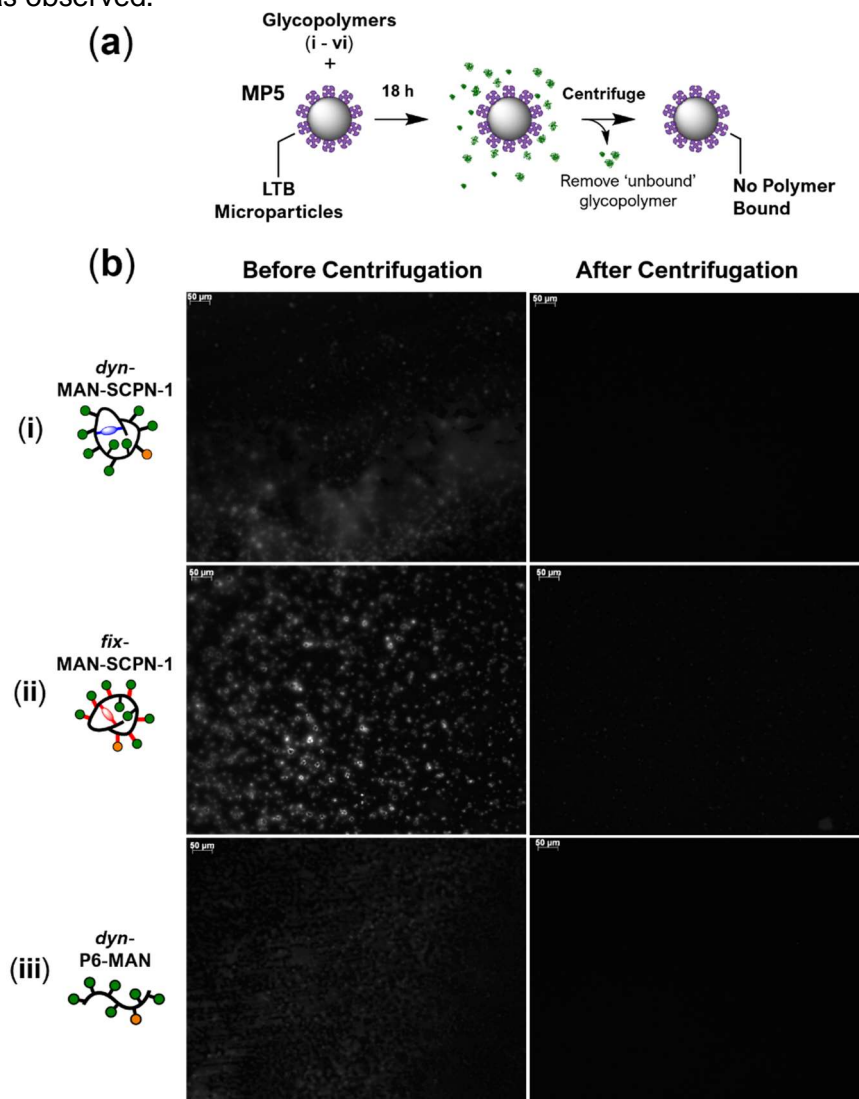


Figure 36: (a) Control experiment in which LTB-functionalized microparticles (**MP5**) were ‘wrapped’ or ‘coated’ with glycopolymers (**i-iii**). (b) Fluorescence microscope images were obtained before and after centrifugation to remove ‘unbound’ glycopolymer chains. No emission was observed upon **MP5** after centrifugation, and thus it was concluded that all glycopolymers (**i-iii**) had been successfully removed.

Further control experiments were performed with glycine-capped particles (**MP4**, Table 1) – a 5 μm microparticle whose surface is absent of any carbohydrate-binding receptors. This experiment also revealed that glycopolymers (**i-vi**) exhibited negligible non-specific binding onto the glycine particle (**MP4**) surface (see, Fig. 37b), as evidenced by low MGVs after centrifugation and washing to remove ‘unbound’ glycopolymer chains. Figure 37 provides a summary of MGVs obtained for all ‘shrink-wrapping’ and control experiments. MGVs reported in Fig. 37 are the average MGV ‘wrapped’/‘coated’ particles after steps to remove the surface-bound glycopolymers.

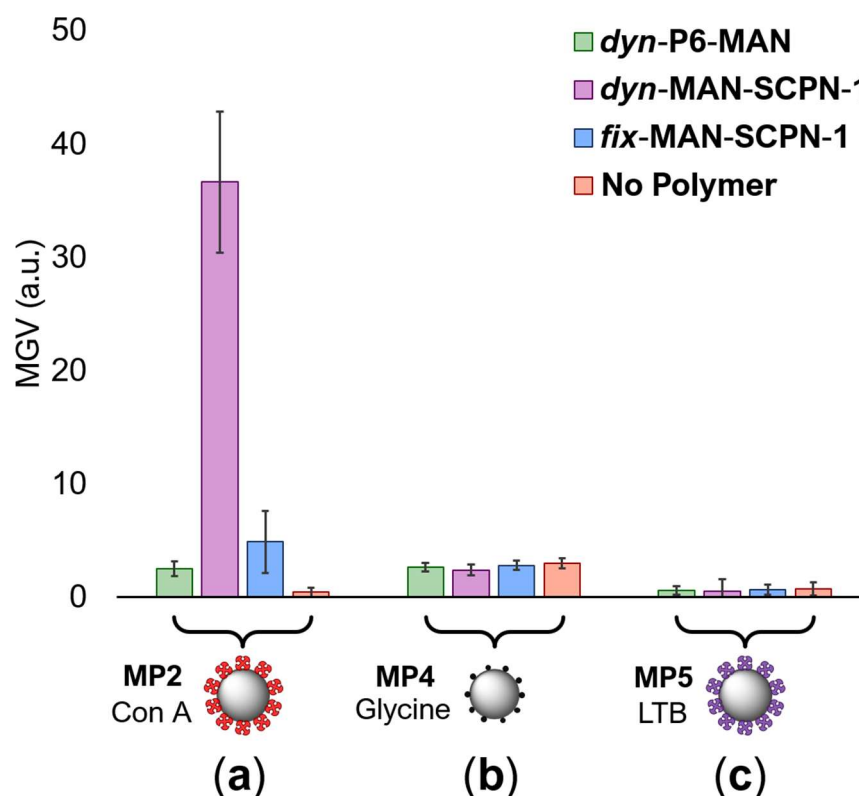


Figure 37: MGVs obtained from ‘wrapping’ and control experiments with 5 μm silica particles displaying (a) Con A (**MP2**), (b) glycine only (**MP4**) and (c) LTB (**MP5**). These MGVs were calculated from images obtained after steps to displace the glycopolymer ‘wrappings’/‘coatings’ from the particle surfaces. The bars report average MGVs measured for > 100 individual particles and error bars represent the standard deviation. A no polymer control experiment was included (**orange bars**), which reveal the brightness of the ‘naked’ particles, in the absence of any glycopolymer.

With strong evidence of ‘shrink-wrapping’ now in hand, future work will investigate the on-demand ‘unwrapping’ of Con A microparticles – a spontaneous process which can be triggered by exposure of the surface-bound glycopolymer films to a solution of hydroxylamine. This highly nucleophilic amine is anticipated to react with acyl hydrazone crosslinks located within the glycopolymer film through component exchange, and thus fully displace all acyl hydrazone linkages in favour of forming the more thermodynamically stable oxime bond. It was hypothesized that this process will ‘etch’ crosslinked polymer films from the Con A microparticle surface, thus providing scope to engineer the on-demand ‘unwrapping’ and ‘release’ of the underlying particle substrate.

3.4. Conclusion

Specific carbohydrate-receptor interactions were exploited to trigger the ‘structural metamorphosis’ of discrete polymer chains into intermolecularly crosslinked polymer films located upon the surface of 3D nano- and microscale objects. Fluorescence microscopy experiments highlighted that the dynamic covalent nature of crosslinks contained within the glyco-SCPNs were of instrumental importance to the ‘shrink-wrapping’ process. Glycopolymers which lack covalent crosslinkers (**P6-MAN**) or possess non-dynamic crosslinks (**fix-MAN-SCPN-1**) did not facilitate ‘wrapping’ of microparticle surfaces. These observations were entirely consistent with the proposed hypothesis that hydrazone exchange is crucial to the ‘shrink-wrapping’ process. Furthermore, key control experiments demonstrated that successful ‘wrapping’ of lectin-functionalized silica microparticles occurs only when carbohydrate appendages displayed upon the glyco-SCPNs are complementary to the receptors located at the particle surface. These observations confirmed that specific molecular recognition events between carbohydrate-receptor pairs are responsible for concentrating glyco-SCPNs onto particle surfaces, and thus must drive ‘shrink-wrapping’ of lectin-displaying micro-objects. These findings constitute the very first step towards the end goal of ‘wrapping’ complex biological objects, such as lectin-displaying bacteria. It is anticipated that further development of this chemistry may present dynamic covalent glyco-SCPN architectures which can selectively recognise, bind, and thus ‘neutralize’ harmful pathogens within crosslinked polymer films. Finally, it should be acknowledged that the successful ‘shrink-wrapping’ of microscale objects was largely owed to the development of a highly hydrophilic PEG-based polymer scaffold (**P6**), which features excellent aqueous solubility and displays negligible levels of non-specific binding to particle surfaces. Now that the appropriate polymer building blocks have been discovered, ‘shrink-wrapping’ can finally progress towards the encapsulation of 3D nanoscale objects of increased complexity. With this ambitious goal in mind, Chapter 4 now explores the synthesis of polymer ‘wrapping agents’ with the capacity to selectively recognise carbohydrate receptors displayed upon the surface of **SV40** virus-like particles.

3.5. Experimental

3.5.1. General Experimental

All chemicals were purchased from Sigma-Aldrich, Fisher Scientific or Alfa Aesar and were used as received without further purification. All nano- and microparticles were purchased from Micromod Partikeltechnologie GmbH (NHS-functionalized silica particles) and Sigma Aldrich (**smNPs**, **smMPs**). All solvents were dried prior to use according to standard methods. *N,N*-dimethylacrylamide was purified by vacuum distillation at 60 °C. All solvents used for flash chromatography were GPR grade, except hexane and ethyl acetate, when HPLC grade was used. Unless state otherwise, all synthetic procedures were performed in oven-dried glassware under a N₂(g) atmosphere.

4.5.2. Instrumentation

¹H and ¹³C NMR spectra of synthesised compounds were recorded on a Bruker Avance 300 spectrometer (300 and 75 MHz respectively), Bruker Avance 400 spectrometer (400 MHz and 100 MHz, respectively), Bruker Avance III HD spectrometer (at 500 MHz and 125 MHz, respectively), or Bruker 700 Avance III HD spectrometer (700 MHz and 175 MHz, respectively). In all cases, the residual solvent signal was used as an internal standard. High-resolution mass spectrometry was performed on a Waters LCT Premier mass spectrometer^a. Gel permeation chromatography (GPC) was conducted on a on a Varian ProStar instrument (Varian Inc.) equipped with a Varian 325 UV-Vis dual wavelength detector with a 254 nm laser, a Dawn Heleos II multi-angle laser light scattering detector (Wyatt Technology Corp.), a Viscotek 3580 differential refractive index detector and two PL gel 5 µm Mixed D 300 × 7.5 mm columns with guard column (Polymer Laboratories Inc.) in series. Chromatogram analysis was performed on Galaxie software (Varian Inc.) and analyzed with the Cirrus software (Varian Inc.) and Astra software (Wyatt Technology Corp.). Near monodisperse poly(methyl methacrylate) standards (Agilent Technologies) were used for calibration. DLS and zeta potential measurements were performed on a Malvern Instruments Nano ZS. Fluorescence microscopy images were obtained were obtained using Zeiss Axioskop 2 Plus. pH measurements were made using a Hanna HI 90103 instrument which was calibrated before use using commercial buffer solutions (Sigma-Aldrich).

3.5.3. Nomenclature for Gluco-Configured Monosaccharides

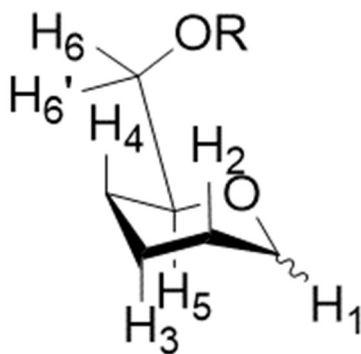
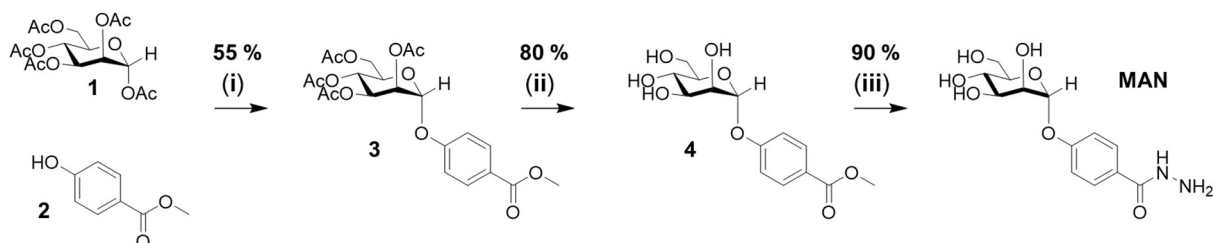


Figure 38: Proton numbering in ^1H NMR data for gluco-configured monosaccharides.

3.5.4. Synthesis of Mannose Hydrazone (MAN)



Scheme 1: Synthesis of mannose hydrazone residue (**MAN**). Step (i) $\text{BF}_3\text{Et}_2\text{O}$, dichloroethane, 50°C , 18 h. Step (ii) NaOMe , anhydrous MeOH . Step (iii) H_2NNH_2 , MeOH , reflux, 18 h.

4-Methoxycarbonylphenyl 2,3,4,6-tetra-O-acetyl- α -D-mannopyranoside (**3**):

β -D-Mannose pentaacetate **1** (5.25 g, 13.3 mmol) and 4-(methoxycarbonyl)phenol **2** (3.05 g, 26.7 mmol) were dissolved in 1,2-dichloroethane (30 mL), followed by the dropwise addition of boron trifluoride diethyl etherate (5.44 mL, 40.0 mmol). The reaction mixture was stirred 24 h at 50°C and quenched by the addition of aq. NaHCO_3 (30 mL). The organic extract was washed with aq. NaCl (50 mL), dried over MgSO_4 , evaporated to dryness and purified by column chromatography (SiO_2 , 2:1 \rightarrow 1:1 hexane-EtOAc) and the semi-crude product spontaneously recrystallised from the column fractions, affording **3** (3.54 g, 55 %) as colourless plates; m.p. $137\text{--}140^\circ\text{C}$ (from methanol); ^1H NMR (500 MHz, CDCl_3) δ (ppm): 8.01 (d, $J = 8.9$ Hz, 2H), 7.13 (d, $J = 8.9$ Hz, 2H), 5.60 (d, $J_{1,2} = 1.8$ Hz, 1H, H-1), 5.55 (dd, $J_{3,4} = 10.0$ Hz, $J_{3,2} = 3.5$ Hz, 1H, H-3), 5.46 (dd, $J_{2,3} = 3.5$ Hz, $J_{2,1} = 1.8$ Hz, 1H, H-2), 5.37 (t, $J_{4,3} = 10.2$ Hz, $J_{4,5} = 10.2$ Hz, 1H, H-4), 4.28 (dd, $J_{6,6'} = 12.3$ Hz, $J_{5,6} = 5.6$ Hz, 1H, H-6), 4.09 – 4.02 (m, 2H, H-5, H-6'), 3.90 (s, 3H, OCH_3), 2.21 (s, 3H, COCH_3), 2.06 (s, 3H, COCH_3), 2.04 (s, 3H, COCH_3), 2.02 (s, 3H, COCH_3); ^{13}C NMR (75 MHz, CDCl_3) δ (ppm): 170.48, 169.95, 169.69, 166.44 (C=O), 158.99, 131.60, 124.84, 115.94 (ArC), 95.41 (C-1), 69.41, 69.14, 68.68, 65.73, 61.98 (C-6), 52.07 (OCH_3), 20.87, 20.70, 20.69, 20.67 (COCH_3); HRMS: Found $[\text{M}+\text{Na}]^+$ 505.1316, $\text{C}_{22}\text{H}_{26}\text{O}_{12}\text{Na}$ requires 505.1316.

4-Methoxycarbonylphenyl α -D-mannopyranoside (**4**):

A solution of 4-methoxycarbonylphenyl 2,3,4,6-tetra-O-acetyl- α -D-mannopyranoside **3** (3.00 g, 6.22 mmol) in anhydrous methanol (60 mL) was charged with sodium methoxide (670 mg, 12.4 mmol). After stirring at room temperature for 24 h the reaction mixture was neutralized with amberlite IRC 50 H⁺ resin, filtered and evaporated to afford **4** (1.56 g, 4.98 mmol, 80 %) as a colourless glassy solid; ¹H NMR (500 MHz, D₂O) δ (ppm): 7.92 (d, J = 7.5 Hz, 2H, ArH), 7.15 (d, J = 7.5 Hz, 2H, ArH), 5.65 (d, $J_{1,2}$ = 1.8 Hz, 1H, H-1), 4.11 (dd, $J_{2,3}$ = 3.1 Hz, $J_{2,1}$ = 1.8 Hz, 1H, H-2), 3.99 (dd, $J_{3,4}$ = 9.7 Hz, $J_{3,2}$ = 3.1 Hz, 1H, H-3), 3.83 (s, 3H, OCH₃), 3.72 – 3.63 (m, 3H, H-4, H-6, H-6'), 3.59 – 3.56 (m, 1H, H-5); ¹³C NMR (75 MHz, D₂O) δ (ppm): 168.91 (C=O), 159.47, 131.45, 123.40, 116.26 (ArC), 97.43 (C-1), 73.41, 70.22, 69.63, 66.39 (C-2, C-3, C-4, C-5), 60.51 (C-6), 52.37 (OCH₃).

4-Benzoylhydrazide α -D-mannopyranoside (**MAN**):

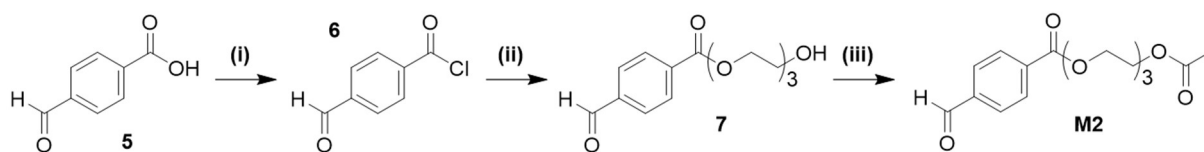
4-Methoxycarbonylphenyl α -D-mannopyranoside **4** (1.51 g, 4.80 mmol) was dissolved in methanol (3 mL), hydrazine monohydrate (707 μ L, 14.4 mmol) was added and the solution was refluxed for 4 h. The solution was then concentrated and lyophilized from water to afford **MAN** (1.36 g, 4.32 mmol, 90%) as a colourless lyophilizate; ¹H NMR (500 MHz, MeOD) δ (ppm): 7.81 (d, J = 8.8 Hz, 2H), 7.23 (d, J = 8.8 Hz, 2H), 5.61 (d, $J_{1,2}$ = 1.8 Hz, 1H, H-1), 4.06 (dd, $J_{2,3}$ = 3.5 Hz, $J_{2,1}$ = 1.8 Hz, 1H, H-2), 3.95 (dd, $J_{3,4}$ = 9.5 Hz, $J_{3,2}$ = 3.5 Hz, 1H), 3.84 – 3.71 (m, 3H, H-4, H-6, H-6'), 3.59 (ddd, $J_{5,4}$ = 9.8 Hz, $J_{5,6}$ = 5.3 Hz, $J_{5,6'}$ = 2.6 Hz, 1H, H-5); ¹³C NMR (125 MHz, MeOD) δ (ppm): 169.33 (CONHNH₂), 160.61, 130.02, 127.98, 117.46 (ArC), 100.00 (C-1), 75.71 (C-5), 72.43 (C-3), 71.89 (C-2), 68.34 (C-4), 62.70 (C-6); J_{C1-H1} = 171.00 Hz (consistent with α -configuration); 8 HRMS: Found $[M+H]^+$ 315.1189, C₁₃H₁₉N₂O₇ requires 315.1189.

3.5.5. Synthesis of Acrylamide-based Aldehyde Polymer Scaffolds **P1** - **P5**

M1 was prepared as reported in the experimental section of Chapter 2 (pages 80-81).

Polymer scaffolds **P1** - **P5** were prepared according to the experimental procedure reported in Chapter 2, page 83.

3.5.6. Synthesis of PEG Aldehyde Monomer **M2**



Scheme 2: Synthesis of aldehyde-TEGA monomer, **M2**. Step (i) 5 eqv. SOCl₂, 18 h reflux in toluene. Step (ii) Intermediate **6** was added dropwise into triethylene glycol, Et₃N, CH₂Cl₂, 8 h at 0 °C. Step (iii) acryloyl chloride, Et₃N, CH₂Cl₂, 18 h at 0°C.

4-Formylbenzoyl chloride (**6**):

4-Formylbenzoic acid **5** (4.38 g, 29.17 mmol) and thionyl chloride (27.7 g, 232.7 mmol) was dissolved in toluene (150 mL), placed under nitrogen atmosphere and refluxed overnight (18 h). White PTT was isolated by filtration and the filtrate was dried under high vacuum to afford the title product as a pale yellow solid (4.34 g, 89 % yield), used without any further purification. ^1H NMR (300 MHz, CDCl_3) δ (ppm): 9.89 (s, 1H), 8.31 (d, 2H, J = 8.2 Hz), 8.06 (d, 2H, J = 8.2 Hz). ^{13}C NMR (75 MHz, CDCl_3) δ (ppm): 191.13, 167.96, 140.55, 137.72, 131.93, 129.93.

2-(2-(2-Hydroxyethoxy)ethoxy)ethyl 4-formylbenzoate (**7**):

Triethylene glycol (24.85 g, 165.48 mmol) and Et_3N (6.08 g, 60.08 mmol) were dissolved in anhydrous CH_2Cl_2 (40 mL) and stirred under nitrogen atmosphere at 0 °C. 4-formylbenzoyl chloride **5** (4.92 g, 29.17 mmol) was dissolved in CH_2Cl_2 (20 mL) and added dropwise to the solution, which was allowed to gently warm to rt with overnight stirring. The reaction mixture was evaporated to dryness and the crude residue dissolved in EtOAc (150 mL) and washed with 0.1 M NaOH (3 x 75 mL). The organic extract was dried over MgSO_4 , filtered and dried *in vacuo* to afford the crude product as a yellow oil (514 g, 63 % Yield). The title product was further purified by column chromatography (SiO_2 , 75:25 EtOAc/hexane, product R_f = 0.35) to afford a colourless oil (3.93 g, 48 %). ^1H NMR (300 MHz, CDCl_3) δ (ppm): 10.10 (s, 1H), 8.23 (d, 2H, J = 8.2 Hz), 7.96 (d, 2H, J = 8.2 Hz), 4.53 (t, 2H), 3.86 (t, 2H), 3.71 (m, 6H), 3.61 (t, 2H). ^{13}C NMR (75 MHz, CDCl_3) δ (ppm): 191.78, 165.70, 139.35, 135.15, 130.46, 129.65, 72.63, 70.86, 69.26, 64.65, 61.95, 60.54.

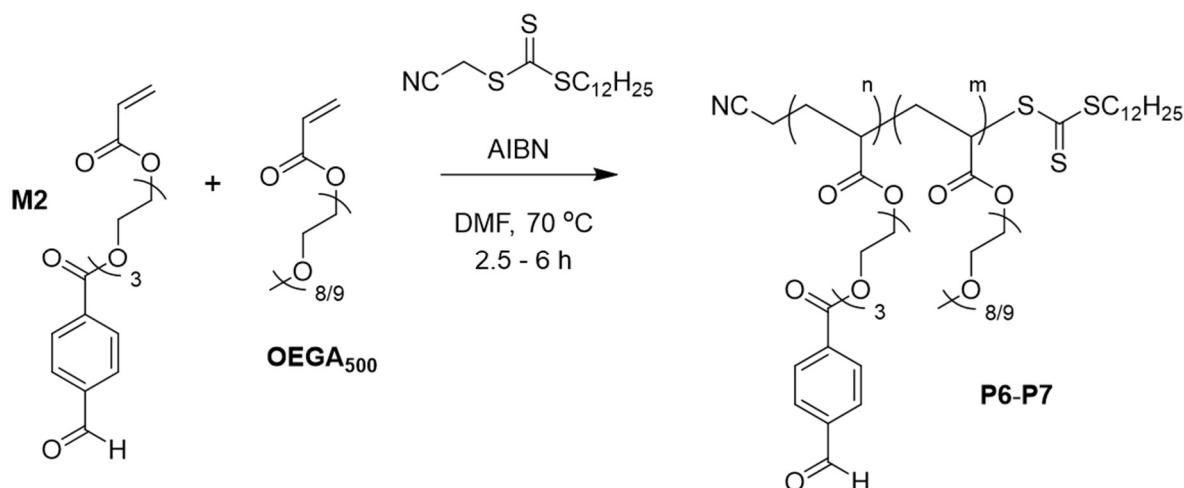
2-(2-(2-(Acryloyloxy)ethoxy)ethoxy)ethyl 4-formylbenzoate (**M2**):

2-(2-(2-Hydroxyethoxy)ethoxy)ethyl 4-formylbenzoate **7** (2.50 g, 8.84 mmol) and Et_3N (1.82 g, 17.96 mmol) were dissolved in CH_2Cl_2 (40 mL) and stirred under nitrogen atmosphere at 0 °C. Acryloyl chloride (0.884 g, 9.76 mmol) dissolved in CH_2Cl_2 (30 mL) was added dropwise to the solution, which gently warmed to rt with overnight stirring. The reaction mixture was concentrated under vacuum and the product partitioned between brine (100 mL) and EtOAc (3 x 75 mL). The organic layer was dried over MgSO_4 , filtered, and dried under vacuum to afford a crude yellow oil which was immediately purified by column chromatography (40:60 EtOAc/petroleum ether). The title product was obtained as colourless oil (2.59 g, 87 %). ^1H (300 MHz, CDCl_3) δ (ppm): 10.10 (s, 1H), 8.22 (d, 2H, J = 8.4 Hz), 7.95 (d, 2H, J = 8.4 Hz), 6.42 (dd, 1H, J = 17.0, 1.3 Hz), 6.15 (dd, 1H, J = 17.0, 10.2), 5.83 (d, 1H, J = 10.2, 1.3 Hz), 4.52 (d, 2H), 4.32 (d, 2H), 3.86 (d, 2H), 3.83 - 3.63 (m, 6H). ^{13}C NMR (75 MHz, CDCl_3) δ (ppm): 191.58, 166.02, 165.43, 139.15, 134.98, 130.96, 130.21, 129.42, 128.17. HRMS $^+$, $[\text{C}_{17}\text{H}_{20}\text{O}_7][\text{Na}]$, Theoretical: 359.1, Actual: 359.1.

The product was observed to readily auto-polymerize at rt. To avoid such auto-polymerization processes the aldehyde monomer was diluted to give a 200 mM stock solution in anhydrous CH₂Cl₂ and stored at - 20 °C.

3.5.7. Preparation of PEG Aldehyde Copolymer Scaffolds (P6 - P7)

Aldehyde scaffolds (**P6 – P7**) were prepared by RAFT polymerization of aldehyde monomer **M1** and water-soluble comonomer **OEGA**₅₀₀ in DMF at 70 °C.



Scheme 3: RAFT polymerization of aldehyde monomer **M2** with **OEGA**₅₀₀ afforded scaffolds **P6 - P7**.

RAFT Polymerization Protocol: **OEGA**₅₀₀ (1.16 g, 2.32 mmol), **M2** (780 mg, 2.32mmol, 75 eq), **2-(Dodecylthiocarbonothioylthio)-2-methylpropanoic acid** (DDMAT) (11.27 mg, 30.91 μmol, 1.0 eq) and **α,α' -Azoisobutyronitrile** (AIBN) (1.01 mg, 6.18 μmol, 0.2 eq) were combined in a Schlenk tube equipped with a magnetic stirrer bar and degassed by six consecutive freeze-pump-thaw cycles. The reaction was backfilled with nitrogen and subjected to 2 further freeze-pump-thaw cycles. The reaction vessel was heated in an oil bath to 70 °C and the reaction was stirred for 6 h (**P6**) or 2.5 h (**P7**). The polymer was purified by dialysis (Spectra por, 3 kDa MWCO) against DI water (3 x 3 L) to afford **P6/P7**. ¹H NMR (300 MHz, CDCl₃) δ 10.09 (br), 8.18 (br), 7.95 (br), 4.48 (br), 4.15 (br), 3.84 (br), 3.63 (br), 3.37 (br), 0.88 (br). The final polymer composition was determined by ¹H NMR spectroscopy revealing that **M2** / **OEGA**₅₀₀ = 1 : 1.23. ¹H NMR spectroscopic end group analysis showed $M_n \approx 27.4$ kDa, in close agreement with the feed ratio (1:1 **M2** : **OEGA**₅₀₀). The aldehyde copolymer was purified by dialysis against methanol (3 x 2L), water (2 x 2L), then lyophilized to afford a viscous yellow oil (731.4 mg, 26.7 μmol).

3.5.8. Preparation of Mannosylated Polymer Scaffolds

Aldehyde polymer scaffold (**P3**) was dissolved in 50 mM acetate/D₂O buffer (pD = 4.5), to afford a polymer solution with [**P3**] = 1.2 mM (**Solution A**), which was vortexed (1 min) and sonicated (5 min) to ensure complete dissolution of **P3**. Mannose hydrazide (**MAN**) was dissolved in 50 mM acetate/D₂O buffer (pD = 4.5), to afford **Solution B**, containing 30.2 mM **MAN**. A 500 μ L aliquot of **Solution B** (**MAN**) was added to **Solution A** (**P3**) to afford **Solution C**, in which the **P3** : **MAN** stoichiometry is 1 : 25.5 (i.e. 1.50 eqv **MAN** relative to the number of aldehyde groups on **P3**). **Solution C** was stirred at room temperature for 2 - 6h and the reaction was monitored by ¹H NMR spectroscopy, which revealed total disappearance of aldehyde signal (δ 10.04 ppm), thus confirming that the 'decoration' **P3** had complete. The mannosylated polymer scaffold (**P3-MAN**) was purified by dialysis (Spectra por, 3 kDa MWCO) against water (3 x 3L) to remove small molecule impurities, and then lyophilized to afford **P3-MAN** as a white solid. Mannosylated scaffolds **P1-MAN**, **P2-MAN**, **P4-MAN** – **P6-MAN** were prepared according the above procedure, but concentration of **MAN** in **Solution B** was adjusted to compensate for differences in the number of aldehyde units located upon the polymer scaffolds (i.e. concentration of **Solution B** was adjusted to ensure 1.50 eqv. of **MAN** per aldehyde unit).

Polymer scaffolds **P4** - **P5** were relatively hydrophobic in nature, and thus required small volumes (0.25 % v/v) of *d*₆-DMSO or *d*₄-MeOD cosolvent in **Solution A** to ensure complete dissolution of the polymer chains.

3.5.9. Preparation of Acrylamide- and PEG-Based *dyn*-MAN-SCPNs

P3-MAN solution (400 μ L, 1.12 μ mol) was diluted with 800 μ L of 50 mM acetate/D₂O buffer (pD 4.5) to afford [**P3-MAN**] = 0.913 mM (26.5 mM hydrazone unit). Succinic dihydrazide (82 μ L, 0.164 mg, 1.12 μ mol, 1 eqv) was added to the polymer solution, which was stirred overnight at rt. An identical protocol was employed for the preparation of *dyn*-MAN-SCPNs with higher densities of crosslinker, however, the concentration of succinic dihydrazide solution was adjusted. This protocol was also employed for the synthesis of PEG-based *dyn*-MAN-SCPNs, however, the molar concentrations were adjusted to (i) account for differences in the number of hydrazone reactive sites displayed upon the polymer scaffold, and (ii) to achieve different densities of crosslinker moieties within the resultant SCPN architecture.

3.5.10. Preparation of *fix*-MAN-SCPNs and *fix*-P6-MAN

Solution R: NaCNBH₃ (50 – 80 mM) in 100 mM AcOH-H₄NOAc/H₂O (pH 4.5).

dyn-MAN-SCPNs (and *dyn*-P6-MAN) were chemically reduced by addition of NaCNBH₃ (**Solution R**, 100 μ L 2.0 eqv relative to the number of hydrazone units) and the solution was stirred overnight at room temperature. Concentration of **Solution R** was adjusted to compensate for differences in the concentration of hydrazone units upon the polymer scaffold.

3.5.11. Preparation of Buffer Solutions

General Procedure: pH meter was calibrated prior to use. All buffer solutions were passed through a 0.45 µm syringe filter immediately before use to remove unwanted particulates.

D₂O Acetate Buffer: 50 mM H₄NOAc-AcOH, pD 4.5.

Acetate Buffer: 2 mM MnCl₂, 2 mM CaCl₂, 100 mM H₄NOAc-AcOH, pH 4.5.

Phosphate Buffer: 2 mM MnCl₂, 2 mM CaCl₂, 10 mM Na₂HPO₄/NaH₂PO₄, pH 7.4.

Bicarbonate Buffer: 2 mM MnCl₂, 2 mM CaCl₂, 10 mM NaHCO₃, pH 8.5.

3.5.12. Preparation of Con A-functionalized Nanoparticles

Lectin-Functionalization of NHS-Functionalized Silica Particles: NHS-functionalized silica particles (Micromod Partikeltechnologie) were suspended in 10 mM bicarbonate buffer (pH 8.5) with sonication for 5 min to afford **Solution A** (10 mg/mL). Stock solutions of Rhodamine-labelled Concanavalin A (Rh-Con A) or unmodified Concanavalin A (Con A) were diluted in bicarbonate buffer to afford **Solutions B – E** (2000 - 2 µg/mL protein concentration). Aliquots of **Solutions B - E** were added to the NHS particles (**A**), such that the final protein dose was 0 - 5000 µg protein per mg NHS particles. Particle/protein solutions were incubated at 4 °C for 4 h with 950 rpm shaking, then a 100 µL aliquot of 200 mM glycine (in 10 mM bicarbonate buffer) was added to 'cap' unreacted NHS-ester sites. The protein-functionalized particles were stirred overnight at 4 °C, purified by four centrifugal wash cycles (10 min at 15 krpm) to remove the unconjugated protein, then resuspended in phosphate buffer (pH 7.4) for a final particle concentration of 12.5 mg/mL.

Lectin-Immobilization onto Streptavidin-Modified Polystyrene Particles: Streptavidin-modified polystyrene nanoparticles (**smNPs**, diameter: 100 nm) (Sigma Aldrich) were suspended in 10 mM phosphate buffer (pH 7.4) with sonication for 5 min to afford **Solution A'** (5 mg/mL). Stock solutions of biotinylated Concanavalin A (**b-Con A**) were diluted in 10 mM phosphate buffer to afford **Solution B'** (500 µg/mL protein concentration). An aliquot of **Solution B'** was added to the suspension of particles (**Solution A'**), such that the final protein dose was 500 µg **b-Con A** per mg of particles. Particle/protein solutions were then incubated at 4 °C for 4 h with 950 rpm shaking, then purified by four centrifugal washes (10 min at 15 krpm) to remove the unconjugated protein, then resuspended in phosphate buffer (pH 7.4) for a final particle concentration of 5 mg/mL. **b-Con A** was immobilized onto streptavidin-modified microparticles (**smMPs**, diameter: 5 µm) (Sigma Aldrich) using the same procedure, and the protein dose was also 500 µg **b-Con A** per mg of particles.

3.5.13. B4F Assay

Biotin-4-fluorescein (**B4F**, Sigma Aldrich)(25 mg) was dissolved in DMSO (250 μ L) to afford stock solution A (**B4F_A**), 155.1 mM concentration. **B4F_A** was divided into 50 μ L aliquots and stored at - 20 °C prior to use. **B4F_A** then diluted with 50 mM phosphate buffer (pH 7.4) to afford working solutions **B4F_B** (10 mM), **B4F_C** (1 mM), **B4F_D** (0.5 mM), **B4F_E** (100 μ M), **B4F_F** (50 μ M), **B4F_G** (10 μ M), **B4F_H** (1 μ M), **B4F_I** (0.5 μ M), **B4F_J** (100 nM).

An aqueous suspension containing 0.5 mg/mL nanoparticles (**smNPs**, **NP1**, or biotin-saturated **smNPs**) prepared with 10mM phosphate buffer, the dispersion was mixed 25 times with a 200 μ L micropipette and an emission spectrum was measured (λ_{em} = 500 – 650 nm). Small volumes of **B4F** solutions (**B4F_B**-**B4F_J**) were titrated into the nanoparticle dispersion, the solution was mixed 25 times and an emission spectrum was recorded after each **B4F** addition. Normalized emission profiles are shown in Figure 13e.

3.5.14. Normalization of Emission Profiles

The production of normalized emission profiles shown in Fig. 13e, i – iii, required the measured values of emission at λ_{em} = 490 nm to be normalized affording to **Eqn. 1**:

$$\text{Normalized Emission, } I_{Norm} = \frac{\text{max}' - \text{min}'}{(\text{max} - \text{min})} \times (I_x - \text{max}) + \text{max}' \quad (\text{Eqn. 1})$$

Where **max'** and **min'** are the new maximum (100) and minimum (0) values of normalized emission (I_{Norm}), respectively. I_x is the measured emission value prior to normalization. **max** and **min** are the maximum and minimum values of measured emission prior to normalization (I_x).

3.5.15. Protocol for DLS ‘Shrink-Wrapping’ Experiments

Con A particles (50 μ L of 12.5 mg/mL **NP1** in 10 mM phosphate buffer) were diluted with acetate buffer, pH 4.5 (475 μ L) and mixed rapidly 10 times with a 200 μ L micropipette. 100 μ L of glycopolymer solutions (0 - 5000 μ g/mL) were added to the suspension of Con A particles and the solution mixed by rapidly pipetting 10 times. The solutions were incubated at rt with 900 rpm shaking for 4 h, purified by five consecutive centrifuge-wash-resuspend cycles and then analyzed by DLS. After analysis, α -methyl mannose (200 μ L, 2M) was added and the solution were incubated for 24 h and then underwent five centrifugal washes, before reanalysing by DLS.

3.5.16. Protocol for Fluorescence Microscope ‘Shrink-Wrapping’ Experiments

50 μ L of Con A particles **MP1** or **MP2** (12.5 mg/mL in 10 mM phosphate buffer) were diluted with 20 mM acetate buffer, pH 4.5 (525 μ L) and then 100 μ L of glycopolymer solutions (1 - 5000 μ g/mL) were added to achieve a polymer dose of 0 – 10000 μ g per mg of particles, final particle concentration of 1.0 mg/mL. Microparticle suspensions were mixed rapidly 10 times with a 200 μ L micropipette. The solutions were incubated at rt with 900 rpm shaking prior to imaging by fluorescence microscopy. 0 - 24 h after mixing, ‘unbound’ glycopolymers were removed from the samples by five consecutive centrifugal wash cycles. 3 \times 5 μ L aliquots were removed from purified samples, deposited onto a clean glass slide, and then imaged under the fluorescence microscope to monitor film formation upon microparticle surfaces. This analysis was performed at different time points after mixing to monitor the formation of glycopolymer layers upon the microparticle surfaces. Displacement of glycopolymer films was achieved by incubation with α -methyl mannose (2M, 200 μ L) which was added to each sample, and solutions were incubated for 24 h at 37 $^{\circ}$ C. Samples were purified by centrifugal washes, before re-imaging by fluorescence microscopy to determine whether glycopolymer layers had been displaced from the particle surfaces. **Control Experiments:** Control experiments were performed with microparticles **MP3** - **MP5** exact as above. Additional control experiments were performed in the absence of polymer solution, where the 40 μ L was substituted for the same volume of aqueous buffer.

3.5.17. Image Analysis to obtain Mean Gray Values (MGVs)

ImageJ software (1.5i) software was used to process all images. Briefly, images were imported into ImageJ and the thresholding tool (default setting) was employed to highlight bright areas of the image (emissive particles) (see Fig. 39, **red highlighted areas**). A region of interest (ROI) was generated for each individual particle (Fig. 39, **yellow circles** labelled with numerical identifiers). Greater than 50 ROIs (i.e. 50 particles/particle clusters) were generated from each fluorescence micrograph and the MGV was determined for each individual ROI (i.e. MGV_{ROI1} MGV_{ROI2} etc) and this data was tabulated (see Fig. 39c). The average MGV (see Fig. 39d) obtained for particles within that micrograph was then calculated by summing the MGVs for each region of interest (MGV_{ROI1} MGV_{ROI2} etc)(Fig. 39c) and dividing by the number of ROIs. The standard deviation was of MGVs within each image was also reported. The MGV of the ‘background’ (MGV_{bg}) was determined in two steps: (1) The threshold tool was employed to isolate the darkest areas of the image and a ROI was generated. (2) MGV for this ROI was measured. The ‘background’ emission was accounted for by subtracting of the MGV was subtracted from each individual particle (MGV_{ROI1} MGV_{ROI2} etc).

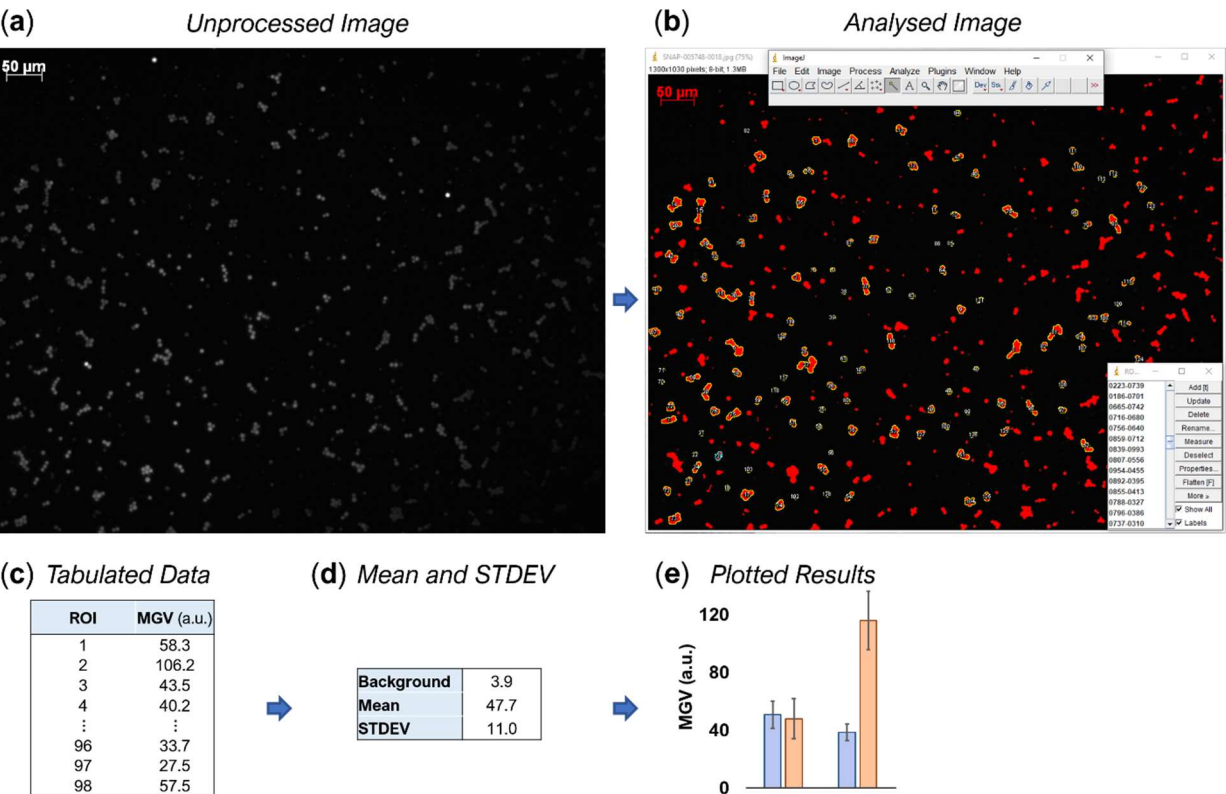


Figure 39: Fluorescence micrographs of emissive particles were analyzed to determine their mean gray values (MGVs) using ImageJ software. (a) An unprocessed fluorescence micrograph. (b) ImageJ screenshot the analyzed fluorescence micrograph. Brightly emissive particles (**highlighted red**) were selected using the threshold tool. Yellow circles indicate regions of interest (ROIs). A separate MGV was obtained from each ROI shown in the image above, and the data was tabulated (c). Greater than 50 individual particles (ROIs) were selected from each image to calculate the mean brightness (average MGV) and STDEV (d) for the particles within the image, allowing for the results to be plotted as a bar graph (e).

3.6. References

- [1] (a) R. A. Dwek, *Biochem. Soc. Trans.*, 1996, **96**, 683–720. (b) Y. C. Lee and R. T. Lee, *Acc. Chem. Res.*, 1995, **28**, 321–327. (c) C. R. Bertozzi and L. L. Kiessling, *Science*, 2001, **291**, 2357–2364.
- [2] C. S. Mahon, C. J. McGurk, S. M. D. Watson, M. A. Fascione, C. Sakonsinsiri, W. B. Turnbull and D. A. Fulton, *Angew. Chem. Int. Ed.*, 2017, **56**, 12913–12918.
- [3] A. Imberty and A. Varrot, *Curr. Opin. Struct. Biol.*, 2008, **18**, 567–576
- [4] M. E. Woolhouse, S. Gowtage-Sequeria, *Emerg. Infect. Dis.*, 2005, **11**, 1842–1847.
- [5] W. C. W. S. Putri, D. J. Muscatello, M. S. Stockwell, A. T. Newall, *Vaccine*, 2018, **36**, 3960–3966.
- [6] (a) C. Reed, S.S. Chaves, P. Daily Kirley, R. Emerson, D. Aragon, E.B. Hancock, et al., *PLoS One*. 2015, 103, e0118369. (b) V. J. Lee, Z. J. Marc Ho, E. H. Goh et. al., *Influenza Other Respir.*
- [7] A. D. Iuliano, K. M. Roguski, H. H. Chang et al., *Lancet*, 2018, **391**, 1285–1300.
- [8] S. Finch, M. J. McDonnell, Hani Abo-Leyah, S. Aliberti and J. D. Chalmers, *Ann. Am. Thorac. Soc.*, 2015, **12**, 1602–1611.
- [9] (a) J. Vila et al., *FEMS Microbiol. Rev.*, 40, 2016, 437–463. (b) Olivier T., D. Skurnik, B. Picard and E. Denamur, *Nat. Rev. Microbiol.*, 2010, **8**, 207–217.
- [10] J. De Smet, H. Hendrix, B.G. Blasdel, K. Danis-Wlodarczyk, R. Lavigne, *Nat. Rev. Microbiol*, 2017, **15**, 517–530.
- [11] (a) G.I. Bell GI, *Science*, 1978, **200**, 618–627. (b) W.E. Thomas, E. Trintchina, M. Forero, V. Vogel, E. V. Sokurenko, *Cell*, 2012, **109**, 913–923. (c) B. T. Marshall, M. Long, J. W. Piper, T. Yago, R.P. McEver, C. Zhu, *Nature*, 2003, 423, 190–193.
- [12] R. Robinson, *PLoS Biology*, 2006, **4**, 1473–1485.
- [13] (a) L. Coutte et al., *J. Exp. Med.*, 2003, **197**, 735–742. (b) A. M. Krachler and K. Orth, *Virulence*, 2014, **4**, 284–294 (c) P. Klemm, M. A. Schembri, *Int. J. Med. Microbiol.*, 2000, **290**, 27–35 (d) K. A. Kline et al., *Cell Host Microbe.*, 2009, **5**, 580–592.
- [14] D. F. Senear, and D. C. Teller, *Biochemistry*, 1981, **20**, 3076–3083.
- [15] C. A. Stark and A. D. Sherry, *Biochem. Biophys. Res. Commun.*, 1979, **87**, 598–604.
- [16] S. Goto, Kyoko Masuda et al., *Chem. Pharm. Bull.*, 2002, **50**, 445–449.
- [17] (a) J. D. Badjić, A. Nelson, S. J. Cantrill, W. B. Turnbull and J. F. Stoddart, *Acc. Chem. Res.*, 2005, **38**, 723–732. (b) U. Boas and P. M. H. Heegaard, *Chem. Soc. Rev.*, 2004, **33**, 43–63.
- [18] P. Frank, A. Prasher, B. Tuten, D. Chao and E. Berda, *Appl. Petrochem. Res.*, 2015, **5**, 9–17.
- [19] G. Houen and K. Hansen, *J. Immunol. Methods*, 1997, **210**, 115–123.

Chapter 4

Progress Towards the 'Shrink-Wrapping' of SV40 Viral Capsid

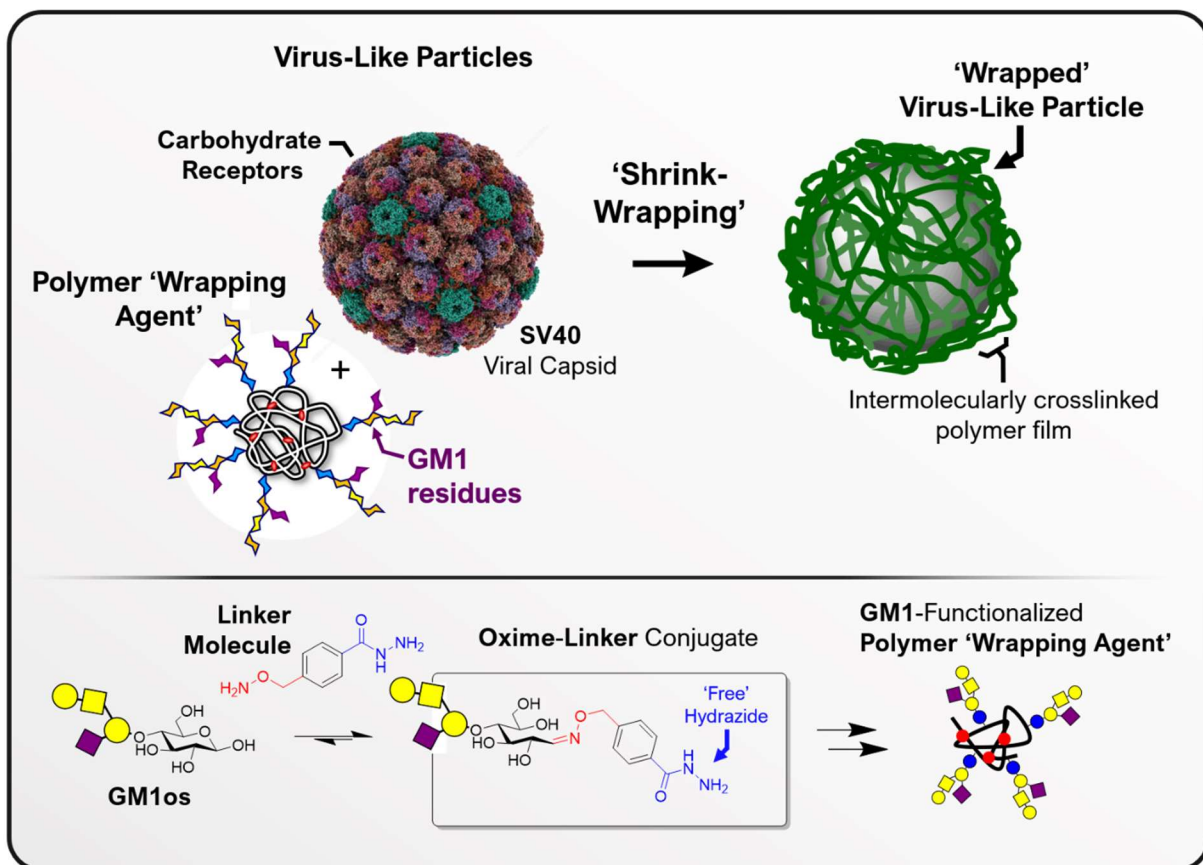


Table of Contents

4.1. Abstract	146
4.2. Results and Discussion	147
4.2.1. Preparation of GM1os	148
4.2.2. Proposed Strategy for the Synthesis of GM1-SCPNs	149
4.2.3. Preparation of <i>bis</i> -Functional Linker 3	150
4.2.4. Validating the Chemoselectivity of Linker 3	151
4.2.5. Optimizing the Glycoconjugation of Linker 3	153
4.2.6. Glycoconjugation of Linker 3 to GM1os	157
4.2.7. Rationalizing the Observed Chemoselectivity of Linker 3 with Carbohydrate Electrophiles	160
4.2.8. Functionalization of Aldehyde Polymer Scaffold with GM1-Linker Glycoconjugates	161
4.2.9. Barriers to the Preparation of GM1-SCPNs	162
4.2.10. An Alternative Synthetic Route to GM1-SCPNs	164
4.2.11. Glycoconjugation of Boc-Linker 18 to D-Lactose	165
4.2.12. Future Work	167
4.3. Conclusion	168
4.4. Experimental	170
4.5. References	174

4.1. Abstract

Chapter 3 has demonstrated that ‘shrink-wrapping’ of 3D microscale objects can be achieved when the ‘wrapping’ process is driven by specific molecular recognition events between polymers and the object surface. ‘Shrink-wrapping’ of simian virus 40 (**SV40**), a small icosahedral capsid, was thus envisaged to form an intermolecularly crosslinked glycopolymer film (Fig. 1) upon the viral surface. This crosslinked polymer ‘wrapping’ is anticipated to protect the ‘shrink-wrapped’ viral ‘cargo’ from dehydrating conditions of the external environment and may also serve to ‘neutralize’ the pathogen by masking the virus surface. An overarching aim of this thesis was to exploit specific ligand-receptor interactions to drive the ‘shrink-wrapping’ of **SV40** viral capsid, a small and biologically relevant object. This goal first required the synthesis of SCPNs ‘decorated’ with residues of the complementary carbohydrate ligand **GM1**, which is recognized by receptors located upon **SV40** exterior. Progress towards the preparation of **GM1**-functionalized SCPNs (**GM1**-SCPNs) is reported within this chapter.

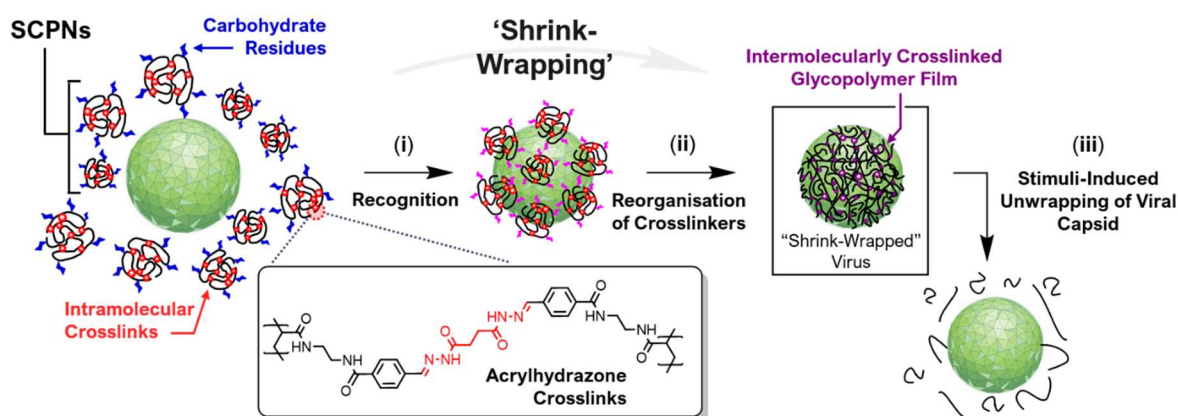


Figure 1: ‘Shrink-wrapping’ of a viral capsid within an intermolecularly crosslinked polymer film. In step (i) single-chain polymer nanoparticles (**SCPNS**) decorated with carbohydrate residues bind selectively to receptors situated on the periphery of the capsid. This process ‘concentrates’ the **SCPNS**, allowing their dynamic covalent crosslinkers to undergo intra- to inter-chain reorganisation in step (ii), resulting in the ‘shrink-wrapping’ of the capsid within a thin layer of intermolecularly crosslinked polymer chains. In step (iii) the application of a stimuli such as a drop in pH or increase in redox potential would be anticipated to induce cleavage of the crosslinkers, triggering the ‘unwrapping’ of viral capsid. In this chapter, work towards the synthesis of a suitable glyco-SCPNS is reported.

4.2. Results and Discussion

This chapter reports progress towards the goal of ‘shrink-wrapping’ virus-like particles. Simian virus 40 (**SV40**) capsid (Fig. 2a) was selected as a target on account of its availability from our collaborators in the laboratory of Professor Bruce Turnbull at University of Leeds. **SV40** is a small ($D_h \approx 50$ nm) non-enveloped DNA tumour-virus with a total surface area of 7854 nm². The **SV40** capsid is composed of 360 copies of the **VP1** major capsid protein (Fig. 2b), organised into 72 pentamers that assemble to form an icosahedral architecture (Fig. 2a). Each **VP1**-pentamer contains five carbohydrate binding sites, thus the capsid possesses a total of 360 carbohydrate binding sites displayed upon the viral surface. Although **SV40** capsid features a relatively high density of carbohydrate binding sites (1 site per 21.8 nm²), their interaction with the complimentary pentasaccharide **GM1** (Fig. 2d) is relatively weak (**VP1-GM1**, $K_d = 5.8$ mM).¹ Although these binding constants appear relatively low, this issue is readily circumnavigated by multivalent expression² of carbohydrates upon a polymer scaffold, where an ensemble of low-affinity carbohydrate-receptor interactions reinforce one another to facilitate high-affinity

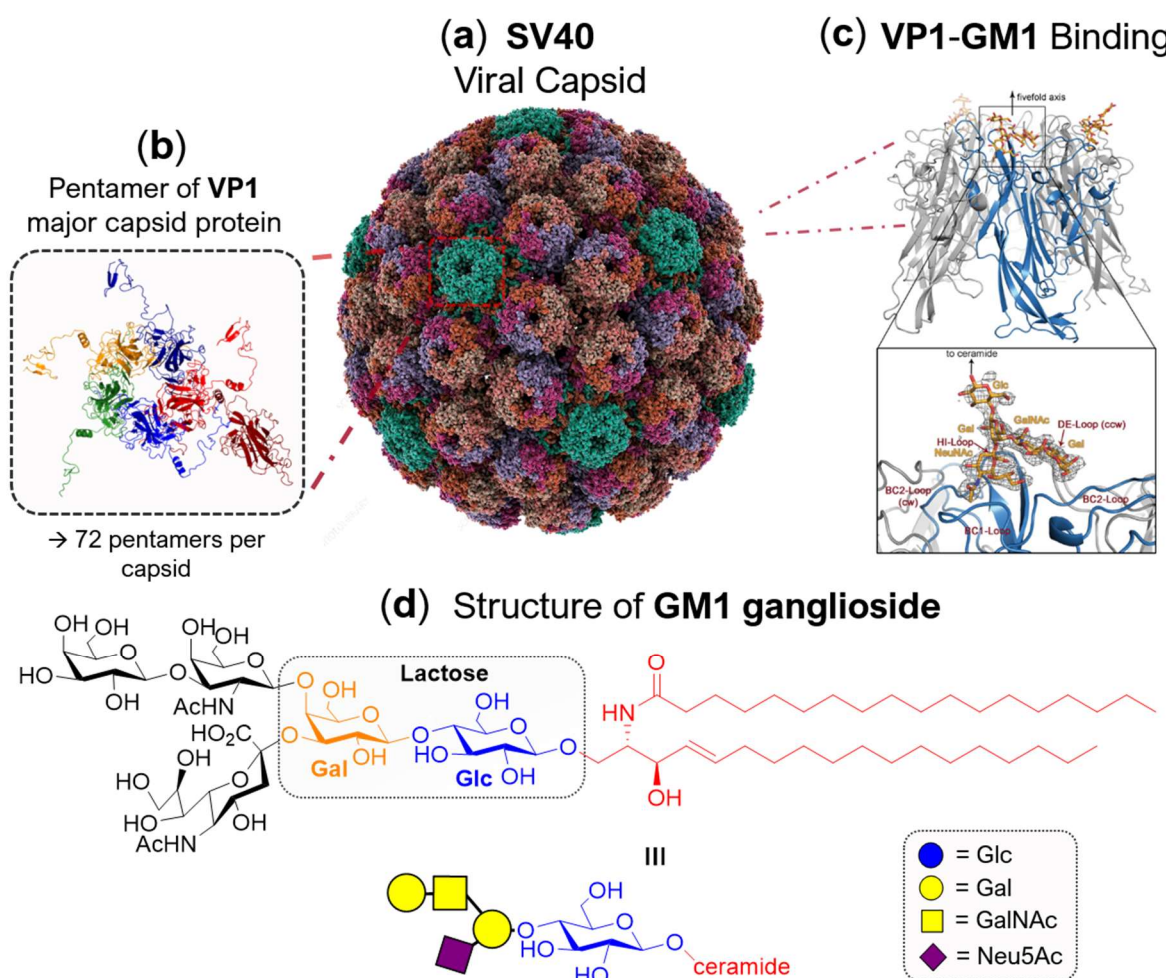


Figure 2: (a) **SV40** viral capsid is a small non-enveloped DNA tumour-virus, composed from 360 copies of the major capsid protein, **VP1** (b) which are organised into 72 pentamers that assemble to form the icosahedral capsid architecture. Each **VP1** protein subunit contains a single carbohydrate binding site (c), which binds selectively to the branched oligosaccharide **GM1** ganglioside (d). **SV40** viral capsid, thus, displays 360 **GM1** binding sites upon its surface.

binding to the viral surface. It is anticipated that multivalent display of carbohydrates will encourage **GM1-SCPNs** to bind onto viral capsid. Thus, this effect can be exploited to achieve high affinity polymer-virus interactions, which are anticipated to help drive the ‘shrink-wrapping’ process by effectively concentrating **GM1-SCPNs** onto the periphery of **SV40**.

4.2.1. Preparation of GM1os

GM1 oligosaccharide (**GM1os**) was synthesized³ (Fig. 3a) by enzymatic cleavage of the **ceramide tail** from **GM1 ganglioside** (see structure in Fig. 3c) to yield the carbohydrate product with a reactive hemiacetal (masked aldehyde group) at its reducing end (Fig. 3a, ii). In aqueous solution, the reducing end of **GM1os** (Fig. 4a) predominantly exists as a ring-closed hemiacetal (i) which is in equilibrium with the ring-opened (ii) aldehyde form (< 3 % CHO).

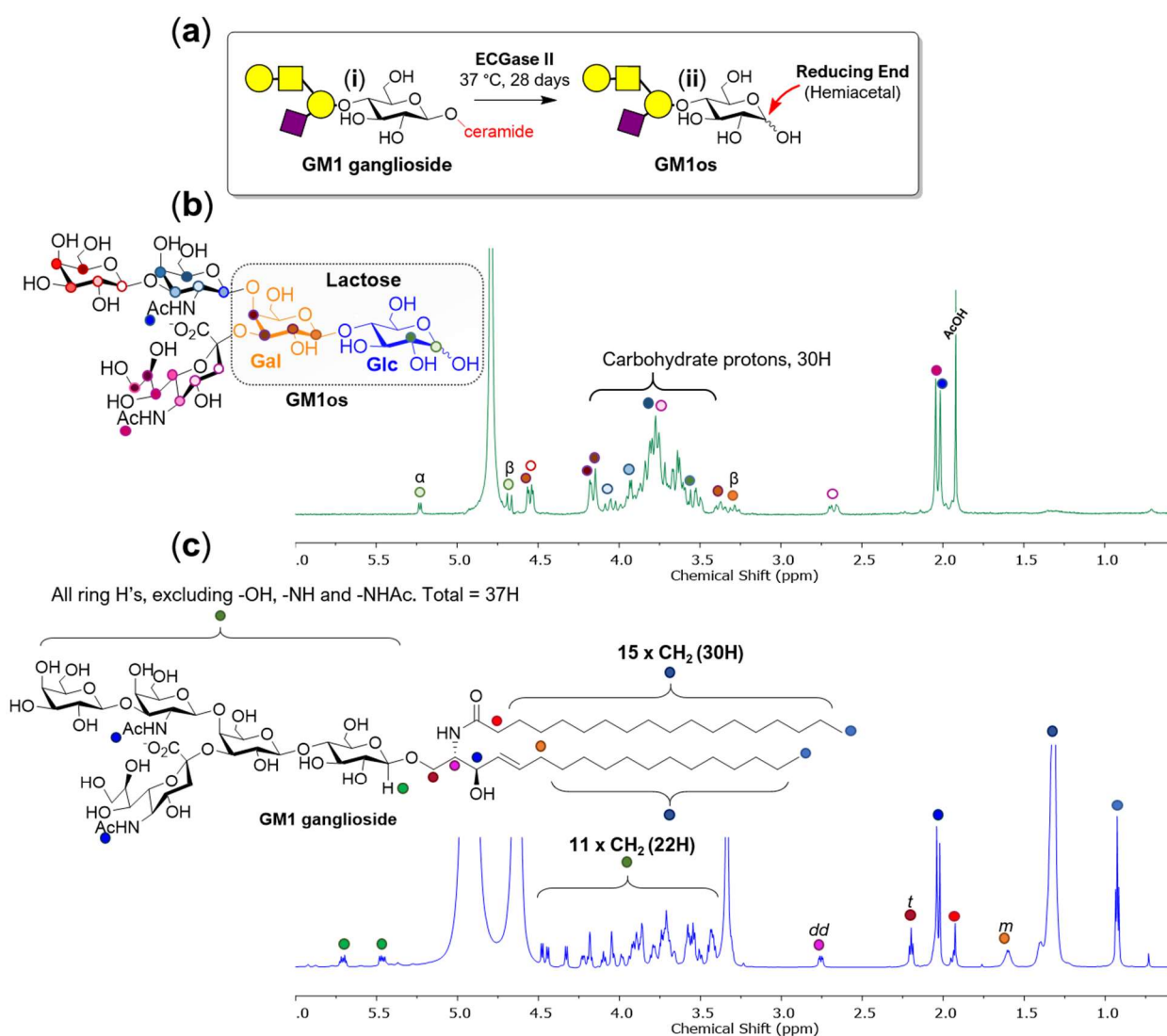


Figure 3: (a) Enzymatic cleavage of ceramide moiety from **GM1 ganglioside** by **ECGase II** afforded **GM1** oligosaccharide (**GM1os**) with a terminal hemiacetal group at its reducing end. Partial ¹H NMR spectra of **GM1os** (700 MHz, D₂O)(b) and **GM1 ganglioside** starting material (700 MHz, d₄-MeOD) (c).

Following purification (see experimental), **GM1os** was lyophilized and isolated as a white solid (254 mg, 78 % yield). Figures 3b-c show the partial ^1H NMR spectra of **GM1os** product and **GM1 ganglioside** starting material, respectively, the assignment of which was consistent with literature reports.⁴ The ^1H NMR spectrum of **GM1os** (Fig. 3b) revealed that quantitative cleavage of the ceramide moiety was successful, as evidenced by the total disappearance of the associated ceramide signals ($\delta = 0.89 - 2.90$ ppm) and the emergence of new signals (●) at $\delta = 5.22$ ppm ($J_{1,2} = 3.66$ Hz) and $\delta = 4.67$ ppm ($J_{1,2} = 7.86$ Hz), which were assigned to the GlcH1 α/β positions on the reducing end of **GM1os**. Attempts to characterize **GM1os** by mass spectrometry proved unsuccessful on account of difficulties in ionizing the carbohydrate.

4.2.2. Proposed Strategy for the Synthesis of GM1-SCPNs

Considerable thought was given to identify functional groups that react efficiently and selectively with unmodified carbohydrates. Reactions of alkoxyamine or hydrazide groups with ‘free’ carbohydrates are known to be chemoselective and have been widely exploited for the synthesis of neoglycopeptides,⁵ neoglycoconjugates⁶ and carbohydrate-functionalized surfaces.⁷ Consequently, these processes were chosen for the site-specific covalent immobilization of ‘free’ carbohydrates onto polymer scaffolds. In the selected strategy for preparing **GM1**-grafted **SCPNs**, the reducing end (electrophilic site) of **GM1os** was anticipated to react with a nucleophilic Linker **3** (Fig. 4c) to yield an **GM1-linker** conjugate (Fig. 4d).

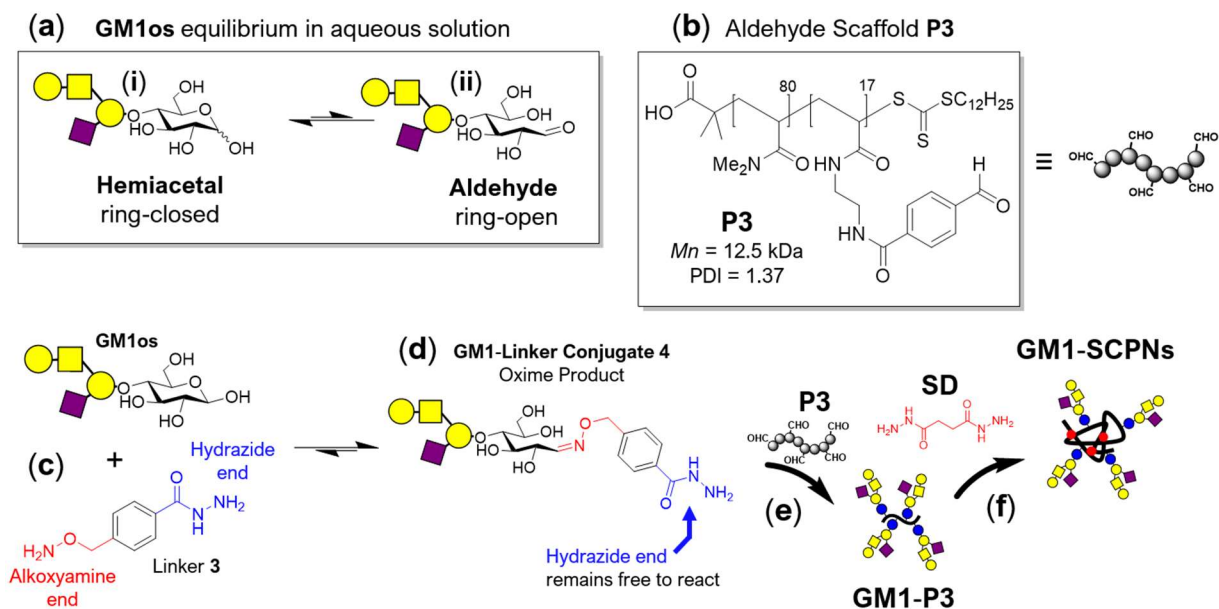


Figure 4: (a) In aqueous solution, the reducing end of **GM1os** predominantly exists as a ring-closed hemiacetal (i) which is in equilibrium with the ring-opened (ii) aldehyde form (< 3 % CHO). (b) Structure of aldehyde-functionalized polymer scaffold **P3**, the synthesis of which was reported in Chapter 3 (pages 97 - 98). (c) Reaction of **GM1os** with linker **3** was expected to yield oxime-linked glycoconjugate **4** as the majority product under thermodynamic control. (c-d) Proposed synthetic strategy for the preparation of **GM1**-grafted polymers by reacting the ‘free’ hydrazide end of **GM1-Linker Conjugate 4** (d) with an aldehyde-functionalized polymer scaffold **P3** (b) to afford **GM1-P3** (e). Intramolecular crosslinking of **GM1-P3** with succinic dihydrazide (**SD**) (f) was anticipated to afford **GM1-SCPNs**.

Linker **3** (Fig. 4c) has two nucleophilic sites: A **hydrazide** and an **alkoxyamine**, which react with carbonyls to form acyl hydrazones and oximes, respectively. Oxime bonds are known to be more hydrolytically^{8a} and thermodynamically^{8b} stable than are acyl hydrazones, and it was thus anticipated that **3** would react selectively through its **alkoxyamine end** to yield the stable oxime-linked glycoconjugate **4** (Fig. 4d), in preference to forming the analogous hydrazone product. On the reasonable assumption that oxime conjugate **4** is the majority product obtained under thermodynamic control, it was thus envisioned that the ‘free’ **hydrazide end** of **4** could be grafted (Fig. 4e) onto an aldehyde-functionalized scaffold **P3** (Fig. 4b) to afford **GM1-P3**, a hydrazone-functionalized polymer scaffold ‘decorated’ with pendant **GM1** carbohydrate residues. This approach leaves the reducing end of **GM1os** in its ring-open form – however, this should not affect its binding with the capsid, which is predominantly facilitated by the terminal sialic acid and galactoside residues.¹ Intramolecular crosslinking (Fig. 4f) of **GM1-P3** with succinic dihydrazide (**SD**) was anticipated to afford **GM1-SCPNS**. The synthesis and characterization of the parent polymer scaffold **P3** is reported in Chapter 3 (see pages 97 - 98 for details).

4.2.3. Preparation of *bis*-Functional Linker **3**

In order to facilitate grafting of **GM1** to the aldehyde scaffold **P3** (Fig. 4c), *bis*-functional linker molecule **3** was prepared (Fig. 5a) in two steps. In step (i) alkylation of *N*-hydroxyphthalimide with bromide **1** yielded intermediate **2**. Subsequent hydrazine reflux (ii) of **2** with hydrazine monohydrate afforded tandem hydrazinolysis of both methyl ester and *N*-hydroxyphthalimide to furnish linker **3**, which contains both **hydrazide** and **alkoxyamine** nucleophilic sites. Linker **3** was isolated as an off-white solid (62 % yield)

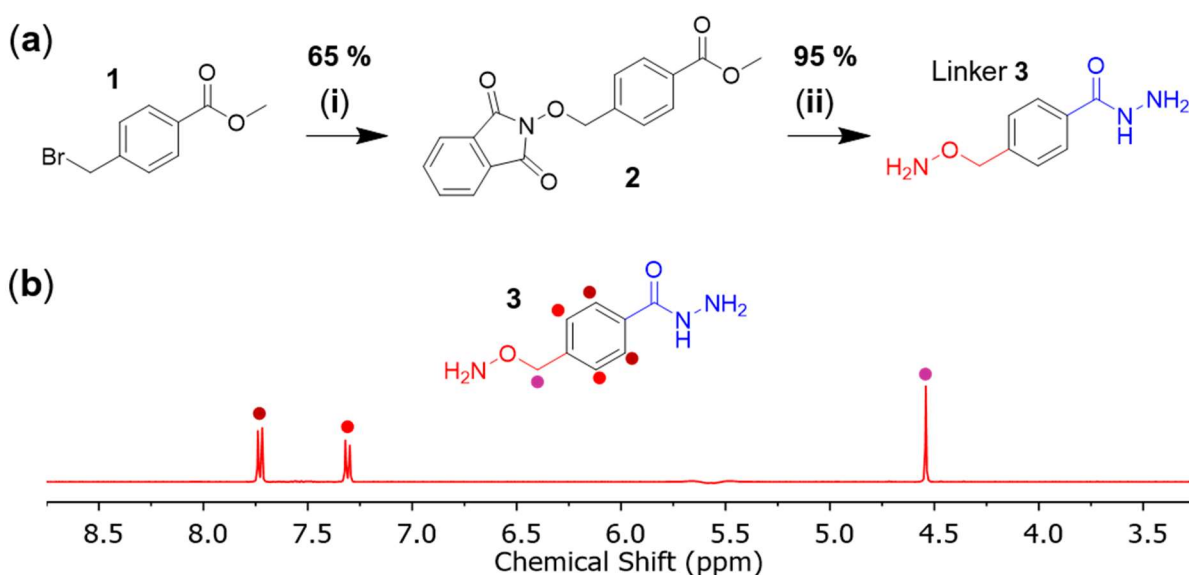


Figure 5: (a) Synthesis of alkoxyamine linker **3**. Step (i) *N*-Hydroxyphthalimide, DIPEA, CH₂Cl₂, 18 h, rt. Step (ii) N₂H₄·H₂O/EtOH, 4 h, rt. (b) Partial ¹H NMR spectrum (*d*₆-DMSO, 300 MHz) of linker **3**.

4.2.4. Validating the Chemoselectivity of Linker 3

Linker **3** (Fig. 6a) may react with carbonyl compounds through its **alkoxyamine end** to form oximes, or through its **hydrazide end** to form acyl hydrazones. To evaluate linker chemoselectivity towards carbonyl-containing electrophiles, control experiments were undertaken in which **3** (86 mM, in d_6 -DMSO with 50 mM AcOH) was reacted with 0.95 eqv. benzaldehyde (Fig. 6b) or 0.95 eqv. acetone (Fig. 6c). These processes were monitored as a function of time by ^1H NMR spectroscopy (Fig. 6e-f) and the associated kinetics traces were derived (Fig. 6g-h). Reaction progress was monitored over an 18 h timeframe and upon reaching equilibrium the hydrazone : oxime product distributions, % yield, and equilibration time (T_{eq}) were determined (Table 1) by integral analysis of 'diagnostic' ^1H NMR signals (Fig. 6e-f).

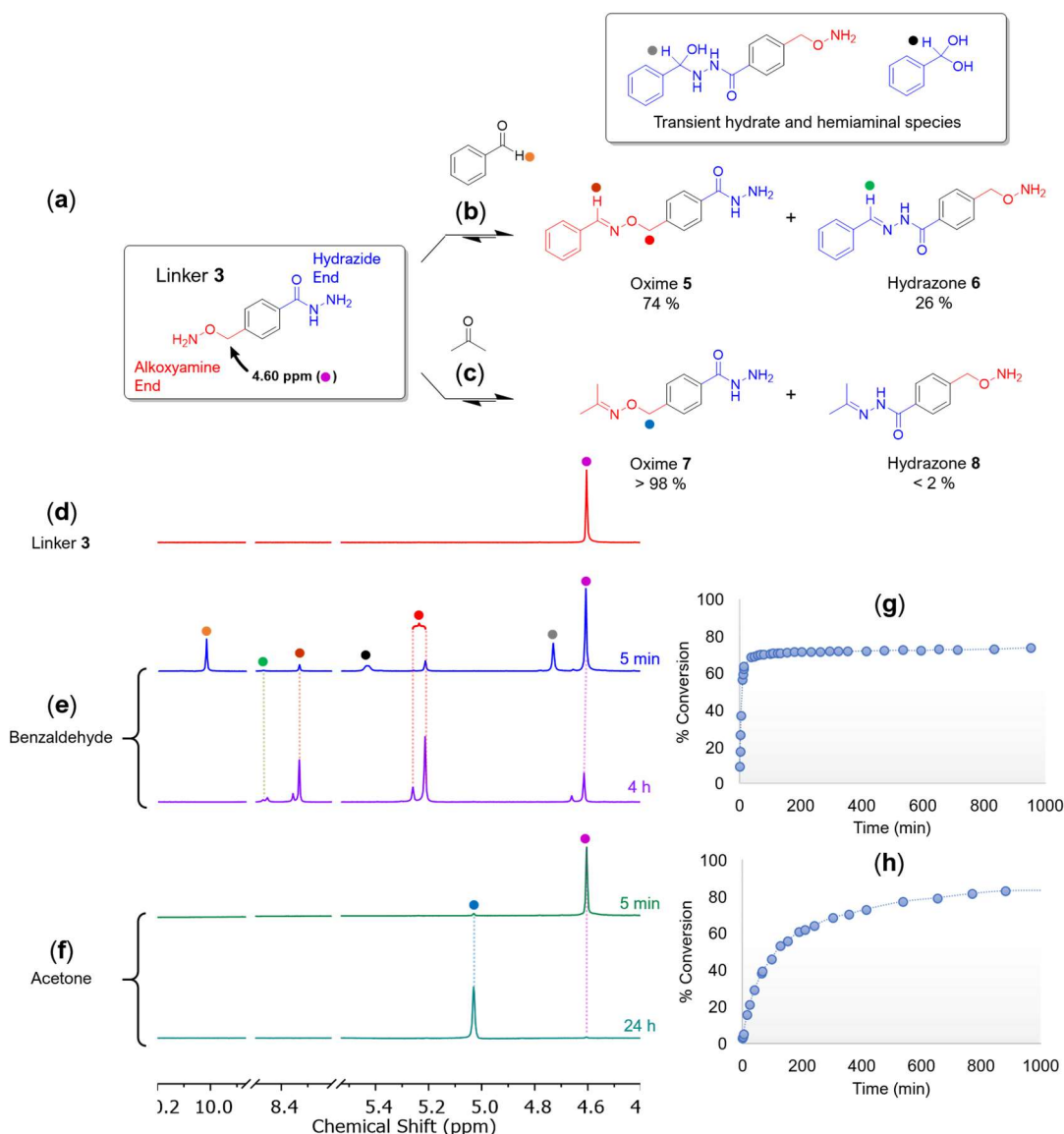


Figure 6: (a) Linker **3** (86 mM in d_6 -DMSO with 50 mM AcOH) can react through **alkoxyamine end** to form oximes, or through **hydrazide end** to form hydrazones. Reaction of **3** with 0.95 eqv. benzaldehyde (b) or 0.95 eqv. acetone (c) both afforded the oxime product with > 74 % selectivity, as determined by ^1H NMR spectroscopic studies (d-f). Partial ^1H NMR (d_6 -DMSO, 400 MHz) spectra of linker **3** in isolation (d), during reaction of **3** with benzaldehyde (e) and acetone (f). Kinetic traces for reaction of **3** with benzaldehyde (g) and acetone (h).

Substrate	T _{eq} (min)	Oxime	Hydrazone	Yield
Acetone	< 2820	> 98 %	0 %	> 98 %
Benzaldehyde	203	74 %	26 %	> 98 %

Table 1: Equilibration time (T_{eq}), oxime/hydrazone product distributions and % yield for reaction of linker **3** with carbonyl-containing substrates, acetone or benzaldehyde.

During the reaction of **3** with benzaldehyde (Fig 6b) ¹H NMR spectroscopy revealed the formation of multiple short-lived species (Fig. 6b/e, ● and ●). However, by timepoint T = 11 min, these transient species had been consumed and the spectra had simplified such that the identity of all the species could be assigned. ¹H NMR spectra revealed the complete disappearance (Fig. 6e) of aldehyde signal (●)(10.02 ppm), rapid consumption of the ‘diagnostic’ alkoxyamine signal (●)(4.61 ppm) belonging to the unreacted linker **3** and concomitant appearance of new ¹H NMR signals (●)(5.21 and 5.26 ppm).^{*} The emergence of these new signals was attributed to the formation of an oxime product (see Fig. 6b, ●), a reaction which had achieved completion by 203 min. The observation that aldehyde signal (●) had been fully consumed, yet the unreacted alkoxyamine signal (●) persisted revealed that oxime **5** was the predominant product (74 % yield), with hydrazone product **6** accounting for the remaining 26 %. The reaction with acetone (Fig. 6c) also showed rapid disappearance of the alkoxyamine signal (●) (Fig. 6f) and emergence of a new oxime signal (●)(5.03 ppm), which indicated quantitative formation of an oxime product after 2820 minutes. From these initial chemoselectivity studies it was concluded that linker **3** has a preference to react with carbonyl compounds through the **alkoxyamine end**, with oxime product typically formed in > 74 % yield.[†] Alkoxyamine linker **3** was thus progressed to trial oxime ligations with carbohydrate substrates (Fig. 7), where **3** was also anticipated to display a preference for oxime formation by reaction through its **alkoxyamine end**.

^{*} Two ¹H NMR signals were observed for the ‘diagnostic’ benzylic protons (●) of benzaldehyde oxime product **5** on account of E/Z isomerization of the oxime bond. In contrast, E/Z isomerization was not observed in the case of acetone, which is a symmetrical ketone and thus affords only single product, oxime product **7**. See the ¹H NMR spectrum in Fig. 6f, where benzylic protons (●) of oxime **7** show only a single peak at δ = 5.30 ppm.

[†] Intriguingly, linker **3** reacts with acetone to form oxime **7** in > 98 % yield, yet benzaldehyde forms hydrazone **5** and oxime **6** in a 74:26 ratio. Under the assumption that reactions were operating under thermodynamic control, the observation that benzaldehyde forms a mixture of products implies that the hydrazone and oxime are of similar energy. In contrast, reactions of **3** with acetone revealed a clear difference in stability of the hydrazone and oxime products, with a strong preference for the latter.

4.2.5. Optimizing the Glycoconjugation of Linker 3

The proposed synthesis of **GM1-SCPNs** (Fig. 4) required oxime-linked glycoconjugate **4** (Fig. 4d) to be isolated in a high yield. Working with unprotected **GM1** was, however, synthetically challenging and presented little scope for purification on account the highly hydrophilic nature of this complex carbohydrate and its inherent incompatibility with organic solvents. Furthermore, **GM1os** was time-consuming and costly to produce[‡] and therefore only available in a limited supply of < 250 mg. Investigations thus focussed on optimizing the linker-sugar conjugation chemistry, such that glycoconjugate **4** could be isolated in a high yield and then directly grafted onto polymer scaffolds without requiring tedious and wasteful purification procedures. The reducing end of **GM1os** (Fig. 3b) is isostructural with **D-Lactose**, thus this low-cost and commercially available disaccharide served as a suitable model for glycoconjugations involving **GM1**. A range of experimental conditions were screened to optimize the glycoconjugation of linker **3** to **D-Lactose** (Fig. 7) and the conjugation efficiency was quantified by ¹H NMR spectroscopy, which the reported % conversion values listed in Table 2.[§]

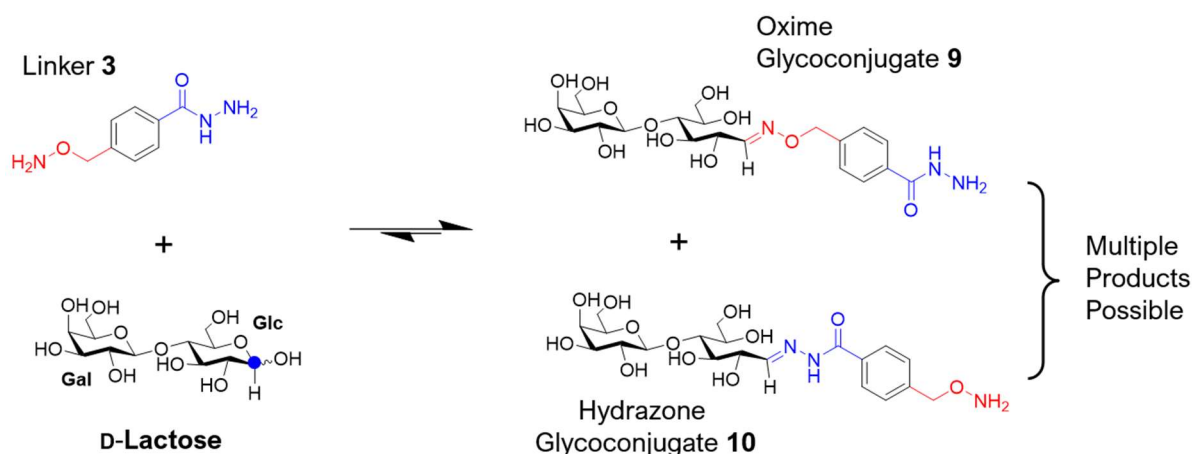


Figure 7: Conjugation of linker **3** with **D-Lactose** was monitored by ¹H NMR spectroscopy. Disappearance of the α- and β- anomeric ‘diagnostic’ ¹H NMR signals (●) were employed to monitor the progress of the glycoconjugation reaction to form products **9/10**.

[‡] Production of 250 mg **GM1os** requires three weeks for enzymatic cleavage of the ceramide tail from GM1-ganglioside. GM1-ganglioside starting material costs £310 for 500 mg (Carbosynth UK, September 2018) and the enzyme for ceramide cleavage (EGCase II) cost £309.

[§] The reported % conversion values (Table 2) were calculated by integral analysis of the ‘diagnostic’ **D-lactose** anomeric (H1α) signals relative to an internal standard within the ¹H NMR spectra. Aromatic ¹H NMR signals (δ 7.38 and 7.78 ppm) of linker **3** were chosen as the internal ¹H NMR standard for two reasons: (i) their chemical shifts remained unchanged throughout the course of the reaction and (ii) no overlap was observed with adjacent signals.

Time-resolved ^1H NMR spectroscopy permitted *in-situ* monitoring of glycoconjugation reactions, where the steady disappearance of ‘diagnostic’ anomeric (●) signals** associated with **D-Lactose** (Fig. 7) revealed consumption of the carbohydrate starting material and thus reported reaction progress. Although this glycoconjugation reaction may yield two potential products: (i) Oxime **9** or (ii) hydrazone **10**, it was anticipated that oxime **9** (Fig. 7) would be the predominant product. Thus, experimental conditions were initially optimized to improve the yield of the carbohydrate-linker condensation process with little consideration for the oxime/hydrazone product distribution, which was challenging to interrogate on account of the complexity observed in ^1H NMR spectra.†† Discussion of the products isolated from this reaction is, however, provided on page 155.

Table 2 summarizes the conditions explored to optimize ligation of linker **3** to **D-Lactose**. Entries 6 and 9 employed 4-aminophenol (**4-AP**) as a nucleophilic organocatalyst, which was anticipated to catalyze oxime formation,⁹ and thus improve the yield of glycoconjugate products. The following parameters were adjusted to achieve the highest % conversion of lactose substrate: (i) Solvent type and composition, (ii) presence of **4-AP** organocatalyst, (iii) linker concentration, (iv) carbohydrate concentration, (v) reaction temperature.

Entry	Solvent	Catalyst	[Lactose] (mM)	[Linker] (mM)	Temperature	% Conversion
1	AcOH/D ₂ O	-	134	150	rt	35 %
2	1:1 AcOH/D ₂ O : MeOH	-	150	150	rt	47 %
3	1:1 AcOH/D ₂ O : MeOH	-	150	450	rt	41 %
4	AcOH/D ₂ O	-	150	150	rt	49 %
5	AcOH/D ₂ O	-	86	86	rt	47 %
6	AcOH/D ₂ O	4-AP	86	86	50 °C	60 %
8	AcOH/d ₆ -DMSO	-	108	94	rt	> 95 %
9	AcOH/d ₆ -DMSO	4-AP	108	94	rt	94 %
10	AcOH/d ₆ -DMSO	-	108	119	rt	89 %

Table 2: Summary of reaction conditions for ligation of linker **3** to **D-Lactose**. Entry 8 was determined as the optimal experimental conditions for ligation of linker **3** to **D-Lactose**, on account of these conditions affording the highest % consumption values. The % conversion values were calculated from the consumption of **D-Lactose** starting material, which was determined by ^1H NMR spectroscopy. Solvent conditions: AcOH/D₂O is 50 mM AcOH in D₂O, pD \approx 3.4; AcOH/d₆-DMSO is 150 mM AcOH in d₆-DMSO. In entries 6 and 9 the concentration of 4-aminophenol organocatalyst was 50 mM.

** Reaction progress was monitored by integral analysis of the α -anomer ^1H NMR signal only. The integral of the β -anomer (δ 4.17 ppm) was affected by signal overlap, thus could not be employed to reliably monitor the reaction. α - and β -anomers rapidly interconvert in solution, however their ratio should remain constant, and thus consumption of the α -anomer is expected to be representative of the reaction progress.

†† ^1H NMR spectra obtained during the monitoring of glycoconjugation processes were highly complex and difficult to interrogate, on account of a number of factors: (i) Carbohydrates exist as an equilibrium mixture of α - and β -anomers, the exact composition of which was directly affected by the glycoconjugation process; (ii) a mixture of carbohydrate-linker adducts were obtained, the diagnostic signals of which displayed significant overlap with signals of the carbohydrate region (δ 2.80-4.50 ppm); (iii) carbohydrate-linker adducts were observed to exist as a mixture of isomers; (iv) glycoconjugation reactions were initially conducted in acetate buffered D₂O (Table 2, entries 1-6), where the diagnostic alkoxyamine signal (Fig. 8a, ●) of linker **3** was masked beneath the HOD peak.

Inspection of Table 2 reveals that anhydrous conditions afforded the highest % conversions for glycoconjugation, with entry 8 exceeding 95 % conversion within 24 h. In contrast, oxime ligation reactions performed in aqueous solution (pD \approx 4.9) typically afforded low % conversions of < 60 %. Oxime formation is a condensation reaction and thus the conjugation of linker **3** to carbohydrates was anticipated to be disfavoured by an aqueous environment. The observation that % conversion values were initially low but could be slightly improved by increasing the carbohydrate concentration in aqueous solution (see entries 1 and 3), was entirely consistent with this hypothesis. It was also concluded that linker-carbohydrate conjugation chemistry preceded in a cleaner fashion at room temperature than was observed at elevated temperatures, and that the presence of 4-aminophenol catalyst did not significantly improve % conversion in organic solvents. Conditions from entry 8 were found to be optimal for conjugation of linker **3** to carbohydrate substrates, on account of the highest % conversion value, thus were employed for all subsequent glycoconjugation reactions. Under these conditions it was demonstrated that linker **3** conjugates to **D-Lactose** with a high efficiency. However, the oxime/hydrazone product distribution had not yet been interrogated and this will now be discussed by consideration of the observed ^1H NMR spectra (Fig. 8b).

Figure 8b shows a series of time-resolved ^1H NMR spectra obtained during the reaction of **D-Lactose** with linker **3** in 150 mM AcOH/ d_6 -DMSO (Table 2, entry 8). These spectra revealed that the ‘diagnostic’ **alkoxyamine** signal (δ 4.60 ppm, \bullet) was surprisingly not consumed during the reaction, thus indicating that the expected oxime conjugate **9** had not formed. The observation that ‘diagnostic’ **D-Lactose** GalH2 and GlcH1 signals ($\bullet\alpha,\beta$ + $\bullet\alpha,\beta$) were consumed and new carbohydrate signals appeared (δ 4.89 and 4.21 ppm, $\bullet\alpha,\beta$) but the **alkoxyamine end** of **3** (\bullet) remained unreacted strongly indicates that hydrazone **10** was a likely product. The emerging doublet at δ 6.99 ppm (\bullet) was consistent with the chemical shift of a hydrazone CH, again suggesting that hydrazone **10** had been isolated as the predominant product. It should be acknowledged, however, that the signal at δ 6.99 ppm (\bullet) does not integrate to the anticipated value and thus this conclusion should be treated with caution. The two carbohydrate doublet signals at δ 4.89 ($\bullet\alpha$) and 4.21 ppm, ($\bullet\beta$) were assigned to glycoconjugate **12**, a species which is formed by ring-closure of hydrazone **10**.

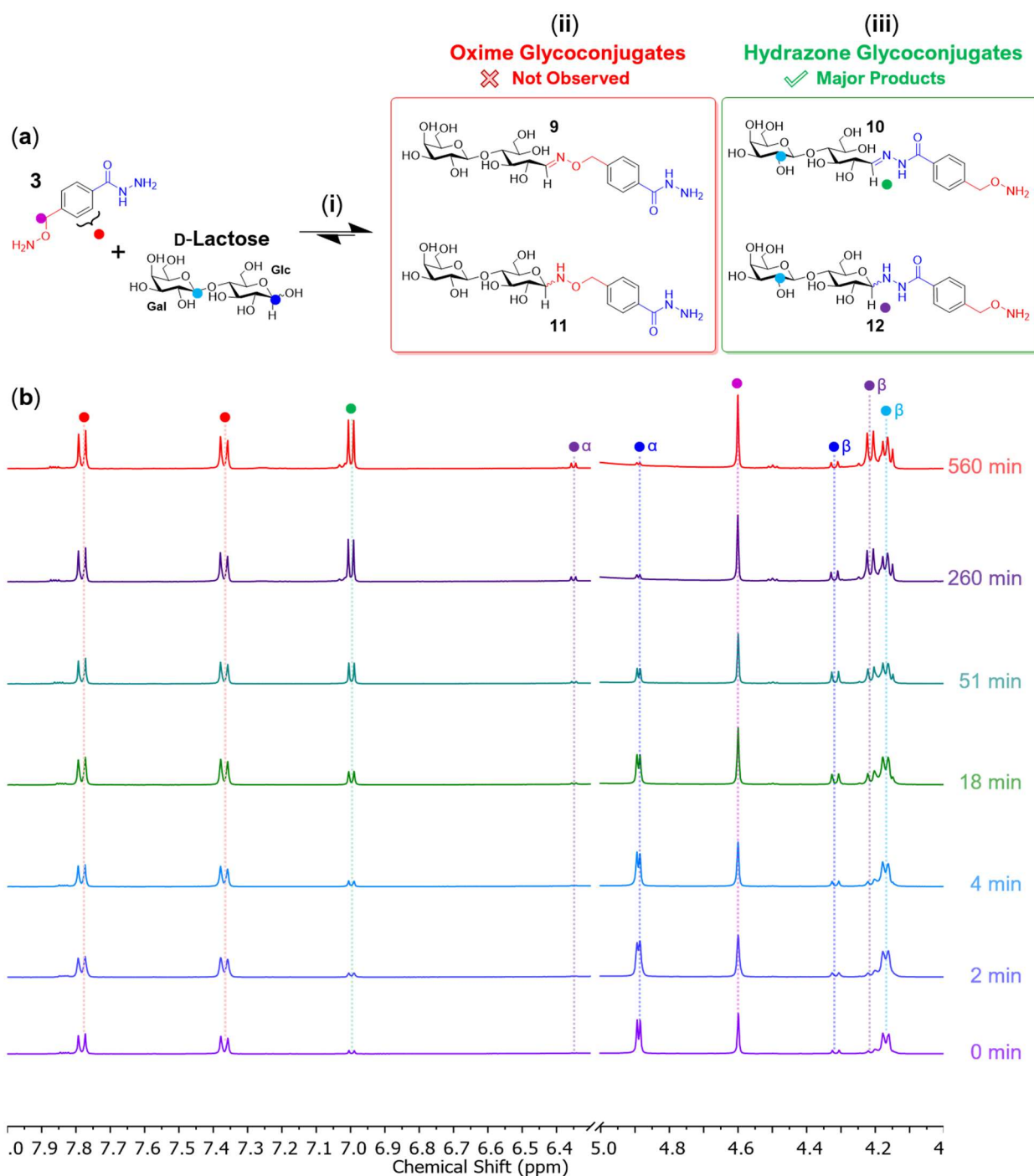


Figure 8: (a) Conjugation of linker **3** (94 mM) with D-Lactose (108 mM) was monitored by ^1H NMR spectroscopy. Disappearance of the 'diagnostic' α -anomeric ^1H NMR signal at δ 4.89 ppm was employed to follow the progress of the glycoconjugation reaction as a function of time. Step (i) was performed under conditions optimized for glycoconjugation. See Table 2, entry 8. (b) Partial ^1H NMR spectra (400 MHz, d_6 -DMSO) obtained during reaction of **3** with D-Lactose.

Reactions between carbohydrates and hydrazides are known to yield both acyclic (Fig. 9a) and cyclic (Fig. 9b) adducts. Acyclic hydrazide adducts are known to undergo ring-closure reactions⁷ in which OH5 attacks the hydrazone bond (Fig. 9a) to form cyclic hemiaminal species (b) such as **12** (Fig. 8a). ¹H NMR spectra (Fig. 8b) have provided evidence that **D-Lactose** reacts with linker **3** to yield a mixture of hydrazide adducts which may exist in a cyclic (**12**) and acyclic (**10**) form. The expected oxime product (**9**), however, was not isolated. These intriguing observations will later be rationalized on pag 159, but first the conjugation of linker **3** to **GM1os** must be discussed.

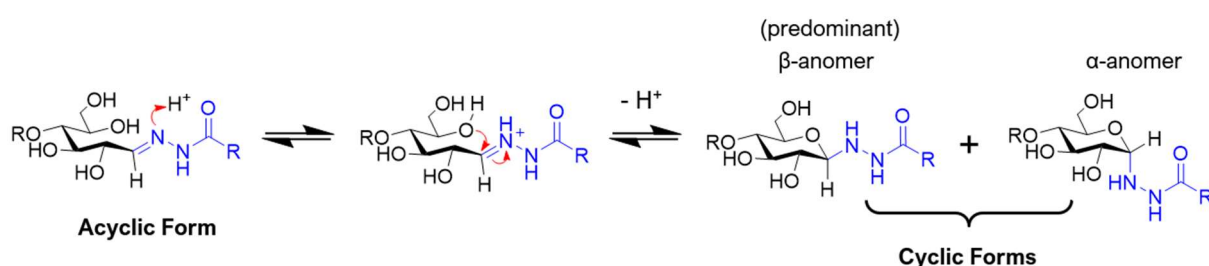


Figure 9: Carbohydrate-hydrazide adducts may exist as acyclic (i) or cyclic (ii) forms. Acyclic hydrazone form (i) converts into the cyclic form (ii) by ring closure reaction, in which OH5 attacks the hydrazone bond to afford predominantly the β -anomer.⁷

4.2.6. Glycoconjugation of Linker **3** to **GM1os**

GM1os was conjugated to linker **3** (Fig. 10a) under conditions determined to be optimal for glycoconjugation.^{‡‡} The conjugation reaction was monitored by ¹H NMR spectroscopy (Fig. 10b), where integral analysis of ‘diagnostic’ signals (δ 4.60 ppm, ●) associated with the **alkoxyamine end** of linker **3**, **GM1os** starting material (δ 4.89 ppm, ●), glycoconjugate products **13** (δ 6.90 ppm, ●) and **14** (δ 7.55 ppm, ●) were employed to monitor reaction progress. Reactions were monitored for T \geq 72 h.

^{‡‡} 108 mM carbohydrate, 94 mM linker **3** with 50 mM AcOH in *d*₆-DMSO, rt. Note that the linker : sugar stoichiometry of 1 : 1.15 equivalents was chosen as a precautionary measure to ensure that the ‘free’ linker molecule had been entirely consumed by reaction with carbohydrate. Residual linker molecules may directly react with and thus potentially crosslink the aldehyde polymer scaffold **P3**. An excess of carbohydrate ensures that oxime-linked glycoconjugate **4** contains negligible quantities of unreacted linker **3**, thus reducing risk of unwanted crosslinking.

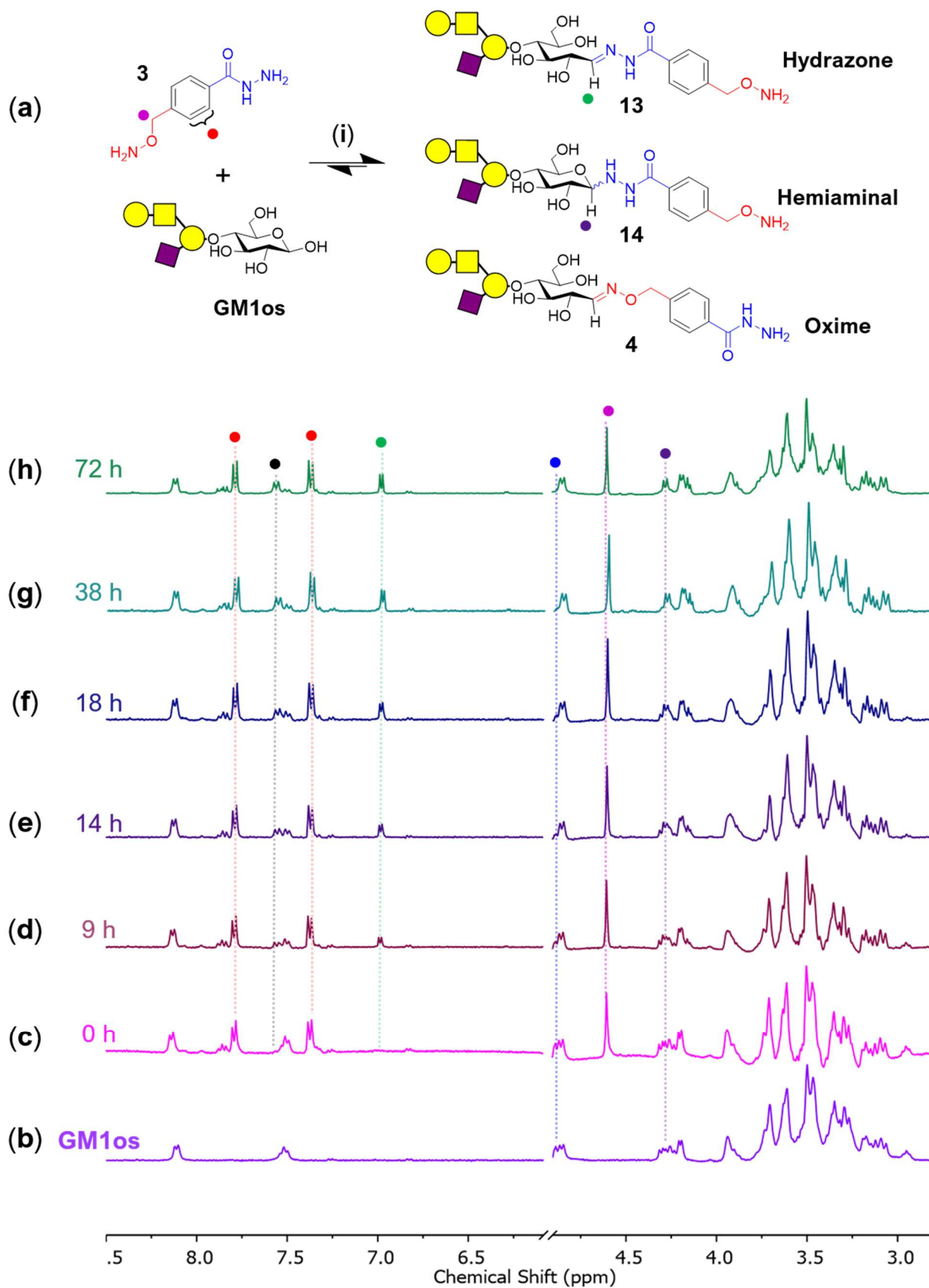


Figure 10: (a) Conjugation of linker **3** to **GM1os** may afford three possible products: Ring-opened hydrazone **13**, ring-closed hemiaminal **14** or the desired oxime product **4**. Partial ^1H NMR spectra (d_6 -DMSO, 400 MHz) of **GM1os** (b) and of **GM1os** during its reaction with linker **3**; reaction time 0 h (c), 9 h (d), 14 h (e), 18 h (f), 38 h (g) and 72 h (h)

Analysis of the ^1H NMR spectra (Fig. 10b-h) revealed that after reaction of linker **3** with **GM1os** (Fig. 10d) the 'free' **alkoxyamine end** of **3** (δ 4.60 ppm, ●) remained completely unreacted, indicating that the desired oxime conjugate **4** had not formed. However, the intensity of the **GM1os** anomeric signals at δ 4.85 (●, H1 α) and 4.25 ppm (●, H1 β) had radically decreased, almost disappearing from the spectrum obtained at $T > 72$ h (Fig. 10h), signifying that the carbohydrate reducing end had been almost entirely consumed. These observations, in conjunction with the new signals (Fig. 10d) which emerged at δ 6.90 ppm (●) and 7.55 ppm (●), were consistent with the formation of carbohydrate-hydrazide adducts (Fig. 10a) which may exist either as (i) a ring-opened hydrazone (**13**) or (ii) as a ring-closed hemiaminal (**14**). The formation of **13** and **14** was entirely consistent with the results obtained with **D-Lactose** (Fig. 8), but the isolation of these unexpected products lies in stark contrast with the hypothesis that oxime bonds are more thermodynamically stable than hydrazones.^{8b, 9a} Linker **3** displayed the expected chemoselectivity in control experiments with simple carbonyl compounds (acetone and benzaldehyde)(Fig. 6a), where oximes were observed as the majority products, whilst reactions with carbohydrate electrophiles (Figs. 10 and 11), **3** showed the opposite chemoselectivity, with hydrazone glycoconjugates being the major products. These conflicting but equally intriguing observations demonstrate that, despite both being carbonyl-containing electrophiles, carbohydrates demonstrate a very different reactivity to simple carbonyl compounds. Rationale for the observed differences in reactivity will now be discussed.

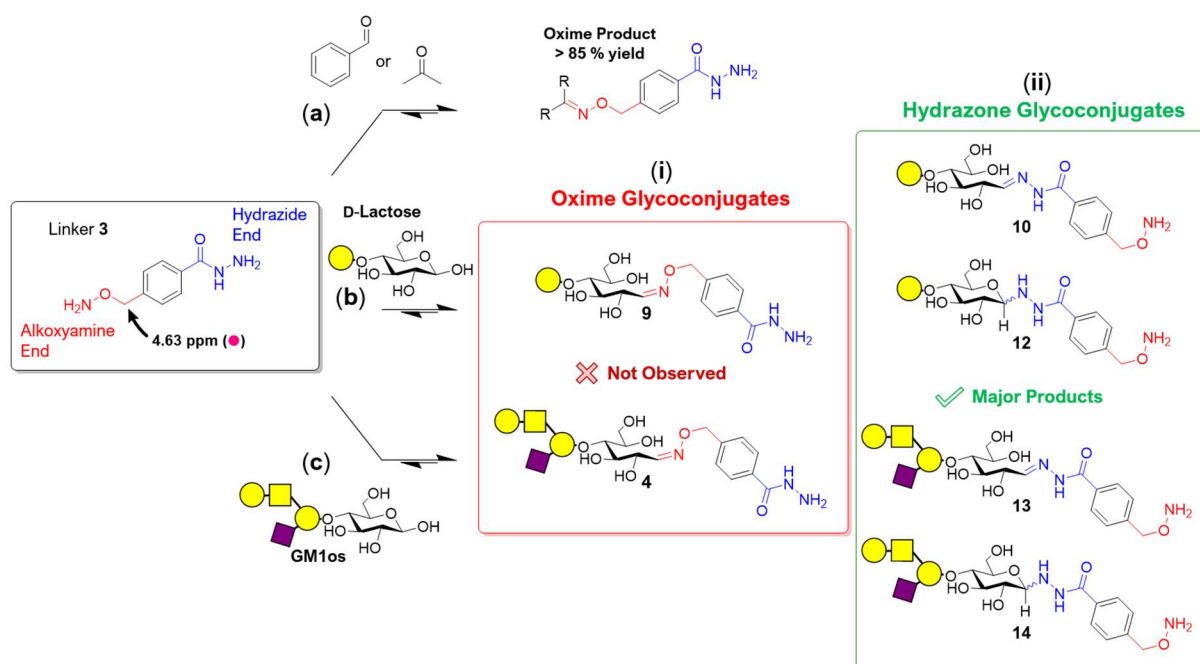


Figure 11: (a) Reaction of *bis*-functional linker **3** with acetone or benzaldehyde (a) rapidly afforded oxime product in > 75 % yields. In contrast, reaction of **3** with **D-Lactose** (b) or **GM1os** (c) both yielded 0 % oxime glycoconjugates (**9**, **4**), as evidenced by ^1H NMR studies (Fig. 8, 10) which showed no change in the integral of the 'diagnostic' signal at δ 4.60 ppm.

4.2.7. Rationalizing the Observed Chemoselectivity of Linker 3 with Carbohydrate Electrophiles

Nucleophilic attack of carbohydrate substrates by hydrazides will initially afford an acyclic hydrazone product (Fig. 12c). However, subsequent the ring-closure can occur in which OH5 attacks the hydrazone bond (see Fig. 9) to afford a cyclic aminal-like product. It is known that reactions between carbohydrates and substances containing **alkoxyamine** groups (Fig. 12a) generate acyclic products preferentially.⁷ In contrast, it has been reported that cyclic adducts (Fig. 12c) with β -configuration are produced predominantly in reactions of carbohydrates with **hydrazide** nucleophiles.¹⁰

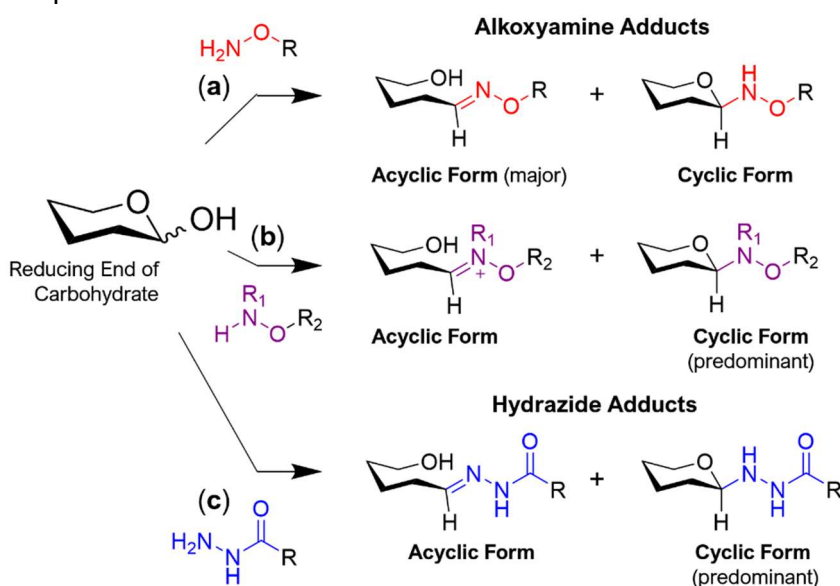


Figure 12: Adducts obtained from reactions of carbohydrates with (a) **alkoxyamine**, (b) **N-alkylated alkoxyamine** and (c) **hydrazide** groups.

Literature suggests that the cyclic forms of hydrazide-carbohydrate adducts (Fig. 12c) are more thermodynamically favourable than the corresponding acyclic forms.⁷ However, in the case of the alkoxyamine-carbohydrate adducts (Fig. 12a) the more favourable cyclic isomer is not always kinetically accessible, thus the less stable acyclic isomer is typically observed.^{7,10} In this chapter, it was thus hypothesized that carbohydrates react preferentially with the **hydrazide end** of linker 3 to form hydrazones, on account of ring-closure reactions (Fig. 9) which afford more thermodynamically stable cyclic forms of the carbohydrate. Although oxime bonds are typically more thermodynamically stable than hydrazones,^{8b} the ring-closure of hydrazide-carbohydrate adducts was hypothesized to bring additional stabilization of hydrazone-linked glycoconjugates which is simply not observed for the corresponding oxime conjugate. This hypothesis rationalizes why **GM1os** and **D-Lactose** reacted selectively with the **hydrazide end** of linker 3 to form hydrazone-linked glycoconjugates, leaving **alkoxyamine end** of 3 completely untouched. These observations have important consequences on the proposed synthesis of **GM1-SCPNs**, which will be later discussed on pages 162 – 163.

4.2.8. Functionalization of Aldehyde Polymer Scaffold with GM1-Linker Glycoconjugate

The 'free' **alkoxyamine end** of hydrazone-linked **GM1** glycoconjugates **13/14** were grafted onto aldehyde-functionalized copolymer **P3** (Fig. 13a) to afford carbohydrate-decorated scaffold **GM1-P3**. ^1H NMR spectroscopy (Fig. 13b-d) showed total disappearance of the 'diagnostic' **P3** aldehyde (δ 9.80 ppm) and alkoxyamine **3** (δ 4.60 ppm) signals, indicating complete functionalization of **P3** to afford **GM1**-grafted scaffold **GM1-P3**. **GM1-P3** was purified by aqueous dialysis to remove small molecule impurities including any unbound **GM1** conjugates **13/14**. After dialysis, the ^1H NMR spectrum of **GM1-P3** (Fig. 13d) revealed that **GM1** carbohydrate signals are still present, indicating that **GM1** was successfully immobilized onto the polymer scaffold. Although this strategy was successful in grafting **GM1** to the polymer backbone, the precise order in which the dynamic covalent bonds were assembled upon the polymer scaffold was incompatible with the proposed synthesis of **GM1-SCPNs**, for reasons which will now be discussed.

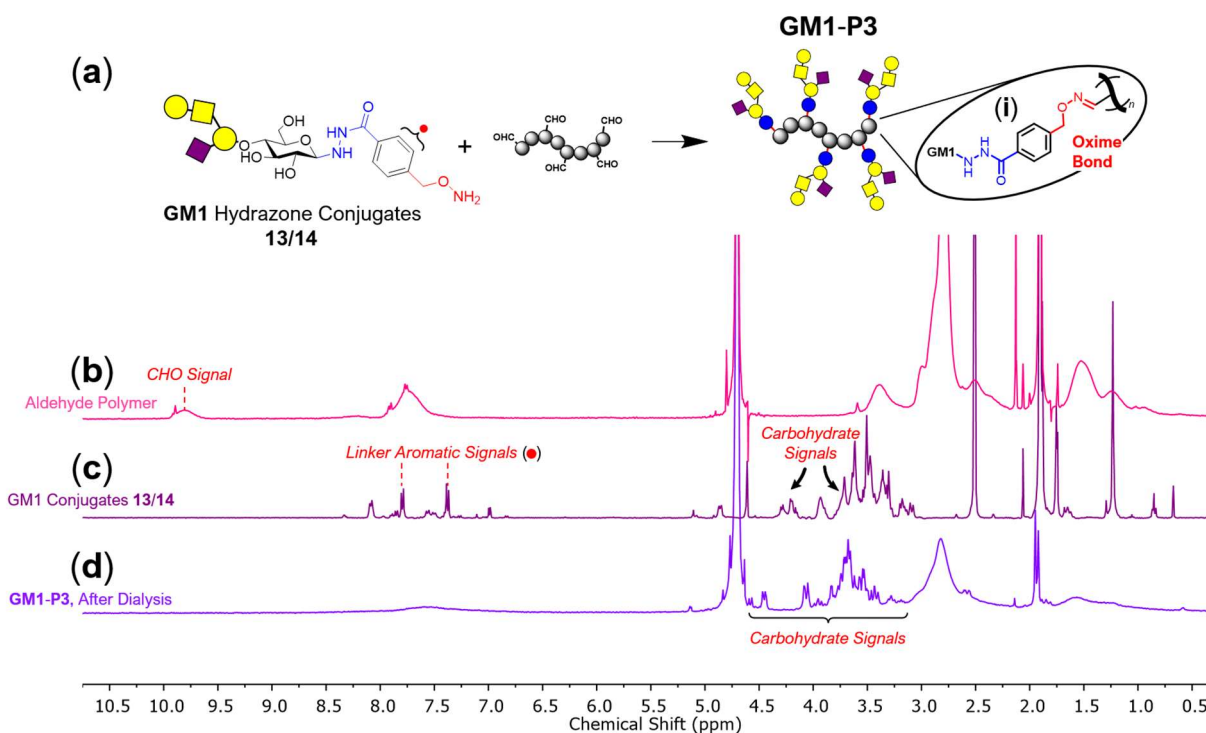


Figure 13: (a) **GM1** 'decorated' glycopolymer **GM1-P3** was prepared by grafting **GM1** hydrazone conjugates **13/14** onto aldehyde-functionalized polymer scaffold **P3**. **GM1-P3** is functionalized with oxime bonds (i), a covalent linkage which is not labile towards component exchange with hydrazide nucleophiles. (b-d) Partial ^1H NMR spectra of (b) aldehyde polymer **P3** (D_2O , 300 MHz), (c) **GM1** hydrazone conjugates **13/14** (d_6 -DMSO, 300 MHz) and (d) **GM1-P3** after dialysis (D_2O , 300 MHz).

4.2.9. Barriers to the Preparation of GM1-SCPNs

The proposed synthesis (Fig. 14a-c) of **GM1-SCPNs** required the glycopolymer scaffold to be entirely functionalized with dynamic covalent acyl hydrazone linkages.^{§§} In the above case, however, **GM1-P3** was functionalized through oxime bonds on account of grafting **P3** with **alkoxyamine**-displaying **GM1** conjugate **4** (Fig. 14d). Whilst oximes are sometimes considered a dynamic covalent bond,¹¹ these linkages are generally not labile towards component exchange with hydrazide nucleophiles (Fig. 14e).^{8b} Thus, it was expected that crosslinking of **GM1-P3** with succinic dihydrazide would be unsuccessful and ‘dynamic’ **GM1-SCPNs** may not be isolated from this synthetic route. The exact rationalization as to why **GM1-SCPNs** could not be directly synthesized from hydrazone-linked **GM1**-conjugates **13/14** is summarized schematically within Figure 14.

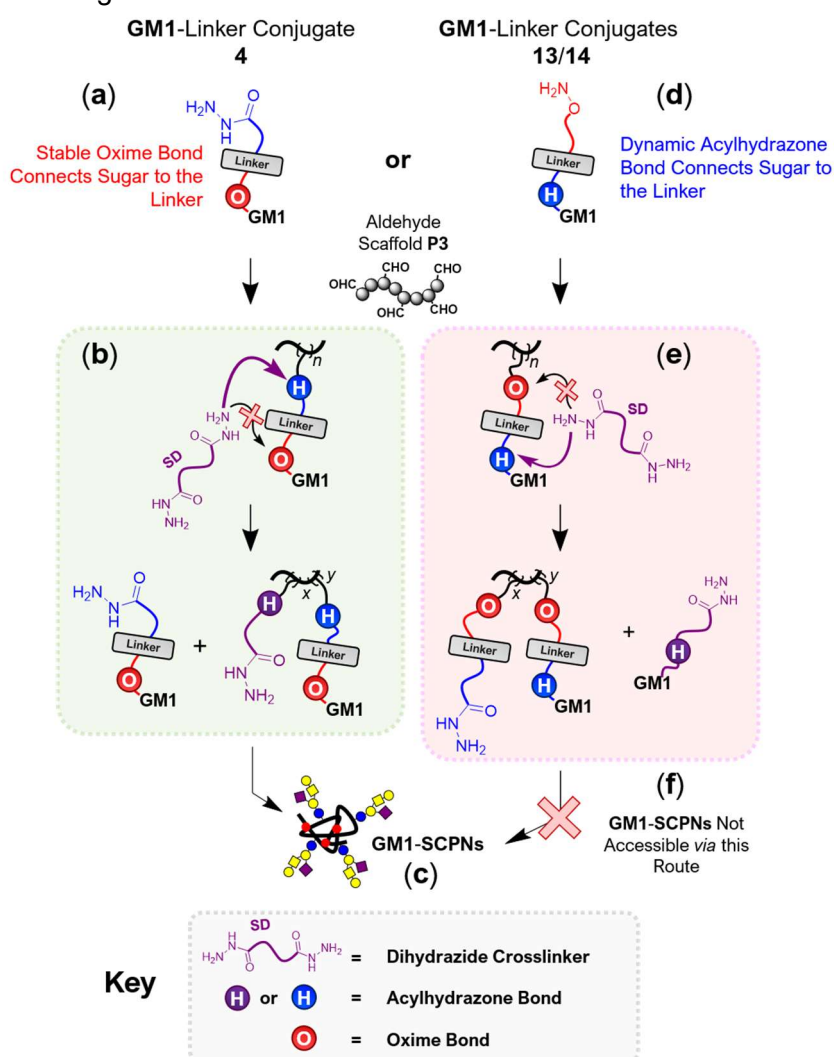


Figure 14: The precise order of connectivity of stable (oxime) and dynamic (acyl hydrazone) covalent bonds upon the glycopolymer scaffold determines whether **GM1-SCPNs** can be successfully synthesized. (a-c) Proposed synthetic strategy for the preparation of **GM1-SCPNs**. (d-f) An unsuccessful synthetic route to **GM1-SCPNs**.

^{§§} This feature was a crucial requirement for obtaining **GM1-SCPNs** which are capable of ‘shrink-wrapping’, as this process depends upon the component exchange of ‘dynamic’ acyl hydrazone crosslinkers to facilitate ‘structural metamorphosis’ of **SCPNs** into intermolecularly crosslinked polymer films

The precise order of connectivity of stable (oxime) and dynamic (acyl hydrazone) covalent bonds upon the glycopolymer scaffold predetermines whether **GM1-SCPNS** can be successfully synthesized or not by a given synthetic route. Figure 14a-c shows the proposed synthetic route to **GM1-SCPNS** (*Route A*). Here, the **GM1** sugar moiety is connected to linker molecule *via* a stable oxime linkage, leaving a pendant hydrazide group. The ‘free’ hydrazide of linker-**GM1** conjugate **4** might then react with aldehyde polymer scaffold **P3**, affording a hydrazone-functionalized polymer scaffold that is grafted with pendant carbohydrate (**GM1**) residues. Intramolecular crosslinking of this glycopolymer is initiated by addition of crosslinker (**SD**), which is anticipated to attack the dynamic covalent acyl hydrazone linkage in preference to the thermodynamically stable oxime bond (Fig. 14b). As a result, the crosslinker residue is incorporated onto the glycopolymer scaffold, and a single **GM1**-linker molecule is displaced through the process of hydrazone exchange. Under high dilution, the embedded crosslinker residue (purple) will undergo further hydrazone exchange reactions to yield the desired **GM1**-functionalized SCPNs (**GM1-SCPNS**) (Fig. 14c).

Figure 14d-f shows a synthetic route to **GM1-SCPNS** (*Route B*), which was explored on account of linker **3** reacting with **GM1os** to form predominantly the hydrazone-linked glycoconjugates **13/14**. This route is very similar to *Route A* (Fig. 14a-c), except that **GM1** is now attached to the linker *via* a dynamic covalent acyl hydrazone linkage (Fig. 14e), leaving a pendant alkoxyamine free to be grafted onto the aldehyde functionalized polymer scaffold **P3**. This subtle discrepancy between the two synthetic routes has a drastic knock-on effect, which results in the failure of *Route B* to yield structurally dynamic **GM1-SCPNS**. Briefly, grafting of the ‘free’ alkoxyamine of **GM1** conjugates **13/14** (Fig. 14d) onto **P3** was undertaken and is hypothesized to result in an oxime-functionalized glycopolymer scaffold (Fig. 14e). Addition of **SD** was then hypothesized to undergo nucleophilic attack at the dynamic covalent acyl hydrazone in preference to the stable oxime linkage (Fig. 14e). **SD** attacks the electrophilic carbohydrate (**GM1**) component of this hydrazone bond, thus hydrazone exchange results in the displacement of a single **GM1**-crosslinker conjugate from the glycopolymer scaffold. Although further hydrazone exchange reactions are possible, none of these processes lead to intramolecular crosslinking, and thus **GM1-SCPNS** cannot be synthesized by this route (Fig. 14f). An alternative synthetic strategy (Fig. 15) will now be discussed, which was employed to facilitate the successful synthesis of **GM1-SCPNS** *via* the oxime-linked **GM1** conjugate **4** (Fig. 14a-c).

4.2.10. An Alternative Synthetic Route to GM1-SCPNs

To address the observed issue with the chemoselectivity of linker **3**, an alternative linker **18** which features a **Boc-protected hydrazide** moiety was prepared (Fig. 15a). It was anticipated that Boc-protection would prevent the **hydrazide end** from reacting with carbohydrates, thus oxime-linked **GM1** conjugate **4** (Fig. 16c) is expected in place of the previously observed hydrazone conjugates **13/14** (see Fig. 14b).

Boc-linker **18** was prepared (Fig. 15a) in three steps. In step (i), nucleophilic attack upon acid chloride **15** by *tert*-butyl carbazate afforded intermediate **16**. In step (ii) **16** was furnished with a pendant *N*-hydroxyphthalimide moiety to yield intermediate **17**. Hydrazinolysis of **17** then afforded the final compound, Boc-linker **18**, which was isolated as a white solid (43 % yield). ^1H NMR spectroscopic analysis of **18** (Fig. 15b) was consistent with the proposed structure. The ^1H NMR (Fig. 15b) spectrum showed two secondary amide *NH* (br, s) signals and the characteristic Boc methyl peak (9H, s) at δ 1.45 ppm, thus confirming the presence of the Boc-protected hydrazide group. The chemoselectivity of Boc-linker **18** towards carbonyl compounds (benzaldehyde and acetone) was verified ^1H NMR studies, revealing identical results to those observed for linker **3**.

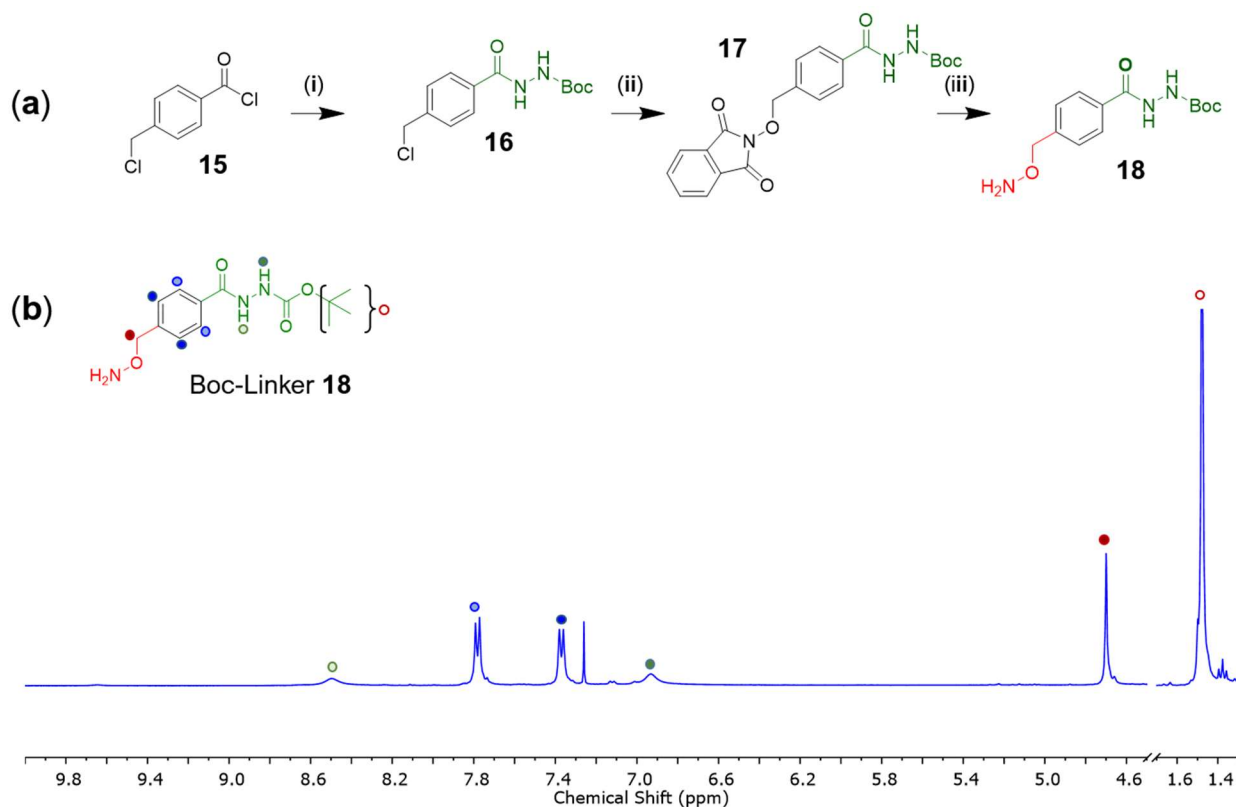


Figure 15: (a) Synthesis of Boc-linker **18**. Step (i): *tert*-butyl carbazate, DIPEA, CH_2Cl_2 , 18 h, rt. Step (ii): DMF, reflux, 18 h. Step (iii): $\text{N}_2\text{H}_4 \cdot \text{H}_2\text{O}/\text{EtOH}$, 4 h, rt. (b) Partial ^1H NMR spectrum (CDCl_3 , 300 MHz) of Boc-linker **18** with structural assignments shown.

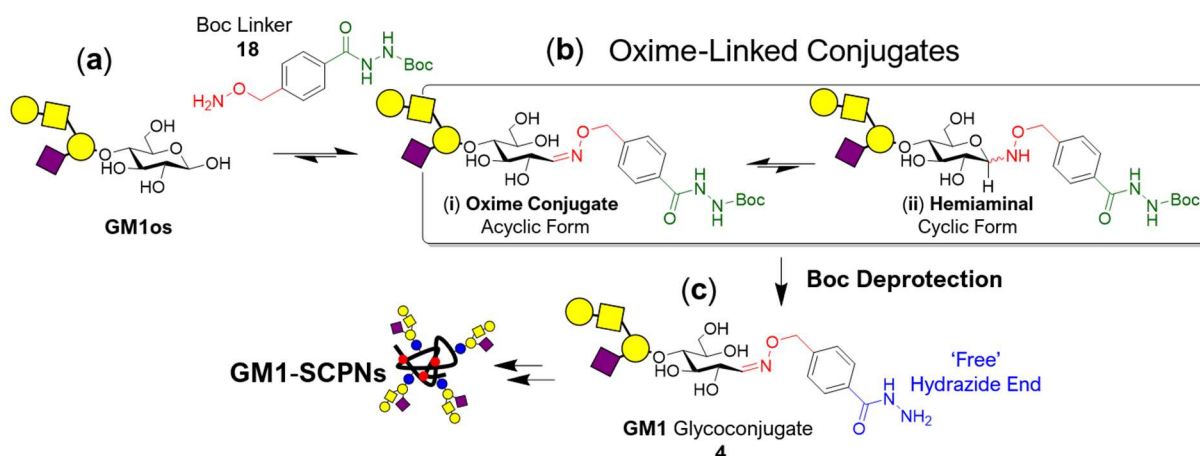


Figure 16: An alternative synthetic route towards **GM1-SCPNs**. It was hypothesized that oxime ligation (a) of **GM1os** with Boc-linker **18** would permit the selective formation (b) of oxime-linked conjugates (i) and (ii). It was expected that Boc-deprotection (c) would yield oxime glycoconjugate **4** which possesses a 'free' hydrazide moiety for grafting onto aldehyde-functionalized polymer scaffolds, thus allowing hydrazone-functionalized **GM1-SCPNs** to be successfully prepared.

4.2.11. Glycoconjugation of Boc-Linker 18 to D-Lactose

Reaction of **D-Lactose** with Boc-linker **18** (Fig. 17a) was performed in 50 mM AcOH/*d*₆-DMSO and monitored by ¹H NMR spectroscopy (Fig. 17b-d). Integral analysis of ¹H NMR spectra (Fig. 17b-d) revealed that anomeric signals of **D-Lactose** starting material at δ 4.85 (●, H1α) and 4.25 ppm (●, H1β) were not consumed and the 'diagnostic' alkoxyamine signal at δ 4.60 ppm (●) remained unchanged over the 72 h period during which reaction monitoring took place. It was thus concluded that although 'free' alkoxyamine end is the only available nucleophile, Boc-linker **18** does not react with carbohydrate electrophiles, suggesting that either (i) formation of oxime conjugate **9** was not a thermodynamically favourable product, or (ii) there is a kinetic barrier preventing oxime formation between the alkoxyamine end of **18** and **D-Lactose**. It has been reported that the conjugation of primary alkoxyamines (such as linkers **3** and **18**) to the reducing end of carbohydrates can be low yielding in the case of some carbohydrates.⁷ One study has demonstrated that reactions of carbohydrates with *N*-alkylated alkoxyamine groups (Fig. 12b) afford predominantly stable cyclic hemiaminal adducts, which are anticipated to improve the yield of oxime ligation. These studies suggest that oxime linked **GM1** conjugates (Fig. 17a, **9**) cannot be easily accessed by reactions of primary alkoxyamine linkers (**3**, **18**) with **GM1os**. Although investigations towards the 'shrink-wrapping' of **SV40** viral capsids were progressing well, issues with linker chemoselectivity and time constraints forced the premature termination of experimental work.

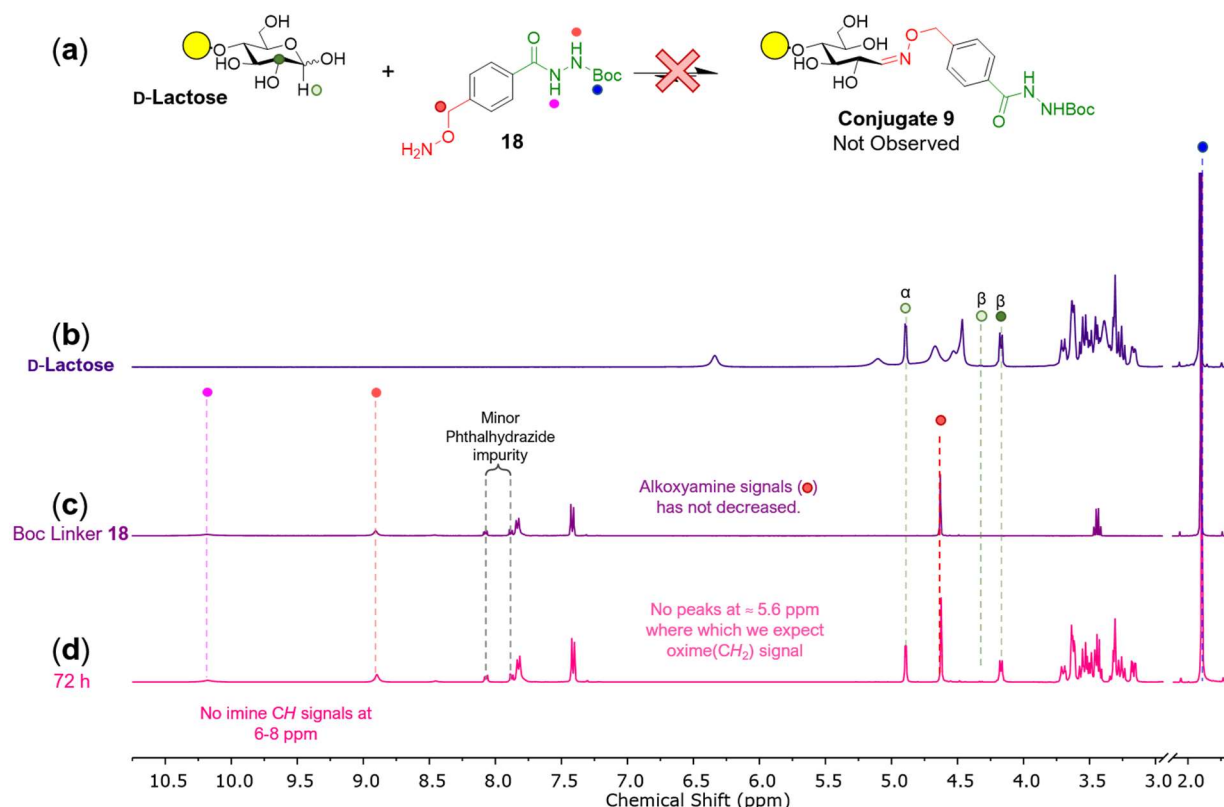


Figure 17: (a) Glycoconjugation of Boc-linker **18** to **D-Lactose**. (b-d) Partial ¹H NMR spectra (*d*₆-DMSO, 400 MHz) of **D-Lactose** (b), Boc-linker **18** (c) starting materials and their reaction after 72 h (d). The formation of the anticipated oxime conjugate **9**, was not observed

In summary, three synthetic strategies for the preparation of **GM1-SCPNs** have been explored and good progress has been made towards this goal. **GM1os** was successfully functionalized with linker **3**, and this glycoconjugate (**13/14**) was then grafted onto polymer scaffolds to afford **GM1**-decorated glycopolymers. Crucially, the ‘shrink-wrapping’ project required precise ordering of acyl hydrazone (dynamic) and stable oxime (non-dynamic) linkages within the SCPN architecture, and thus this synthetic route was ultimately not achieved within the time available. Alternative synthetic routes will be required to grant access to the desired **GM1-SCPN** architecture, and these will now be proposed in the research outlook.

4.2.12. Future Work

Thorough review of the literature in conjunction with results reported in this chapter has revealed two alternative synthetic strategies from which **GM1-SCPNs** may be constructed, and these will now be discussed.

1. Oxime ligation with a Secondary Alkoxyamine Linker

The *N*-alkyl (**R**) group of **19** is anticipated to significantly increase the yield of oxime ligation by facilitating formation of the stable cyclic isomer.⁷ It is thus hypothesized that linker **19** will undergo more efficient oxime ligation than did linker **18**, thereby allowing **GM1** conjugate **20** to be isolated. In this strategy, the hydrazide end should remain Boc-protected to prevent unwanted competing reactions that lead to hydrazide-carbohydrate adducts.

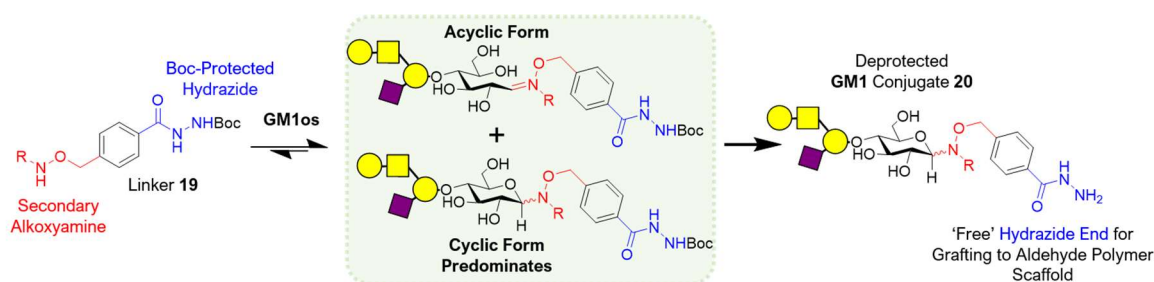


Figure 18: Proposed synthesis of oxime-linked **GM1** conjugate **20** from which **GM1-SCPNs** can be prepared. Oxime ligation of secondary alkoxyamine nucleophiles, such as linker **3** are known¹⁰ to afford carbohydrate conjugates with reasonable yields. The presence of an alkyl substituent (**R**) upon nucleophilic nitrogen N¹ favours the formation of the thermodynamically favourable cyclic form of the oxime-linked glycoconjugate.⁷ It is thus anticipated that secondary alkoxyamine linker **19** affords **GM1** conjugate **20** with improved yields (relative to linker **3**), such that **GM1-SCPNs** can successfully be prepared.

2. Thioglycoside Formation

The synthetic strategies discussed in this chapter utilized *bis*-functional alkoxyamine/hydrazide and relied on oxime formation to attach **GM1** onto linker molecules. Oxime ligation was surprisingly low yielding, and thus an alternative covalent linkage should be considered between the linker and **GM1** carbohydrate molecules. Thioglycoside formation (Fig. 19) at the reducing end of carbohydrates has become a popular glycoconjugation strategy, as this chemistry can be performed on unmodified carbohydrates in aqueous solution under mild conditions, and this would be an ideal approach to derivatize **GM1** with the required acyl hydrazide.

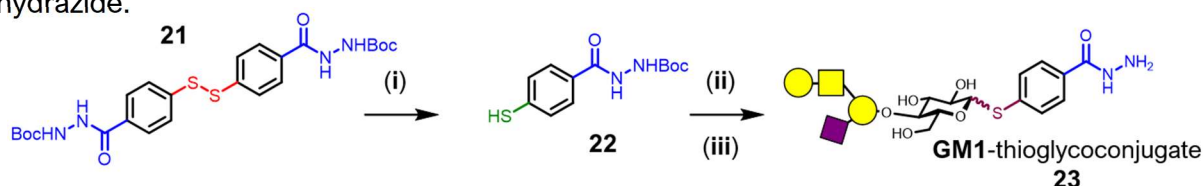


Figure 19: Proposed synthesis of **GM1**-thioglycoconjugate **24**. Step (i): Disulfide cleavage of **22** to yield the thiol-containing linker **23**. Conditions: Tris(2-carboxyethyl)phosphine (**TCEP**), 4.5:1.0 H₂O/MeCN, rt, 4 h. Step (ii): Thioglycoside formation. Conditions: **GM1os**, 2-chloroimidazolium chloride (**DMC**), 4.5:1.0 H₂O/MeCN, rt, 18 h. Step (iii): Deprotection of Boc-hydrazide. 100 °C, 2 h.

4.3. Conclusion

The 'shrink-wrapping' of **SV40** capsid through complementary recognition events requires SCPNs that are decorated with complex carbohydrate appendages of **GM1**, the native ligand which binds selectively to sialic acid receptors located upon the virus surface. This chapter explored three synthetic routes to **GM1-SCPNs** in which the reducing end of **GM1os** was functionalized with a linker molecule (**3**) and then grafted onto aldehyde polymer scaffolds *via* oxime or hydrazone linkages. The synthesis of a *bis*-functional alkoxyamine / hydrazide linker (**3**) was reported and its chemoselectivity towards both carbonyl and carbohydrate electrophiles was interrogated by ¹H NMR spectroscopy. As anticipated, carbonyls such as acetone and benzaldehyde reacted with a strong preference for the alkoxyamine end of linker **3** and formation of the corresponding oxime products was essentially quantitative within several hours. Surprisingly, linker **3** displayed the opposite chemoselectivity with carbohydrate electrophiles **D-Lactose** and **GM1os**, preferring to react through its hydrazide end to form the corresponding carbohydrate-hydrazide adducts. Upon exposure to **GM1os**, linker **3** afforded acyl hydrazone (**13**) and hemiaminal (**14**) adducts, but not the anticipated oxime conjugate (**4**).

A rationale for these intriguing observations was proposed by comparison of experimental results to existing literature reports.^{7,10} Although oximes are widely accepted to be more thermodynamically stable than hydrazones,⁸ the results in this chapter demonstrate that such predictions do not always hold true and cannot be applied when considering reactions upon complex carbohydrate electrophiles such as **GM1os**. Carbohydrate-hydrazide adducts are known to undergo ring-closure reactions to afford cyclic hemiaminal species which are more thermodynamically stable than the corresponding acyclic hydrazone form.⁷ In contrast, carbohydrate-alkoxyamine adducts are reported to exist predominantly as the acyclic oxime form, with the trace quantities of the cyclic hemiaminal form.¹⁰ It was thus hypothesized that carbohydrate-hydrazide (predominantly cyclic) adducts are more energetically stable than the corresponding oxime (predominantly acyclic) glycoconjugates, on account of the additional thermodynamic stability which is introduced by the ring-closure reaction that may occur for carbohydrate-hydrazide adducts. This hypothesis was consistent with the observation that linker **3** prefers to react with carbohydrate electrophiles through its hydrazide end to yield the corresponding hemiaminal (cyclic) and acyl hydrazone (acyclic) products in preference to forming the oxime (acyclic) glycoconjugate. Although functionalization of **GM1os** with linker **3** afforded predominantly acyl hydrazone (**13**) and hemiaminal (**14**) adducts, the decision was made to persist with the preparation of **GM1-SCPNs** by grafting these glycoconjugates onto the aldehyde-functionalized polymer scaffold (**P3**). ¹H NMR spectroscopy revealed that grafting was successful, with polymers displaying characteristic **GM1** carbohydrate signals after

purification by dialysis. Attempts to intramolecularly crosslink these polymer scaffolds were, however, unsuccessful on account of the dihydrazide crosslinker (**SD**) being unable to displace the stable oxime linkages by which the **GM1** glycoconjugates were connected to the polymer scaffold.

An alternative synthetic route to **GM1-SCPNS** was explored to assess if carbohydrates can be selectively conjugated to linker molecule through oxime linkages. Judicious attempts were made to isolate the model oxime glycoconjugate (**9**) by functionalizing **D-Lactose** with linker **18**, where the **hydrazide end** is Boc-protected to prevent formation of carbohydrate-hydrazide adducts. However, attempts to isolate oxime **9** were unsuccessful, despite linker **18** **alkoxyamine end** being the only nucleophilic site available to react with **GM1os**. These observations were consistent with literature reports^{7,10} that oxime ligation of primary alkoxyamines to carbohydrate electrophiles are occasionally low-yielding and can be highly dependent on the nature of the carbohydrate employed. Future work looks to build upon this work and further the synthesis of **GM1-SCPNS** *via* the strategies proposed on page 167.

4.4. Experimental

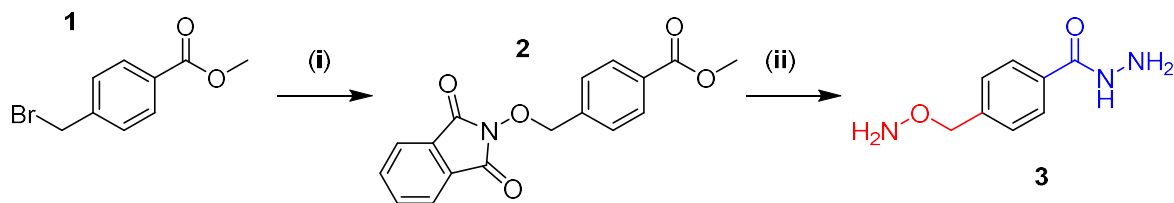
4.4.1. General Experimental

All chemicals were purchased from Sigma-Aldrich, Alfa Aesar, Fisher Scientific or Carbosynth UK (**GM1 ganglioside**) and were used as received without further purification. All solvents were dried prior to use according to standard methods. All solvents used for flash chromatography were GPR grade, except hexane and ethyl acetate, when HPLC grade was used. Unless stated otherwise, all synthetic procedures were performed in oven-dried glassware under a N₂ (g) atmosphere. Simian virus 40 (**SV40**) major capsid protein **VP1** and the enzyme ECGase II were produced by recombinant expression from *E. Coli* and purified by the laboratory of Prof. Bruce Turnbull, University of Leeds. Assembly of the **SV40** capsid was achieved by dialysis against ammonium sulfate to induce molecular crowding of **VP1** pentamers. ¹H and ¹³C NMR spectra of synthesised compounds were recorded on a Bruker Avance 300 spectrometer (at 300 and 75 MHz respectively), Bruker Avance 400 spectrometer (at 400 MHz and 100 MHz, respectively), Bruker Avance III HD spectrometer (at 500 MHz and 125 MHz, respectively), or Bruker 700 Avance III HD spectrometer (at 700 MHz and 175 MHz, respectively). High-resolution mass spectrometry was performed on a Waters LCT Premier mass spectrometer^a

4.4.2. Preparation of GM1os

GM1os was prepared with slight modification of the published literature protocol.⁹ **GM1 ganglioside** (500 mg, 319 μmol) and BSA (10 mg) were dissolved in 25 mM NH₄OAc, pH 5.0, 0.2 % Triton X (45 mL). ECGase II (1.3 mL at 67 μM in 20 mM Na₂HPO₄, pH 7.0, 500 mM NaCl) was added. The solution was split into 450 μL aliquots and incubated at 37 °C for 25 days, after which the reaction was judged complete by TLC (product spot *R_f* = 0.1 in 6:2:1 CHCl₃:MeOH:H₂O, with H₂SO₄/MeOH TLC stain). The solutions were combined and washed with Et₂O (4 x 15 mL). The combined aqueous fraction was diluted with H₂O (10 mL), passed through a 0.45 μm syringe filter, then loaded onto a C18 solid phase extraction cartridge and eluted with H₂O. Fractions containing **GM1os** were combined and twice lyophilised from H₂O, yielding **GM1os** as a white solid (253.5 mg, 249 μmol, 78% yield). The product was used without further purification. ¹H NMR (D₂O, 700 MHz) δ (ppm): 5.22 (d, 1H, α-anomer, *J*₃ = 3.78 Hz), 4.66 (d, 1H, β-anomer, *J*₃ = 7.98 Hz), 4.54 (t, 1H, *J*₃ = 7.49 Hz), 4.12-4.18 (m, 2H), 4.04 (t, 1H, *J*₃ = 14.0 Hz), 3.55-4.00 (complex m, carbohydrate ring H's, 25H), 3.47-3.54 (2 x d, 2H), 3.29 (t, 1H, *J*₃ = 9.03 Hz), 2.03 (s, 3H), 2.01 (s, 3H), 1.91 (s, 3H).

4.4.3. Preparation of Linker 3



Scheme 1: Synthesis of linker (**3**). (i) *N*-hydroxyphthalimide, DIPEA, CH₂Cl₂, 18 h, rt. (ii) N₂H₄·H₂O/EtOH, 4 h, rt.

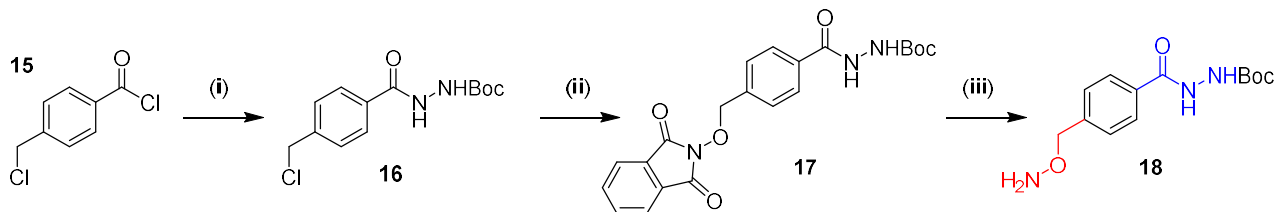
Synthesis of Methyl 4-(((1,3-dioxoisindolin-2-yl)oxy)methyl)benzoate (**2**):

Methyl 4-(bromomethyl)benzoate **1** (4.85 g, 21.2 mmol) was dissolved in CH₂Cl₂ (90 mL) and DIPEA (5.44 g, 42.1 mmol) added afford a clear red solution. *N*-hydroxyphthalimide (4.50 g, 27.7 mmol) was added and the suspension was stirred under nitrogen for 18 h. The reaction was judged complete by TLC (product *R_f* ≈ 0.4, CH₂Cl₂), then washed with H₂O (4 x 50 mL) and the organic phase was dried over MgSO₄, filtered, and then evaporated to dryness. The product was obtained as a white solid (4.23 g, 65 % yield) and used without further purification. ¹H NMR (CDCl₃, 300 MHz) δ (ppm): 8.03 (d, 2H, aromatic, *J*₃ = 8.13 Hz), 7.79 (m, 2H, aromatic), 7.73 (m, 2H, aromatic), 7.61 (d, 2H, aromatic, *J*₃ = 8.13 Hz), 5.25 (s, 2H, -HN-O-CH₂-Ar), 3.90 (s, 3H, -O-CH₃), ¹³C NMR (75 MHz, CDCl₃) δ (ppm): 166.65, 163.39, 138.59, 134.55, 130.87, 129.79, 129.46, 128.78, 123.59, 79.04, 52.21.

Synthesis of 4-((Aminooxy)methyl)benzohydrazide (**3**):

Methyl 4-(((1,3-dioxoisindolin-2-yl)oxy)methyl)benzoate **2** (713 mg, 2.35 mmol) was dissolved in EtOH (5 mL) and hydrazine monohydrate (1.0 mL, 20 mmol) was added. The solution was stirred at rt for 18 h, and the reaction was judged complete by TLC (product *R_f* ≈ 0.65, 1:1 MeOH/CH₂Cl₂, red by ninhydrin stain). The phthalhydrazide by-product formed a white precipitate from EtOH and was removed by filtration. Residual hydrazine was removed by exhaustively drying the sample for 12 h under high vacuum. The product was judged pure by TLC and ¹H NMR spectroscopy, then twice lyophilized to afford the pure product as a white solid (405 mg, 95 % yield). ¹H NMR (*d*₆-DMSO, 300 MHz) δ (ppm): 9.74 (broad s, 1H, NH), 7.80 (d, 2H, aromatic, *J*₃ = 8.40 Hz), 7.38 (d, 2H, aromatic, *J*₃ = 8.40 Hz), 4.61 (s, 2H, H₂N-O-CH₂-Ar). ¹³C NMR (75 MHz, *d*₆-DMSO) δ (ppm): 166.19, 156.12, 142.05, 132.46, 127.96, 76.70.

4.4.4. Preparation of Boc-Hydrazide Linker 18



Scheme 1: Synthesis of Boc-linker (**18**). **Step (i):** *tert*-Butyl carbazate, DIPEA, CH₂Cl₂, 18 h, rt. **Step (ii)** DMF, reflux, 18 h. **Step (iii):** N₂H₄·H₂O/EtOH, 4 h, rt.

Synthesis of *tert*-butyl 2-(4-(chloromethyl)benzoyl)hydrazine-1-carboxylate (**16**):

tert-Butyl carbazate (4.80 g, 36.3 mmol) and Et₃N (3.93 g, 30.3 mmol) were dissolved in CH₂Cl₂ (100 mL) and stirred under N₂ atmosphere at 0 °C for 10 min. 4-(chloromethyl)benzoyl chloride **15** (5.72 g, 30.27 mmol) was dissolved in CH₂Cl₂ (50 mL), then added dropwise to the ice-cold mixture over 2 h. The reaction was then allowed to gently warm to rt, with overnight stirring. Product formation was confirmed by TLC (product *R_f* = 0.42, 20 : 1 CH₂Cl₂ / MeOH). The reaction mixture was washed with water (3 x 75 mL) and the organic extract dried over MgSO₄, filtered, and evaporated to afford the crude product as a white solid. The product was further purified by precipitation, by dissolving the crude in a minimum volume of hot EtOAc and adding dropwise to ice-cold hexane (400 mL). The product was isolated by filtration as a white solid (6.57 g, 76 % yield). ¹H NMR (CDCl₃, 300 MHz) δ (ppm): 8.50 (br s, 1H, NH), 7.72 (d, 2H, aromatic, *J*₃ = 8.1 Hz), 7.34 (d, 2H, aromatic, *J*₃ = 8.1 Hz), 6.77 (br s, 1H, NH), 4.51 (s, 2H, -HN-O-CH₂-Ar), 1.42 (s, 9H, O-C(CH₃)₃). ¹³C NMR (75 MHz, CDCl₃) δ (ppm): 166.22, 155.94, 146.19, 141.54, 128.75, 127.75, 82.18, 45.28, 28.17

Synthesis of *tert*-butyl 2-(4-(((1,3-dioxoisindolin-2-yl)oxy)methyl)benzoyl)hydrazine-1-carboxylate (**17**):

tert-Butyl 2-(4-(chloromethyl)benzoyl)hydrazine-1-carboxylate **16** (1.30 g, 4.55 mmol), *N*-hydroxyphthalimide (840.5 mg, 5.15 mmol), Na₂CO₃ (766.5 mg, 5.55 mmol) and NaI (78.5 mg, 0.50 mmol) were dissolved in DMF (40 mL) and heated at 80 °C for 48 h. Product formation was confirmed by TLC (product *R_f* = 0.75, 12 : 1 CH₂Cl₂ / MeOH). The reaction mixture was diluted with EtOAc (100 mL) and the organic layer was washed with distilled H₂O (5 x 75 mL) to ensure all residual DMF and *N*-hydroxyphthalimide was removed. The organic extract was dried over MgSO₄, filtered, and then evaporated to afford the crude product as a clearly colourless oil, which quickly crystallized into a white solid (819 mg, 64 % yield). ¹H NMR (CDCl₃, 300 MHz) δ (ppm): 8.10 (br s, 1H, NH), 7.85 – 7.69 (m, 6H, Ar), 7.60 (d, 2H, Ar, *J*₃ = 7.8 Hz), 6.76 (br s, 1H, NH), 5.25 (s, 2H, R₂N-O-CH₂-Ar), 1.49 (s, 9H, O-C(CH₃)₃). ¹³C NMR (75 MHz, CDCl₃) δ (ppm): 165.36, 164.98, 150.18, 143.54, 138.01, 134.56, 129.85, 128.79, 127.48, 123.62, 82.12, 78.91, 28.15.

tert-Butyl 2-(4-((aminooxy)methyl)benzoyl)hydrazine-1-carboxylate (**18**):

tert-Butyl 2-(4-(((1,3-dioxoisindolin-2-yl)oxy)methyl)benzoyl)hydrazine-1-carboxylate **17** (521.0 mg, 1.27 mmol) and hydrazine monohydrate (126.9 mg, 2.53 mmol) were dissolved in EtOH (7.5 mL) and stirred at rt overnight. Product formation was confirmed by TLC (product R_f = 0.60, 16 : 1 CH₂Cl₂ / MeOH), white precipitate (phthalhydrazide) was removed by filtration and reaction was evaporated to dryness. The crude residue was evaporated under high vacuum to ensure residual hydrazine was removed. The product was further purified to remove residual phthalhydrazide by precipitation from EtOH. The product was isolated by as a white solid (356.4 g, 91 % yield). ¹H NMR (CDCl₃, 300 MHz) δ (ppm): 8.00 (br s, 1H, NH), 7.78 (d, 2H, Ar, J_3 = 8.0 Hz), 7.41 (d, 2H, Ar, J_3 = 8.0 Hz), 6.77 (br s, 1H, NH), 5.09 (s, 2H, H₂N-O-CH₂-Ar), 1.49 (s, 9H, O-C(CH₃)₃). ¹³C NMR (75 MHz, CDCl₃) δ (ppm): 168.40, 155.69, 144.62, 139.79, 127.90, 127.43, 82.17, 74.53, 28.31.

4.4.5. Synthesis of Aldehyde Polymer Scaffold **P3**

Synthesis and characterization of aldehyde-functionalized copolymer scaffold **P3** is reported in Chapter 3, pages 97 – 98, whilst the experimental procedure for synthesis of **P3** is given in Chapter 2, pages 80 – 81.

4.4.6. Preparation of **GM1-Scaffold P3**

The crude reaction mixture of **GM1** conjugates **13/14** (42 μ mol, 500 μ L) was added directly to aldehyde scaffold **P3**. Complete disappearance of the aldehyde ¹H NMR signal was observed within 10 minutes of mixing the components. The **GM1**-functionalized scaffold (**GM1-P3**) was purified by dialysis (Spectra Por, 3 kDa MWCO) against distilled water (3 x 600 mL) and then lyophilized to afford the purified glycopolymer as a white solid.

4.5. References

1. U. Neu, K. Woellner, G. Gauglitz and T. Stehle, Structural basis of GM1 ganglioside recognition by simian virus 40, *Proc. Natl. Acad. Sci. U.S.A.*, 2008, **105**, 5219–5224.
2. (a) J. D. Badjić, A. Nelson, S. J. Cantrill, W. B. Turnbull and J. F. Stoddart, Multivalency and Cooperativity in Supramolecular Chemistry, *Acc. Chem. Res.*, 2005, **38**, 723–732. (b) U. Boas and P. M. H. Heegaard, Dendrimers in Drug Research, *Chem. Soc. Rev.*, 2004, **33**, 43–63. (c) S. L. Mangold and M. J. Cloninger, Binding of Monomeric and Dimeric Concanavalin A to Mannose-Functionalized Dendrimers, *Org. Biomol. Chem.*, 2006, **4**, 2458–2465.
3. W. B. Turnbull, B. L. Precious and S. W. Homans, Dissecting the Cholera Toxin - Ganglioside GM1 Interaction by Isothermal Titration Calorimetry, *J. Am. Chem. Soc.*, 2004, **126**, 1047–1047.
4. R. L. Ong and R. K. Yu, ¹H-NMR Assignments of GM1 Oligosaccharide in Deuterated Water at 500 MHz by Two-Dimensional Spin-Echo J-Correlated Spectroscopy, *Arch. Biochem. Biophys.*, 1986, **245**, 157–166.
5. Y. Hatanaka, U. Kempin and P. Jong-Jip, Facile Preparation of Carbohydrate Microarrays by Site-Specific, One-Step Synthesis of Biotinyl Photoprobes from Unprotected Carbohydrates, *J. Org. Chem.* 2000, **65**, 5639–5643.
6. (a) F. Peri, L. Cipolla, B. La Ferla, P. Dumy and F. Nicotra, A highly convergent approach to O- and N-linked glycopeptide analogues, *Glycoconj. J.*, 2000, **16**, 399–404. (b) M. R. Carrasco, R. T. Brown, I. M. Serafimova and O. Silva, Synthesis of N-Fmoc-O- (N'-Boc-N'-methyl)-aminohomoserine, an Amino Acid for the Facile Preparation of Neoglycopeptides, *J. Org. Chem.*, 2003, **68**, 195–197. (c) M. R. Carrasco, M. J. Nguyen, D. R. Burnell, M. D. Maclaren and S. M. Hengel, Synthesis of neoglycopeptides by chemoselective reaction of carbohydrates with peptides containing a novel N'-methyl-aminoxy amino acid, *Tetrahedron Lett.*, 2002, **43**, 5727–5729. (d) S. E. Cervigni and P. Dumy, Synthesis of Glycopeptides and Lipopeptides by Chemoselective Ligation, *Angew. Chem. Int. Ed.*, 1996, **35**, 1230–1232. (e) Y. Zhao, S. B. Kent and B. T. Chait, Rapid, Sensitive Structure Analysis of Oligosaccharides, *Proc. Natl. Acad. Sci. U.S.A.*, 1997, **94**, 1629–1633. (f) E. C. Rodriguez, K. A. Winans, D. S. King, C. R. Bertozzi and R. V May, A Strategy for the Chemoselective Synthesis of O-Linked Glycopeptides with Native Sugar–Peptide Linkages, *J. Am. Chem. Soc.*, 1997, **119**, 9905–9906.
7. M. Lee and I. Shin, *Org. Lett.*, Facile Preparation of Carbohydrate Microarrays by Site-Specific, Covalent Immobilization of Unmodified Carbohydrates on Hydrazide-Coated Glass Slides, 2005, **7**, 4269–4272.
8. (a) J. Kalia and R. T. Raines, Hydrolytic Stability of Hydrazones and Oximes, *Angew. Chem. Int. Ed.*, 2008, **47**, 7523–7526. (b) C. S. Mahon, C. J. McGurk, S. M. D. Watson, M. A. Fascione, C. Sakonsinsiri, W. B. Turnbull and D. A. Fulton, Molecular Recognition-Mediated Transformation of Single-Chain Polymer Nanoparticles into Crosslinked Polymer Films, *Angew. Chem. Int. Ed.*, 2017, **56**, 12913–12918.
9. (a) D. K. Kölmel and E. T. Kool, Oxime and Hydrazones in Bioconjugation: Mechanism and Catalysis, *Chem. Rev.*, 2017, **117**, 10358–10376. (b) D. Larsen, M. Pittelkow, S. Karmakar and E. T. Kool, New Organocatalyst Scaffolds with High Activity in Promoting Hydrazone and Oxime Formation at Neutral pH, *Org. Lett.*, 2015, **17**, 274–277. (c) S. A. Loskot, J. Zhang and J. M. Langenhan, Nucleophilic catalysis of MeON-neoglycoside formation by aniline derivatives, *J. Org. Chem.*, 2013, **78**, 12189–12193.
10. F. Peri, P. Dumy and M. Mutter, Chemo- and stereoselective glycosylation of hydroxylamino derivatives: A versatile approach to glycoconjugates, *Tetrahedron*, 1998, **54**, 12269–12278.
11. (a) V. A. Polyakov, M. I. Nelen, N. Nazarpak-Kandlousy, A. D. Ryabov and A. V. Eliseev, Imine exchange in O -aryl and O -alkyl oximes as a base reaction for aqueous 'dynamic' combinatorial libraries. A kinetic and thermodynamic study, *J. Phys. Org.*, 1999, **363**, 357–363. (b) P. T. Corbett, J. Leclaire, L. Vial, K. R. West, J. Wietor, J. K. M. Sanders and S. Otto, Dynamic Combinatorial Chemistry, *Chem. Rev.*, 2006, **106**, 3652–3711

Chapter 5

Enhancing the Kinetics of Hydrazone Exchange Processes at Neutral pH

This chapter was based upon the following article:

Patrick L. Higgs, Antonio J. Ruiz-Sanchez, Milene Dalmina, Benjamin R. Horrocks, Andrew G. Leach and David A. Fulton, *Org. Biomol. Chem.*, 2019, **17**, 3218-3224.

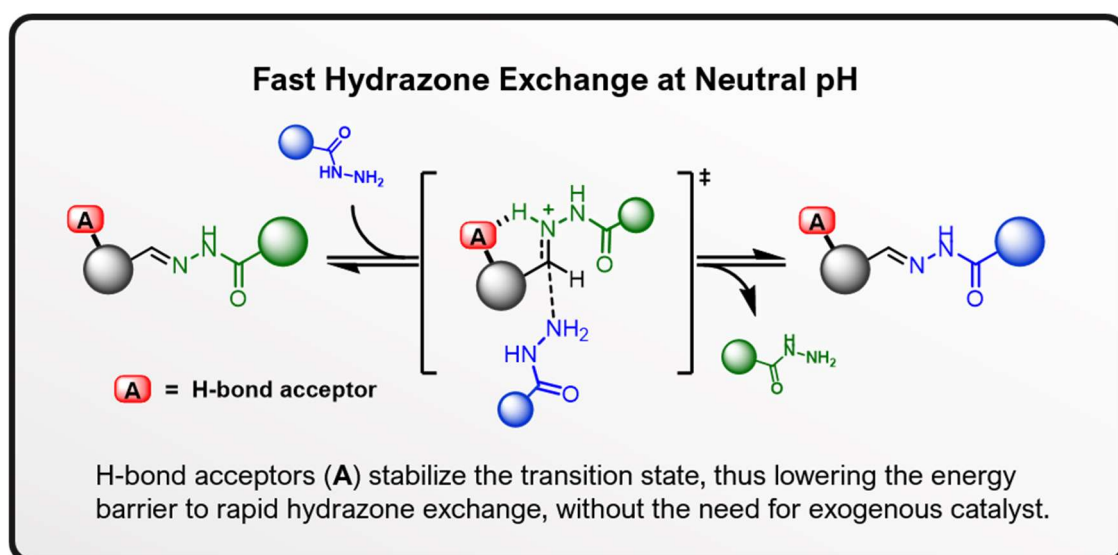


Table of Contents

5.1. Abstract	177
5.2. Introduction	178
5.2.1. Mechanism of Hydrazone Exchange	179
5.3. Results and Discussion	180
5.3.1. Experimental Hydrazone Exchange Studies	180
5.3.2. Computational Hydrazone Exchange Studies	183
5.3.3. Exchange Kinetics of BenzoDHP (1g)	187
5.4. Conclusion	189
5.5. Experimental	190
5.6. References	196
5.7. Appendix A	198

5.1. Abstract

This thesis has described the successful ‘wrapping’ of micron-sized objects within crosslinked polymer films. Results demonstrated that ‘wrapping’ occurs only when: (i) There are complementary recognition events between polymer and object, and (ii) crosslinks located within the polymer ‘wrapping agents’ are dynamic covalent in nature and may freely undergo processes of component exchange. Fluorescence microscopy experiments have provided strong evidence of the ‘wrapping’ process, and the development of a highly hydrophilic poly(ethylene glycol)-based ‘wrapping agent’ has permitted ‘wrapping’ to be successfully accomplished in aqueous media. These research outcomes have motivated progress towards the ‘wrapping’ of smaller, biologically relevant objects such as virus-like particles (VLPs) and bacteria. One remaining challenge, however, is the requirement of the ‘wrapping’ process to operate under mildly acidic (pH 4.5) conditions, which are necessary to catalyze the structural rearrangement of dynamic covalent acyl hydrazone crosslinkages located within the polymer ‘wrapping agents’. Kinetics of hydrazone exchange are optimal at pH 4.5, yet exceptionally slow at pH 7.4, where most biological targets are stable. This discrepancy presents a bottleneck in the biocompatibility of the ‘wrapping’ approach, as relatively few biomacromolecules will tolerate acidic conditions for prolonged timescales. To address that limitation, improve biocompatibility and maximize biological utility of the ‘shrink-wrapping’ approach, this chapter reports a combined computational and experimental study, which was conducted to identify a palette of hydrazone linkages that undergo rapid component exchange at neutral pH. In these studies, judiciously placed *N*- or *O*-hydrogen bond acceptors within the carbonyl-derived moiety of the hydrazone were shown to stabilize transition states *via* hydrogen bonding interactions, providing a valuable boost to exchange kinetics at neutral pH. Incorporation of these rate-enhancing structural features onto polymer scaffolds was thus hypothesized to afford a second generation of ‘wrapping agents’, which could be engineered for their capacity to ‘shrink-wrap’ biological objects in water at physiological pH.

5.2. Introduction

The field of dynamic covalent chemistry¹ requires chemical bonds that readily undergo component exchange processes. One of the most utilized is the hydrazone bond, (Fig. 1) which has optimal exchange kinetics at pH 4.5, being considerably slower at neutral pH.^{1b, 2} The requirement to operate at lower pH limits significantly the scope and application of hydrazone-based dynamic covalent chemistry as many interesting biological targets are only stable at near neutral pH values, and thus it would be advantageous if hydrazone exchange were able to operate on an experimentally useful timescale at pH values closer to neutral. Inspired by the work³ of Jencks in the 1960s, Dawson and co-workers demonstrated⁴ that aniline can successfully catalyze exchange processes at neutral pH, and aniline catalysis was applied⁵ successfully in a hydrazone-based dynamic combinatorial library for the discovery of inhibitors of glutathione S-transferase. The relatively high concentrations of aniline required (100 mM) to enhance the rate of component exchange can limit significantly the wider biocompatibility of the organocatalyst approach, and to this end Kool *et al.* have developed⁶ improved catalysts which can provide rate enhancements of up to eight times that of aniline catalysis at lower concentrations of catalyst.



Figure 4: Hydrazones undergo reversible component exchange through transimination processes where a hydrazone reacts with a hydrazide to afford a new hydrazone and hydrazide.

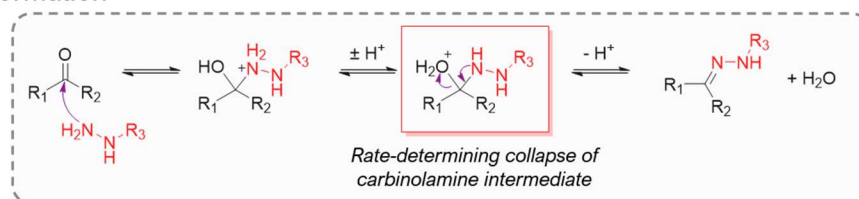
While investigating hydrazone and oxime formation at neutral pH, Kool and co-workers also studied^{6a} an alternative approach to organocatalysis in which structural modifications of aldehyde components can increase the rate of hydrazone or oxime formation at neutral pH. These structural modifications involve the inclusion of neighbouring acidic or basic functional groups or atoms within the carbonyl-derived moiety of the hydrazone that assist proton transfer within the rate limiting step, thereby lowering transition state energies and enhancing the rate of hydrazone formation. It was anticipated that these structural modifications would also enhance the rate of hydrazone exchange processes at neutral pH, which are typically slow under basic conditions. The exchange kinetics were thus investigated for a small pool of hydrazones containing acidic or basic functional groups/atoms and their observed order of reactivity was rationalized by computational studies. Computational modelling indicated that the observed rate enhancements most likely arise on account of the abilities of ‘neighbouring’ functional groups/atoms to form stabilizing hydrogen bond interactions within the transition state structure. Furthermore, this model correctly identified benzodihydropyran (benzoDHP)

as a candidate rate-enhancing group. Although this prediction was initially surprising given the absence of any acidic or basic moieties within benzoDHP, the expected rate-enhancement was subsequently verified by experiment to be the fastest performing substrate, demonstrating that useful enhancements in rate can be obtained.

5.2.1. Mechanism of Hydrazone Exchange

Although hydrazone formation and hydrazone exchange reactions proceed *via* similar condensation mechanisms (Fig. 2), there exist several key differences between these two processes: (i) At neutral pH, the rate-determining step in hydrazone formation is collapse of the tetrahedral carbinolamine intermediate (Fig. 2a), whereas in hydrazone exchange the rate-limiting step is nucleophilic attack upon the hydrazone (Fig. 2b), which was entirely consistent with the results from computational studies (see Fig. 6). (ii) In hydrazone formation, a single water molecule – a poor leaving group – is ejected from the carbinolamine intermediate, whilst in hydrazone exchange the departing hydrazine/hydrazide constitutes a much better leaving group. (iii) In hydrazone exchange, nucleophilic attack by the incoming hydrazide requires protonation at the hydrazone nitrogen (N^1) to increase the electrophilicity at the hydrazone C^1 position. Yet, in hydrazone formation nucleophilic attack is rapid, and does not require protonation of the carbonyl oxygen. Although there are substantial mechanistic similarities between hydrazone formation (Fig. 2a) and hydrazone exchange (Fig. 2b), the above discrepancies (i-iii) between the two reactions mean that it should not take for granted that structural features which enhance the rate of hydrazone formation would also enhance the kinetics of hydrazone exchange.

(a) Hydrazone Formation



(b) Hydrazone Exchange

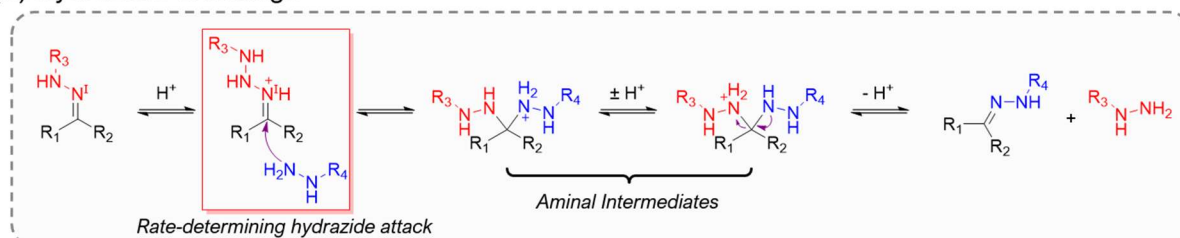


Figure 2: Proposed mechanisms of hydrazone formation (a) and hydrazone exchange (b), which was consistent with the computational studies. The rate-determining step in hydrazone formation (a) is ejection of water from the carbinolamine intermediate, whereas in hydrazone exchange (b) the rate-limiting step is nucleophilic attack by the incoming hydrazide.

5.3. Results and Discussion

5.3.1. Experimental Hydrazone Exchange Studies

When considering the application of hydrazone bonds in dynamic combinatorial chemistry, one must take account of several important requirements. It is crucial that equilibria lie very much on the side of product hydrazone, and thus aromatic aldehyde partners are often used as the extended conjugation of the resultant hydrazone ensures product stability, especially important when operating in aqueous solutions. Aliphatic aldehydes, on the other hand, tend to form hydrazones where the equilibrium is less towards the desired hydrazone. Furthermore, acyl hydrazide reaction partners are used to ensure reasonable rates of component exchange as other classes of hydrazides/hydrazines often form hydrazones which undergo component exchange on a timescale too slow to be practically useful. With these considerations in mind, investigations focused upon a small pool of hydrazones **1a-f** (Fig. 3) (for synthetic procedures see experimental). Hydrazones **1a-c** and **1e-f** contain a basic nitrogen or acidic group either upon or within the aromatic moiety of the carbonyl components which it was postulated would likely influence the kinetics of exchange. These specific substrates were chosen based upon the work^{6a} of Kool *et al.*, where they exhibited relatively high rate enhancements for hydrazone formation and thus were sensible starting points to investigate their influence on hydrazone exchange. Hydrazone **1d**, however, is an exception in that it contains no potential rate-enhancing structural features, and thus serves as a control.

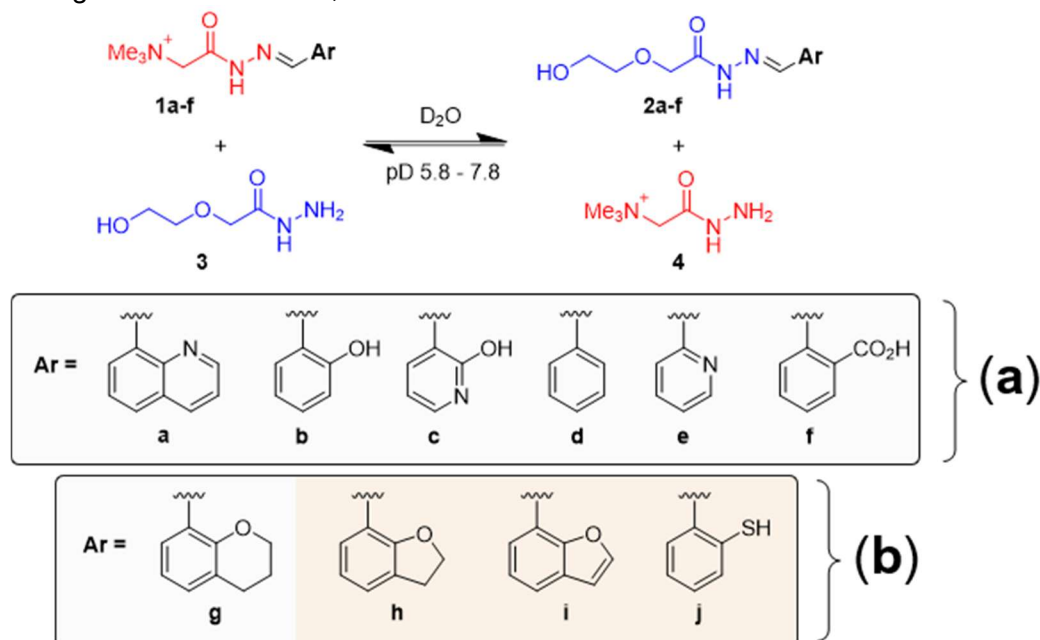


Figure 3: Component exchange of hydrazones **1a-f** with acyl hydrazide **3** to form hydrazones **2a-f** and acyl hydrazide **4**, a process which was studied by 1H NMR spectroscopy. (a) Exchange of **1a-f** was studied both experimentally and modelled computationally as a symmetrical exchange process, where $AcNHNH_2$ is both the attacking nucleophile, and hydrazide component of the hydrazone. (b) Substrates **h-j** were only studied computationally, and based upon the outcomes of this work, **g** was progressed to experimental study.

Component exchange to form hydrazones **2a-f** was accomplished by reaction of hydrazones **1a-f** with an excess of acyl hydrazide **3** (see experimental for details). Acyl hydrazides **3** and **4** possess hydroxyl and quaternary ammonium groups, respectively, which ensure water solubility of their associated hydrazones. Exchange reactions (see experimental for details) were monitored by ^1H NMR spectroscopy at room temperature over a range of pD values (5.8–7.8).^{*} The mole fraction of each species in solution was determined at each time point from the normalized integrals of ‘diagnostic’ protons. Although it was found that any ‘diagnostic’ signal could be used as a spectral ‘handle’ to quantify the rate of hydrazone exchange, for reasons of experimental simplicity, the trimethylammonium ($-\text{NMe}_3^+$) signals associated with hydrazones **1a-f** (●) and exchange product **4** (●) (Fig. 4a) were chosen. Integral analysis of time-resolved ^1H NMR spectra (Fig. 4a) afforded kinetics traces (Fig. 4b) (see page 199, Fig. 10) from which the second order rate constants (k_f and k_r) (page 200, Table 1) were obtained

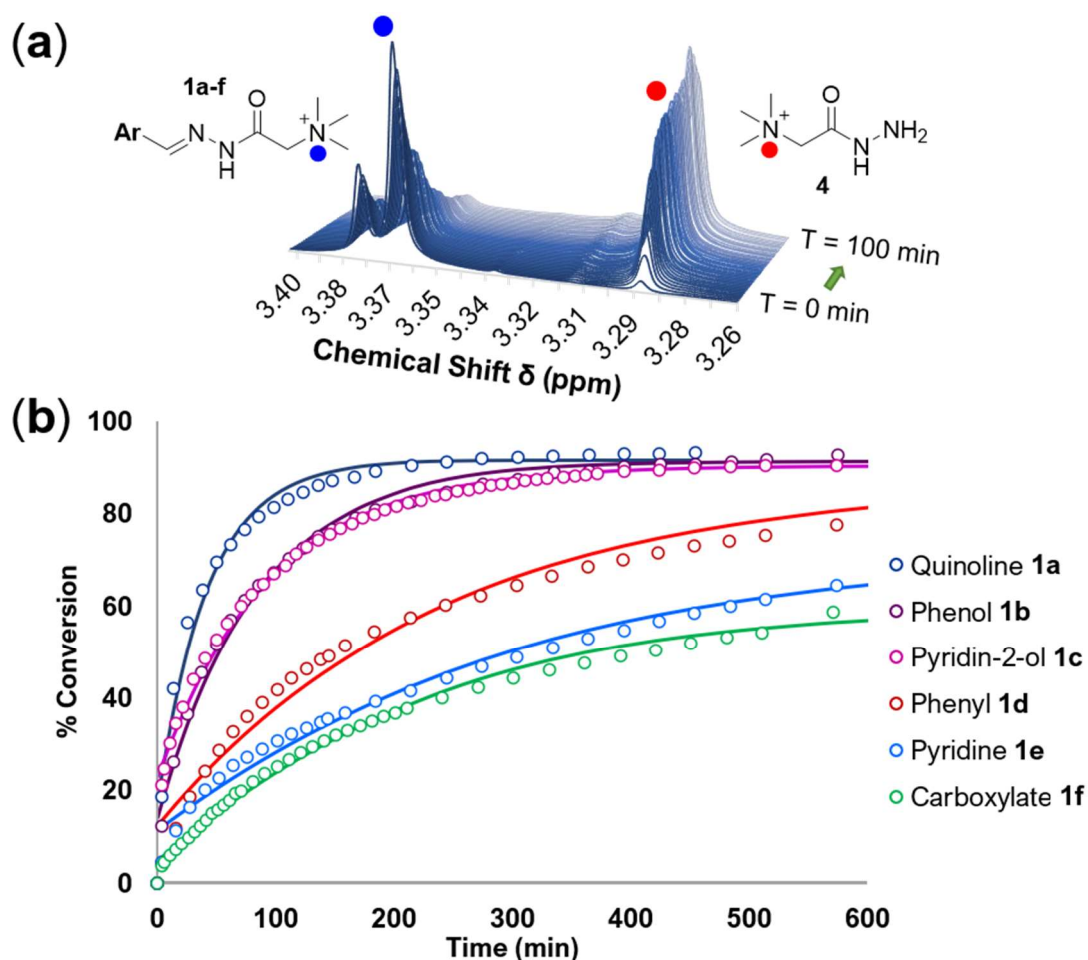


Figure 4: Hydrazone exchange reactions were monitored by ^1H NMR spectroscopy. (a) A series of time-resolved ^1H NMR spectra are shown for a representative exchange process (**1d**, pD 7.8). Integration of ‘diagnostic’ quaternary ammonium ($-\text{NMe}_3^+$) signals associated with the starting hydrazone (●) and exchange product **4** (●) allowed for the kinetics traces (b) to be deduced. (b) Kinetics traces of hydrazones **1a-f** undergoing component exchange with glycol hydrazide **3** at pD 7.8.

^{*} All experimental studies are performed in D_2O and thus acidities were measured in pD. Computational studies which were modelled in H_2O with acidity measured in pH. pD can be related to pH by the simple calculation $\text{pD} = \text{pH} + 0.42$.²¹

(see experimental for details). Division of each of the forward rate constants (k_f) by the that of the slowest exchange process (with the smallest k_f value), allowed for the relative rates (k_{rel}) of hydrazone exchange to be deduced (Fig. 5). As anticipated, the exchange kinetics (Fig. 5) of all examples were faster as the pD decreased. The rates of exchange are 2-8 times faster at the lowest pD investigated (5.4) compared to the highest pD (7.8), observations consistent with component exchange being accelerated by protonation.

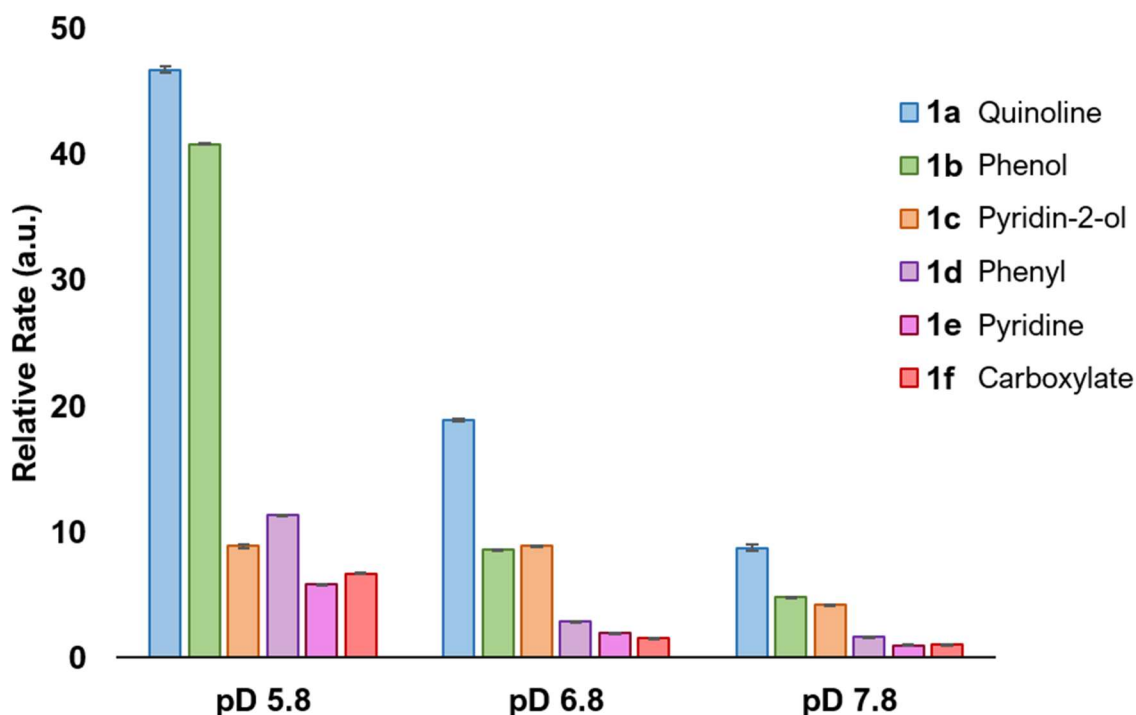


Figure 5: Relative rates of component exchange for hydrazones **1a-f**, which were obtained from the forward rate constant values k_f (see experimental for details). Error bars show $\pm 1\sigma$ confidence intervals.

Component exchange was fastest with hydrazone **1a**, being approximately 5 times faster than control hydrazone **1d** at all pD values investigated, suggesting that the inclusion of a proximal basic nitrogen may catalyze hydrazone exchange. Surprisingly, hydrazones **1e** and **1f** – both of which possess proximal acid/basic groups – were observed to undergo slower component exchange processes (at all pD values) than the control hydrazone **1d**. This result was initially surprising, as it had been anticipated that the hydrazone containing the most basic group would best catalyze the hydrazone exchange process as it would exhibit the greatest likelihood of being protonated and so be able to transfer a proton in the rate limiting step; the pK_a of the pyridyl nitrogen is estimated to be 5.14,⁷ which is higher than that of the quinoline ($pK_a = 4.85$)⁷ and the benzoic acid ($pK_a = 4.20$)⁷ suggesting that pyridine **1e** should undergo the fastest hydrazone exchange. The observed order of reactivity (quinoline > phenol > phenyl > pyridine \approx carboxylate) does not correlate with the pK_a value of the proximal acid/basic groups, an observation which suggests that the rate enhancement is not caused by protonation of this group.

5.3.2. Computational Hydrazone Exchange Studies

In order to better understand the experimental observations, computational studies were undertaken. All computational work was conducted by Dr Andrew Leach at Liverpool John Moores University. Three possible hydrazone exchange mechanisms were considered and studied at the M06-2X/6-31G* level⁸ of theory, a level that is expected to produce reasonable agreement with barrier heights. All calculations were performed in Gaussian09⁹ and included implicit solvation using the PCM protocol.[†] To simplify calculations, the hydrazide employed in modelling the exchange processes was AcNHNH₂, which was also used as the hydrazide component within the hydrazone. The overall process modelled was therefore a symmetrical exchange reaction.

[†] All species were characterized by frequency calculations.

Firstly, process (1) (Fig. 6a) was considered, in which no protons were added into the system. In the calculated transition state (**P1TS**), proton shuttling between the incoming nucleophile and the hydrazone was required, and a single water molecule can fulfil this role by simultaneously removing a proton from the incoming hydrazide and protonating the hydrazone. This proton shuttling leads to a neutral tetrahedral intermediate (**P1Int**) that would be expected to collapse either to reactants or products through similar barriers. In process (2) (Fig. 6b), groups located within the aldehyde derived moiety of the hydrazone were protonated to give reaction precursors (**P2Prot**) before nucleophilic attack by the hydrazide, a process that proceeds through a similar transition state (**P2TS**) to process (1). This mechanism leads to a protonated intermediate (**P2PI**) that can either rearrange (intramolecular proton transfer) or return a proton to the surrounding environment. The computed energetics (see ΔG^\ddagger values in Fig. 6) are those calculated for pH 7, while those for pH 5 (where different) are in brackets. The calculated values reveal that process (2) features a high energy barrier, with ΔG^\ddagger values exceeding 30 kcal/mol, indicating that protonation of the functional group/atom within the aldehyde-derived moiety likely impedes the exchange process. Next, process (3) (Fig. 6c) was considered, which represents a specific acid-catalysed reaction where the hydrazone nitrogen (N^1) is protonated prior to nucleophilic attack by the hydrazide. This protonation gives protonated hydrazone (**P3PH**) that is attacked by hydrazide through transition state **P3TS** to

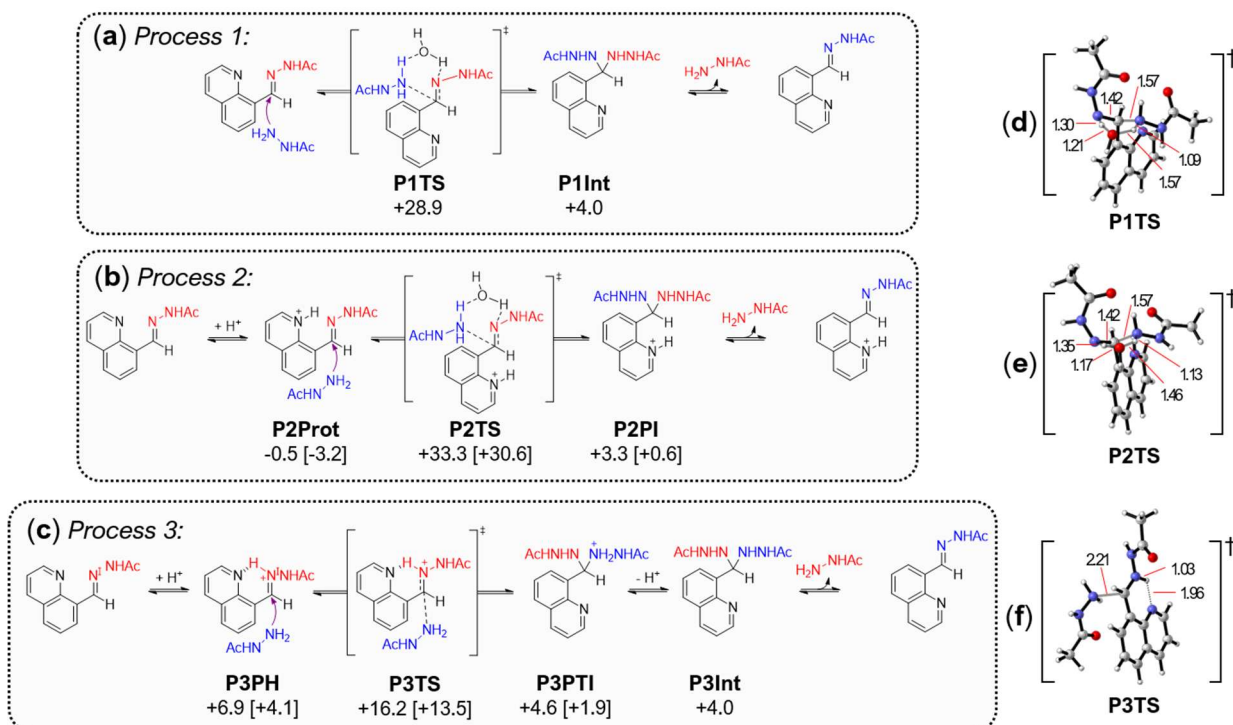


Figure 6: Three mechanisms of hydrazone exchange which were explored computationally. (a) Process (1): No protonation of hydrazone prior to hydrazide attack (uncatalyzed reaction). (b) Process (2): Protonation of proximal acid/base group within aldehyde component of hydrazone. (c) Process (3): Protonation of hydrazone nitrogen (N^1) prior to attack. Energetics (ΔG^\ddagger values, kcal/mol) were calculated at pH 7, whilst values for pH 5 are in brackets. Process (3) represents the most likely mechanism for hydrazone exchange, on account of having low energy barriers, relative to Processes (1) and (2). (d-f) Transition state structures **P1TS**, **P2TS** and **P3TS**, respectively.

give a protonated tetrahedral intermediate **P3PTI**. For process (3) the calculated free energy barrier (see ΔG^\ddagger values, Fig. 6) is significantly lower than those obtained for processes (1) and (2), indicating that process (3) constitutes the most likely mechanism for hydrazone exchange. Although the pathway with the lowest free energy barrier is likely to be the one that is operational there are significant uncertainties in these comparisons and therefore the ability of each process to explain the relative reactivity of the different hydrazones was also considered.

For process (1), the lowest computed free energy barrier (and therefore fastest reaction) is for carboxylate **1f**[†] (see page 207, Table 4) whilst the highest energy barrier (and therefore slowest process) involves quinoline **1a**, observations that are not consistent with experiment and therefore process (1) was discounted. The energetics calculated for process (2) (page 207, Table 5) predict that: (i) the most reactive substrate is control compound **1d** – which is absent of any acid/basic groups to catalyze the reaction; and (ii) the least reactive substrate is **1a** – which was experimentally observed to have the fastest hydrazone exchange kinetics. Process (2) was not consistent with the observed order of reactivity and was discounted. The computed barrier heights for process (3) (page 207, Table 6) however, predict an order of reactivity (pH

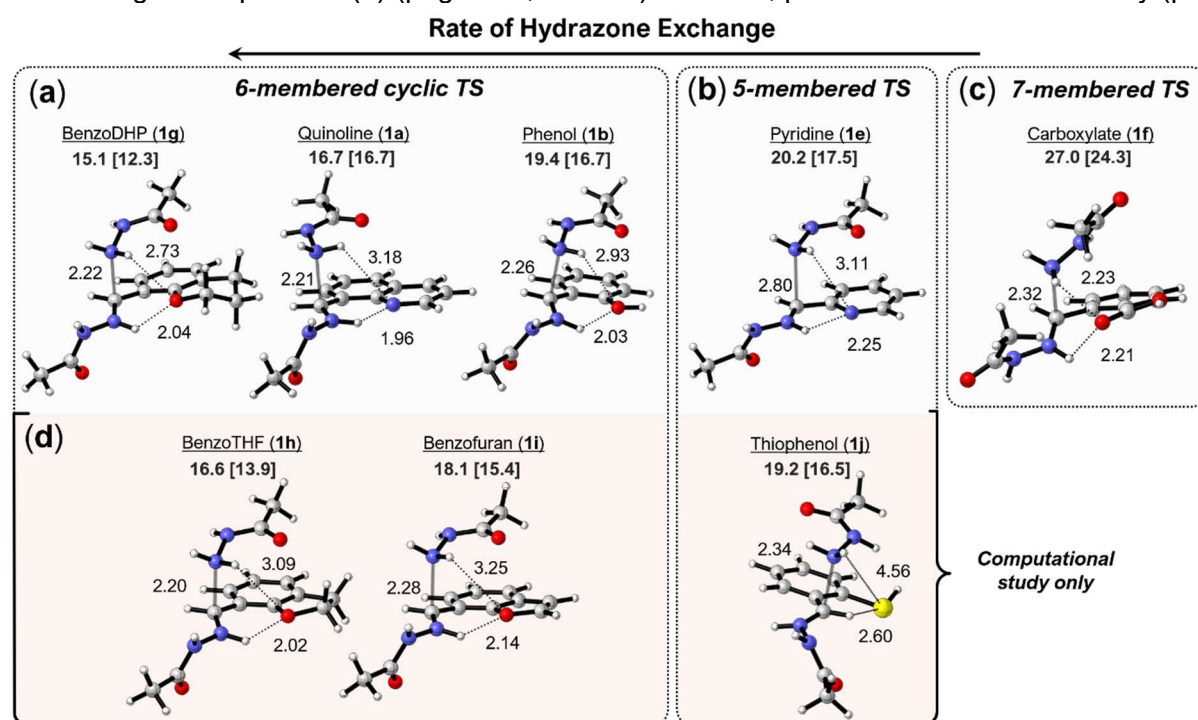


Figure 7: Hydrogen bonding interactions stabilise the transition states for hydrazone exchange. The energy barriers (ΔG^\ddagger) corresponding to each TS structure were calculated at pH 7.4 and pH 5.4 [brackets]. (a) 6-membered cyclic TS (benzoDHP **1g**, quinoline **1a**, phenol **1b**) have the lowest energies and exhibit the fastest hydrazone exchange. (b) 5-membered cyclic TS (pyridine **1c**, thiophenol **1j**), (c) 7-membered TS (carboxylate **1f**). (d) Substrates **1h-j** were only studied computationally.

[†] Further modelling of **1f** revealed that the carboxylate moiety may ring-close upon the aminal-like intermediate to form a meta-stable 5-membered cyclic structure (see page 209, Fig. 16), although no evidence of this species was observed during ¹H NMR experiments. This meta-stable presented a local minimum on the potential energy surface, making it challenging to reliably compute energetics that were consistent with a single exchange mechanism. Energetics of all other substrates however, were in close agreement with process (3).

7.4: **1a** > **1b** > **1d** \approx **1e** > **1f**; pH 5.4: **1a** \approx **1b** > **1d** \approx **1e** > **1f**) that was consistent with the observed relative rates (Fig. 3), further supporting the idea that process (3) constitutes the most likely mechanism of hydrazone exchange.

In process (3), the key species that governs the reactivity was the transition state for hydrazide attack (**P3TS**). The origin of the high reactivity of **1a** was revealed in the corresponding transition state structure (Fig. 7a), which features two hydrogen bonds from the quinoline nitrogen to both the incoming hydrazide (N-H distance: 3.18 Å) and the protonated hydrazone (N-H: 1.96 Å), that stabilize the transition state.¹⁰ Crucially, these stabilizing interactions help to lower the energy barrier for hydrazone exchange, thus providing a boost in the exchange kinetics. In the analogous transition states for pyridine **1e** (N-H: 2.93 Å, 2.25 Å) (Fig. 7b) and carboxylate **1f** (O-H: 2.23 Å, 2.21 Å) (Fig. 7c) these distances are longer, suggesting that of the two interactions it is the hydrogen bond to the protonated hydrazone that governs reactivity. It has been noted previously¹¹ that 6-membered ring intramolecular hydrogen bonding interactions (such as those that operate for quinoline **1a**) are slightly favoured over their 5-membered equivalent (as for pyridine **1e**) and much favoured compared to their 7-membered equivalent (carboxylate **1f**). Thus, it is the ideal spatial positioning and orientation of hydrogen bond acceptor atoms/groups within the transition state, rather than simply the presence of acidic or basic moieties, that leads to increased reactivity in hydrazone exchange. With this thought in mind, alternative oxygen-containing substrates **1g-i**, and thiophenol **1j** (Fig. 7) were considered computationally as a test of this model, as such substrates contain hydrogen bond acceptors, but lack the suitably acidic/basic groups required to catalyze the reaction *via* intramolecular proton transfer. Amongst these examples, benzoDHP **1g** was predicted to be faster than all other compounds studied experimentally and was therefore selected for synthesis. The origin of this predicted rate enhancement was clear in the structure of the relevant transition state for **1g** (Fig. 7a). The heterocyclic oxygen atom in this species is positioned in such a way that it can form two stabilizing interactions through a favoured 6-membered ring: one with the protonated hydrazone (2.04 Å, O-H) and a second with the incoming nucleophile (2.73 Å, O-H). Short hydrogen bonding interactions within the transition state indicate stronger stabilizing interactions, the likes of which lower the transition state energy to a greater extent, thus resulting in faster hydrazone exchange. The transition state of benzoDHP **1g** features two such short hydrogen bonds, which are considerably shorter (and therefore presumably stronger) than analogous bond lengths calculated for quinoline **1a** (N-H: 1.96 Å, 3.18 Å) and phenol **1b** (O-H: 2.03 Å, 2.93 Å). This observation suggests that **1g** would offer significantly improved exchange kinetics over quinoline **1a**, an already fast exchanging hydrazone. This hypothesis was then experimentally validated by determining the hydrazone exchange kinetics of benzoDHP **1g** (Fig. 8).

5.3.3. Exchange Kinetics of BenzoDHP (1g)

Hydrazones **1a**, **1d** and **1g** were exchanged with hydrazide **5** (Fig. 8a), and the kinetics were monitored by ^1H NMR spectroscopy and the relative rates of exchange were deduced (see page 203, Table 2). It was necessary to study this exchange process with morpholine hydrazide (**5**) instead of glycol hydrazide **3**, as exchange of **1g** with **3** resulted in product precipitation that convoluted the exchange kinetics (see page 201, Fig. 11). Gratifyingly, **1g** displayed a 2-fold rate enhancement with respect to quinoline **1a** (Fig. 8b), highlighting the predictive power of the deduced computational model for hydrazone exchange.

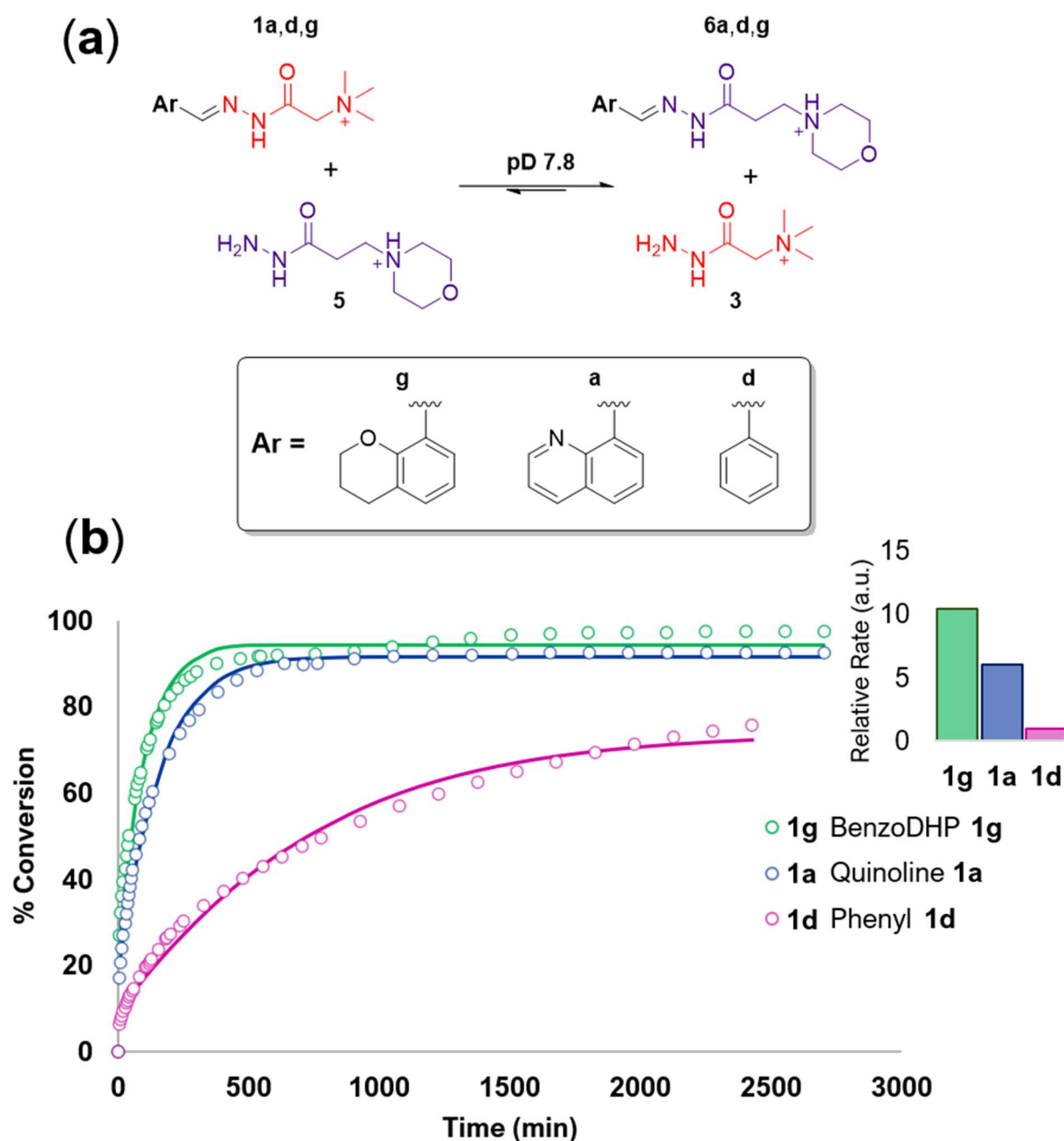


Figure 8: Hydrazone exchange kinetics of **1a**, **1d** and **1g** were studied at pD 7.8 by ^1H NMR spectroscopy. (a) Exchange of hydrazones **1a, d, g** with hydrazide **5**. (b) Kinetic traces of **1a**, **1d**, **1g**. Experimental data and theoretical fit are shown as circles and solid lines, respectively. Inset: derived relative rates for hydrazone exchange. See page 203, Table 2 for second order rate constants.

Despite mechanistic differences between hydrazone exchange and formation processes, it was hypothesized that the rate-enhancing effects observed for proximal acid/base groups upon hydrazone formation may also arise on account of hydrogen bonding interactions which lower the activation energies (by stabilising the transition states). The ability of those groups to facilitate intramolecular proton transfer, as postulated by Kool *et al.*^{6a-d}, will also be a contributing factor. Preliminary experiments (Fig. 9a) revealed that chroman-8-carbaldehyde (the aldehyde from which benzoDHP **1g** was derived) exhibited rapid hydrazone formation, reacting 15-fold faster than quinoline-8-carbaldehyde, and 26-fold faster than benzaldehyde, which lacks any rate-enhancing features. The intriguing observation that the benzoDHP moiety catalyses rapid hydrazone formation despite its lack of a significantly acidic or basic group to facilitate intramolecular proton transfer processes, supports the hypothesis that hydrogen-bonding interactions play an important role in organocatalysed hydrazone formation, and most likely also the mechanistically similar processes of imine and oxime formation.

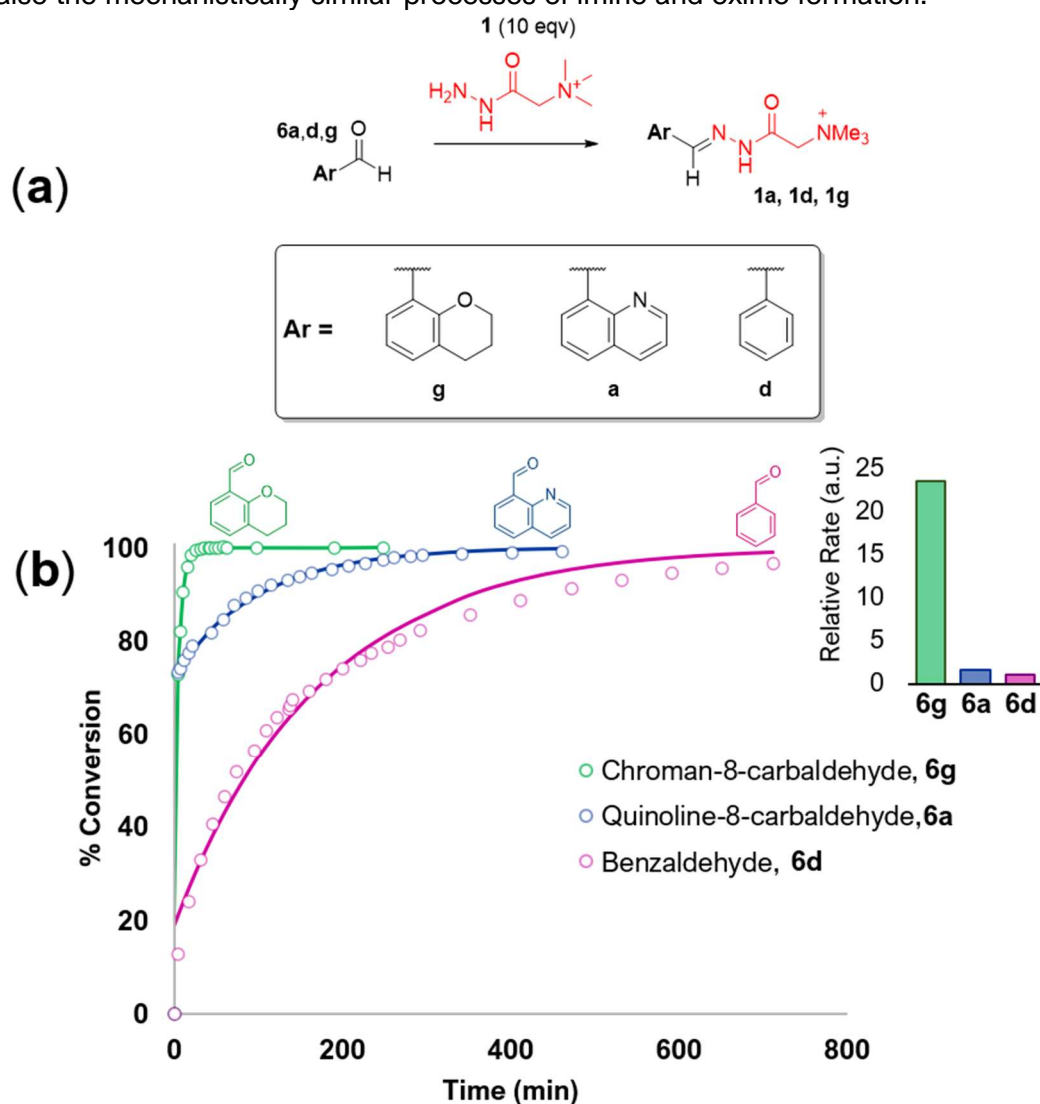


Figure 9: (a) Hydrazone formation of aromatic aldehydes **6a**, **6d**, **6g** with Girard's Reagent T (**5**) to form hydrazone products **1a**, **1d** and **1g**, respectively. ^1H NMR monitored the reaction kinetics at pD 7.8. (b) Kinetics traces of hydrazone formation of aldehydes **6a**, **6d**, **6g**. Inset: Relative rates of hydrazone formation. See Appendix A, page 205, Table 3 for second order rate constants.

5.4. Conclusion

The results in this chapter demonstrated that the judicious placement of neighbouring hydrogen-bond acceptors within the carbonyl-derived fragment of a hydrazone compound leads to significant enhancements in rates of hydrazone exchange. Computational modelling identified the most likely reaction pathway for this process, the energetics of which were entirely consistent with experimentally determined exchange rates. Furthermore, modelling supported the hypothesis that the rate-determining step in hydrazone exchange is nucleophilic attack on the protonated hydrazone, which is an important distinction between hydrazone exchange and hydrazone formation, where the rate-limiting step is collapse of the carbinolamine tetrahedral intermediate. Crucially, modelling revealed that the origin of the observed rate enhancements lies in the ability of neighbouring functional groups to form a stabilizing hydrogen bonds within the transition state, and that geometries where 6-membered ring intramolecular hydrogen bonding interactions can be adopted are particularly important. The reliability of this model was demonstrated by its prediction that a benzoDHP group – containing a very weakly basic but optimally placed oxygen atom that acts as a hydrogen-bond acceptor – displayed fast exchange kinetics, which was gratifyingly supported by experimental observation. Preliminary experiments revealed that chroman-8-carbaldehyde (from which BenzoDHP **1g** was derived) also catalyses rapid hydrazone formation. Remarkably, chroman-8-carbaldehyde was found to react 15-fold faster than previously reported quinoline-8-carbaldehyde,^{6a} despite its lack of an acidic/basic group. These observations suggest that the inclusion of hydrogen-bond acceptor moieties within the aldehyde component may also play an important role in catalysing hydrazone formation, alongside the previously reported^{6a-d} catalytic effect of proximal acid/base groups. At neutral pD, benzoDHP **1g** was observed to afford a 2-fold enhancement in the rate of hydrazone exchange, relative to the kinetics of quinoline **1a**, and was observed to be 10-fold faster than control hydrazone **1d**. With regards to the DAF groups interest in dynamic combinatorial chemistry, this work suggests that valuable gains in rate of exchange can be made, which in turn would permit the design and fabrication of a polymer-scaffolded DCLs¹² operating with reasonable kinetics at near-neutral pH – a crucial requirement for interfacing DCLs with biomacromolecules.¹³ Furthermore, given the importance of hydrazone exchange within dynamic covalent polymers,¹⁴ materials,¹⁵ surfaces,¹⁶ molecular machines,¹⁷ interlocked molecules,¹⁸ cages¹⁹ and functionalized nanoparticles,²⁰ where component exchange processes endow structural adaptivity, thus these findings may offer insight to the design and optimization of new systems. It was also anticipated that this work would benefit the development of new organocatalyst for hydrazone/oxime formation and exchange processes, indicating that computational studies, on account of their ability to ‘pick winners’, might minimise tedious preliminary screenings for catalytic activity.

5.5. Experimental

5.5.1. General Experimental

All chemicals, including Girard's reagent T (**R1**) were purchased from Sigma-Aldrich or Alfa Aesar and were used as received without further purification. ^1H and ^{13}C NMR spectra of synthesised compounds were recorded on a Bruker Avance 300 spectrometer (at 300 and 75 MHz respectively), Bruker Avance 400 spectrometer (at 400 MHz and 100 MHz, respectively), or a Bruker Avance III HD spectrometer (at 500 MHz and 125 MHz, respectively). High-resolution mass spectrometry was performed on a Waters LCT Premier mass spectrometer^a or an Agilent 6550 iFunnel Q-TOF LC/MS^b. The synthesis and characterization of morpholine hydrazide **5** was reported in Chapter 2 (see pages 39 and 86).

Synthetic Procedures:

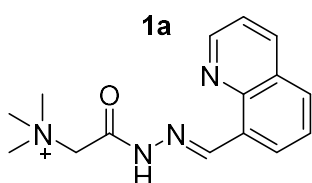
5.5.2. General Procedure for Preparation of Hydrazone Compounds (1a-1g)

Aromatic aldehyde (1.00 eqv.) was dissolved in MeOH (2.5 mL) and stirred at room temperature. Girard's Reagent T (0.9 eqv) was dissolved in MeOH (2.5 mL), then added in one portion to the aldehyde solution. Reactions were judged complete by TLC (7:2 MeOH/2M H_4NCl), evaporated to dryness and the crude residue washed with dichloromethane (7 mL) and sonicated for 5 min. The final products were isolated by filtration and dried for 30 min under high vacuum.

5.5.3. Characterization of Hydrazones 1a-1g

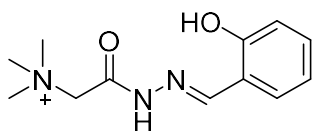
^1H and ^{13}C NMR spectra of compounds **1a-1g** appear complex on account of *syn/anti* isomerization about the C-N amide bond that exhibits hindered rotation, consistent with previous literature reports.²² The *syn/anti* ratio was typically in the range 50:50 to 30:70, with the *anti*-isomer being the preferred conformer in most cases.

N,N,N-Trimethyl-2-oxo-2-(2-(quinolin-8-ylmethylene)hydrazineyl)ethan-1-aminium (**1a**) ^1H NMR (D_2O , 400 MHz) δ (ppm): 8.81(*anti*) + 8.64(*syn*) (1H, s, Ar- $\text{HC}=\text{N}$ -), 8.75(*anti*) + 8.68(*syn*) (1H, d, Ar), 8.36(*anti*) + 8.25(*syn*) (1H, d, Ar), 8.10 (1H, d, Ar), 7.96(*anti*) + 7.87(*syn*) (1H, d, Ar), 7.55 (2H, m, Ar), 4.74(*syn*) + 4.31(*anti*) (2H, s, $-\text{C}=\text{N}-\text{N}-\text{CH}_2-$), 3.43 (9H, s, $-\text{N}(\text{Me})_3$). ^{13}C NMR (101 MHz, D_2O) δ (ppm): 160.91, 150.23, 149.58, 149.30, 147.38, 144.24, 131.94, 131.15, 128.40, 127.05, 126.55, 122.05, 121.87, 63.98, 62.90, 54.49, 54.40. HRMS⁺ $\text{C}_{15}\text{H}_{19}\text{N}_4\text{O}^+$, Theoretical: 271.1559 Actual: 271.1556^b. mp. 159 °C.



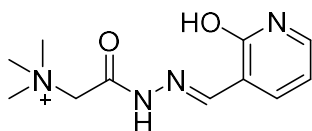
2-(2-(2-Hydroxybenzylidene)hydrazineyl)-N,N,N-trimethyl-2-oxoethan-1-aminium (1b) ¹H NMR (D₂O, 400 MHz) δ (ppm): 8.12(*anti*) + 7.95(*syn*) (1H, s, Ar-HC=N-), 7.35 (2H, m, Ar), 6.89 (2H, m, Ar) 4.54(*syn*) + 4.12(*anti*) (2H, s, -C=N-N-CH₂), 3.30 (9H, s, -N(Me)₃). ¹³C NMR (101 MHz, D₂O) δ (ppm): 164.70, 160.08, 156.67, 155.87, 152.76, 148.08, 132.91, 132.53, 131.07, 129.93, 120.64, 120.47, 118.24, 117.48, 116.46, 116.33, 63.88, 62.58, 54.47. HRMS⁺ C₁₂H₁₈N₃O₂⁺, Theoretical: 236.1399, Actual: 236.1409.^β mp. 206 °C.

1b



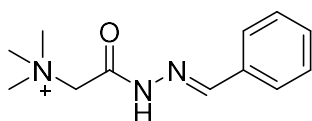
2-((2-(2-Hydroxypyridin-3-yl)methylene)hydrazineyl)-N,N,N-trimethyl-2-oxoethan-1-aminium (1c) ¹H NMR (D₂O, 400 MHz) δ (ppm): 8.35(*anti*) + 8.10(*syn*) (1H, s, Ar-HC=N-), 8.25(*anti*) + 8.20(*syn*) (1H, d, Ar) 7.71(*anti*) + 7.65(*syn*) (1H, d, Ar), 6.65 (1H, m, Ar), 4.74(*syn*) + 4.26(*anti*) (2H, s, -CH₂-N(Me)₃) 3.40 (9H, -CH₂-N(CH₃)₃). ¹³C NMR (75 MHz, D₂O) δ (ppm): 165.59, 162.75, 162.70, 160.84, 147.22, 142.60, 141.24, 140.58, 138.26, 137.44, 122.79, 122.24, 108.96, 63.99, 62.82, 54.43, 54.32. HRMS⁺ C₁₁H₁₇N₄O₂⁺, Theoretical: 237.1232, Actual: 237.1345.^β mp. 159 °C.

1c



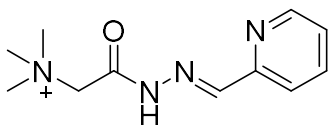
2-(2-Benzylidenehydrazineyl)-N,N,N-trimethyl-2-oxoethan-1-aminium (1d) ¹H NMR (D₂O, 400 MHz) δ (ppm): 8.18(*anti*) + 7.95(*syn*) (1H, s, Ar-HC=N-), 7.70(*anti*) + 7.67(*syn*) (2H, d, Ar), 7.43 (3H, m, Ar), 4.65(*syn*) + 4.15(*anti*) (2H, s, -C=N-N-CH₂-), 3.30 (9H, s, -N(CH₃)₃). ¹³C NMR (101 MHz, D₂O) δ (ppm): 165.61, 160.81, 153.19, 148.32, 133.08, 132.47, 131.74, 131.06, 129.09, 128.99, 127.95, 127.44, 64.06, 62.88, 54.45. HRMS⁺ C₁₂H₁₈N₃O⁺, Theoretical: 220.1432, Actual: 220.1450.^α mp. 175 °C.

1d



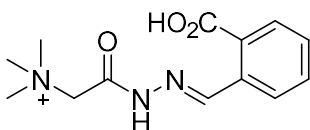
N,N,N-Trimethyl-2-oxo-2-(2-(pyridin-2-ylmethylene)hydrazineyl)ethan-1-aminium (1e) ¹H NMR (D₂O, 400 MHz) δ (ppm): 8.57 (1H, dd, Ar), 8.23(*anti*) + 8.04(*syn*) (1H, s, Ar-CH=N-N), 7.95 (2H, m, Ar) 7.51 (1H, dd, Ar), 4.29 (2H, s, -C=N-N-CH₂-), 3.39 (9H, s, -N(CH₃)₃). ¹³C NMR (101 MHz, D₂O) δ (ppm): 166.11, 161.38, 150.80, 150.65, 150.60, 149.22, 149.11, 146.17, 138.39, 126.02, 125.63, 122.85, 122.55, 63.87, 62.85, 54.47, 54.34. HRMS⁺ C₁₁H₁₇N₄O⁺, Theoretical: 221.1402, Actual: 221.1393.^α mp. 190 °C.

1e



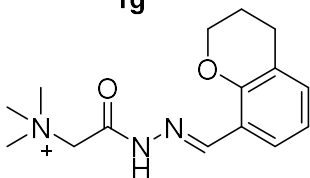
2-(2-(2-Carboxybenzylidene)hydrazineyl)-*N,N,N*-trimethyl-2-oxoethan-1-aminium (1f) ¹H NMR (D₂O, 400 MHz) δ (ppm): 8.34(*anti*) + 8.28(*syn*) (1H, s, br, Ar-HC=N-), 7.90-7.42 (4H, m, Ar), 4.66(*syn*) + 4.13(*anti*) (2H, s, -C=N-N-CH₂-), 3.28 (9H, s, -N(CH₃)₃). ¹³C NMR (101 MHz, D₂O) δ (ppm): 171.26, 161.57, 146.74, 135.37, 133.19, 131.82, 131.07, 130.56, 129.38, 126.67, 63.94, 62.80, 54.33. HRMS⁺ C₁₃H₁₈N₃O₃⁺, Theoretical: 264.1348, Actual: 264.1355.^β mp. 162 °C.

1f



2-(2-(Chroman-8-ylmethylene)hydrazineyl)-*N,N,N*-trimethyl-2-oxoethan-1-aminium (1g) ¹H NMR (D₂O, 300 MHz) δ (ppm): 8.48(*anti*) + 8.21(*syn*) (1H, s Ar-HC=N-), 7.64 (1H, d, Ar), 7.23 (1H, d, Ar), 6.94 (1H, dd, Ar), 4.67(*syn*) + 4.21(*anti*) (2H, s, -CH₂-N(Me)₃), 4.24 (2H, t, -OCH₂-), 3.29 (9H, s, -N(CH₃)₃), 2.77 (2H, t, -OCH₂-CH₂-CH₂-), 1.98 (2H, t, -OCH₂-CH₂-CH₂-). ¹³C NMR (75 MHz, D₂O) δ (ppm): 165.28, 160.41, 153.99, 153.54, 148.98, 144.14, 133.58, 132.86, 124.62, 124.20, 120.48, 120.38, 119.87, 67.23, 64.06, 62.82, 54.41, 54.33, 24.05, 21.41, 21.34. HRMS⁺ C₁₅H₂₂N₃O₂⁺, Theoretical: 276.1721, Actual: 276.1712.^β mp. 173 °C.

1g



Preparation of Kinetics Experiments

5.5.4. Study 1 + Study 2 (See Appendix A, pages 198 and 202, respectively)

Hydrazones **1a-1g** were dissolved in 500 μL deuterated buffer solution ($\text{pD} = 5.8\text{-}7.8$), and hydrazide residue **3** (or **5** for **Study 2**) (5.0 eqv. dissolved in 500 μL buffer) was added, and solution mixed thoroughly by rapidly pipetting up and down 10 times. The sample was loaded into the NMR spectrometer to monitor the exchange kinetics over a minimum of 16 h at 25°C . The kinetics traces were corrected for the time delay between initial mixing of reagents, and the time at which the first spectrum was acquired. The absolute rate constants were obtained according to the method described on page 194.

Final prepared sample contains: 23.4 mM hydrazone (**1a-1g**), 117 mM (5.0 eqv.) hydrazide residue **3** (or **5** for **Study 2**) dissolved in a total volume of 1.00 mL phosphate/ D_2O buffer, pD 7.8.

5.5.5. Study 3 (See Appendix A, page 204)

Stock solutions of aldehydes **6a**, **6d** and **6g** were prepared by dissolving in d_6 -DMSO. Concentrations were as follows: **6g** (87 mg/mL, 536.4 mM), **6a** (67.5 mg/mL, 429.5 mM), **6d** (84 mg/mL, 791.6 mM). A 304.8 mg/mL, 1.82 M stock solution of Girard's Reagent T (**4**) in 100 mM phosphate/ D_2O buffer, pD 7.8.

A typical ^1H NMR experiment was prepared by adding aldehyde stock (29.5 – 54.4 μL) and d_6 -DMSO (345.6 – 370.5 μL) to a clean NMR tube, then diluting with 100 mM phosphate/ D_2O , pD 7.8 (389.3 μL). The reaction was initiated by addition of the Girard's Reagent T stock solution (128.4 μL), the sample was rapidly mixed by pipetting up and down 10 times, then loaded into the NMR instrument for analysis. The kinetics traces were corrected for the time delay between initial mixing of reagents, and the time at which the first spectrum was acquired. The absolute rate constants were obtained according to the method described on page 195.

Final prepared sample contains: 25.5 mM aldehyde (**6a**, **6d**, or **6g**), 254.4 mM Girard's Reagent dissolved in a total volume of 400 μL d_6 -DMSO + 517.7 μL phosphate/ D_2O buffer, pD 7.8. d_6 -DMSO was necessary to solubilize the aldehyde starting material.

5.5.6. Determination of Second Order Reversible Rate Constants

The kinetic data for hydrazone exchange reactions (**Study 1** and **Study 2**) were analyzed according to a second order reversible reaction mechanism:



Where A is the starting hydrazone (**1a-g**), B is glycol hydrazide **3** (**Study 1**) or morpholine hydrazide **5** (see **Study 2**), C is product hydrazone (**2a-g**) and D is the free hydrazide (Girard's Reagent T, **4**) liberated by the exchange process.

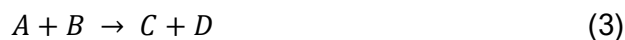
Differential rate law:

$$\frac{\delta[A]}{\delta t} = -k_f [A][B] + k_r [C][D] \quad (2)$$

Where k_f is the second order rate constant of the forward process and k_r is the second order rate constant for the reverse process. The differential rate law (2) was integrated numerically by explicit finite difference using the experimental time data, the initial values of the concentrations and trial values of k_f and k_r . The values of the two rate constants and the initial mole fraction of A (χ_A) were then optimized by least square fitting of the integrated rate law to the experimental data for [A] obtained by integration of the trimethylammonium (-NMe_3^+) signals associated with the starting hydrazone (**1a-g**) and exchange product **4** (Girard's Reagent T) in the ^1H NMR spectra recorded during the reaction. Each spectrum required about 2 minutes to collect, which is a much shorter time than the half-life of the reactions at the concentrations employed.

Statistical errors on the fitted values of rate constant are reported as $\pm 1 \sigma$ confidence intervals estimated under the usual assumption of independent and identically distributed (i. i. d.) variables and normal measurement errors.

The kinetics of hydrazone formation (**Study 3**) were analyzed according to a second order irreversible reaction mechanism:



Where *A* is the starting aldehyde (**a, d, g**), *B* is Girard's Reagent T **4**, *C* is the product hydrazone (**2a-g**) and *D* is the water molecule liberated by the condensation reaction.

Differential rate law:

$$\frac{\delta[A]}{\delta t} = -k[A][B] \quad (4)$$

Where *k* is the second order rate constant. The differential rate law (4) was integrated numerically in Microsoft Excel by explicit finite difference method, using the experimental time data, the initial values of the concentrations and trial values of *k*. The values of rate constant *k* and the initial mole fraction of A (χ_A) were then optimized by least square fitting (using Excel Solver Function) of the integrated rate law to the experimental data for [A] obtained by integration of the aldehyde (-CHO) signal and signals (*syn*- and *anti*-) associated with the hydrazone (-HC=N-N-) product in the ¹H NMR spectra recorded during the reaction. Acquisition of each ¹H NMR spectrum took approximately 2 minutes, a timescale which (at the concentration of reagents employed) was significantly shorter than the half-lives of the reactions being monitored.

Statistical errors on the fitted values of rate constant are reported as $\pm 1 \sigma$ confidence intervals estimated under the usual assumption of independent and identically distributed (i. i. d.) variables and normal measurement errors.

5.6. References

- [1] (a) S. J. Rowan, S. J. Cantrill, G. R. L. Cousins, J. K. M. Sanders, and J. F. Stoddart, *Angew. Chem. Int. Ed.*, **41**, 2002, 898–952; (b) P. T. Corbett, J. Leclaire, L. Vial, K. R. West, J. L. Wietor, J. K. M. Sanders and S. Otto, *Chem. Rev.*, 2006, **106**, 3652–3711; (c) A. Wilson, G. Gasparini and S. Matile, *Chem. Soc. Rev.* **43**, 2014, 1948–1962.
- [2] (a) Z. Rodriguez-Docampo and S. Otto, *Chem. Commun.*, **42**, 2008, 5301–5303; (b) A. Dirksen and P. E. Dawson, *Bioconjug. Chem.*, **19**, 2008, 2543–2548.
- [3] (a) W. P. Jencks, *J. Am. Chem. Soc.*, 1959, **81**, 475–481; (b) E. H. Cordes and W. P. Jencks, *J. Am. Chem. Soc.*, 1962, **84**, 832–837; (c) E. H. Cordes and W. P. Jencks, *J. Am. Chem. Soc.*, 1962, **84**, 826–831; (d) E. H. Cordes and W. P. Jencks, *J. Am. Chem. Soc.*, 1962, **84**, 4319–4328.
- [4] (a) A. Dirksen, S. Dirksen, T. M. Hackeng and P. E. Dawson, *J. Am. Chem. Soc.*, 2006, **128**, 15602–15603; (b) A. Dirksen, T. M. Hackeng and P. E. Dawson, *Angew. Chem. Int. Ed.*, 2006, **45**, 7581–7584.
- [5] B. Shi, R. Stevenson, D. J. Campopiano and M. F. Greaney, *J. Am. Chem. Soc.*, 2006, **128**, 8459–8467.
- [6] (a) E. T. Kool, D. H. Park and P. Crisalli, *J. Am. Chem. Soc.*, 2013, **135**, 17663–17666; (b) P. Crisalli and E. T. Kool, *J. Org. Chem.*, 2013, **78**, 1184–1189; (c) E. T. Kool, P. Crisalli and K. M. Chan, *Org. Lett.*, 2014, **16**, 1454–1457; (d) D. Larsen, M. Pittelkow, S. Karmakar and E. T. Kool, *Org. Lett.*, 2015, **17**, 274–277; (e) D. K. Kölmel and E. T. Kool, *Chem. Rev.*, 2017, **117**, 10358–10376. (f) L. H. Yuen, N. S. Saxena, H. S. Park, K. Weinberg and E. T. Kool, *ACS Chem. Biol.*, 2016, **11**, 2312–2319. (g) D. Larsen, A. M. Kietrys, S. A. Clark, H. S. Park, A. Ekebergh and E. T. Kool, *Chem. Sci.*, 2018, **9**, 5252–5259.
- [7] H. C. Brown *et al.* in E. A. Braude and F. C. Nachod Determination of Organic Structures by Physical Methods, Academic Press, New York, 1955.
- [8] (a) Y. Zhao and D. G. Truhlar, *Theor. Chem. Acc.*, 2008, **120**, 215–241; (b) Y. Zhao and D. G. Truhlar, *Acc. Chem. Res.*, 2008, **41**, 157–167.
- [9] Gaussian 09, Revision C.01, M. J. Frisch, G. W. Trucks, H. B. Schlegel, G. E. Scuseria, M. A. Robb, J. R. Cheeseman, G. Scalmani, V. Barone, B. Mennucci, G. A. Petersson, H. Nakatsuji, M. Caricato, X. Li, H. P. Hratchian, A. F. Izmaylov, J. Bloino, G. Zheng, J. L. Sonnenberg, M. Hada, M. Ehara, K. Toyota, R. Fukuda, J. Hasegawa, M. Ishida, T. Nakajima, Y. Honda, O. Kitao, H. Nakai, T. Vreven, J. A. Montgomery, Jr., J. E. Peralta, F. Ogliaro, M. Bearpark, J. J. Heyd, E. Brothers, K. N. Kudin, V. N. Staroverov, T. Keith, R. Kobayashi, J. Normand, K. Raghavachari, A. Rendell, J. C. Burant, S. S. Iyengar, J. Tomasi, M. Cossi, N. Rega, J. M. Millam, M. Klene, J. E. Knox, J. B. Cross, V. Bakken, C. Adamo, J. Jaramillo, R. Gomperts, R. E. Stratmann, O. Yazyev, A. J. Austin, R. Cammi, C. Pomelli, J. W. Ochterski, R. L. Martin, K. Morokuma, V. G. Zakrzewski, G. A. Voth, P. Salvador, J. J. Dannenberg, S. Dapprich, A. D. Daniels, O. Farkas, J. B. Foresman, J. V. Ortiz, J. Cioslowski, and D. J. Fox, Gaussian, Inc., Wallingford CT, 2010.
- [10] (a) Y. Lam, M. N. Grayson, M. C. Holland, A. Simon and K. N. Houk, *Acc. Chem. Res.* 2016, **49**, 750–762; (b) R. Wolfenden and M. J. Snider, *Acc. Chem. Res.* 2001, **34**, 938–945.
- [11] B. Kuhn, P. Mohr and M. Stahl, *J. Med. Chem.*, 2010, **53**, 2601–2611.
- [12] (a) D. A. Fulton, *Org. Lett.* 2008, **10**, 3291–3294. (b) C. S. Mahon, A. W. Jackson, B. S. Murray and D. A. Fulton, *Chem. Commun.* 2011, **47**, 7209–7211. (c) C. S. Mahon, A. W. Jackson, B. S. Murray and D. A. Fulton, *Polym. Chem.* 2013, **4**, 368–377.

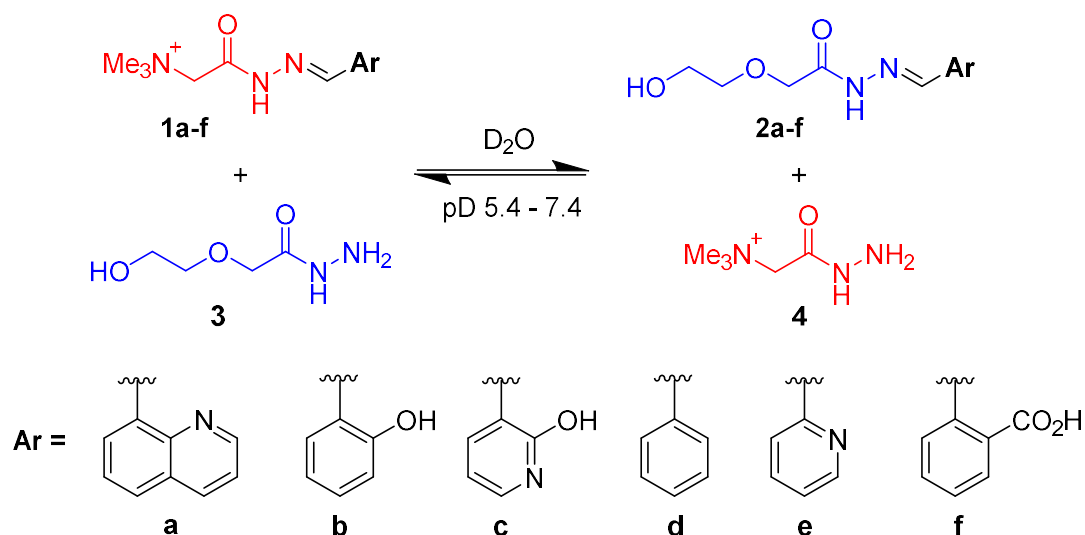
- [13] (a) A. J. Ruiz-Sanchez, P. L. Higgs, D. T. Peters, A. T. Turley, M. A. Dobson, A. J. North and D. A. Fulton, *ACS Macro Lett.*, 2017, **6**, 903–907; (b) C. S. Mahon, M. A. Fascione, C. Sakonsinsiri, T. E. McAllister, W. Bruce Turnbull and D. A. Fulton, *Org. Biomol. Chem.*, 2015, **13**, 2756–2761.
- [14] (a) C. S. Mahon, C. J. McGurk, S. M. D. Watson, M. A. Fascione, C. Sakonsinsiri, W. B. Turnbull and D. A. Fulton, *Angew. Chem. Int. Ed.*, 2017, **56**, 12913–12918; (b) C. S. Mahon and D. A. Fulton, *Chem. Sci.*, 2013, **4**, 3661–3666; (c) D. E. Whitaker, C. S. Mahon and D. A. Fulton, *Angew. Chem. Int. Ed.*, 2013, **52**, 956–959; (d) R. P. Brinkhuis, F. De Graaf, M. B. Hansen, T. R. Visser, F. P. J. T. Rutjes and J. C. M. Van Hest, *Polym. Chem.*, 2013, **4**, 1345–1350.
- [15] (a) J. F. Folmer-Andersen and J. M. Lehn, *J. Am. Chem. Soc.*, 2011, **133**, 10966–10973; (b) K. S. Kim, H. J. Cho, J. Lee, S. Ha, S. G. Song, S. Kim, W. S. Yun, S. K. Kim, J. Huh and C. Song, *Macromolecules*, 2018, **51**, 8278–8285; (c) G. Deng, F. Li, H. Yu, F. Liu, C. Liu, W. Sun, H. Jiang and Y. Chen, *ACS Macro Lett.*, 2012, **1**, 275–279; (d) D. D. McKinnon, D. W. Domaille, J. N. Cha and K. S. Anseth, *Chem. Mater.*, 2014, **26**, 2382–2387.
- [16] (a) N. Sakai and S. Matile, *J. Am. Chem. Soc.*, 2011, **133**, 18542–18545; (b) P. Charbonnaz, Y. Zhao, R. Turdean, S. Lascano, N. Sakai and S. Matile, *Chem. A Eur. J.*, 2014, **20**, 17143–17151; (c) J. Areephong, E. Orentas, N. Sakai and S. Matile, *Chem. Commun.*, 2012, **48**, 10618–10620.
- [17] (a) G. De Bo, S. Kuschel, D. A. Leigh, B. Lewandowski, M. Papmeyer and J. W. Ward, *J. Am. Chem. Soc.*, 2014, **136**, 5811–5814; (b) S. Kassem, A. T. L. Lee, D. A. Leigh, A. Markevicius and J. Solà, *Nat. Chem.*, 2016, **8**, 138–143; (d) S. Kassem, A. T. L. Lee, D. A. Leigh, V. Marcos, L. I. Palmer and S. Pisano, *Nature*, 2017, **549**, 374–378.
- [18] (a) D. A. Leigh, V. Marcos, T. Nalbantoglu, I. J. Vitorica-Yrezabal, F. T. Yasar and X. Zhu, *J. Am. Chem. Soc.*, 2017, **139**, 7104–7109; (b) S. Erbas-Cakmak, S. D. P. Fielden, U. Karaca, D. A. Leigh, C. T. McTernan, D. J. Tetlow and M. R. Wilson, *Science*, 2017, **343**, 340–343.
- [19] W. Drożdż, C. Bouillon, C. Kotras, S. Richeter, M. Barboiu, S. Clément, A. R. Stefankiewicz and S. Ulrich, *Chem. A Eur. J.*, 2017, **23**, 18010–18018.
- [20] (a) F. Della Sala and E. R. Kay, *Angew. Chemie Int. Ed.*, 2015, **54**, 4187–4191; (b) W. Edwards, N. Marro, G. Turner and E. R. Kay, *Chem. Sci.*, 2017, **9**, 125–133.
- [21] A. Krężel, W. Bal, *J. Inorg. Biochem.*, **98**, 2004, 161–166.
- [22] B. Levrand, W. Fieber, J. M. Lehn and A. Herrmann, *Helv. Chim. Acta*, 2007, **90**, 2281–2314.

5.7. Appendix A

Kinetics Traces, Absolute Rate Constants and Preliminary NMR Spectra

5.7.1. Study 1

Hydrazones **1a-f** (23.4 mM) were exchanged with hydrazide **3** (117 mM) in buffered D₂O at pD 7.8, pD 6.8 and pD 5.8. See Fig. 10 for kinetics traces.



Scheme 1: Hydrazones **1a-f** undergoing component exchange with hydrazide **3** to afford product hydrazones **2a-f**.

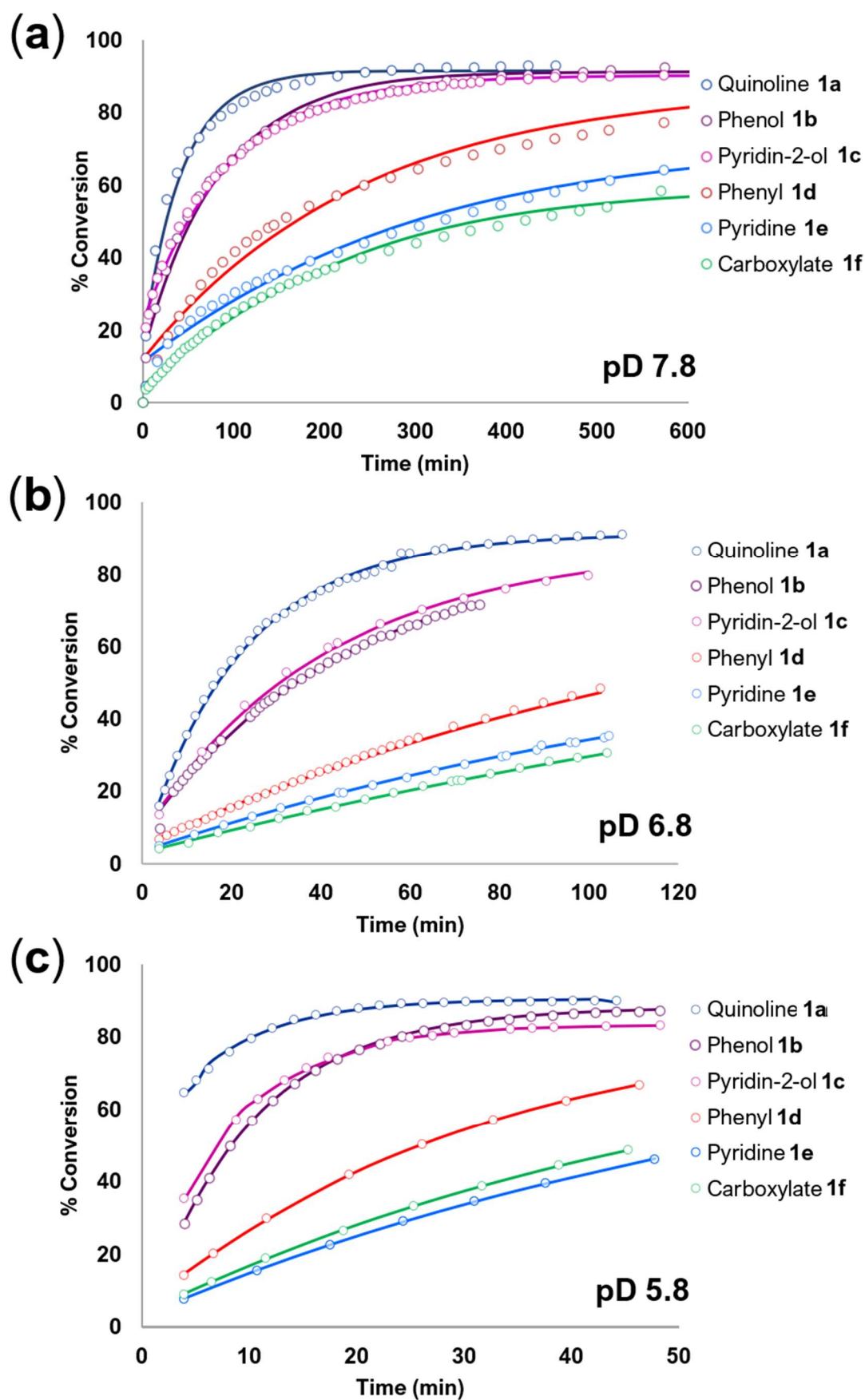


Figure 10: Kinetics traces of hydrazones **1a-1f** reacting with hydrazide **3** at pD 7.8 (Study 1) (a), pD 6.8 (b) and pD 5.4 (c). Experimental data and theoretical fit are shown as circles and solid lines, respectively. The fitting procedure and treatment of statistical errors is described on page 194.

Second Order Rate Constants:

	k_{rel}	k_f (M ⁻¹ s ⁻¹)			k_r (M ⁻¹ s ⁻¹)		
		pD 7.8	pD 6.8	pD 5.8	pD 7.8	pD 6.8	pD 5.8
1a	30.3	0.159 (± 2.9 %)	0.344 (± 0.6 %)	0.852 (± 0.5 %)	0.107 (± 10.6 %)	0.154 (± 4.3 %)	0.858 (± 2.2 %)
1b	26.5	0.087 (± 1.9 %)	0.156 (± 0.4 %)	0.744 (± 0.1 %)	0.055 (± 0.6 %)	0.116 (± 2.6 %)	0.368 (± 0.7 %)
1c	5.7	0.076 (± 0.9 %)	0.162 (± 0.5 %)	0.162 (± 1.6 %)	0.071 (± 3.3 %)	0.128 (± 1.0 %)	0.776 (± 1.3 %)
1d	7.4	0.030 (± 2.4 %)	0.052 (± 0.4 %)	0.207 (± 0.2 %)	0.030 (± 9.3 %)	0.043 (± 2.7 %)	0.206 (± 0.6 %)
1e	3.8	0.018 (± 2.1 %)	0.036 (± 0.3 %)	0.107 (± 0.1 %)	0.067 (± 12.3 %)	0.220 (± 5.9 %)	0.090 (± 1.4 %)
1f	4.4	0.020 (± 1.1 %)	0.028 (± 0.2 %)	0.122 (± 0.1 %)	0.121 (± 4.9 %)	0.035 (± 1.1 %)	0.157 (± 0.3 %)

Table 1: Second order rate constants (k_f , k_r) for hydrazone exchange of **1a-1f** with glycol hydrazide **3** (**Study 1**). Where, k_f is the rate constant for the forward reaction and k_r is that of the reverse process. The statistical errors are reported as percentages. They correspond to 68 % (1 σ) confidence intervals (see page 194 for details).

5.7.2. Preliminary Kinetics Experiment

Hydrazone **1g** was exchanged with hydrazide **2** (Fig. 11a) to form product hydrazone **2g**, which precipitated from aqueous solution and thus disappeared from the ^1H NMR spectra (Fig. 11b) which made it impossible to monitor reaction progress using ^1H NMR as the analytical method. It was therefore necessary to study an alternative exchange process (Study 2) involving morpholine hydrazide **5** (Scheme 2).

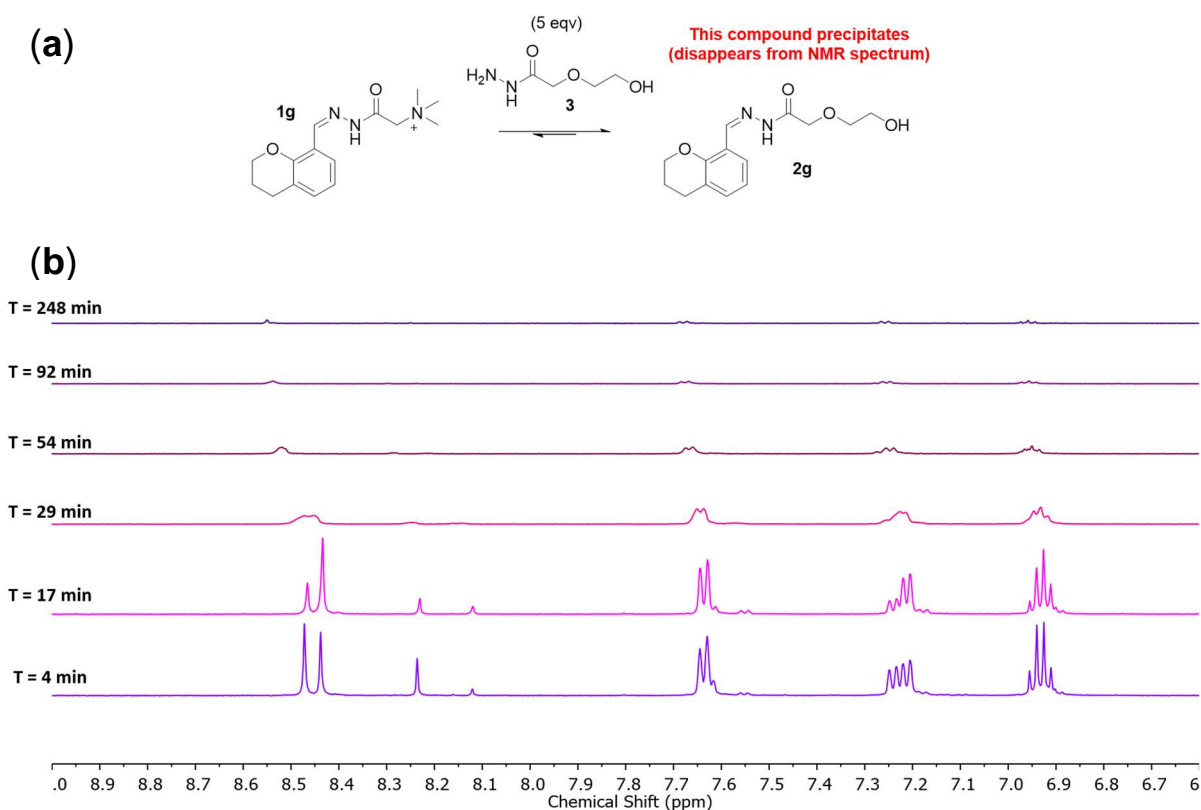
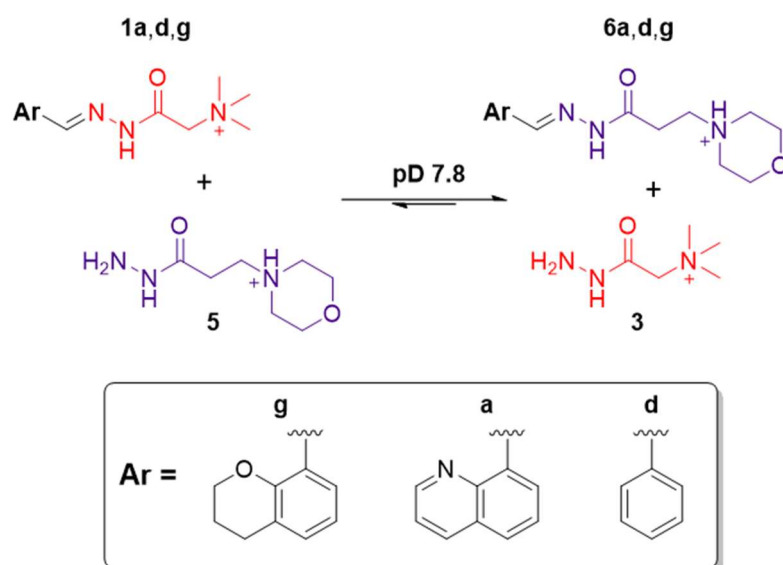


Figure 11: A preliminary experiment revealed that hydrazone exchange of **1g** with hydrazide **3** (a) resulted in precipitation of the product hydrazone (**2g**), which led to signal broadening in the ^1H NMR spectra. (b). Convolution of the NMR spectra ultimately prevented accurate monitoring of the hydrazone exchange kinetics, thus an alternative exchange process (Study 2) was investigated (see Scheme 2).

5.7.3. Study 2

Hydrazones **1a**, **1d** and **1f** (23.4 mM) were exchanged with hydrazide **4** (117 mM) in buffered D₂O at pD 7.8. See Fig. 12 for kinetics traces.



Scheme 2: Hydrazones **1a**, **1d** and **1g** undergo component exchange with hydrazide **3** to afford product hydrazones **6a**, **6d** and **6g**.

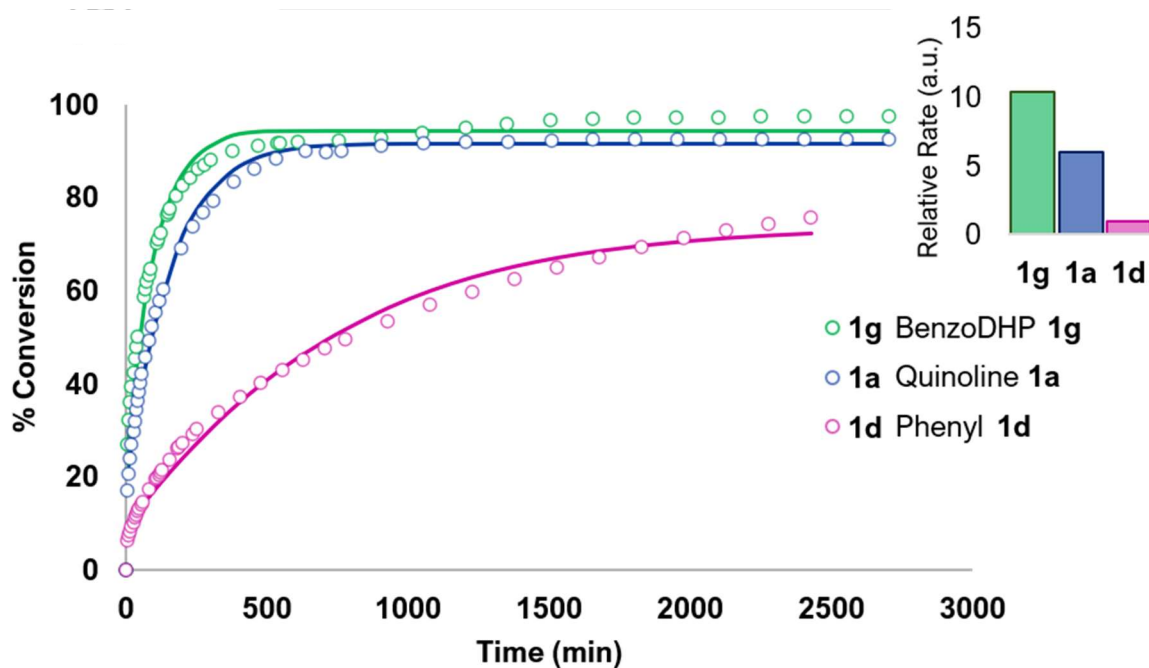


Figure 12: Kinetics traces of BenzoDHP **1g**, Quinoline **1a** and Phenyl **1d** reacting with hydrazide **5** at pD 7.8. Inset shows relative rates of hydrazone exchange. Experimental and fitted data are shown as circles and solid lines, respectively. See page 194 for details of fitting the kinetics data.

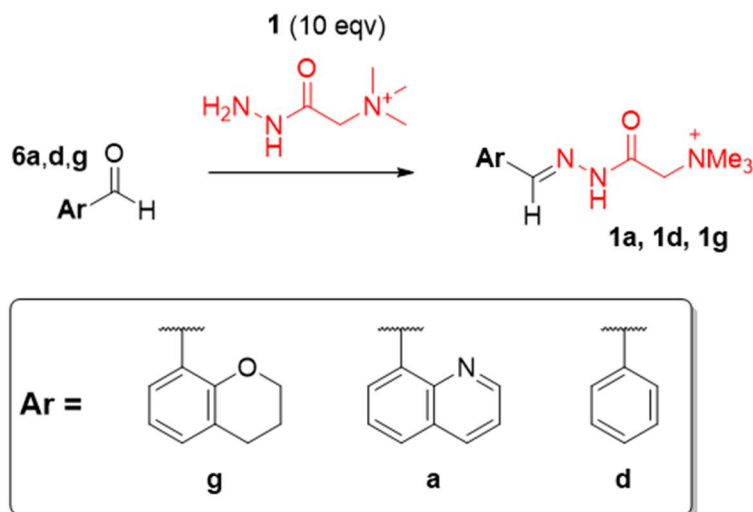
Second Order Rate Constants:

		k_f (M ⁻¹ s ⁻¹)	k_r (M ⁻¹ s ⁻¹)
	k_{rel}	pD 7.8	pD 7.8
1a	10.3	0.078 (± 9.9 %)	0.037 (± 30.4 %)
1d	6.0	0.046 (± 9.3 %)	0.032 (± 22.2 %)
1g	1.0	0.008 (± 2.5 %)	0.021 (± 10.1 %)

Table 2: Second order rate constants (k_f , k_r) for hydrazone exchange of **1a,d,g** with morpholine hydrazide **5** (Study 2). Where, k_f is the rate constant for the forward reaction, k_r is that of the reverse process and k_{rel} is the relative rate as deduced from k_f . The statistical errors are reported as percentages. They correspond to 68 % (1 σ) confidence intervals.

5.7.4. Study 3

Hydrazone formation kinetics of aldehydes **6-8** with Girard's Reagent T was studied by ^1H NMR spectroscopy. Hydrazone formation was observed to be significantly faster than hydrazone exchange under similar conditions. See page 193 for details on sample preparation.



Scheme 3: Aldehydes **6a**, **6d** and **6g** undergo condensation reactions with hydrazide **1** to afford product hydrazones **1a**, **1d** and **1g**. ^1H NMR spectroscopy was employed to monitor the kinetics of this reaction at pD 7.8

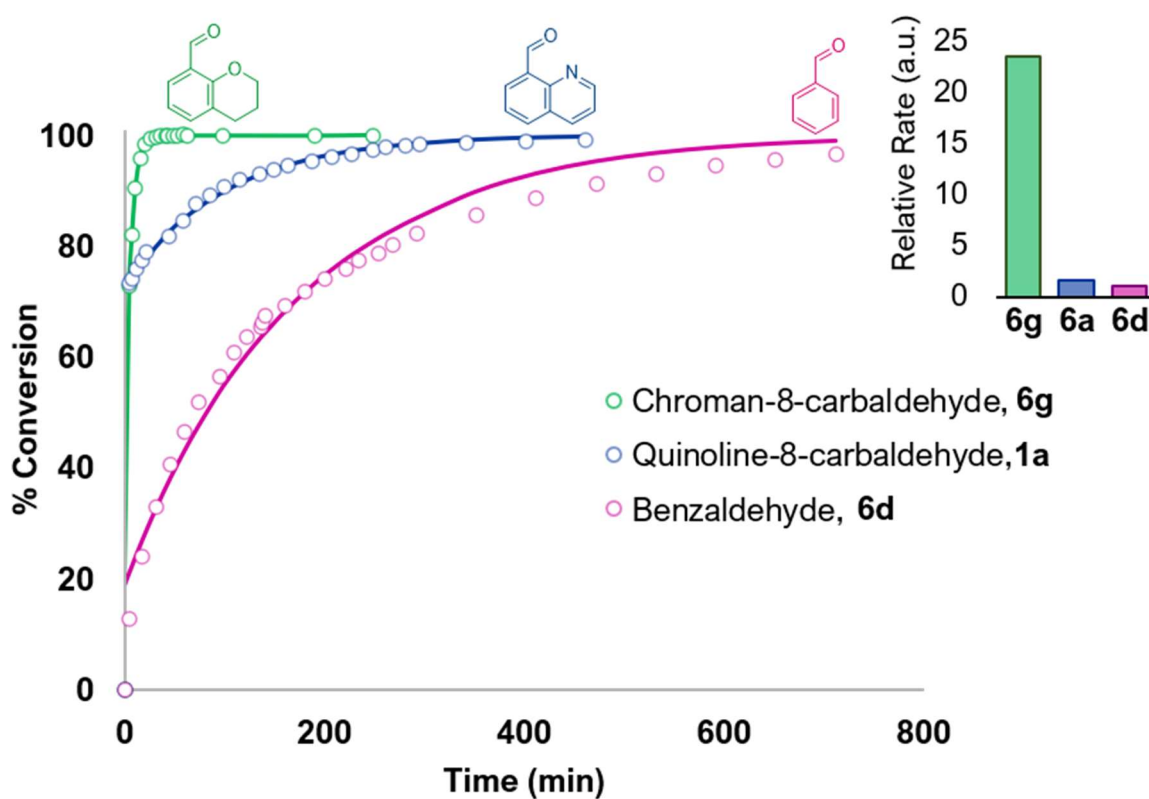


Figure 13: Hydrazone formation kinetics obtained for aldehydes **6a, d, g** in their condensation reaction with hydrazide **1**. Inset shows the relative rates of hydrazone formation.

Second Order Rate Constants:

		k_2 (M ⁻¹ s ⁻¹)
	k_{rel}	pD 7.8
Chroman-8-carbaldehyde, 6g	23.6	1.266 (± 0.5 %)
Quinoline-8-carbaldehyde, 6a	1.6	0.024 (± 13.8 %)
Benzaldehyde, 6d	1.0	0.002 (± 6.9 %)

Table 3: Second order rate constants (k) for hydrazone formation of **6a**, **6d** and **6g** with Girard's reagent T (**4**) (Study 3). The statistical errors are reported as percentages. They correspond to 68 % (1 σ) confidence intervals (see page 195 for details).

5.7.5. Computational Studies

Hydrazone Exchange Studies: In order to gain insights to our experimental observations, computational studies were undertaken. Reaction mechanisms were studied at the M06-2X/6-31G* level of theory. To simplify the calculations, the hydrazide employed in modelling the exchange processes was AcNHNH₂, which was also used as the hydrazide component within the hydrazone. The process modelled is therefore a symmetrical exchange but provided the mechanistic insight required. Protonation free energies were computed using H₃O⁺ as the proton source and corrected by adding the difference between the computed and experimental values of *K_w*. Corrections to 1 M concentrations were applied using an ideal gas approximation. Concentrations of H⁺ and ⁻OH that are appropriate to the pH were applied and water was assumed to be present at 55.5 M.

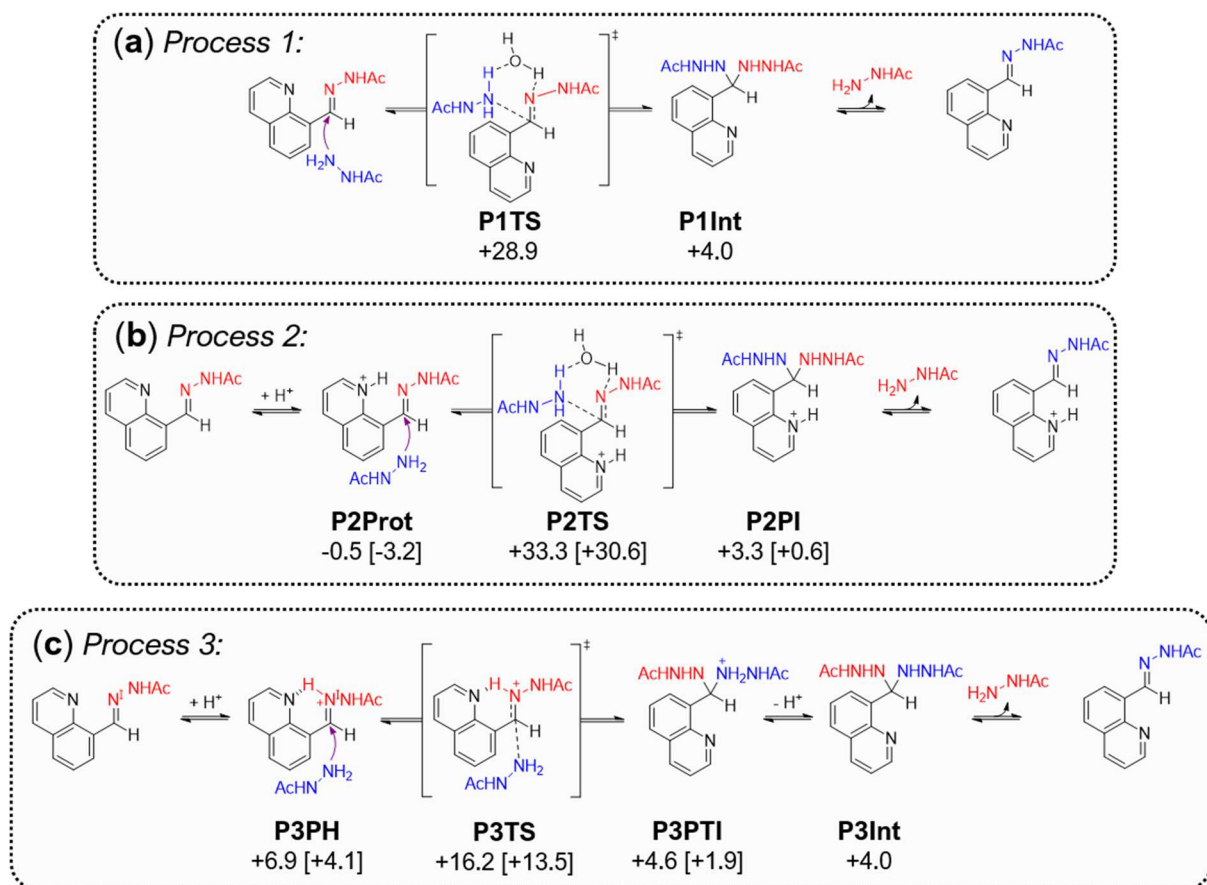


Figure 14: Three mechanisms of hydrazone exchange which were explored computationally. (a) Process (1): No protonation of hydrazone prior to hydrazide attack (uncatalysed reaction). (b) Process (2): Protonation of proximal acid/base group within aldehyde component of hydrazone. (c) Process (3): Protonation of hydrazone nitrogen (N¹) prior to attack. See page 207, Tables 4 - 6 for all energetics (ΔG^\ddagger) values.

Process 1:

Substrate	P1TS	P1Int
quinoline 1a	+28.9	+4.0
phenyl 1d	+27.1	+3.0
pyridine 1e	+26.2	+3.7
carboxylate 1f	+23.0	+3.0

Table 4: Free energies (ΔG^\ddagger) computed for intermediates and transition states of **1a-f** at pH 7.4. Values computed at pH 5.4 are in brackets (where given).

Process 2:

Substrate	P2Prot	P2TS	P2PI	ΔG^\ddagger
quinoline 1a	-0.5 [-3.2]	+33.3 [+30.6]	+3.3 [+0.6]	+33.8 [+33.8]
phenyl 1d	0.0	+27.1	+3.0	+27.1
pyridine 1e	+3.4 [+0.7]	+33.2 [+30.5]	+3.2 [+0.5]	+33.2 [+30.5]
carboxylate 1f	-16.2 [-19.0]	+15.3 [+12.7]	-14.4 [-17.1]	+31.6 [+31.6]

Table 5: Free energies (ΔG^\ddagger) computed for intermediates and transition states of **1a-f** at pH 7.4. Values computed at pH 5.4 are in brackets (where given).

Process 3:

Substrate	P3PH	P3TS	P3PTI	ΔG^\ddagger
quinoline 1a	+6.8 [+4.1]	+16.2 [+13.5]	+4.6 [+1.9]	+16.7 [+16.7]
phenol 1b	+11.1 [+8.3]	+19.4 [+16.7]	+23.2 [+20.4]	+19.4 [+16.7]
phenyl 1d	+15.0 [+12.2]	+20.3 [+17.6]	+7.9 [+5.2]	+20.3 [+17.6]
pyridine 1e	+13.4 [+10.6]	+20.2 [+17.5]	+6.7 [+3.9]	+20.2 [+17.5]
carboxylate 1f	-4.3 [-9.8]	+10.8 [+5.3]	+4.3 [-1.1]	+27.0 ^a [+24.3]

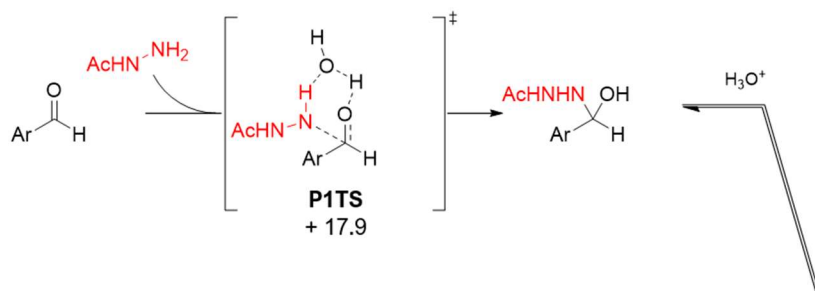
^a this is the free energy relative the lowest free energy state available pre-rate-limiting transition state, **P2Prot**

Table 6: Free energies (ΔG^\ddagger) computed for intermediates and transition states of **1a-f** at pH 7.4. Values computed at pH 5.4 are in brackets (where given).

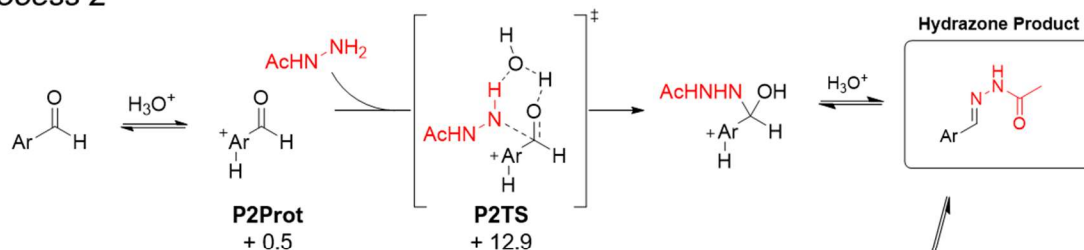
Hydrazone Formation versus Hydrazone Exchange

In order to gain insight to the mechanistic differences between hydrazone exchange and hydrazide, both reactions were studied in an identical way, with three possible mechanisms being considered: Process (1) hydrazide directly attacks the unprotonated aldehyde (Fig. 15a); process (2) protonation of acid/base groups within the aldehyde, followed by hydrazide attack (Fig. 15b); process (3) protonation of the aldehyde, followed by hydrazide attack (Fig. 15c).

(a) Process 1



(b) Process 2



(c) Process 3

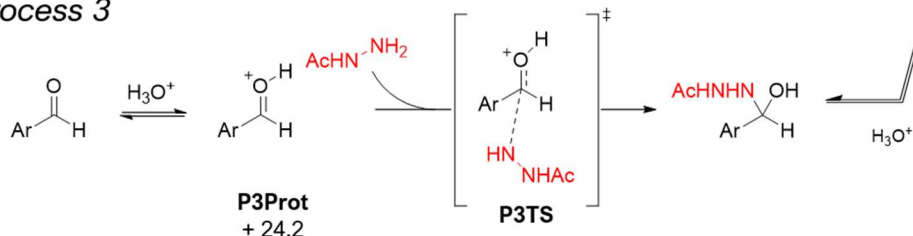


Figure 15: Three potential mechanisms of hydrazone formation were explored computationally for quinoline-8-carbaldehyde (Ar = quinoline). Free energy barriers (kcal/mol) were calculated relative to the lowest energy species. (a) No protonation prior to hydrazide attack on aldehyde (uncatalysed reaction). (b) Protonation of proximal acid/base group within the aromatic aldehyde, and subsequent hydrazide attack to form the hemiaminal intermediate. (c) Protonation of aldehyde oxygen prior to hydrazide attack.

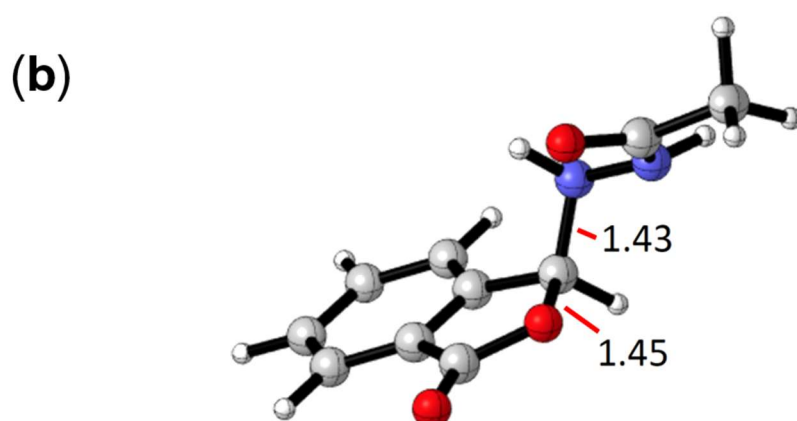
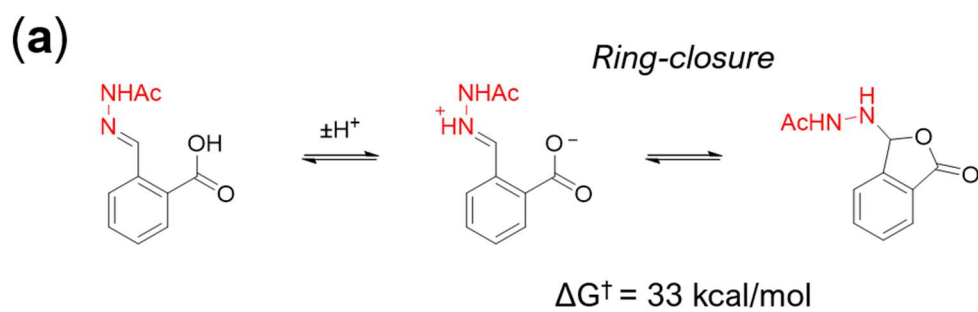


Figure 16: Computational modelling revealed that hydrazone **1f** forms a meta-stable cyclic intermediate, formed by carboxylate ring-closing upon tetrahedral (aminal) intermediate to form a 5-membered ring (a). Annotations indicate key bond lengths: 1.45 Å (O-C), 1.43 Å (C-N) are shown for the computed structure of the ring-closed intermediate (b).

Chapter 6

Research Outlook

6.1. Abstract

This thesis set out to explore the ‘shrink-wrapping’ of nano- and microscale objects – a process which is thought to occur through the adsorption of discrete polymer chains onto object surfaces followed by their ‘structural metamorphosis’ into covalently crosslinked polymer films. It was hypothesized that ‘structural metamorphosis’ could be exploited to achieve the ‘wrapping’ complex biological targets such as virus-like particles or bacteria, which may improve their stabilities and permit engineering of their surface properties. Chapter 1 proposed an incremental approach towards this ambitious goal (Fig. 1), beginning with the ‘wrapping’ of readily available model systems (Fig. 1a-b). Whilst it was initially envisaged that ‘simple’ nano-objects (**Model System I** and **II**) (Fig. 1a-b) would be straightforward to ‘wrap’ compared to complex biological targets (Fig. 1c-d), results later demonstrated that the ‘wrapping’ of nanoscale objects is often more challenging to investigate than microscale objects, as nano-objects often prone to unwanted processes of particle-particle aggregation and may suffer irreversible polymer-object binding on account of their large surface areas and high surface energies. Considering these challenges, a top-down approach for investigating the ‘shrink-wrapping’ of biological targets is now proposed. Studies should first explore the ‘wrapping’ of large objects, such as micron-sized bacteria, the surface-coating of which can be readily monitored by the fluorescence microscopy protocol established in Chapter 3.

‘Shrink-Wrapping’ Biological Targets of Increasing Complexity:

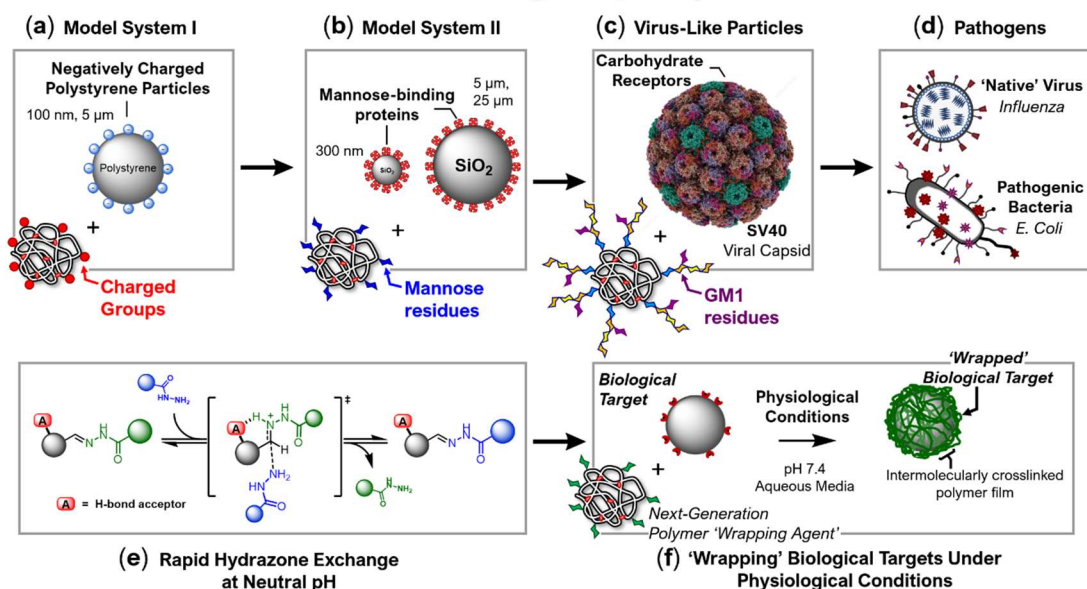


Figure 1: Proposed research strategy for progressing the ‘shrink-wrapping’ concept towards biological targets of increasing complexity. **(a) Model System I:** Electrostatically charged SCPNs were adsorbed onto oppositely charged polystyrene nano- or microscale particles. Electrostatic interactions drive the ‘shrink-wrapping’ process. **(b) Model System II:** Protein-functionalized silica nano- and microspheres displaying mannose-binding receptors were ‘shrink-wrapped’ with mannose decorated glyco-SCPNs. **(c) Virus-Like Particles:** Investigations towards the ‘shrink-wrapping’ Simian virus 40 viral capsid. **(d) ‘Shrink-wrapping’** of ‘native’ viruses such as influenza, or pathogenic bacteria such as *E. Coli*. **(e)** Rate-enhancing structural features (**A**) facilitate rapid hydrazine exchange at neutral pH, and thus their inclusion upon polymer scaffolds may permit ‘wrapping’ of biological targets under physiological conditions **(f)**.

6.2. The Challenges of ‘Wrapping’ Nano-Objects

The ‘metamorphosis’ of polymer chains upon object surfaces was found to be a subtle and thus difficult to interrogate process. The ‘shrink-wrapping’ of 3D nanoscale objects proved particularly difficult to investigate for two key reasons: (i) Nano-dimensional objects have high surface areas, and thus may exhibit unwanted processes of non-specific binding and particle-particle aggregation. These processes both can inhibit objects from being ‘wrapped’ within a homogeneous layer of polymer film. (ii) DLS is one of the few readily available analytical techniques that can monitor the ‘shrink-wrapping’ of nanoscale objects within nanometer-thick polymer films in real-time and in aqueous solution. However, the process of attaching or removing polymer chains from the particle surface was observed to modulate the colloidal stability of nano-objects, which can trigger their aggregation and may have a drastic impact on the accuracy with which DLS analysis can characterize the thickness of object-bound polymer films. In only the most well-behaved systems does DLS provide truly informative data from which judgements can be made to optimize the ‘shrink-wrapping’ chemistry. Because of the significant analytical challenges associated with monitoring the formation of thin polymer films upon nanoscale objects, future work should first explore the ‘wrapping’ of microscale objects, which can be readily interrogated *via* the established fluorescence microscopy protocol, and thus may serve as a reliable model for the ‘wrapping’ of nanoscale objects.

6.3. Success in ‘Wrapping’ Microscale Objects

Whilst ‘wrapping’ of nanoscale objects proved difficult to investigate, excellent progress has been made in the ‘shrink-wrapping’ of microscale objects. In Chapter 3, fluorescence microscopy experiments granted direct access to monitor the formation of polymer films upon microparticle surfaces, and thus provided a strong characterization handle with which to investigate the ‘shrink-wrapping’ phenomenon. Successful ‘wrapping’ was observed only for polymer ‘wrapping-agents’ which contain dynamic covalent acyl hydrazone crosslinks, thus highlighting that hydrazone exchange reactions are key to the ‘wrapping’ process. Specific ligand-receptor interactions were also observed to play a crucial role in concentrating polymer chains upon the particle periphery through complementary recognition events, which were hypothesized to drive the ‘shrink-wrapping’ process. Since ‘wrapping’ only occurs in the presence of complementary recognition between polymer ‘wrapping-agent’ and the object surface, it may be possible to selectively ‘wrap’ target objects within complex mixtures – a feature which could later be exploited to sequester biologically-relevant objects, such as viruses or pathogenic bacteria, from their local environment. ‘Wrapping’ may also stabilize these species, increase their shelf-lives, and improve their performance – in much the same way that plastic wrappers and films do for everyday objects.

6.4. Development of Next-Generation Polymer ‘Wrapping-Agents’

In future research, the ‘shrink-wrapping’ of sensitive biological targets will require hydrazone exchange processes which operate with reasonable kinetics at neutral pH. A combined computational-experimental study in Chapter 5 identified the key structural features of hydrazone bonds which undergo rapid component exchange at neutral pH (Fig. 1e). Incorporating the structures of these fast-exchanging hydrazones into polymer scaffolds (Fig. 1f) is anticipated to provide a useful boost to the kinetics of ‘shrink-wrapping’ at neutral pH, thus permitting this chemistry to be interfaced with biological targets under their ‘native’ (physiological) conditions.

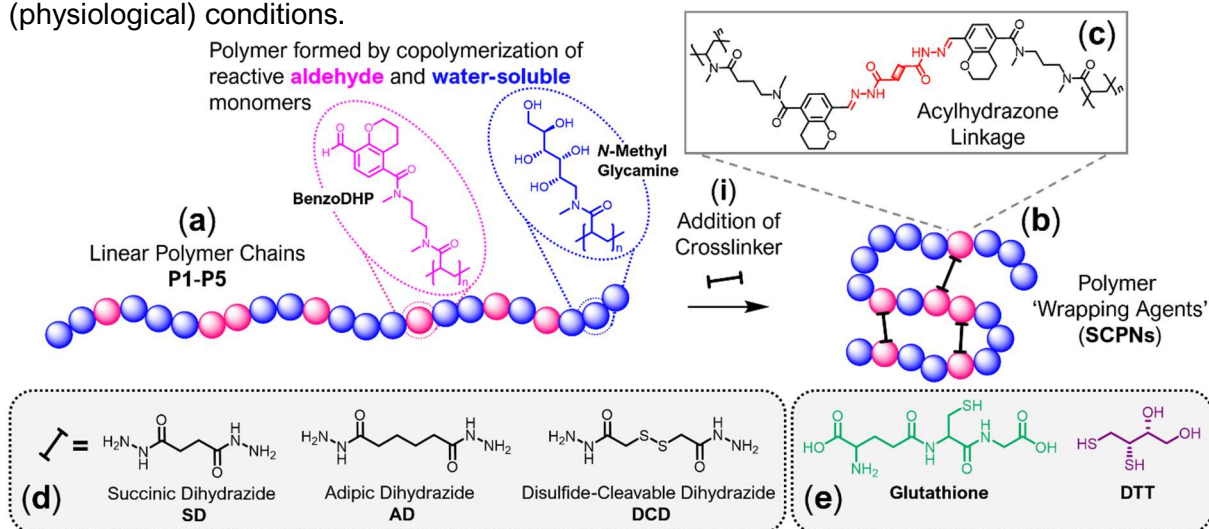


Figure 2: Proposed synthesis of next-generation polymer ‘wrapping-agents’ which should be hydrophilic, highly water-soluble and capable of rapid hydrazone exchange at neutral pH. (a) Linear polymer chains (**P1 - P5**) produced by copolymerization of reactive **aldehyde** (**BenzoDHP**) and **water-soluble** (**N-Methyl Glycamine**) monomers. A range of linear polymer chains (**P1 - P5**) should be produced, which contain varying densities of **aldehyde** ‘anchor-points’ which can be intramolecularly crosslinked (i) to form polymer ‘wrapping-agents’ (**SCPNs**) (b). **SCPNs** should be constructed with **acyl hydrazone crosslinks** (c), but varied crosslinker functionality can be achieved by employing a range of crosslinker types (d), including a disulfide-cleavable linker (**DCD**) which is anticipated to allow the triggered ‘un-wrapping’ of objects, by addition of reducing agents such as **glutathione** or **DTT** (e).

Figure 2 outlines the proposed synthesis of next-generation polymer ‘wrapping-agents’ which should be hydrophilic, highly water-soluble, and capable of rapid hydrazone exchange at neutral pH. Hydrophilic polymer scaffolds (Fig. 2a) bearing reactive **aldehyde** (**BenzoDHP**) ‘anchor-points’ and highly **water-soluble** (**N-Methyl Glycamine**) moieties can be constructed by copolymerization of the corresponding acrylamide monomers. In Chapter 5, **BenzoDHP** was shown to established rapid hydrazone exchange at physiological pH, on account of its ability to stabilize the transition state through hydrogen-bonding interactions (Fig. 1e), and thus inclusion of these moieties upon polymer scaffolds (Fig. 2a) is anticipated to afford ‘wrapping-agents’ capable of ‘shrink-wrapping’ at physiological pH. In order to facilitate ‘triggered’ object ‘un-wrapping’, future work should incorporate alternative crosslinker types, such as disulfide-cleavable linker **DCD** (Fig 2d) into polymer ‘wrapping agents’, as these linkages could be cleaved by addition of reducing agents such as **glutathione** or **DTT** (Fig. 2e).

6.5. Beyond the ‘Wrapping’ of Nanoscale Objects

Beyond the idea of ‘shrink-wrapping’ nano- and microscale objects, it was hypothesized that the ‘wrapping’ approach may also be applied to the capture individual water droplets suspended in air – an impressive feat which is achieved in nature by the bacterial hydrophobin **BsIA** (Fig. 3a, iv).

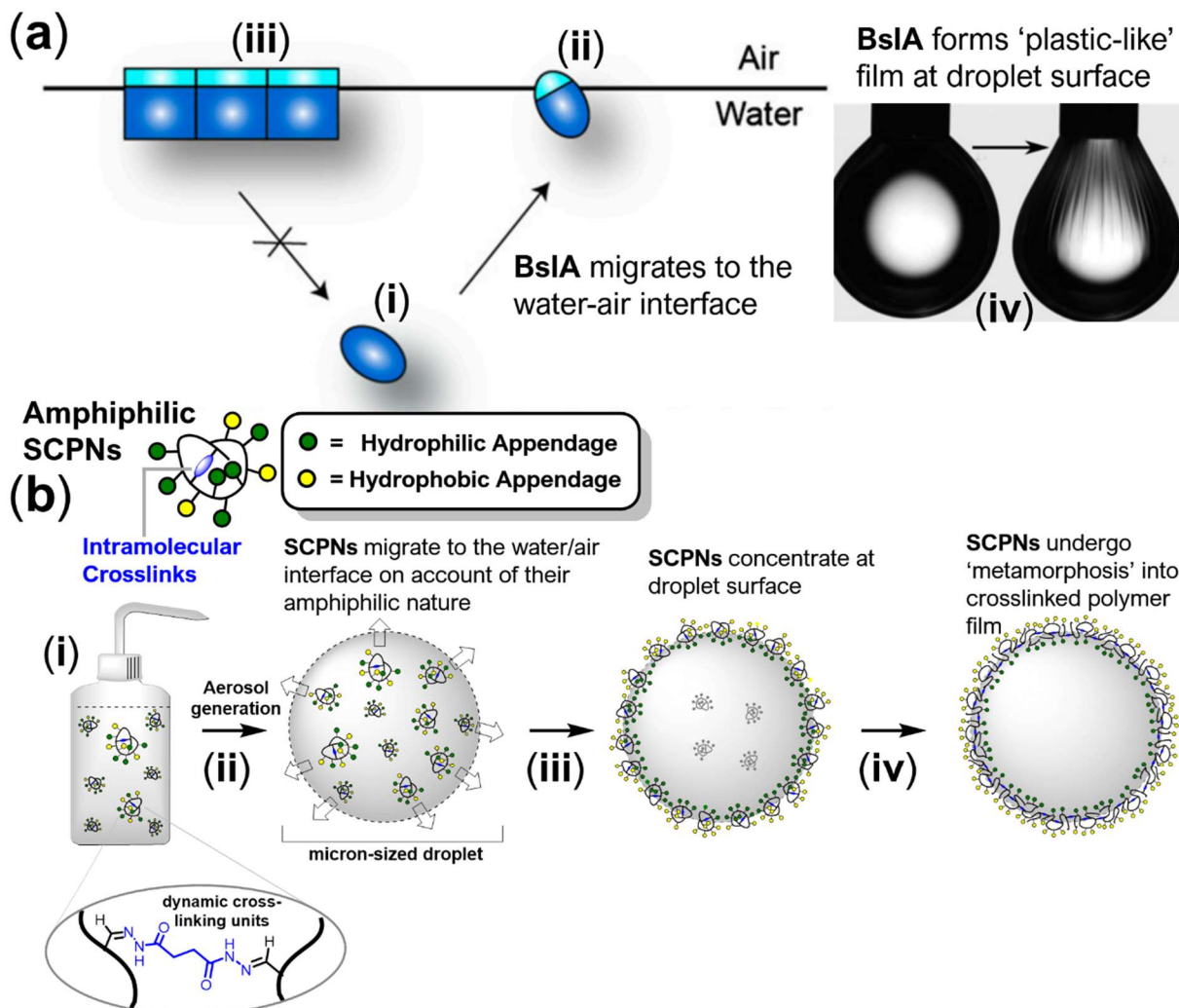


Figure 3: (a) ‘Structural metamorphosis’ of the bacterial hydrophobin **BsIA**, a crucial protein component of bacterial biofilms. Wild-type **BsIA** (i) migrates to the water/air interface and the protein spontaneously undergoes a conformational ‘switch’ (ii), which drives the irreversible formation of a polymer-like ‘crosslinked’ protein film (iii) upon the droplet surface. Droplet compression experiments (iv) revealed that **BsIA** films are elastic in nature, encapsulating the water droplet within plastic-like layer. (b) ‘Shrink-wrapping’ of aqueous droplets by **Amphiphilic SCPNs**, which are ‘decorated’ with hydrophilic (green) and hydrophobic (yellow) appendages. In dilute solutions (i) with low interfacial areas, these **SCPNS** will be kinetically stable and they will not aggregate. However, after generation of an aerosol (ii), a dramatic increase in interfacial area is expected, which thus drives **SCPNS** to migrate and concentrate at the water/air interface (iii). This process brings the **SCPNS** into close spatial proximity with one another, thus allowing their ‘metamorphosis’ into crosslinked polymeric film (iv) which is anticipated to encapsulate the droplet surface, much like **BsIA** (a, iv).

BsIA is a relatively hydrophobic protein component which plays a crucial role in biofilm formation. When dissolved in aqueous solution, **BsIA** spontaneously migrates to the water/air interface (Fig. 3a, **ii**) on account of its amphiphilic nature. This process triggers a 'switch' in the protein conformation to 'display' a hydrophobic patch upon its periphery, which subsequently 'locks' the proteins together (Fig. 3a, **iii**) in a plastic-like film (Fig. 3a, **iv**) at the droplet surface. Inspired by this elegant form of 'structural metamorphosis', it was hypothesized that amphiphilic polymer 'wrapping agents' (Fig. 4b) displaying an appropriate balance of hydrophilic (**green**) and hydrophobic (**yellow**) appendages may also migrate to the water/air interface, concentrate themselves at the droplet surface, and thus could trigger the 'metamorphosis' of neighbouring polymer chains to form a crosslinked polymer film (Fig. 3b, **i** - **iv**) upon the droplet exterior. Future work should further develop this concept, as it presents scope to 'capture' aqueous droplets within polymer films, and thus an entirely new class of 'smart' materials may be engineered. Polymer 'wrappings' are anticipated to (i) prevent unwanted droplet coalescence, (ii) protect and stabilize aerosol cargos in their environments, (iii) allow control over when cargos are released, and (iv) allow us to isolate and store droplets of tailored size, concentration and composition. Furthermore, the dynamic covalent nature of the crosslinks within polymer film permits scope to achieve triggered 'un-wrapping' of aqueous droplets, or even to perform component exchange of residues located within polymer films at the droplet interface.

6.6. Research Outlook

This chapter has proposed a basic research framework and outlined the key concepts which should be explored during future work. With firm evidence of the 'wrapping' of microscale objects now in hand, the outlook for this research program is very optimistic. Chapter 3 established a robust fluorescence microscopy protocol by which the 'wrapping' of microscale objects can be monitored with confidence. Whilst the 'wrapping' of nanoscale objects has proven difficult to achieve – on account of nano-objects having a high propensity to exhibit irreversible and non-specific binding polymer-object binding – it is now anticipated that the highly hydrophilic poly(ethylene glycol) based 'wrapping agents' developed in Chapter 3 will circumnavigate these issues, and should thus permit successful 'shrink-wrapping' of nanoscale targets. Chapter 5 elucidated candidate hydrazone structures, which may undergo hydrazone exchange at neutral pH, and this constitutes the first step in preparing the next-generation of polymer 'wrapping-agents', capable of 'wrapping' biological targets under their 'native' physiological conditions. Finally, the novel concept of 'wrapping' aqueous droplets within polymer films was proposed – a process in which hydrophobic interactions could be exploited in tandem with dynamic covalent chemistry to deliver an entirely new class of smart materials.

Manuscript A

Molecular Recognition-Mediated ‘Wrapping’ of Micron-Sized Spherical Objects

Manuscript Submitted July 2020

Patrick L. Higgs, Jordan L. Appleton, W. Bruce Turnbull
and David A. Fulton

**Chemistry – School of Natural
and Environmental Sciences**
Newcastle University
Newcastle upon Tyne
NE1 7RU United Kingdom

16/07/2020

Dear Steve

Molecular Recognition-Mediated ‘Wrapping’ of Micron-Sized Spherical Objects

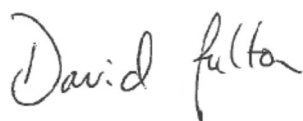
We would like to present the above manuscript for your consideration as an *Edge* article in *Chemical Science*.

There has been a growing interest in developing methods to isolate or stabilize nano- and micron-sized objects through their inclusion within protective coatings. Polymer films make particularly appealing protective coatings, but to the best of our knowledge, there are no reported methods to ‘wrap’ tiny objects within polymer films.

In this work we demonstrate how a molecular-recognition mediated ‘wrapping’ approach can be applied to successfully ‘wrap’ micron-sized particles within a layer of cross-linked polymer film. This involves the utilisation of polymer ‘wrapping’ agents that can concentrate upon the microparticle surface then cross-link with one another to form polymer films. The concentration process is driven by specific molecular recognition between the polymer and the surface, and cross-linking is facilitated by intramolecular dynamic covalent bonds within the polymer that rearrange to intermolecularly cross-link the polymer chains. This work is significant because it suggests that the approach will also be compatible with virus-like particles, which are of significant interest as next generation vaccines but which suffer from poor stability in warm or dehydrating conditions and would thus benefit from their inclusion within ‘wrappers’ that improve their stabilities. This work will be of considerable general interest, especially in the field of ‘smart’ materials, stimulate discussion and inspire the development of new materials

We hope that you will consider this manuscript for publication in *Chemical Science*, and we look forward to hearing from you shortly.

Yours faithfully



David A Fulton

Molecular Recognition-Mediated 'Wrapping' of Micron-Sized Spherical Objects

Patrick L. Higgs,^a Jordan L. Appleton,^a W. Bruce Turnbull^b and David A. Fulton^{*a}

Received 00th January 20xx,
Accepted 00th January 20xx

DOI: 10.1039/x0xx00000x

There is growing interest in developing methods to 'wrap' nano- and micron-sized biological objects within films that may offer protection, enhance their stability or improve performance. We describe the successful 'wrapping' of lectin-decorated microspheres, which serve as appealing model micron-sized objects, within cross-linked polymer film. This approach utilizes polymer chains decorated with complementary carbohydrates that drive the concentration of polymer onto microparticle surfaces, thus bringing the polymer chains into close spatial proximity with one another. Dynamic covalent crosslinkers then undergo intra- to interpolymer chain crosslinking, leading to the formation of polymeric film coating the microparticles. Experiments demonstrate that both complementary molecular recognition and the dynamic covalent nature of the crosslinker are required for successful 'wrapping' to occur. The utilization of poly(oligoethylene glycol) polymers, which may prevent non-specific interactions that can lead to unsuccessful outcomes, was also crucial to ensuring successful 'wrapping'. This work is significant as it suggests that nano- and micron-sized biological objects such as virus-like particles, bacteria or mammalian cells – all of which may benefit from additional environmental protection or stabilization in emerging applications – could also be 'wrapped' by this approach.

Introduction

Crosslinked polymer films are ubiquitous in the modern world, acting as barriers to protect objects from their environments, providing stabilization or improving performance.¹ Scientific advances are continually leading to the development of new nano- and micron-sized biological objects that may also benefit from their inclusion within crosslinked polymer films able to act as a protective 'wrapper'. For example, virus-like particles (VLPs) are nanoscale components of vaccines^{2a-c} that often lack robustness towards temperature, pressure and humidity,^{2d} and methods to 'wrap' them may improve their stability in hot or dehydrating conditions.^{2e} Engineered bacteria, such as those able to produce biofuels, can also suffer from stability issues, and their inclusion within a 'wrapper' that helps to maintain membrane integrity may also improve their performance.³ It has also been demonstrated⁴ that electrostatic layer-by-layer approaches can be used to coat platelets (red blood cells), showing that the inclusion of cells within a coating can be harnessed to present novel approaches to manipulate their biological functions.

To address the challenge of 'wrapping' nano- or micron-sized objects, we propose a new molecular recognition-mediated approach whereby polymer chains bind to the object surface then

crosslink with one another. This can be achieved with polymers decorated with ligands that recognize and bind to complementary receptors displayed upon the object (Fig. 1a), driving the concentration of the polymer chains upon the surface. The polymer chains then crosslink with one another (Fig. 1b) through an intra- to inter-polymer chain crosslinking process (Fig. 1c) that can only occur when the polymers are spatially close to one another, resulting in the formation of crosslinked polymer film. The polymer crosslinking process exploits the component exchange

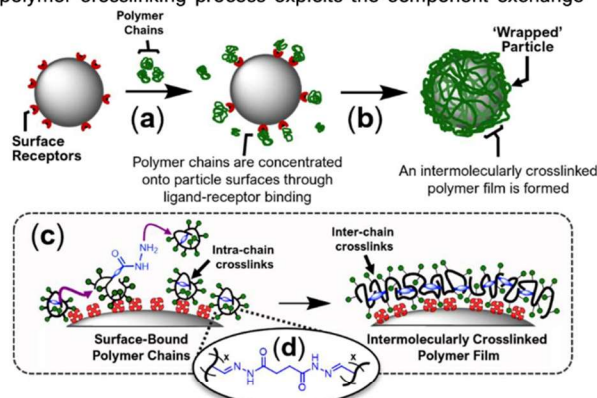


Figure 1: Molecular recognition-mediated 'wrapping' of nano- and micron-sized objects. (a) Polymer chains bind through specific molecular recognition to receptors located upon the object surface. (b) Now spatially close to one another, polymer chains undergo intra- to intermolecular crosslinking with their neighbouring chains to form a crosslinked polymer film upon the particle surface. (c) Film formation is driven by the conversion of intra-chain crosslinks into inter-chain crosslinks. This process relies upon the ability of dynamic covalent acyl hydrazone bonds (d) to undergo component exchange process.

^a Chemistry-School of Natural and Environmental Sciences, Bedson Building, Newcastle University, Newcastle upon Tyne, NE1 7RU.

^b School of Chemistry, University of Leeds, LS2 9JT.

† Footnotes relating to the title and/or authors should appear here.

Electronic Supplementary Information (ESI) available: [details of any supplementary information available should be included here]. See DOI: 10.1039/x0xx00000x

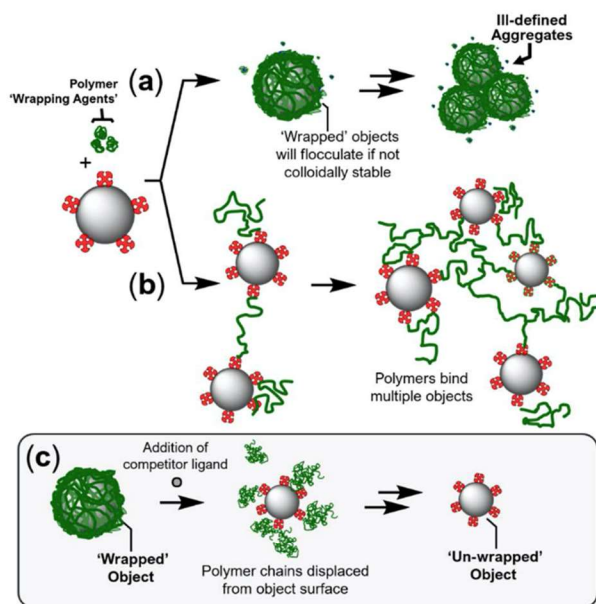
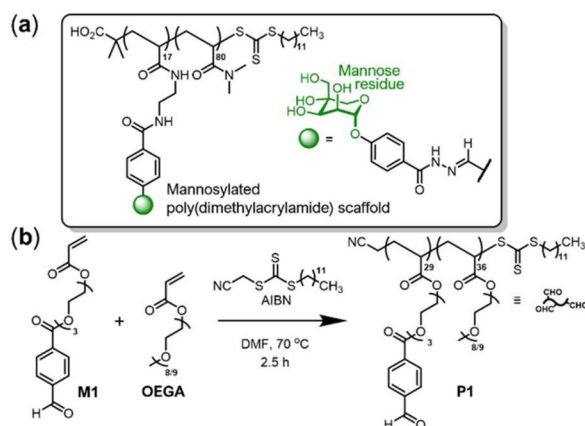


Figure 2: The challenges of 'wrapping' nano- and micron-sized objects. (a) The 'wrapped' objects flocculate to form unwanted crosslinked aggregates. (b) Polymer chains bind to multiple objects, again leading to the unwanted formation of aggregates. (c) Control experiment in which the polymer 'wrapping' is displaced from the particle by addition of a competitor ligand which binds receptors upon the object surface.

properties of dynamic covalent acyl hydrazone bonds⁵ used to intramolecularly crosslink the polymer chain (Fig. 1d). These well-known bonds can exchange their components to form new bonds, and this molecular-level process facilitates intra- to inter-polymer chain crosslinking, driving polymer film formation.

The successful application of this approach to 'wrap' a dispersion of nano- or micron-sized objects, however, presents some considerable challenges. After successful 'wrapping', it is important that the objects do not subsequently flocculate as this would likely lead to further component exchange process involving the dynamic covalent linkers, leading to the formation of an ill-defined aggregate bound together by crosslinked polymer chains (Fig. 2a). Polymer chains must also not bind multiple objects, otherwise the outcome of the experiment may also tend towards the formation of aggregates (Fig. 2b). This unwanted outcome can be minimized by the elimination of non-specific interactions between polymer and object and the careful choice of experimental conditions, in particular the polymer:object stoichiometries and concentrations. The elimination of non-specific aggregation between polymers and objects is also required for what we consider to be the key experiment (Fig. 2c) to prove that successful 'wrapping' has occurred. This experiment requires that excess small molecule competing ligand be added in an attempt to displace the bound polymer chains from the surface of the object. If the polymer chains cannot not be displaced then it suggests they have successfully crosslinked with one another; if they are displaced, then crosslinking between chains has not occurred, and the 'wrapping' process has therefore not been successful. Unwanted non-specific interactions between polymer and object may lead to polymers remaining bound to the object even if they have not crosslinked with one another to form a film,



Scheme 1: (a) Mannose-decorated polyacrylamide used in unsuccessful preliminary studies, presumably on account of being overly hydrophobic. (b) Preparation of hydrophilic aldehyde-functionalized copolymer scaffold P1. The oligo(ethylene glycol) side chains provide exceptional hydrophilicity.

thus making it difficult to ascertain if the intra- to interpolymer crosslinker rearrangement has occurred successfully.

Here, we describe a polymer 'wrapping agent' that can eliminate non-specific binding effects and thus successfully 'wrap' a micron-sized object. This polymer was based upon a poly(oligoethylene glycol acrylate) (p(OEGA)) scaffold, that on account of its outstanding hydrophilicity does not participate in non-specific binding, eliminating the unwanted outcomes described in Fig. 2 and thus helping to ensure effective 'wrapping' occurs.

Results and Discussion

As a stepping stone towards the 'wrapping' of nano- and micron-sized biological objects we focused on 'wrapping' spherical silica microparticles with diameters of approximately 5 μm , as these provided a readily-available low-cost target with which to develop the 'wrapping' chemistry. Silica microparticles can be easily functionalized with protein receptors that provide a means for polymer chains decorated with complementary ligands to concentrate upon their surfaces. Their relatively large size also means they can be visualised easily by fluorescence and optical microscopy. This feature circumvents a reliance upon dynamic light scattering techniques, where the formation of even small quantities of multiparticle aggregates can skew measured hydrodynamic radii and polydispersities, rendering the technique unable to provide convincing evidence for the formation of 'wrapped' objects. We chose to coat silica microparticles with the mannose-binding lectin concanavalin A (ConA)⁸ (**MP-ConA**) (see ESI). Lectins are particularly relevant receptors as many viruses^{7a} and bacteria^{7b} are decorated with lectins whose purpose is to bind complementary carbohydrates upon the surfaces of mammalian cells.^{7c}

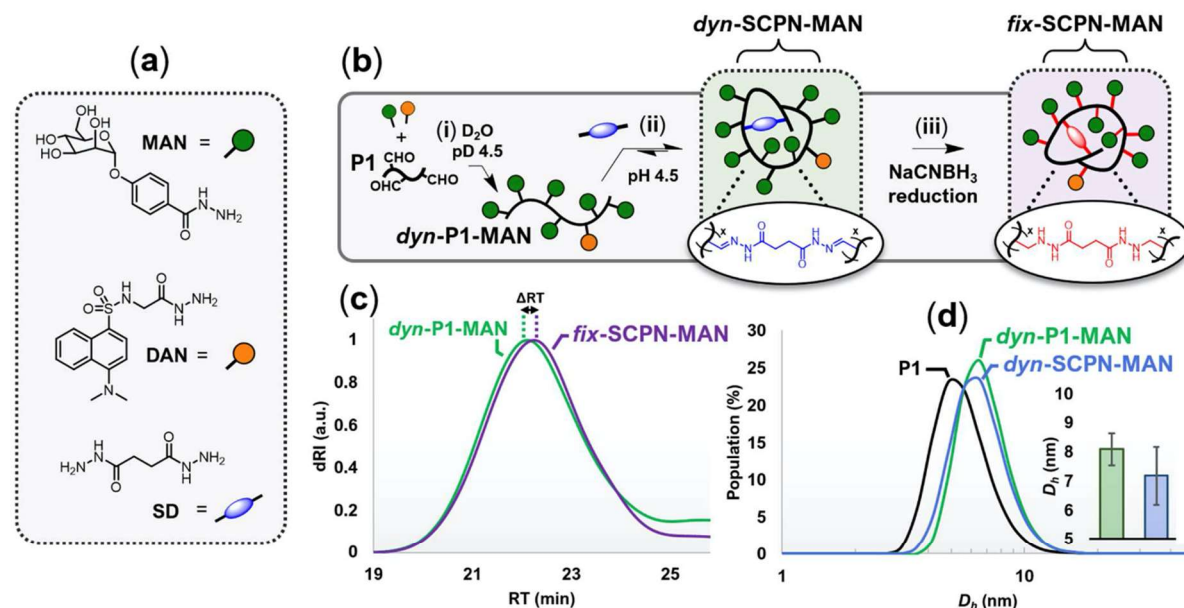


Figure 3: Synthesis and characterization of mannosylated polymer species; *dyn*-P1-MAN, *dyn*-SCPN-MAN and *fix*-SCPN-MAN. (a) Structures of mannose hydrazide (MAN) ligand, dansyl hydrazide (DAN) fluorescent label and succinic dihydrazide (SD) crosslinker. (b) P1 was 'decorated' (step i) with hydrazide residues MAN and DAN to afford mannosylated polymer scaffold *dyn*-P1-MAN. Addition of dihydrazide SD (1 eqv) (step ii) afforded intramolecularly crosslinked polymer *dyn*-SCPN-MAN. Reduction of *dyn*-SCPN-MAN (step iii) afforded *fix*-SCPN-MAN, whose crosslinks were no longer dynamic. (c) GPC analysis of conversion of *dyn*-P1-MAN into *dyn*-SCPN-MAN. Normalized differential refractive index (dRI) traces revealed a small increase in retention time (Δ RT) for *fix*-SCPN-MAN (purple) relative to *dyn*-P1-MAN (green), consistent with chain collapse. (d) DLS (*D_h*) particle size distributions of P1 (black), *dyn*-P1-MAN (green) and *dyn*-SCPN-MAN (blue) at [polymer] = 1 mg mL⁻¹. Inset: Mean *D_h* values of *dyn*-P1-MAN (green) and *dyn*-SCPN-MAN (blue). Error bars indicate standard deviation.

Preliminary attempts at 'wrapping' microparticles using mannose-decorated polymers based upon poly(dimethylacrylamide) (Scheme 1a) were unsuccessful, with significant multiparticle aggregates being observed. We speculate that on account of their utilization of relatively hydrophobic aromatic aldehyde-functionalized co-monomers, which are required as 'anchor points' for dynamic covalent crosslinkers, these copolymers display a propensity to engage in non-specific interactions that lead to the unsuccessful outcomes described in Fig. 2. Furthermore, it is likely that the hydrophilicity imparted by the dimethyl acrylamide co-monomers does not sufficiently mask this hydrophobicity, further compounding the problem.

Synthesis of the Hydrophilic Polymer 'Wrapping Agent'

We thus chose to base our next generation of polymer 'wrapping agents' upon p(OEGA) copolymers, where we anticipated that the superior solubilizing effects of the OEGA moieties meant these copolymers could comfortably accommodate poorly water-soluble benzaldehyde units, and thus would be less likely to participate in non-specific binding. PEGylation is a well-established strategy in drug-development,⁸ where the incorporation of non-toxic, non-immunogenic, highly hydrophilic PEG fragments onto relatively hydrophobic pharmaceutical 'cores' has afforded therapeutic agents with enhanced aqueous solubility, biodistribution and pharmacokinetic profiles, lower levels of hydrophobic aggregation,⁹ less off-target toxicity and has brought substantial improvements to therapeutic index.¹⁰ Inspired by this tried-and-tested approach, our decision to improve hydrophilicity and eliminate non-specific binding by inclusion of PEG units within copolymer scaffolds was thus anticipated to also enhance biocompatibility of the 'wrapping agents'.

The synthesis of the polymer 'wrapping agent' was based upon the linear aldehyde-functionalized copolymer P1 (Scheme 1b), which was prepared by the RAFT-copolymerization of aldehyde-containing acrylate monomer M1 (ESI) with the commercially-available hydrophilic comonomer OEGA. Analysis by gel permeation chromatography (GPC) revealed (ESI) a monomodal distribution of reasonably low polydispersity (PDI = 1.4), consistent with a controlled polymerization process. The monomer composition (M1:OEGA of 1:1.24) and the number-average molecular weight (*M_n* = 27.4 kDa) were determined by ¹H NMR spectroscopy. The reaction (Fig. 3b, step i) of P1 with excess mannose hydrazide (MAN) and dansyl hydrazide (DAN) afforded the mannosylated copolymer *dyn*-P1-MAN. The mannose residues are complementary ligands for the ConA receptors upon the peripheries of target microsphere MP-ConA, and the fluorophore DAN, which was appended in small quantities, allows visualization of polymer films by microscopy. Purification by dialysis against water and subsequent characterization by ¹H NMR spectroscopy indicated that all aldehyde functions had reacted and unconjugated MAN/DAN had been successfully removed. We chose to intramolecularly crosslink P1 with dynamic covalent acyl hydrazone bonds, which we have previously¹¹ shown are able to undergo intra- to interchain crosslinking when concentrated. Thus, treatment of *dyn*-P1-MAN with succinic dihydrazide (SD) (Fig. 3b, step ii) induces^{12b} component exchange through a transimination-type process, resulting in intra-polymer chain crosslinking to yield the desired polymer 'wrapping agent' *dyn*-SCPN-MAN. The crosslinking process was monitored (Fig. 3d) by GPC analysis of aliquot of reactions which were treated with NaBH₃CN to reduce the dynamic hydrazone bonds (Fig. 3b, step iii); this 'fixing' of all dynamic bonds was required to ensure the species cannot undergo any

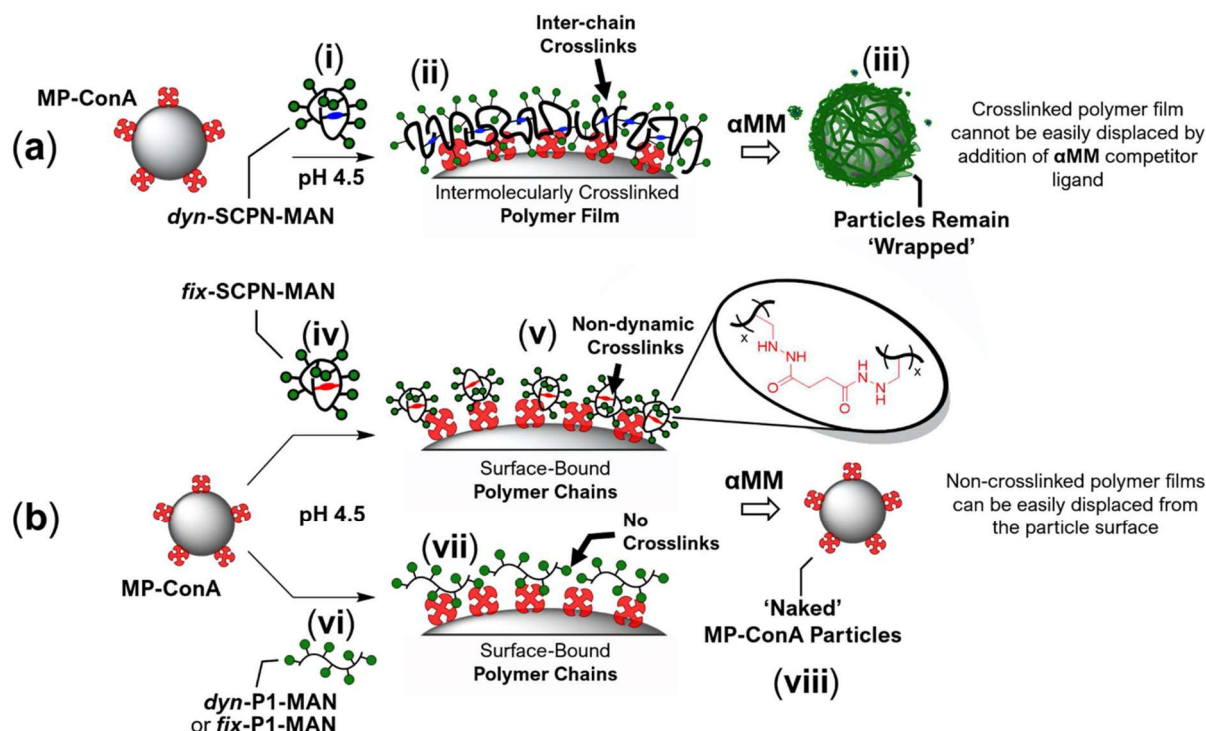


Figure 4: (a) Treatment of microparticles (MP-ConA) with *dyn-SCPN-MAN* (step i) leads to the successful 'wrapping' of the microparticle within a polymer film (ii) where the polymers are intermolecularly crosslinked with one another. This film cannot be displaced from the particle surface by incubation with competitor ligand α MM (iii). (b) Control experiments performed with *fix-SCPN-MAN* (non-dynamic crosslinks) (iv) and *dyn-P1-MAN* (no crosslinks)(vi) lead to non-crosslinked particle surfaces (v and vii), and thus these polymer layers are readily displaced by incubation with α MM to reveal the 'naked' ConA microparticles (MP-ConA)(viii). These control experiments aim to demonstrate that (1) 'shrink-wrapping' introduces additional stability to polymer films generated upon particle surfaces and (2) the crosslinks must have a dynamic covalent character in order for 'shrink-wrapping' to successfully occur.

component exchange process during analysis. This revealed an increase in retention time of *fix-SCPN-MAN* (purple) compared to *dyn-P1-MAN* (green), an observation that indicates collapse of polymer chains to form species of decreased volume,¹³ and is consistent^{13b,14a} with successful intramolecular crosslinking. DLS analysis (Fig. 3d) revealed a subtle decrease in the hydrodynamic diameter (D_h) of *dyn-SCNP-MAN* (blue) relative to that of the linear (non-crosslinked) *dyn-P1-MAN* (green), an observation that was also suggestive of successful intramolecular crosslinking. The intramolecular nature of the crosslinking means *dyn-SCNP-MAN* possesses the so-called single chain polymer nanoparticle (SCNP) architecture,^{14a} an emerging class of polymer nanoparticle which has received much attention from researchers over the last decade or so.^{14b-i}

It was anticipated that after binding to MP-ConA, the polymer chains would then crosslink with one another to afford a crosslinked polymer 'wrapper' (Fig. 4a). For control experiments (Fig. 4b), we used mannose-decorated polymers able to bind onto the microsphere but unable to then crosslink with one another as they do not possess crosslinks (*dyn-P1-MAN* and *fix-P1-MAN*), or their dynamic covalent crosslinks had been kinetically fixed (*fix-SCNP-MAN*). *fix-P1-MAN* was prepared by the reduction of *dyn-P1-MAN* with NaBH_3CN . It was anticipated that these controls would be displaced from the particle surface by the addition of excess α -D-methyl mannopyranoside (α MM), a small molecule ligand that binds ConA.¹⁵

Microparticles are Successfully 'Wrapped' when Treated with the Polymer 'Wrapping Agent'

In 'wrapping' experiments, microparticles MP-ConA (1 mg/mL) were incubated with dansyl-labelled *dyn-SCNP-MAN* or control polymers (*dyn-P1-MAN*, *fix-P1-MAN* or *fix-SCNP-MAN*) (2.5 mg/mL) in 100 mM acetate buffer (pH 4.5) for 18 h and unbound polymers were removed from the particle surfaces by centrifugal washing steps (ESI). Aliquots of each sample ($3 \times 5 \mu\text{L}$) were then deposited onto a clean glass slide, dried, and then carefully imaged by fluorescence microscopy (Fig. 5a-d). As anticipated, fluorescence was observed around the microparticles (Fig. 5, columns C1, C2), indicating all polymers were able to successfully bind onto the surfaces of the microparticles. These images also predominately show individual microparticles or relatively low-number aggregates; no significant numbers of larger many-particle aggregates were observed, suggesting the effectiveness of the oligoethylene glycol appendages of the polymers in preventing unwanted aggregation. Excess α MM was then added and each sample left to incubate at 37 °C for 24 h then purified by centrifugation to remove unbound polymer, and the samples imaged by microscopy (Fig. 5, columns C3, C4). Significant fluorescence was still observed upon the microparticles originally treated with *dyn-SCNP-MAN* (Fig. 5d), an observation indicating that the polymer coating was not displaced from the microparticle surface upon treatment with an excess of α MM. The images of the microparticles originally treated with

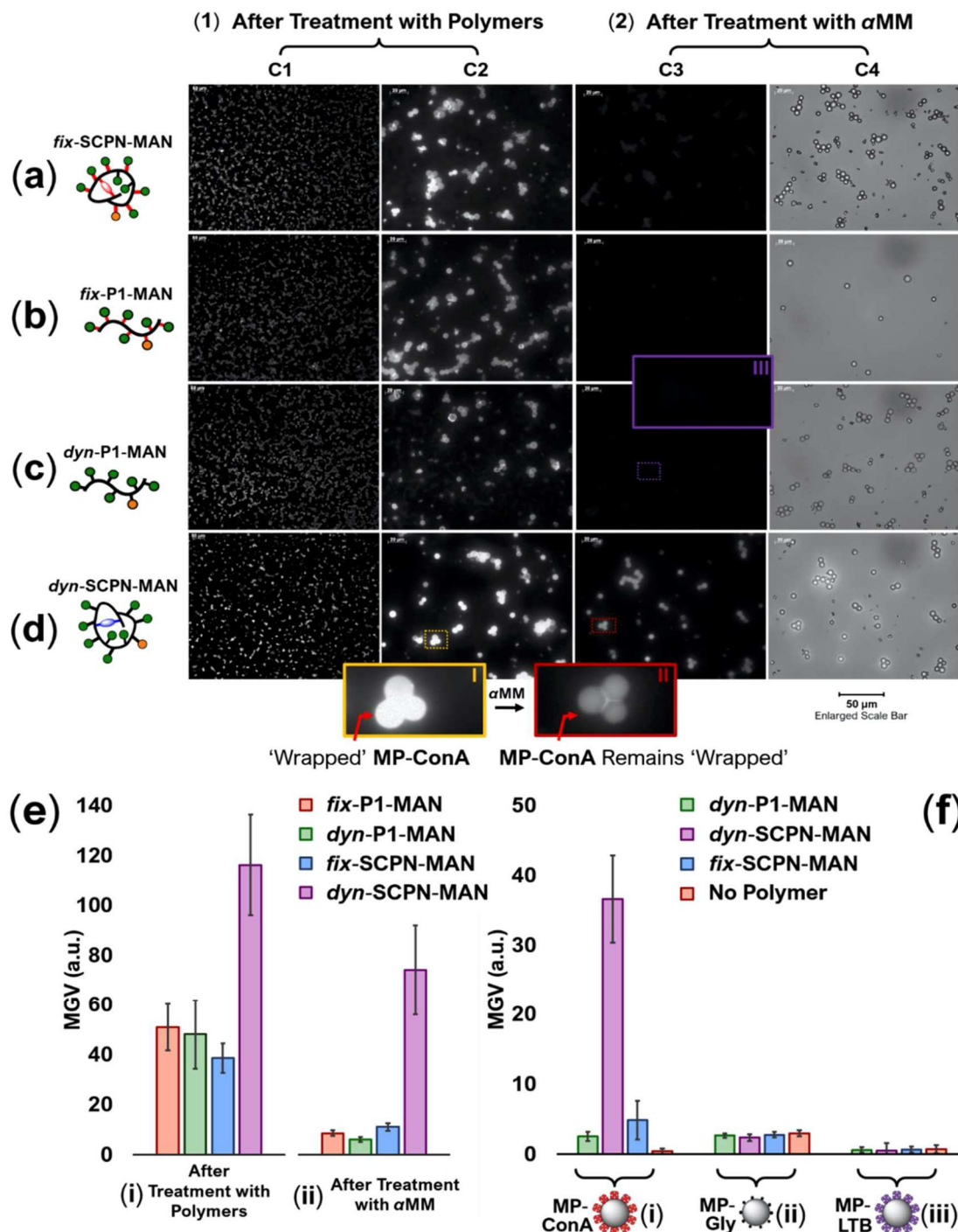


Figure 5: Representative fluorescence microscope images of 'wrapping' experiments. Images show microparticles (MP-ConA) after treatment with polymers (Image group (1), column C2 is a magnification of column C1) and then after incubation with α MM (Image group (2) shows the same particles both under normal light (C4) and under UV irradiation (C3); this comparison was required to demonstrate the presence of non-emissive particles). After treatment of microparticles with control polymers (a) *fix*-SCPN-MAN (non-dynamic), (b) *fix*-P1-MAN (non-dynamic) and (c) *dyn*-P1-MAN (no crosslinks,) fluorescence was observed around all microparticles, indicating polymers have bound to the microparticle surfaces. After treatment with α MM, however, all polymers were fully displaced from the surfaces, indicating polymer crosslinking has not occurred. (d) After microparticle treatment with polymer 'wrapping agent' *dyn*-SCPN-MAN fluorescence was observed around all microparticles. This fluorescence remains after treatment with α MM, indicating the polymer chains have successfully crosslinked and thus cannot be displaced. Insets I-III: Further magnified images produced for regions of interest (see highlighted areas) within selected micrographs. (e) Mean gray-values (MGVs) obtained for 'wrapped' MP-ConA (i) before and after (ii) incubation with α MM to displace polymer 'wrappings'. (f) MGVs obtained from 'wrapping' and control experiments with three microparticle types: (a) MP-ConA, (b) MP-Gly and (c) MP-LTB. MGVs were determined from images after α MM incubation to attempt to displace the polymers from the particle surfaces. Bars represent the average MGVs were measured for > 100 individual particles. Error bars indicate standard deviation. A no polymer control experiment was included (orange bars), which reveal the 'background' brightness of 'naked' microparticles in the absence of polymer. Bars in (e-f) represent average MGVs determined for < 100 particles. Error bars indicate standard deviation.

controls (**fix-SCNP-MAN**, **dyn-P1-MAN** and **fix-P1-MAN**) (Fig. 5a-c) show a significant reduction in the fluorescence associated with the microparticles, indicating that excess **α MM** has been able to successfully displace these polymers from the surface of these objects. Taken together, these observations suggest that upon their binding to the microparticle surface, polymer 'wrapping agent' **dyn-SCNP-MAN** had successfully undergone dynamic intra- to interpolymer chain linking to form a crosslinked polymer 'wrapping' around the microparticle which could not be displaced upon the addition of excess **α MM**. Control polymers (**fix-SCNP1-MAN**, **dyn-P1-MAN** and **fix-P1-MAN**), on the other hand, were not able to form crosslinked coatings, and thus were displaced from the microparticle surface upon the addition of excess **α MM**.

The relative levels of binding of polymers to the microspheres was estimated by measuring the magnitude of the fluorescence for each sphere using image analysis software which calculates mean gray values (MGVs) for each sphere (see ESI for details). Comparison of MGv values after treatment with polymers indicate (Fig. 5e) that all microparticles are of similar brightness (MGV values ~ 37 – 51), except the sample treated with **dyn-SCNP-MAN** (pink bars), which is considerably brighter (MGV ~ 116 \pm 21). Previous work has shown^{12b} that crosslinked films prepared by molecular recognition-mediated film formation are often thicker than a single layer of polymer chains because the initially formed layer is able to recruit further chains from solution into the crosslinked network. This possibility is not available to the control polymers as they lack dynamic crosslinkers, and hence there is less fluorescence associated with their coated microparticles. After treatment with excess **α MM**, there was a fall in MGv from 116 to 74 for the microparticle treated with **dyn-SCNP-MAN**, suggesting that some polymer was only weakly bound to the microparticle surface. This observation was rationalized by the hypothesis that not all **dyn-SCNP-MAN** chains will successfully crosslink upon the microparticle surface because of the relatively low intramolecular crosslinking density (each chain has on average only one crosslinker, and thus it is likely that a portion of the population contains no crosslinker and cannot incorporate into the film). The final MGv of 74, however, is still significantly larger than those observed for the control polymers before their displacement with **α MM**, further supporting the idea that **dyn-SCNP-MAN** forms a crosslinked polymer film around the microparticle.

The control polymers experience a significant decrease in MGv upon treatment with excess **α MM** (from ~ 46 to ~ 8.6), suggesting that most, but not all, of the polymers are displaced from the microparticle surfaces. This observation suggests the possibility of a small degree of non-specific binding between the polymers and microparticle surfaces, perhaps also involving the relatively hydrophobic dansyl residues appended to the polymer chains.

Specific Molecular Recognition Events are Required for 'Wrapping' to Occur

To confirm that specific molecular recognition events are required to drive the successful 'wrapping' of the microsphere, 5 μ m microparticles (**MP-LTB**) decorated with heat-labile toxin (LTB),¹⁶ a lectin that does not bind mannose, and a glycine-capped

microparticle (**MP-Gly**), which is absent in any carbohydrate receptors, were prepared (ESI). These microparticles were incubated with solutions of polymers and centrifuged to remove unbound polymers. Samples were then treated with **α MM** and reanalysed by fluorescence microscopy (images not shown) and MGVs calculated (Fig. 5f). There was no significant fluorescence observed around microparticles **MP-LTB** and **MP-Gly**, indicating that the polymers do not bind to microparticles unable to engage in complementary molecular recognition, thus confirming complementary molecular recognition between polymer and microparticles is required to drive 'wrapping'.

Conclusion

We have successfully demonstrated the molecular recognition-mediated 'wrapping' of lectin-functionalized silica microspheres that serve as low-cost and readily-available models for developing 'wrapping' chemistry. This goal was accomplished using polymers displaying mannose residues that drive their concentration upon the microparticle surfaces, and dynamic covalent crosslinkers able to undergo intra- to interpolymer interconversion to form a crosslinked polymer film. This structural rearrangement of the polymer chains, which occurs without the addition or subtraction of any molecular components, can be considered as an example of a 'structural metamorphosis'.¹⁷ Crucial to the successful outcome was the use of a **p(OEGA)**-based polymer 'wrapping agent' that eliminated non-specific interactions that can drive unwanted aggregation processes and also make 'wrapping' difficult to prove. As 'wrapping' only occurs in the presence of complementary recognition between the polymer 'wrapping agent' and the object, it may be possible to selectively 'wrap' target objects within mixtures.

This work is significant because it demonstrates that small objects can be 'wrapped' within crosslinked polymer films, thus suggesting that smaller and biologically-relevant objects such as VLPs and bacteria may also be successfully 'wrapped'. 'Wrapping' may stabilize these species, increase their shelf-lives and improve their performance, in much the same way that plastic wrappers and films do for everyday objects. Indeed, recent work^{2e} has shown the encapsulation of brome mosaic virus, a small icosahedral plant virus, within a layer of tannic acid crosslinked with Fe³⁺ ions was stabilized towards dehydrating conditions that would otherwise lead to virus disassembly, and suggests that 'wrapping' VLPs can indeed improve stability. We envisage that the molecular recognition-mediated approach described here will help address stability issues associated with nano- and micron-sized biological objects, and we are working towards applying this method to 'wrap' VLPs.

Conflicts of interest

There are no conflicts to declare.

Notes and references

- 1 (a) W. Knoll, R. C. Advincula, *Functional Polymer Films*, Wiley-VCH, Weinheim, 2011. (b) *Protective Coatings: Film Formation and Properties*, ed. M. Wen, K. Dušek, Springer International Publishing AG, Cham, Switzerland, 2017.
- 2 (a) B. V. Syomina and Y. V. Ilyinb, *Mol. Biol.*, 2019, **53**, 323. (b) D. Yan, Y. Wei, H. Guo, S. Sun, *Appl. Microbiol. Biotechnol.*, 2015, **99**, 10415. (c) G. Guillen, J. C. Aguilar, S. Duenas *et al.*, *Adv. Nat. Sci. Nanosci. Nanotechnol.*, 2013, **4**, 1. (d) M. G. Mateu, *Protein Eng. Des. Sel.*, 2011, **24**, 53. (e) L. Delalandea, I. B. Tsvetkovaa, C. Zenga, K. Bonda, M. F. Jarrolda and B. Dragnea, *Nanoscale*, 2016, **8**, 16221.
- 3 W. Youn, J. Y. Kim, J. Park, N. Kim, H. Choi, H. Cho and I. S. Choi, *Adv. Mater.*, 2020, 1907001.
- 4 H. Ai, M. Fang, S. A. Jones and Y. M. Lvov, *Biomacromolecules* 2002, **3**, 560-564.
- 5 (a) P. T. Corbett, J. Leclaire, L. Vial, K. R. West, J. Wietor, J. M. Sanders and S. Otto, *Chem. Rev.*, 2006, **106** 3652. (b) A. Wilson, G. Gasparini and S. Matile, *Chem. Soc. Rev.*, 2014, **43**, 1948. (c) P. Chakma and D. Konkolewicz, *Angew. Chem. Int. Ed.*, 2019, **58**, 9682.
- 6 (a) K. D. Hardman and C. F. Ainsworth, *Biochemistry*, 1972, **11**, 4910. (b) C. A. Stark and A. D. Sherry, *Biochem. Biophys. Commun.*, 1979, **87**, 598. (c) D. F. Seneart and D. C. Telle, *Biochemistry*, 1981, **20**, 3076.
- 7 (a) U. Neu, K. Woellner, G. Gauglitz and T. Stehle, *PNAS*, 2008, **105**, 5219. (b) G. E. Soto and S. J. Hultgren, *J. Bacteriol.*, 1999, **181**, 1059. (c) A. Imberty and A. Varrot, *Curr. Opin. Struct. Biol.*, 2008, **18**, 567.
- 8 (a) F. M. Veronese and G. Pasut, *Drug Discov. Today*, 2005, **10**, 1451. (b) K. Knop, R. Hoogenboom, D. Fischer, and U. S. Schubert, *Angew. Chem. Int. Ed.*, 2010, **49**, 6288. (c) J. Milton Harris and R. B. Chess, *Nat. Rev.*, 2003, **2**, 214.
- 9 (a) G. Molineu, *Pharmacotherapy*, 2003, **23**, 3S. (b) C. S. Fishburn, 2008, *J. Pharm. Sci.*, 97, 4167. (c) M. Swierczewska, K. C. Lee and S. Lee, *Expert Opin. Drug. Deliv.*, 2016, **13**, 531.
- 10 (a) G. Pasut and F. M. Veronese, *Drugs Today*, 2009, **45**, 687. (b) P. Mishra, B. Nayak and R. K. Dey, *Asian J. Pharm. Sci.*, 2016, **11**, 337.
- 11 B. S. Murray and D. A. Fulton, *Macromolecules* 2011, **44**, 7242-7252.
- 12 (a) D. E. Whitaker, C. S. Mahon and D. A. Fulton, *Angew. Chem. Int. Ed.*, 2013, **125**, 990. (b) C. S. Mahon, C. J. McGurk, S. M. D. Watson, M. A. Fascione, C. Sakonsinsiri, W. B. Turnbull and D. A. Fulton, *Angew. Chem. Int. Ed.*, 2017, **56**, 12913.
- 13 P. Frank, A. Prasher, B. Tuten, D. Chao and E. Berda, *Appl. Petrochemical Res.*, 2015, **5**, 9.
- 14 (a) C. K. Lyon, A. Prasher, A. M. Hanlon, B. T. Tuten, C. A. Tooley, P. G. Franka and E. B. Berda *Polym. Chem.*, 2015, **6**, 181. (b) T. Terashima, T. Mes, T. F. A. De Greef, M. A. J. Gillissen, P. Besenius, A. R. A. Palmans and E. W. Meijer, *J. Am. Chem. Soc.*, 2011, **133**, 4742. (c) I. Perez-Baena, F. Barroso-Bujans, U. Gasser, A. Arbe, A. J. Moreno, J. Colmenero, and J. A. Pomposo, *ACS Macro Lett.*, 2013, **2**, 775. (d) D. Chao, X. Jia, B. Tuten, C. Wangb and E. B. Berda, *Chem. Commun.*, 2013, **40**, 4178. (e) E. Huerta, P. J. M. Stals, E. W. Meijer and A. R. A. Palmans, *Angew. Chem. Int. Ed.*, 2013, **125**, 2978. (f) T. S. Fischer, D. Schulze-Sünninghausen, B. Luy, O. Altintas and C. Barner-Kowollik, *Angew. Chem. Int. Ed.*, 2016, **55**, 11276. (g) A. P. P. Kröger, N. Hamelmann, A. Juan, S. Lindhoud and J. M. J. Paulusse, *ACS Appl. Mater. Interfaces*, 2018, **10**, 37. (h) H. Rothfuss, N. D. Knöfel, P. W. Roesky and C. Barner-Kowollik, *J. Am. Chem. Soc.*, 2018, **140**, 5875. (i) Y. Liu, S. Pujals, P. J. M. Stals, T. Paulöhr, S. I. Presolski, E. W. Meijer, L. Albertazzi and A. R. A. Palmans, *J. Am. Chem. Soc.* 2018, **140**, 3423.
- 15 S. L. Mangold and M. J. Cloninger, *Org. Biomol. Chem.*, 2006, **4**, 2458.
- 16 (a) E. A. Merritt, T. K. Sixma, K. H. Kalk, B. A. M. van Zanten and W. G. J. Hol, *Mol. Microbiol.*, 1994, **13**, 745. (b) E. A. Merritt and W. G. J. Hol, *Curr. Opin. Struct. Biol.*, 1995, **5**, 165.
- 17 (a) L. Hobley, F. V. Rao, K. M. Bromley, M. Porter, A. R. Prescott, C. E. Macphee and D. M. F. Van Aalten, Interfacial self-assembly of a bacterial hydrophobin. *Proc. Natl. Acad. Sci. U.S.A.*, 2015, **112**, 5419. (b) R. K. Kumar, R. L. Harniman, A. J. Patil and S. Mann, Self-transformation and structural reconfiguration in coacervate-based protocells, *Chem. Sci.*, 2016, **7**, 5879. (c) H. Sun, C. P. Kabb, Y. Dai, M. R. Hill, I. Ghiviriga, A. P. Bapat and B. S. Sumerlin, *Nat. Chem.*, 2017, **9**, 817.